

AS
SL

ASTROPHYSICS AND
SPACE SCIENCE LIBRARY

SCIENTIFIC DETECTORS FOR ASTRONOMY

The Beginning of a New Era

PAOLA AMICO
JAMES W. BELETIC
JENNA E. BELETIC
Editors



KLUWER ACADEMIC PUBLISHERS

SCIENTIFIC DETECTORS FOR ASTRONOMY

ASTROPHYSICS AND SPACE SCIENCE LIBRARY

VOLUME 300

EDITORIAL BOARD

Chairman

W.B. BURTON, National Radio Astronomy Observatory, Charlottesville, Virginia, U.S.A.
(burton@starband.net); University of Leiden, The Netherlands (burton@strw.leidenuniv.nl)

Executive Committee

J. M. E. KUIJPERS, *Faculty of Science, Nijmegen, The Netherlands*
E. P. J. VAN DEN HEUVEL, *Astronomical Institute, University of Amsterdam,
The Netherlands*
H. VAN DER LAAN, *Astronomical Institute, University of Utrecht,
The Netherlands*

MEMBERS

I. APPENZELLER, *Landessternwarte Heidelberg-Königstuhl, Germany*
J. N. BAHCALL, *The Institute for Advanced Study, Princeton, U.S.A.*
F. BERTOLA, *Università di Padova, Italy*
J. P. CASSINELLI, *University of Wisconsin, Madison, U.S.A.*
C. J. CESARSKY, *Centre d'Etudes de Saclay, Gif-sur-Yvette Cedex, France*
O. ENGVOLD, *Institute of Theoretical Astrophysics, University of Oslo, Norway*
R. McCRAY, *University of Colorado, JILA, Boulder, U.S.A.*
P. G. MURDIN, *Institute of Astronomy, Cambridge, U.K.*
F. PACINI, *Istituto Astronomia Arcetri, Firenze, Italy*
V. RADHAKRISHNAN, *Raman Research Institute, Bangalore, India*
K. SATO, *School of Science, The University of Tokyo, Japan*
F. H. SHU, *University of California, Berkeley, U.S.A.*
B. V. SOMOV, *Astronomical Institute, Moscow State University, Russia*
R. A. SUNYAEV, *Space Research Institute, Moscow, Russia*
Y. TANAKA, *Institute of Space & Astronautical Science, Kanagawa, Japan*
S. TREMAINE, *CITA, Princeton University, U.S.A.*
N. O. WEISS, *University of Cambridge, U.K.*

SCIENTIFIC DETECTORS FOR ASTRONOMY

The Beginning of a New Era

Edited by

PAOLA AMICO

JAMES W. BELETIC

and

JENNA E. BELETIC

*California Association for Research in Astronomy (CARA),
W.M. Keck Observatory, Hawaii, U.S.A.*

KLUWER ACADEMIC PUBLISHERS

NEW YORK, BOSTON, DORDRECHT, LONDON, MOSCOW

eBook ISBN: 1-4020-2527-0
Print ISBN: 1-4020-1788-X

©2004 Springer Science + Business Media, Inc.

Print ©2004 Kluwer Academic Publishers
Dordrecht

All rights reserved

No part of this eBook may be reproduced or transmitted in any form or by any means, electronic, mechanical, recording, or otherwise, without written consent from the Publisher

Created in the United States of America

Visit Springer's eBookstore at:
and the Springer Global Website Online at:

<http://www.ebooks.kluweronline.com>
<http://www.springeronline.com>

TABLE OF CONTENTS

FOREWORD	xiii
LIST OF PARTICIPANTS	xvii
THE NERD GALLERY	xxi
MAPS AND MASTER PLAN	xxxiii

Ian S. Mclean

A Golden Era for Astronomy - The Advent of CCDs and Infrared Arrays	1
--	----------

SECTION I: DETECTOR MANUFACTURERS	9
--	----------

Ken J. Ando, Peter J. Love, Nancy A. Lum, David J. Gulbransen, Alan W. Hoffman, Elizabeth Corrales, Robert E. Mills, Mark E. Murray

Overview of Astronomy Arrays at Raytheon Infrared Operations (RIO)	11
---	-----------

Giovanni Bonanno, Massimiliano Belluso, Antonio Calì, Alessandro. Carbone, Rosario Cosentino, Angelo Modica, Salvo Scuderi, Cristina Timpanaro, Michela Uslenghi

A New Photon Counting Detector: Intensified CMOS-APS	21
---	-----------

Giovanni Bonanno, Rosario Cosentino, Massimiliano Belluso, Salvo Scuderi, Cinzia Di Franco, Pier Giorgio Fallica, Delfo Sanfilippo, Emilio Sciacca, Salvatore Lombardo

Preliminary test measurements of the SPAD array	29
--	-----------

Morley M. Blouke, Denis L. Heidtmann, J. Eriksen and Archibald Barter

Preliminary Characterization of Two High-Speed, Back-Illuminated CCD Image Sensors	33
---	-----------

Barry E. Burke, James A. Gregory, Andrew H. Loomis, Steven D. Calawa, Paul M. Nitishin, Thomas A. Lind, Michael J. Cooper, Douglas J. Young, Peter W. O'Brien, Bernard B. Kosicki, Gerald A. Luppino, and John L. Tonry

Broadband (200-1000 nm) Back-Illuminated CCD Imagers	41
---	-----------

Albert M. Fowler, K. Michael Merrill, William Ball, Arne Henden, Fred Vrba, Craig McCreigh

Orion: A 1-5 Micron Focal Plane for the 21st Century	51
--	-----------

James D. Garnett, Majid Zandian, Roger E. DeWames, Michael Carmody, John G. Pasko, Mark Farris, Craig A. Cabelli, Donald E. Cooper, G. Hildebrandt, J. Chow, John T. Montroy, Jose Arias, Jagmohan Bajaj, and Kadri Vural, and Donald N.B. Hall

Performance of 5 Micron, Molecular Beam Epitaxy HgCdTe Sensor Chip Assemblies (SCAs) for the NGST Mission and Ground-based Astronomy	59
---	-----------

<i>Don Groom</i>	
Cosmic rays and other nonsense in astronomical CCD images	81
<i>Steve Holland</i>	
An Overview of CCD Development at Lawrence Berkeley National Laboratory	95
<i>James Janesick, Ferry Gunawan, Taner Dosluoglu, John Tower, Niel McCaffrey</i>	
Scientific CMOS Pixels	103
<i>Paul R Jorden, Peter Pool, Simon M. Tulloch</i>	
Secrets of E2V Technologies CCDS (ex Marconi CCDs)	115
<i>Lester J. Kozlowski</i>	
Progress in Ultra-low Noise Hybrid and Monolithic FPAs for Visible and Infrared	123
<i>J. Rainer Kramm, Horst Uwe Keller, Reinhard Müller, Dietmar Germerott and Georg Tomasch</i>	
A Marconi CCD42-40 with Anti-Blooming - Experiences with the OSIRIS CCDs for the ROSETTA Mission	131
<i>Michael Lesser</i>	
Very Large Format Back Illuminated CCDs	137
<i>David Lumb, Alan Owens, Anthony Peacock, Marcos Bavdaz, Christian Erd</i>	
Compound Semiconductor Detectors, Development activities at ESA	145
<i>David Lumb, Peter Verhoeve, Roland den Hertog, Anthony Peacock, Didier Martin, Nicola Rando</i>	
Optical Photon-Counting STJ Activities at ESA	149
<i>Vyshnavi Suntharalingam, Barry E. Burke, and Michael J. Cooper</i>	
Silicon-on-Insulator-Based Single-Chip Image Sensors - Low-Voltage Scientific Imaging	155
<i>Paul Vu</i>	
Large Format and Scientific Detectors at Fairchild Imaging	163
<i>Augustyn Waczynski, Terry Beck, Ray Boucarut, Edward Cheng, Dave Cottingham, Gregory Delo, Dale Fixsen, Robert J. Hill, Scott Johnson, Peter Kenny, Wayne Landsman, Eliot Malumuth, Joel Offenber, Elizabeth Polidan, Anne Marie Russell, David Schlossberg, Elmer Sharp, Edward Wassell, Yiting Wen, John Yagelowich</i>	
HgCdTe Detectors for the Hubble space telescope wide field camera 3 IR Channel	175
<i>Guy F.W. Woodhouse, Nicholas R. Waltham, Marcus J. French, Mark L. Prydderch, Quentin R. Morrissey, Renato Turchetta, Andy J. Marshall, James M. King</i>	
CMOS Active Pixel Sensor developments at the Rutherford Appleton Laboratory	183

SECTION II: OBSERVATORY STATUS/PLANS	195
<i>Dietrich Baade</i>	
ESO's Optical detector systems in the VLT operations era	197
<i>James W. Beletic, Paola Amico, Randall Campbell and Robert Goodrich</i>	
The Detector Systems of the Keck Observatory - UV to 25 microns	205
<i>Gert Finger, Reinhold J. Dorn, Hamid Mehrgan, Manfred Meyer, Alan F.M. Moorwood, and Joerg Stegmeier</i>	
IR Detector Developments at ESO	219
<i>Jason Griesbach</i>	
Controller Developments – at the Anglo-Australian Observatory	225
<i>Derek Ives, Nagaraja Bezawada, Maureen Ellis</i>	
Detector Work at the UKATC - The optical to the sub-millimetre	231
<i>Ralf Kohley, Marcos Suárez, Juan Manuel Martín, Greg Burley, Lluís Cavaller and Rafael Vilela</i>	
CCD camera systems for the GTC	239
<i>Ricardo Schmidt</i>	
Detectors at CTIO: Present Status and Future Plans	247
<i>Roger Smith</i>	
Strange Happenings in the Dungeons - A new detector group at Caltech	255
<i>Barry Starr</i>	
NOAO Observatory plans	261
<i>Barry M. Starr, Nicholas Buchholz, Gustavo Rahmer, Jerry Penegor, Ricardo Schmidt, Michael Warner, K. Michael Merrill, Charles F. Claver, Y. Ho, Kaviraj Chopra, Eduardo Mondaca, Chirag Shroff, D. Shroff</i>	
MONSOON Image Acquisition System	269
SECTION III: INSTRUMENTATION	277
<i>Keith H. Burrell, Punit Gohil, Richard J. Groebner, David H. Kaplan, John I. Robinson, Daniel M. Thomas, and David G. Nilson</i>	
Improved CCD Detectors for High Speed, Charge Exchange Spectroscopy Studies on the D III-D Tokamak	279
<i>Cyril Cavadore, Claudio Cumani, Francis Franza and Enrico Marchetti</i>	
CCD wavefront sensing system for the ESO Multi-Conjugate Adaptive Optics Demonstrator (MAD)	283
<i>Jean-Charles Cuillandre</i>	
CFHT's SkyProbe: true atmospheric attenuation measurement in the telescope field	287
<i>Jean-Charles Cuillandre, James Beletic, Reinhold Dorn, James Beletic, Gerard Luppino, Sidik Isani, Nicolas Gorceix, Olivier Lai, Thomas Craven-Bartle, Barry Burke, François Ménard</i>	
CFHT's FlyEyes: assessing on-sky performance of the new MIT/LL CCID35 CCD curvature wavefront sensor	299

Sebastian Deiries, Olaf Iwert, Cyril Cavadore, Christof Geimer, Evi Hummel

Ultra-clean CCD Cryostats – CCD contamination can be kept under control	305
<i>M. Bonner Denton, Andrew K. Knight, Stephen C. Denson, Roger P. Sperline, Erick T. Young, James H. Barnes, Gary M. Heiftje, Mahadeva Sinha, Mark Wadsworth, David W. Koppenaal, Charles J. Barinaga, Christopher A. Gresham</i>	
The Impact of Astronomy Technologies on Chemical Analysis	311
<i>Reinhold J. Dorn, Barry E. Burke, James W. Beletic</i>	
A CCD based curvature wavefront sensor for adaptive optics in astronomy	319
<i>Philippe Feautrier, Reinhold J. Dorn, Gerard Rousset, Cyril Cavadore, Julien Charton, Claudio Cumani, Norbert Hubin, Pierre Kern, Jean-Louis Lizon, Pascal Puget, Didier Rabaud, Patrick Rabou, Eric Stadler, Thierry Fusco, Yves Magnard</i>	
Performance and results of the NAOS visible wavefront sensor	325
<i>Jean-Luc Gach, Olivier Hernandez, Jacques Boulesteix, Claude Carignan</i>	
Fabry Perot Observations using a new GaAs Photon Counting System	335
<i>Mario Gai, Leonardo Corcione, Giuseppe Massone</i>	
Near IR fringe tracking for VLTI: the FINITO detection system	341
<i>Enrique Joven, José V. Gigante and Francis Beigbeder</i>	
OSIRIS Detectors - First tests and Control System	345
<i>Fernando Pedichini and Roberto Speziali</i>	
The Optimized Cryostat for the LBC Camera	349
<i>Klaus Reif, Günter Klink, Phillip Müller and Henning Poschmann</i>	
The OmegaCam Shutter - A low acceleration, impact-free device for large CCD mosaics	367
<i>Martin Roth, Thomas Fechner, Dieter Wolter, Andreas Kelz, Thomas Beckner</i>	
Ultra-deep Optical Spectroscopy with PMAS – using the Nod-and-Shuffle Technique	371
<i>Roger Smith, David Walker and Hugo E. Schwarz</i>	
The Tololo All Sky Camera – TASCA	379
<i>John Tonry, Barry Burke, Gerald Luppino, Nicholas Kaiser</i>	
The Orthogonal Parallel Imaging Transfer Camera	385
<i>John Tonry, Gerald A Luppino, Nicholas Kaise¹, Barry Burke, George H. Jacoby</i>	
Giga-pixels and Sky Surveys	395
<i>Augustyn Waczynski, Terry Beck, Ray Boucarut, Edward Cheng, Dave Cottingham, Gregory Delo, Dale Fixsen, Robert J. Hill, Scott Johnson, Peter Kenny, Wayne Landsman, Eliot Mahumuth, Joel Offenberg, Elizabeth Polidan, Anne Marie Russell, David Schlossberg, Elmer Sharp, Edward Wassell, Yiting Wen, John Yagelowich</i>	
The Hubble Space Telescope Wide Field Camera 3 Instrument Charge- Coupled Device Detectors - CTE Performance and Mitigation	403
<i>Guy F.W. Woodhouse, Nicholas R. Waltham, James M. King, Gary R. Burton, Duncan L. Drummond, Andy J. Marshall, John A. Rainnie, Marcus J. French</i>	
Camera and detector development in the Space Science and Technology Department of the Rutherford Appleton Laboratory	407

Zhaowang Zhao and Binxun Ye
Compact CCD Camera

413

SECTION IV: ELECTRONICS

417

Paul D. Berry, Rene Doyon, Philippe Vallee, Daniel Nadeau

The design and testing of a cryogenic pre-amplifier for the Rockwell Hawaii and Hawaii II Detector Arrays

419

Giovanni Bonanno, Roario Cosentino, Massimiliano Belluso, Pietro Bruno, Fabio Bortoletto, Maurizio D'Alessandro, Daniela Fantinel, Enrico Giro, Leonardo Corcione, Alessandro Carbone, Gioacchino Evola

The new generation CCD controller: first results

423

Marco Bonati, Michael Ashe

ISPI's software- an infrared application of the ArcVIEW system.

427

Greg Burley, Ian Thompson, Charlie Hull

Compact CCD guider camera for Magellan

431

Gert Finger, Reinhold J. Dorn, Alan W. Hoffman, Hamid Mehrgan, Manfred Meyer, Alan F.M. Moorwood and Joerg Stegmeier

Readout techniques for drift and low frequency noise rejection in infrared arrays

435

Michael Lesser and Madhuvanesh Parthasarathy

AzCam: A Windows-based CCD/CMOS/Client/Server Data Acquisition System

445

Javier Reyes-Moreno, Christoph Geimer, Andrea Balestra, Nicolas Haddad

Upgrade of ESO's FIERA CCD Controller and PULPO subsystem

449

Martin Riopel, René Doyon, Daniel Nadeau and Christian Marois

An Optimized Data Acquisition System Without Reset Anomaly for the HAWAII and HAWAII-2 Arrays

453

Marcos Suárez, Ralf Kohley, Greg Burley, Lluís Cavaller, Rafael Vilela, Albert Tomás

GTC Acquisition Cameras and Wavefront Sensors

459

Mingzhi Wei and Richard Stover

A New CCD Controller at UCO/Lick Observatory

463

Guy F.W. Woodhouse, Nicholas R. Waltham, Marcus J. French, Lawrence L. Jones

The Use of ASIC Technology in the Development of Compact, Low-Power CCD Cameras

467

SECTION V: DETECTOR TESTING AND CHARACTERIZATION

479

Randall D. Campbell

Characterization of the Si:As Blocked Impurity Band (BIB) Detector in Keck's Long Wavelength Spectrometer, LWS

481

Fabrice Christen, Cyril Cavadore, Dietrich Baade, Olaf Iwert, Konrad Kuijken, Boris Gaillard, Stéphane Darbon

Characterizing the CCDs of the OmegaCam wide-angle camera 485

Jose J. Díaz, Fernando Gago, Francis Beigbeder, Francisco Garzón, Jesús Patrón

EMIR Hawaii-2 Detector test bench 489

Jose J. Díaz, Fernando Gago, Francis Beigbeder, Francisco Garzón, Jesús Patrón

EMIR Hawaii-2 first test results 493

Gert Finger, Reinhold J. Dorn, Hamid Mehrgan, Manfred Meyer, Alan F.M. Moorwood, and Joerg Stegmeier

Test results with 2Kx2K MCT arrays 497

Klaus W. Hodapp, Robert Thornton, Jeff Kuhn, Everett Irwin, Hubert Yamada, Mark Waterson

The HAWAII-2 2048x2048 HgCdTe Detector Arrays 501

Binxun Ye and Qian Song

How Accurate Are QE Measurements? 511

SECTION VI: FOCAL PLANE MOSAICS	515
--	------------

Jean de Kat, Olivier Boulade, Xavier Charlot, P. Abbon, Stéphan Aune, Pierre Borgeaud, Pierre-Henri Carton, Dominique Eppel , Pascal Gallais, Remy Granelli, Michel Gros, Jean Y. Rouss , Pierre Starzynski, Laurent Vigroux

The Electronic Controller of the 40 CCDs Megacam Mosaic 517

Reinhold J. Dorn, Gert Finger, Gotthard Huster, Jean Louis Lizon, Hamid Mehrgan, Manfred Meyer, Joerg Stegmeier and Alan F.M. Moorwood

Design of the CRIRES 512 x 4096 pixel Aladdin InSb focal plane array detector mosaic 523

Takashi Ichikawa, Yuka Katsuno, Ryuji Suzuki, Chihiro Tokoku and Tetsuo Nishimura

Performance of HAWAII-2 FPA for SUBARU Multi-Object Near-Infrared Camera and Spectrograph 529

Derek Ives, Ken Laidlaw and Naidu N. Bezawada.

Wide Field Focal Plane Arrays for UKIRT and VISTA 535

Michael Lesser, David Oulette

Fully Buttable Imagers 539

David Mason, Scott Horner, Earl Aamodt

Mosaic Focal Plane Development 547

SECTION VII: SPACE MISSIONS	553
------------------------------------	------------

Mark Clampin, Marco Sirianni, George F. Hartig, Holland C. Ford, Garth D. Illingworth, Mr. Bill Burmester, William Koldewynd, Andre R. Martel, Adam Riess, Ronald J. Schrein, and Pamela C. Sullivan

In flight Performance of the Advanced Camera for Surveys Detectors 555

<i>Mario Gai, Deborah Busonero</i>	
On the Implementation and Calibrations of the Focal Plane for GAIA	565
<i>Yann Hello, Jérôme Parisot, Sébastien Barde, Tristan Buey, Bertrand Le Ruyet, Alain Sémary, Didier Tiphène</i>	
Behaviour of a Raytheon IRFPA (438x270) under high energy protons	573
<i>David Lumb</i>	
Radiation damage effects in XMM-Newton Epic MOS CCDs	577
<i>Robert Philbrick, John Geary, Edward Dunham, David Koch</i>	
95 Million Pixel Focal Plane for Use On The Kepler Discovery Mission	581
<hr/>	
SECTION VIII: SUB-ELECTRON NOISE FOCAL PLANE ARRAYS	591
<hr/>	
<i>Alastair Basden, Craig Mackay, Chris Haniff</i>	
L3CCDs: Fast Photon Counting for Optical Interferometry - Statistics of Photon Counting	593
<i>Alastair Basden, Craig Mackay, Bob Tubbs</i>	
L3CCDs: Low Readout Noise CCDs in Astronomy – Lucky Exposure Technique	599
<i>Jean-Luc Gach, David Darson, Christian Guillaume, Michel Goillandeau, Olivier Boissin, Jacques Boulesteix, Cyril Cavadore</i>	
Zero noise CCD - a new readout technique	603
<i>Jean-Luc Gach Christian Guillaume, Cyril Cavadore, Olivier Boissin</i>	
First results of an L3CCD in photon counting mode	611
<hr/>	
GLOSSARY OF ACRONYMS	615
THE NERD BOAT	625

FOREWORD

Dear Friends,

It seems like it was only yesterday that we drove the last of you to the airport. The memories and the spirit of the Scientific Detectors for Astronomy Workshop (SDW2002) remain fresh and strong. For us, this was a very special event, a great gathering of what may be one of the friendliest and most cooperative technical communities on our little planet.

We have tried to capture the spirit of the Workshop in these Proceedings and we hope you are able to relive your week in Hawaii. For those readers who did not attend, we invite you into this community.

As you probably noticed, there is a new name on the cover: Jenna Beletic was the ace up our sleeve for these Proceedings. As a summer intern at Keck, she took up the task of organizing, proofreading, editing and formatting the papers. She also made the graphics (her artistic talents shine on pages xxxiii and xxxv), contacted authors and prepared the mountain of paperwork which goes with producing a book. Jenna's enthusiasm at learning, her passion for the job and creativity (e.g. find 100 ways to get Paola and Jim to do their jobs) have been a motivating addition to our team of "old workshop foxes"..... and a source for a good deal of paternal pride. We are honoured to have her as a fellow editor.

The success of this workshop was achieved with the help of many people, who, as their only reward, were promised our gratitude and a nebulously defined "eternal glory." In order to keep our promise, here are our public thanks. We want to start recognizing the efforts of those in Hawaii who made the workshop happen. Special thanks go to our *factotums*: Gale Kihoi at Keck, who helped us organize the logistics and worked tirelessly during the workshop's week to make sure everything ran smoothly; Lali Acdal at the Hawaii Preparatory Academy (HPA), who helped us provide facilities, food and lodging for the 155 participants and guests.

Many thanks to: Laurie Ainslie and her staff at HPA for the excellent hosting services; Kim Sweeney, the inspired artist who made the wonderful cartoons for the nerds' gallery; Elise Beletic, Adam and Veronica "Molokai" Contos who stayed up late to help us prepare the workshop giveaways; they and the other Beletic Girls also listened patiently to our "crazy ideas", as early as one year before the event. Their support and encouragements have kept us going. We thank Doug Arnott and his drivers who helped organizing the first-ever summit visit for 120 people, and the staff at the CFH, Keck, Gemini and Subaru telescopes who offered their services as chaperons during the visit; Alan Hara who organized our lunch at

Hale Pohaku; Dick Bredthauer, Jean-Charles Cuillandre and Sidik Isani for their entertaining shows on Monday night; Jean Charles Cuillandre for volunteering as the photographer for the nerds' gallery (see page xxi); the line dancers, Chris Hunt and his Band and the "paniolas" of Parker Ranch for showing us how Hawaiian cowboys can party; our friends of the Keauhou Canoe Club, for opening the premises of the club and organizing a wonderful "Barbie at the Beach" event ; Mrs. La Roma Tomasada who put together a wonderful Gala dinner at the Mauna Kea Beach Resort; Sharon Shutes who helped us organize transportations and Jenda Johnson, the geologist who accompanied us during the visit of the Volcano National Park. Many thanks to Pat Goude, who helped edit these Proceedings.

Our gratitude goes to Ian McLean, our invited speaker, who opened the workshop with an interesting and fun talk (see page 1). Many thanks to all of you who, in spite of being workshop guests, helped us whenever it was needed: among many, we wish to thank Dave Mason and Martin Roth, our "good Samaritans." A very special "grazie" goes to Fernando Pedichini, who, like all true friends, is always available when help and support are needed. Many thanks to our colleagues Randy Campbell and Bob Goodrich, who helped us with the final preparation and refereeing of the Proceedings. Many thanks to the photographers who sent us their photos and in particular to Cyril Cavadore and Peter Sinclaire who took the pictures of the rainbow (on the first day of the workshop) and of the "moonbow" (on the last day) shown on the cover.

Our gratitude (eternal, of course) goes to some other key-players that made the SDW2002 different from the previous Workshops. For the first time we had a Scientific Organizing Committee: Barry Starr (NOAO), Bob Goodrich (Keck Observatory), Bruce Atwood (OSU), Cyril Cavadore (ESO), Derek Ives (ROE), Doug Simons (Gemini Observatory), Gerry Luppino (IfA), Gert Finger (ESO), Ian McLean (UCLA), Jean-Charles Cuillandre (CFHT), John Geary (CfA), Klaus Hodapp (IfA), Lothar Strueder (MP Semiconductor Lab), Mark Clampin (STScI), Randy Campbell (Keck Observatory), Richard Stover (UCSC), Roger Smith (Caltech) and Tetsuo Nishimura (Subaru Telescope).

Also, for the first time we had sponsors, whose financial contribution made the workshop possible and the cost to participants the best deal west of Fiji (\$850 for 6 nights, inclusive lodging, meals, excursions, conference fee, proceedings and the goodies): Greg Fahlman on behalf of CFH, Doug Simons on behalf of Gemini and Tetsuo Nishimura on behalf of Subaru.

Finally, we want to thank all of the participants and their guests, for their contributions, and their active participation in all events (for a list see page xvii). We thank you for your sense of humour and good sportsmanship. Beside the fun and camaraderie we shared, this was an excellent technical meeting and this book is proof of the quality and energy of our community.

We are looking forward to seeing you all and many more at the next workshop, SDW2005.

Paola & Jim



**Lords of the Chips, Fellowship of the Nerds,
we wish you all low noise and high QE!**



Jenna Beletic, moments after reaching “Nerdvana”

PS: Read the Proceedings thoroughly; if you find something “strange” in one of the title/abstract sections, send an email. The first one wins a price!

LIST OF PARTICIPANTS

Amico, Paola	W.M. Keck Observatory, USA	pamico@keck.hawaii.edu
Ando, Ken	Raytheon Infrared Operations, USA	kjando@west.raytheon.com
Aspin, Colin	Gemini Observatory, USA	caa@gemini.edu
Atwood, Bruce	Ohio State University, USA	atwood@ohstpy.mps.ohio-state.edu
Baade, Dietrich	European Southern Observatory, Germany	dbaade@eso.org
Barriga, Pablo	European Southern Observatory, Chile	pbarriga@eso.org
Basden, Alastair	Cambridge University, UK	a.g.basden.97@cantab.net
Beletic, James	W.M. Keck Observatory, USA	jbeletic@keck.hawaii.edu
Berry, Paul	Laboratoire d'Astrophysique Experimental, Canada	berry@astro.umontreal.ca
Bezawada, Nagaraja	UK Astronomy Technology Centre, UK	nmb@roe.ac.uk
Blouke, Morley	Scientific Imaging Technologies, Inc., USA	Morleyb@site-inc.com
Bonanno, Giovanni	Istituto Nazionale di AstroFisica, Italy	gbo@ct.astro.it
Bonati, Marco	Caltech, USA	mbonati@astro.caltech.edu
Bredthauer, Richard	Semiconductor Technology Associates, USA	r.bredthauer@sta-inc.net
Bristow, Paul	European Southern Observatory, Germany	bristowp@eso.org
Burke, Barry	MIT Lincoln Laboratory, USA	bburke@ll.mit.edu
Burley, Greg	OCIW, USA	burley@ociw.edu
Burrell, Keith	General Atomics, USA	Keith.Burrell@gat.com
Campbell, Randy	W.M. Keck Observatory, USA	randyc@keck.hawaii.edu
Carter, David	South African Astronomical Observatory, South Africa	dbc@sao.ac.za
Cavadore, Cyril	European Southern Observatory, Germany, now at Thales Group	cyril.cavadore@fr.thalesgroup.com
Chin, Jason	W.M. Keck Observatory, USA	jchin@keck.hawaii.edu
Christen, Fabrice	Kapteyn Instituut / ESO, Germany	fchrste@eso.org
Clampin, Mark	STScI, USA	clampin@stsci.edu
Clark, Paul	University of Durham, UK	paul.clark@durham.ac.uk
Conrad, Al	W.M. Keck Observatory, USA	aconrad@keck.hawaii.edu
Cook, Kem	Lawrence Livermore National Laboratory, USA	kcook@llnl.gov
Cuillandre, Jean-Charles	Canada-France-Hawaii Telescope, USA	jcc@cft.hawaii.edu
de Kat, Jean	Commissariat a l'Energie Atomique, France	jean.dekat@free.fr

Deiries, Sebastian	European Southern Observatory, Germany	sdeiries@eso.org
Denton, M. Bonner	University of Arizona, USA	mbdenton@u.arizona.edu
Diaz, José	Instituto de Astrofísica de Canarias, Spain	jdg@ll.iac.es
Dorn, Reinhold	European Southern Observatory, Germany	reinhold.dorn@eso.org
Downing, Mark	Australian National University, Australia	mark@mso.anu.edu.au
Ellerboek, Brent	Gemini Observatory, USA	bellerbroek@gemini.edu
Ellis, Maureen	UK Astronomy Technology Centre, UK	mae@roe.ac.uk
Feautrier, Philippe	Grenoble Observatory, France	Philippe.Feautrier@obs.ujf- grenoble.fr
Finger, Gert	European Southern Observatory, Germany	gfinger@eso.org
Fochi, Peter	Marconi Applies Technologies, USA	peter.fochi@marconi.com
Fowler, Albert	NOAO, USA	fowler@noao.edu
Gach, Jean-Luc	Mairselle Observatory, France	gach@observatoire.cnrs-mrs.fr
Gago Rodriguez, Fernando	Instituto de Astrofísica de Canarias, Spain	fgago@ll.iac.es
Gai, Mario	Turin Observatory, Italy	gai@to.astro.it
Garcia Yus	Gemini Observatory, Chile	ygarcia@gemini.edu
Garnett, James	Rockwell Scientific Company, USA	ygarnett@rwsc.com
Geary, John	S.A.O., USA	geary@cfa.harvard.edu
Gigante, José	Instituto de Astrofísica de Canarias, Spain	gigante@ll.iac.es
Gilmore, David	University of California at Santa Cruz, USA	gilmore@ucolick.org
Goodrich, Robert	W.M. Keck Observatory, USA	rgoodrich@keck.hawaii.edu
Griesbach, Jason	Anglo-Australian Observatory, Australia	jsg@aaoepp.aao.gov.au
Groom, Donald	Lawrence Berkeley National Laboratory, USA	DEGroom@lbl.gov
Guillaume, Christian	OHP/Marseille/CNRS, France	guillaume@obs-hp.fr
Haddad, Nicolas	European Southern Observatory, Chile	nhaddad@eso.org
Hall, Donald	University of Hawaii, USA	hall@ifa.hawaii.edu
Hanna, Kevin	University of Florida, USA	hanna@astro.ufl.edu
Hardy, Tim	National Research Council Canada, Canada	Tim.Hardy@nrc.ca
Harris, Frederick	U.S. Naval Observatory, USA	fhh@nofs.navy.mil
Hello, Yann	CNRS, France	yann.hello@obspm.fr
Hodapp, Klaus	Institute for Astronomy, UH, USA	hodapp@ifa.hawaii.edu
Holland, Steve	Lawrence Berkeley National Laboratory, USA	seholland@lbl.gov

Honey, Allan	W. M. Keck Observatory, USA	ahoney@keck.hawaii.edu
Ichikawa, Takashi	Tohoku University, Japan	ichikawa@astr.tohoku.ac.jp
Isani, Sidik	Canada-France-Hawaii Telescope, USA	isani@cfht.hawaii.edu
Ives, Derek	UK Astronomy Technology Centre, UK	dji@roe.ac.uk
Janesick, James	Sarnoff Corporation, USA	CMOSCCD@aol.com
Jorden, Paul	Marconi Applied Technologies, UK	paul.jorden@marconi.com
Joven, Enrique	Instituto de Astrofisica de Canarias, Spain	eja@ll.iac.es
Keller, Horst Uwe	Max-Planck-Institut für Astronomie, Germany	keller@linmpi.mpg.de
Klougart, Jens	Copenhagen University Observatory, Denmark	klougart@astro.ku.dk
Kohley, Ralf	Grantecan, Spain	rkohley@ll.iac.es
Kozlowski, Lester	Rockwell Scientific Company, USA	lkozlowski@rwsc.com
Kramm, Rainer	Max-Planck-Institut für Astronomie, Germany	kramm@linmpi.mpg.de
Kwiatkowski, Kris	LANL, USA	krisk@lanl.gov
Lazo, Manuel	Gemini Observatory, USA	mlazo@gemini.edu
Lesser, Michael	University of Arizona, USA	mlesser@as.arizona.edu
Love, Peter	Raytheon Infrared Operations, USA	pjlove@west.raytheon.com
Lumb, David	European Space Agency, Netherlands	dlumb@rssd.esa.int
Luppino, Gerry	University of Hawaii, USA	ger@ifa.hawaii.edu
Martin Fleitas	Grantecan, Spain	jmartin@ll.iac.es
Mason, David	Lockheed Martin, USA	dave.mason@lmco.com
McArthur, Scot	Ball Aerospace & Technologies Corp., USA	smcarthu@ball.com
McLean, Ian	UCLA, USA	mclean@astro.ucla.edu
McLeod, Brian	Smithsonian Observatory, USA	bmcleod@cfa.harvard.edu
Miyazaki, Satoshi	Subaru Telescope, Japan	satoshi@anela.mtk.nao.ac.jp
Montroy, John	Rockwell Scientific Company, USA	jmontroy@rwsc.com
Müller, Philipp	University of Bonn, Germany	philipp@astro.uni-bonn.de
Murowinski, Richard	National Research Council Canada, Canada	Richard.Murowinski@nrc.ca
Nakaya, Hidehiko	Subaru Telescope, USA	nakaya@naoj.org
Nishimura, Tetsuo	Subaru Telescope, USA	nishimura@subaru.naoj.org
Nolan, Robert	Gemini Observatory, USA	rnolan@gemini.edu
Norregaard, Preben	Copenhagen University Observatory, Denmark	preben@astro.ku.dk
Onaka, Peter	Institute for Astronomy, UH, USA	onaka@ifa.hawaii.edu
Parisot, Jerome	Paris Observatory, France	jerome.parisot@obspm.fr
Pedichini, Fernando	Rome Observatory, Italy	pedik@mporzio.astro.it

Philbrick, Robert	Ball Aerospace & Technologies Corp., USA	rphilbri@ball.com
Philip, A.G. Davis	ISO and Union College, USA	AGDP@union.edu
Pool, Peter	Marconi Applied Technologies, UK	peter.pool@marconi.com
Rahmer, Gustavo	NOAO/CTIO, USA	grahmer@ctio.noao.edu
Reif, Klaus	University of Bonn, Germany	reif@astro.uni-bonn.de
Reiss, Roland	European Southern Observatory, Germany	rreiss@eso.org
Reyes Moreno, Javier	European Southern Observatory, Germany	jreyes@eso.org
Riopel, Martin	University of Montreal (LAE), Canada	mriopel@sympatico.ca
Roth, Martin	Astrophysical Institute Potsdam, Germany	mmroth@aip.de
Salmon, Derrick	Canada-France-Hawaii Telescope, USA	salmon@cfht.hawaii.edu
Schmidt, Ricardo E.	NOAO/CTIO, USA	rschmidt@noao.edu
Simons, Doug	Gemini Observatory, USA	dsimons@gemini.edu
Sinclair, Peter	European Southern Observatory, Chile	psinclair@eso.org
Smith, Roger	Caltech, USA	rsmith@astro.caltech.edu
Starr, Barry	NOAO, USA	Barry_M_Starr@raytheon.com
Stover, Richard	University of California, Santa Cruz, USA	richard@ucolick.org
Suarez Valles, Marcos	Grantecan, Spain	msuarez@ll.iac.es
Suntharalingam, Vyshnavi	MIT Lincoln Laboratory, USA	vyshi@ll.mit.edu
Tonry, John	University of Hawaii, USA	jt@ifa.hawaii.edu
Torborg, Scott D.	W.M. Keck Obsevatory, USA	storborg@keck.hawaii.edu
Vu, Paul	Fairchild Imaging, USA	paul.vu@fcimg.com
Vural, Paul	Rockwell Scientific Company, USA	kvural@rwsc.com
Waczynski, Augustyn	GSFC/GST, USA	aw@tophat.gsfc.nasa.gov
Walther, Dolores M.	Gemini Observatory, USA	dwalther@gemini.edu
Ward, Jeff T.	Canada-France-Hawaii Telescope, USA	ward@cfht.hawaii.edu
Wei, Mingzhi	University of California Santa Cruz, USA	wmz@ucolick.org
Wilcox, Mavournee K.	Institute for Astronomy, UH, USA	mkwilcox@ifa.hawaii.edu
Woodhouse, Guy	Rutherford Appleton Laboratory, UK	g.f.w.woodhouse@rl.ac.uk
Yamashita, Takuya	Subaru Telescope, USA	takuya@naoj.org
Ye, Binxun	National Astronomical Observatory, China	bxye@bao.ac.cn , bxye@public.bta.net.cn
Zhao, Zhaowang	National Astronomical Observatory, China	sky.ccd@bao.ac.cn

The Lords of the Chips The Fellowship of the Nerds

The Nerd Gallery

Abiding by the Lords of the Chips theme, each participant assumed the identity of one of three Tolkien characters, Orcs, Ents or Wizards, for the portrait gallery. Initially, most of the participants enrolled as wizards, but we set up a trial to reveal their true nature...



The SDW2002 picture stand.

The roll of a die unmasked their allegiances: only true wizards can roll a six, a roll of 4 or 5 is the undoing of an ent, 3, 2 and 1 the signature of an orc. The photos on the following pages present our esteemed colleagues in their true form...

Orcs

Servants of the Dark Current

The Orcs were first bred by the dark PMT of the north in the Elder Days. These creatures, being filled with angst of the unknown, quickly developed many barbarous dialects. They speak in acronyms and are often unintelligible even to their own kind (see Glossary of Acronyms pg. 615). In appearance Orcs are squat, swarthy creatures. Most of them prefer darkness and are blinded by the sun (not to be confused with astronomers).



Dietrich Baade



Pablo Barriga



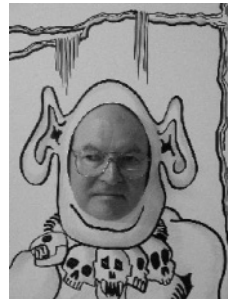
Alastair Basden



James Beletic



Paul Berry



Morley Blouke



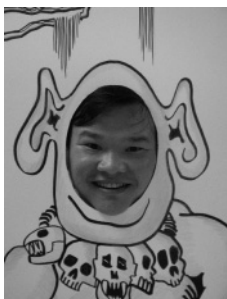
Richard Bredthauer



Paul Bristow



David Carter



Jason Chin



Fabrice Christen



Paul Clark



Jean de Kat



Jose Diaz



Maureen Ellis



Jean-Luc Gach



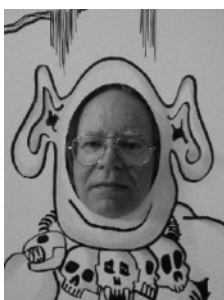
Mario Gai



Jorge Garcia-Yus



James Garnett



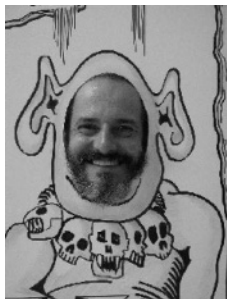
John Geary



Nicholas Haddad



Yann Hello



Klaus Hodapp



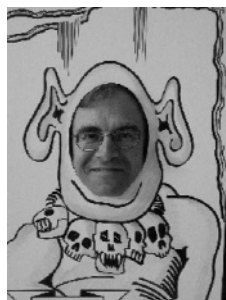
Derek Ives



Enrique Joven



Ralf Kohley



Lester Kozlowski



Rainer Kramm



Gerry Luppino



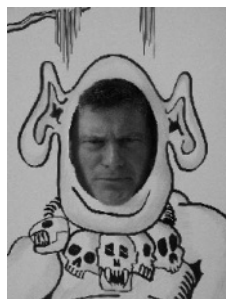
Phillip Mueller



Richard Murowinski



Tetsuo Nishimura



Preben Norregard



Peter Onaka



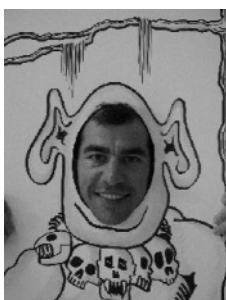
Peter Pool



Klaus Reif



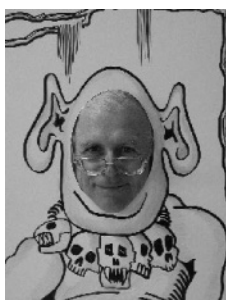
Roland Reiss



Javier Reyes-Moreno



Martin Riopel



Derrick Salmon



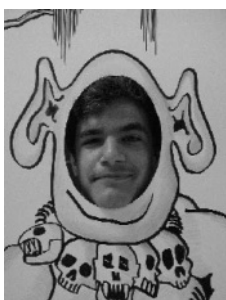
Barry Starr



Richard Stover



Vyshnavi Suntharalingam



Scott Torborg



Zhao Zhaowang

Ents

Shepherds of the Electrons

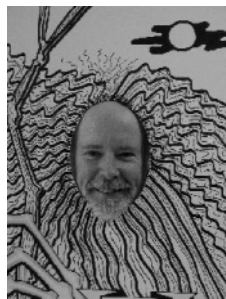
The Ents are a race of giant, tree-like people. Their purpose is to protect the electrons, although some align themselves with holes. However, as the great arrays have grown, the number of Ents has dwindled. Now they are said only to be found in the darkest and most mysterious of laboratories.



Paola Amico



Ken Ando



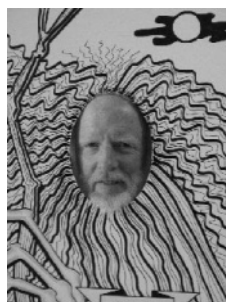
Bruce Atwood



Giovanni Bonanno



Greg Burley



Keith Burrell



Cyril Cavadore



Jean-Charles Cuillandre



Sebastian Deiries



Bonner Denton



Reinhold Dorn



Philippe Feautrier



Gert Finger



*Fernando Gago-
Rodriguez*



Jose Gigante



David Gilmore



Robert Goodrich



Kevin Hanna



Fred Harris



Steve Holland



Takashi Ichikawa



Sidik Isani



Paul Jorden



Jens Klougart



Michael Lesser



David Lumb



David Mason



Ian McLean



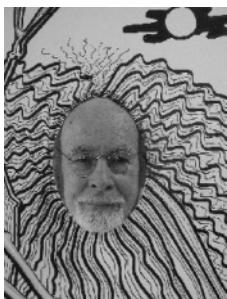
Brian McLeod



Jerome Parisot



Robert Philbrick



A.G. Davis Philip



Martin Roth



Ricardo Schmidt



Roger Smith



John Tonry



Jeff Ward



Mavourneen Wilcox

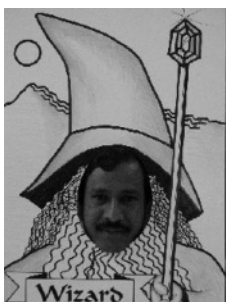


Guy Woodhouse

Wizards

The Vanguard of Low Noise

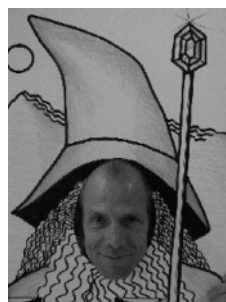
Wizards are supremely powerful and can use that power for good or for evil, depending on where their hearts lie. They first appeared in the 1970's to aid the silicon against the PMT. They have since diversified and some live on a diet of Mercury, Cadmium and Telluride. They lead the search for the Holy Grail: sub-electron noise.



Nagaraja Bezawada



Barry Burke



Randy Campbell



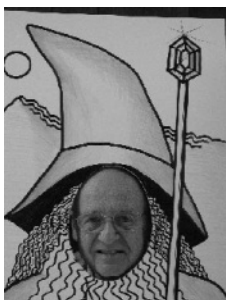
Peter Fochi



Albert Fowler



Jason Griesbach



Donald Groom



Christian Guillaume



Tim Hardy



Horst-Uwe Keller



Kris Kwiatkowski



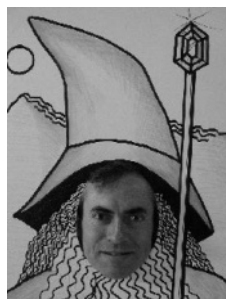
Peter Love



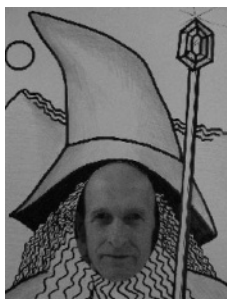
Fernando Pedichini



Gustavo Rahmer



Peter Sinclair



Augustyn Waczynski



Mingzhi Wei

'Ringwraiths'

Black Riders of the AR coating

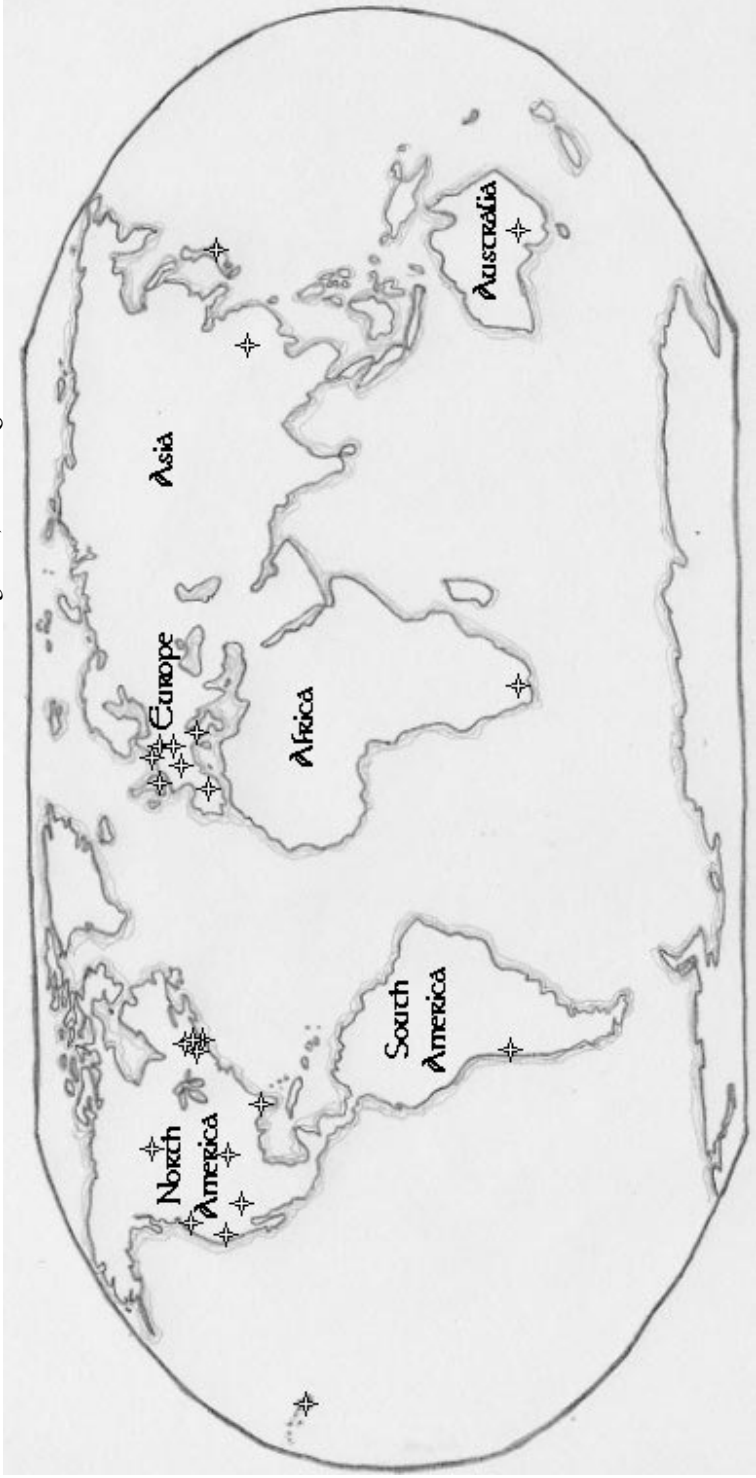
These are the Ones seduced by the power of nothingness. Preferring to dress in many coats, although some only wear in a single 50 nm layer, they are doomed to sleepless nights hunting for a better match between air and crystal structure. They cannot be pictured because no light reflects from their faces.

<i>Marco Bonati</i>	<i>Mark Clampin</i>	<i>Al Conrad</i>	<i>Kem Cook</i>
<i>Mark Downing</i>	<i>Brent Ellerbroek</i>	<i>Donald Hall</i>	<i>Allan Honey</i>
<i>James Janesick</i>	<i>Manuel Lazo</i>	<i>Juan Manuel</i> <i>Martin Fleitas</i>	<i>Scot</i> <i>McArthur</i>
<i>Satoshi Miyazaki</i>	<i>John Montroy</i>	<i>Hidehiko Nakaya</i>	<i>Robert Nolan</i>
<i>Doug Simons</i>	<i>Marcos Suarez</i> <i>Valles</i>	<i>Paul Vu</i>	<i>Kadri Vural</i>
<i>Dolores Walther</i>	<i>Takuya Yamashita</i>	<i>Binxun Ye</i>	

World Cap

The Origins of the Nerds

(6 continents, 14 countries, 26 observatories, every major designer/manufacturer)



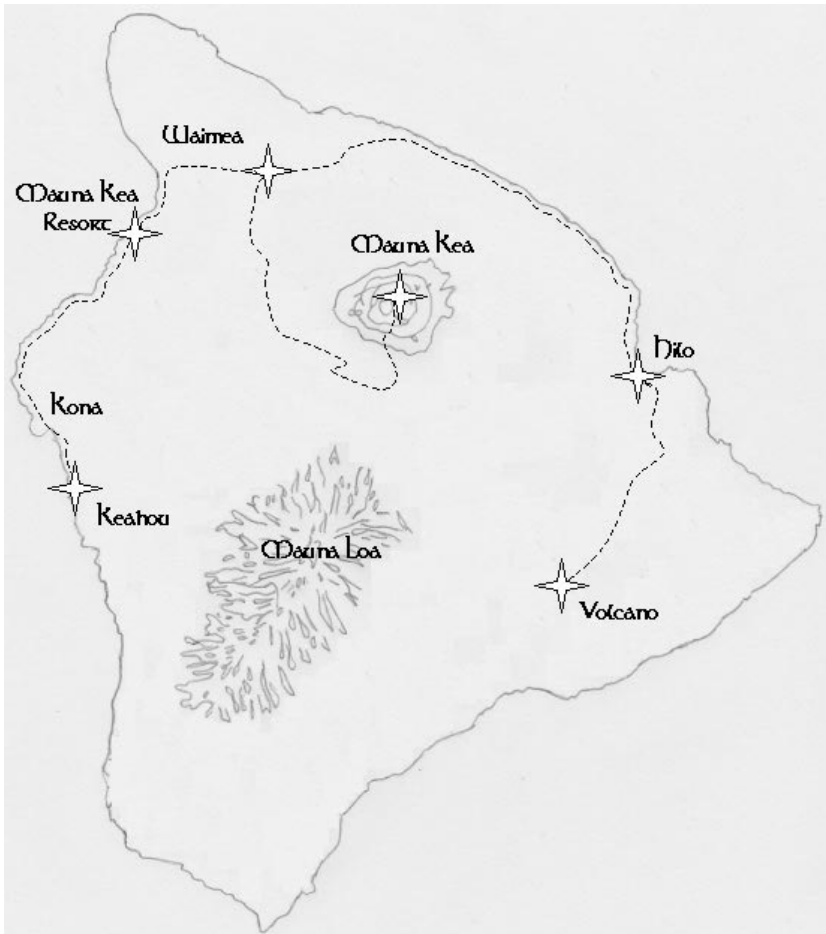
SDW2002 MASTER PLAN

The following is an overview of the events of the workshop. Hopefully this will refresh memories of SDW2002 and all the “work” that was accomplished there.

<p>Day 1, SUN, June 16</p> <p>Check in. Sports at HPA campus. Registration reception at HPA campus.</p>	<p>Day 2, MON, June 17</p> <p>Talks: Detector Manufacturers. Roundtable: <i>Shoot the Manufacturers</i> Roundtable: <i>Detector technologies</i> Public talks: Richard Bredthauer and Jean-Charles Cuillandre.</p>
<p>Day 3, TUE, June 18</p> <p>Talks: Observatory Status/Plans Departure to summit. Lunch at Hale Pohaku Summit visit: CFH Telescope, Keck Subaru and Gemini Observatories. Movie night at HPA – “The Dish”.</p>	<p>Day 4, WED, June 19</p> <p>Talks: Instrumentation Sports afternoon at HPA campus. “Paniolo” night</p>
<p>Day 4, THU, June 20</p> <p>Talks: Electronics Roundtable: <i>Detector Electronics</i>. Talks: Detector Testing and Characterization. Roundtable: <i>Detector Characterization</i>. Snorkelling at Kealakekua Bay and outrigger canoeing. Barbecue at Keauhou Canoe Club with Volleyball and Hula lessons</p>	<p>Day 5, FRI, June 21</p> <p>Talks: Focal Plane Mosaics Talks: Space Missions and Sub-electron Noise Focal Plane Arrays Roundtable: <i>Sub-electron Noise FPAs</i>. Gala dinner and Hula show at the Mauna Kea Resort.</p>
<p>Day 6, SAT, June 22</p> <p>Check out. Optional Visit to the Volcanoes National Park. Dinner at Café Pesto.</p>	

Big Island Map

SOW2002 Master Plan



Waimea: Conference Venue, Registration Reception, Talks, Sports, Movie Night, “Paniolo” Night
Mauna Kea: Summit Visit
Keahou: Snorkeling and “Barbie at the Beach”
Mauna Kea Resort: Gala Dinner, Hula Show
Volcano: Volcanoes National Park Visit
Hilo: Café Pesto

A GOLDEN ERA FOR ASTRONOMY: THE ADVENT OF CCDS AND INFRARED ARRAYS

Ian S. McLean

University of California, Los Angeles

Abstract: *The advent of solid-state imaging devices transformed astronomy. Beginning with the introduction into astronomy of charge-coupled devices in 1976, followed a decade later by infrared arrays, astronomers gained access to near-perfect imaging devices. The consequences have been nothing short of revolutionary, perhaps especially so in the infrared. Witness, for example, the spectacular pictures from the Hubble Space Telescope cameras, or the impressive infrared imagery from the 2MASS project. Within the last decade CCD formats deployed or planned for use in ground-based cameras have become huge. Infrared mosaics, stimulated by the Next Generation Space Telescope, are coming soon. In addition, new technologies such as CMOS (Complementary Metal Oxide Semiconductors) and STJs (Superconducting Tunnel Junctions) are being developed and the future of astronomical detectors looks very exciting, especially in an era of giant telescopes performing at their diffraction-limit.*

Key words: *Charge-Coupled Devices (CCDs), Infrared Arrays*

1. INTRODUCTION

It is an honor and a privilege to say a few words at the beginning of this exciting and timely meeting. As I looked over the program for the meeting I could not help but think of the many remarkable advances in detectors that have been made over the last 30 years since I entered astronomy.

I was between my sophomore and junior years at the University of Glasgow, Scotland in 1969 when men from the planet Earth first stood upon the surface of the Moon. It was a fantastic time, and there was a feeling that astronomy and space science was on the edge of great discoveries. It was

clear to me that although the thirst for knowledge was the driver, the vehicle was technology. So I felt then as I do now, that pushing the limits of technology is the key to improving our understanding of the universe.

When I began my Ph.D. research in the summer of 1971, my first task was to build a photon counting system for a cooled photomultiplier tube (PMT) that would be part of a new astronomical polarimeter. The idea of observing one object at a time, even with a photoelectric device, was frustrating, but I had no alternatives. Little did I know that just one year earlier, on the other side of the Atlantic, a new development had occurred that would affect all of astronomy, including my own career.

1.1 The development of the CCD

Toward the end of 1969, researchers at the Bell Labs in Murray Hill, New Jersey were investigating new ways of imaging with solid-state silicon methods in an effort to develop a Picturephone. Research on magnetic bubble memory, three-phase plasma display panels and silicon vidicons was in full swing at Bell Labs when executive director of the semiconductor division, Willard (Bill) Boyle, and his close friend George Smith, department head in charge of developing silicon diode arrays, got together one afternoon. In front of a blackboard they began musing about the idea of an "electric bubble" which could be passed through silicon by analogy with passing a magnetic domain from one site to another. It was already known that a charge could be "stored" by the electric potential created by a small insulated metal plate on the surface of a silicon crystal. It was the concept of stringing these storage sites together and using voltage differences between sites to "couple the charge" that was new. Within a few weeks of that afternoon George had a small linear CCD array under test and their paper appeared in the Bell System Technical Journal, Vol. 49, No. 4 in April 1970. And so a new era was born. Years later, around 1987, when I had the privilege to interview Bill Boyle at his retirement home in Nova Scotia, he recalled reactions to the invention of the CCD ranging from "I should have thought of that" to "that will never work." But it did work!

Ironically, the invention of the CCD occurred just as vidicon technology reached a peak in perfection, and many astronomers and planetary scientists were using vidicons for research. One of these, Jim Westphal of Caltech, was quick to realize the potential of the CCD and proposed it as an alternative technology for a camera for an orbiting space observatory. That camera was WF/PC 1, and the orbiting observatory became the Hubble Space Telescope.

During the period from 1973-1979, Texas Instruments under the leadership of Morley Blouke, who is with us at this meeting, worked with NASA JPL to develop CCD arrays for what would become the Galileo and

Hubble Space Telescope missions. One of the test engineers on the program at JPL was Jim Janesick. Realizing the importance of demonstrating a CCD camera on a telescope, Jim approached a leading astronomer at a national institute to enquire about getting time to test a CCD on the sky, and was turned down. Fortunately he did not give up, and he found a more forward-looking supporter in Dr. Brad Smith a planetary scientist at the University of Arizona. In 1976, using the 61-inch telescope on Mt. Bigelow, they obtained the first images of astronomical objects with a CCD. As Brad recalled for me, "all who participated and who saw those images agreed that the potential of the CCD was superior to the other imaging equipment of the time." (For the *full* history, including IR arrays see [1]).

As luck would have it, I became a post-doc at the University of Arizona in 1977 and became friends with Brad's post-doc, Harold Reitsema, now at Ball Aerospace, and through him learned about the CCDs that were being tested on Mt. Bigelow. I was hooked. Soon after, I began to develop instruments based on CCDs and five years later branched into IR arrays.

I recall that the opening words at the detector meeting organized by David Latham and John Geary at Harvard-Smithsonian in June 1981 were something like "enough evidence has been amassed to suggest that CCDs are here to stay." Having just flown to Massachusetts from Arizona (in blue jeans and tartan tie) where I had commissioned a CCD-based spectropolarimeter, I heartily agreed. Our instrument made the first use of the unique ability of CCDs to shuffle charge back and forth on the chip as the polarization state was modulated. The device I used was a thinned, backside-illuminated RCA 512×320 chip. Even with the charge transfer efficiencies of the time, the method worked [2].

There was a period of worry in the late seventies and early eighties when good CCDs were difficult to obtain in the general community. Around that time GEC (now E2V Technologies) chips became available and protagonists like Craig Mackay developed very low-noise systems. Not long after, other manufacturers appeared and the "foundry" approach became popular. I recall standing at the back of the Tucson SPIE meeting in 1986 and sharing remarks with Jim Janesick on how far CCDs had come since astronomical "first light" in 1976.

Of course, much, much more has happened since those early days! Thanks to the dedicated efforts of people like Morley Blouke, Dick Bredthauer, Barry Burke, Paul Jorden and many others too numerous to mention, the formats increased enormously to the huge mosaics (40 2K×4K pixel CCDs in a single focal plane) and the devices themselves have been improved in significant ways.

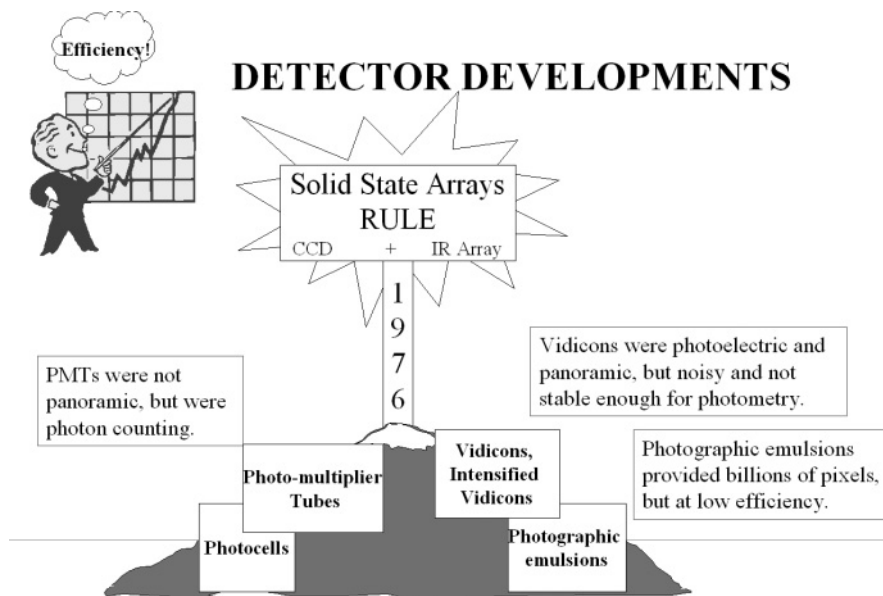


Figure 1. A cartoon representation of detector developments over the last 30 years. CCDs were first introduced into astronomy in 1976. Infrared arrays for astronomy followed about a decade later. But as the cartoon illustrates, there are two newcomers to the party, CMOS and STJ devices.

The demand for "more pixels" is accompanied by a demand for less read noise, better charge transfer efficiency and more response (or quantum efficiency). CCDs are ubiquitous. They have found their way into everything from the commercial video-camera world to the amateur astronomy market. CCDs have become a powerful tool for X-ray astronomers as well.

1.2 The advent of Infrared Arrays

Unfortunately, the band-gap of silicon does not allow astronomers to explore beyond $1.1\ \mu\text{m}$, and so the true infrared remained inaccessible during the rise of the CCD. Nevertheless, infrared astronomy was a rapidly developing field in the seventies because it was recognized as a key regime for understanding how stars form, hidden from view within dusty, gaseous cocoons.

Frank Low introduced the gallium-doped germanium bolometer in 1961 and the use of lead sulfide cells enabled the original $2\ \mu\text{m}$ sky survey by Leighton, Neugebauer, Becklin and others to make many discoveries. Don Hall replaced lead sulfide by indium antimonide [3] and a new generation of 3-4-m class telescopes, like UKIRT and the IRTF, optimized for infrared wavelengths began operations in 1979. With the launch of the Infrared

Astronomical Satellite in 1983, infrared astronomy made another huge leap, all without the aid of a panoramic detector.

Almost as soon as CCDs were invented, however, people tried to make infrared sensitive versions out of InSb and HgCdTe. None of these efforts to use charge-coupling in low band-gap semiconductors were successful. Instead, a new "hybrid" approach was adopted in which the detection of the infrared photons was separated from the function of handling the signal charge. Of course, these efforts were driven by the extreme importance of the infrared for military applications. The infrared sensitive array was typically a grid of photodiodes or photoconductors bump bonded to a readout array through a matching grid of indium columns. Surface channel silicon CCDs were tried as the read out device, but better methods were soon found. Some small-format infrared arrays were in the hands of astronomers in the late seventies and early eighties. Even by 1982, however, when I carried out a survey for the Royal Observatory, Edinburgh and UKIRT, formats were very small; the devices were not really for sale and virtually none had low-background performance capability.

It was about that time that I met Alan Hoffman at SBRC (now Raytheon Infrared Operations) and Jon Rode at Rockwell Science Center (now Rockwell Scientific). UKIRT wanted to develop an infrared array camera that would work from 1-5 μm . The best option for the detector material at that time was InSb, but what was the most suitable silicon read out device or multiplexer? Fortunately, Al Fowler at the Kitt Peak National Observatory (now NOAO) had the answer. He had been experimenting with a platinum silicide Schottky Barrier device hybridized to an interesting silicon readout chip that had an associated source follower for each infrared detector, and a multiplex scheme that allowed each pixel to be addressed and reset individually. In 1984 UKIRT and NOAO teamed up and placed orders with SBRC for the development of an astronomy-optimized infrared array with 58 \times 62 pixels using this source follower per detector (SFD) approach. That development enabled me to deliver the first of three facility-class cameras (IRCAM) based on this chip to UKIRT in September 1986.

Fortunately, a call for next generation Hubble instruments would stimulate the development of short-wave Mercury-cadmium-telluride (HgCdTe) arrays as well. Since the Hubble Telescope's primary mirror is warm, a detector with a response from 1-2.5 μm was all that was needed for the NICMOS instrument proposed by Rodger Thompson of the University of Arizona. HgCdTe was ideally suited to this application since its band-gap was variable depending on the concentration of mercury. The NICMOS chips developed by Rockwell under the leadership of Kadri Vural were a precursor to an extensive family of devices that have found wide application in ground-based astronomy.

Around this time too, serious developments began toward longer wavelength arrays to support another great observatories mission, SIRTf. Craig McCreight at NASA Ames was one of the pioneers in these efforts. Subsequently, excellent arrays with 256×256 pixels were produced by two companies—DRS Technologies (formerly Boeing/Rockwell, Anaheim) and Raytheon (SBRC). SIRTf is due to launch in the second half of 2003.

By March of 1987, when Eric Becklin, Gareth Wynn-Williams and I organized a "workshop" on infrared array detectors in Hilo, Hawaii, several groups had operational arrays, and a new era in infrared astronomy was born. Six years later when Eric and I hosted a similar meeting at UCLA in July 1993, plans were already in hand for $1K \times 1K$ formats and many of the newcomers to the field of infrared *astrophysics* had already forgotten the long road to success that others had trod [4].

Today, some near-infrared arrays have noise levels in single digits and dark currents are low enough for high-resolution spectroscopy, making instruments like NIRSPEC on the Keck telescope possible. Formats of $2K \times 2K$ pixels exist already, with two- and three-side buttable versions being developed for the Next Generation Space Telescope and for ground-based applications in large mosaic cameras. Longer wavelength arrays for 10-20 μm are not far behind; for example, $1K \times 1K$ arrays of arsenic doped silicon (As:Si) have been produced.

IR arrays and CCDs have many similarities. Note however, that IR arrays are not CCDs. There is no charge-coupling involved, therefore charge transfer efficiency is not an issue. There are other significant differences too. Sky backgrounds are higher, well depths (and capacitances) larger, and readout electronics are faster.

I think it is fair to say that the advent of IR arrays has caused an even greater revolution in infrared astronomy than CCDs have for optical astronomy. The fundamental reason for this is the absence of any kind of panoramic detector for the infrared. Optical astronomers had photographic emulsions since the late 19th century and vidicon technology in the sixties.

Today, CCDs and infrared arrays are the detectors of choice. But, as illustrated in Fig. 1, two new technologies are coming to join the party. In recent years, CMOS imaging devices have rapidly become competitive, and the completely new technology of Superconducting Tunnel Junctions (STJs) holds promise of obtaining spectral energy information during imaging.

2. WHERE DO WE GO FROM HERE?

Closely associated with the advances in array detectors is the development in electronics and computers to control and handle the huge data stream that our instruments are now capable of generating. While the

basic principles are the same, almost every observatory has developed their own controllers, sequencers, analog systems, and software. About the only thing we have in common is that the final data must be saved in FITS format. We should be able to do better than that! It would help all of us if there could be a much higher level of compatibility among hardware, software and terminology. At the very least we should strive to have common interfaces. Several groups are thinking along these lines and perhaps that might emerge as a topic at this meeting.

Another issue facing observatories in the future is the huge cost of large detector mosaics, especially for the more costly infrared detectors. Is there anything that can be done to increase yields and bring down costs?

Where do we go from here? Presumably at this workshop we will hear about the competition between CMOS and CCDs, about "designer CCDs," about efforts to compress CCD and infrared array external electronics into application specific integrated circuits (ASICs), and about other efforts to maximize the "shutter open" time.

As we contemplate building even larger ground-based telescopes, issues such as optical matching to detector pixels will become increasingly challenging in the seeing-limited mode, and we will have to think more carefully about what information is to be packed onto our detector arrays. The impact of adaptive optics systems mitigates the matching problem, but drives format and low-background performance.

The angular size of a pixel on the sky in arc seconds is related to the physical pixel size, the diameter of the telescope and the $f/\#$ of the camera lens by

$$\theta_{\text{pix}} = 206265 \, d_{\text{pix}} / D_{\text{tel}} \, F/\#_{\text{cam}} \quad (1)$$

To sample good seeing on a very large telescope pushes the $f/\#$ to faster values for the same pixel size. So don't forget the poor optical designer when deciding to make the physical pixels smaller.

Also, quantum efficiency (QE) is not DQE. The Detected Quantum Efficiency or DQE is the quantum efficiency of an ideal detector with no readout noise producing the same signal to noise ratio as the real one.

$$\text{DQE} = \text{QE} \left[1 + R^2 / N_e \right]^{-1} \quad (2)$$

where R is the rms readout noise in detectors and N_e is the number of detected photoelectrons in the pixel.

So the $\text{DQE} < \text{QE}$ and it depends on the signal. To keep the DQE within 10% of the real QE then the read noise $R < 0.316\sqrt{N_e}$. For faint object

spectroscopy and applications with diffraction-limited pixels, 1 e^- noise is needed.

More effort too will be needed on data reduction pipelines to ensure that near "final form" results can be obtained within minutes of an observation.

3. SNEAK PREVIEW

Looking over the program, I am intrigued and excited to hear the discussions by Jim Janesick of the battle between CMOS and CCDs, but I don't believe for one second that Paul Jorden will reveal the "secrets of Marconi" ... still, you never know! You will find papers on everything from novel orthogonal transfer CCDs to gigantic low-impact shutters, to sub-electron noise devices and cameras with up to 40 chips in a single focal plane. It is significant that we have the infrared detector manufacturers here in force as well as the CCD and CMOS makers. I am also looking forward to learning more about STJs from David Lumb, and both the CCD and infrared array detector manufacturers will tell us about the biggest and best detectors available. There will be several roundtable discussions and special evening talks. I predict a week of information overload, but a most enjoyable one. Aloha and mahalo.

4. ACKNOWLEDGEMENTS

I would like to thank Jim Beletic and Paola Amico for inviting me to give this opening talk and for organizing such an excellent meeting. I would also like to thank Fred Chaffee for his kind introduction, and Don Hall, Jim Janesick and Al Fowler for helpful comments.

5. REFERENCES

- [1] McLean, I.S., 1997, *Electronic Imaging in Astronomy: detectors and instrumentation*, Praxis Publishing Ltd., Chichester, UK. [Please note that this book is not out of print but it can no longer be obtained from John Wylie & Sons. Instead, you can go directly to Praxis Publishing at www.praxis-publishing.co.uk/]
- [2] McLean, I.S., Reitsema, H., 1983, *High-resolution polarization images of Crab Nebula with a charge-coupled device camera*, *Nature*, **304**, p. 243.
- [3] Hall, D.N.B, Aikens, R.S., Joyce, R., and McCurnin, T.W., 1975, *Johnson noise limited operation of photovoltaic InSb detectors*, *Applied Optics*, **14**, p. 450.
- [4] McLean, I.S. 1994, *Infrared Arrays: the next generation*, Kluwer Academic Publishers, Dordrecht, Netherlands.

SECTION I:

DETECTOR MANUFACTURERS

OVERVIEW OF ASTRONOMY ARRAYS AT RAYTHEON INFRARED OPERATIONS (RIO)

Ken J. Ando, Peter J. Love, Nancy A. Lum, David J. Gulbransen, Alan W. Hoffman, Elizabeth Corrales, Robert E. Mills, Mark E. Murray

Raytheon Vision Systems

Abstract: *We review the various types of astronomy arrays currently available from RIO for wide-field imaging and spectroscopy. Arrays for infrared astronomy became available from RIO (previously the Santa Barbara Research Center) with the introduction of the 58×62 InSb in 1984. Since the introduction of this first array, RIO has developed and produced increasingly larger format arrays, including the 256×256 InSb array for SIRTf (Space Infrared Telescope Facility) and the Aladdin $1K\times 1K$ array. Over 70 Aladdin arrays have been delivered and are currently deployed on a number of major telescopes throughout the world. RIO is currently developing the next generation of $2K\times 2K$ format arrays. These include the $2K\times 2K$ ORION InSb array, and the VIRGO $2K\times K$ SWIR HgCdTe array for ground-based applications and the $2K\times 2K$ InSb array for the NGST program. In addition, RIO is currently developing the next generation large format $1K\times 1K$ Si:As Impurity Band Conduction (IBC) arrays for the NGST MIR instrument.*

Key words: *Infrared (IR) arrays, InSb, HgCdTe, Si:As Impurity Band Conduction (IBC), large-format arrays, Focal Plane Array (FPA), module*

1. INTRODUCTION

Since the first utilization of the 58×62 InSb staring array in the early 1980s, astronomers have been demanding larger and larger formats to increase the field of view and observational utility of the large imaging and spectroscopic instruments of 8-m class telescopes such as Gemini, Keck, Subaru, and the VLT. RIO has been actively developing large-format

infrared arrays for both ground and space-based astronomy applications since the early 1980s. The Aladdin 1K×1K element array has been in continuous production since 1994 and has been incorporated into a number of the prime instruments in these telescopes. InSb arrays with formats of 2K×2K are currently under development for ground-based (ORION) and space-based (NGST) applications. These arrays will provide a 4-fold increase in the number of pixels with the same sensitivity, quantum efficiency, and spectral coverage realized with the thinned Aladdin arrays. In addition, 2K×2K SWIR HgCdTe arrays (1-2.5 μm) are also under development for ground-based imaging and spectroscopy in the J, H, K bands. Finally, Si:As IBC and Si:PIN arrays with increased performance and larger formats (1K×1K) are currently under development for future applications. Figure 1 summarizes the chronology of large-format infrared array development at RIO for ground-based and space-based applications.

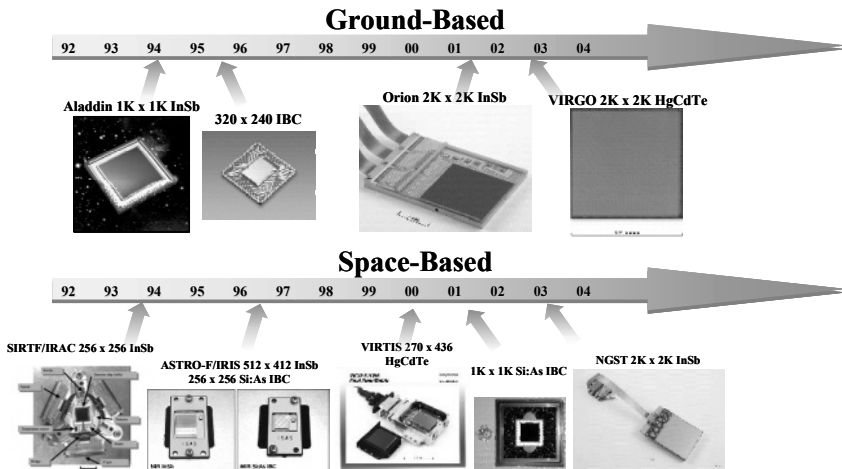


Figure 1. Development of large-format astronomy arrays at RIO for ground-based and space based applications.

2. ALADDIN INSB PERFORMANCE

RIO InSb detector arrays have been successfully integrated into two space-based astronomy missions. The SIRTIF Infrared Array Camera (IRAC) instrument utilizes a 256×256 InSb array and the ASTRO-F Infrared Camera (IRC) instrument utilizes a 512×412 InSb array. The maturity of RIO's InSb is highlighted by the delivery of over 30 Aladdin science grade arrays to the astronomical community. Over the past 20 years, the InSb process, including the ion implantation of the n-type bulk to form the p-on-n type junction, and

the subsequent passivation and thinning, has been refined and is in full-scale production at RIO. One significant advantage of InSb is the fact that, since it is thinned after hybridization, it remains “flexible” and is thereby forced to match the thermal expansion of the much thicker Si ROIC substrate. Consequently, in contrast to HgCdTe on CdZnTe substrates, the thermal mismatch does not lead to pixel outages as the array is cooled. In addition, since the InSb is thinned, and the input surface is passivated and anti-reflection coated, visible response can be realized. Because of the excellent characteristics of the InSb substrate material and the ability to thin it to less than 10 μm , InSb has excellent spectral response and quantum efficiency. Figure 2 shows the quantum efficiency of a typical Aladdin InSb array. Quantum efficiencies of greater than 90% with 99.7% operability are routinely achieved.

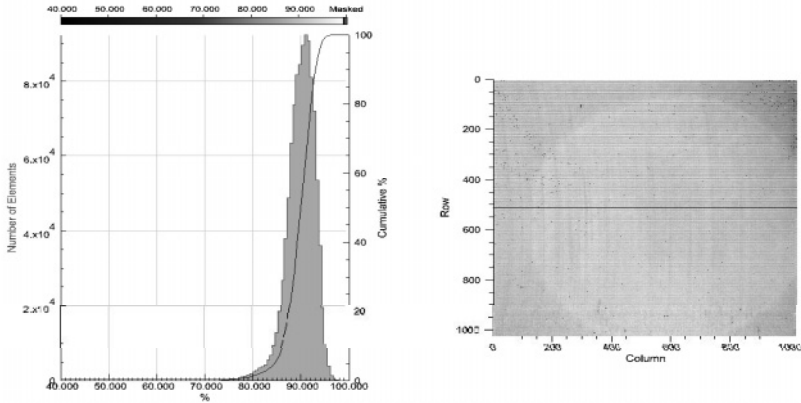


Figure 2. Quantum efficiency for a typical InSb Aladdin 1Kx1K array is greater than 90% with more than 99.7% operability.

3. Si:As IMPURITY BAND CONDUCTION (IBC) ARRAY PERFORMANCE

Si:As Impurity Band Conductor (IBC) arrays have been developed at RIO for both ground-based and space-based applications [1]. For ground-based applications, a 320x240 IBC array, the CRC-774, has been developed and is currently deployed in a number of large telescopes for spectroscopy in the 5 to 28 μm region. RIO has also developed and delivered a 256x256 low-background Si:As IBC array for space-based applications. Flight units are incorporated in the IRAC and IRC instruments of the SIRTf and Astro-F missions, respectively. Figures 3 and 4 show the typical responsive quantum efficiency, noise and spectral response measured for the 256x256 Si:As IBC

arrays on the SIRTf program. More recently, a 1K×1K Si:As IBC array was fabricated utilizing an Aladdin 1K×1K multiplexer. Figure 5 shows the dark current characteristics of this array and a SIRTf 256×256 array as measured by the NASA Ames Research Laboratories. Additional work is in progress now to further improve the dark current and other performance characteristics of the array in the 1K×1K format for the NGST MIR instrument.

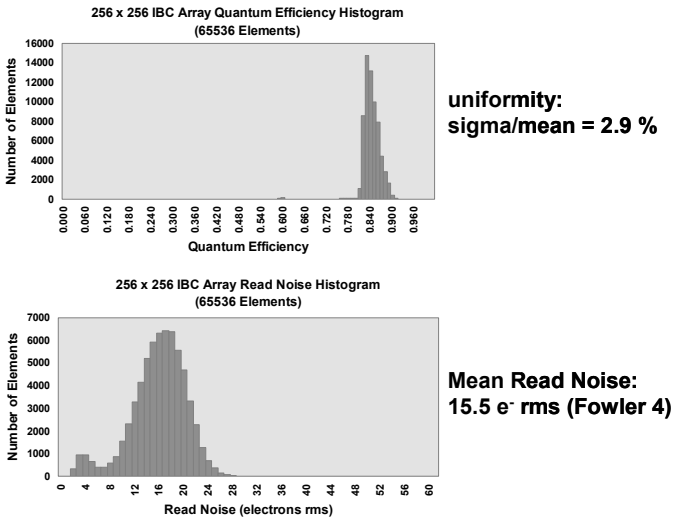


Figure 3. Typical quantum efficiency, read noise, and spectral response for a SIRTf/IRAC 256×256 Si:As IBC array.

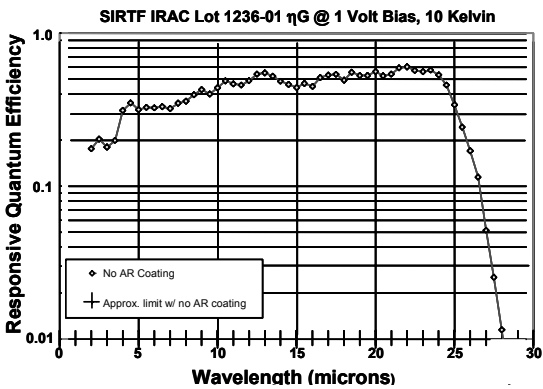


Figure 4. Typical quantum efficiency, read noise, and spectral response for a SIRTf/IRAC 256×256 Si:As IBC array.

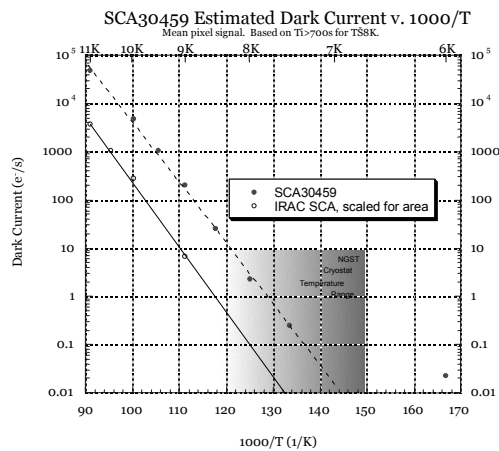


Figure 5. Typical dark current versus operating temperature for a SIRTf/IRAC 256x256 Si:As IBC Array and a 1024x1024 Si:As IBC array.

4. ORION AND NGST 2Kx2K InSb MODULES AND FPAS

To meet the increasing demand for larger formats, RIO is developing both InSb and HgCdTe/CdZnTe 2Kx2K format arrays [2]. InSb wafers are now available in sizes up to 100 mm in diameter, and development efforts to scale the growth to 150 mm are in progress. Under the ORION program, a 2Kx2K InSb array with 64 outputs has been demonstrated for ground-based astronomy. This array is two-side buttable for packaging into a 4Kx4K module. Figures 6 and 7 show the first ORION engineering module and the associated response uniformity map from this array.

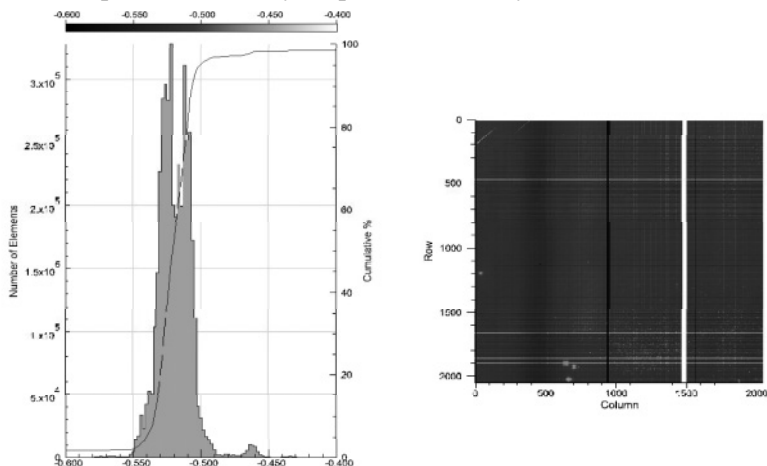


Figure 6. Performance of the first Orion 2Kx2K InSb engineering module.

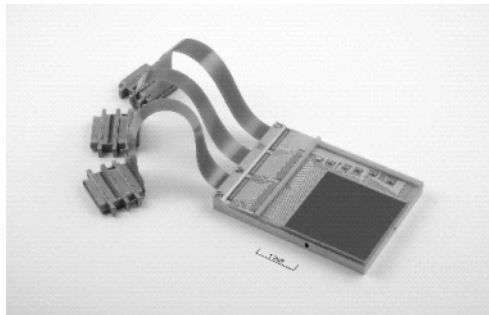


Figure 7. Photo of the 2-side butttable module. The module has three 37-pin MDM cables/connectors to accommodate 64 outputs and the clock and bias supplies.

A $2K \times 2K$ InSb array with 4 outputs and 3-side buttability is also under development for the NGST program. Three-side buttability allows packaging modules into $4K \times 2nK$ ($n = 1, 2, 3, \dots$) FPAs. Figure 8 shows a photograph of a 6" ROIC wafer and the first prototype $2K \times 2K$ NGST module.

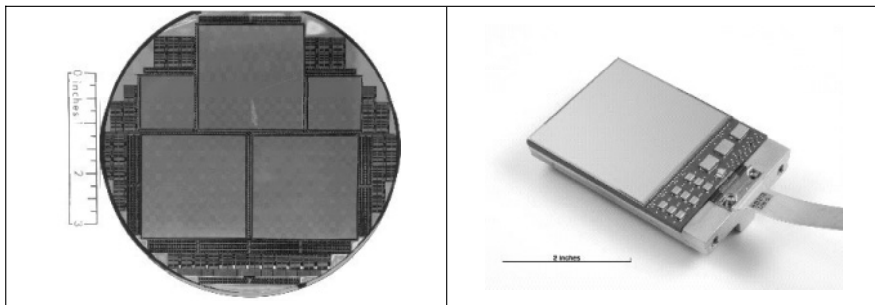


Figure 8. NGST 6" ROIC wafers with three $2K \times 2K$ die per wafer and first Prototype NGST $2K \times 2K$ "plug-and-play" Module for the NIR FPA. The module is 3-side butttable for construction of $4K \times 2nK$ ($n = 1, 2, 3, \dots$) mosaic FPAs. Module is shown with a "bare" NGST SB290 readout array. The unit cell pitch is $25 \mu m$.

Figure 9 shows the design evolution of the $4K \times 4K$ FPA housing for the NGST NIR FPA. Beginning in 1999, the $4K \times 4K$ FPA was based on four $2K \times 2K$ butted modules with each module consisting of four $1K \times 1K$ SCAs. By 2002, the FPA had evolved into a FPA with four close-butted $2K \times 2K$ modules with each module consisting of a single $2K \times 2K$ InSb SCA.

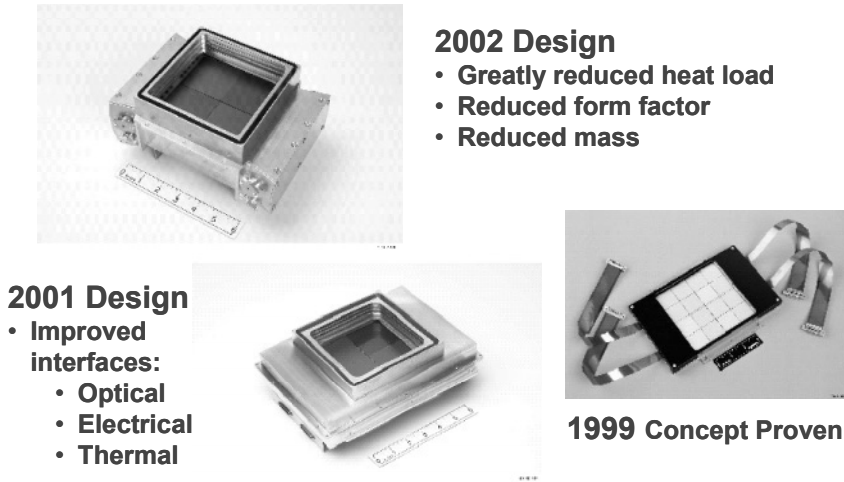


Figure 9. Design evolution of the NGST 4Kx4K NIR InSb FPA Package.

5. VIRGO 2Kx2K SWIR HgCdTe DEVELOPMENT

InSb detectors [3], which respond out to almost $5.5 \mu\text{m}$, must be operated at low temperatures (25 to 35 K) to suppress dark current. Recently, RIO started development of SWIR LPE HgCdTe/CdZnTe 2Kx2K arrays which operate at temperatures near 80 K. For imaging and spectroscopy in the J, H, and K bands, the detector cutoff wavelength can be tuned to about $2.5 \mu\text{m}$ at 80 K. RIO has funded and completed the design (called VIRGO) of a new 2Kx2K Readout Integrated Circuit (ROIC) designed to mate with the SWIR HgCdTe detectors. The readout derives all needed clock waveforms from just two input clocks – a master clock (at $\frac{1}{2}$ the video rate) and a frame start clock. Very careful attention to the layout and design of the digital logic should result in a low glow multiplexer. “Mux glow” (readout self emissions seen by the detector array) have plagued many previous readout designs for astronomy applications using submicron CMOS. The VIRGO readout is composed through the Reticle Image Composition Lithography (RICL) technique using a basic 1024(vertical)x512(horizontal) array of unit cells. This allows a wide variety of array formats to be achieved with the same mask set. A later lot is planned that will pattern 4Kx4K readouts – the VIRGO-4K.

The VIRGO-2K design can be electrically configured to use 4 or 16 output drivers with corresponding readout frame rates of 1.43 Hz or 0.376 Hz. The outputs are designed to run at a 400 KHz data rate. If faster frame

rates are desired, the data rate can be increased to at least 4 MHz by increasing the output and unit cell source follower currents. At this rate, the chip can be readout at a 14 Hz rate. Each output addresses a consecutive block of columns in the array in both the 4 and 16 output modes. A second control line allows the selection of global or row-by-row reset of the unit cell integration capacitance. Finally, a third control line allows the unit cell reset to be suppressed for a frame to allow a non-destructive readout of the integrated image data. This non-destructive read capability allows a variety of output sampling techniques such as correlated double sampling (sometimes called Fowler-1) or Fowler-N sampling to be used to eliminate reset noise reduce low frequency drift over the long integration periods.

The first lot of VIRGO readout wafers has been received and tested. The results were excellent. Every device was functional with nearly 50% meeting the readout test specification. One of the wafers yielded 7 of the 8 1K \times 1K and 4 of the 9 2K \times 2K readouts. Each readout was tested for power dissipation, offset uniformity, and source follower gain. The power dissipation in 16 output mode was well under 10 mW. The typical offset uniformity distribution had a 25 mV standard deviation and a 150 mV peak-peak spread. The source follower gain was about 0.97 with a <1% sigma/mean distribution at room temperature (see Fig. 10).

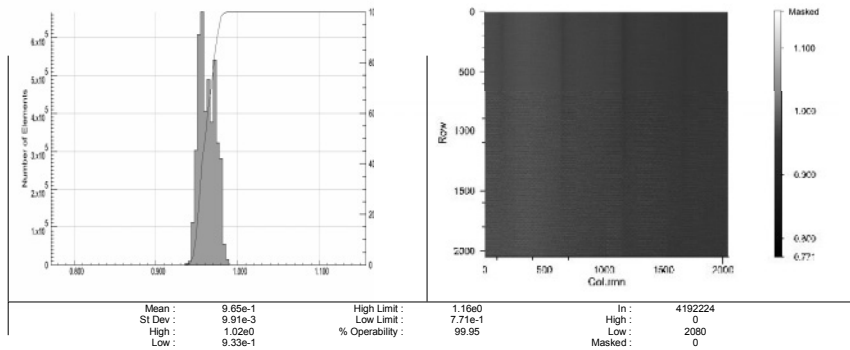


Figure 10. VIRGO 2K \times 2K ROIC source follower gain is about 0.97 at room temperature and greater than 0.98 at 80 K. The sigma/mean of the distribution is about 1%.

HgCdTe grown by LPE on lattice-matched CdZnTe substrates is also a very mature technology at RIO [4]. The bulk CdZnTe substrates have a cut-on wavelength of about 0.85 μm , so that these devices do not respond in the visible unless the CdZnTe substrate is removed after hybridization. The main advantage of HgCdTe detectors over InSb detectors is that the cutoff wavelength can be tuned to any desired value between 2 μm and 13 μm and beyond. These devices are fabricated by growing an n-type absorbing base layer on a CdZnTe substrate, followed by growth of a p-type cap layer. Etching mesas through the p-type cap layer into the n-type base layer

delineates individual photodiodes. Because the bulk CdZnTe substrates are relatively expensive and difficult to obtain in large areas, this detector technology does not easily scale to fabrication of large-format arrays. The largest area CdZnTe substrates suitable for LPE growth of HgCdTe are typically no larger than about 30 cm². Moreover, the substantial thermal expansion mismatch (CTE) between HgCdTe/CdZnTe and Si becomes problematic for large-area arrays. Unless the relatively thick bulk CdZnTe substrate is removed, some mechanical means must be used to either force the Si ROIC to match the HgCdTe/CdZnTe detector or vice versa. Current array sizes for these devices are 640×480, 1K×1K, and most recently 2K×2K with 20 μm×20 μm pixels have been fabricated for use with the VIRGO-2K readouts. Figure 11 shows a photo of a VIRGO 8" ROIC wafer with 9 patterned 2K×2K die and 8 1K×1K die. Also shown is a typical SWIR LPE HgCdTe/CdZnTe detector spectral response which shows high in-band quantum efficiency and a sharp cut-on and cutoff.

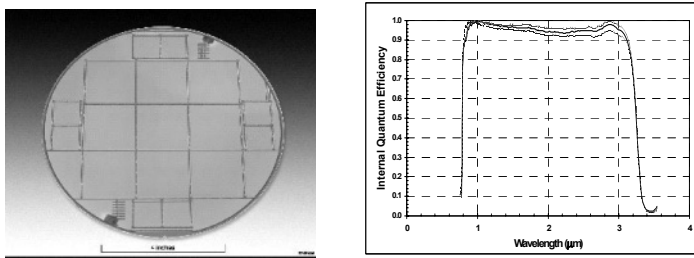


Figure 11. VIRGO 8" ROIC wafers are patterned with nine 2K×2K ROIC die. The VIRGO unit cell pitch is 20 μm. Typical SWIR HgCdTe/CdZnTe spectral response shows high quantum efficiency from 0.85 μm to the cutoff wavelength of the detector.

6. SUMMARY AND CONCLUSION

InSb arrays have reached a high degree of maturity at RIO with the demonstrated producibility and performance of the Aladdin array. These arrays are characterized by low dark current ($<0.1\text{e}^-/\text{sec}$), high QE ($>90\%$) and high operability ($>99\%$). RIO is currently developing the next generation 2K×2K InSb arrays [5]. These include the ORION and NGST arrays. The first prototype ORION array was successfully fabricated and achieved an operability of 98%. The NGST ROIC have been tested and NGST InSb arrays will be available shortly. An advanced packaging design for a 4K×4K FPA with greatly reduced heat load, reduced form factor and reduced mass was demonstrated for NGST. A 1K×1K Si:As IBC with improved performance is under development for the NGST MIR instrument. Development of a 2K×2K SWIR HgCdTe array for ground-based JHK

astronomical applications is well underway. The first lot of VIRGO ROICs has been fabricated and tested with excellent results. The ROICs will be mated with detector arrays fabricated with our well established LPE HgCdTe growth process. Excellent performance in the JHK bands is expected with these arrays.

7. ACKNOWLEDGEMENTS

The results summarized here would not have been possible without the contributions of all of the members of the RIO Astronomy team and all the personnel at RIO who were involved in the design, fabrication and test of the InSb, HgCdTe and Si:As arrays. In addition, special thanks to Al Fowler of NOAO, Craig McCreight of NASA Ames Research Center, and members of the University of Rochester team including William Forrest, Judy Pipher, Andrew Moore and Craig McMurtry for their testing and technical support.

8. REFERENCES

- [1] Estrada, A., Domingo, G., Garnett, J., Hoffman, A., Lum, N., Love, P., Solomon, S., Venzon, J., Chapman, G., and Sparkman, K., 1998, *Si:As IBC IR Focal Plane Arrays for Ground-Based and Space-Based Astronomy*, Proc. SPIE vol. **3354-11**, p. 99.
- [2] Hoffman, A., Ando, K., Estrada, A., Garnett, J., Lum, N., Love, P., Rosbeck, J., and Sparkman, K., 1998, *Near IR Arrays for Ground-Based and Space-Based Astronomy* Proc. SPIE vol. **3354-03**, p. 24.
- [3] Ando, K., Love, K., Garnett, J., Lum, N., Rosbeck, J., Smith, M., and Sparkman, K., 2000, *Infrared Detectors for Ground-Based and Space-Based Astronomy Applications*, Proc. SPIE vol. **4008-159**, p. 1254.
- [4] Ando, K., Bornfreund, R., Brazier, C., Holcombe, R., Kasai, I., Love, P., and Smith, M., 2000, *270×436 HgCdTe FPA Module for the Rosetta VIRTIS-H and -M Instruments*, Proc. SPIE vol. **4131**, p. 348.
- [5] Love, P., Ando, K., Bornfreund, R., Corrales, E., Mills, R., Cripe, J., Lum, N., Rosbeck, J., and Smith, M., 2001, *Large-Format Infrared Arrays for Future Space and Ground-Based Astronomy Applications*, Proc. SPIE vol. **4486-38**, p. 373.

A NEW PHOTON COUNTING DETECTOR: INTENSIFIED CMOS-APS

Giovanni Bonanno¹, Massimiliano Belluso¹, Antonio Cali¹, Alessandro Carbone², Rosario Cosentino¹, Angelo Modica³, Salvo Scuderi¹, Cristina Timpanaro¹, Michela Uslenghi⁴

¹*Istituto Nazionale di AstroFisica -Osservatorio Astrofisico di Catania*, ²*Elettromare La Spezia*, ³*Xilinx Ireland*, ⁴*Istituto di Astrofisica Spaziale e Fisica Cosmica - Milano*

Abstract: *A new type of position sensor (CMOS-APS) used as readout system in MCP-based intensified photon counter is presented. Thanks to CMOS technology, the pixel addressing and the readout circuits as well as the analogue-to-digital converters are integrated into the chip. These unique characteristics make the CMOS-APS a very compact, low power consumption, photon counting system. The more classical Photon Counting Intensified CCDs (PC-ICCD), the selected CMOS-APS, the driving and interface electronics based on Field Programmable Gate Array (FPGA), and the adopted algorithm to compute the center of the luminous spot on the MCP phosphor screen are described.*

Key words: *Complementary Metal Oxide Semiconductor Active Pixel Sensor (CMOS-APS), intensified photon counter*

1. INTRODUCTION

In a photon counting system, there are several advantages of using a CMOS-APS instead of a CCD. In a CCD the charge is shifted sequentially from a pixel to pixel until it reaches a single or a small number of output nodes. In an APS the charge in each pixel can be readout by addressing the pixel directly, because the preamplifier is integrated on each pixel and the timing control and pixel addressing is integrated on chip. Thanks to CMOS technology, pixel processing and analogue-to-digital converters are integrated into the chip. The highly parallel structure of the APS allows a

count rate dynamic range larger than that obtainable with photon counting systems based on intensified CCD. Two other important characteristics, fundamental in space applications, must also be considered: CMOS devices use a single 3.3 V power supply and show a better radiation hardness than CCDs.

The CCD technology, developed more than twenty years ago and improved during these years, is well known and appreciated in many fields for the high quantum efficiency and the low readout noise even at relatively high scan rates. The novel CMOS-APS technology is in continuous evolution [1], and, at the moment, is characterized by higher readout noise. This parameter can be overcome in photon counting systems by setting a higher MCP gain. The other difference, which favors the CCD, is the fill factor, which is 100 % for CCDs, is not higher than 60 % for CMOS-APS. However this parameter is not very critical for the performance of intensified systems.

2. THE CMOS-APS PHOTON COUNTING SYSTEM

The developed system basically constitutes of a Micro Channel Plate (MCP) with a phosphor screen coupled to a CMOS-APS through relay optics. A block diagram of the complete system is shown in Fig. 1.

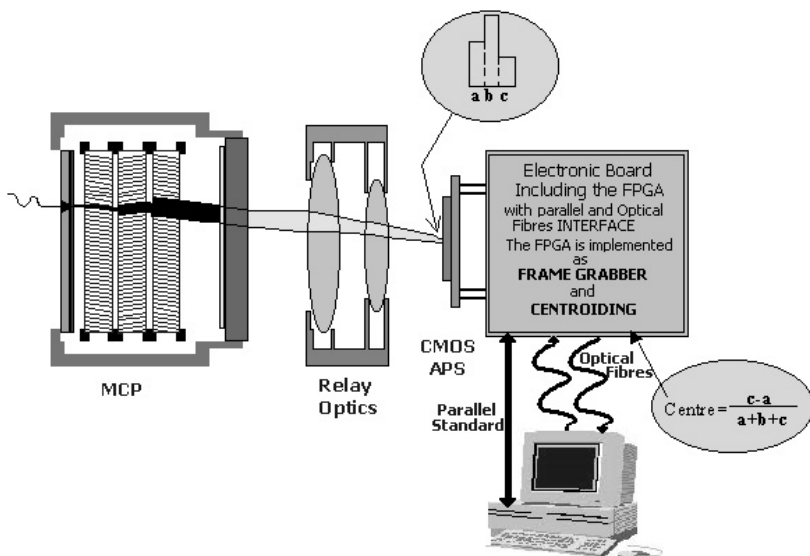


Figure 1. Block diagram of the CMOS-APS photon counting system

The electrons generated in a photocathode are multiplied by the MCP, and the emerging electron cloud impinges on a phosphor screen giving a luminous spot. Relay optics re-image this spot onto the CMOS-APS. The APS and a high density Field Programmable Gate Array (FPGA) are located on the same board that is connected to a PC through a parallel interface and a fast serial connection (1.2 GBit/sec) based on fiber optic. The FPGA is configured to drive the APS, to readout the pixels and to make computations. The various functions are obtained by downloading the configuration file via the parallel interface by using a standard protocol, or via the optical fibers by using a dedicated DLL. Finally, the data corresponding to the coordinates of each valid event are acquired by the computer and stored in a file.

2.1 Optical and mechanical layout

The CMOS-APS is usually delivered covered with a window, and, as we did for CCDs, we planned to replace the window with a fiber optic taper. For the first tests we decided to use an optical objective, the Rodenstock model HR-Heligaron 35, with a very small numerical aperture (for better spatial resolution) and few optical components (to minimize the signal loss due to the transmittance of each element). The main characteristics of this objective are shown in Table 1. Figure 2 shows the mechanical layout.

Table 1. Characteristics of the HR-35

First lens diameter	31 [mm]
Max object diameter	35 [mm]
Field image diameter	8 [mm]
Total number of lenses	9
Transmission @ 550 nm	>98 [%]
Focal length	17 [mm]
Numerical Aperture	0.32
Demagnification	1 : 4.3
MTF @ 33.5 lp/mm	90 - 85 [%]
MTF @ 67 lp/mm	80 - 50 [%]
Relative Brightness	99.5 [%]

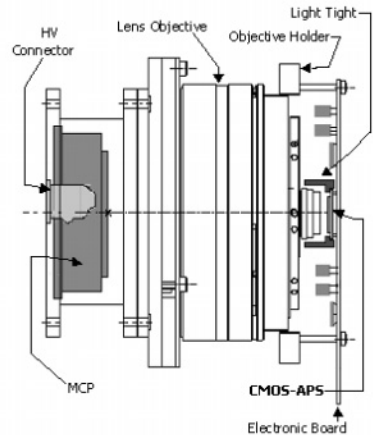


Figure 2. Mechanical layout of the system

2.2 The CMOS-APS

For the position sensor of the photon counting system we used a CMOS-APS PB-1024 manufactured by Photobit that, with 500 frames/sec, assures a high count rate and thus increases the system dynamic range. The internal architecture is shown in Fig. 3. The PB-1024 has been designed to have pixel row parallelism, and in fact includes the timing and control circuitry to treat

a row at a time on chip (see the Row Timing Block in Fig. 3), and 1024 8 bit A/D converters to digitize simultaneously the analog signal from an entire pixel row. Furthermore the chip contains special self-calibrating circuitry that allows reduction of the fixed pattern noise. To speed up the data output a “ping pong” memory array is used. This type of memory stores the 1024 8 bit digitized data, which is read during the next conversion cycle. Eight pixels (a 64 bit word wide) can be read at a time, through the eight ports which have 8 bits. Thus in 128 clock pulses an entire row is read out. The device can be considered a “digital device” in the sense that it receives digital signals and sends digitized data. Thus, only a “digital controller”, like a Field Programmable Logic Array (FPGA), is required to run the sensor.

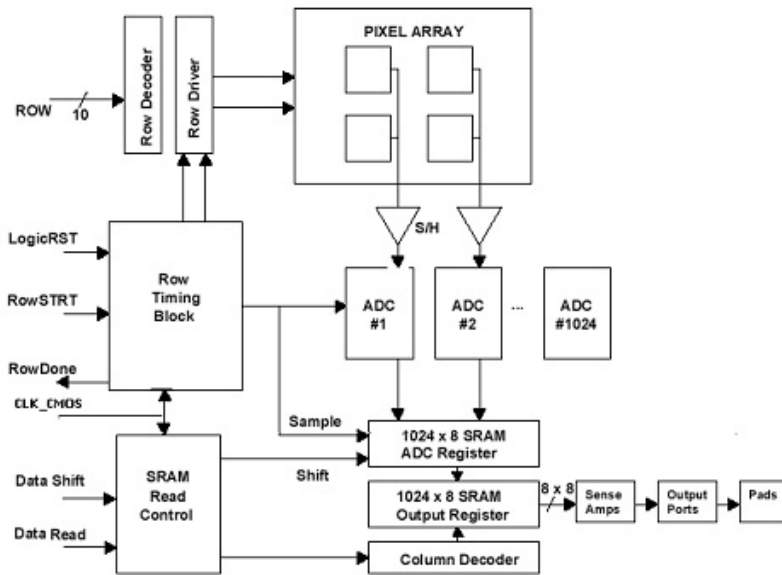


Figure 3. Block diagram of the internal architecture of CMOS-APS PB-1024

3. THE CMOS-APS DRIVING ELECTRONICS

The block diagram of the detector front-end electronics is shown in Fig. 4, while the Fig. 5 shows a picture of the electronic board.

The APS has almost all the electronics needed on chip to operate it as an imager, the FPGA provides the rest of necessary signals. The implemented circuits on the FPGA provide the bias signals, their telemetry, the power supply, and the interface to the host PC. A 128 KWords 32 bits ZBT RAM is used to store the acquired image, which is then subsequently read at a different data rate. The heart of the controller consists of the implementation

on the FPGA of the centroid algorithm, which is divided into two parts. The event validation locates the peak signal of all events above a specific discrimination level, and the centroid computation carries out a three point truncated center of gravity. If the pixel values are **a**, **b**, **c**, with **b** being the highest, the coordinate of the center will be $(c-a)/(a+b+c)$. Figure 6 shows the block diagram of the implemented circuit.

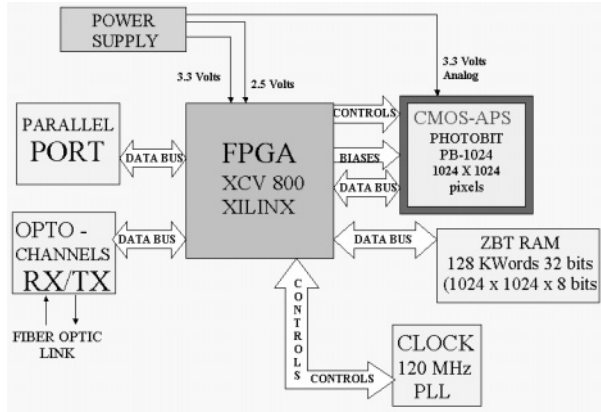


Figure 4. Block diagram.

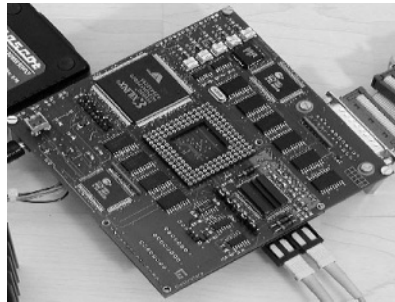


Figure 5. Picture of the electronic board.

The 64 bits data, corresponding to 8 pixels, are stored on synchronous FIFOs at each pulse of the CLK_CMOS , and when the first three rows are completely packed on FIFOs, the computation procedure continues. A set of D-Latches are used to obtain 8 windows of 3×3 pixels. The center computation and the event validation circuits operate simultaneously on these 8 windows, and, at each clock pulse, another eight 3×3 pixels windows are stored in the D-Latches. This process continues until the end of frame. When the four synchronous FIFOs receive the validation event signal, they store the row and column data (contained in the respective registers) and the sub-pixel value (given by the center computation circuitry) to form a 32-bit

word with the event x-y coordinates. This is sent, through 4 asynchronous FIFOs and a multiplexer, to the host computer via the parallel interface or the fast serial link.

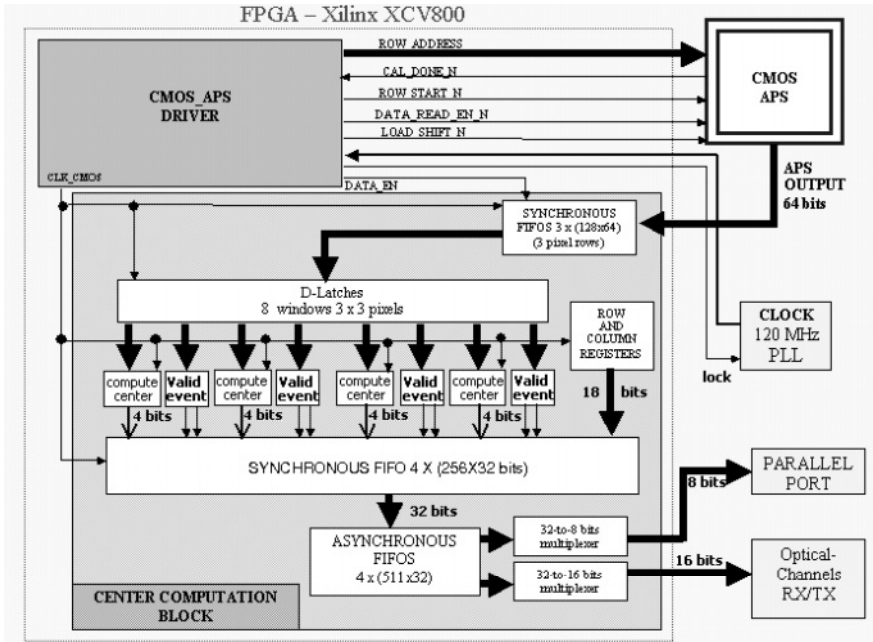


Figure 6. Block diagram of the FPGA circuit implementation for the centroiding

4. FIRST RESULTS

Before operating in centroid mode, we took lots of images while varying the MCP gain, the objective focus and the APS working frequency. From the analysis of the spot profile with respect to the noise level we derived the best operating conditions. An image of 512×512 pixels acquired at a frequency of 20 MHz is shown in the lower left panel of the Fig. 7. Surface plots of sub areas of 150×150 pixels of images taken at 20 MHz, 40 MHz and 50 MHz are also shown. It can be seen that the noise increases with the increasing frequency, while the events are always well discriminated.

The measured APS fixed pattern noise is negligible (3-6 ADU rms.) at all readout frequencies. A maximum frequency of 50 MHz (400 frames/sec) is achievable without affecting the total noise and then the lower discrimination level. By windowing to half frame the system works at 800 frames/sec and a higher dynamic range is obtainable. We can conclude that the CMOS-APS used as position sensor in MCP based systems can perform

better than a faster CCD and with some important advantages: compactness, simplicity, radiation hardness, low power consumption and low cost.

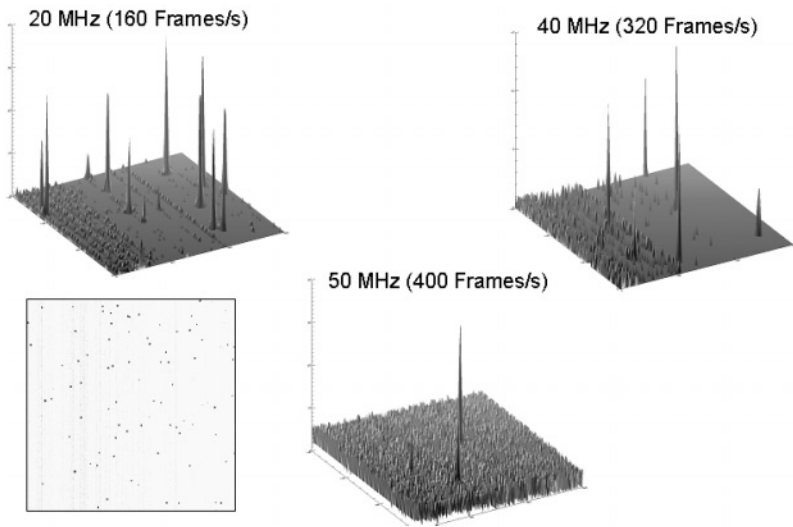


Figure 7. Image of 512x512 pixel acquired at a frequency of 20 MHz and surface plots of sub-areas of 150x150 pixels of images taken at 20 MHz, 40 MHz and 50 MHz.

5. REFERENCES

- [1] Janesick, J. et al., 2002, *Scientific CMOS Pixels*, these proceedings, pg. 103



Reinhold Dorn (right) keeps smiling despite discovering that his handkerchief has already been used. Gert Finger (center) and Guy Woodhouse (left) have been also awarded a prize for best-dressed paniolos (Hawaiian cowboys).



Nerd Enrollment: Klaus Reif and Tim Hardy sign in, while Paola Amico and Gale Kihoi welcome them at the official opening of SDW2002.

PRELIMINARY TEST MEASUREMENTS OF THE SPAD ARRAY

Giovanni Bonanno¹, Rosario Cosentino^{1,2}, Massimiliano Belluso¹, Salvo Scuderi¹, Cinzia Di Franco³, Pier Giorgio Fallica³, Delfo Sanfilippo³, Emilio Sciacca⁴ Salvatore Lombardo⁴

¹Istituto Nazionale di AstroFisica - Osservatorio Astrofisico di Catania, ²Telescopio Nazionale Galileo (TNG), ³ST Microelectronics - Catania, ⁴Consiglio Nazionale delle Ricerche – Istituto per la Microelettronica e microsistemi – sez. Catania

Abstract: *This is a progress report on preliminary test measurements aimed to evaluate the performance of new Single Photon Avalanche Diodes (SPAD) developed by ST Microelectronics. Various samples with different dimensions (from 10 to 100 μm diameter) and two 5x5 arrays (20 and 40 μm) are manufactured by STM; some of which have been characterized. A brief description of the device and its main characteristics (dark, quantum efficiency and linearity) are presented.*

Key words: *Single Photon Avalanche Diodes (SPAD), detector, photon counting, quantum efficiency*

1. THE SINGLE PHOTON AVALANCHE DIODE

SPAD is a p-n junction biased above the breakdown. In this operative condition a hole-electron pair, generated in the depletion layer, causes an avalanche, which is measurable as a current. The diode works as a single photon detector with an infinite gain. Figure 1 shows the structure of the last generation SPAD and that of the layout of an array.

The current flows in the diode until the drive circuit, the Active Quenching Circuit (AQC), turns off the polarisation for a dead time and then restores it. This prepares the SPAD for another event. This turn off time, defined ‘hold off’ time, depends on the quality of the SPAD. Figure 2 shows

the block diagram of the quenching circuit that is made by a DRIVER that provides the polarization, a COMPARATOR that triggers the monostable when an event occurs. The monostable generates the hold-off pulse.

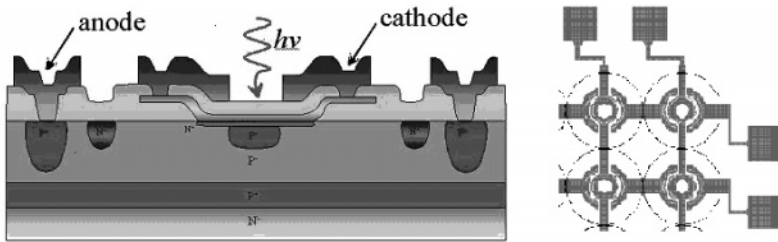


Figure 1. The structure of SPAD device (left) and array layout (right).

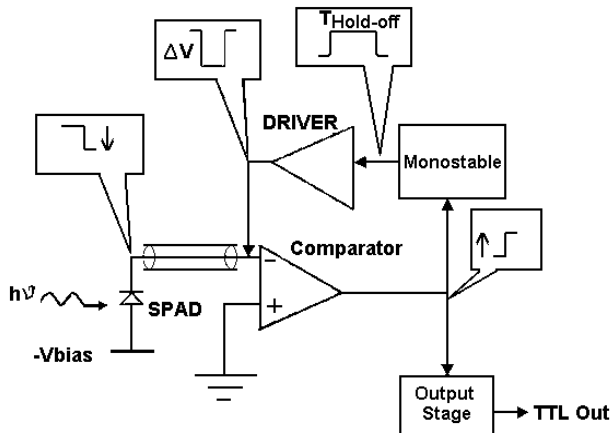


Figure 2. Active Quenching Circuit block diagram.

2. SPAD CHARACTERIZATION

2.1 Quantum Efficiency (QE)

The instrumental apparatus used for the quantum efficiency measurements was designed at the Catania Astrophysical Observatory. The system is a modified version of a previous system, already operating for CCDs QE measurements [1]. It is usually operated in a vacuum and has a modular structure. The first module accommodates an optical system whose purpose is to have the beam emitted by the radiation source matching the monochromator focal ratio. The second module along the radiation beam

path is the monochromator. The monochromator has three 1200 g/mm ruled gratings to cover efficiently the whole spectral range. The nominal spectral resolution is 0.1 nm. After being dispersed the beam enters an integrating sphere, where the SPAD and a calibrated photodiode are mounted. The acquisition system reads the counts of the SPAD and the current measured by the calibrated photodiode at the same time. Before measuring the QE of SPADs of different active areas (10, 20, 50 and 100 μm), we measured the breakdown voltage of each device and set the polarization voltage value between 10% and 20% above this value.

A typical breakdown voltage is about 30 V. The SPAD quantum efficiency, measured in a range 350-1050 nm, is typical of a silicon based detector and shows a peak of about 60 % at 550 nm for 100 μm diameter devices. We measured the QE at different polarization voltages and found that the QE increases with the polarization voltage. The measurements also show an increase in the efficiency with the SPAD diameter. This result is unexpected because the QE measurements are normalized by area. One hypothesis is that there is a small area around the pixel with poorer sensitivity due to fabrication process. In fact, the effect becomes less evident for devices with larger area.

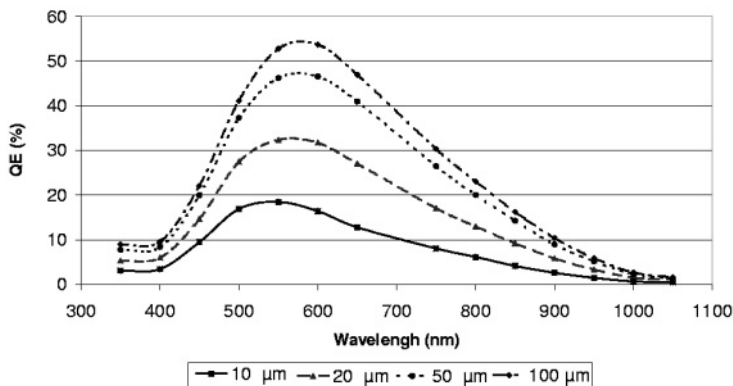


Figure 3. Quantum efficiency at polarization voltage 20% above the breakdown voltage.

2.2 Dark counts

Dark current can be produced by thermal generation and after pulsing. Dark counts increase with the bias voltage because the higher electric field increases the probability of avalanche and the depletion volume. After pulsing depends on the following phenomenon: during the avalanche, some carrier can be trapped in the depletion layer and released after a time delay. If this time delay is greater than the hold-off time, the carrier generates an avalanche named “after pulsing”. To reduce the after pulsing effect, the

hold-off time had to be increased even though this reduces the count rate. Both causes of dark counts depend on the defects in the depletion volume and can be reduced with a cleaner fabrication process. Dark counts are measured at 20 °C, with a hold-off time of 360 nsec that reduces the after pulsing effect. In Table 1 the results of dark measurements of 20 μm SPAD versus bias voltages are shown. The results highlight the dependence of dark counts by the bias voltage.

Table 1. Dark Counts of 20 μm SPAD at 20 °C.

Bias Voltage [V]	QE [%] @ 550 nm	Dark Counts
36.87	12.96	6.2
40	18.25	8.2
41	19.82	12.2
42	21.64	10.4
43	21.10	14.8
44	22.75	18

2.3 Linearity

The linearity is measured using a standard method, consisting of illuminating the detectors at different signal levels with a uniform source of radiation. The deviation from linearity is shown in Table 2. The measurements show that the deviation from linearity is very low and that there is no variation in QE in the range of measurements.

Table 2. Linearity of 50 μm SPAD.

Photodiode (pA)	Spad (count)	QE (%)	Deviation from linearity
1072	6650	22.526	1.003
911	5650	22.521	1.003
467	2850	22.161	0.987
122	760	22.621	1.007

2.4 Future developments

Two arrays of 5×5 elements, with pixel size 20 and 40 μm of diameter, have been developed by STM and a series of measures are scheduled in Summer 2002. A new active quenching circuit, to allow array readout, is under development. A smart controller to drive the array and provide all necessary circuitry to acquire the image is under study.

3. REFERENCES

- [1] Bonanno, G., Bruno, P., Cali A., Cosentino, R., Di Benedetto R., Puleo M., Scuderi S., 1996, *The Catania Astrophysical Observatory facility for UV CCD characterization*, SPIE Proc., Vol. **2808**, p. 242.

PRELIMINARY CHARACTERIZATION OF TWO HIGH-SPEED, BACK-ILLUMINATED CCD IMAGE SENSORS

Morley M. Blouke¹, Denis L. Heidtmann¹, James Eriksen¹ and Archibald Barter²

¹Scientific Imaging Technologies Inc., ²PixelVision of Oregon Inc.

Abstract: *This paper discusses the performance of two new sensors: a 2K×2K and a 4K×4K pixel array. These thinned arrays are intended for high frame rate, scientific applications*

Key words: *Charge-Coupled Device (CCD), large format, thinned, back-illuminated*

1. INTRODUCTION

For a number of years, one of the standard CCD imagers has been the thinned 1K×1K image sensor. This device has large, 24 μm pixels, read noise at 50 Kpix/sec of $\sim 5\text{ e}^-$ rms, high quantum efficiency, and a dynamic range typically in excess of 16 bits. More recently the demands of the market have placed emphasis on higher resolution, higher speed operation while maintaining a high dynamic range and high QE. In this paper we report on two new devices from SITE. These devices are 2K×2K and 4K×4K pixel arrays with 12 μm pixels. The chips are intended to be thinned using our new thinning process for high frame rate, scientific applications.

2. DEVICE DESCRIPTION

2.1 Architecture

The SITE SI-028A (2K×2K) and SI-029A (4K×4K) CCD sensors are designed for low light level scientific and industrial imaging applications.

Both devices are n-buried channel chips fabricated using a two level polysilicon gate process. The parallel section is intended to operate in a four-phase mode, while the serial is a two-phase register.

Figure 1 presents a functional diagram of the architecture of the 4K×4K device (with the exception of pixel count, the 2K×2K chip is identical.) The imaging section is segmented into an upper and lower half. The upper and lower serial registers are split at the midpoint. A two stage source follower amplifier is located at each end of each of the serial registers. Consequently, the devices may be read out through one, two, or four amplifiers in the usual manner characteristic of 4 output full frame devices.

The parallel array is operated as a four phase CCD. Each 12 μm pixel consists of four 3 μm -wide electrodes, fabricated using two levels of polysilicon. In the MPP version, the phase one gates serve as the barrier phase. The parallel section is isolated from the serial registers by a transfer gate. The transfer gate is also a barrier phase. There are twelve columns on each side of the array, which serve to collect excess dark current and photo-generated charge in the field region and can be used as dark reference columns. Similarly, in each half of the array, there are eight extra rows covered by the light shield. The light shield defines the 2K×2K (4K×4K) active imaging area.

The serial registers are built as two-phase registers. They are wider than the parallel pixels, so they can accommodate charge in excess of 200 ke⁻. Each half of the register is terminated in a 2× summing well, providing support for 2×2 binning. There are 32 lead-in pixels at each end of the serial. Each gate of the serial register, *i.e.* each barrier and each well electrode, is separately connected. By appropriate choice of which pair of gates are connected together, the serial register can be made to run in either direction or in split mode using both output amplifiers.

The four output amplifiers are two stage source followers and are all identical. The load for the first stage is an on-chip, buried-channel MOSFET, while the load for the larger, second stage is off chip, usually a resistor. The output has been carefully designed for reduced capacitance of the sense node to increase the conversion gain and reduce noise. There are two last gates, so that with appropriate biasing of the gate next to the node, the conversion gain can be reduced.

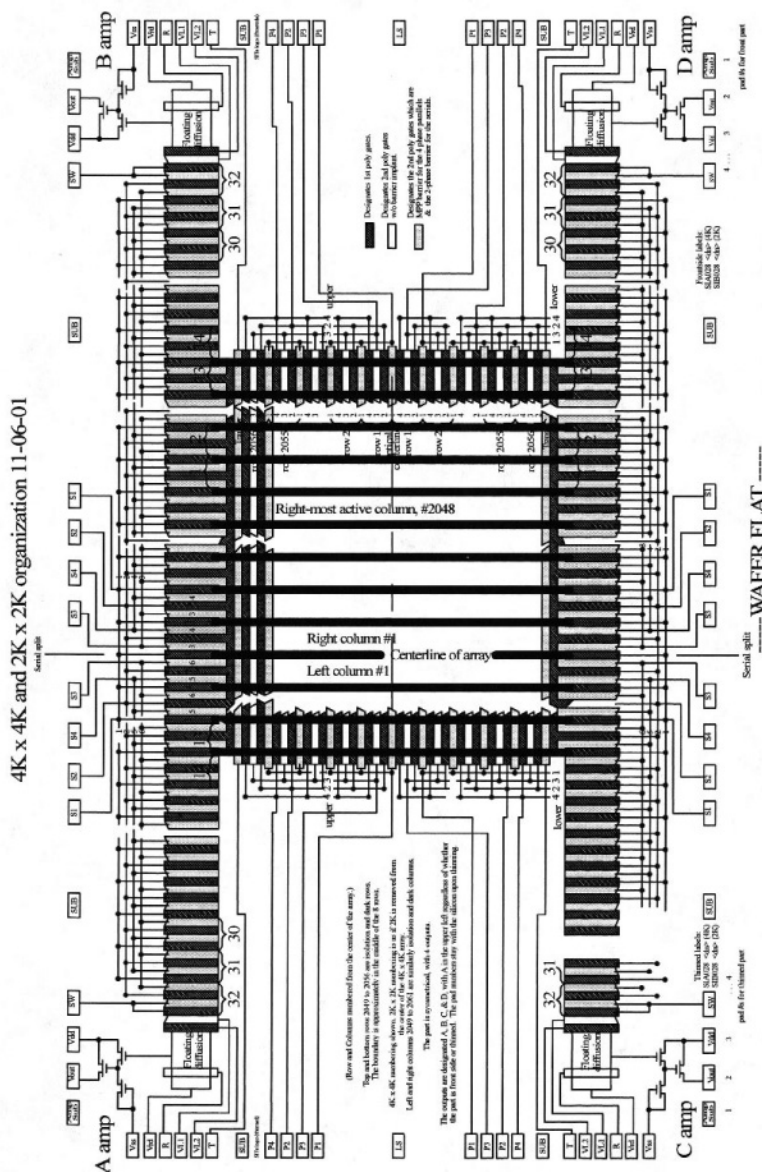


Figure 1. Functional diagram of the SI029A, the 4Kx4K CCD. The organization of the 2Kx2K device is similar.

2.2 Packaging

Figure 2 presents a photo of a front-illuminated 4Kx4K device in its package and a back-illuminated 2Kx2K device, also packaged, with a

standard unit of measure. The size of the $2K \times 2K$ chip is essentially the same as the SITe SI003A $1K \times 1K$ chip. The package is a black ceramic material with four rows of pins, two on each side of the package. Additionally, the package has bolt down holes to permit easy and intimate attachment of the device to the cold finger. A window is not normally supplied with the package, although the package normally supports such a cover.

The CCD is organized and laid out such that the device can be plugged in and rotated 180° without injuring the chip. Indeed, one need only permute the parallel clocks and the rotated device will function properly.

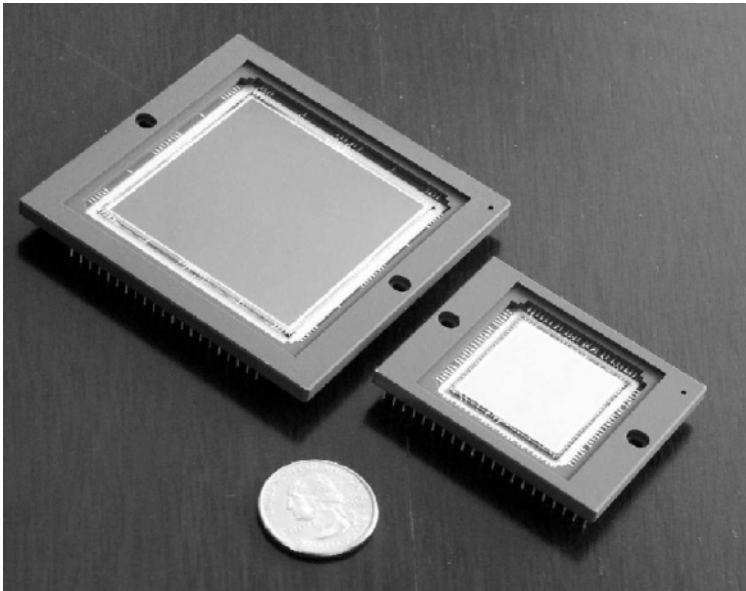


Figure 2. Photograph of the SI-029A and the SI-028A.

3. DEVICE PERFORMANCE

3.1 Electrical

A typical photon transfer curve is shown in Fig. 3. These data were taken in a high-speed camera running at 2.6 Mpix/sec using a thinned $2K \times 2K$ chip. The row shift time for this device was $4.7 \mu\text{sec/row}$ or approximately 210 Kpix/sec. At this speed, the full well was in excess of 160 Ke^- . Noise of the system plus device was $34 \text{ e}^- \text{ rms}$. The conversion sensitivity of the device in the high gain stage is approximately $6.8 \mu\text{V/e}^-$ with a standard deviation of $0.5 \mu\text{V/e}^-$ as measured at the output of the chip. The low gain state is achieved by applying a positive bias to the gate next to the output node such that its potential is higher than the reset potential.

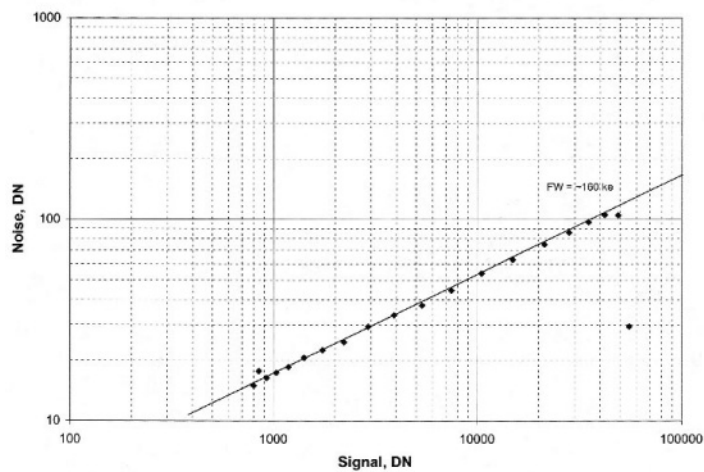


Figure 3. Photon transfer curve for 2Kx2K chip. Data taken at 2.6 Mpix/sec and 4.7 μ sec/row.

The effect is to increase the effective area of the output node, thereby increasing the capacitance of the node. In the low gain condition the gain is approximately one half the high gain value or 3.5 μ V/e⁻. Table 1 summarizes the performance and physical characteristics of these new devices.

Table 1. Performance summary.

Parameter	Value	
	SI-028A	SI-029A
Format	2Kx2K	4Kx4K
Dark ref. Columns	12 per side	
Dark ref. Rows	8 per half	
Clocking: Parallel	Four phase	
Serial	Two phase	
Amplifiers	Four, 2 stage source followers	
Lead-in pixels	32	
Sensitivity: High gain	6.8 \pm 0.5 μ V/e ⁻	
Low gain	3.5 μ V/e ⁻	
Noise	7.9 \pm 1 e rms at 50 Kpix/s and -45 $^{\circ}$ C	
Dark current	30 pA/cm ²	
CTE: Parallel	0.999988	
Serial	0.999966	
Full Well: Parallel	> 100 Ke ⁻	
Serial	400 Ke ⁻	
Cap./phase: Parallel	30 nF	120 nF
Serial	128 pF	256 pF
Row shift time	< 4 μ s/row	

3.2 Optical

Figure 4 exhibits an image of a resolution target taken with the 2K×2K device. The data were taken at -45°C and 50 Kpix/sec.

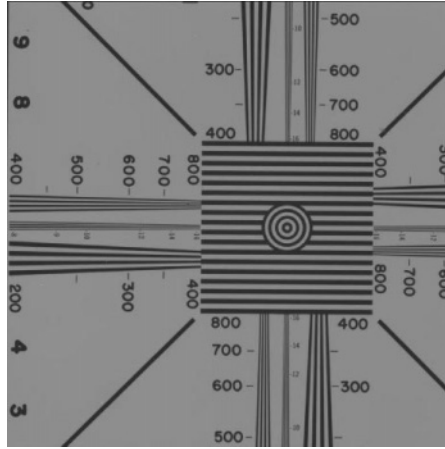


Figure 4. Low level image taken with a 2K×2K device.

The thinned devices are treated with an antireflection coating. The process is a modified version of the process developed at the University of Arizona by Mike Lesser and the flash gate process developed by Janesick, et al., at JPL [1]. There are two options: a single layer coating tuned to peak in the blue part of the spectrum at 400 nm, and a two-layer, wider band coating for the visible. Both coatings give high QE as illustrated in Fig. 5. The data extend to 200 nm but are uncorrected for quantum yield below 350 nm. Figure 6 presents data of quantum efficiency as a function of temperature for the two-layer coating. This coating is much more stable against variation in temperature than coatings supplied earlier. The single layer coating behaves in a similar fashion.

4. SUMMARY

SITe has produced a pair of large area, small pixel CCD sensors designed for high speed, scientific imaging applications. The devices have 2K×2K and 4K×4K formats with $12\ \mu\text{m}$ sq. pixels. The sensors are intended to be thinned and, coupled with the new AR coating process, have high quantum efficiency that is stable against changes in temperature. Front-illuminated versions of the devices are also available. High-speed camera testing shows good performance at 2.6 Mpix/sec and preliminary testing suggests that good performance can be achieved at 10 Mpix/sec.

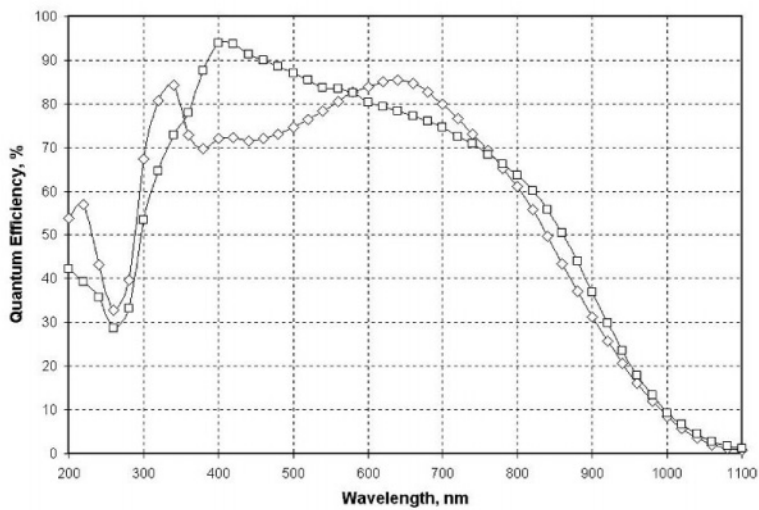


Figure 5. Typical quantum efficiency curves for two different AR coatings.

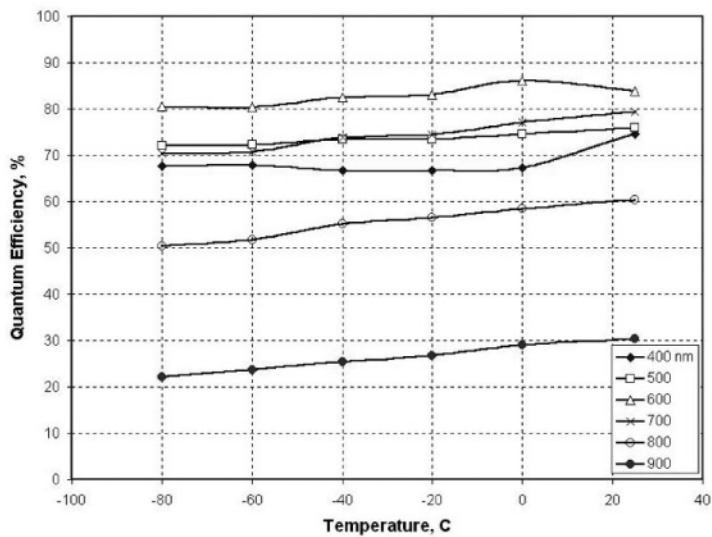


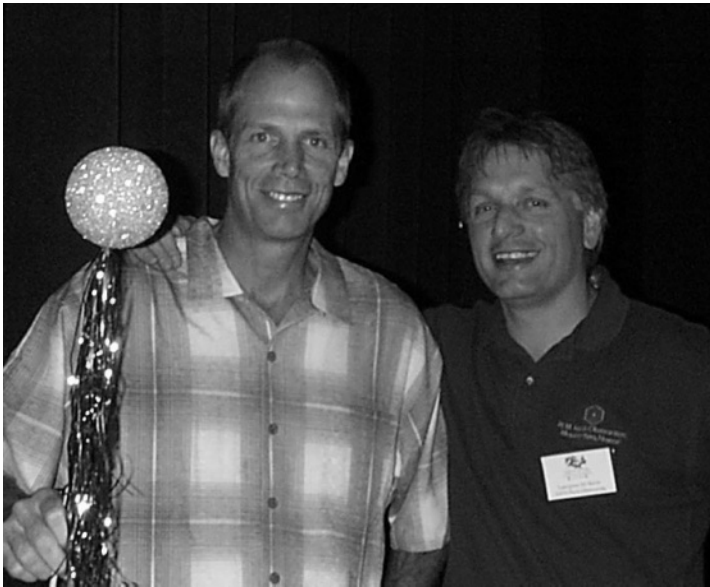
Figure 6. Quantum efficiency as a function of temperature for selected wavelengths.

5. REFERENCES

[1] Janesick, J.R., Elliott, T., Frascchetti, G., Collins, A.S., Blouke, M.M., Corrie, B., 1989, *Charge-coupled Device Pinning Technologies*, Optical Sensors and Electronic Photography, M.M. Blouke and D. Pophal, Editors, Proc. SPIE **1071**, p. 153.



A nerd's life. It doesn't get any better than this, does it? Peter Love, Guy Woodhouse and Ken Ando (left to right) on their way to Kealahou Bay (courtesy of G. Woodhouse).



Randy Campbell (left) wishes he could make his boss disappear with the flick of the wand.....tough luck, Jim's still here. Jim Beletic, unaware of the danger, moments before disappearing from the stage (he eventually came back at the gala dinner).

BROADBAND (200–1000 NM) BACK-ILLUMINATED CCD IMAGERS

Barry E. Burke¹, James A. Gregory¹, Andrew H. Loomis¹, Steven D. Calawa¹, Paul M. Nitishin¹, Thomas A. Lind¹, Michael J. Cooper¹, Douglas J. Young¹, Peter W. O'Brien¹, Bernard B. Kosicki¹, Gerald A. Luppino², and John L. Tonry²

¹Lincoln Laboratory, Massachusetts Institute of Technology, ²Institute for Astronomy, University of Hawaii

Abstract: *Improved and stable blue/UV quantum efficiency has been demonstrated on 2K×4K imagers using molecular-beam epitaxy to create a thin doped layer on the back surface. Quantum efficiency data on thick (40–50 μm) imagers with single and dual-layer anti-reflection coatings is presented that demonstrates high and broadband response. Measurements of the optical point-spread response show the devices to be fully depleted with good response across a broad spectrum, but interesting features appear in the near-IR as a result of deeply penetrating light being scattered off the surface structure of the CCD.*

Key words: *Charge-Coupled Device (CCD), molecular-beam epitaxy, Quantum Efficiency (QE), point-spread response*

1. INTRODUCTION

This paper describes recent work at MIT Lincoln Laboratory in collaboration with the U. of Hawaii to enhance the performance of large-area CCD imagers and to characterize these devices for use in astronomy. This collaboration began in 1994 between Lincoln Laboratory and a consortium of astronomy groups led by Gerald A. Luppino of the U. of Hawaii. The

focus has been the development of 2K×4K imagers (15 μm pixels), as well as technology developments for improved device performance. Among the latter is the development of thick (40–50 μm), back-illuminated devices for improved red response and reduced fringing, the orthogonal-transfer CCD, customized anti-reflection coatings, and blooming control. These have been described in the prior proceedings of this conference [1,2].

2. ENHANCED BLUE/UV RESPONSE

The challenges of making a back-illuminated imager with a high and stable Quantum Efficiency (QE) below 400 nm have been described in literature for more than two decades. The difficulty in this case is the extremely shallow penetration depth α^{-1} of the radiation ($\alpha^{-1} < 10$ nm from $\lambda = 200\text{--}360$ nm), which makes photoelectrons vulnerable to recombination losses at the back surface.

Two general approaches have been pursued to avoid this loss. One has been to grow a thin, low-temperature oxide layer on the back surface and deposit a metal that induces a negative charge in the oxide via chemisorption charging [3]. In the past, this method resulted in devices that required careful environmental control or periodic UV illumination to maintain stable response, though recent work by Lesser indicates that this problem has been overcome [3].

The other approach is to create a repulsive field by introducing a thin-doped layer on the back surface. What makes this method challenging is that: a) the doped layer must be introduced after the CCD is thinned, and b) doping of silicon must be carried out at elevated temperatures. In our previous work we described the use of a shallow boron implant followed by a pulsed laser anneal to activate the implant [1, 2]. The laser pulse, about 50 ns in duration, is sufficient to melt the silicon to a depth of about 100 nm, after which the molten silicon recrystallizes to form a p^+ layer. Since this layer is much thicker than the absorption lengths in the UV, most photoelectrons generated by these wavelengths are created in the non-depleted, field-free p^+ layer. Here the photoelectrons move by diffusion and hence are as likely to diffuse to the back surface as to the p^+/p^- junction, where the fields would propel them toward the front of the device. As a result, the internal quantum efficiency tends to be well below unity and to vary according to ambient conditions.

The epitaxial deposition of a thin p^+ layer on a CCD chip (as opposed to wafer) by a technique known as Molecular-Beam Epitaxy (MBE) was first described a decade ago [4], and the results showed that stable, near-unity internal quantum efficiencies could be achieved in the UV. We have applied

the MBE process to our 2K×4K imager wafers. The process begins with a fully processed, 150 mm CCD wafer which is then chemically thinned to about 40–50 μm except for a narrow rim around the perimeter. Though fragile, the wafer can be handled by the rim and is sufficiently robust to allow the required cleaning steps prior to epitaxial growth and subsequent mounting on a handle wafer. MBE growth is done at a wafer temperature of about 400 °C and consists of about 5 nm of heavily boron-doped silicon (roughly 37 atomic layers). The chosen growth temperature represents a compromise between the upper limit to which a wafer with aluminum metallization can be subjected and the fact that higher growth temperatures lead to higher quality layers. Nevertheless, the results to date suggest that layers of sufficient quality can be grown without causing device failures related to the metallization.

Figure 1 shows the resulting QE measurements at room temperature on uncoated back-illuminated devices processed with II/LA (ion implant/laser anneal) and MBE. For comparison, a calculated curve assuming reflection-limited response is shown as the dashed line, and shows that the MBE process produces essentially unity internal quantum efficiency. Note that the definition of QE used here is the ratio of *detected photons* (as opposed to detected electrons) to incident photons. This distinction is important for $\lambda < 300$ nm where the number of photoelectrons generated per absorbed photon is greater than one.

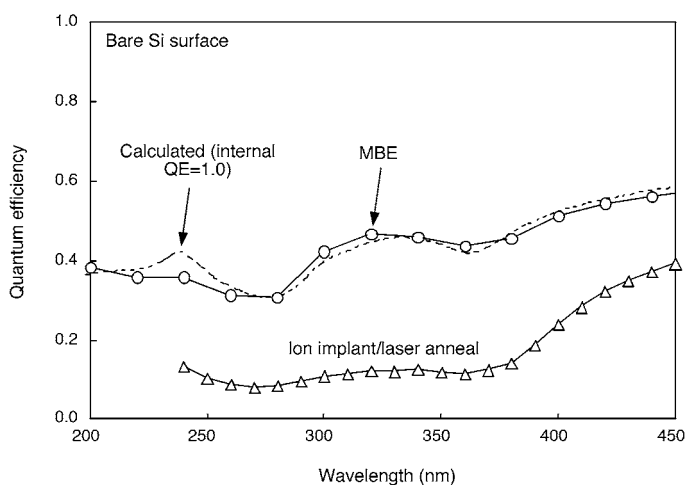


Figure 1. Measured quantum efficiencies at room temperature of a bare CCD with an MBE-deposited p^+ layer and a p^+ layer created by ion implantation and activated by a pulsed layer anneal. The calculated QE assuming unity internal QE is plotted for comparison.

Because of the historical experience of QE instability at UV wavelengths in earlier generations of back-illuminated CCDs, it is important to monitor

the performance of these devices over time. We have periodically measured the QE of a small (512×1024) test imager that resides on the same wafers as the $2K \times 4K$ devices for 13 months. Half of this device is coated with an antireflection coating of HfO_2 while the other half is uncoated.

Figure 2 shows measurements of the QE of both halves of the device over this period. The device has been stored most of the time in a nitrogen vented dry box, but has also been periodically placed in a vacuum cryostat for testing at low temperatures. No evidence of QE instability has been seen thus far under any test conditions.

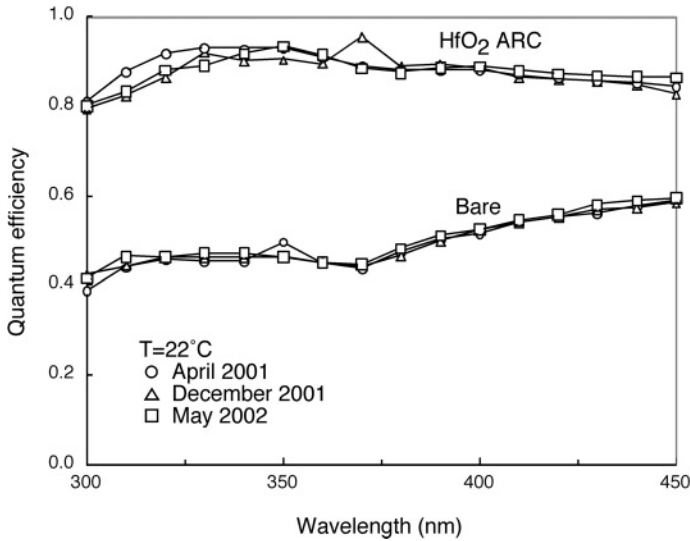


Figure 2. Measured quantum efficiency taken over a period of 13 months on a device, half of which is uncoated and the other half coated with a HfO_2 anti-reflection coating.

3. BROADBAND QUANTUM EFFICIENCY

In addition to extending the response down to 200 nm, we have also improved the near-IR response by using high-resistivity ($\approx 5000 \, \Omega \cdot \text{cm}$) p-type silicon. The depletion depths on non-thinned devices can readily exceed $50 \, \mu\text{m}$ under normal gate biases. This means that devices thinned to $<50 \, \mu\text{m}$ will be fully depleted, which is essential if good point-spread response in the blue is to be obtained. Our wafers are thinned to about $45 \, \mu\text{m}$, and as a result the QE is better and the fringing lower for $\lambda > 800 \, \text{nm}$ than that obtained from the typical device thicknesses of $10\text{--}20 \, \mu\text{m}$.

Figure 3 shows data on the QE versus wavelength for two MBE-treated devices, each with a different anti-reflection coating. For maximum UV/blue response we use a single layer of HfO_2 , in this case optimized for

about 330 nm. The other coating is a dual layer of HfO_2 and SiO_2 which is designed to give maximum response around 850 nm while giving up as little blue and UV response as possible. In previous work we had described a dual-layer coating for enhanced near-IR response consisting of TiO_2 and Al_2O_3 [2], but we found that these materials require special precautions in order to maintain stoichiometry during evaporation. Unless deposited in a high back pressure of O_2 they can be metal rich and optically lossy.

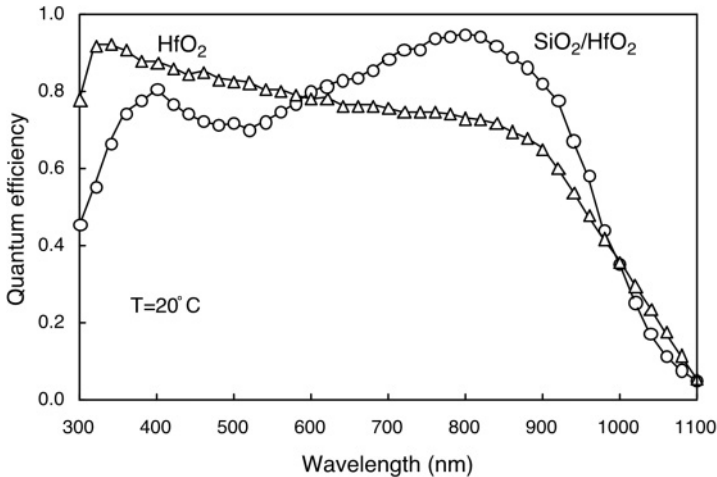


Figure 3. Measured quantum efficiency of MBE devices with two types of anti-reflection coatings.

The data of Figure 3 were taken at room temperature, but most astronomical observations are taken with devices at low temperatures. Because the bandgap of silicon increases with temperature, the long wavelength rolloff in the QE moves to shorter wavelengths as the temperature is reduced. This is shown in Figure 4, where the long-wavelength QE of a device with the dual-layer coating is plotted for three temperatures.

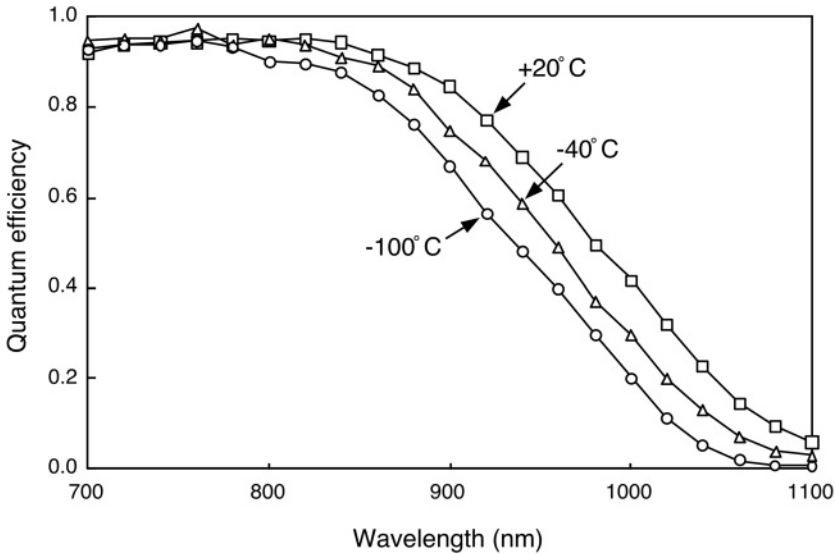


Figure 4. Measured quantum efficiency in the near IR for three temperatures.

4. POINT-SPREAD RESPONSE

An important characteristic of a sensor is the optical point-spread response, which is the device response to a small optical spot scanned over the pixel array. The point-spread response is particularly important for verifying a condition of full depletion, which is critical for minimizing lateral charge spreading and obtaining sharp images. A system for performing this measurement was recently described [5] in which a focused spot about 3 μm in diameter is stepped in a raster pattern over a small subarray of pixels while monitoring the signal from a given pixel at the center of the array. Figure 5 shows the results of one-dimensional scans through the center of a pixel both along and orthogonal to the channel direction at a wavelength of 430 nm. At this wavelength the photoelectrons are generated close to the back surface (the absorption length in silicon is $<0.3 \mu\text{m}$), and this provides a worst case test of charge spreading. This data, from a 47 μm thick imager, shows a smooth response with position, and the low signal levels measured when the spot is one pixel or more away indicate full depletion.

From the full two-dimensional scans we have found that when the spot is centered in a pixel, the charge collected by that pixel is 83 and 90% of the total signal for devices of 48 and 43 μm thickness. These results no doubt depend on the gate voltage levels, since these voltages determine the

strength of electric fields driving the carriers toward the CCD wells. For these measurements we held two of the three phases high at +4 V, while the third phase was held at -6 V.

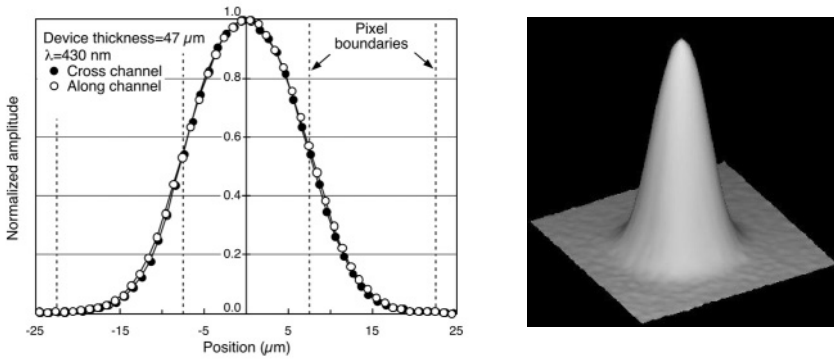


Figure 5. Point-spread response at 430 nm. (left) Curves of one-dimensional scans through the center of the pixel across and along the channel. (right) Surface plot showing full two-dimensional response.

In the near IR the point-spread response is at least as good as in the blue, as expected, but there are additional significant features in the response. These are best seen in the surface plots shown in Fig. 6, which were taken at a wavelength of 950 nm. The plot on the left is from a device which had a thin film of Al deposited on the CCD gates before the wafer was mounted on a handle wafer for thinning, while the device on the right had no such film. The purpose of the film was to explore improvements in the near-IR QE that result from more light being reflected back into the CCD.

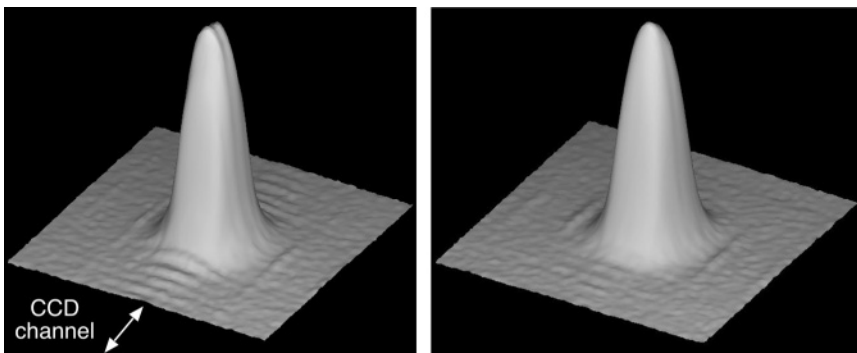


Figure 6. Surface plots of the optical response at 950 nm for a device with (left) and without (right) a thin-film metal mirror deposited on the CCD gates.

The interesting features in these plots are the ridges seen as the spot is scanned in neighboring pixels. Two prominent ridges can be seen running

parallel to the channel direction, and a series of closely spaced ridges can be seen perpendicular to the channel in front of and behind the main response lobe. These features give rise to what is termed the “red halo,” which are low-level spurious signals or cross-talk in adjacent pixels. The red halo is seen at wavelengths for which the light penetrates through to the device gate structure on the front.

The origin of these features can be understood with the aid of Fig. 7, where light is shown reflecting off the surface features of the device.

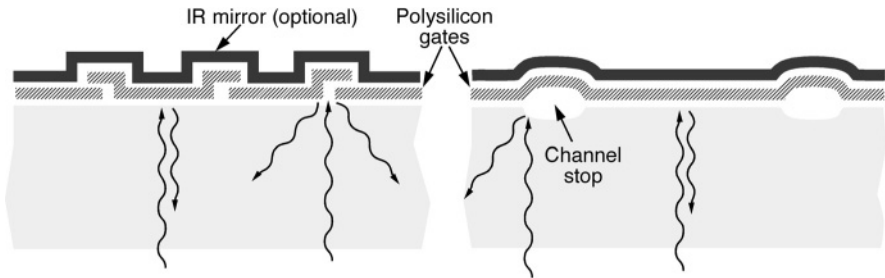


Figure 7. Illustration of the long-wavelength optical scattering off surface features on the front of the CCD.

Light that is incident normal to a flat portion of the interface will be reflected back in the direction of the incident illumination. However, the device has periodic surface structures that lead to scattering and reflections of the light at substantially different angles. Because the absorption lengths at the wavelengths involved are deeper than the device thickness and the fact that the device is much thicker than the pixel size ($15 \times 15 \mu\text{m}$), this scattered light can be absorbed in neighboring pixels. In the cross-channel direction this scattering results in “ghost images” of the channel stops parallel to the CCD channel. In the along-channel direction it results in effects arising from scattering off the polysilicon-gate gaps and gate-gate overlaps, and these can be seen more clearly in the device with the mirror.

It is clear from Fig. 6 that the mirror enhances this scattering (by about a factor of 2). In addition, we have found that the improvement in quantum efficiency with the IR mirror is marginal, and we therefore conclude that it is inadvisable to use this technique.

These results demonstrate the utility of point-spread-response data in diagnosing the optical performance of a sensor. This measurement is more appropriate in most astronomical applications where the images are point-like than the frequency-domain counterpart, which is the MTF or modulation transfer function. It is not likely that an MTF measurement could diagnose the source of the pixel crosstalk illustrated in Fig. 6.

5. ACKNOWLEDGEMENTS

The authors wish to thank Victor Dolat for testing, Kay Johnson for CAD layout of the devices, and Pete Daniels and Debbie Landers for packaging, as well as the many technicians in the Lincoln Microelectronics Laboratory (MEL) for the excellent device fabrication.

The Lincoln Laboratory portion of this work was performed under a Collaboration Program between MIT Lincoln Laboratory and the University of Hawaii Consortium. Opinions, interpretations, conclusions, and recommendations are those of the authors, and do not necessarily represent the view of the United States Government.

6. REFERENCES

- [1] B. E. Burke, J. A. Gregory, R. W. Mountain, B. B. Kosicki, E. D. Savoye, P. J. Daniels, V. S. Dolat, T. A. Lind, A. H. Loomis, and D. J. Young, 1998, *Large-area back-illuminated CCD imager development*, Optical Detectors for Astronomy, Kluwer Academic Publishers, Dordrecht, pp. 19-28.
- [2] B. E. Burke, J. A. Gregory, G. A. Luppino, J. L. Tonry, A. H. Loomis, C. C. Cook, D. J. Young, M. J. Cooper, and T. A. Lind, 2000, *CCD imager technology development at Lincoln Laboratory*, Optical Detectors for Astronomy II, Kluwer Academic Publishers, pp. 187-199.
- [3] M. Lesser and V. Iyer, 1998, *Enhancing back illuminated performance of astronomical CCDs*, Proc. SPIE, vol. **3355**, pp. 446-456.
- [4] M. E. Hoenk, P. J. Grunthaner, F. J. Grunthaner, R. W. Terhune, M. Fattahi, and H.-F. Tseng, 1992, *Growth of a delta-doped silicon layer by molecular beam epitaxy on a CCD for reflection-limited ultraviolet quantum efficiency*, Appl. Phys. Lett., vol. **61**, pp. 1084-1086.
- [5] T. A. Lind, R. K. Reich, W. H. McGonagle, and B. B. Kosicki, 1999, *Intrapixel response test system for multispectral characterization*, Proc. SPIE, vol. **3649**, pp. 232-238.



*Marooned.
(Courtesy G. Burley)*



"Your FPA is nothing...once I built one that was this big..." says Augustyn Waczynski to Gert Finger. The audience around shows signs of interest, bewilderment and desperation (right).

ORION: A 1-5 MICRON FOCAL PLANE FOR THE 21ST CENTURY

Albert M. Fowler¹, K. Michael Merrill¹, William Ball¹, Arne Henden², Fred Vrba², Craig McCreight³

¹NOAO, ²USNO Flagstaff, ³NASA Ames Research Center

Abstract: *The Orion program is a project to develop a 2K×2K infrared focal plane using InSb p-on-n diodes for detectors. It is the natural follow-up to the successful Aladdin 1K×1K program started in the early 90's. The work is being done at the Raytheon Infrared Operations Division (RIO, previously known as the Santa Barbara Research Center) by many of the same people who created the Aladdin focal plane. The design is very similar to the successful Aladdin design with the addition of reference pixels, whole array readout (no quadrants), two-adjacent-side buttability, and a packaging design that includes going directly to the ultimate focal plane size of 4K×4K. So far we have successfully made a limited number of hybrid modules with InSb detectors. In this paper we will describe the design features and test data taken from some of these devices.*

Key Words: *Complementary Metal Oxide Semiconductor (CMOS), focal plane, buttability, infrared*

1. INTRODUCTION

With funding support in late 2000 from the National Optical Astronomy Observatory (NOAO), the United States Naval Observatory (USNO), and NASA, we commenced a program to develop a 2K×2K InSb focal plane at RIO similar to the successful Aladdin 1K×1K program. The program was formally started in early 2001, and the first bare readouts were available for testing at RIO in late 2001. So far, we have produced four functional hybrid arrays using this short and, thus far, successful program. Most of the test data herein are derived from testing at RIO and by the Rochester University

group as NOAO still does not have control electronics to adequately run an Orion focal plane.

The design has several features, which have not appeared in any previous work and that we feel makes this device superior in many ways to Aladdin. The first is two-adjacent-side buttability and a module-packaging concept that leads directly to future 4K×4K focal plane applications. Second is the addition of several types of reference pixels for noise and uniformity correction. Other improvements include a single 2K×2K readout instead of a quadrant readout, and the use of blocked (stripe) rather than interleaved column readout.

The processing used for this design is 2 μm p-well CMOS, single Poly-Double Metal. From previous projects, we know using PMOS transistors for the analog circuitry will produce the lowest noise and highest performance at 30K. The use of double metal instead of the single metal used in the Aladdin program was a new aspect of the program. This was necessary because of the excessive line impedance and conversely long time constants that would develop if poly was used for the reset and enable buses. This change reduced the readout yield somewhat but not significantly.

2. DESIGN

2.1 Specifications

The first requirement of any program is a list of the specifications and goals for the project. Table 1 is a list of the Orion focal plane design goals and performance characteristics.

2.2 Packaging

The packaging concept used for Orion is a major change from the leadless chip carrier (LCC) concepts used in Aladdin or the Pin Grid package in use on other focal planes. There are two major motivations for this change. First, the detector is over 50 mm square and this required a thermally compatible and stable platform to prevent delamination of the indium bumps and cracking after multiple cryocycles. Second is the need for a package that is easily integratable into a larger 4K×4K focal plane. We believe the design we have chosen meets these goals. Figure 1 is a picture of the Orion focal plane module.

Table 1. Orion program specifications and goals

Format	2K×2K
Pixel Size	25 × 25 μm
Array Active Area	51.2 × 51.2 mm
Optical Fill Factor	> 98%
Architecture	Two Side Buttable (Adjacent sides) Designed to make a larger 4K×4K module 64 outputs : read out in stripes of 32 columns each Built in current source per output Read out as a single 2K×2K device
Readout Structure	Three transistor Single-Stage Floating Diffusion (SFD) Unit Cell P-well CMOS Control Logic On Chip Buffers for all clocks and control signals Control Logic - 2 phase shift registers
References	First (#1) and last columns (#2048) are reference columns Additional references on each output as follows: 1) reference, 32 data pixels 2) reference, 32 data pixels 3) 32 data pixels only
Reset Modes	Global (all detectors) Ripple (reset by row pairs)
Output Performance	1. 5 μsec per pixel Frame rate ~ 10 frames per sec
Detector Material	Backside-illuminated Thinned p-on-n InSb
Well Capacity	150×10 ³ e ⁻ at 0.5v applied bias
Read Noise	< 25 e ⁻ rms for Fowler 1 sampling
Dark Current	< 0.2 e ⁻ per sec/ pixel at 30 K
Quantum Efficiency	> 95% at 1.7 μm s
	Quarter wave AR coating at 1.7 μm s
Response	0.6 to 5 μm s with appropriate AR coating
Operating Temperature	25-35 K
Operability	Typically > 99.5%

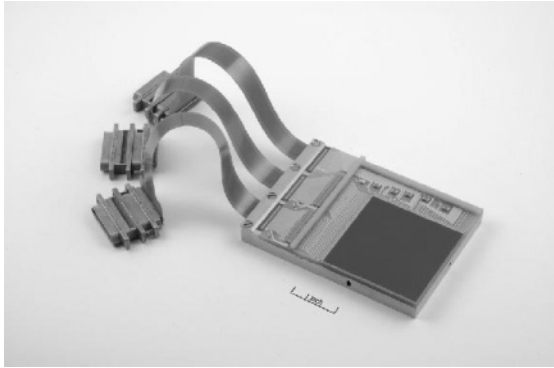


Figure 1. Orion focal plane module.

The base material is 6^+ mm of Invar36, which has been used to package CCD's for many years because of its thermal compatibility with silicon. Next, we bonded an aluminum nitride (AlN) motherboard to the pedestal (also used for the LCCs in the large focal planes). The motherboard approach was chosen so we would have electrical isolation from the metal pedestal, a place to route the wiring from the multiplexer chip to the edge of the module, and a place to mount filter capacitors and support components. In addition, it allowed us to mount the detector focal plane chip close to the edges for 2-side buttability and future 4K \times 4K modules. The electrical interface is made via 3-flat cables terminated in 37 pin Micro-D Metal connectors. These connectors were chosen because of their previous reliability in cryogenic applications.

Two 2.5 \times 0.6 mm bars surround the detector-silicon chip to provide a means to baffle the detector from outside light sources. The bottom of the pedestal has several threaded holes for mounting the module to a larger detector mount. In addition, there is one hole located at the optical center of the detector for maintaining alignment with respect to an instrument, if needed. For 4K \times 4K modules there are provisions for pins and corresponding holes in the side of the pedestal for alignment of multiple 2K \times 2K sub-modules.

The thermal compatibility with the silicon readout, flatness, and structural rigidity of the Invar36 pedestal results in a design which does not delaminate or crack during cooling. We have fabricated four complete focal plane modules and cooled some of them many times with no sign of delamination or crack development. Therefore we are satisfied that our design goals have been met. Figure 2 is a picture of a possible 4K \times 4K focal plane using the Orion 2K \times 2K modules.

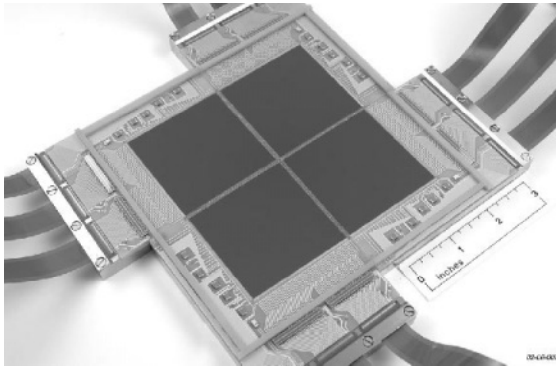


Figure 2. A possible 4K×4K focal plane using the Orion 2K×2K modules.

3. GENERAL READOUT ARCHITECTURE

This design has a number of features novel to large IR arrays. The first, is read out as a single 2K×2K array rather than in quadrants. In the past the quadrant design was used because of concerns about yield. These were put to rest during our experience in fabricating the Aladdin 1K×1K readouts. Also, this approach was required by the desire for two-adjacent-side buttability.

Next, we used a double metal process, as the continued use of poly for the larger chip would have created unacceptable time constants when resetting and addressing rows. We have continued to use the 2 μm p-well approach as this yields the lowest noise and minimizes the LED effects. Another feature of this chip is that it reads out in blocks of 32 columns to each of its 64 outputs rather than the interleaved columns used in the past. We did this to reduce the capacitance of the output bus and increase speed. Also, an output failure will only take out a small section rather than 64 individual columns scattered across the array.

Other changes are the addition of many different types of reference pixels in the readout data stream. We incorporated current sources for the output transistors on the module. Source resistors can also be used, but the current source provides the highest gain with output transistors, which should yield lower noise. We also incorporated a feature, which allows us, via a single control line, to shut down the output amplifiers during long integrations to eliminate any potential photon background effects.

are reset like the detectors, but they do not have the dark current and uniformity issues related to real detectors. Like the output references, the pixels in column 2048 are tied directly to the detector substrate bias. Both of these references can be used to remove row odd/even patterns or other non-uniformities along the row direction. The usefulness of the various references will have to be answered over time by the users. We feel some of the reference use will fall by the wayside in time.

5. OUTPUTS

The Orion chip has 64 outputs however, unlike previous designs where the columns are interleaved columns, this chip reads out in blocks of 32 columns per row. This was done for two reasons:

- The first and most important of these was the reduction of line capacitance loading due to the over 50⁺ mm size of this chip. Since the effective number of outputs for Orion (64) is half that of the Aladdin chip, it is important to preserve the 1.5 μ sec/pixel readout time. The unit cell must drive the column bus and the other 2047 diffusions on the bus, but now we have reduced the capacitance on the output bus to a minimum.
- The second reason was that if a failure of an output occurs, it only affects a 32-column-wide stripe rather than every 64th column across the whole array. We feel this is an improvement over previous approaches.

The output transistors are distributed across the whole width at the edge of the readout to reduce and distribute any emission from them. Because of the integral current source, which can easily be switched off by a single line, the output transistors can be shut down during long integrations to eliminate any photon contributions from them.

6. PERFORMANCE

6.1 Fabrication

To date, four complete hybrid modules have been fabricated. In all cases each yielded a very high operability but of course not without some problems. The major problem is what has been coined as PEDs (photon emitting defects) caused by shorts either between the detector and the readout or in the readout itself. Fortunately, a method of dealing with these defects was worked out during the Aladdin program and it does not cause us

much concern. The removal of each PED results in the removal of a 5×5 pixel area at the defect location.

6.2 Testing

Between RIO and NOAO, we have cryogenically cycled the four initial hybrid modules over 20 times with no evidence of cracking or pixel delamination. There is minimal test and performance data at NOAO because the required controller for the Orion test system is still being produced. We have been able to get a limited amount of noise data from the reference pixels, but the University of Rochester has been able to do more work in that area. This data shows that the Orion readout noise is slightly lower than the latest Aladdin devices. At NOAO, slow scan noise in the reference channels was $34 \mu\text{V rms}$ with Fowler 1 sampling and similar results were obtained by the University of Rochester. Rochester was also able to confirm that the noise decreases as expected with further Fowler sampling. In fact, they were able to achieve a noise level of $5 \mu\text{V rms}$ at 32 Fowler pairs. Since the Orion pixels are 85% of the Aladdin size, we can expect the read noise to be in the range of $<20 e^- \text{ rms}$. RIO, as well as NOAO, is hoping to achieve similar results in the near future.

We have run gain and linearity tests on this readout and the device has an overall gain of 0.75 and a linear operating range of over 1V. For these tests we used the integral output current source and a drain current (I_d) of $100 \mu\text{A}$. The linear range of the unit cell and output amplifier is adequate for a 1 V detector bias.

7. ACKNOWLEDGEMENTS

We want to recognize the extraordinary efforts of the Astronomy Team at Raytheon Infrared Operations. Their work, which involved going from concept to the delivery of the largest infrared focal plane in less than 18 months, is a great achievement. We also wish to acknowledge the financial support of Sidney Wolff of NOAO, NASA, and USNO, without whom this program would not have been possible.

PERFORMANCE OF 5 MICRON, MOLECULAR BEAM EPITAXY HgCdTe SENSOR CHIP ASSEMBLIES (SCAs) FOR THE NGST MISSION AND GROUND-BASED ASTRONOMY

James D. Garnett¹, Majid Zandian¹, Roger E. DeWames¹, Michael Carmody¹, John G. Pasko¹, Mark Farris¹, Craig A. Cabelli¹, Donald E. Cooper¹, G. Hildebrandt¹, J. Chow¹, John T. Montroy¹, Jose Arias¹, Jagmohan Bajaj¹, and Kadri Vural¹ and Donald N.B. Hall²

¹Rockwell Scientific Company, ²Institute for Astronomy, University of Hawaii

Abstract: *Low background applications place the most stringent requirements on detector material, requiring the lowest possible dark currents, highest quantum efficiencies, negligible image persistence (image latency or “ghosts”), high operability, and good uniformity. Rockwell Scientific’s MWIR ($\lambda_{co}=5\mu m$) MBE HgCdTe/CdZnTe consistently meets these stringent requirements due to a number of growth techniques unavailable to other MWIR materials. The first part of this paper focuses on the advantages offered by MBE HgCdTe on CdZnTe detectors. The second part focuses on the functional capabilities of our most recent multiplexers, the HAWAII-1RG and HAWAII-2RG. Finally, the paper briefly concludes with a look at the future of SCA control with Rockwell Scientific’s new NGST ASIC for control and digitization of the HAWAII-RG series multiplexers.*

Key words: *HgCdTe, multiplexer, Readout Integrated Circuit (ROIC), Next Generation Space Telescope (NGST), Application Specific Integrated Circuit (ASIC)*

1. INTRODUCTION

Over the last few years, molecular beam epitaxy grown mercury cadmium telluride on cadmium zinc telluride substrates (HgCdTe MBE on

CdZnTe) has proven to be the highest performance MWIR (1-5 μ m) detector material for low background applications compared to any other MWIR material, including the historical “standard,” indium antimony (InSb).

Low background applications place the most stringent requirements on detector material, requiring the lowest possible dark currents, highest quantum efficiencies, negligible image persistence (image latency or “ghosts”), high operability, and good uniformity. Rockwell Scientific’s MWIR MBE HgCdTe/CdZnTe consistently meets these stringent requirements due to a number of growth techniques unavailable to other MWIR materials, either grown as a boule and sliced, grown by liquid phase epitaxy (LPE), or even grown by MBE on alternative substrate materials.

The first part of this paper focuses on the advantages offered by MBE HgCdTe on CdZnTe detectors. The second part focuses on the functional capabilities of our most recent multiplexers, the HAWAII-1RG and HAWAII-2RG. When MBE HgCdTe on CdZnTe is hybridized to a state-of-the-art “HAWAII” series multiplexer, the sensor ship assembly (SCA) combination results in one the finest sensor chip assemblies available. Finally, the paper briefly concludes with a look at the future of SCA control with Rockwell Scientific’s new NGST ASIC for control and digitization of the HAWAII-RG series multiplexers.

2. DETECTOR ARCHITECTURE

Rockwell Scientific’s MBE is grown in a double layer planar heterstructure (DLPH) architecture, illustrated in Fig. 1.

The growth on the CdZnTe substrate begins with the bulk HgCdTe, which represents the active absorbing layer of the detector structure. This bulk material is grown as n-type with indium doping. The cut-off of the bulk material is determined by the mole fraction (x) of Cd. The cut-off of HgCdTe is tuned by adjusting the value of x in the $\text{Hg}_{(1-x)}\text{Cd}_x\text{Te}$ composition; the smaller the fraction of x , the longer the cut-off wavelength. After the bulk HgCdTe is grown to the desired thickness, the layer is capped off with a thin, higher bandgap energy composition ($x_{\text{cap}} > x_{\text{bulk}}$) layer. The higher bandgap energy composition reflects minority carriers ($\text{Force} \propto -\partial E_{\text{gap}}/\partial z$, where z is the dimension in the growth direction, normal to the substrate plane) away from the frontside.

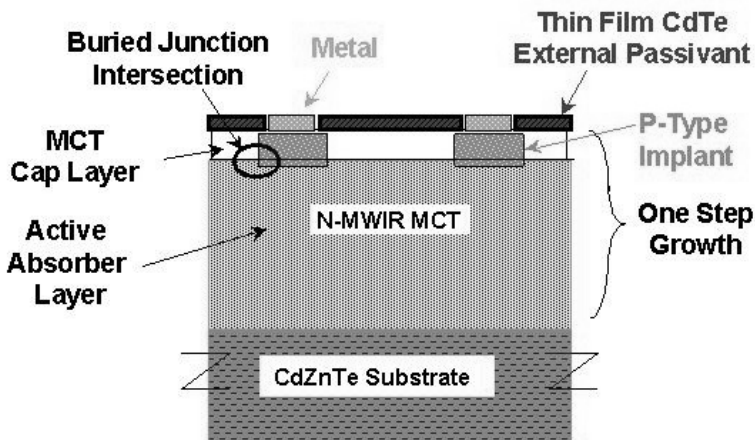


Figure 1. Detector cross section of the double layer planar heterostructure (DLPH) grown by MBE HgCdTe on CdZnTe. The base and cap layer are doped with indium. The p-n junction is formed by arsenic implantation and passivated with CdTe.

This greatly reduces potential problems associated with frontside trapping. In addition, because of the exacting control of the bulk growth provided by molecular beam epitaxy, a compositional gradient is routinely built into the bulk material that also drives the minority carriers away from the backside. This gradient improves crosstalk, quantum efficiency, intra-pixel sensitivity, and potential problems associated with backside trapping. The ability to obtain these very low defect $\text{Hg}_{(1-x)}\text{Cd}_x\text{Te}$ layers has been previously discussed and presented in earlier papers [1-3].

After detector growth, the detector array is defined by processing the detector layer into a chosen pixel format by creation of p-type implants arranged in an $n \times m$ matrix with a given pixel pitch. The p-type implants now create the p-n junctions that define the individual pixels. The p-type “buried” junction pixels are defined by arsenic ion implantations. The junction is called “buried” because the majority of the implant resides in the capping layer of the structure with only a small volume intersecting the bulk n-type material. The detectors are completed by MBE deposition of a frontside CdTe passivation layer. Contact is made to the p-side of the p-n junction with metal deposition. Indium bumps are evaporated onto the metal contacts and the detector array is ready for bump bonding to a matching silicon readout array, as illustrated in Fig. 2. The indium contacts provide the electrical connection that allows the detector photocurrent to be integrated and sensed by the silicon readout as an equivalent voltage (transimpedance amplification) and eventually multiplexed to the outside world. For a $2K \times 2K$ array, over 4 million individual indium bumps are bonded together.

The major advantage of molecular beam epitaxy HgCdTe on CdZnTe over all other detector growth techniques is its ability to “bandgap” engineer the growth of the detector. As the detector is grown on the substrate, the detector process parameters can be monitored in situ and adjusted real time to create the desired detector architecture with precise and repeatable control. “Bandgap” engineering allows exact definition of the epi thickness, doping profile, compositional structure, and capping layer of the detector. By growing the MWIR HgCdTe on near perfectly lattice matched CdZnTe, detectors are produced with the lowest levels of dislocations and defects of any MWIR detectors in the world today. This produces the lowest dark currents, and virtually no problems associated with persistence due to the trapping of photo-generated minority carriers by defects and dislocations.

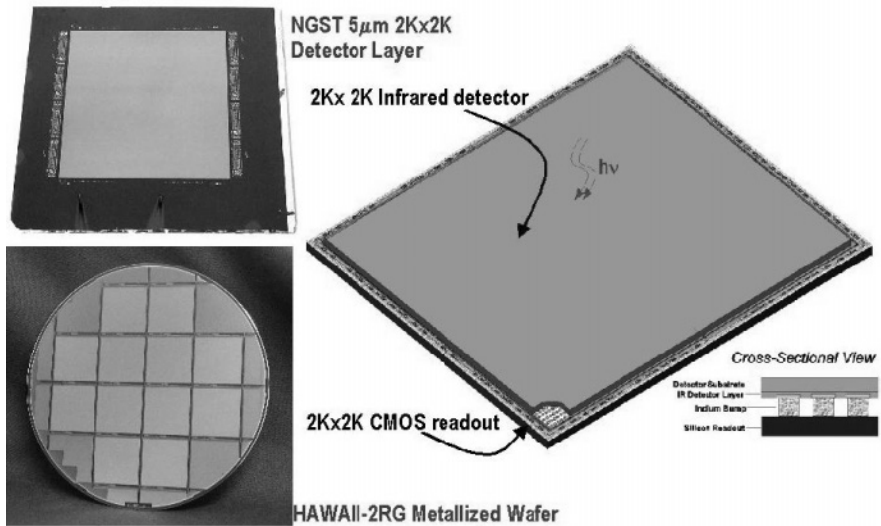


Figure 2. The hybrid sensor chip assembly consists of bonding a detector array to a matching silicon array via indium bump contacts. This figure shows the hybridization components for the NGST 2048x2048, 5 μm MBE HgCdTe SCAs.

3. DETECTOR EVALUATION METHODS

Detector performance is evaluated before producing hybrid assemblies (see Fig. 2 above) by testing variable area test diodes processed on the same detector layers, or wafers, as the detector arrays themselves.¹ These process

¹ The silicon readout die are also evaluated before hybridization via wafer probing both at initial receipt of the wafers from the silicon foundry and after backend processing, which evaporates the indium bumps onto the individual pixel “unit cells” of each readout die.

evaluation control (PEC) diodes or chips are diced from the detector layer, mounted and wire bonded in leadless chip carriers, and tested to assess the quality of the grown and processed layer.

PEC testing includes current versus voltage (I-V) characterization of the individual diodes and spectral quantum efficiency (QE) measurements. The functional dependence of the current versus diode bias voltage is an indicator of the goodness of the diodes. The QE spectral provides the detector layer cut-off wavelength and the possible presence of traps or dislocation problems through the relative change in QE with wavelength.

Analysis of the slope of the I-V curve in forward bias provides information on the dark current mechanisms present in the diode. This is a very useful technique because the forward bias current dependence is given by the simple empirical formula,

$$I \propto \exp(eV_{fb}/(nkT)) \quad (1)$$

where e is the electronic charge, $V_{fb} > 0$ the forward bias voltage, n a “mechanism parameter” discussed below, k Boltzmann’s constant, and T the temperature of operation. Forward bias operation provides an exponentially amplified look at the dark current, which insures that the dark current measurement is well above test set limitations.

The ultimate dark current performance is set by diffusion-limited performance, the most fundamental dark current mechanism.² The other mechanisms can, in principle, all be reduced or eliminated by appropriate device design or through the elimination of surface and bulk defects. Diffusion current is the thermally driven creation of electron-hole pairs in the bulk material (in both the n-type and p-type regions, but usually dominated by the n-type bulk since the p-type is doped much higher than the n-type and the thermal generation rate is inversely proportional to the doping). In forward bias, the slope of the logarithm of the current versus the bias voltage is given by $e/(nkT)$. For diffusion dominated dark current, $n = 1$, and for generation-recombination (g-r) currents, the slope is given by $n = 2$ (for mid-gap trapping states). If the measured “slope” value n deviates from unity, it is indicative of non-ideal behavior, implying a significant trap contribution. For tunneling or surface leakage currents $n > 2$, typically ~ 3 -5. Typically, MWIR diodes operate at relatively high temperatures, *e.g.*, greater than 150 K, are dominated by the diffusion dark current and only start to show deviations as the temperature is dropped below ~ 100 K. As

² Since the theoretical limit for ideal dark current performance is set by the diffusion current, with $n=1$ the “ideal” diffusion limited dark current, n is often referred to as the “ideality” factor. Values of n greater than 1 represent deviations from the ideal dark current limit.

diffusion and g-r currents become competitive at the lower temperatures the value of n lies somewhere between 1 and 2.

The overall quality of the diode under reverse bias, the actual bias for operation of the detector arrays, is determined by the dependence of the reverse bias current. Ideal diode behavior has a flat (constant) current versus reverse bias, whereas non-ideal behavior shows a soft breakdown with approximately linearly increasing (negative) dark current versus reverse bias³ or “abrupt” breakdown with a dramatic increase in dark current over a very small (~ 10 mV reverse bias change) variation in reverse bias. Both of these latter scenarios are indicative of poor dark current behavior of the diode due to excess currents. Figure 3 is illustrative of these three I-V characteristics.

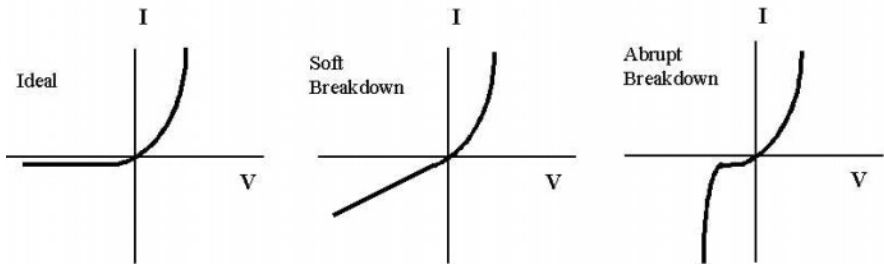


Figure 3. Typical I-V curve characteristics showing ideal diode behavior, soft breakdown under reverse bias and abrupt breakdown under reverse bias.

Finally, the RoA product (product of dynamic impedance at zero bias with junction area⁴ can be calculated for the slope of the I-V curve near zero bias. This product provides an indication of quality of the diode, with large RoA products implying very low dark current devices for a given temperature. From the RoA product, the saturation diffusion current in reverse bias can be estimated.

Unfortunately, at very low temperatures, this very small current cannot simply be read off the I-V graph in reverse bias. At these low dark current levels other current mechanisms, such as “shunt” resistance currents (with

³ G-R dominated dark currents will actually show a natural “soft” breakdown with reverse bias because the magnitude of the g-r current depends on the detector junction depletion width, which itself increases with increasing (negative) reverse bias.

⁴ For smaller area diodes it is necessary to substitute the “optical” area of the diode rather than the physical junction area. This is because for small area diodes the diffusion length of the minority carriers, which defines the length outside the depletion region from which charge carriers can be collected, becomes a significant fraction of the diode area.

Rshunt < Rdet) or photo-currents which result from small light leaks in the test dewars,⁵ dominate due to test set limitations.

Once the RoA is accurately calculated, the magnitude of the current density can be estimated for diffusion limited behavior under reverse bias saturation from

$$J_{diff} = (kT/e^-)/(RoA) \quad (2)$$

From this current density, the estimated diffusion limited dark current for the detector array pixels is calculated by $I_{diff} = A_{pix} \cdot J_{diff}$, where A_{pix} is the pixel area.

The PEC I-V characteristics are analyzed at different temperatures, which provides insight into when and what non-ideal dark current behavior becomes important as the detector is cooled. The best detectors show diffusion-limited behavior at the lowest temperatures. As mentioned previously, good detector diodes show diffusion-limited behavior above ~120-150 K and then, depending on the quality of the detector, show deviations as the temperature decreases.

The spectral QE data provides the cut-off wavelength for the detector layer as well as the uniformity when measured on several PECs located all around the detector array. The relative QE versus wavelength provides information on the quality of the back and front-sides of the detector. The overall magnitude of the QE provides information about the diffusion length and hence the quality of the bulk material (in terms of lifetime and trap density). Ideally, one looks for a relatively flat QE versus wavelength. At shorter wavelengths, where the photons are absorbed much closer to the backside of the diodes, a drop in QE is indicative of traps and dislocations.⁶ One also looks for a sharp fall-off in QE versus wavelength near the cut-off. A slowly decreasing or “soft” slope is indicative of process non-uniformities and/or a large number of traps located near the conduction band edge. For MWIR HgCdTe, the theoretical maximum QE for non anti-reflection coated material is somewhere near 74-78 % (it is somewhat process dependent).

⁵ Dr. Majid Zandian, Rockwell Scientific Company, has recently pioneered a technique of “ganging” a large number of high quality diodes from the same detector layer to overcome these low temperature limitations by effectively magnifying the total dark current of the multiple diodes to a level above the test set limitations.

⁶ This is not always the case, since there are situations where a drop in QE at shorter wavelengths is part of the detector design. We are not talking about such detectors in this paper.

4. MWIR DETECTOR AND SCA PERFORMANCE RESULTS

4.1 Dark Current

For NASA's Next Generation Space Telescope (NGST) technology demonstration program, a large number of detector layers were grown with cut-offs near $\sim 5.0 \mu\text{m}$ at 77 K. The cut-off at the NGST operational temperature for HgCdTe material, 37 K, is longer by $\sim 0.3\text{-}0.4 \mu\text{m}$.⁷ All the layers grown in the last two years, after we had tuned the appropriate growth technique, show the same consistent PEC characterization results, spanning five detector lot runs and consisting of over 20 individual detector layers. For the 1024×1024 format we processed eleven $5\text{cm} \times 5\text{cm}$ layers, each layer containing 4 detector arrays, and for the 2048×2048 format we processed ten $6\text{cm} \times 6\text{cm}$ CdZnTe substrates, each layer containing 1 detector array. To date, we have characterized over one dozen 1024×1024 SCAs hybridized and tested for the NGST demonstration program and we have just begun to hybridize our first 2048×2048 SCAs. Figure 2 above shows a representative $6\text{cm} \times 6\text{cm}$ CdZnTe substrate with $5 \mu\text{m}$ MBE HgCdTe grown and processed into a $2048 \times 2048 \times 18.0 \mu\text{m}$ pixel format.

Representative I-V curves are shown in Fig. 4 and 5.

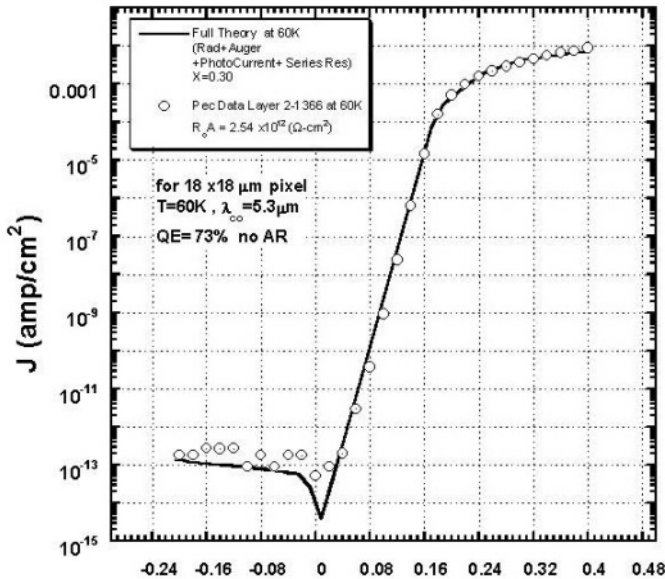


Figure 4. I-V curve for PEC data from layer 2-1366 at 60 K. Current density is plotted as the absolute value current density, so negative currents in reverse bias appear positive on this graph.

⁷ For MWIR HgCdTe, the material bandgap decreases with decreasing temperature.

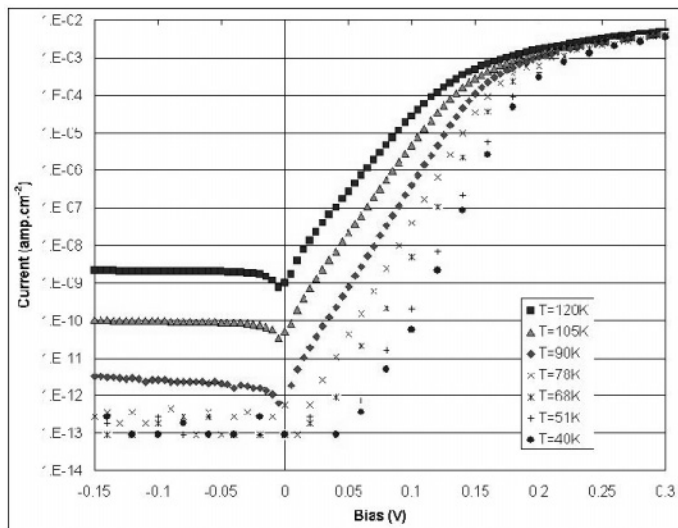


Figure 5. I-V curves versus temperature for the same layer shown in Fig. 4 above.

These curves clearly show the stunning performance of Rockwell Scientific's MWIR HgCdTe. Diffusion limited behavior is seen throughout the forward bias region with no indication of a break in the $n \sim 1$ slope; furthermore, this ideal detector behavior is maintained all the way down to 60 K. Below this temperature there is a slight indication of non-diffusion dark current noticeable only at the lowest biases and temperatures. The most likely mechanism for this current is tunneling.

The layer associated with Fig. 4 is processed in a 1024×1024 format detector array, grown on $5\text{cm} \times 5\text{cm}$ CdZnTe substrate. The test data in Fig. 4 are the circles and the black curve is a theoretical fit to the data. An RoA value of $2.5 \times 10^{12} \Omega\text{-cm}^2$ translates into a detector array current of ~ 0.04 e-/sec at 60 K. Note that the reverse bias saturation current is higher than the actual dark current of the detector. This is due to the lack of light tight dewar out to $5 \mu\text{m}$; therefore, photo-current was included in the theoretical calculation.⁸

The data in Fig. 5 show the remarkable diffusion limited behavior down to about 60 K. The current densities in reverse bias are flat as expected for good devices. Below about 80 K, the reverse bias dark current is photo-current limited and doesn't represent the actual reverse bias current density. The rollover in current at high forward bias is expected and is due to series resistance of the contacts to the diode.

⁸ For routine, production PEC testing the dewars are designed for rapid turnaround to provide basic detector layer quality information. Ultimate dark current performance is tested on the SCAs in custom-designed, light tight SCA dewars.

The reverse bias characteristics are flat and the extracted RoA's versus temperature shown in Fig. 6 are the highest RoA MWIR values in the published literature. Assuming diffusion limited dark current, the implied dark current level for Rockwell Scientific's 18.0 μm pixel arrays is less than 30 e^-/sec at 77 K for measured median RoAs in excess of $5 \times 10^9 \Omega\text{-cm}^2$. And measured (median) RoAs near $2.5 \times 10^{12} \Omega\text{-cm}^2$ at 60 K, imply pixel dark currents below 0.1 e^-/sec .

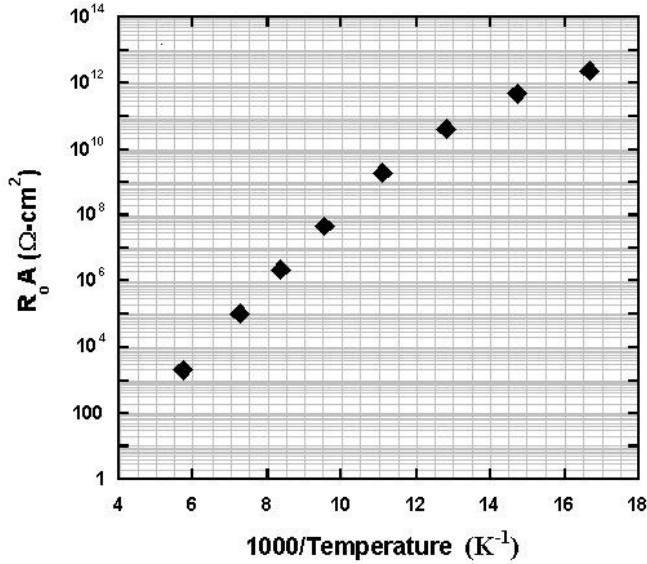


Figure 6. RoA values versus inverse temperature showing the excellent performance of 5 mm MWIR MBE HgCdTe on CdZnTe.

Beyond about $1\text{E}+09 \Omega\text{-cm}^2$, the PEC diodes must be “ganged” together to overcome test set limits. This allows the evaluation of PEC diodes to extend down into the sub-77 K regime and confirm the high quality of the grown detector layers.

These amazing detector dark current values predicted from the PEC test data are corroborated by hybridized SCA data shown in Fig. 7. Figure 7 shows dark current versus inverse temperature (1000/K) on a log-linear scale.

As with forward bias operation, in reverse bias operation the saturation current shows an exponential dependence that also contains the “mechanism” parameter n , shown in Equation (1). In this case

$$I \propto \exp(-E_{\text{gap}}/(nkT)) \quad (3)$$

where E_{gap} is the bandgap of the detector material. The linear slope in the logarithm of dark current versus $1/T$ in Fig. 7 is very clear and allows an easy extraction of the slope factor n .

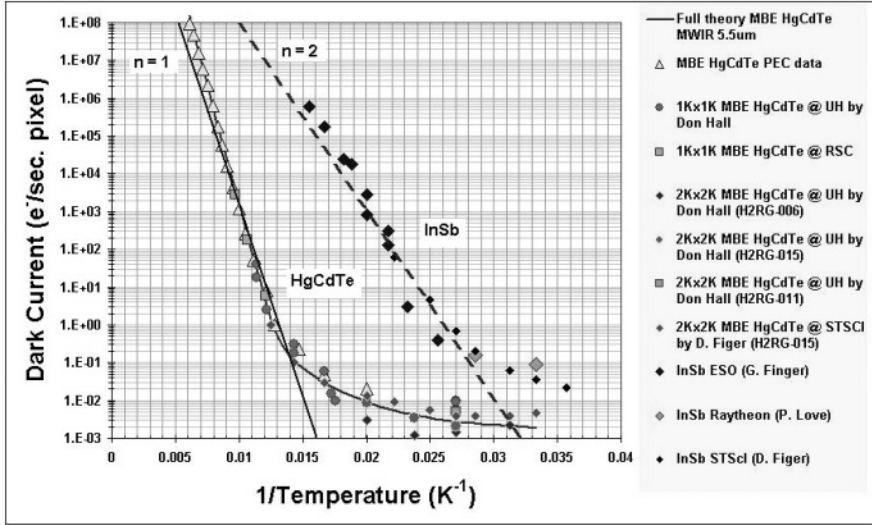


Figure 7. Comparison of dependence of dark current on temperature between MBE grown MWIR HgCdTe SCAs and the best reported values for InSb arrays. HgCdTe 1024x0124 arrays with 18x18 μm pixels, whereas InSb arrays are 27x27 μm pixels for the 1024x1024 arrays and 30x30 μm pixels for the 256x256 arrays. HgCdTe cutoff=5.3 μm .

As can be seen in Fig. 7, the HgCdTe data follows a near perfect $n = 1$ slope, whereas InSb, the other competitive MWIR material, follows an $n = 2$ slope, as measured by Dr. Gert Finger at ESO [4]. From this graph, it is clear that InSb is dominated by g-r currents, driven by mid-bandgap traps, which lead to higher dark currents compared to HgCdTe for any given temperature down to about 30 K. Below 30 K, data does not exist for HgCdTe⁹. Below ~ 40 K, 5 μm MBE HgCdTe dark current levels off to a constant level on the order of a few $\text{e}^-/1,000$ sec. This dark current is probably due to surface leakage or a tunneling mechanism (e.g., band-to-band) since it is relatively temperature independent.

The point of both of this graph is to show that 5 μm HgCdTe shows superior dark current compared to InSb for any given temperature down to

⁹ Since MBE HgCdTe easily meets the stringent dark current needs for the NGST mission well above the 30 K minimum operating temperature for the NGST 5 μm detector bands, there is no need to test below this lower temperature limit. Below 37 K the HgCdTe dark current levels off to a few electrons per thousand seconds.

about 30 K. This is understood from the fact that HgCdTe dark current is diffusion limited while InSb dark current is g-r limited. Both materials have demonstrated sub-10 $e^-/K\cdot sec$ level, InSb at a temperature below 30 K and HgCdTe at temperatures below 40 K. But the focal plane array data for 5 μm MBE HgCdTe dark currents are *consistently* measured at the $\sim 10 e^-/K\cdot sec$ level below 40 K.

The situation for large format 1024 \times 1024 5 μm MBE HgCdTe is impressive: dark currents well below 0.01 e^-/sec (36 $e^-/hour$) at temperatures from ~ 30 to 40 K operation have been measured for 13 of 15 tested 1024 \times 1024 MWIR HgCdTe SCAs. At the time this paper was written (August, 2002) our first 2048 \times 2048 SCA had been hybridized and showed a mean dark current below 0.01 e^-/sec at 37 K [5].¹⁰

4.2 Quantum Efficiency and Spectral Response

The PEC diode spectral responses are measured with a Fourier transform infrared spectrometer and the 50% spectral cutoff wavelength (λ_{co}) is used to determine the energy gap of the HgCdTe. The spectral response for these devices is near classical. A typical spectral response curve for a device with λ_{co} of 5.14, 5.36, and 5.44 μm at 78, 40, and 30 K, respectively, is illustrated in Fig. 8. Note that the cutoff wavelength is sharp at all temperatures and corresponds well to the designed HgCdTe composition of the epilayer.

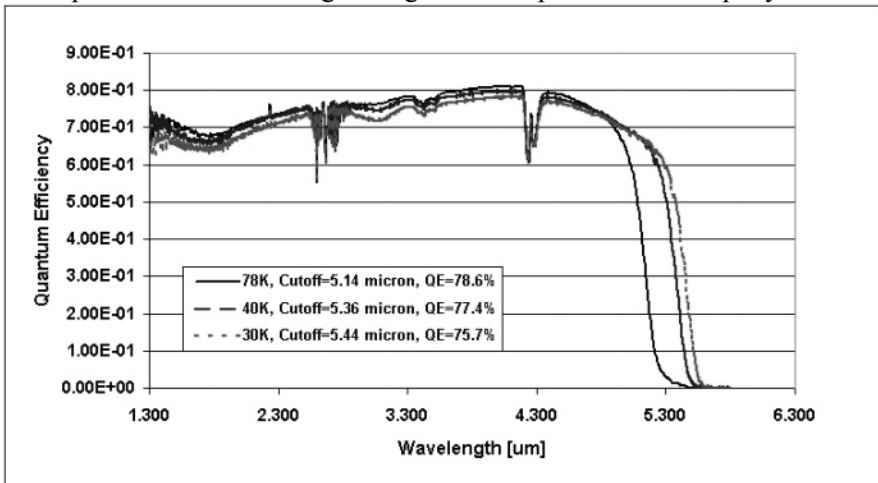


Figure 8. Spectral response and narrow band filter QE measurement of MWIR 1024 \times 1024 array process evaluation control (PEC) chips at three different temperatures of 78, 40, and 30 K. The various dips in the relative response near 2500 nm and 4200 nm are absorption features of H₂O and CO₂. The PEC chips are not anti-reflection coated.

¹⁰ Due to the publication date of this paper, some of that 2Kx2K data has been included in the data in Figure 7.

The relative QE is tied to an absolute value with a narrow band filter measurement taken at $3.5\ \mu\text{m}$ with a calibrated, high temperature blackbody source. The absolute QEs for all of the devices measured are all consistently above 70 %. The spectral response is also relatively independent of device operating temperature from 78 K down to 30 K.

Rockwell Scientific has also developed substrate removal of HgCdTe/CdZnTe epilayers at the SCA level and subsequent passivation of the backside of the bare HgCdTe. Removal of the CdZnTe substrate permits detection of visible photons, allowing the useable range of MWIR HgCdTe SCA wavelength detection to range from $0.4\text{--}5.5\ \mu\text{m}$. We have measured dark current, QE, operability, and uniformity on almost half a dozen 1024×1024 MWIR HgCdTe arrays, two devices both prior to and after substrate removal and again after final backside passivation. No detectable change or degradation in performance of these SCAs was observed. Full spectral scans for substrate removed SCAs only exist at the present time on SWIR ($\lambda_{\text{co}} \sim 2.2\text{--}2.5\ \mu\text{m}$) HgCdTe devices that pioneered the substrate removal technology on other programs. Those spectra show very flat spectral response from $\sim 0.4\ \mu\text{m}$ to λ_{co} . The ability to develop anti-reflection coatings that allow the QE of the MBE HgCdTe SCAs to exceed 80 % is a well-developed capability within the thin films optics group at Rockwell Scientific. Figures 9 and 10 show a MWIR SCA delivered under NASA's Deep Impact program with a $1\text{--}5\ \mu\text{m}$ anti-reflection coating.

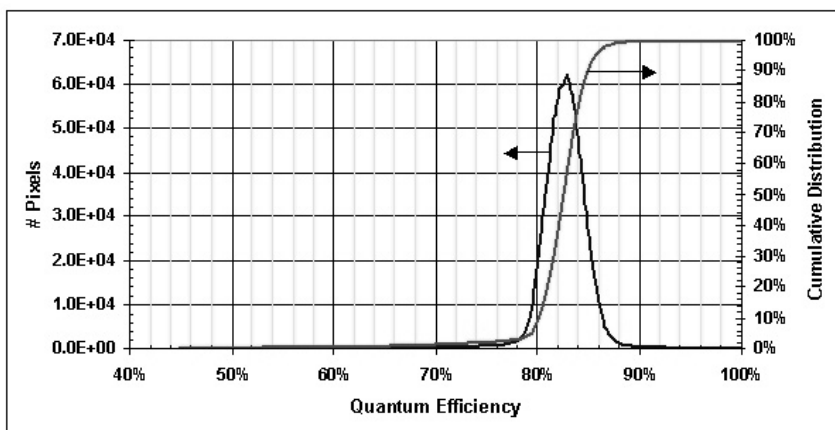


Figure 9. Histogram for an anti-reflection coated $4.8\ \mu\text{m}$ MBE HgCdTe SCA hybridized to the HAWAII-1R ROIC.



Figure 10. Responsivity gray scale for an anti-reflection coated 4.8 μm MBE HgCdTe SCA hybridized to the HAWAII-1R ROIC.

This image is taken in K-band (2.1-2.4 μm). Mean QE is 82.6% and operability is $> 99.4\%$. The dark border around the greyscale image is the embedded reference pixels (see Fig. 10).

Table 1 below summarizes the PEC results for the most recent layers grown for the NGST technology demonstration of 2048 \times 2048 detector arrays. These layers are grown on 6 cm \times 6 cm CdZnTe substrates. All the layers show excellent cut-off wavelength and thickness uniformity.

Table 1. NGST technology demonstration 6 cm \times 6 cm layer inventory. All of the layers have been processed into 2048 \times 2048 detector array formats with 100% yield.

Lot #	Wafer ID	λ_{co} @ 77K	QE @ 77K	Median RoA @ 77K
		[μm]	[%]	[$\Omega\text{-cm}^2$]
1	1487	5.1	78.2	1.10E+09
1	1488	4.8	77.1	1.30E+09
1	1489	5.0	75.5	5.01E+08
1	1490	5.2	76.2	3.30E+09
1	1491	5.1	77.6	4.88E+08
2	1492	4.9	75.1	2.63E+09
2	1493	5.0	76.1	3.78E+08
2	1494	5.0	72.6	6.30E+09
2	1495	5.0	73.8	6.60E+08
2	1496	5.0	76.4	2.78E+09

Figure 11 shows a photograph of one of the MBE grown NGST demonstration detector layers on a 36 cm² CdZnTe substrate and corresponding statistics of the layer. Note that the 2048 \times 2048 \times 18.0 μm detector array spans less than 3.7 cm on a side and is processed in the “sweet spot” center of the layer, improving the already impressive uniformity statistics.

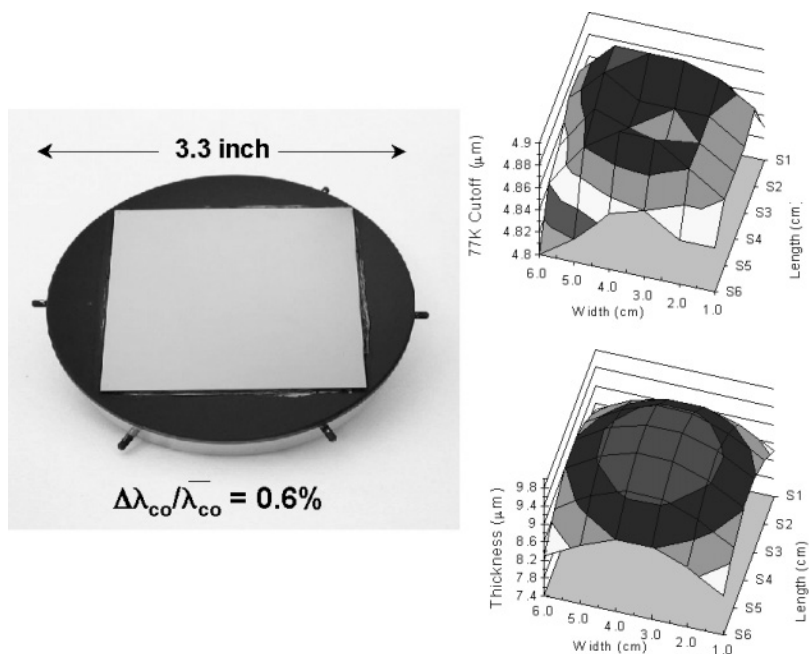


Figure 11. Photograph of an MBE grown NGST demonstration detector layer and corresponding uniformity statistics.

5. HAWAII-RG SERIES LARGE FORMAT MULTIPLEXERS

The latest readout integrated circuits (ROICs) or multiplexers from Rockwell Scientific continue the successful evolution of the HAWAII¹¹-series multiplexers. The HAWAII series ROICs are all source-follower per detector unit cell architectures with increasing functionality as they have evolved over the last eight years. Each evolutionary step of the HAWAII-series' ROICs has witnessed a gain in functionality and migration to the latest state-of-the-art design rules at the most sophisticated silicon foundries in the world. Each of the readouts has been designed and fabricated with first pass success. The HAWAII-1, a 1024×1024×18.5 μm format, 0.8 μm CMOS ROIC, was introduced in 1994 with first pass design success. It was followed in 1998 with the HAWAII-2, a 2048×2048×18.0 μm format, 0.8 μm CMOS ROIC. The HAWAII-2 became Rockwell Scientific's workhorse for its 2048×2048 production SCAs, the so called PACE¹² technology,

¹¹ HAWAII is an acronym for HgCdTe Astronomy Wide Area Infrared Imager. The ROICs were pioneered by a collaboration between Rockwell Scientific and Dr. Donald N.B. Hall at the Institute for Astronomy, University of Hawaii.

¹² PACE is an acronym for Producible Alternative to Cd(Zn)Te Epitaxy.

utilizing liquid phase epitaxy HgCdTe on a sapphire substrate. These arrays were first produced in 1998 and moved into full production in 2000. Presently these arrays are produced at a rate of 1 yielded science grade device per month.

In 2000, the HAWAII-1R, a $1024 \times 1024 \times 18.0 \mu\text{m}$ format, $0.5 \mu\text{m}$ CMOS ROIC was introduced. The HAWAII-1R was produced jointly under the NGST technology demonstration program and the Hubble Space Telescope's Wide Field Camera 3 (WFC-3) program. It will be flown on both NASA's Hubble Space Telescope and Deep Impact comet interception missions. This ROIC features reference pixels (the "R" in -1R) embedded in the pixel format as well as a separate reference output available at the end of each row readout. The reference pixels are used to eliminate any long integration time electronic drifts in the baseline of the ROIC due either to system $1/f$ noise or possible thermal drifts. The HAWAII-1R also successfully introduced glow suppression techniques in the design to eliminate the edge glow seen by the detector under extremely low background conditions.¹³ The dominant sources of this glow are the output amplifiers and clock drivers.

In 2001 the HAWAII-1RG, a $1024 \times 1024 \times 18.0 \mu\text{m}$ format, deep sub- μm CMOS ROIC was designed and tested. The HAWAII-1RG was designed under NASA's NGST technology demonstration program as the stepping stone for the larger format HAWAII-2RG. The HAWAII-1RG has had 100% of its functionality confirmed. And because the HAWAII-1RG was processed at UMC, one of the world's leading silicon foundries, the yield of perfect science grade die is extremely high, in excess of 40 %!

The HAWAII-1RG features embedded reference pixels, a separate reference output available whenever an active pixel is read out, and a separate guide window output (the "G" in -1RG). Again, the reference pixels allow the user to eliminate long integration time electronic drifts due to system $1/f$ noise or thermal drifts of the focal plane array. The guide window, among many possible application advantages, allows very stable tracking of a guide star. The guide window is an arbitrarily sized rectangular window located anywhere within the pixel format. The window output is read out at speeds up to 5 MHz and interleaved with the full frame "science"

¹³ This glow is always present in any silicon circuitry. All semiconductor chips emit both infrared and visible light photons when they are running. These emissions occur during the normal operation of a chip. These normal emissions are due to either thermal effects, driven by temperature changes due to localized heating within the chip, or non-thermal, driven by energy band structure considerations. These emissions are often extremely faint, but can be seen by the very sensitive infrared detectors. For most emissions seen by infrared detectors the emission is driven by the silicon energy band structure and typically falls in the range near $\sim 1.0 \mu\text{m}$, although hot electron/bremsstrahlung effects extend this response further into the infrared.

data. The HAWAII-1RG completed the successful glow suppression techniques begun with the HAWAII-1R to the point that the upper limit to measured glow is less than 0.02 e- per pixel per frame readout.

The readout noise measured at the time of this paper is < 15 e- rms CDS at 375 kHz bandwidth for a 125 kHz slow readout mode operation and for temperatures from 37 K to room temperature. This read noise number is preliminary since a new test system has been implemented. In addition, it has already been demonstrated by independent testing at the University of Hawaii that multiple sampling up to 8 sample pairs shows a $1/\sqrt{N}$ improvement and preliminary single sample CDS readout noise is closer to ~ 12 e-rms [5]. The ~ 12 e-rms CDS noise level is consistent with what has been verified by multiple astronomers on the previous HAWAII-series ROICs. All quoted input referred noise figures are with actual SCAs which have the full capacitance of the integration node with a detector hybrid present.

It appears very likely that multiply sampled (Fowler sampling or sampling-up-the-ramp) readout noise below 3 e- rms is easily achievable. This noise level is the goal readout noise for the NGST mission; however, the NGST readout noise goal *includes* the contribution from dark current and hence drives the indirect requirement for dark currents below 0.01 e-/sec. The NGST nominal integration time is 1000 sec and with a dark current, e.g., of 0.1 e-/sec the associated shot noise will be 10 e-rms. This provides a fundamental limit to the lowest readout noise attainable, no matter how many samples are taken. For MBE HgCdTe, with dark currents below 10 e-/Ksec, the associated shot noise is below 3 e-rms. With multiple sampling, the multiplexer readout noise contribution must be brought below ~ 1 e-rms to achieve the NGST goal. This seems achievable, but has yet to be demonstrated.

The HAWAII-2RG multiplexer has been fabricated at the UMC foundry, the second largest silicon foundry in the world. The HAWAII-2RG is functionally identical to the HAWAII-1RG, but with a $2048 \times 2048 \times 18.0$ μm pixel format. The HAWAII-2RG has the identical functionality as the HAWAII-1RG and essentially only differs in the number of selectable outputs: 1, 4, or 32 outputs compared with the selectable 1, 2, or 16 outputs of the HAWAII-1RG. The functionality of the ROIC has been 100% confirmed and hence, the HAWAII-2RG represents the 5th consecutive first pass design and fabrication success in the HAWAII-series ROICs. Once again, the yield from the UMC foundry is remarkable: $> 22\%$ yield of perfect die and $> 60\%$ yield of science grade die¹⁴.

¹⁴ Science grade die is defined as a ROIC with functional operability $> 99.9\%$. This is achieved with ≤ 2 column outages.

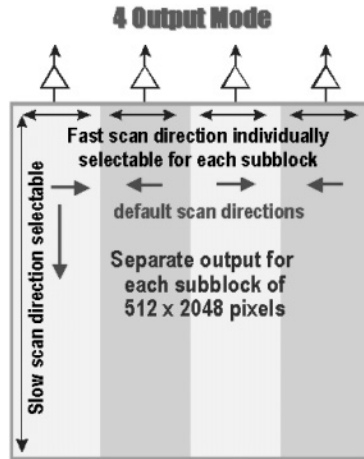


Figure 12. Example of the organization of the output channel structure for the HAWAII-2RG. Shown here is the organization for 4-output mode. The shaded border around the entire array is the 4 columns and 4 rows of embedded reference pixels. Note the ability to select the direction of the readout shift registers to provide for seamless temporal coincidence at output channel borders.

The HAWAII-1RG and -2RG arrange their outputs as blocks of columns, *e.g.*, the 4-output mode of the HAWAII-2RG has each output channel handling 2048 rows by 512 columns, as illustrated in Figure 12 below. All the previous HAWAII-series designs utilized a quadrant format. The present design is more “monolithic” in the sense that there are no longer independent biases and clocks for the individual quadrants that exists in the previous designs. This has allowed the -RG series ROICs to evolve with bond pads on only a single side of the die. This makes both readouts 3-side buttable and 4th side near-buttable for mosaicing of the SCAs into much larger focal plane arrays, much like the way the CCD world has progressed with huge mosaics.

Figure 13 shows an illustrative 8K×8K mosaic possible with the HAWAII-2RG design.

To date almost two dozen orders are in-house or almost in-house for individual HAWAII-2RG SCAs for use in mosaics of 4K×4K and 6K×6K designs. A summary of the key features of the HAWAII-2RG/1RG include:

- Bi-directional shift registers for seamless output boundaries
- Selectable 1, 4, or 32 analog outputs (1, 2, or 16 outputs for the HAWAII-1RG)
- Selectable global, row-by-row, or single pixel reset
- Separate reference and window outputs (although the window image can be read out via one of the conventional analog outputs)

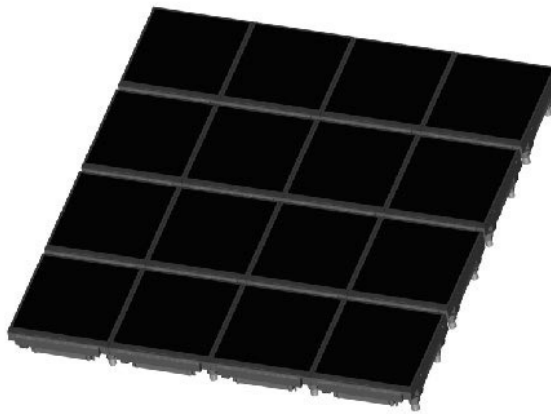


Figure 13. Schematic of an 4x4 mosaic, 8Kx8K pixel mosaic of HAWAII-2RG SCAs. Gaps at the close-butable sides are under 2.3 mm and between the near-butable side are 5.1 mm. Full spatial extent of this 64 Mpixel focal plane array is almost 155 mmx165 mm.

- Selectable “slow” operation mode (100-500 kHz per output data rate) or “fast” operation mode (~1-5 MHz per output data rate with 16 selectable gains from 1-16)
- Simplified clocking with internal re-generation of the clock pulses
- Complete suppression of all amplifier and clock driver “glow”
- “Enhanced” clocking mode that includes the capability for sub-frame or sub-row integration times
- Programmable serial interface for all of the available operational modes

The HAWAII-2RG is the 2048x2048 ROIC for the 5 μ m MBE HgCdTe demonstration SCAs for NGST.

6. FUTURE TRENDS FOR ROCKWELL SCIENTIFIC

Rockwell Scientific is presently designing an application specific integrated circuit (ASIC) for NGST that will provide full command and control of many of Rockwell Scientific’s ROICs, specifically the HAWAII-1RG/2RG ROICs.

Motivated by the desire to simplify SCA implementation, RSC has developed this ASIC to manage all aspects of SCA operation and output digitization. The relatively small size of the ASIC (~ 22 mmx14 mm) allows for nearby mounting and easy implementation on either warm or cold system components. Close mounting to the SCA(s) keeps analog signal paths as

short as possible and provides flexibility in configuring the focal plane/drive electronic sub-system. These factors result in drastic reduction in space, weight and power consumption of the drive electronics as compared with traditional component drive electronics. Accordingly, the “SIDE CAR” represents a tremendous saving for space-based telescopes and earth science satellites. Ground based astronomy benefits from commonality, lower overall cost, ease of programming from a host computer, and simplicity of electronics. All applications benefit from improved reliability.

A summary of the key features of the NGST ASIC include:

- 32 input channels
- 4 additional channels for reference output, window output, temperature sensors
- Up to 500 kHz A/D conversion per channel with 16 bit resolution
- Up to 10 MHz A/D conversion per channel with 12 bit resolution
- Preamplifier gain = 0 dB - 27 dB in steps of 3 dB
- 32 programmable digital I/O (clock generation)
- 20 programmable bias voltages/currents
- 16 bit Microcontroller
- In-flight programmable
- Excellent arithmetic capabilities (smart chip!)
- Efficient power-down modes
- 1 - 24 digital output channels for data transfer (LVDS or CMOS)
- <100 mW at 100 kHz 32-channel operation
- Chip dimensions are 22 mm×14 mm using state of the art deep submicron CMOS processing
- Only requires one power supply, one fixed reference and one master clock for operation

7. CONCLUSION

Beginning in early 2000, Rockwell Scientific embarked on the design of a “next generation” MWIR ($\lambda_{co} = 5 \mu\text{m}$) SCA. We determined the necessary growth processes to produce consistently high performance MBE HgCdTe detector arrays. In addition, we took the traditional SFD architecture of the astronomy ROIC and carried it to the next level of sophistication with 100% design success. These two accomplishments have resulted in a revolutionary step in MWIR SCA performance for both space-based and ground-based astronomy.

Rockwell Scientific is now executing a dramatic technology advancement in command, control, and digitization of infrared SCAs by designing a revolutionary application specific chip to provide full command

and control of the SCA operations with minimal inputs and providing digitized data at the output. This advancement will maximize the impact of the SCA performance improvements that we have already achieved. The next generation of SCAs with ASIC controller will soon arrive, providing a complete command, control, and digitization package system for the entire astronomy community.

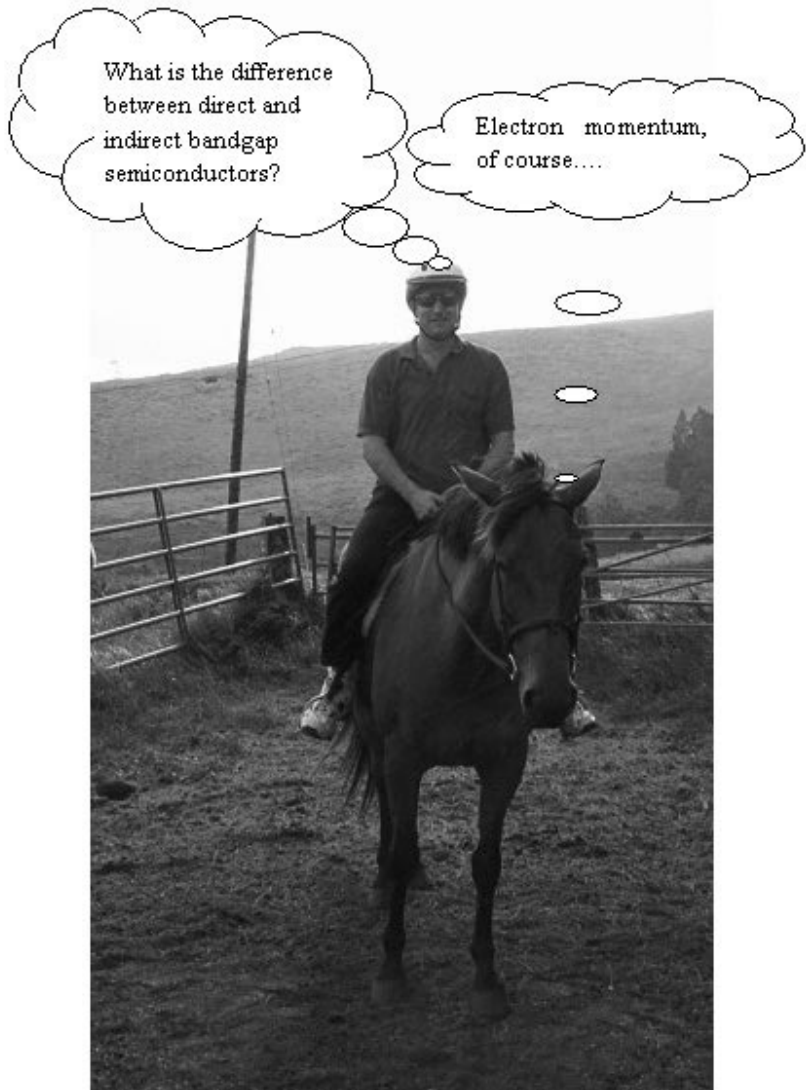
Rockwell Scientific is now in the final phases of producing 5 μm , MBE HgCdTe 2048 \times 2048 \times 18.0 μm pixel arrays for the NGST technology demonstration. As of the end of August 2002 we have hybridized 4 full-up SCAs. Initial tests have begun and results should be available in the early Fall of 2002.

8. ACKNOWLEDGEMENTS

This work is supported by NASA Ames Research Center through contract NAS2-98077 to the University of Hawaii and Z005035 to RSC. Ames Contract Technical Monitor Dr. Craig McCreight and UH Principal Investigator Dr. Donald N. B. Hall.

9. REFERENCES

- [1] M. Zandian, 1999, *A kinetic study of growth induced defects in HgCdTe grown by MBE* Proceedings of IRIS Specialty Group on IR Materials and also MCT Workshop .
- [2] J. M. Arias, 1994, *Properties of Narrow Gap Cadmium-based Compounds*, edited by P. Capper (EMIS Data review Series No. 10), p. 30.
- [3] M. Zandian, J.M. Arias, R. Zucca, R.V. Gil and S.H. Shin, 1991, *HgCdTe Double Heterostructure Injection Laser Grown by Molecular Beam Epitaxy*, Appl. Phys. Lett. **59**, 1022.
- [4] G. Finger, P. Biereichel, H. Mehrgan, M. Meyer, A.F.M. Moorwood, G. Nicolini and J. Stegmeier, 1998, *Infrared Detector Programs for the VLT Instruments at the European Southern Observatory*, *Proceedings SPIE*, **3354**, pp. 87-98.
- [5] Dr. Donald N.B. Hall, Institute for Astronomy, University of Hawaii, personal communication.



*Matching the right horse with the right nerd.
(Courtesy M. Downing)*

COSMIC RAYS AND OTHER NONSENSE IN ASTRONOMICAL CCD IMAGERS

Don Groom

Lawrence Berkeley National Laboratory

Abstract: *Cosmic-ray muons make recognizable straight tracks in the new-generation CCD's with thick sensitive regions. Wandering tracks ("worms"), which we identify with multiply-scattered low-energy electrons, are readily recognized as different from the muon tracks. These appear to be mostly recoils from Compton-scattered gamma rays, although worms are also produced directly by beta emitters in dewar windows and field lenses. The gamma rays are mostly byproducts of ^{40}K decay and the U and Th decay chains. Trace amounts of these elements are nearly always present in concrete and other materials. The direct betas can be eliminated and the Compton recoils can be reduced significantly by the judicious choice of materials and shielding. The cosmic-ray muon rate is irreducible. Our conclusions are supported by tests at the Lawrence Berkeley National Laboratory low-level counting facilities in Berkeley and 180 m underground at Oroville, California.*

Key words: Charge-Coupled Device (CCD), cosmic rays, high resistivity, fully depleted, back illuminated, Compton scattering, gamma ray

1. INTRODUCTION

The ability of ionizing radiation to generate electron-hole pairs in silicon is the bane of optical astronomy, where "cosmic rays" contribute confusion and loss of imaging pixels in CCD's. Multiple exposures and elaborate software are used to eliminate these artifacts.

Genuine cosmic rays near the bottom of the atmosphere consist almost exclusively of relativistic muons produced by secondary meson decay. These muons even penetrate meters of material without interaction or deflection.

But other radiation artifacts usually dominate, and these are not irreducible. Most seem to be Compton recoil electrons from scattered ambient gamma rays, but in some situations, such as when a high-potassium glass like BK7 is present in the dewar, direct β rays produced near the surface of the glass can strike the CCD.

In thin CCD's a radiation event usually occupies 3 or so pixels, and in most cases it is distinctively sharp compared to a star. With the advent of thicker high-resistivity CCD's [1-6], the story is somewhat different. The straight cosmic-ray muon tracks are often quite long, and there are abundant wandering tracks which we call "worms." There are also localized events, usually with fewer counts than would be expected from cosmic-ray muons, which we call "spots." Muon tracks and worms are shown in Fig. 1. Those familiar with nuclear emulsion experiments readily recognize the worms as multiply-scattered low-energy electrons.

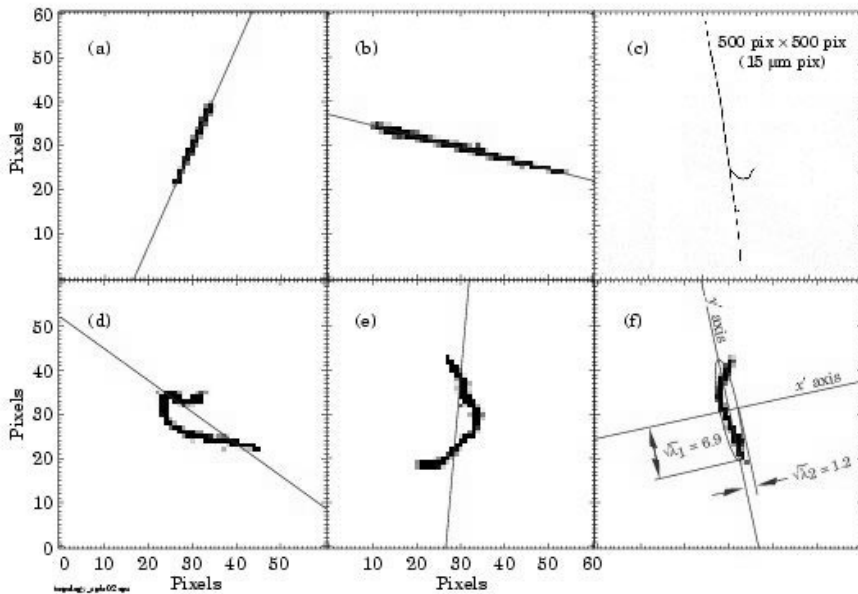


Figure 1. Examples of cosmic-ray muons (a–c) and worms (d–f) in a totally depleted 200 μm thick LBNL CCD. (c) shows one of the longest tracks found, and two δ rays (knock-on electrons) can be seen. (f) also indicates the definition of λ_1 and λ_2 , the principal moments of the distribution.

We have made a study of these events, in most (but not all) cases in totally depleted LBNL CCD's [1-4] 200–300 μm thick. Long dark images were obtained under different conditions at a variety of places: the UCO/Lick and NOAO CCD laboratories, in a low-background room at LBNL, deep underground at Oroville, CA, at Kitt Peak, Cerro Tololo, the

Keck Observatory, and Lick Observatory. Here we explore the nature of the events and the use of lead shielding to reduce the number of spots and worms.

2. COSMIC RAYS

The vertical flux of cosmic rays in the atmosphere as a function of composition and height is shown in Fig.23.3 of [7]. At sea level, 98% of cosmic rays are muons (mean energy ≈ 4 GeV); most of the remainder is protons and neutrons. The muons are decay products of mesons produced in hadronic cascades initiated by primary cosmic rays, which are mostly protons. Maximum intensity occurs at an altitude of about 10 km, and for $E \geq 1$ GeV there is an approximately exponential decrease in intensity below 500 g/cm^2 (≈ 6 km). At low energies the angular distribution is usually approximated as $\cos^\alpha \theta$, where θ is the zenith angle, and $\alpha \approx 2$ for $E \sim 3$ GeV. For $\alpha = 2$ the flux in a horizontal detector is $\pi/2$ times the vertical intensity. For a vertical detector the flux is half this, but the tracks are longer. The vertical intensity is uncertain because of the low energy threshold and low-energy flux uncertainties, but the flux in a horizontal detector is expected to be $0.84\text{--}0.94 \text{ cm}^{-2}\text{min}^{-1}$ at sea level. At an altitude of 2500 m (typical of many large observatories) it is 1.6 times greater, and on Mauna Kea it is 2.1 times greater. The proton/neutron flux is $\sim 2\%$ at sea level, but on Mauna Kea it adds another $\sim 30\%$ to the total flux.

Energy deposit by a muon is a highly stochastic process, and because large energy deposits are rare the most probable deposit depends strongly on thickness [8]. At -100°C it is about 75 electron-hole (e^- -h) pairs/ μm for a $300 \mu\text{m}$ active region, 56 e^- -h pairs/ μm for a $20 \mu\text{m}$ thickness, and only 27 e^- -h pairs/ μm for the $13 \mu\text{m}$ thick SITE CCD's used in CTIO's MOSAIC.

3. EVENT CHARACTERIZATION

A long dark exposure shows a zoo of muons (straight lines), worms, and spots. Software has been developed which is at least partly successful in distinguishing between them. The events are isolated using standard astronomical software. An event is defined as a group of connected pixels with counts above background, with at least one pixel having a significantly higher number of counts. The code generates a number of parameters for each object, including the second moments of the distribution about the centroid.

The number of counts (or e -h pairs) produced by a normally incident muon is expected to distribute about some most probable value, tailing on

the high side. It is thus convenient to scale the number of counts by the active region thickness divided by the track length as calculated from the projected length and the thickness. This number is almost proportional to the number of e-h pairs produced by a normally incident muon. For lack of a good name, we call it “perpendicular counts” or “perp counts.” This reduction distorts the energy deposit information for other kinds of events, but we are mainly using it to help separate muons from the rest.

The distribution of this quantity for a series of long dark exposures under extremely clean conditions at the LBNL Low-level Background Facility (LBF) [9] is shown in Fig. 2. The vertical dashed line indicates the most probable number of counts. The vertical cuts above and below the peak are chosen conservatively to include essentially all of the muons.

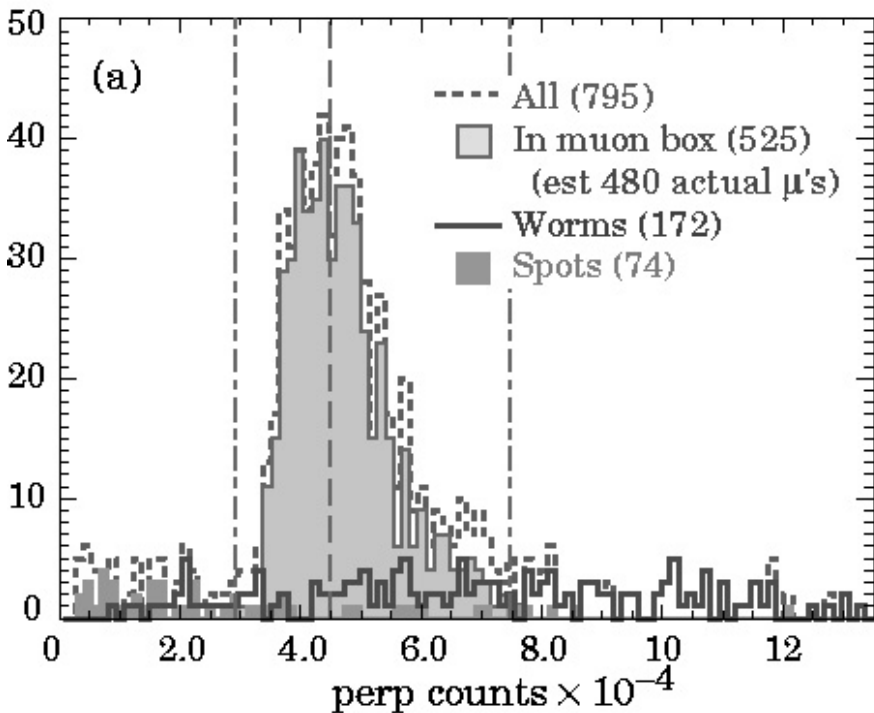


Figure 2. Total exposure of 4800 s at the LBNL Low Background Facility (LBNL LBF): distribution of the normal projection of the number of counts (“perp counts”). The cuts chosen for the “muon region” are shown by the dash-dotted lines

A muon track should be a straight line. A measure of “straightness” can be obtained from the second moments matrix. One can imagine rotating the coordinate system, as shown in Fig. 1(f), so that the matrix is diagonal. With the labels as shown, the $x'x'$ moment is minimal for a straight line (muon),

while the $y'y'$ moment can have any value. The $x'y'$ moment is zero, by the definition of the transformation. These moments are simply the eigenvalues of the original matrix, so the transformation does not need to be made explicitly. We define $\lambda_1(\lambda_2)$ as the maximum (minimum) eigenvalue of the second moments matrix, normalized by dividing by total number of counts in the event so that the result is independent of amplifier gain.

A plot of “perp counts” as a function of λ_2 for the muon-rich exposures at the LBF is shown in Fig. 3.

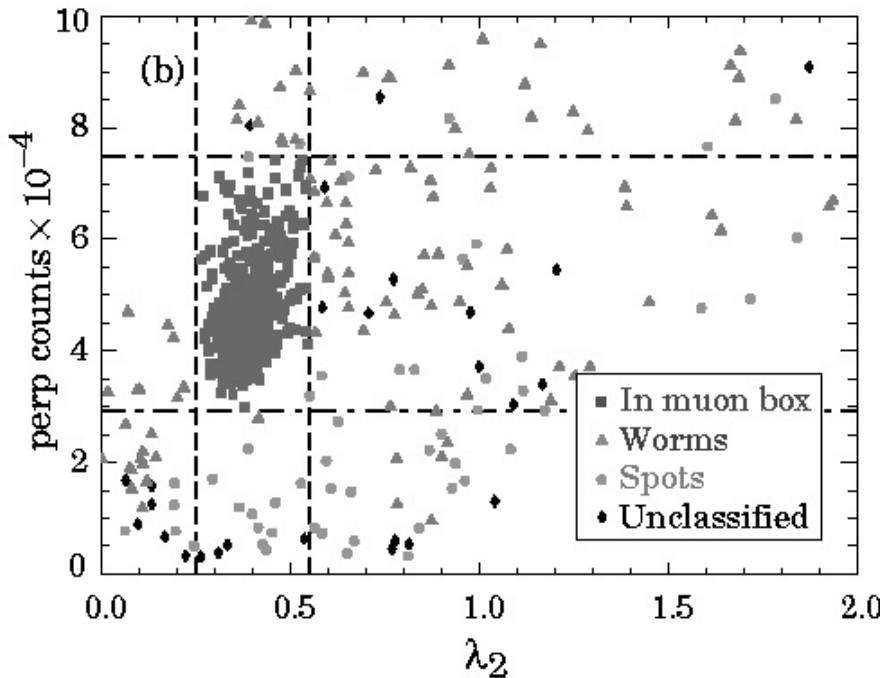


Figure 3. Total exposure of 4800 s at the LBNL Low Background Facility (LBNL LBF): distribution “perp counts” as a function of the smallest eigenvalue λ_2 . The “perp counts” cut and the additional cut $0.25 < \lambda_2 < 0.55$ define the “muon box”.

In this case most cosmic-ray muons are in the interval $0.25 < \lambda_2 < 0.55$; in other situations limits are chosen differently because of different CCD bias, thickness, and other factors. Our “muon box” is defined by the cuts on “perp counts” and λ_2 . Non-muon events similar to those outside the box also occur inside, although in this example the estimated contamination is less than 10%. Hand-scans of a muon-free run (discussed below) verify that non-muon events in this box are genuinely indistinguishable from muons. On the other hand, some muons escape from the box. Scanning shows these to be mostly unusual muon events with a small δ -ray track or other artifact

superimposed on an obvious muon track. In even dirty situations, we usually observe “muon box” rates of $0.7\text{--}1.0\text{ cm}^{-2}\text{min}^{-1}$ in horizontal CCDs, consistent with the cosmic ray rates discussed in the last section. We observe roughly half this rate when the CCD is vertical.

4. THE NATURE OF COSMIC RAYS, WORMS, AND SPOTS

Four sets of long dark exposures were obtained, using the same CCD, dewar, and controller configuration:

- (a) In the basement UCO/Lick CCD laboratory in Santa Cruz. About a third of the events were muons (at the expected rate); the remainders were worms and spots.
- (b) In the LBNL Low Background Facility [9], a room with 1.5 m thick concrete walls; the special concrete has very low radioisotope content. Most events were muons.
- (c) Near the power plant of the Oroville (California) dam, 480 meters-water-equivalent underground, where cosmic rays are attenuated by 10^3 . Worms and spots were observed, but no muons.
- (d) Again at Oroville, this time in an ultra-clean lead vault built for demanding low-level counting experiments. Almost nothing was observed — 120 events in 7400 s. Surprisingly, 113 of the 119 events outside the muon box fell above the upper cut on muon energy deposit. This is also reflected in the high worm/spot ratio (≈ 3) as compared with the ratio outside the vault (≈ 1). Given other experience with the vault, these events are thought to originate in the dewar assembly itself.

These results are summarized in Table 1. The conclusions are simple: Events identified with cosmic ray muons are observed inside or outside a well-shielded room, but are not seen underground. Worm and spot rates are much reduced in an environment without the normal traces of U, Th, and K in the walls, and are essentially zero in an ultra-clean environment.

Further evidence for the Compton electron nature of the worms and spots was provided by a series of measurements at the Lick Observatory 3-m Coudé spectrometer room. Figure 4 shows the “perp counts” spectrum obtained with a CCD without (much) shielding. The muon rate was about as expected, but the rate outside the muon box was $1.6\text{ cm}^{-2}\text{min}^{-1}$. As layers of 0.16 mm Pb were wrapped around the dewar, the “outside the box” rate fell below the muon rate. (We consider this a reasonable goal for all instruments).

Table 1. Evidence for Compton nature of worms and spots. There is usually contamination in the muon box, hence the apparently greater muon rate at UCO/Lick than at LBNL. Since some events could not be classified, the spot + worm rate is in general less than the “outside muon box” rate.

Experiment	Integration time [s]	Spots	Worms	Muon box [cm ⁻³ min ⁻¹]	Outside box
UCO/Lick (Santa Cruz)	1000	0.87±0.08	0.97±0.08	0.93±0.08	2.16±0.12
LBNL, shielded room	4800	0.10±0.01	0.22±0.02	0.71±0.03	0.37±0.02
Oroville, 180 m underground	7843	0.21±0.01	0.20±0.02	0.06±0.01	0.47±0.02
Same, inside lead vault	7400	0.02±0.00	0.07±0.01	0.00±0.00	0.10±0.01

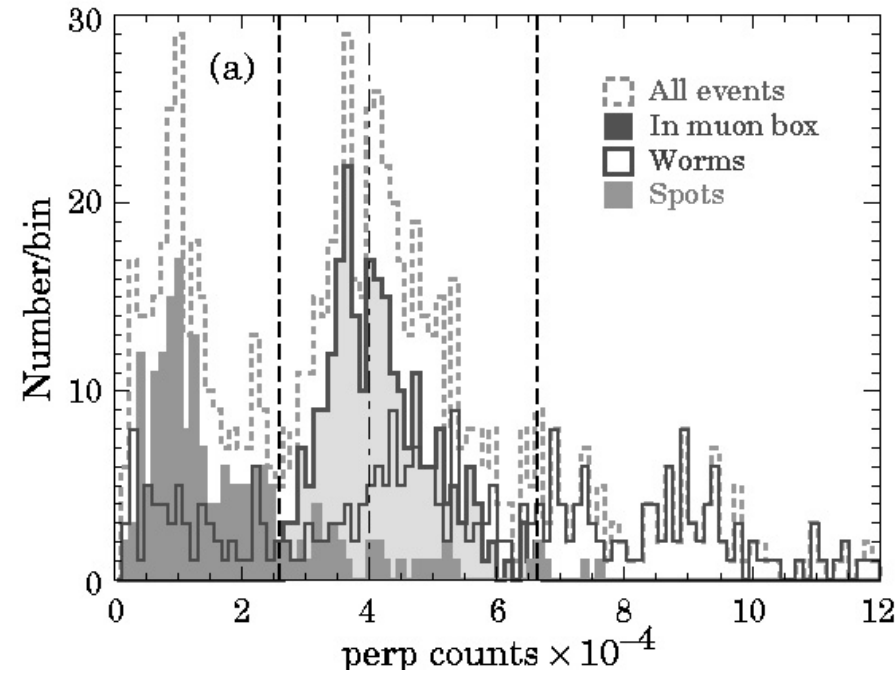


Figure 4. Lick 3-m Coudé spectrograph room: distribution of the normal projection of the number of counts (“perp counts”) in two long darks with nearly no shielding

We also obtained spectra with a cryogenic Ge gamma spectrometer, shown in Fig. 5.* Results are consistent with the typical potassium, uranium, and thorium abundances found in ordinary concrete and rock. There is no evidence for ^{60}Co , an occasional contaminant of steel. The addition of 1 cm lead around the detector reduced the rate by 80%, mostly at low energies (500 KeV) where the Compton scattering probability in the CCD is highest. We view this reduction as a function of energy consistent with the reduction in the rate outside the muon box when 1 cm of Pb shielding is used. There is an important corollary: Since most of the problem is with low-energy gamma rays with short interaction lengths, there is little point to using massive shielding. One centimeter of shielding seems to be sufficient.

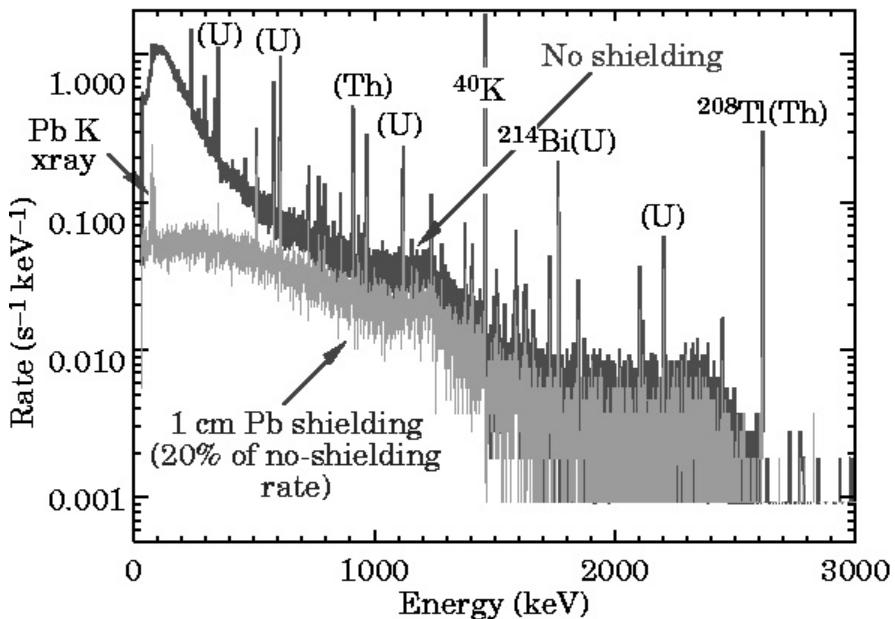


Figure 5. Lick 3-m Coudé spectrograph room: Gamma spectra in the spectrometer room, without and with a 1 cm lead shield. Characteristic lines correspond to gamma rays produced in ^{40}K decay and in the U and Th decay chains.

* If the spectrometer were exposed to a monochromatic gamma source, one would see a very sharp line representing complete containment of the event, a valley on the low-energy side, and a plateau at smaller energies due to partially contained events, mostly recoils from Compton scattering. The spectrum shown can be understood as a superposition of many such monochromatic gamma spectra plus low-energy events due to a sea of low-energy gammas already degraded by Compton scattering.

Most of our observations are consistent with the worms and spots being the tracks of low-energy electrons, the recoils from elastic-scattering (Compton scattering) gamma and x rays in the few hundred KeV range. There is an important exception: Our NOAO collaborators observed an increase of $2.8 \text{ cm}^2\text{min}^{-1}$ over the normal background in the room when a BK7 field lens was inside the dewar, and no increase if it were immediately outside the dewar. This observation is consistent with beta rays from ^{40}K decay close enough to the surface of the glass that the particles can escape. Other groups have encountered the same problem with BK7 [10,11], which has a high potassium content.[†] (Except under bizarre circumstances, alpha particles are never a problem because of their very short range.)

5. OTHER OBSERVATIONS

Long dark exposures were made at UCO/Lick with an MIT/LL CCID20, a deep-depletion device intended for the DEIMOS spectrometer at the Keck Observatory [5-6]. The sensitive thickness is estimated to be $40 \text{ }\mu\text{m}$. The distributions show the familiar peak in “perp counts” and a populated muon box with about the expected rate. The distributions were much broader than in our thick devices, and a clean muon/Compton separation was not possible. Rates outside the box were very much reduced by shielding with 5 cm of Pb. We estimate that the ratio of Compton rates for an unshielded MIT/LL thick CCD to that in the LBNL CCD is 0.65, with $\sim 10\%$ – 15% uncertainty. The thickness ratio is 0.15. The difference provides evidence that many of the Compton recoil electrons do not originate in the sensitive volume of the CCD. Sensitivity to Compton recoil electrons (and, obviously, direct β rays if potassium is present in the dewar) is not limited to thick CCD’s.

Dark exposures were obtained at CTIO with MOSAIC (horizontal orientation), which consists of 8 SITE CCD’s with $\approx 13 \text{ }\mu\text{m}$ sensitive regions. In spite of the lack of useful pattern recognition, the distributions show peaks at the expected most probable number of e-h pairs. The rate was $4.3 \text{ cm}^2\text{min}^{-1}$, as compared with an expected cosmic ray rate at that altitude of about $1.4 \text{ cm}^2\text{min}^{-1}$.

An 800×1980 pixel ($15 \text{ }\mu\text{m}$)² LBNL fully-depleted CCD on the RC spectrograph at the KPNO 4-m telescope (60 deg. angle from vertical) obtained a muon box rate of $0.66 \text{ cm}^2\text{min}^{-1}$, and the rate outside the muon box was $0.51 \text{ cm}^2\text{min}^{-1}$. The muon rate is consistent with the expected rate for this altitude and CCD orientation. The Compton rate is the lowest recorded in any of the observations without shielding. Perhaps the mechanical housing provides shielding. The same CCD in a vertical

orientation at the NOAO laboratory in Tucson measured $0.60 \text{ cm}^{-2}\text{min}^{-1}$ in the muon box (OK) and $2.00 \text{ cm}^{-2}\text{min}^{-1}$ outside it (among the highest Compton rates we have ever observed in the absence of BK7 glass).

After the tests showing that 1 cm of lead reduced the Compton rate to an acceptable level in the Lick 3-m spectrometer room, a lead box was built to shield the dewar on the spectrometer. It seemed to have no effect. Measurements with the Ge gamma spectrometer are scheduled in an attempt to understand the situation.

Tests with the “standard” CCD setup used for the Oroville and other measurements were also made at the Keck I telescope—horizontal and vertical, on the floor and on the Nasmyth deck, inside and outside of a lead box built for the purpose. Controller problems prevented characterization of the events, but total rates of about $5 \text{ cm}^{-2}\text{min}^{-1}$ were observed. The horizontal/vertical rate difference was consistent with expectation, but rates inside/outside the lead box were about the same. Long high-altitude exposure[‡] of the stainless steel alloy used in the dewar ruled out cosmogenic activation of the dewar on the flight to Hawaii as the source of the problem. It is still not understood.

6. ASSAY RESULTS

We have characterized the U, Th, and K content of most materials in the dewar which might act as radiation sources. The results are given in the upper section of Table 2. The “black socket” for our test CCD was a radiation source, as seems to be expected for materials with black dye. Indium is naturally radioactive, but the thin ($\sim 500 \text{ \AA}$) In/Sn coating we use as a rear window in our CCD’s makes a negligible contribution.

We also characterized the concrete at the Lick 3-m telescope and the lava used as concrete aggregate at the Keck and other telescopes on Mauna Kea.[◊] These results are shown in Table 2. In both the Lick 3-m and UCO/Lick environments the Compton rate was $2.2 \text{ cm}^{-2}\text{min}^{-1}$, in contrast to $0.8\text{--}0.9 \text{ cm}^{-2}\text{min}^{-1}$ for cosmic rays. In rooms or on dome floors made from such concrete, enough shielding to achieve gamma-ray attenuation by a factor of three or more would be desirable.

[‡] The stainless steel was characterized underground at Oroville, sent on four overnight Federal Express delivery trips from LBNL to Harvard and back, and again characterized. Cosmogenic activation was observed, but at a totally insignificant level.

[◊] No lava was harmed in making these tests, and except for a few decayed atoms all of it has been returned to the Mauna Kea summit.

Characterization results from an NOAO sample of BK7 optical glass are given at the end of the table. The potassium content is tentative pending chemical analysis.

Table 2. Radiological assay results for common materials found in CCD dewars and nearby concrete. Numbers in parentheses indicate the error in the last place, and “ND” indicates “none detected.” The approximate conversion factors to decay rate are 0.66 (pCi/g)/ppm for chemically pure uranium, 0.11 (pCi/g)/ppm for thorium, and 8.5 (pCi/g)/percent for potassium.

Sample	U (ppm)	Th (ppm)	K (%)
CCD black socket	0.64(4)	1.38(6)	0.011(1)
Si wafers (3 in box)	0.025(6)	0.16(2)	ND
Aluminium nitride	0.010(2)	0.019(5)	ND
Aluminium sputter	ND	0.044(14)	ND
Circuit boards (Lick)	0.064(4)	2.07(8)	0.016(2)
Epoxy (Lick)	0.012(3)	0.010(3)	ND
INVAR, bar stock	ND	ND	ND
Molybdenum, bar stock	0.020(3)	0.020(3)	ND
Sn/In alloy	5.0(1)	4.6(1)	ND
Lick 3-m core	1.35	4.0	0.72
UCO/Lick lab core	1.2	1.2	1.23
Mauna Kea Lava [◇]	1.5	4.7	1.52
BK7 glass (NOAO)	0.10(5)	0.7(2)	3.5(1)

7. OBSERVATIONS AND CONCLUSIONS

We are not the first to find non-cosmic-ray events in CCD’s, nor the first to recognize the distinctive energy deposit of a (normally incident) cosmic-ray muon. In his 1986 review [10], Mackay discusses the rate excess over that expected from cosmic rays, and in one case diagnoses much of the problem as radiation from the glass dewar window. He reports rates of $10 \text{ cm}^{-2}\text{min}^{-1}$, more than 10 times the cosmic-ray rate. Florentin-Nielsen and Anderson [11] describe experiments in which the device was operated 37 m below ground level in a chalk mine, with a reduction to 33% of the surface rate, to $0.56 \text{ cm}^{-2}\text{min}^{-1}$. In other experiments they identified a UBK-7 lens as

[◇] No lava was harmed in making these tests, and except for a few decayed atoms all of it has been returned to the Mauna Kea summit.

producing very high rates because of its ^{40}K content. An old ESO report lists cosmic-ray rates in a dozen CCD's ranging from $6\text{ cm}^{-2}\text{min}^{-1}$ in RCA SIC 501 CCD's to $1.4\text{ cm}^{-2}\text{min}^{-1}$ in a GEC 8603 [12].

Deep-depletion CCDs have been used in x-ray astronomy for a long time. Walton et al. [13] describe a study in which signal size is used to discriminate against cosmic rays—the x-ray mirror response cutoff was at 10 keV, and only 10% of the cosmic-ray signals were this small.

There is anecdotal evidence of hotspots in a concrete telescope pier (Hugo Schwarz, reported on CCD-world), drywall (Roy Tucker, reported on CCD-world), radioactive dewar windows (BK7 seems notorious in this regard), and thorium-containing lenses. There is also continued worry about radioisotope tracers such as the ^{60}Co used in steel process control.

Our study is unique, however, in that the thicker CCD's have made it possible to do a moderately good job in isolating the muon and non-muon components. It again emphasizes the need for care and careful characterization for every material used in the vicinity of the CCD, especially inside the dewar. The gamma ray background from ubiquitous potassium, uranium, and thorium decay can be reduced to an acceptable level by careful shielding. But we are left with mysteries: Shielding usually worked as expected, but in some cases had no apparent effect. Work continues.

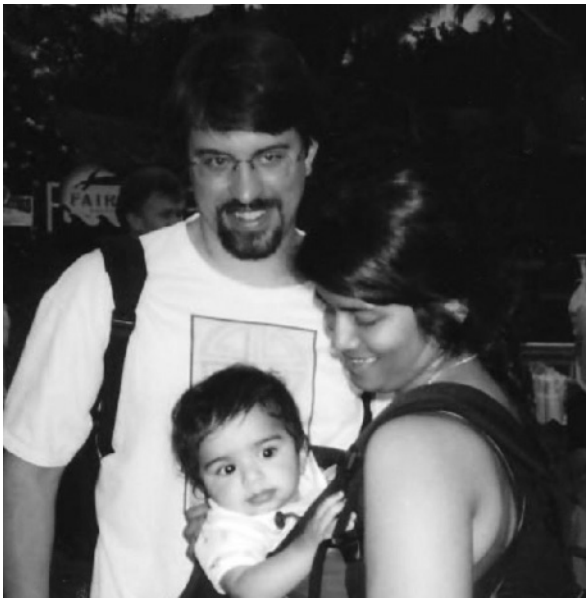
8. ACKNOWLEDGMENTS

This work was supported by the U.S. Department of Energy under contract No. DE-AC03-76SF00098 and by the U.S. National Science Foundation ATI program. The author gratefully acknowledges contributions from many people, but especially his collaborators Al Smith, Dick McDonald, Donna Hurley, Bill Brown, Kirk Gilmore, Steve Holland, Richard Stover, and Mingzhi Wei.

9. REFERENCES

- [1] S. E. Holland et al., 1996, *A 200x200 CCD Image Sensor Fabricated on High-Resistivity Silicon*, IEDM Tech. Digest, pg. 911.
- [2] S. E. Holland et al., 1999, *Large Format CCD Image Sensors Fabricated on High Resistivity Silicon*, Proc. 1999 IEEE Workshop on Charge-Coupled Devices and Advanced Image Sensors, pgs. 179-182.

- [3] S. E. Holland, 2003, *An Overview of CCD Development at Lawrence Berkeley National Laboratory*, these Proceedings, pg 95.
- [4] S. E. Holland, D. E. Groom, N. P. Palaio, R. J. Stover, and M. Wei, to be published, *Fully-depleted back-illuminated charge-coupled devices fabricated on high-resistivity silicon*, IEEE Trans.Elec. Dev
- [5] B. E. Burke et al., 1998, *Large-area back-illuminated CCD imager development*, in Optical Detectors for Astronomy, Kluwer Academic Publishers, Dordrecht, pgs. 19–28.
- [6] B. E. Burke et al, 2000, *CCD imager technology development at Lincoln Laboratory*, in Optical Detectors for Astronomy II, Kluwer Academic Publishers, pgs. 187–199.
- [7] K. Hagiwara et al., 2002, Phys. Rev. D **66** 010001; also available at <http://pdg.lbl.gov/>
- [8] H. Bichsel, 1988, Rev. Mod. Phys.**60**, pgs. 663–699.
- [9] <http://user88.lbl.gov/lbf/index.htm>
- [10] C. D. Mackay, 1986, Ann. Rev. Astron. Astrophys. **24**, pgs. 255–283. See especially p.268
- [11] R. Florentin-Nielsen, M. I. Andersen, & S.P. Nielsen, 1995, *Cosmic ray events and natural radioactivity in CCD cryostats*, New developments in Array Technology and Applications, eds. A. G. Philip et al., IAU Symp pg. 167.
- [12] *On the Rates of Radiation Events in CCD's*, (excerpt from an ESO report), available at <http://www.pv-inc.com/tutorial/tutorial.htm>
- [13] D. Walton, R. A. Stern, R. C. Catura, & J. L. Culhane, 1984, SPIE **501**, pgs. 306–316.



Vyshnavi Suntharalingam with husband and son at the arrival of the snorkeling cruise.



*Nothing like a good conch blowing to digest....
(Courtesy G. Burley)*

AN OVERVIEW OF CCD DEVELOPMENT AT LAWRENCE BERKELEY NATIONAL LABORATORY

Steve Holland

Lawrence Berkeley National Laboratory

Abstract: *Fully depleted, back-illuminated charge-coupled devices fabricated at Lawrence Berkeley National Laboratory on high-resistivity silicon are described. Device operation and technology are discussed, as well as the results on telescopes and future plans.*

Key words: *Charge-Coupled Device (CCD), fully depleted, back illuminated, high-resistivity silicon*

1. INTRODUCTION

A new type of scientific charge-coupled device (CCD) has been developed at Lawrence Berkeley National Laboratory (LBNL) [1]. This development was motivated by the LBNL Supernova Cosmology Project (SCP), which studies cosmology via distant, red-shifted supernovae [2]. Conventionally thinned, back-illuminated CCDs typically have poor red response and fringing at the near-infrared wavelengths of interest to the SCP. The device described here has a much improved red response and negligible fringing by virtue of a thick depletion region.

The CCDs described in this work have been fabricated at the LBNL Microsystems Laboratory, a Class 10 clean room facility that emphasizes fabrication of devices on high-resistivity silicon. Recent interest in volume production for the proposed Supernova/Acceleration Probe (SNAP) space-based imager has led us to begin a technology transfer effort with a commercial CCD manufacturer. Initial results of this effort are described as

well as some results from the use of this type of CCD at the National Optical Astronomy Observatory (NOAO) and Lick Observatory.

1.1 Fully-depleted, back-illuminated CCD technology

Figure 1(a) shows the cross-section of the CCD described in this work. A 3-phase CCD is fabricated on n-type high-resistivity silicon, typically 10-12 $\text{k}\Omega\text{-cm}$. A backside bias voltage in combination with the extremely low substrate doping allows for full depletion of the substrate at reasonable operating voltages (see Fig. 1(b)). The substrate doping is typically about 4 orders of magnitude lower than that in the channel. This results in low sensitivity of the channel potential to the backside bias voltage since only a small fraction of the field lines in the channel terminate in the substrate. Hence, to the first order, the backside bias voltage used to fully deplete the substrate is independent of the bias voltages on the CCD gate electrodes as opposed to deep-depletion CCDs where the depletion depth in the substrate is determined by the voltages on the gate electrodes.

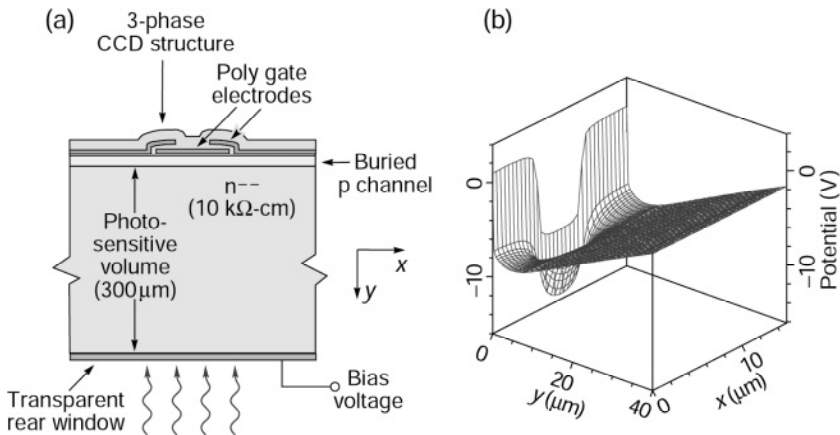


Figure 1 (a) Cross section of a fully-depleted, back-illuminated CCD fabricated on high resistivity silicon. (b) A two-dimensional simulation showing the potential in the fully-depleted substrate that directs the photo-generated holes to the conventional potential wells generated by the voltages on the CCD gate electrodes.

As a practical matter it is not convenient to make a physical contact to the backside of the CCD as shown in Fig. 1. In the actual implementation the contact is made on the front side [3,4]. An n⁺ substrate contact surrounds a series of floating p⁺ guard rings that terminate on a grounded p⁺ guard ring. The function of the floating p⁺ guard rings is to gradually drop the substrate bias voltage between the n⁺ contact and the grounded p⁺ guard ring. The n⁺ contact is located beyond the depletion edge in the quasi-neutral n-type substrate. For low-level light applications the photocurrent-generated voltage

drop across the high-resistivity substrate is negligible, hence the CCD can be fully depleted from the circuit side.

Figure 2 shows a photograph of a 100 mm diameter CCD wafer fabricated at LBNL. The wafer contains $2K \times 2K$ $(15 \mu m)^2$ CCDs as well as smaller format devices. The substrate resistivity is 10-12 $k\Omega\text{-cm}$, which results in the full depletion of 300 μm thick substrates at bias voltages of 20-25 V.

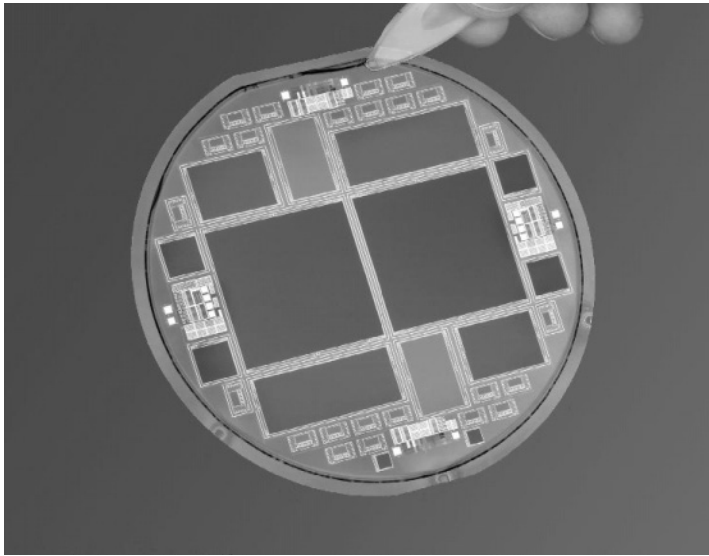


Figure 2. Photograph of a 100 mm diameter CCD wafer fabricated at LBNL.

Lick Observatory has measured that these CCDs achieve quantum efficiency of 60% at 1 μm wavelength (Fig. 3), noise of 4-6 e^- rms at 8 μs sample time each for reset and signal, and CTE exceeding 0.999995. Our most recent amplifier design has a noise level of approximately 2 e^- rms. Dark currents of less than 10 $e^-/\text{pix}/\text{hr}$ at -120 $^{\circ}\text{C}$ have been demonstrated [4]. The latter is achieved by inverting the CCD channel surface with electrons between frames and taking advantage of the long time constant for electrons trapped at interface states at cryogenic temperatures [5,6].

CCDs from this processing run have been installed on telescopes. Figure 4 shows a near-infrared spectrum of NGC 7662 taken at the NOAO 4-m telescope with a 1980×800 , $15 \mu m^2$ CCD on the RC spectrograph [7]. The lack of fringing and high quantum efficiency at near-infrared wavelength is evident in the good resolution of spectral lines at wavelengths longer than 8000 \AA . The image of NGC7662 shown in inset of Fig. 4 was taken at the Lick Observatory 1-m telescope on an early 200×200 prototype high-resistivity CCD. LBNL CCDs are also in use at the NOAO Multiple-

Aperture Red Spectrometer and the Lick Observatory Hamilton Spectrograph.

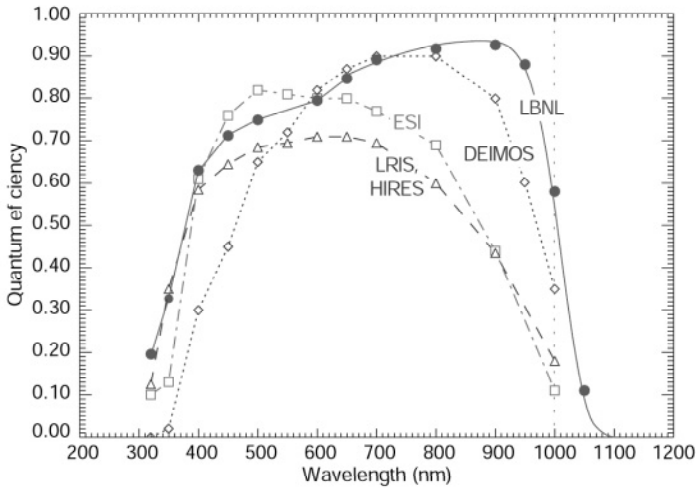


Figure 3. Measured quantum efficiencies comparing a 300 μm thick, fully depleted LBNL CCD versus CCDs in use at the Keck Telescope. The ESI and DEIMOS CCDs were fabricated at MIT Lincoln Laboratory [8], and the HIRES/LRIS CCDs were fabricated at Scientific Imaging Technologies.

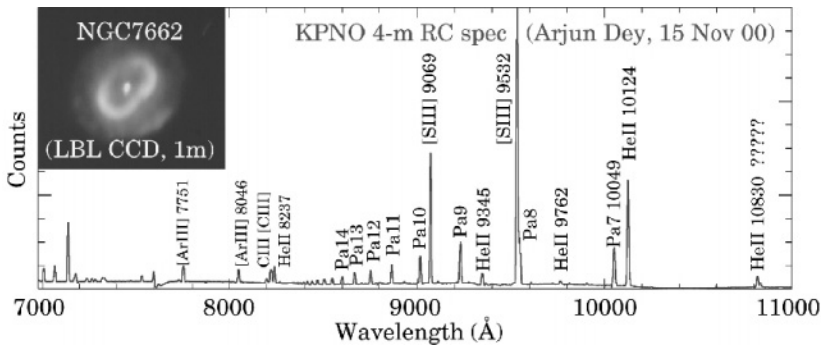


Figure 4. Near-infrared spectrum of NGC7662 taken with a 1980 \times 800, 15 μm^2 LBNL CCD at the NOAO RC spectrograph. Courtesy of Arjun Dey of NOAO.

1.2 Work in progress and future plans

The LBNL SCP group and others have proposed a space-based project (SNAP) to study large numbers of supernovae. A gigapixel imager containing CCDs and infrared detectors is envisioned, requiring significant quantities of both types of detectors. As a result, we have begun a technology transfer effort with DALSA Semiconductor. Figure 5 shows a

150-mm-diameter, high-resistivity wafer processed at DALSA Semiconductor. CCDs on this wafer include $2K \times 4K$ $(15\ \mu\text{m})^2$ devices for ground-based astronomy, prototype $(12\ \mu\text{m})^2$ and $(10.5\ \mu\text{m})^2$ pixel SNAP CCDs, as well as other experimental devices. High-quality front-illuminated CCDs have been produced and initial technology transfer efforts of the LBNL back-illumination technology have begun. Figure 6 shows results from a back-illuminated, 300 μm thick, fully-depleted CCD fabricated at DALSA Semiconductor. The only processing step performed at LBNL was the deposition of anti-reflection coatings on the backside of the wafer. Although substantial technology development remains, this is an encouraging and significant result.

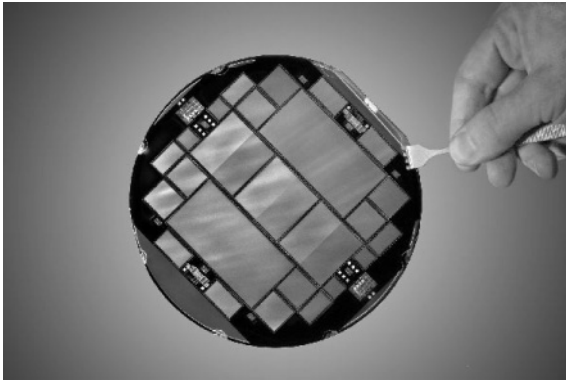


Figure 5. Photograph of a 150 mm diameter, high-resistivity CCD wafer fabricated at DALSA Semiconductor (Bromont, Quebec, Canada).

In addition to the manufacturing challenges for SNAP, small pixels are desired for the wide-field CCD imager. In order to take advantage of smaller pixel size the point spread function (PSF) of the CCD imager must be consistent with the smaller pixel size. In a fully-depleted CCD the PSF is determined by lateral diffusion of the photogenerated holes during their transit to the potential wells [9,10]. Conversely, in a conventionally thinned CCD the field-free region at the back surface of the CCD typically has the dominant effect on the PSF.

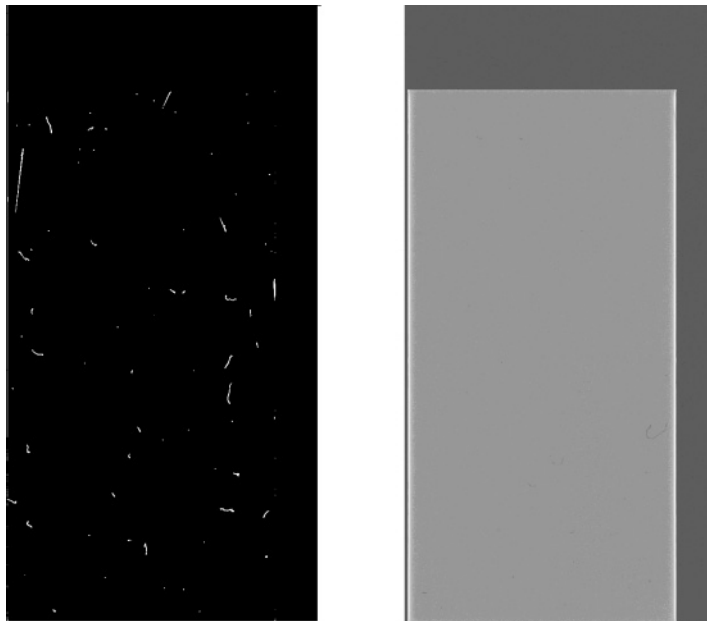


Figure 6. Dark current (*left*) and 500 nm flat field (*right*) images taken on a 1024×512 (15 μm)² pixel fully-depleted, back-illuminated CCD fabricated at DALSA Semiconductor. The dark current at -150 °C was 3e⁻/pixel-hour. For this experiment, the substrate bias voltage was set very high (80 V), which overdepleted the CCD. This would be the worst case scenario for dark current. The bright spots and lines in (*left*) are trails left by particles such as cosmic rays (muons) and radioactive decay of materials at the observatory and in the dewar.

For the overdepleted case the width, σ , of the resulting Gaussian charge distribution at the CCD potential wells approaches the constant field limit given by

$$\sigma = \sqrt{2 \frac{kT}{q} \frac{z_{sub}^2}{(V_{sub} - V_J)}} \quad (1)$$

where z_{sub} is the substrate thickness, V_{sub} is the substrate bias voltage, V_J is an average potential near the CCD potential wells generated by the applied gate voltages, and kT/q is the thermal voltage. Hence, the PSF can be improved by decreasing the substrate thickness and/or increasing the substrate bias voltage. A target CCD thickness for SNAP is 200 μm . This

thickness is also advantageous in terms of reducing loss of pixels to cosmic ray hits, but with the disadvantage that the long wavelength quantum efficiency is degraded slightly. Reliable operation of CCDs at substrate bias voltages compatible with the desired SNAP PSF will be the subject of major study during the R&D phase of detector development for SNAP.

2. ACKNOWLEDGEMENTS

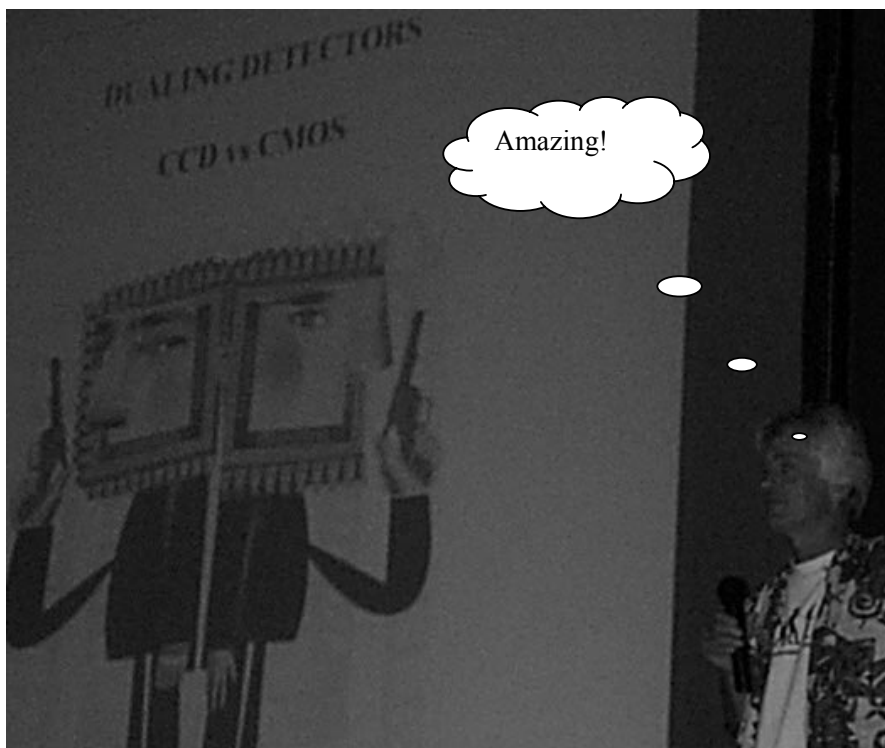
This work was supported by DOE contract No. DE-AC03-76SF00098 and the National Science Foundation ATI program. The author gratefully acknowledges the many people who have made contributions to this effort including Richard Stover, Mingzhi Wei, Don Groom, Nick Palaio, Guobin Wang, Bill Brown, Kirk Gilmore, Armin Karcher, Bill Kolbe, Chris Bebek, Michael Levi, John Bercovitz, Robert Groulx, Raymond Frost, Eric Janelle, Arjun Dey, Rich Reed, and Debra Fischer.

3. REFERENCES

- [1] Holland, S.E., Godhaber, G., Groom, D.E., Moses, W.W., et al., 1996, *A 200×200 CCD image sensor fabricated on high-resistivity silicon*, IEDM Technical Digest, p. 911.
- [2] Perlmutter, S., Aldering, G., della Valle, M., Deustua, S., Ellis, R.S., Fabbro, S., Fruchter, A., Goldhaber, G., Groom, D.E., Hook, I.M., Kim, A.G., Kim, M. Y., Knop, R.A., Lidman, C., McMahon, R.G., Nugent, P., Pain, R., Ranagia, N., Pennypacker, C.R., Ruiz-Lapuente, P., Schaefer, B., Walton, N., 1998, *Discovery of a supernova explosion at half the age of the Universe*, Nature, **391**, p. 51.
- [3] U.S. Patent 6,259,085, July 10th, 2000, *Fully depleted back illuminated CCD*.
- [4] S.E. Holland, D.E. Groom, N.P. Palaio, R.J. Stover, and M. Wei, *Fully-depleted, back-illuminated charge-coupled devices fabricated on high-resistivity silicon*, to be published, IEEE Trans. Elec. Dev.
- [5] B.E. Burke and S.A. Gajar, 1991, *Dynamic suppression of interface-state dark current in buried-channel CCDs*, IEEE Trans. Elec. Dev., **38**, 2, p. 285
- [6] P. Jorden, 2002, *Secrets of E2V Technologies CCDs*, these proceedings, pg. 115
- [7] Arjun Dey, private communication.
- [8] B.E. Burke, J.A. Gregory, M.W. Bautz, G.Y. Prigozhin, S.E. Kissel, B.B. Kosicki, A.H. Loomis, and D.J. Young, 1997, *Soft x-ray CCD imagers for AXAF*, IEEE Trans. Elec. Dev., **44**, 10, p. 1633.
- [9] Holland, S.E., et al., 1997, *Development of back-illuminated, fully-depleted CCD image sensors for use in astronomy and astrophysics*, presented at the 1997 IEEE Workshop on Charge-Coupled Devices and Advanced Image Sensors, Bruges, Belgium.
- [10] Groom, D.E., Eberhard, P.H., Holland, S.E., Levi, M.E., Palaio, N.P., Perlmutter, S., Stover, R.J., Wei, M., 1999, *Point-spread function in depleted and partially depleted CCD's*, Proc. 4th ESO Workshop on Optical Detectors for Astronomy, Garching, Germany.



Moments before his turn at the Karaoke, the “Shoot the manufacturers” roundtable members are smiling. Left to right; J. Garnett, B. Burke, P. Vu, L. Kozlowski, K. Ando and M. Blouke. Continues on page 298.



SDW2002 reports on the war between CCDs and CMOS. From our special envoy Jim Janesick.

SCIENTIFIC CMOS PIXELS

James Janesick, Ferry Gunawan, Taner Dosluoglu, John Tower, Niel McCaffrey
Sarnoff Corporation

Abstract: *High performance CMOS pixels are introduced and their development is discussed. 3T (3-transistor) photodiode, 5T pinned diode, 6T photogate and 6T photogate back illuminated CMOS pixels are examined in detail, and the latter three are considered as scientific pixels. The advantages and disadvantages of these options for scientific CMOS pixels are examined. Pixel characterization, which is used to gain a better understanding of CMOS pixels themselves, is also discussed.*

Key words: *Complementary Metal Oxide Semiconductor (CMOS), Charge-Coupled Device (CCD), pixel, transistor, Metal Oxide Semiconductor Field Effect Transistor (MOSFET)*

1. INTRODUCTION

A decade has passed since complementary metal oxide semiconductor (CMOS) imaging detectors began to make their move into the charge-coupled device (CCD) arena. The imaging community is now well aware of CMOS imager advantages for commercial use, however, it is unclear if the technology can be applied scientifically. Imaging scientists have shown a reluctance to applying CMOS detectors because they are content with the CCD and its near perfect output performance [1]. If CMOS is to compete with the CCD, its technology must demonstrate similar qualities. Low cost, low power, high on-chip system integration and high-speed operation are very attractive CMOS features. However, the lack of high performance is currently restraining CMOS from scientific use. This paper introduces high performance scientific CMOS pixels and presents plans to realize their development.

2. CMOS PIXELS

2.1 3T Photodiode Pixel

The majority of CMOS arrays are based on a 3-transistor (3T) photodiode pixel design because of its simplicity and conformity to conventional CMOS processes. The 3T will not be considered a scientific pixel because the pixel exhibits high dark current and high read noise performance. However, advanced CMOS pixels for potential scientific use are extensions of the 3T, and therefore, the pixel will be examined in detail here.

The 3T is comprised of four components as shown in Fig. 1.

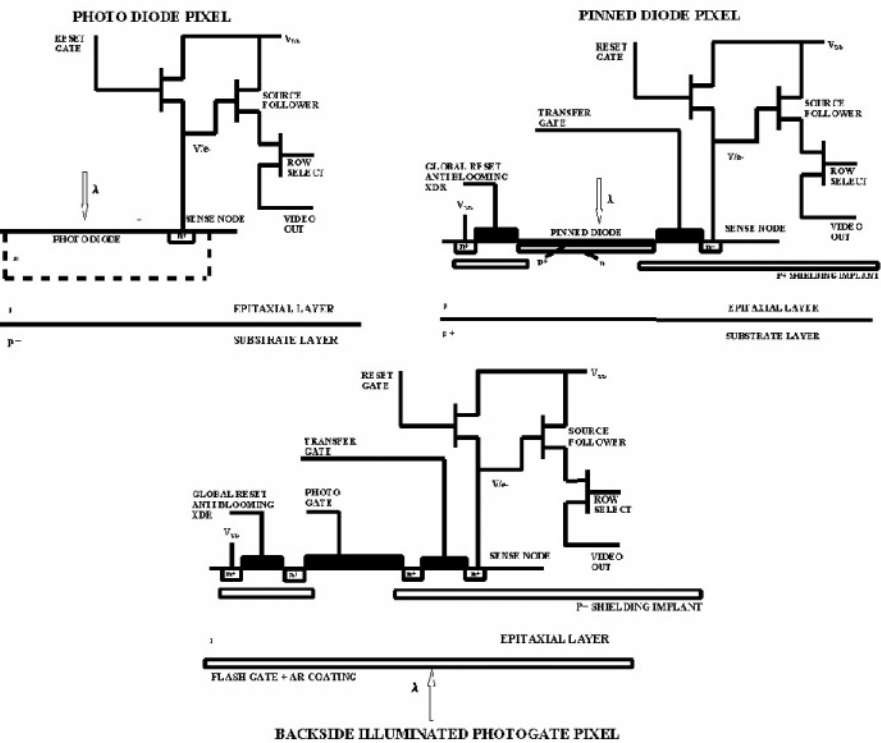


Figure 1. CMOS pixels discussed in text.

The photodiode region is responsible for generating and collecting signal charge. Three metal oxide semiconductor field effect transistors (MOSFETs) are required to measure the charge on the diode. They include a: 1) source follower MOSFET that converts charge to an output voltage, 2) reset MOSFET that resets the photodiode before charge is integrated and 3) row select MOSFET that selects the row (or line) for readout.

The maximum voltage swing that takes place on the diode is limited by the pixel supply voltage (V_{DD}) minus the threshold and bulk effect voltages related to the reset MOSFET (V_{THR}), and the thermal voltage level where charge begins to thermally escape from the diode through the reset switch (V_{th}). Charge capacity for the pixel is the voltage swing divided by the photodiode sensitivity (V/e^-). For example, assuming $V_{DD} = 3.3$ V, $V_{THR} = 1.4$ V, $V_{th} = 0.9$ V (36 kT), and $S_V = 33$ μ V/ e^- a full well level of 30,000 e^- is calculated. It should be noted that saturation could also take place if the source follower threshold voltage, V_{THS} , is greater than V_{th} . Figure 2 shows a photon transfer curve generated by a 3T, 4 μ m pixel DVGA CMOS detector that delivers a charge capacity in agreement with these assumptions [2]. Driving the reset gate to a voltage greater than V_{DD} can increase charge capacity for the 3T. For example, driving the reset gate to $V_{DD} + V_{THR}$ will result in a charge capacity of 115,000 e^- based on assumptions above. An external voltage or on-chip charge-pumping circuits are provided to generate the required drive [3]. An additional benefit to over driving the reset MOSFET is the elimination of floating diffusion image lag problems [2].

The photodiode pixel exhibits a nonlinear output response because the depletion capacitance of the photodiode decreases as it charges. In turn, the node sensitivity (V/e^-) decreases. The effect is seen in Fig. 2 where the chip gain constant ($e^-/\text{digital number (DN)}$) varies from 30 to 40 e^-/DN .

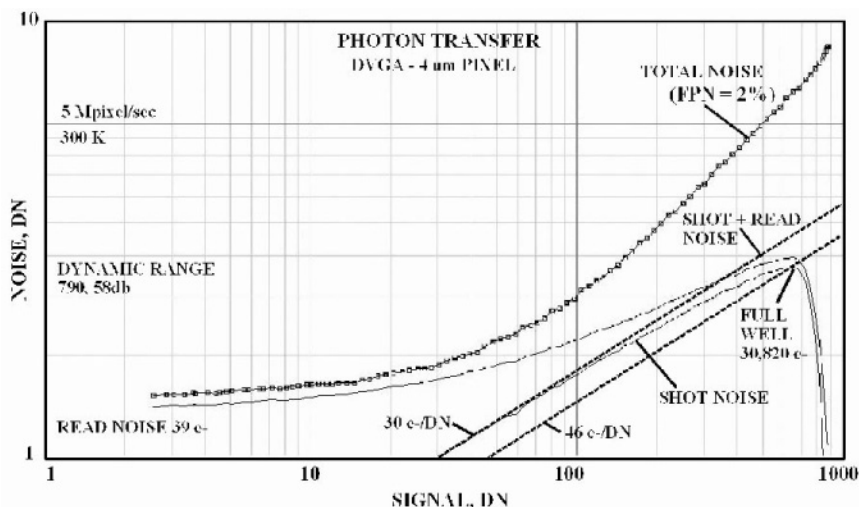


Figure 2. Photon transfer generated by a 3T DVGA CMOS array.

Nonlinearity increases with photodiode doping, however, charge capacity also increases. The nonlinearity effect works in the designer's favor because the sense node sensitivity (V/e^-) is highest, and reset noise lowest at low signal levels. Computer-processing algorithms can readily remove nonlinearity.

The 3T pixel uses *rolling shutter* readout. Charge integration time, or the time period where the photodiode is allowed to discharge to photon input, is governed by leaving the reset switch off a specified number of line periods before a row is selected for readout. For example, minimum integration time occurs when the reset switch is inhibited one line before a row is selected. Rolling shutter exhibits image smear and motion artifacts because charge integration takes place over the entire readout period (1/30 sec for standard video rates). Advanced pixel designs discussed below minimize the effect. The readout scheme also inherently exhibits high read noise because it is incompatible with CDS signal processing. Here we find that the reference and video levels are not referenced to the same reset pulse (i.e., a reset occurs between the two samples). The resultant noise is limited by kTC reset noise, which varies from 20 to 70 e^- depending on the diode capacitance. Nevertheless, CDS processing is almost always employed to minimize fixed pattern noise (FPN) generated from column to column gain and offset differences (a CDS circuit is usually employed in each column of the array).

The 3T pixel exhibits relatively high thermal dark current (typically 0.3 to 1 nA/cm^2 at 300 K) compared to CCD arrays. In addition, bright pixels (i.e., dark spikes) usually accompany the dark floor. The spikes are often generated at the n^+ sense node contact where process induced damage exists. Dark spikes and associated dark FPN can be eliminated by cooling the detector or by despiking the image via computer processing. Advanced pixel designs discussed below can eliminate the n^+ contact dark current problem.

To achieve good charge collection efficiency (CCE) and low pixel cross talk (i.e., high MTF), the n -diode implant (typically phosphorus) is driven as far as possible. In doing so, an ohmic region and corresponding depletion region extends deep into the silicon to collect near-IR photoelectrons efficiently.

2.2 5T Pinned Diode CMOS pixel

The 5T pinned diode CMOS pixel corrects 3T photodiode performance deficiencies, and therefore, the pixel is considered for scientific use here. Signal charge is generated and collected in a pinned diode region that is at a fixed potential. Note from Fig. 1 that the pinned diode is isolated from the sense node and 3T readout MOSFETs by a transfer gate (4th T). The transfer gate, when activated high, transfers charge from the pinned region to a sense node. In that the pinned region is fully depleted, complete charge transfer takes place without image lag problems (similar to CCD operation). Also shown is a global reset gate (5th T), which serves several purposes (e.g., extended dynamic range [3]).

It is important that the sense node sensitivity (V/e^-) matches the diodes charge capacity. If, during charge transfer, the sense node potential swings to a potential equal to the diode potential (when empty) incomplete transfer will

take place. Node sensitivity and associated swing are adjusted by the source follower gate capacitance. Therefore, source follower geometry typically scales with pixel size. Also note that nonlinearity is less for a 5T compared to a 3T because node capacitance is dominated by the source follower capacitance (diode capacitance dominates the 3T pixel resulting in more nonlinearity).

Like the 3T pixel, a pinned diode exhibits high quantum efficiency (QE) depending on pixel fill factor. For example, a 5T pinned diode 9 μm pixel layout can exhibit approximately 80% fill factor using current CMOS design rules (i.e., 0.18 or 0.25 μm). For short UV wavelengths, reflection is the main QE loss. At 4000 \AA approximately 40 % QE is achieved for light collecting areas of the pixel.

There are a few disadvantages with the 5T pinned pixel. Low charge capacity usually limits the technology to large pixel applications. This limitation is because the pinned diode potential needs to be set approximately mid way between the potential of the transfer gate when low and the potential of the sense node after reset (refer to Fig. 3). Also, the pinned diode requires two custom implants similar to how pinned CCD pixels are processed [1]. The first implant (typically phosphorus) defines the potential of the diode region, whereas the second implant (typically boron) is a very shallow but concentrated implant that pins the surface potential (and hence, diode potential) to ground potential. The implants employed must be very accurately aligned or charge transfer problems will result. For example, a trap problem often develops when the p+ pinning implant encroaches under the transfer gate during high temperature processing. This decreases the potential at the leading edge of the gate resulting in a barrier for electron transfer as demonstrated in Fig. 3. The fringing fields between the transfer gate and sense node region do not overcome the barrier because the potential difference between regions is very small. Although CCDs exhibit similar trap problems they are not as vulnerable as CMOS because clock and bias voltages and corresponding fringing fields are much greater and normally prevail over the traps. The CMOS trap problem described here can be corrected by offsetting (or angling) the pinning implant from the transfer gate slightly (less than 0.4 μm).

Several readout modes are possible for the 5T pinned pixel. Two popular modes are referred to as *snap* and *progressive scan* readout. Rolling shutter with true CDS is another readout scheme. Readout is initiated by resetting all pixels using the global reset gate. Next, charge is integrated on the diode for a given exposure period. During this time the sense node is reset to eliminate any dark current or signal charge build up there. Then signal charge is transferred to the sense node for all pixels at one time. After transfer, readout commences line-by-line using CDS-like processing (i.e., sample 1, reset, sample 2). The readout

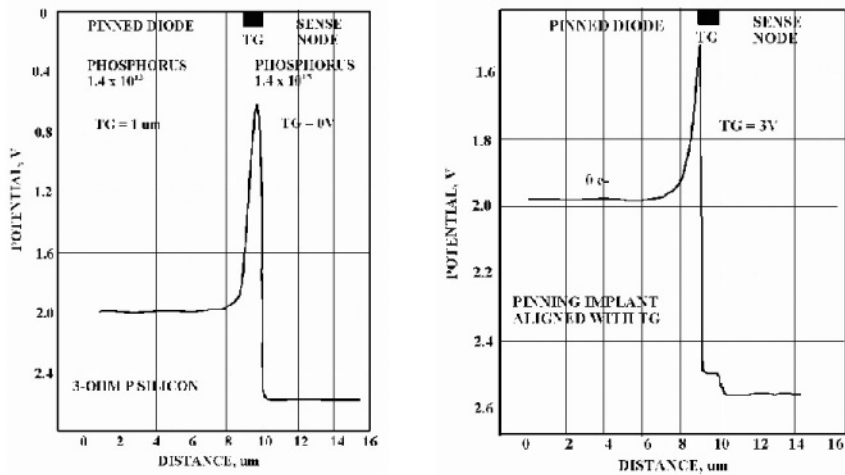


Figure 3. Potential diagrams for a pinned diode CMOS pixel.

scheme is referred to as snap because very short exposures can be taken compared to the readout time. This allows freeze-action photography not allowed by rolling shutter readout. As with 3T operation, true CDS is not possible for snap readout, limiting noise performance to kTC noise. However, reset noise is lower than 3T because only the sense node capacitance is involved (the diode capacitance is absent). The pixel will also exhibit high dark current like the 3T because the n+ sense node stores charge during readout.

It should be noted that the sense node must be protected from charge that blooms over the transfer gate during readout. Sense node blooming can occur when the integration time is less than the readout time. The problem can be circumvented by setting the global reset gate to a potential lower than the transfer gate allowing charge to escape through the global reset gate drain instead of to the sense node.

Snap readout can also take place as the next frame is integrated (similar to frame and interline transfer CCDs). Here the exposure and readout periods are equivalent. Signal charge collected on the diode can be controlled by activating the global reset switch for a specified time during integration (a form of electronic exposure).

Image cross talk is an important issue for snap readout. Light shields above the pixel prevent photons from interacting directly with the transfer gate and sense node regions (the light shield typically defines the fill factor for the pixel). But, signal charge generated in deep regions of the silicon can diffuse to the sense node during readout resulting in image cross talk. The isolation problem is

most conspicuous for very short near-IR exposures. Providing a shielding implant beneath the sense node and transfer gate as shown in Fig. 1 can minimize the effect. The implant gradient produces a self-induced electric field that forces signal charge from the region into the diode region. Normally the sense node and read MOSFETs are placed in a highly doped p-well that naturally reflects signal carriers from the regions.

The second readout scheme, progressive scan, allows for true CDS readout and low dark current generation. For this mode of operation, a mechanical shutter (or pulsed light source) is normally used for long exposure periods (e.g., astronomical applications). After exposure, charge is read line-by-line using true CDS readout (i.e., reset, sample-1, charge transfer, sample-2). Progressive scan offers low dark current because the sense node can be continuously reset until a line of pixels is read. In addition, the diode region exhibits low dark current because of the pinning action at the Si-SiO₂ interface similar to MPP operation for CCDs [1]. The problem of image cross talk is also less concerning because charge that diffuses to the sense node during readout is eliminated through the reset switch. In this case, the charge diffusion problem translates to a QE loss, which as mentioned above, can be minimized through a sense node shielding implant.

2.3 6T Photogate CMOS pixel

A 6T photogate pixel is similar to the 5T pinned diode pixel except that a photogate replaces the pinned diode. The pixel is based on conventional CMOS processes making the pixel much easier to fabricate. Charge transfer to the sense node takes place by clocking the photo and transfer gates similar to CCD operation. The readout modes discussed above (e.g., snap, progressive scan, rolling shutter) are also applicable to photogate array. Charge capacity for the photogate is greater than the pinned diode because the gate can be clocked to V_{DD} volts or more.

The main disadvantages for the conventional photogate pixel are low QE performance and image lag. The QE problem is particularly critical for blue/UV incoming wavelengths where the poly silicon gate is absorbing. QE performance can be enhanced by employing photogates that partially cover the active region (similar to poly hole CCDs [1]). Image lag is inherent to the pixel because of n+ material typically located between gates. Because these regions cannot be fully depleted, charge transfer will be incomplete resulting in image lag. Custom photogate designs exist that can provide full depletion and complete charge transfer (e.g., overlapping poly gates as employed by CCDs).

In general, CMOS pixels suffer from charge diffusion problems [2]. CCD manufacturers have reduced charge diffusion effects by using high resistivity silicon wafers and high voltage clocking to take advantage of the fact that the

electric field depth varies as a function of the square-root of resistivity and applied voltage. CCD electric fields typically extend 7 to 10 μm , allowing full spectral coverage into the near-IR spectral region (7000 to 11000 \AA). In contrast, charge collection efficiency for CMOS arrays has been relatively poor because standard foundry processes use low resistivity silicon and require low voltage drive. Typical electric field depths for CMOS processes extend only 1 to 2 μm , limiting low cross talk spectral coverage to less than 6500 \AA . Also, collection efficiency degrades as the pinned diode and photogate potential wells collapse as signal charge collects. For example, at full well, the depletion depth under the photogate becomes nearly non-existent. The 3T pixel is less sensitive to the problem for reasons given above (i.e., n-region can be implanted deep). Buried channel CCDs will maintain some depletion depth under the barrier phases under full well conditions, and therefore, show relatively constant MTF over the sensors dynamic range. Trading charge capacity for charge collection efficiency and use of high resistivity silicon can minimize charge diffusion effects. Also, the photogate can be driven with a high clock voltage for increased depletion. Lastly, the substrate can be driven negatively for more depletion.

2.4 Photogate 6T Backside Illuminated CMOS Pixel

Ultimate QE sensitivity is achieved by removing the substrate layer and allowing direct illumination of the epitaxial silicon layer from the rear of the device. Thinning CMOS arrays is in its infancy and many problems will need to be resolved. For example, near-IR photons can interact directly with the sense node and MOSFETs resulting in QE loss. Maintaining a large fill factor through state-of-the-art design rules will minimize this loss. Also, charge diffusion to the same structures is important at all wavelengths. As explained above, deep shielding implants will help direct signal charge into the photo region. How effective these shielding implants will be remains to be seen.

Sometimes poor yield has been experienced when CMOS arrays are thinned. Membrane stress during thinning is probably one culprit behind the shorts seen. Compared to CMOS, the CCD is a more robust technology to apply thinning. For example, CMOS arrays employ very thin gate oxides (about 50 \AA thick) where CCD gate insulators are approximately ten times thicker, and therefore, are less vulnerable to stress induced shorts. Also, inter-level metal shorts present a potential problem to CMOS arrays. In contrast, scientific CCDs usually employ a single metal layer circumventing the problem completely. Also, accumulating the backside after thinning can be stressful if high temperature processing is involved (e.g., ion implantation followed by a high temperature activation process). Low temperature accumulation techniques employed on CCD arrays are attractive for this reason (e.g., flash gate technology) [1].

3. CMOS PIXEL CHARACTERIZATION

Unlike CCD characterization, the CMOS test engineer does not have direct access to the pixel output signal. Instead, raw pixel video is processed by on-chip analog circuitry making it impossible to evaluate fundamental pixel performance. To gain understanding about CMOS pixels, stand-alone discrete test pixels are characterized. Such test devices are clocked and readout using the same electronics in testing CCDs. Full well, dark current, linearity, cross talk, read noise, QE, image-lag, etc., are typical data products collected for each test pixel type. The same characterization process is used to find optimal clock and bias conditions. Discrete CMOS analog circuits (e.g., CDS, amplifier, ADC) are also designed and tested to evaluate their impact on pixel performance.

Figure 4(left) shows a test pixel array with nine different 32×32 sub arrays that contain diverse pixel designs. Figure 4(right) shows nine center pixels within a sub array that can be independently clocked and read out. The pixels are designed differently and evaluated to determine optimal design features. As shown, the center pixel is usually completely shielded from light in order to perform cross-talk measurements.

Figure 5 shows a low-light level photon transfer curve generated by a 6T photogate test pixel with the photogate non activated (i.e., no charge transfer takes place). The $2.8 e^-$ noise floor measured is limited by random telegraph signals (RTS) $1/f$ noise generated by the source follower MOSFET. This is a typical response for small MOSFETs using the CDS signal processing parameters indicated [2].

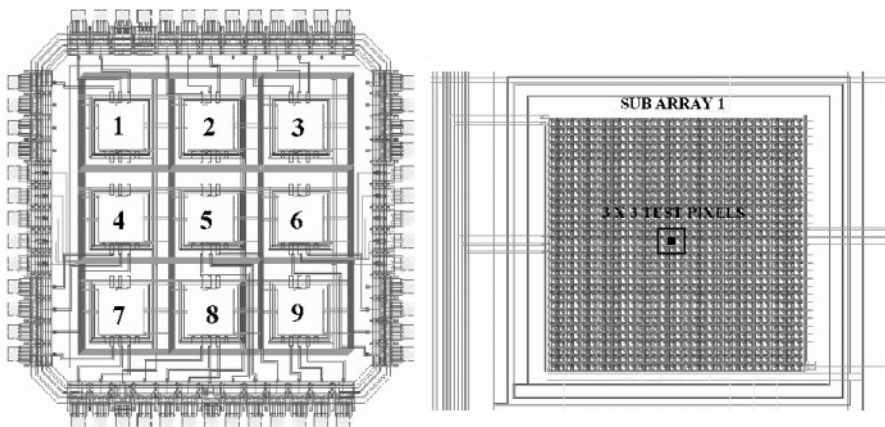


Figure 4. Test pixel array (left) and sub-pixel array showing center nine test pixels (right).

observed for high signals is associated with the source follower MOSFET. Also shown is a video response taken directly from the pixel. Figure 7 shows a line trace of pixels exercised by a LED light source that is cycled on and off to show image lag behavior. Approximately 140 e^- peak-to-peak signal is displayed in conjunction with a 3 e^- noise floor.

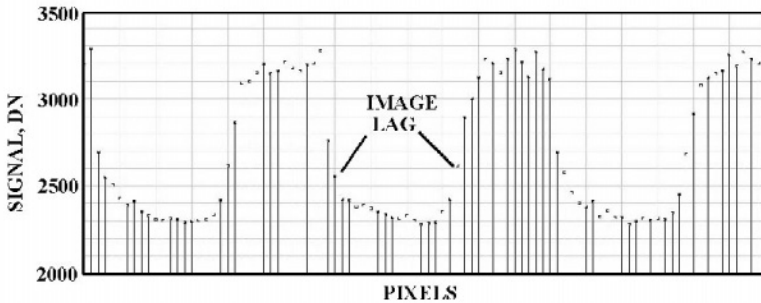


Figure 7. Line trace of pixel responses showing image lag behavior.

4. SUMMARY

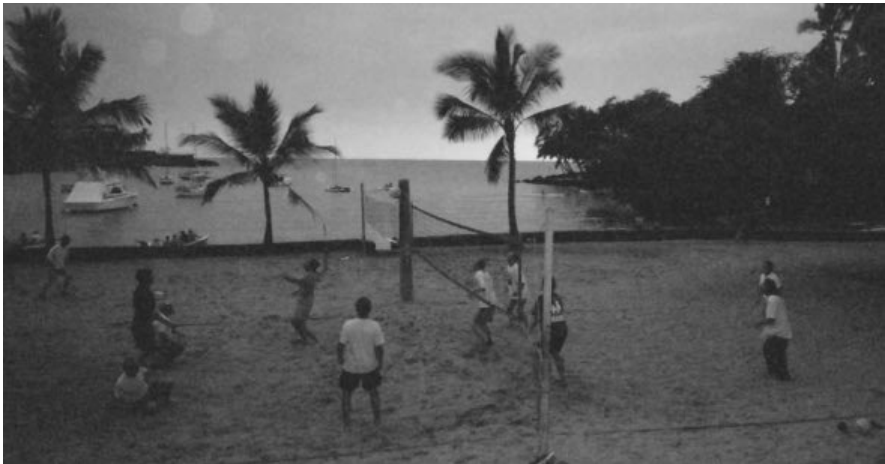
The 3T pixel offers several high-quality attributes for scientific imaging applications. Design and process simplicity, high UV QE, high fill factor, high charge collection efficiency with deep ohmic diode contact, high full well and absence of image lag are well established claims for the pixel. Unfortunately, high reset noise and high dark current have kept the pixel from scientific use. CMOS groups are actively trying to reduce kTC noise by a variety of ingenious techniques [2]. However, the methods usually fall short of what true CDS can achieve and are often plagued with image lag problems. Efforts to reduce 3T read noise (without image lag!) to the noise level of the CCD remains to be seen. The pinned diode pixel can offer low read noise and dark current comparable to the CCD. However, low full well and very custom (and delicate) fabrication requirements are disadvantages for the pixel. Although developmental cost would be high, the pinned CMOS pixel is a good candidate for future scientific use. The primary drawbacks to the photogate pixel are image lag and low QE performance. The QE difficulty can be circumvented by backside illumination, however, significant development will be required to bring this technology to light. Image lag will need to be completely eliminated for scientific use. This requirement may be satisfied by custom photogate designs that can achieve complete charge transfer like the CCD (e.g., double poly process).

In-depth fundamental pixel and on-chip support circuitry characterization will continue at Sarnoff. Work is under way to fabricate photogate pixels without image lag. Efforts include developing a high yield thinning process. CMOS development work will pay close attention to the charge diffusion

problem through use of high resistivity silicon, high voltage drive and thinning to minimize field free material. Timing and logic control for progressive slow-scan readout and true CDS signal processing will be emphasized. For example, CDS *quiet times* will be enforced to avoid on-chip ground bounce problems as employed in low noise CCD camera systems [1]. Lastly, *hybrid* CMOS/CCD arrays will be pursued. Here, the best performance attributes from CMOS and CCD technology will be combined.

5. REFERENCES

- [1] Janesick, J., 2001, *Scientific Charge-Coupled Devices*, SPIE Press, Bellingham, Washington.
- [2] Janesick, J., 2002, *Lux Transfer; CMOS versus CCD*, Proc. SPIE, **4669**, p. 232.
- [3] Blinc, A., 2001, *640x480 CMOS Active Pixel Video Camera with Adaptive Digital Processing, Extended Dynamic Range and Miniature Form Factor*, Proc. SPIE, **4306**, p. 41.



The European "Dark Spikes" team (right) beat the American "Gamma Rays" team during the volleyball finals at the Keauhou Beach party (no wonder, look at the lazy player with the hands in his pockets...).

SECRETS OF E2V TECHNOLOGIES CCDS

(ex Marconi CCDs)

Paul R. Jorden¹, Peter Pool¹, Simon M. Tulloch²

¹E2V Technologies, ²Isaac Newton Group

Abstract: *To complement previously published information on E2V CCDs, we present here some less well-known information about Marconi CCDs. We show details of the performance of deep depletion silicon variants, and discuss other subtleties of performance. We also present an update on L3vision (sub-electron noise) devices, indicating current availability, options, and ongoing development work. Finally, we will give a flavour of the range of custom designs that have been made. Many of these are not commercially available, and may not be familiar to all astronomers or CCD technologists.*

Keywords: *Charge-Coupled Device (CCD), optical sensor, astronomy instrumentation, L3Vision, ultra low noise sensors.*

1. INTRODUCTION

Firstly, to avoid confusion, please note that the company has changed its name to E2V Technologies, from Marconi Applied Technologies (and was previously known as the English Electric Valve Company or EEV), since the date of this workshop presentation. Hereafter, for brevity, we will use the reference E2V for the company name.

E2V CCDs are widely used for astronomical imaging in astronomy, and performance levels (e.g., quantum efficiency and readout noise) of standard scientific sensors as were described at the previous (ESO 1999) workshop [1].

Here we shall discuss some of the less well-known specific features of E2V sensors, although we apologize if the “secrets” of the title are not all revealed! We shall also provide an update on the development status of the new L3Vision ultra low-noise sensors, as well as a flavour of the range of custom sensors, that have been developed specifically for space applications.

2. SPECIFIC PERFORMANCE FEATURES

2.1 “Dither clocking” and dark current

For non-inverted (non-MPP) CCD operation the surface dark current is dominant, and is usually undesirable. However, it is known that when clock phases are switched out of inversion the surface dark current only recovers after a characteristic time (τ). See [2] for more details.

This means that surface dark current can be dynamically suppressed by clock modulation (or “dither” clocking) provided that the phases are occasionally inverted (the clock low level should be sufficiently below the substrate potential). This clock modulation can occur as a deliberate activity during an integration time and also happens by default during a complete CCD clear (or flush) cycle prior to exposure.

We have measured dark current over a range of temperatures from -40°C to -90°C , and over a range of integration times (in darkness) from 1 to 3000 seconds. Not all data can be presented here. As an example, Fig. 1 shows measured dark current rate, and modelled dark current rate at -70°C . [Rate= total measured dark current/ integration time.]

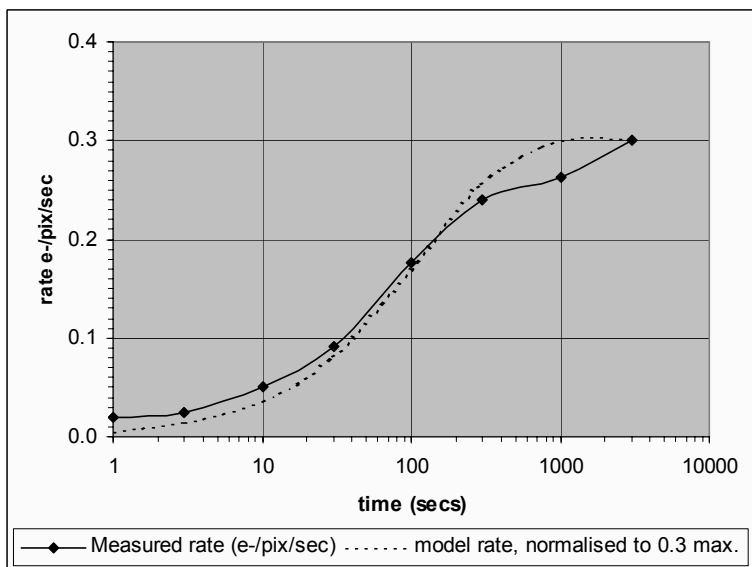


Figure 1. Dark current versus exposure time at -70°C

At short exposure times ($t < \tau$) the dark current is suppressed (potentially to the bulk dark current rate), whereas for long times ($t > \tau$) the full surface dark current rate is observed. The recovery time constant is a strong function

of temperature, and so the time required to change from suppressed dark current to full dark current varies with temperature. Figure 2 shows derived time constants over a range of temperatures. Below -80°C the time constant is ~ 3000 s and at -40°C it is ~ 10 s.

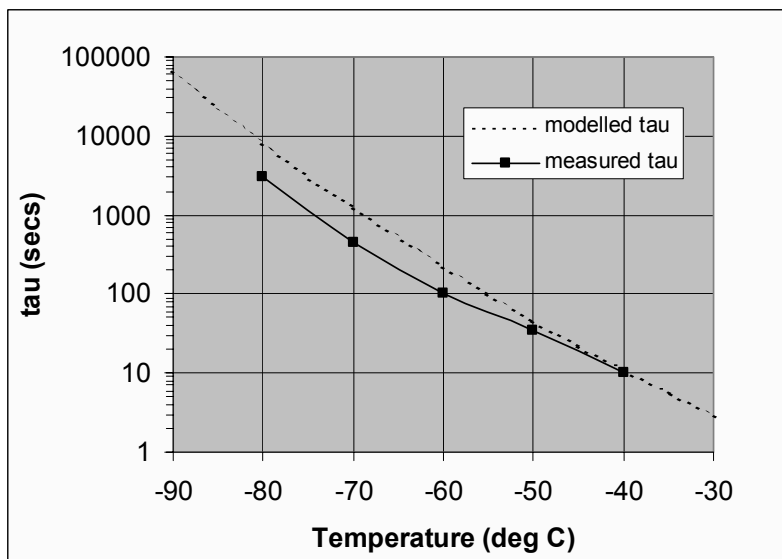


Figure 2. “Dither” time constant at various temperatures.

In summary, surface dark current may be suppressed if exposure times are short compared to the time constant, or if active “dither” clocking is used during the integration. The effect broadly follows the expected behaviour.

2.2 High resistivity silicon CCD performance

Many E2V CCDs are manufactured from “normal” resistivity silicon ($100\ \Omega\text{-cm}$ nominal), which is used for devices that are backthinned to a thickness of $\sim 16\ \mu\text{m}$. However, for maximum red response improvements are possible from the use of a thicker device ($\sim 40\ \mu\text{m}$) made of higher resistivity silicon. Furthermore, since long wavelengths can penetrate to the front side one can enhance these wavelengths a little further by adding a reflective coating to increase internal absorption.

We manufactured a trial deep depletion (high resistivity) device (CCD42-90) having regions with and without this added frontside reflector. Figure 3 shows measured (at the Issac Newton Group (ING) Telescopes) cryogenic quantum efficiency of this device, which had a red ($\sim 750\ \text{nm}$ peak) AR coating. The measurements are seen to agree very well with modelled

values. For comparison, the expected QE of such a chip (with reflector) is shown at +20 °C.

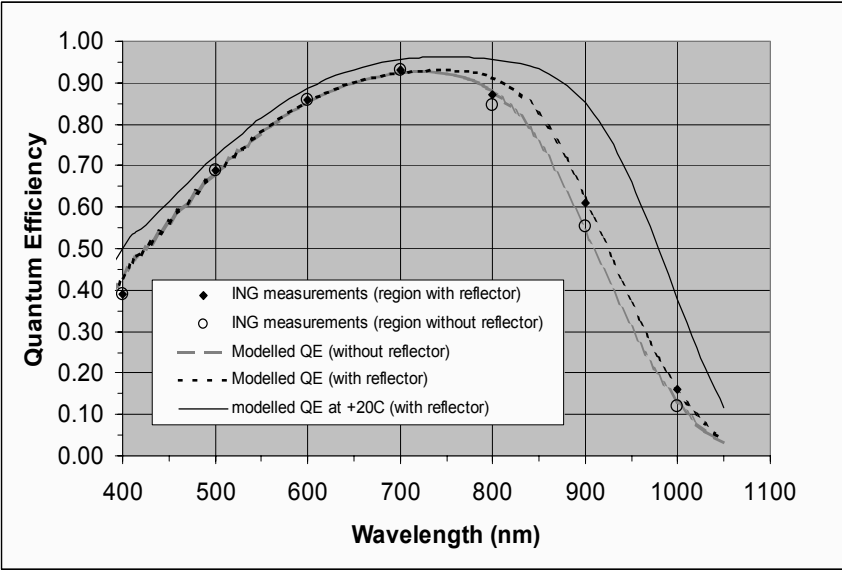


Figure 3. Cryogenic Quantum efficiency of deep depletion CCD.

Backthinned CCDs are known to produce undesirable multi-pass fringes at red wavelengths. The fringing amplitudes (measured on the ING ISIS spectrograph) are shown in Table 1, for a standard silicon E2V sensor, and for the deep depletion variant. As expected for the thicker silicon, fringe amplitude is much reduced for the latter chip. It should be noted that fringe amplitude varies considerably depending on illumination conditions and wavelength dispersion, so these values are indicative only.

Table 1. Measured % fringe amplitudes, for standard and deep depletion CCDs.

Wavelength (nm)	“EEV12” standard CCD (%)	Deep depletion CCD (%)
750	20	4
800	35	6
850	44	9
900	53	14
950	59	20
1000	59	25

Finally, we measured the width of narrow spectral lines (over the red wavelength range of 650-1000 nm), to confirm that spatial resolution was not degraded significantly by the use of thicker silicon (thickness > pixel pitch of 13.5 μm). Measured FWHM (Full-Width Half-Maximum) was

found to be ~ 1.5 pixels ($= 20 \mu\text{m}$). This is similar to values found with standard silicon E2V sensors.

3. L3VISION UPDATE

The novel L3Vision sensors offer sub-electron readout noise through the use of on-chip avalanche gain technology ([3], [4], etc.). Low noise has been demonstrated at high pixel rates, and on-chip gain of up to 1000 can be available. More details are available on the E2V web site [5].

The CCD65 TV-format sensor is available alone or within an analogue camera. This is only manufactured as a frontside illuminated sensor, in ceramic or Peltier packages. Board sets and modules are also available.

The CCD60 sensor, designed for wavefront sensing, is available in frontside form (July 2002). A backside-illuminated version is in development, and expected to be available by late-2002.

The CCD87 (512×512) is a scientific sensor, available from Aug-2002 in frontside form. Early versions of a backside illuminated CCD87 were available in 4Q 2002. In August 2003 an updated compatible CCD97 backthinned sensor will be available.

Other formats are in discussion or development (including a 1024×1024 format). The many application areas remain to be established, but wavefront sensing, high-speed imaging, and low noise detection offer important opportunities for astronomers.

4. NOVEL CCD TYPES

E2V CCDs are used for many applications including astronomy, space, commercial, and defence. In particular, many sensors have been developed for custom contracts, and are not widely known in the ground-based astronomy community. Here we shall indicate some of the variety of custom devices and packages that can be made (although not all that were presented at the workshop can be included here).

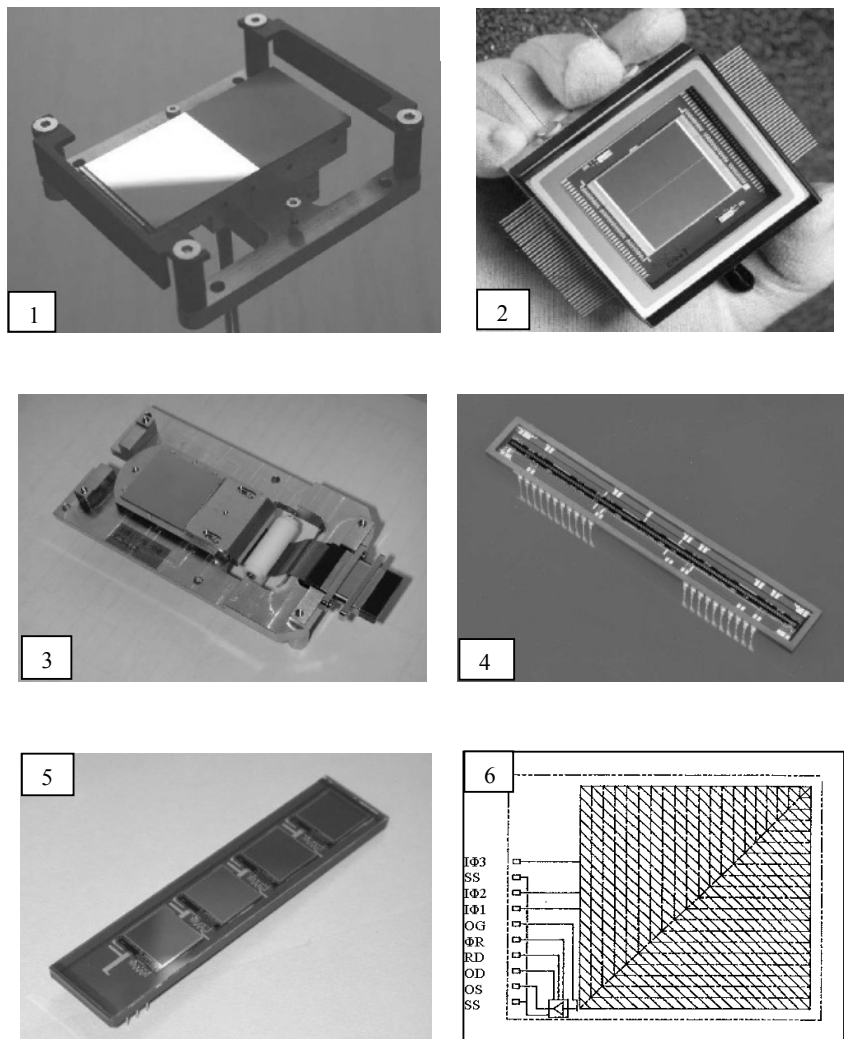


Figure 4. E2V devices: 1) Space- Corot CCD42-80 frame-transfer sensor (on handling jig), 2) Space- Large custom Peltier-cooled sensor, 3) Space-Stereo CCD42-40 on custom mounting plate, 4) CCD21-40 12K (8 μm) pixel linear sensor, 5) D-CIXS set of four CCD54 (1.1 cm^2) x-ray sensors and 6) D-CIXS "swept charge" single pixel architecture

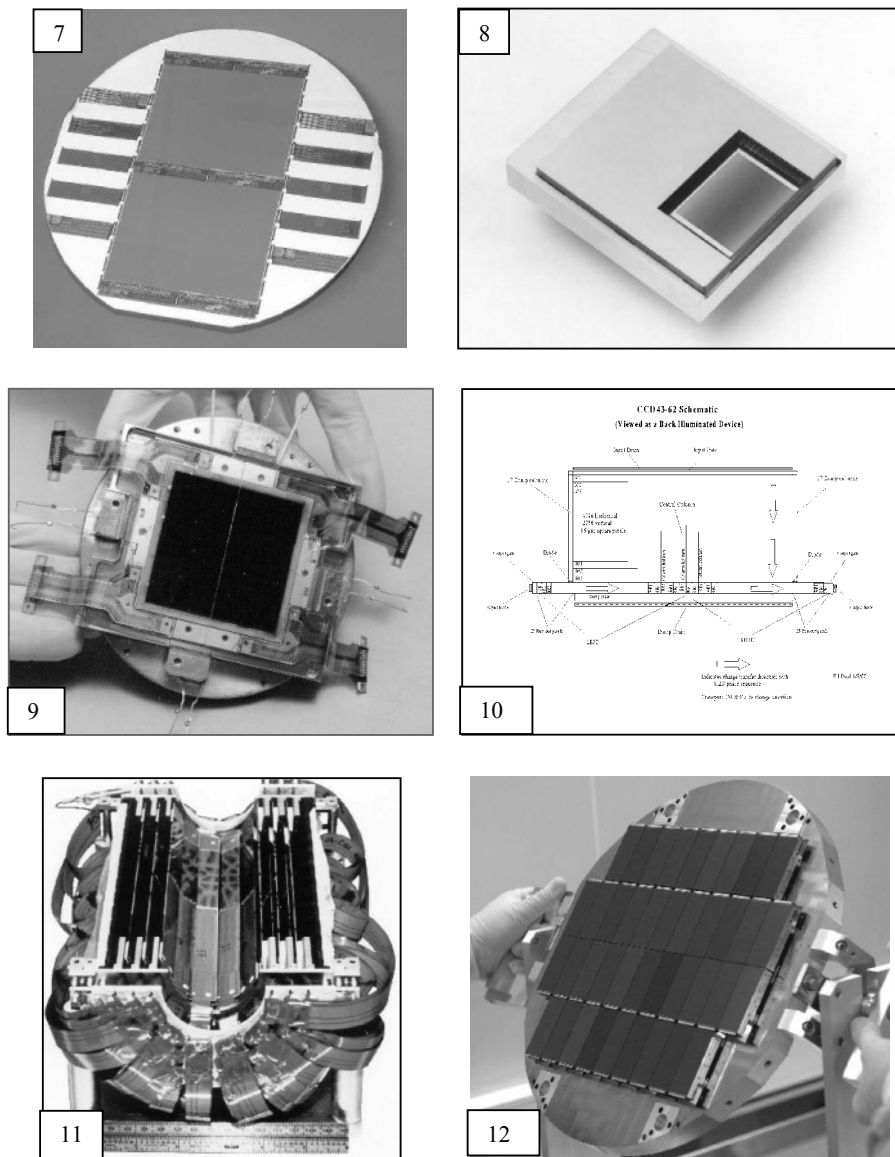


Figure 5. E2V devices: 7) Pair of large CCD46-62 (55×43 mm) sensors on wafer, 8) Space-Envisat CCD25-20 spectrometer sensor (graded AR coating), 9) Space-two CCD43-62 sensors in Hubble WFC3 focal plane assy, 10) CCD43-62 (4096×2050, 15 μm) sensor architecture, 11) Set of 96 CCD32-60 (800×4000) Vertex detectors for SLAC and 12) 40-chip mosaic of CCD42-90 sensors (CFHT).

5. REFERENCES

- [1] Jorden, P.R., Pool, P., Holtom, R., 2000, *Development of a back-illuminated 4K×4K CCD with low-noise outputs*, Kluwer Academic Publishers, Proc. Optical Detectors for Astronomy II, (ESO workshop, Garching, 1999). P. 227.
- [2] Burke, B.E., Gajar, S. A., 1991, *Dynamic suppression of interface-state dark current in buried-channel CCDs*, IEEE Trans. Electron Devices, **38 (no. 2)**, p. 285.
- [3] Jerram, P., Pool, P., Bell, R., Burt, D., Bowring, S., Spencer, S., Hazelwood, M., Moody, I., Catlett, N., Heyes, P., 2001, *The LLCCD: low-light imaging without the need for an intensifier*, Proc SPIE **4306**, p.178.
- [4] Mackay, C., Tubbs, R., Bell, R., Burt, D., Jerram, P., Moody, I., 2001, *Subelectron read noise at MHz pixel rates*, Proc SPIE **4306**, p. 289.
- [5] <http://www.e2vtechnologies.com/ccds>



A highlight of Paniolo night was the fashion show. As paparazzi take photos from the rear of the catwalk, Morley Blouke struts the latest western style from Beaverton, Oregon.

PROGRESS IN ULTRA-LOW NOISE HYBRID AND MONOLITHIC FPAS FOR VISIBLE AND INFRARED

Lester J. Kozlowski
Rockwell Scientific

Abstract: *Deep sub-micron ($\leq 0.25 \mu\text{m}$) CMOS enables the existence of imaging sensors with lower noise at higher video frequencies and lower power dissipation than previously possible. This CMOS-based imaging System-on-Chip (i-SoC) technology hence produces large monolithic and hybrid Focal Plane Arrays (FPAs) that outperform competing CCD-based imaging sensors. The hybrid approach produces visible 2048^2 FPAs and 4096^2 mosaics with $\sim 5e^-$ read noise at 1 MHz and quantum efficiency $>80\%$ from 390 nm to 930 nm. The monolithic approach produces visible 12-bit imaging system-on-chips such as a 1936×1088 with higher quantum efficiency than mainstream CCDs, $< 25e^-$ read noise at 75 MHz and power dissipation $< 180 \text{ mW}$.*

Key words: *infrared (IR), Focal Plane Array (FPA), Complementary Metal Oxide Semiconductor (CMOS), Charge-Coupled Device (CCD), imaging system-on-chip(I-SoC)*

1. INTRODUCTION

Motivated by the compelling need for low-noise, pixel-based amplifiers, infrared Focal Plane Array (FPA) designers quickly moved from CCD readouts to CMOS multiplexers in the mid-1980's. Subsequently leveraging Moore's Law [1] over the intervening years, 2048×2048 focal plane arrays and 4096×4096 mosaics now provide read noise as low as a few e^- for imaging with 12- to 16-bit resolution at high video rates [2, 3]. This paradigm shift presaged the battle now raging between competing visible

sensors by over one decade. While many low-light-level cameras still use CCDs for signal readout, alternative deep sub- μm CMOS technology is justifying a similar pilgrimage for visible camera designers.

Shrinking CMOS feature size is now pushing CMOS-based imaging to larger arrays with smaller pixels. Figure 1 shows the corresponding number of transistors that fit into $5\text{ }\mu\text{m}$ by $5\text{ }\mu\text{m}$, a typical pixel size for a two-dimensional visible imaging array. While the digital processes used to produce microprocessors first enabled integration of several transistors per $5\text{ }\mu\text{m}$ pixel at the start of the 1990's, as shown by the CMOS trendline for microprocessor transistor integration, analog processes and design trades enabled similar integration for visible imaging sensors by ~ 1995 . Thus began the epoch of CMOS-based sensors as a competitive alternative to CCDs.

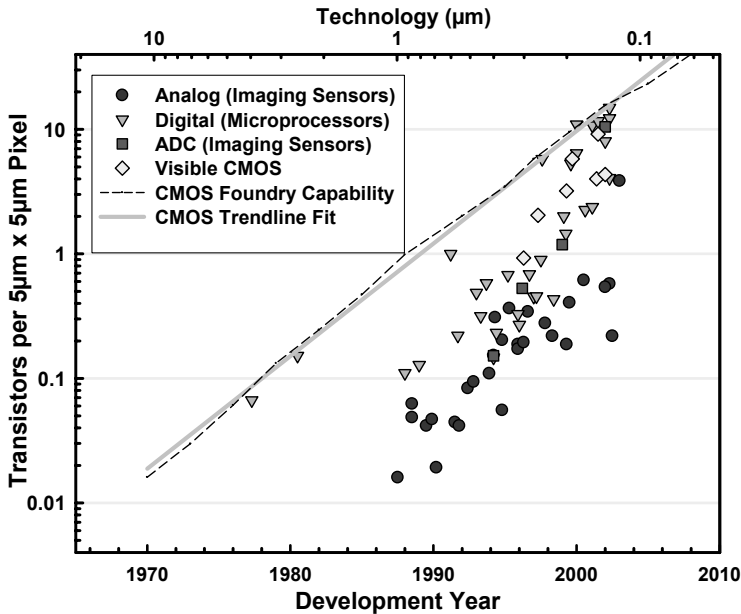


Figure 1. “Practical” number of MOS transistors that fit into a $5\text{ }\mu\text{m}$ by $5\text{ }\mu\text{m}$ pixel vs. year.

The “Analog” group in Fig. 1 focuses on imaging sensors with analog output such as infrared focal plane arrays. The “Digital” grouping translates microprocessor transistor data to the “pixel-centric” domain. The “ADC” set includes imaging sensors for machine vision with pixel-based processing and others with direct-to-digital architecture, such as Yang [4]. “Visible CMOS” accounts imagers with analog pixels and digital output.

1.1 CMOS System-on-Chip Architecture

CMOS-based imagers for both infrared and visible applications now use pixel-based amplifiers in the imaging system-on-chip architecture shown in Fig. 2. The pixel-based amplification enabled by CMOS is best exploited by the latest CMOS technology. While the gated-integrator signal formation in the CMOS pixel amplifier sets the signal bandwidth appropriately, the predominant noise bandwidth of a large format CCD imager is several orders of magnitude higher to read the signal with minimum electrical crosstalk. The read noise of a large format CCD after CDS is hence often dominated by the output amplifier's thermal noise. The CMOS paradigm mitigates this problem because the pixel-based amplifier's bandwidth is better matched to the pixel sampling frequency. This reduces the relevant noise bandwidth so that the CMOS output buffer's noise is negligible.

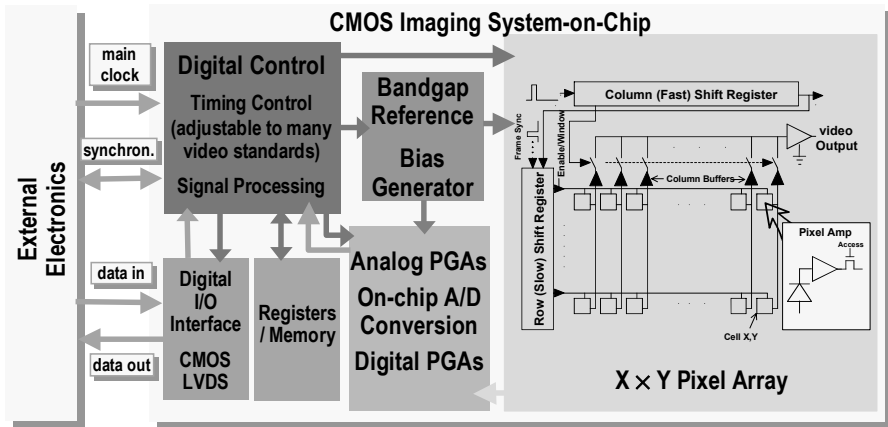


Figure 2. Architecture of representative CMOS imaging system-on-chip.

Unlike the CCD where both charge-to-voltage conversion and video signal buffering occur at the output, these two critical functions are separated in CMOS readouts. The conversion gain is thus optimized for each application. Sense capacitance as small as 0.35×10^{-15} F has thus far been achieved; resulting in measured conversion gains ≥ 100 mV/e⁻ using additional on-chip programmable gain amplifiers.

2. KEY METRICS

CMOS-based imagers hence provide lower temporal noise at video rates along with practical advantages such as on-chip integration of camera related

functions. While monolithic CMOS competes with commercial CCDs, the CMOS-based hybrid facilitates simultaneous optimization of optical fill factor, detector performance and pixel amplifier design. Hybrid manufacture allows the constituents to be fully optimized to the extent that the relevant available technologies allow. In this multi-chip module, signal detection and readout are segregated by flip-chip hybridization where:

- quantum detection is performed in the optimum detector for the specific spectral band and operating temperature.
- low-noise amplification and multiplexing is done in the CMOS readout
- indium interconnects mechanically and electrically interface the detector array and readout.

These advantages have led to the development of CMOS-based hybrids that use silicon detectors [5] or alternative materials with optimized bandgap to reduce dark current, raise operating temperature and optimize the spectral bandpass.

2.1 Read Noise

Mean read noise for various hybrid and monolithic imaging FPAs is summarized in Fig. 3, a plot of read noise vs. “sense” capacitance for various Source Follower per Detector (SFD) and Capacitive TransImpedance Amplifier (CTIA) imaging sensors.

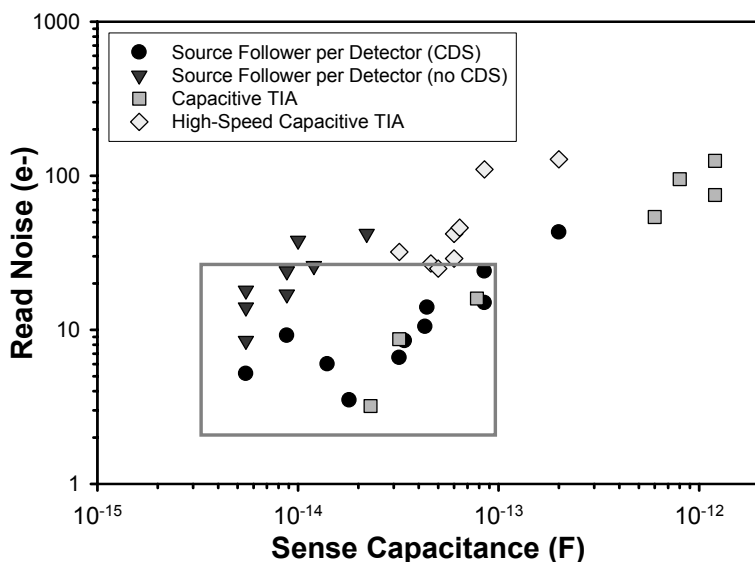


Figure 3. Read noise vs. sense capacitance for CMOS-based imaging sensors at 5 to 75 MHz.

The basic trend toward lower noise for lower capacitance is common to all sensors. However, CMOS read noise is typically $< 20 \text{ e}^-$ for sense capacitance as large as 100 fF. Further, alternative capacitive TIA designs having feedback amplifiers can transmute the relevant noise capacitance from a larger detector-based value to a smaller feedback capacitance to further suppress kTC noise

Figure 4 compares theoretical limits for noise at 8 fF and 12 fF sense capacitance to the read noise reported on CCDs optimized for astronomy, video CCDs available from several manufacturers, the CMOS-based HAWAII-2 IR and visible FPAs, and our monolithic ProCam-HD CMOS sensor.

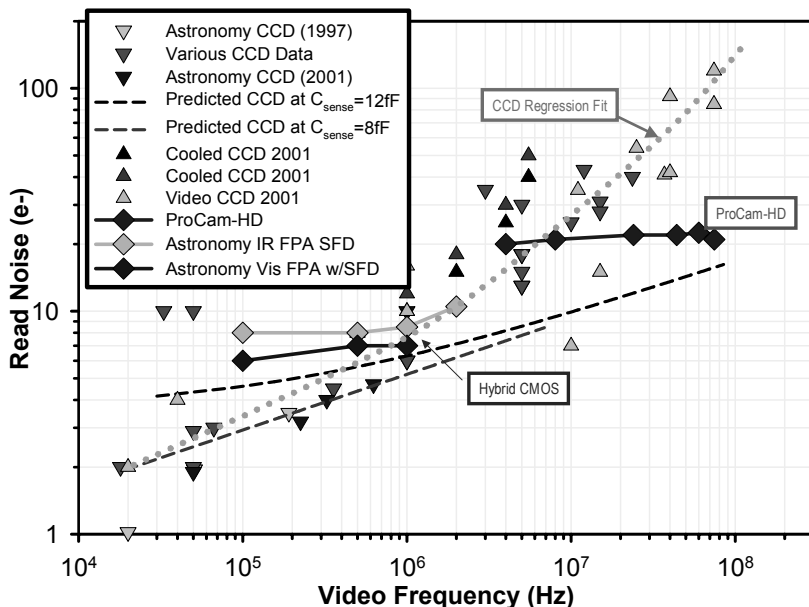


Figure 4. Read noise vs. frequency for various CCDs and CMOS-based imaging sensors.

In good agreement with theory, read noise $< 3 \text{ e}^-$ is repeatedly achieved with astronomy CCD's from the Massachusetts Institute of Technology's Lincoln Laboratory at 10 to 20 kHz. Read noise for video CCDs, on the other hand, increases faster than the amplifier white noise at higher frequencies due to the deleterious impact of excess camera noise stemming from inadequate transimpedance. The ProCam-HD CMOS imager's read noise is significantly lower than the video CCDs at frequencies above 10 MHz with nearly constant read noise of $\sim 20 \text{ e}^-$. The dominant noise mechanisms for this device weakly depend on the video rate and associated

bandwidth. In comparison, HDTV CCDs have $>80\text{ e}^-$ read noise at 75 MHz. Hybrid visible FPA noise is $\sim 6\text{ e}^-$ to 1 MHz. The soon available visible HAWAII-2RG is expected to have read noise approaching 1 e^- at 1 MHz using Fowler sampling at 32 pairs.

2.2 Quantum Efficiency

An optimized silicon detector can offer near-100% quantum efficiency from UV to NIR. Optimization, however, requires decoupling the detection process from the readout process. To produce high performance visible FPAs, we are thus developing visible sensors that combine high sensitivity silicon detector arrays with sub-micron CMOS readout multiplexers and flip-chip hybridization technology that has been developed and optimized over the past 20 years. In addition, the commonality of readouts and controllers to IR channels is another unique attribute. This technology meets high-end visible imaging needs especially when performance, radiation hardness, stability and operability are all important.

Figure 5 shows quantum efficiency (QE) data taken on a hybrid visible silicon imager (HyViSI), labeled HyViSI-1, with $8\text{ }\mu\text{m}$ pixels having anti-reflection coating.

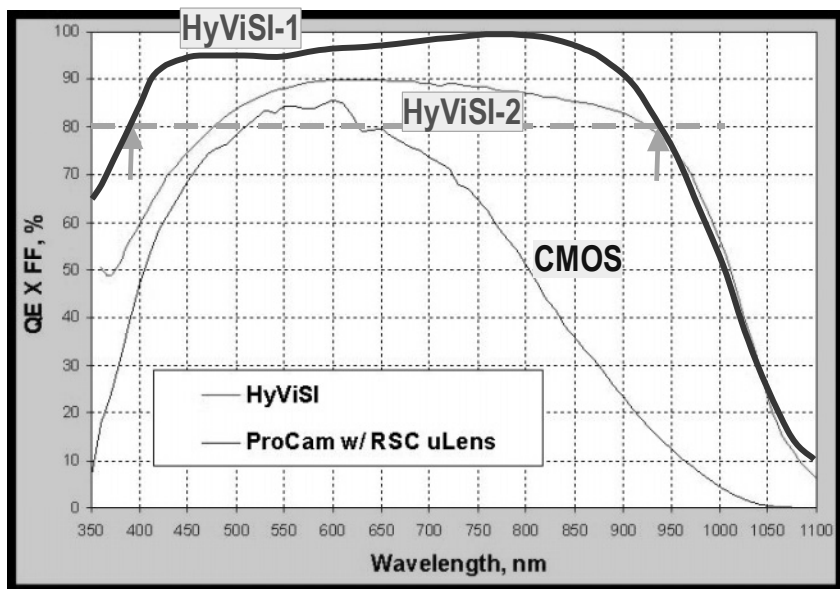


Figure 5. Measured quantum efficiency for hybrid and monolithic CMOS imaging sensors.

The FPA data taken using a set of narrow bandpass filters agrees with PEC QE spectral curve. The spectral response exceeds 90% from 415 nm to 905 nm and 80% from 390 nm to 930 nm. QE loss analysis indicates that optical reflection loss is the dominant loss mechanism. HyViSI-2 hence shows the lower performance due to reflection loss that is achieved with a single-layer a-r coating. Also shown is the QE for a monolithic CMOS ProCam-HD sensor with near-100% fill factor microlenses [6]. Here the dominant loss is inadequate absorption in the near infrared.

3. CONCLUSION

CMOS-based imaging system-on-chip (i-SoC) technology is successfully producing large monolithic and hybrid FPAs that are superior in many respects to competing CCD-based imaging sensors. The hybrid approach produces visible 2048×2048 FPAs with $<6\text{ e}^-$ read noise, quantum efficiency $>90\%$ from 415 nm to 905 nm, and pixel operability of 99.97%; 4096×4096 mosaics are now being developed using the HAWAII-2RG readout [7].

Table 1 compares three visible FPA technologies with respect to over a dozen key parameters. Values that are relatively inferior are italicized, including many of the values for incumbent CCD sensors that are available as Commercial-Off-The-Shelf (COTS) and astronomy sensors.

Table 1. Parametric comparison of CCD, hybrid CMOS and monolithic CMOS.

Parameter	CCD	Hybrid Si	CMOS
Read Noise: 250 KHz	$< 5\text{ e}^-$	$< 2\text{ e}^-$	$< 2\text{ e}^-$
1MHz	$< 10\text{ e}^-$	$< 2\text{ e}^-$	$< 2\text{ e}^-$
75MHz	$< 100\text{ e}^-$	$< 25\text{ e}^-$	$< 25\text{ e}^-$
QE $>70\%$ Science	400-800	375-950	470-680
COTS	<i>Poor</i>	450-950	470-680
Fringing	<i>Yes</i>	None	?
Brickwall Pattern	<i>Yes</i>	No	No
Pitch (μm)	≥ 3	≥ 8	≥ 3
Dark Current	<i>Low-High</i>	<i>High</i>	Moderate
Image Smear	<i>Yes</i>	No	No
MTF @ Nyquist: 250 KHz	$> 65\%$	$> 60\%$	$> 65\%$
75 MHz	$> 5\%$	$> 60\%$	$> 65\%$
Snapshot @ 8 μm	Yes	Yes	Yes
Rad-Hardness	<i>Low</i>	High	High
System-on-Chip	<i>No</i>	Yes	Yes
Romance/Wizardry/Passion	<i>Cult Status</i>	All Business	All Business
Maturity	TRL-9	TRL-7	TRL-7

Based on this objective comparison, the hybrid silicon imager appears superior to both CMOS and CCD technology. CMOS technology appears

generally superior to CCD, except for the fact that many scientists have a compelling need to be intimately involved in optimizing performance at the instrument level. There is consequently a justifiable “cult status” associated with their use for astronomy.

4. REFERENCES

- [1] G.E. Moore, 1965, *Cramming more components onto integrated circuits*, Electronics, Vol. **38**, No. 8.
- [2] M. Loose, L. Lewyn, H. Durmus, J. D. Garnett, D. N. B. Hall, A. B. Joshi, L. J. Kozlowski and I. Ovsiannikov, 2002, *SIDECAR Low-power control ASIC for focal plane arrays including A/D conversion and bias generation*, SPIE **4851**.
- [3] M. Loose, L.J. Kozlowski, A.M. Joshi, A. Kononenko, S. Xue, J. Lin, J. Luo, I. Ovsiannikov, J. Clarke and T. Paredes, 2001, *2/3-inch CMOS Imaging Sensor for High Definition Television*, IEEE Workshop on CMOS and CCD Imaging Sensors.
- [4] D.X.D Yang, A. El Gamal, B. Fowler and H. Tian, 1999, *A 640×512 CMOS Image Sensor with Ultrawide Dynamic Range floating-point pixel-level ADC*, IEEE JSSC **34**(12).
- [5] Y. Bai, J.T. Montroy, J.D. Blackwell, M. Farris, L.J. Kozlowski and K. Vural, 2000, *Development of Hybrid CMOS Visible Focal Plane Arrays*, SPIE **4028**.
- [6] United States Patent 6,301,051.
- [7] M. Loose, M. C. Farris, J.D. Garnett, D.N.B. Hall and L. J. Kozlowski, 2002, *HAWAII-2RG: a 2K×2K CMOS multiplexer for low and high background astronomy applications*, SPIE **4850**.



The winners of the mechanical bull riding competition. Right to left: First Paniolo (T. Hardy), Second Paniolo (P. Bristow) and most pathetic Paniolo (R. Smith).

A MARCONI CCD42-40 WITH ANTI-BLOOMING

Experiences with the OSIRIS CCDs for the ROSETTA Mission

J. Rainer Kramm, Horst Uwe Keller, Reinhard Müller, Dietmar Germerott
and Georg Tomasch
Max-Planck-Institut für Aeronomie

Abstract: *The OSIRIS cameras on-board ESA's spacecraft ROSETTA use a new version of thinned CCD42-40 CCDs with anti-blooming. Marconi employed its lateral shielded anti-blooming technique, which was already developed and applied to the CCD47 production line. The performance of the anti-blooming in particular is described herein as well as other basic detector characteristics such as excellent charge transfer efficiency, low spurious charge generation and dark charge reduction by clock dithering. Furthermore, reduced repeatability performance is reported due to trapped charge in thinned CCD42-40 devices. The release time is temperature dependent. Operations at room temperature require special attention whereas a pre-flash to saturation is widely sufficient to fill the traps in cooled devices for a longer observation period.*

Key words: *Charge-Coupled Devices (CCDs), anti-blooming, Charge Transfer Efficiency (CTE), spurious charge, trapped charge*

1. INTRODUCTION

The ROSETTA spacecraft will be launched in 2003 and will meet comet Wirtanen in 2011 for an observation period of up to 4 years. The OSIRIS camera system on-board ROSETTA consists of two separate sub-units, a wide-angle camera and a narrow-angle camera. Both multi-spectral camera sub-systems use identical CCD detectors.

The OSIRIS CCDs are based on the standard CCD42-40 design and were produced by Marconi under contract of MPAE. Lateral (shielded) anti-blooming overflow protection was introduced to allow observation of weak cometary features near bright regions with partial over-exposures. The advantage of the lateral anti-blooming technique is that the quantum

efficiency is not degraded. Non-MPP devices were used because they provide higher charge capacity of $\geq 100,000 \text{ e}^- \text{ pix}^{-1}$.

2. ANTI-BLOOMING FUNCTION

Full well capacity on devices with shielded anti-blooming is basically determined by the potential of the Anti-Blooming Drain (ABD). Higher drain potential leads to lower charge capacity and to enhanced charge removal capability accordingly. Figure 1(a) shows plots of the charge capacity across the image section for different drain potential levels between 16.5 and 21.5 V. Obviously, the removal structure is homogeneously established across the image array, since the charge capacity appears widely uniform. With a drain potential of 18.5 V (Fig. 1(b)), the anti-blooming works perfectly and the obtained charge capacity of $110,000 \text{ e}^- \text{ pix}^{-1}$ is higher than anticipated.

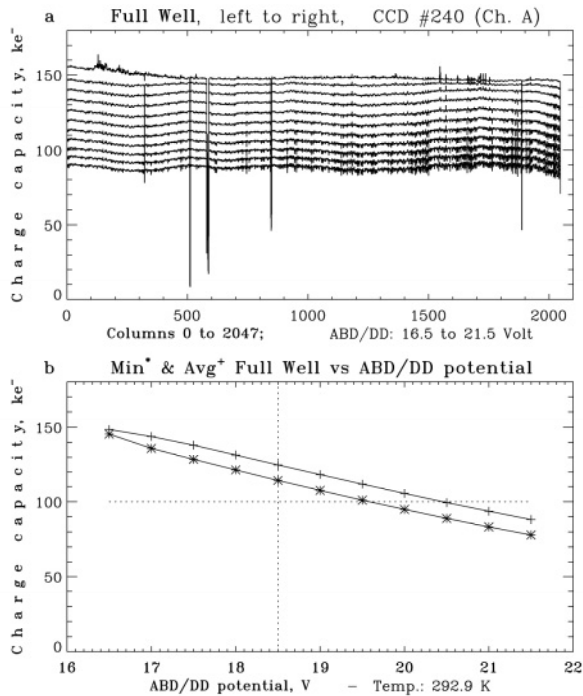


Figure 1. (a) Full well amplitude plots across the top of the image section for different ABD potentials. (b) Minimum and average full well figure plots for the applied potentials.

The achievable charge removal capability is $> 107 \text{ e}^- \text{ s}^{-1} \text{ pix}^{-1}$. On pixels where the charge removal is exceeded, overrunning charge spills over into

almost all directions, so that a locally limited area is filled with charge instead of columns.

3. CLOCK DITHERING

Clock dithering was used during the evaluation of our non-MPP detectors to keep the dark charge low in all operations at higher temperatures. We used full pixel wide dithering at a fixed rate of 80 $\mu\text{s}/\text{cycle}$ that establishes a reasonable compromise between power consumption and charge reduction.

Profitable charge reduction can be obtained only if the Vertical Charge Transfer Efficiency (V-CTE) is high enough and if, in addition, the spurious charge generation is sufficiently low. We found such fast dithering useful at temperatures above 230 K and obtained a highest dark charge reduction rate of up to a factor of 15 at room temperature. Below 230 K clock dithering at this rate is no longer useful, because spurious charge becomes dominant.

We use flat field LED exposures to $\frac{3}{4}$ full well for all CTE measurements and found, as shown in Table 1, excellent vertical CTE.

Table 1. Typical OSIRIS CCD Vertical Charge Transfer Efficiency (V-CTE).

Temperature	V-CTE
295 K	.999 999 58
180 K	.999 999 98
160 K	.999 999 96

Spurious charge generation in the image section can be determined by comparing dark images obtained with and without clock dithering at low temperatures. Figure 2 shows histogram plots of the dark charge amplitudes accumulated in 10 min at 160 K. The spurious charge generation rate here is 1 $e^-/900,000$ clock cycles.

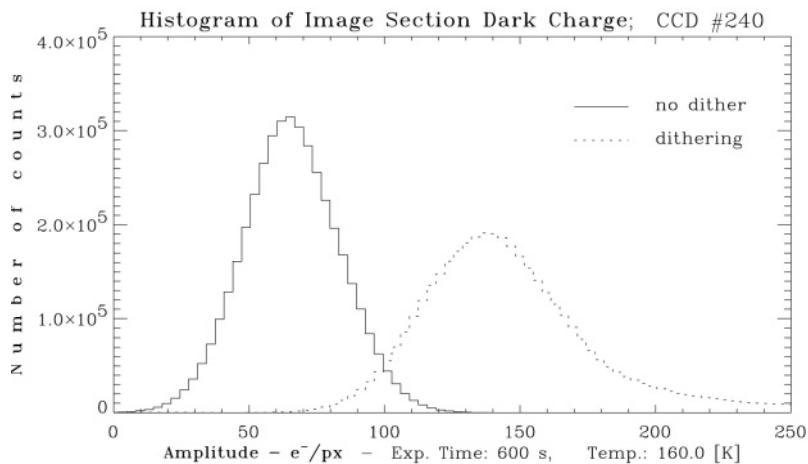


Figure 2. Histogram of dark charge without and with clock dithering at 160 K.

4. TRAPPED CHARGE EFFECTS

The response of the thinned CCD42-40 devices is affected by charge traps that have a density of about 1% of the peak signal storage density. Basically, a fraction of the signal charge is being trapped as long as the traps are not saturated. The magnitude of the signal loss depends on the actual fill factor of the traps. This fill factor is a result of an interaction between previous light stimulation and charge release. The release time is temperature dependent.

At room temperature, the release time is about 6 minutes. Figure 3 shows how under these operation conditions the signal amplitudes depend on the image acquisition rate. All images in this example were identically exposed to about 20% full well amplitude. The effect of previous exposures to succeeding images is clearly visible for acquisition rates of less than 6 minutes. Obviously, at room temperature operations, thinned CCD42-40 devices have limited registration accuracy.

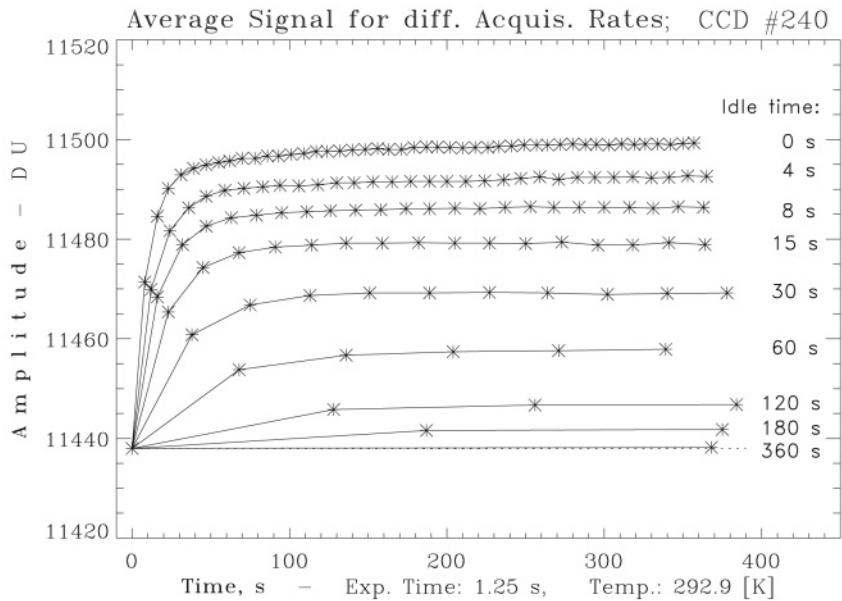


Figure 3. Average image amplitudes for different acquisition rates at 293 K. (Note that all these images were obtained with identical flat field exposures.)

At lower detector temperatures, the release time is in the order of many hours. Consequently, a pre-flash to saturation is sufficient to fill the traps for a longer observation period. Such pre-flash can consist of either a single full well exposure or, alternatively, of multiple exposures with lower light levels.

Figure 4 shows the average signal amplitudes received from the first images after the detector was cooled down to 180 K, or, in other words, with empty traps at the beginning. All 15 images were identically exposed to $\frac{1}{4}$ full well, with 5 consecutive exposures each at the time of the beginning, after 1 hour and, finally, after 3 hours. The signal build-up in the first 5 images is clearly visible. Once, after the CCD was well exposed, the traps are filled with charge, and suitable repeatability can be expected on further images.

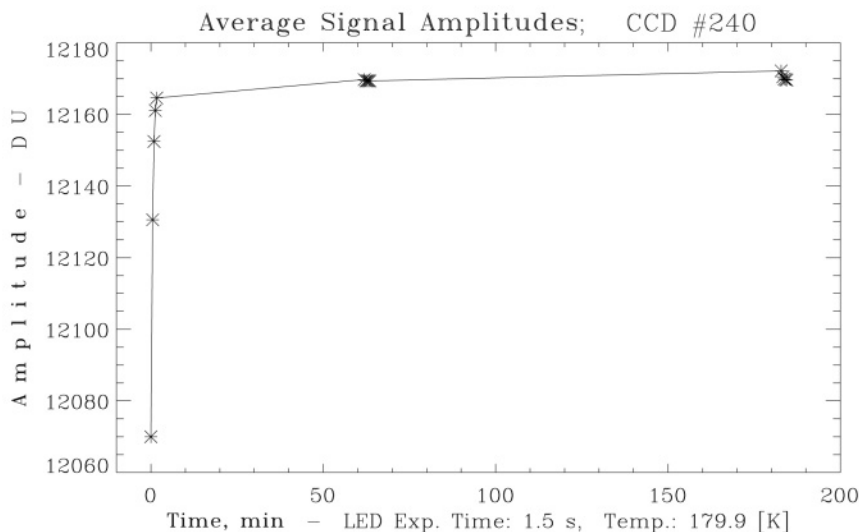
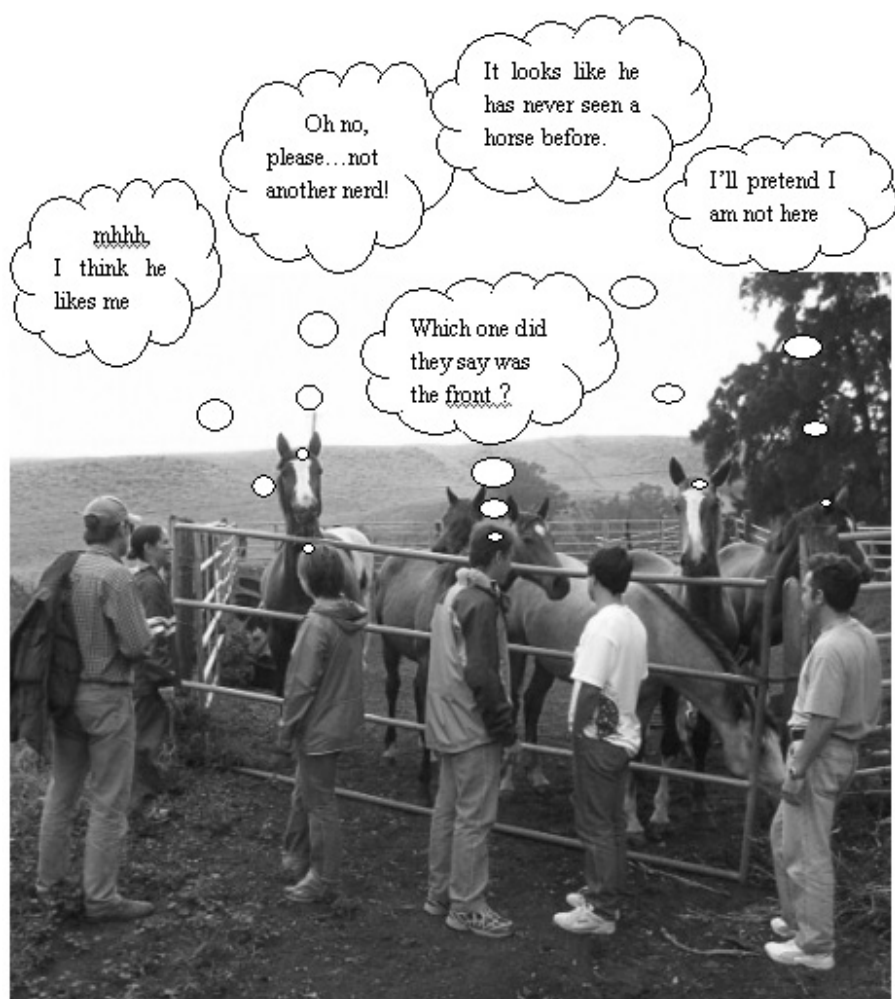


Figure 4. Average signal amplitudes from the first 15 exposures at 180 K with empty traps at the beginning.

5. CONCLUSION

The OSIRIS CCDs passed the detector evaluations with excellent results. The applied anti-blooming overflow protection works perfectly and can be highly recommended to other users searching for instrument improvements. On the other hand, charge traps in thinned CCD42-40 devices make image registrations somewhat complicated, particularly at higher temperatures. Users shall be aware of the charge traps requiring suitable pre-flash stimulation prior to imaging operations.

Nerds and horses
(Courtesy M. Downing)



VERY LARGE FORMAT BACK ILLUMINATED CCDS

Michael Lesser
University of Arizona

Abstract: *The University of Arizona Imaging Technology Laboratory has processed several types of very large format ($> 4K \times 4K$ pixel) charge coupled devices for low light level scientific applications. These back illuminated devices were produced from frontside die fabricated by or for Fairchild Imaging Systems, Semiconductor Technology Associates, the Jet Propulsion Laboratory, and Kodak. A Philips $7K \times 9K$ frontside device has also been processed using similar techniques. The backside sensors yield $>90\%$ quantum efficiency (QE). All devices show excellent charge transfer efficiency ($CTE > 0.999997$) at operating temperatures (typically -100°C). Devices specifically designed for low signal applications have been demonstrated with less than 4 electrons read noise.*

Key words: *Charge-Coupled Device (CCD), astronomy, detectors, silicon, imaging*

1. INTRODUCTION

Very Large Format (VLF) CCDs are defined as devices with $4K \times 4K$ pixels or more. The typical pixel sizes of 9-15 μm s make these devices among the largest integrated circuits in the world, usually over 60 mm per die side. Work at the University of Arizona Imaging Technology Laboratory (ITL) has led to the production of back illuminated VLF CCDs optimized for low light level applications. We have processed devices from several vendors and demonstrated that such sensors are excellent candidates for scientific and industrial imaging programs.

Large telescopes and spectrographs often have focal planes that exceed the maximum diameter of the silicon wafers used to fabricate visible light solid state imagers (currently 150 mm). Therefore a mosaic of devices is required to fully populate these focal planes. In order to minimize the complications of using a large number of individual sensors, it is advantageous to use detectors that are as large as possible. A previous paper publication demonstrated that $4K \times 4K$ $15\text{ }\mu\text{m}$ pixel devices were feasible with devices fabricated at Fairchild Imaging Systems [1]. We have now demonstrated that multiple vendors can produce such devices, all with exceptional performance.

We present here a brief update of our work with the Fairchild devices and present new results from devices fabricated by or for the Jet Propulsion Laboratory, Semiconductor Technology Associates, and Kodak. The backside process developed at ITL and applied here has been published previously [2,3]. First, we briefly discuss our work that led to the development of the VLF CCD process, the front illuminated Philips $7K \times 9K$ CCD.

2. PHILIPS $7K \times 9K$ FRONT ILLUMINATED CCD

The first of the VLF CCDs processed in our laboratory was the Philips $7K \times 9K$ device. While this device was not thinned because it incorporated a vertical antiblooming structure, which limits effective thickness to about $3\text{ }\mu\text{m}$, it was the beginning of our development of very large scale detector packaging techniques. We briefly summarize this work here.

The devices were fabricated on 150 mm wafers with one die per wafer. They were constructed with step and repeat modular mask sets, which define particular areas of the imager on the silicon wafer. Each block consists of a 1024×1024 $12\text{ }\mu\text{m}$ pixel area with different blocks for corners, amplifiers, and wire bond sections. They can be stitched together in any $mK \times nK$ size. The development of this device was a collaboration between American Digital Imaging, Inc., ESO, Max Planck, DLR, and the U. Arizona (for post fabrication processing). The CCD has four amplifiers and utilizes 4-phase parallel and 3-phase serial clocking.

We developed an Invar-36 carrier as the basic device package. Invar-36 was chosen because of its machinability, stiffness, and adequate thermal expansion and conduction properties. We attached to the carrier two identical FR-4 printed circuit boards with gold plated copper traces for wire bonding and I/O fanout. Each board is located at the shorter (serial register) end of the device and contains one 37-pin Nanonics cryogenic connector for

external I/O connection. The two connectors per CCD have identical pinouts.

The Invar-36 carrier was machined and polished flat to a specification of 2.5 μm peak-to-valley, and is 7.62 mm thick to maintain flatness during thermal cycling. We engineered all Invar packages to have less than 1 μm peak-valley flatness deviation. The packages and attachments have been rapidly thermally cycled between liquid nitrogen and room temperature. We have imaged devices as cold as -165 C. The entire CCD and package weighs approximately 1000 g, with no attempt to minimize mass. The CCD is attached to the Invar-36 carrier with an electrically conductive thermoplastic. We imaged several devices and found CTE better than 0.99999 and reasonably good cosmetics. Nearly all amplifiers in the lot were functional. This device was a clear demonstration that 150 mm wafer-scale devices can be produced.

3. FAIRCHILD 4K \times 4K DEVICES

We have previously reported on the backside processing of 4K \times 4K devices fabricated by Fairchild Imaging Systems. These devices included the CD4096JJ, CCD485, and CCD486 CCD imagers. Here we briefly summarize some of the processing considerations of these VLF devices and update final performance data.

All three Fairchild devices are 4096 \times 4096 15 μm pixel devices. The CCD4096JJ was a custom device fabricated for Caltech. The CCD485 and CCD486 devices are commercially available from Fairchild. The CCD4096JJ and CCD485 devices were backside processed at ITL, fabricated on 100 mm diameter wafers and did not have frontside substrate (ground) contacts. The CCD486 devices were fabricated on 125 mm wafers and did have frontside substrate contacts.

Developing a backside substrate contact after thinning proved to be a difficult but important step in producing the first thinned 4K \times 4K devices. The CCDs were received from the fab with metal plating on the backside (gold or aluminum) that was used to improve die attachment for the frontside devices. Because the as-received thickness (450 μm s) was not well suited to the ITL thinning process, and because the metal had relatively poor adhesion to the backside, we had the metal removed and the devices lapped to 250 μm s by an external vendor (Disco Hi-Tec America).

After receiving the newly lapped wafers, 2000 Å of 100% aluminum was deposited onto the wafer backside. This thickness was chosen to provide good ohmic conductivity and to allow for subsequent wire bonding to ensure a clean electrical connection to the backside.

The backside aluminum was left on the devices during dicing and flip chip bonding. Before acid etching, the edges of the device were protected with wax, leaving a border approximately 2 mm wide. A commercial aluminum etch was used to remove the metal over the area to be thinned, leaving aluminum under the protective wax. Following this procedure, the devices were backside thinned.

Wire bonding to the final backside contact did not always pass pull testing, and so each wire was strengthened with conductive epoxy (Epoxy Technologies H-20E). No contact problems have occurred with this process. Several experiments were made with the contact disconnected, and although the device functioned, very long parallel clock overlaps (>100 microseconds) were needed to obtain good vertical CTE. This is expected from a high impedance ground contact, which would degrade the parallel clock waveform in the image area. Since then we have performed experiments to develop a backside contact for such devices using direct ultrasonic indium alloy soldering to the silicon. While we have had some success, the aluminum deposition process has still proven to be the most reliable.

The CCD486 CCD was designed specifically for low noise, scientific applications. It has four single-stage amps and is near-butable on 2 sides (no bond pads). It has been packaged in the same Kovar tub as the CCD485 device and does not require the extra processing of creating a backside ground contact.

The measured performance of both Fairchild $4K \times 4K$ devices is excellent. Noise has been measured at $3.5 e^-$ (50 kHz) for the CCD486 and $6-7 e^-$ for the CCD485. HCTE and VCTE are better than 0.999998. Full well is over $80,000 e^-$ in MPP mode. Because of its dual-stage amplifier, the CCD485 can be read out faster than the CCD486. The full image can be read from 1, 2, or 4 amplifiers. Dark current is about $3 e^-/\text{pixel}/\text{hour}$ at -100°C . These imagers are excellent candidates for many scientific programs requiring a VLF back illuminated CCD. Typical QE curves of several of the VLF CCDs discussed are shown in Fig. 1. The differences in the curves are accounted for by varying antireflection coatings and epitaxial thicknesses (from 10-20 μms).

4. JPL4096

The JPL4096 device is a custom CCD designed by Dr. Mark Wadsworth at the Jet Propulsion Laboratory and fabricated by an external vendor. The device has 4096×4096 $15 \mu\text{m}$ pixels. Backside processing at ITL has been fairly straightforward with no unusual requirements. Of particular interest

with this device are the amplifiers, which have been measure to produce 2.2 e⁻ noise on the frontside parts by Tom Elliot of JPL.

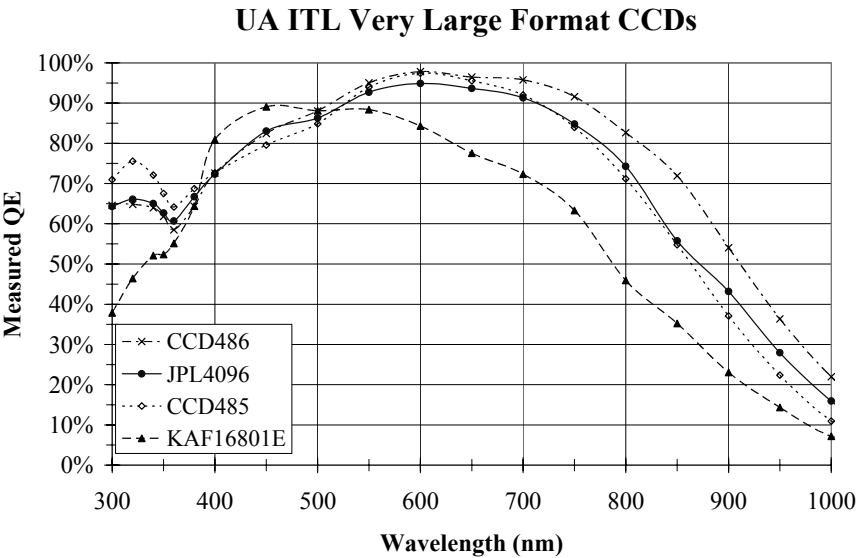


Figure 1. The measured QE of VLF CCDs at room temperature.

CTE is better than 0.99999 at 1620 e⁻ and -100 °C. The backside read noise is under 5 e⁻ at 50 kHz. Additional characterization of the device is underway, but it is clear this is also a viable candidate for VLF imager requirements. This device also demonstrates that such imagers can be built by multiple vendors.

5. STA0700

The STA0700 CCD is a 4K×4K device custom produced by Dr. Richard Bredthauer at Semiconductor Technology Associates for the University of Arizona. The wafer mask was designed to include several different types of CCDs needed by various UA projects, including 800×1200 and 2688×512 spectroscopic format CCDs. These are updated designs of detectors produced many years ago and fabricated by Ford/Loral (designed originally by Dr. John Geary of the Smithsonian Astrophysical Observatory). An interesting aspect of this lot is that two 4K×4K devices have been produced

on each wafer. The 4K devices have low noise amplifiers which were based on the testing of previous CCDs fabricated by STA and others [4].

Initial performance of these devices has only been measured frontside on the ITL cold probe station (-60 °C) since the lot runs were received in the spring/summer of 2002. CTE is better than 0.99999 and cosmetics are excellent. The first lot run showed a fabrication problem, most likely related to insufficient contact etching, and has been replaced with a second run. This lot is currently under test.

6. KODAK KAF16801E

The Kodak 16801E CCD (4K×4K with 9 μm pixels) is available commercially as a front illuminated sensor from Eastman Kodak [5]. Dr. Franz Weber at the Lawrence Livermore National Laboratory has contracted ITL to produce a back illuminated version of the device for X-ray imaging. An interesting requirement of the project has been that the CCD must be pin-compatible with the frontside part in order to make use of existing cameras. This required a significant packaging development utilizing multilayer aluminum nitride (AlN) ceramic technology. The devices also have a relatively thin epitaxial layer (10 μms) which made thinning with high yield difficult and required the development of a modified etching process. All other 4K devices we processed had been fabricated on at least 17 μm thick epitaxial material. Both of these development efforts were successful and several backside KAF16801E devices have been produced. The developed package is shown in Fig. 2.

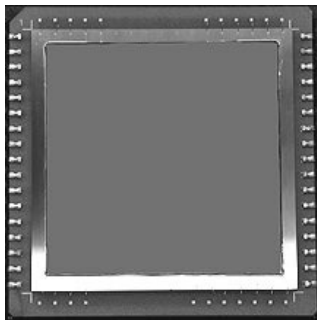


Figure 2. A back illuminated KAF16801E CCD in the AlN package.

The performance of these devices is excellent. CTE is better than 0.999998 at -100 °C, even though previous Kodak parts have been reported to have CTE problems at cold temperatures. The cosmetics are very clean,

and many parts have no defects. We have had some trouble backside charging the devices using our standard process, and hence see lower QE than usual. We are currently working to solve this problem. Overall, the backside processing of the Kodak parts, including the ceramic packaging, is now routine and such devices are well suited for projects requiring VLF devices with smaller pixels and high frame rate capability (pixel rate up to 10 MHz).

7. ACKNOWLEDGEMENTS

This work was supported by the University of Arizona as well as contracts to the UA from Fairchild Imaging Systems, the Jet Propulsion Laboratory, and Lawrence Livermore National Laboratory. The authors wish to thank all members of the UA Imaging Technology Laboratory for their work on VLF CCD processing; especially David Ouellette who designed the packages, Charles Bridges who developed the etching processes, and Teresa Lappin who applied the backside coatings. We also wish to thank Paul Vu at Fairchild Imaging Systems, Dr. Mark Wadsworth at the Jet Propulsion Laboratory, Dr. Richard Bredthauer at Semiconductor Technology Associates, and Dr. Franz Weber at Lawrence Livermore National Laboratory. The 7K×9K development efforts were sponsored by Mr. Jim Foster of American Digital Imaging, Inc. Dr. Albert Theuwissen at Philips provided many helpful discussions regarding the 7K×9K devices.

8. REFERENCES

- [1] Lesser, M. P. and Vu, P., 2001, *Processing of Back-Illuminated 4096x4096 Fairchild CCDs at the University of Arizona*, Proc. SPIE **4306**, p.196
- [2] Lesser, M. P., 1996, *Back Illuminated CCD Processing at Steward Observatory*, Recent Developments in Scientific Optical Imaging, M. B. Denton, R. E. Fields, and Q. S. Hanley, eds., Royal Society of Chemistry, pg.62.
- [3] Lesser, M. P. and Iyer, V., 1998, *Enhancing Back Illuminated Performance of Astronomical CCDs*, Proc. SPIE **3355**, p. 23.
- [4] Lesser, Michael and Bredthauer, Richard, 2000, *Development of a Back Illuminated 4096x4096 15-micron Pixel Scientific CCD*, Further Developments in Scientific Optical Engineering, Proceedings of the International Conference on Scientific Imaging, Royal Society of Chemistry, p. 111
- [5] www.kodak.com



Polywood? Hollywood has nothing over the lifestyle of the rich and famous kingpins of polysilicon.



*The Chinese delegation increases (See page 200 of *Optical Detectors for Astronomy II*.)
From left to right: Binxun Ye, Minghzi Wei and Zhao Zhaowang.*

COMPOUND SEMICONDUCTOR DETECTORS

Development activities at ESA

David Lumb, Alan Owens, Anthony Peacock, Marcos Bavdaz, Christian Erd
Science Payloads Technology Division, Research & Science Support Department, European Space Agency (ESA), European Space Research and Technology Centre (ESTEC)

Abstract: *We describe results obtained in a development programme to procure detectors with high sensitivity to hard X-rays. We note where this programme has broad synergies with developments for ground-based astronomy arrays.*

Key words: *semiconductor detectors, imaging and spectroscopy*

1. INTRODUCTION

CCDs (specially adapted for X-ray response) have become the workhorse detector for X-ray astronomy in the last decade. Future observatory designs highlight detector requirements that suggest that silicon must be replaced as the material of choice: The X-ray luminosity budget of the Universe is dominated by non-thermal emission mechanisms in Active Galactic Nuclei (AGN), and which peaks at energies $\gg 10$ KeV. Unfortunately, the low density of silicon precludes a high stopping efficiency at such energies. Increased emphasis on studies of the high red-shift Universe conversely implies that the important X-ray emission lines of iron will be shifted to *lower* energies (~ 1 KeV), but the energy resolving capability to perform plasma diagnostics must be better than the theoretical limits of the silicon detection process. These two orthogonal requirements are addressed through our developments of compound semiconductors, typically of III-V and II-VI group materials.

Additional requirements are imposed by future observations of planetary surfaces by X-ray fluorescence techniques. The ESA Bepi-Colombo mission to Mercury in particular places stringent requirements for operation at

elevated temperatures, and also for the harsh radiation environment [1]. Operation at room temperature, and after Mega-rad radiation dosages needs to be demonstrated. Semiconductors with a wider bandgap than silicon allow, in principle, a higher temperature operation through reduced dark current.

2. GALLIUM ARSENIDE

The most successful developments to date have been obtained with GaAs substrates, fabricated with high quality epitaxial layers from 40 to 400 μm thick. Relatively low ($\sim 100\text{ V}$) bias is needed to deplete the $\sim 100\text{ }\mu\text{m}$ intrinsic layer formed as part of a p-i-n structure. A 1 mm diameter diode with a resistor-less feed-back amplifier exhibited energy resolutions at 5.9 KeV of 219 eV at 243 K and 266 eV at room temperature [2].

Based on such promising performance we proceeded to fabricate pixelated detectors. 32×32 arrays of 350 μm square pixels were produced. These were measured at a synchrotron beam at HASYLAB. Spatial response was flat to $\sim 2\%$, and energy resolution indistinguishable from single pixel detectors [3].

3. OTHER MATERIALS

Other semiconductor samples have been tested using a variety of material processing techniques, and fabricated into single diode detectors. A sample of measured performance and detector characteristics is shown in Table 1.

Table 1. Summary of properties of various compound semiconductor detectors.

Material	Si	GaAs	CdZnTe	HgI	TlBr
Density	2.33	5.32	~ 6	6.4	7.56
Band gap (eV)	1.12	1.43	0.67	2.15	2.68
Pair creation energy (eV)	3.67	4.2	~ 5.5	4.2	6.5
1/e ⁻ absn. length (mm) 100 KeV	23	3.5	~ 1	0.46	0.32
Detector size (area \times thickness)	1000 mm ² $\times 0.2\text{ mm}$	0.25 \times 0.25 400 μm	3.1 mm ² $\times 2.5\text{ mm}$	7 mm ² $\times 0.5\text{ mm}$	1.7 mm ² $\times 0.5\text{ mm}$
ΔE @5.9 keV	130 (@ -100 $^{\circ}\text{C}$)	260 (@ RT)	311 (@ -37 $^{\circ}\text{C}$)	438 (@ -19 $^{\circ}\text{C}$)	650 (@ -30 $^{\circ}\text{C}$)
ΔE @ 59.5 keV	-	470	824	1540	2300

InP has an even higher stopping power than GaAs, and is undergoing extensive development for LSI (Large Scale Integration) and micro-machine

applications. Liquid encapsulated Czochralski wafers, doped with Fe and Zn, have been fabricated into 1 mm diameter, 180 μm thick detectors. The best resolution demonstrated was 0.8 KeV at 5.9 KeV.

CdZnTe is one of the most widely used semiconductor detector crystals. We characterized a number of high quality commercially grown crystals, selecting the best to fabricate a 2 mm diameter detector which produced ~ 300 eV resolution at 5.9 KeV when cooled to -37°C .

Mercuric Iodide and Thallium Bromide detectors have been investigated for a number of years for their high X-ray stopping capability. Our measured energy resolutions with the best detectors are comparable with the best data reported to date with these types of detectors.

4. INDIUM ANTIMONIDE

The low bandgap that facilitates IR sensitivity in InSb should, in principle, allow the generation of >5 times as many charge carriers per X-ray photon than Si. With a commensurate reduction in statistical fluctuations, the limiting energy resolution in InSb would be more than a factor 2 better. Fig. 1 shows the resulting improvement in spectral diagnosis that could be achieved for the application of measuring the iron-line emission in a highly red-shifted AGN (luminosity $2 \cdot 10^{43}$ erg/sec, $z=4$) with the proposed ESA XEUS Observatory [4].

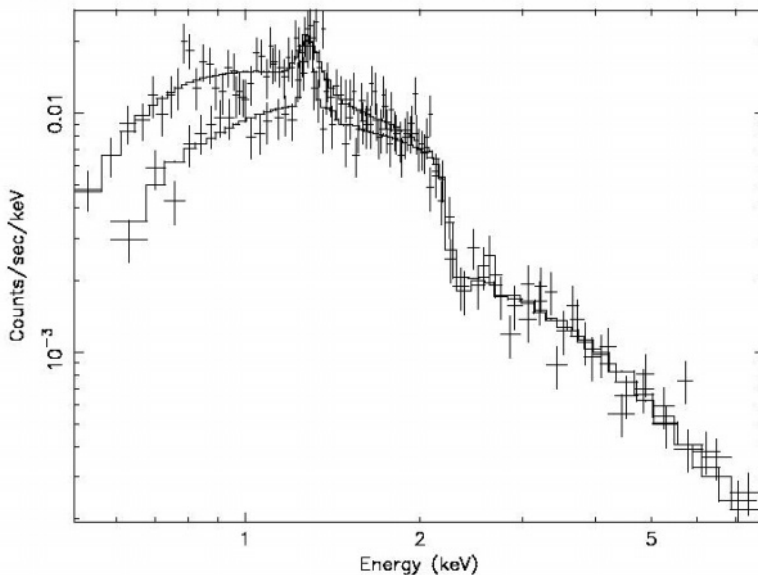


Figure 1. Simulated AGN at $z=4$. Si CCD upper, InSb lower – red-shifted Fe line is more clearly resolved with the InSb detector, allowing metallicity in early Universe to be probed.

We note the long-recognised advantage of characterising optical astronomy CCDs with X-ray sources to define gain and CTI performance. We intend to demonstrate this application in low noise IR InSb astronomy arrays, to the benefit of both disciplines.

5. ASICS

Focusing technologies for high X-ray energies, do not allow high resolution, and modest array sizes (128×128 of pixel size $\sim 200 \mu\text{m}$) are our current goal. The development of readout ASICs (Application Specific Integrated Circuits) for IR arrays, and parallel developments in CMOS imagers in the last few years has been rapid. All the above materials, if processed into such pixel arrays, would be commensurate in size to the ASICs used with IR arrays of the $1\text{K} \times 1\text{K}$ class. If we obtain the very low dark currents promised with the wide bandgap, and low capacitance associated with fully depleted detectors, then the technology for source-follower input readout ASICs should be directly transferable to X-ray applications.

6. ACKNOWLEDGEMENTS

Detector developments have been performed at Metorex, where we acknowledge the work of H. Andersson, H. Sipila, V. Lämsä and S. Nenonen. Important materials developments have been made by V. Gostilo, I. Lisjutin and S Zatoloka at Baltic Scientific Instruments.

7. REFERENCES

- [1] Owens, A., Bavdaz, M., Beijersbergen, M. et al., 2001, Proc. SPIE Vol. **4506**, p. 136-145.
- [2] Owens, A., Bavdaz, M., Peacock, A. et al., 2001, Nucl. Inst. Meth. Phys. Res. A **466**, p. 168.
- [3] Erd, C., Owens, A., Brammertz, G. et al, Nucl. Inst. Meth. In Phys Res A (in press).
- [4] Bleeker, J., Hasinger, G., Inoue, H. et al, 2001, ESA SP-**1242** Xeus Mission Science Report.

OPTICAL PHOTON-COUNTING STJ ACTIVITIES AT ESA

David Lumb, Peter Verhoeve, Roland den Hertog, Anthony Peacock, Didier Martin, Nicola Rando

Science Payloads Technology Division, Research & Science Support Department, European Space Agency, European Space Research and Technology Centre (ESTEC)

Abstract: *Superconducting Tunnel Junction (STJ) detectors offer wavelength-resolved detection of single optical photons with high time resolution. To meet the needs of future astronomical instruments, large detector arrays must be developed. We describe recent activities aimed to secure such performance, and highlight results achieved with prototype arrays when employed at the William Herschel Telescope.*

Key words: *photon-counting, spectroscopy, time resolution, Superconducting Tunnel Junctions (STJs)*

1. INTRODUCTION

The absorption of a photon of energy, E , in a superconductor is followed by a series of fast processes that involve the breaking of Cooper pairs by energetic phonons, created by the hot electrons that are produced when the atom relaxes after the initial photo-absorption. This cascade results in the conversion of photon energy to free charge carriers, (known as *quasi-particles*) in excess of any thermal population. At sufficiently low temperatures (an order of magnitude lower than the superconductor's critical temperature, T_c) the number density of thermal carriers is very small while the average number of excess carriers, N_o , created as a result of the photo-absorption process can be written as: $N_o(E) \sim 7 \times 10^2 E / \Delta(T/T_c)$. Here the photon energy is expressed in eV and the temperature dependent energy gap

$\Delta(T/T_c)$ is in meV. Thus, in a superconductor such as tantalum the initial mean number of free charge carriers created, $N_o(E)$, is $\sim 10^3$ per eV. The variance of $N_o(E)$ depends on the variance in the partition of the absorbed X-ray energy between productive phonons which can break Cooper pairs, and phonons which are essentially lost from the system ($\Omega < 2\Delta$).

The quasiparticles produced through photoabsorption can be detected by applying a DC potential across two such films separated by a thin insulating barrier, forming a Superconducting Tunnel Junction (STJ). This potential bias favours the transfer of quasiparticles from one film to the other through quantum mechanical tunneling across the barrier. After initial tunneling, a quasiparticle can tunnel back, therefore contributing many times (n) to the overall signal. Typically $\langle n \rangle$ is of order 10-100 and depends on the size and nature of the STJ.

Considerable improvements in STJ fabrication led to the first detection of single optical photons several years ago [1], followed by progressive increases in energy resolving capability. Now a practical astronomy instrument needs the demonstration of arrays with a number of elements sufficient to challenge other technologies. A number of different approaches to developing arrays are outlined in Sec. 2. We briefly summarise the colour discriminating properties in Sec. 3 and finally highlight first results obtained with astronomical observations.

2. ARRAY ARCHITECTURES

2.1 Single Junctions

Figure 1 shows a Nomarski photograph of a tantalum 10×12 STJ array: the devices are $25 \mu\text{m}$ square with $1.5 \mu\text{m}$ wide Nb leads and $4 \mu\text{m}$ wide trenches. The Nb bridges crossing the trenches are etched to below $1 \mu\text{m}$ in width to reduce charge diffusion between pixels. Each device in this array has its own Nb top contact wiring, which connects to the top Ta layer via a Silox isolation film. Each device, therefore, operates as a discrete detector with its own signal detection and signal processing chain attached off-chip.

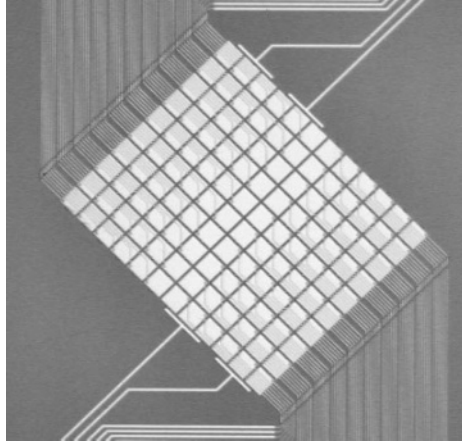


Figure 1. 10×12 array of individually wired Tantalum STJs. The dense layer of parallel tracks running over the top Ta film are easily seen. In this fabrication technology they limit the number of junctions that are easily accommodated in an array, and force an illumination strategy that must be through a semi-transparent rear substrate.

2.2 Matrix Arrays

Figure 2 shows an alternative approach to the direct readout of individual STJs: the so called "matrix readout" array.

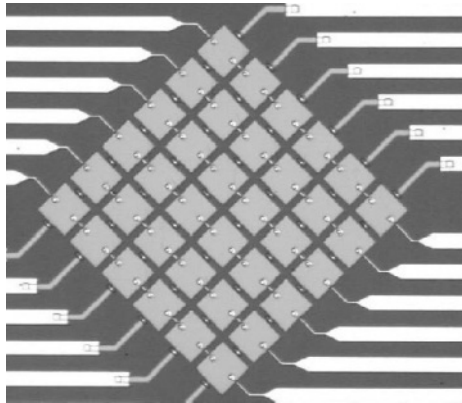


Figure 2. A 6×6 matrix array of Ta STJs. Row connections are made via common base leads, and column connections via common top film leads.

This approach connects the base film of all devices from the same row in an array together, and the top films from a given column in another connection. Events are then read out using a coincidence technique between signals from the two films. This not only reduces the amount of front-end

electronics and the thermal problems associated with the large number of wires entering the cryostat, but also removes the problems associated with dielectrics and contacts obscuring the top film.

2.3 Distributed Readout Arrays

The requirement of individual bias and readout of large format arrays of 1000s of devices is fraught with difficulty. A possible solution is offered by the use of distributed readout imaging devices (DROID) in which photons are absorbed in an epitaxial superconducting film such as tantalum, of large dimension - the absorber - and the signal charges are detected by STJs located at the corners of either a 2D absorber or at the ends of a 1D strip of absorber (see Fig. 3). By time-coincident event measurements it is possible to reconstruct both the absorption position and the energy of the incoming photons. Disadvantages of this approach include the relatively low sustainable count rate (dependant on the chosen geometry) per unit area, and the sensitivity of the absorber to flux trapping.

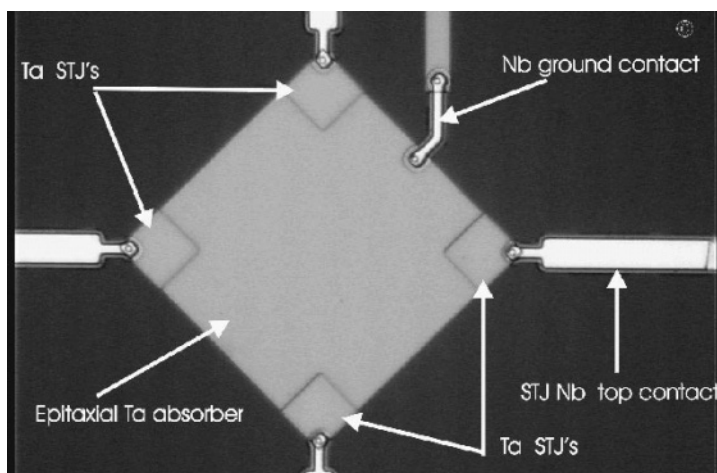


Figure 3. Single 100 μm square Ta absorber with distributed readout via 4 corner STJ readouts.

3. WAVELENGTH RESOLVING PERFORMANCE

Figure 4 illustrates the theoretical limiting energy resolution for a number of materials with different band-gap energies. Also indicated is the measured resolution from near-IR to UV wavelengths for devices based on Ta. This measured resolution approaches the theoretical limit in the UV, whereas the

electronic readout noise still dominates in the near-IR. At $\lambda \sim 200$ nm, the use of lower bandgap material like molybdenum and hafnium would allow a wavelength resolution of 2 or 1 nm respectively compared with our measured value of 7 nm in Ta. However the critical temperature and hence operating temperature is similarly lower in these materials

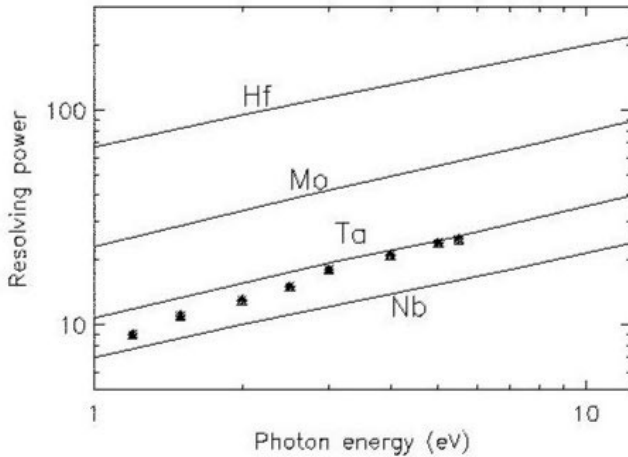


Figure 4. Comparison of theoretically attainable energy resolving power in the wavelength range 1200-100 nm for different materials. Over plotted are measured data for a Ta STJ, highlighting that at longer wavelengths the resolution starts to be dominated by readout noise.

Measurements concerning DROID devices show that there is an additional component relating to spatial non-uniformity. For example, in the current development stage the resolution of a single $50 \mu\text{m} \times 50 \mu\text{m}$ STJ degrades from 7 nm to ~ 14 nm in a $50 \mu\text{m} \times 400 \mu\text{m}$ absorber, due to degradations in response which can be mapped to regions near the Nb base contact and the STJs near the corners.

4. TELESCOPE OBSERVATIONS

To demonstrate the STJ technology in an astronomical context, a prototype camera (S-Cam2) has been taken to the William Herschel Telescope, to observe various targets. S-Cam2 is comprised of a 6×6 array of Ta STJs each $25 \mu\text{m}$ square. The focal plane subtended 4×4 arcseconds square when located at the f/11 Nasmyth-1 focus. The array was operated at a temperature 320 mK, by liquid He cooling. Each junction was read out with conventional room temperature charge sensitive amplifiers recording signals to code the photon energy, and a time stamp of 5 μs accuracy was derived from GPS signals. At a wavelength of 500 nm, the intrinsic Ta

resolution of 12 nm was degraded to ~ 60 nm through a combination of electronic noise and thermal background radiation. The photons were introduced through a "back-illuminated" sapphire substrate, which limited the wavelength response to ~ 310 -720 nm, with a QE ~ 60 -70%.

Measurements of the cataclysmic variables HU Aqr and UZ For have demonstrated the power of spectrally resolved photon-counting investigations that are leveraged with STJ instruments [2]. In HU Aqr the technique of eclipse mapping showed that the accretion stream was comparable in brightness to the accretion region on the white dwarf itself, and that brightness changes in the stream within one orbit indicate an unstable magnetic heating.

QSO redshift machines are another scientific area in which STJs have potential to excel. With a large image array, the energy resolving capabilities would allow direct determination of the QSO redshift of every imaged source, without recourse to an inefficient dispersive element. A test of the technique was made by observations (each ~ 600 -1000 sec) of ~ 18 mag QSO's, comparing the measured energy spectrum with a single QSO template [3]. Redshifts were measured with 1% accuracy, including one object that was found to have an erroneous z value in the literature, after follow-up to confirm the STJ measurement.

5. REFERENCES

- [1] A Peacock, P Verhoeve, N Rando et al, 1996, *Nature* vol **381**, p. 135.
- [2] C M Bridge, M Cropper, G Ramsay et al, 2002, *MNRAS*, in press.
- [3] J H J deBruijne, A P Reynolds, M A C Perryman et al, 2002, *Ast&Aph* **381**, L57.

SILICON-ON-INSULATOR-BASED SINGLE-CHIP IMAGE SENSORS

Low-Voltage Scientific Imaging

Vyshnavi Suntharalingam, Barry E. Burke, and Michael J. Cooper
Lincoln Laboratory, Massachusetts Institute of Technology

Abstract: *A low-voltage (≤ 3.3 V) imaging technology has been developed to enable scientific-grade imagers with low-power complex functions on chip. A 128×128 CCD imager with on-chip clocking and charge-domain analog-to-digital conversion, as well as an exploratory active pixel sensor have been demonstrated. A 640×960 CCD imager with optimized 12 bit charge-domain conversion and an improved active pixel sensor are presently in fabrication.*

Key words: *Charge-Coupled Device (CCD), Active Pixel Sensor (APS), Silicon On Insulator (SOI), Complementary Metal Oxide Semiconductor (CMOS)*

1. INTRODUCTION

In an era where major observatories are envisioning telescopes that are three to five times bigger than present-day systems, focal plane requirements for power consumption and signal processing come to the forefront of instrumentation design. While discrete analog and digital processors for high pixel-count focal planes strain instrument mass and power resources to impractical limits, modern resolution-enhancement techniques, such as adaptive optics, demand even more intelligence from detector systems. Integrating advanced processing on the focal plane can relieve the need for extensive support hardware, lower the power expended in driving signals off chip, and can also bring significant “smarts” to the imager.

However, a significant hurdle to future system integration is the widening divide between the 10-15 V operation of most CCD imagers and the sub-5 V requirements of commercially available support electronics. CMOS-based

imagers, often referred to as active pixel sensors (APS) [1], have captured a significant fraction of the consumer-related market with single-chip sensors capable of region of interest windowing, gain and offset correction, A/D conversion, noise filtering, and high-speed operation. But their imaging performance lags far behind that of the CCDs presently at the core of telescope camera and spectrograph systems. CMOS imagers suffer from high readout noise, narrow spectral response, and poor quantum efficiency resulting from the digital circuit fabrication methods used to produce these imaging devices.

To address future needs for scientific-grade visible imagers we have developed an Imaging/Silicon-On-Insulator-CMOS (I/SOI) technology to build visible imagers with on-chip processing and operation at less than 3.3 V. This monolithic silicon-on-insulator-based approach supports analog and digital circuitry and offers photosensitive devices optimized for low-noise, ultra-high resolution imaging. Our smart CCD- or APS-based focal planes can also be back-illuminated for 100% fill factor and broad spectral response. This low-power, monolithic Imaging/SOI-CMOS technology offers the unsurpassed performance of CCDs as well as complex CMOS circuit functions, for a scalable solution to new scientific needs.

2. TECHNOLOGY DESCRIPTION

2.1 Silicon-On-Insulator

Silicon-on-insulator (SOI) wafers employ a buried silicon dioxide layer (BOX) to separate a thin (~50 nm) silicon layer from the mechanical support of the bulk silicon wafer. Devices fabricated in SOI benefit from reduced parasitic junction capacitances and suppressed short channel effects due to the presence of the insulator below the devices [2]. The 50 nm-silicon active layer causes CMOS devices in the I/SOI technology to operate in the fully depleted (FDSOI) mode, offering further advantages such as reduced channel capacitance, enhanced sub-threshold swing, and minimized floating body effects. In combination, these factors yield circuits where the energy required per computation is lower than for similar circuits implemented in bulk technologies.

Imagers implemented in bulk CMOS employ the p-n junctions formed during transistor fabrication to separate and collect the photogenerated electron-hole pairs. These active pixel sensors cleverly leverage the fabrication technologies standard to digital circuits to achieve detectors with sophisticated functions on chip [3]. However, the imaging performance of

these sensors is ultimately constrained by the optimization of wafer processing steps for digital circuit behavior. The bulk CMOS structure must include a moderately doped epi layer for latchup control and well implants for CMOS isolation. These implants, engineered for sub- μm transistor channel control and high drive current, limit photoconversion efficiency and constrain pixel fill factor.

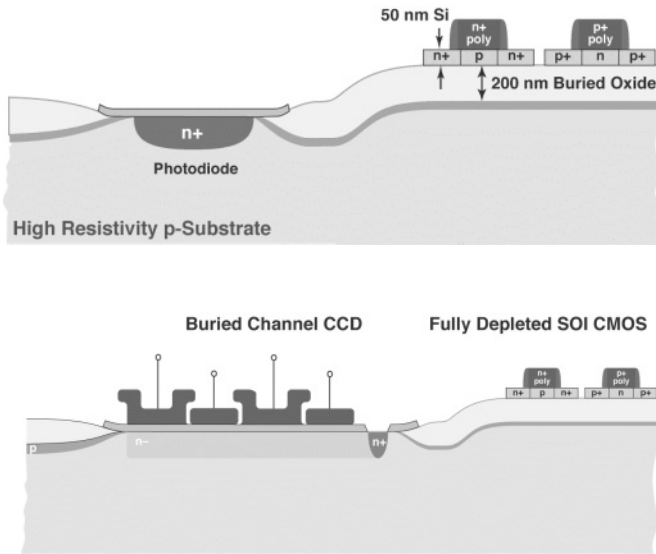


Figure 1. Schematic cross-section through photodiode pixel (top) and CCD imager (bottom) for a monolithic structure that combines photodetectors with SOI-CMOS circuits.

Since SOI-based circuit implementations use only a thin layer of silicon, the bulk material under the buried oxide becomes available for photosensitive devices. Figure 1 shows schematic cross-sections through photodiode (top) and CCD/photogate (bottom) implementations in the I/SOI process technology. The detector elements are fabricated in the bulk high-resistivity wafer and the pixel, clocking, and support functions are fabricated in the thin SOI. The use of a high-resistivity bulk wafer is essential to achieving large depletion depths and thus high QE. An early demonstration of an APS fabricated with 300 $\Omega\text{-cm}$ wafers in the I/SOI technology achieved dramatically improved spectral response to the visible and near infrared, compared to a bulk CMOS design [4]. Further, the buried oxide isolation between SOI transistors and the photosensitive devices in our I/SOI process prevents the signal charge from corruption from the readout electronics.

3. 3.3 V SINGLE-CHIP CCD IMAGER

For initial development the I/SOI technology was targeted for a 3.3 V operating point, to provide sufficient voltage headroom for analog design while significantly reducing CCD power consumption.

3.1 CCD-based Single Chip Imagers

Figure 2(a) is a photomicrograph of the first CCD-based single-chip imager designed in the Imaging/SOI technology. This chip included a four-phase, 128×128 -pixel CCD imager with on-chip clock generation and charge-to-digital conversion. The $8 \mu\text{m} \times 8 \mu\text{m}$ pixel imager demonstrated a charge handling capacity in excess of $125,000 e^-$ at 3.3 V [5]. The imager operated with clock voltages as low as 1.9 V; Fig. 2(b) is an image of the Lexington Minuteman captured with the imager operating at 1.9 V and with off-chip A/D conversion.

Charge-to-digital (QDC) converters are innately suited to imaging applications for they circumvent the charge-to-voltage conversion required when using a conventional ADC by directly converting charge packets non-destructively. This technology also has power and speed advantages over other ADC approaches. The QDC used for this proof-of-concept demonstration was imported from a bulk CMOS 5 V design [6], and was not retargeted for the SOI-based technology. Since the design was not optimized for 3.3 V, nor for SOI device models, the first pass results had 3-4 bits of resolution.

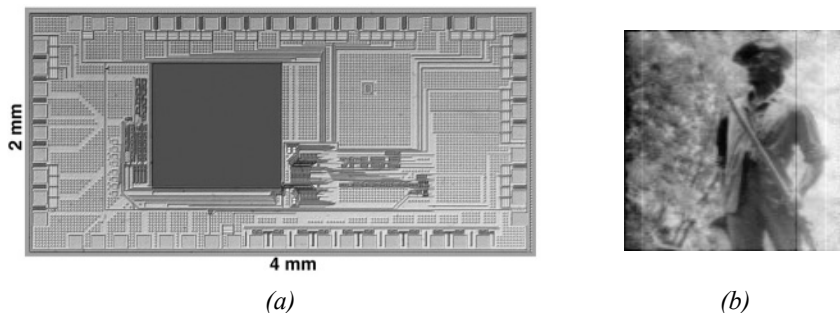


Figure 2. First CCD-based design implemented in Imaging/SOI-CMOS technology. (a) This single-chip sensor consists of a 128×128 array of $8 \mu\text{m} \times 8 \mu\text{m}$ pixels with on-chip clocking and charge-domain A/D conversion. (b) Sample image obtained at 1.9 V with on-chip clocking and off-chip A/D conversion.

3.2 Next Generation CCD/CMOS

The CCD-based single-chip imager presently in fabrication is a significantly larger (640×960) pixel array with on-chip clocking and charge-domain analog-to-digital conversion. It was designed to operate at 3.3 V with 12-effective-bit resolution at 10 MSPS with only 30 mW total power consumption. The imager can be operated in full frame (640×960), frame-transfer (640×480), or TDI modes, and also has the capability of charge binning. The physical extent of the QDC within the chip is similar to that in the earlier design, occupying a mere fraction of a square millimeter. A multi-port configuration with multiple QDCs for higher bandwidth output would not have changed the footprint of the sensor.

3.3 Active Pixel Sensor

Each design of the integrated CCD sensor has been accompanied by an exploratory APS. The first [4] was found to have superior spectral response to a comparable bulk implementation. The second, designed by Lincoln (Laboratory) and presently in fabrication, tests pixel layout variations to minimize dark current and maximize fill factor.

4. NOISE CONSIDERATIONS

Output amplifiers on CCD imagers for scientific applications are carefully optimized to achieve the lowest possible noise values. A fundamental relation governing the noise performance of floating diffusion (as well as floating gate) output circuits using a source follower was given by Ceten [7]:

$$N_e = \frac{e_n(f)C_t}{q} \Delta f \quad (1)$$

where N_e is the rms noise electron count, $e_n(f)$ is the noise voltage of the sense transistor at a frequency f (usually the serial clock frequency), C_t is the total capacitance at the sense or charge collection node, Δf is an effective system bandwidth dictated by the downstream video processing, including correlated double sampling, and q is the electron charge. Another measure of circuit performance is the responsivity, R , or the conversion gain from electrons to volts, which is given by:

$$R = \frac{qA}{C_0} \quad (2)$$

where A is the source-follower gain and C_0 is an effective sense-node capacitance. From these expressions one sees that for best noise performance the total sense-node capacitance must be minimized, CCD designers thus use the smallest possible geometries consistent with the process design rules as well as various tricks to minimize parasitic capacitances [8]. A small capacitance also yields a high responsivity, R , which means that a small charge packet is converted to a high sensor output voltage, which aids in keeping the signal from contamination by external analog and digital sources.

For the standard Lincoln CCD process, as used for the Chandra sensors, the minimum geometries were $2.0\ \mu\text{m}$, and this resulted in $C_t \sim 5\ \text{fF}$ and $R \sim 15\text{--}20\ \mu\text{V/e-}$. Figure 3 illustrates the relative sizes of the standard CCD output circuit and the scaled version enabled by the I/SOI technology. The latter is included as a test circuit on the imager lot currently in fabrication.

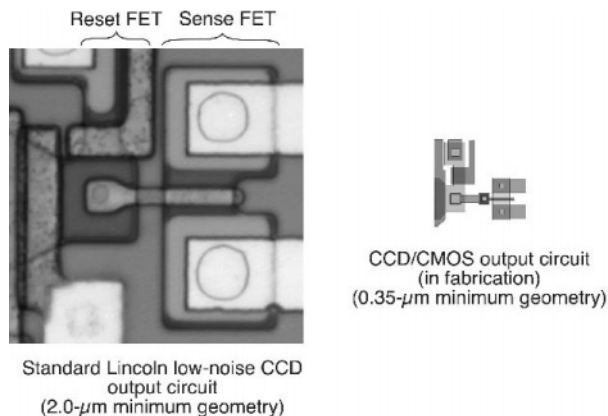


Figure 3. Comparison in output circuit dimensions for standard Lincoln CCD process and for SOI-based CCD/CMOS technology.

The highly scaled charge-sensing circuit should have substantially lower C_t , higher responsivity, R , and potentially even better noise performance than the $2\ \mu\text{m}$ -geometry structure. In this layout the CCD channel and reset field-effect transistor (FET) are located in the bulk handle wafer, while the sense FET is made in the SOI layer.

The major unknown in estimating improvements in noise performance with sub- μm circuits is the noise term e_n . In conventional CCD processes the thermal and $1/f$ noise components in e_n are fairly well characterized, but in

SOI-CMOS transistors there are new issues to deal with. These include the floating-body effect, the kink effect, edge transistors (along the sides of mesa isolated devices), and self-heating (due to the excellent thermal insulation of the buried oxide) [2]. In addition, a CMOS active pixel sensor must contend with additional circuit noise sources such as the access transistor and column amplifier noise.

Yet preliminary noise characterization of SOI-CMOS devices is encouraging. Figure 4 compares the extracted noise spectral voltage for our conventional CCD buried-channel output amplifier to that extracted from a sample FDSOI transistor. Both sets of data exhibit the inverse frequency dependence of the noise voltage and the FDSOI transistor data extrapolates to a manageable value for typical readout rates of a few MHz. We plan to study the noise issues of the SOI transistors using a set of FETs on the current imager lot and find a set of design guidelines for low-noise charge-sensing circuits that could be used by both CCD and APS sensors.

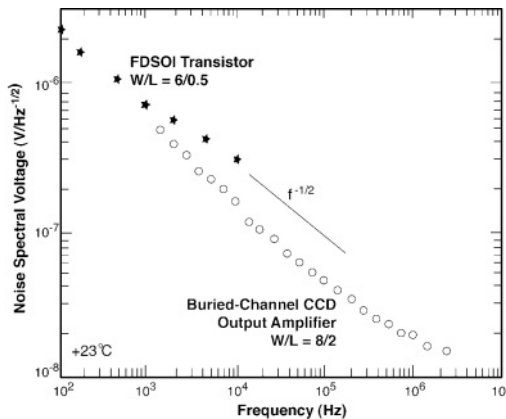


Figure 4. Extracted noise spectral voltage for CCD buried-channel output amplifier and fully depleted SOI transistor.

5. CONCLUSION

We have developed a low-voltage (≤ 3.3 V) imaging technology that merges SOI-CMOS circuits with scientific imaging devices in a monolithic structure. A small (128×128) CCD imager with on-chip clocking and modest A/D conversion as well as an exploratory APS have been demonstrated. A larger CCD imager (640×960) with charge-domain A/D conversion is in fabrication. Noise analysis of SOI-CMOS devices is continuing to with the

goal of an optimized charge-sensing circuit with potential sub-electron noise applicable to CCDs and APSs.

6. ACKNOWLEDGEMENTS

This work was sponsored by the U.S. Air Force under contract F19628-00-C-0002. Opinions, interpretations, conclusions, and recommendations are those of the authors and are not necessarily endorsed by the U.S. Air Force.

7. REFERENCES

- [1] E. R. Fossum, Oct. 1997, *CMOS image sensors: Electronic camera-on-a-chip*, IEEE Trans. Electron Devices, vol. **44**, pp. 1689-1698.
- [2] J.-P. Colinge, 1997, *Silicon-on-Insulator Technology: Materials to VLSI*, 2nd ed., Norwell: Kluwer Academic Press, pp.123-192.
- [3] G. Yang, O. Yadid-Pecht, C. Wrigly, B. Pain, IEDM 1998, *A snap-shot CMOS active pixel imager for low-noise, high-speed imaging*, Technical Digest, pp. 45-48.
- [4] X. Zheng, C. Wrigley, G. Yang, B. Pain, 2000, *High Responsivity CMOS Imager Pixel Implemented in SOI Technology*, Proc. IEEE Int. SOI Conf., pp. 138-139.
- [5] V. Suntharalingam, B. Burke, M. Cooper, D. Yost, P. Gouker, M. Anthony, H. Whittingham, J. Sage, J. Burns, S. Rabe, C. Chen, J. Knecht, S. Cann, P. Wyatt, C. Keast, Dec. 2000, *Monolithic 3.3 V CCD/SOI-CMOS imager technology*, IEEE IEDM Tech. Dig., pp. 697 -700.
- [6] S. Paul, H-S Lee, Dec. 1996, *A 9-b Charge-to-Digital Converter for Integrated Image Sensors*, IEEE J. Solid State Circuits, vol. **31**, no. 12 pp. 1931-1938.
- [7] P. Ceten, May 1991, *CCD on-chip amplifiers: noise performance versus MOS transistor dimensions*, IEEE Trans. Electron Devices, vol. **38**, no. 5, pp. 1206-1216.
- [8] B. E. Burke, J. A. Gregory, M. W. Bautz, G. Y. Prigozhin, S. E. Kissel, B. B. Kosicki, A. H. Loomis, D. J. Young, Oct. 1997, *Soft X-ray CCD imagers for AXAF*, IEEE Trans. Elec. Dev., vol. **44**, no. 10, pp/ 1633-1642.

LARGE FORMAT AND SCIENTIFIC DETECTORS AT FAIRCHILD IMAGING

Paul Vu
Fairchild Imaging

Abstract: *A review of large format and scientific CCD detectors recently developed at Fairchild Imaging is presented. This includes the CCD486, a 4096×4096 monolithic CCD available for front or backside-illumination, the CCD595, a 9216×9216 full frame CCD, and the CCD424, a high-speed back-illuminated CCD developed for the NASA Deep Impact mission.*

Key words: *Charge-Coupled Devices (CCDs), scientific CCD, large format CCD, back-illuminated, backside-thinning*

1. INTRODUCTION

A direct descendant of the Fairchild Semiconductor Company, one of the first companies to start producing CCD imagers commercially as early as 1974, Fairchild Imaging's lineage also includes innovative CCD manufacturers such as Ford Aerospace and Loral Fairchild Imaging Sensors. Fairchild Imaging currently manufactures a growing family of scientific-grade, large area monolithic CCD detectors with imaging areas as large as 80 mm×80 mm for industrial and scientific applications. We also produce a line of high-speed linear CCDs and Time Delay and Integration (TDI) CCDs for industrial inspection and earth resource imaging applications. In addition to our standard product lines, we have successfully developed a number of custom-designed image sensors for space and defense programs.

In this paper, we will review some of the large format products that were recently introduced or revised for enhanced performance.

2. CCD FABRICATION

Fairchild Imaging's modern Charge Coupled Device (CCD) design and manufacturing facilities are located in Milpitas, in the heart of Silicon Valley in northern California.

The CCDs are fabricated in our own wafer fab, on 5 in epitaxial silicon wafers. Our experience in qualifying second source silicon foundries has shown that it is very difficult to yield high quality CCDs using standard process recipes that have not been optimized for large area devices. The manufacturing of CCDs requires precise control of the quality of the starting materials, the appropriate selection of process chemicals, gases, and the proper configuration of the process equipment. Each step of the fabrication process must be fully optimized to achieve the performance expected of scientific grade CCDs. Many of our devices are fabricated using a triple poly, single metal process. An oxide-nitride gate dielectric is employed to optimize yield and device performance. The dimensions of our large area CCDs typically exceed the field of exposure of step-and-repeat photolithographic equipment. Therefore, we have chosen to perform the photolithographic processes using full-field projection aligners rather than relying on step-and-repeat mask aligners. This prevents the inevitable misalignment errors associated with stitching techniques, which result in visible fixed-pattern noise. Fairchild Imaging's scanning projection aligners are equipped with precise automatic alignment capabilities. We have developed special data manipulation methods and photomask specifications to minimize the nearly undetectable sub- μm e-beam registration errors that are normally present in the photomasks.

Dry plasma etching techniques are used to define the polysilicon gate electrodes with exceptional dimensional accuracy, ensuring high response uniformity. Plasma etching is also employed in etching contacts and defining the metal layers. The use of highly automated wafer processing equipment helps reduce manual handling and minimizes defect density. Particulate contamination at every processing step is highly monitored and carefully controlled by regular in-process inspections and measurements. The Fairchild Imaging fabrication process is optimized for large area imaging devices. We have been mass producing 61.4 \times 61.4 mm, 4096(H) \times 4096(V) CCD arrays for more than 6 years, and our wafer fabrication process has been refined to the point that we can routinely achieve exceptionally high yields on ultra large, 80.6 \times 80.6 mm, 9216(H) \times 9216(V) CCD imagers.

3. CCD BACKSIDE THINNING

The Quantum Efficiency of a CCD is greatly enhanced if the device is thinned and back-illuminated. Quantum Efficiency (QE) is simply the ratio of the number of photo-generated electrons sensed by the device and the number of incident photons. QE is a function of the light wavelength, and backside thinned devices significantly increase QE—especially at the shorter wavelengths—because the loss due to absorption and reflection in the polysilicon gate electrodes is effectively eliminated. In the near infrared, the QE of a backside thinned device is comparable to a frontside-illuminated device of comparable epitaxial silicon thickness. Figure 1 compares the QE of the CCD486 when back-illuminated and front-illuminated. Since a bare silicon surface reflects almost 30% of the incident light, QE is further enhanced by the application of special antireflection coatings over the active area. Fairchild Imaging back-illuminated CCDs are available with either a blue-enhanced or broadband AR coating, which are tailored to optimize the QE of these devices in the selected spectral band.

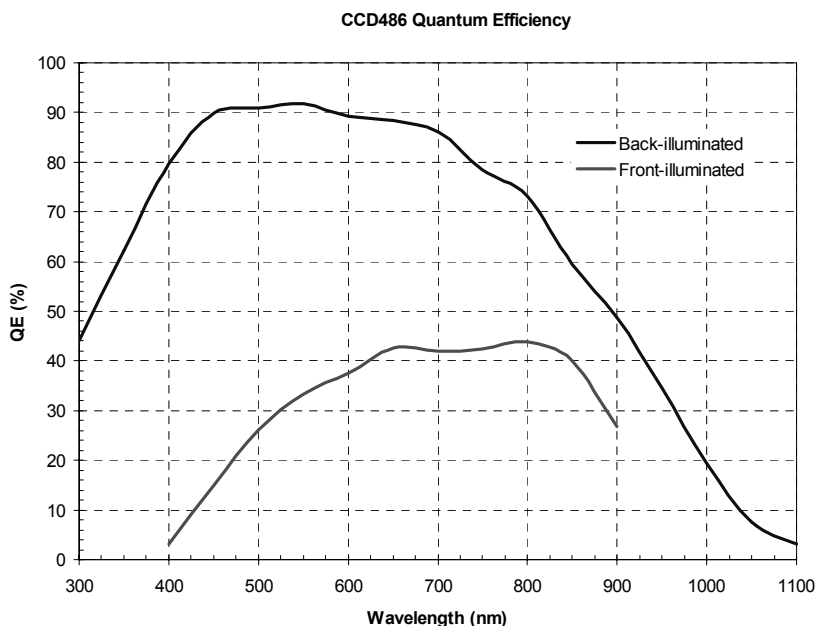


Figure 1. CCD486 Quantum Efficiency.

The Fairchild Imaging CCD backside thinning process is based on highly selective chemical etching techniques, which result in a thinned surface with low defect density, providing accurate control of the final thickness. The

large difference in etch rates between the heavily doped p-type substrate and the epitaxial silicon layer allows us precise control over the final thickness of the active area to within a few microns from its original thickness. Our process also allows us to perform selective ‘window thinning’, which is particularly well suited for back-illuminated frame transfer devices. Using this technique only the active imaging area is thinned, while thick silicon is left intact under the storage sections. Our process yields a uniform, flat active area by providing a flat, rigid epoxy supporting layer under the thinned regions.

Fairchild Imaging performs the CCD backside thinning process in-house. The process is carried out in a dedicated semiconductor wafer fabrication clean room area by qualified technical staff to ensure exacting control of the key process parameters, which is necessary to achieve reliable and consistent yields. The CCD thinning operation is set up for high volume production. In addition to the CCD424, a 1024×1024 frame transfer CCD with 21 μm pixels, Fairchild Imaging’s current backside thinned products include the CCD447, a 2048×2048 full frame CCD with 15 μm pixels, and the CCD486, a 4096×4096 full frame CCD with 15 μm pixels.

A key component of the Fairchild Imaging thinning process is the special backside treatment to accumulate the back surface. Without the treatment, the potential well that exists at the back surface of the device immediately after thinning will prevent photo-generated electrons from reaching the frontside of the device, and result in poor quantum efficiency. Our backside treatment forms a layer of negatively charged ions on a thin, thermally grown oxide layer by chemisorption to induce the underlying silicon surface into accumulation. This condition yields the desired potential profile to drive the photogenerated charge to the CCD collecting wells at the frontside of the devices. It is important to note that our approach does not require the use of ion implantation and laser annealing which cause the well-known “brick wall” pattern in captured images.

The Fairchild Imaging thinning process is performed at the die level, which tends to improve the consistency from die to die since every device can be processed under the same exacting conditions. After complete electrical characterization, the product wafers are lapped and polished to a designated thickness with tight uniformity tolerance across the entire wafer. The wafer thickness is judiciously determined to ensure that sub-surface lattice damage from the lapping process does not extend near the CCD epitaxial layer. The wafers are subsequently diced into individual CCDs and special gold interconnects are formed in the bonding pad openings.

The CCD is then bonded to a substrate carrier that contains matching bonding pads. A low-outgassing epoxy with compatible thermal and

mechanical properties is used to fill the space between the CCD and the substrate and reinforce the bond between the CCD and the substrate carrier.

A selective chemical etching process is used to thin the device to the final desired thickness. A method of over-thinning (etching into the epitaxial layer) is also performed to reduce the field-free region in the device and improve its MTF characteristics.

Immediately following chemical etching, the recombination velocity and surface state density at the silicon surface are extremely large, primarily due to the abrupt termination of the silicon lattice. This results in a high density of dangling bonds. These conditions lead to extremely poor QE and excessively high dark current. A low temperature oxidation process is performed to tie up the dangling bonds and restore the surface integrity.

An antireflection coating is then deposited to optimize the device QE response. A single layer is used to peak the response in the UV, while a 2 layer coating is used if a broadband response is desired. After AR coating, the device is complete and ready to be packaged for final test.

Fairchild Imaging's CCD thinning is performed in a class 100 cleanroom environment. This level of cleanliness is extremely important to achieve near defect-free devices and maintain a consistent yield.

4. LARGE FORMAT CCD IMAGE SENSORS

4.1 CCD486

The CCD486 is a 4096×4096 full frame CCD with 15 μm sq. pixels, tailored especially for low noise scientific applications. The device, still in its early development stages at the 1999 ESO CCD Workshop, has since evolved into a mature product in full volume production. The active area is 61.44 mm by 61.44 mm. The device has four low noise output amplifiers, and is designed to operate in Multi-Pinned Phase (MPP) mode. The full well capacity in MPP has been optimized, making the device particularly well suited for applications requiring high dynamic range (86 dB). The CCD486 is available in two configurations: conventional frontside illuminated and back-illuminated for optimal quantum efficiency. The CCD486 is the largest commercially available 4096(H)×4096(V) monolithic, back-illuminated CCD currently in production.

4.1.1 CCD486 Device Architecture

The CCD486 is a three-phase CCD fabricated with a triple-poly, single metal, n-buried channel process. The imaging area is electrically divided into four quadrants. There are two horizontal readout registers located at the top and the bottom of the imaging area. All of the bonding pads are placed along these two sides of the device, thus the device is edge-butable at the other two sides. The three-phase serial shift registers are evenly split so that the image frame can be read out simultaneously from the four single stage output amplifiers. Figure 2 shows the architecture of the CCD486.

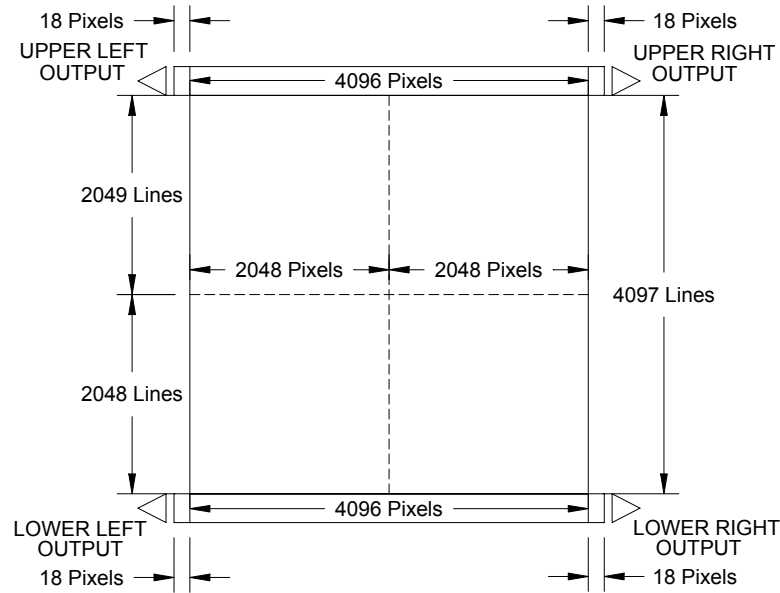


Figure 2. CCD486 architecture.

4.1.2 CCD486 Device Characteristics

The CCD486 (see Fig. 3) is equipped with four low noise output amplifiers capable of less than 4 e⁻ noise floor at relatively low readout speeds, and less than 11 e⁻ readout noise at the maximum data rate of 4 million pix/sec, reading out of all four ports.

Charge Transfer Efficiency (CTE) is typically better than 0.999998 in both the vertical and horizontal shift registers. The device features special notch sub-channels for improved radiation tolerance at low signal levels.

Vertical full well has been optimized to yield 100,000 e⁻ in MPP. Full well is determined from photon transfer curves.

In MPP mode, the dark current is typically less than 0.02 e⁻/pix/sec at – 60°C.

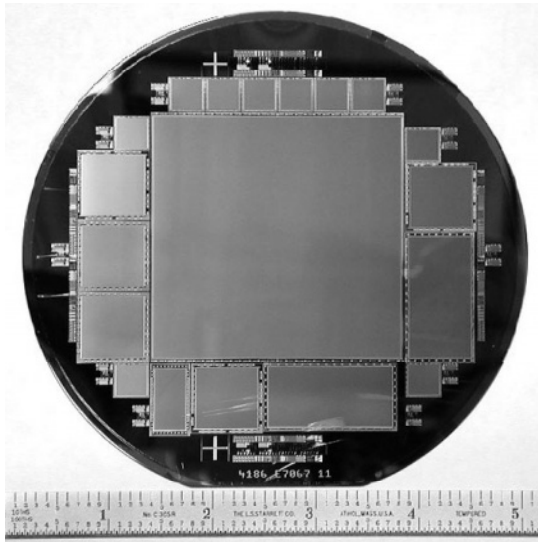


Figure 3. CCD486 on 125mm wafer.

4.1.3 CCD486 Packaging

The CCD486 is completed in a number of different packages:

- Frontside illuminated CCD in Kovar tub package.
- Frontside illuminated CCD in ceramic PGA package.
- Backside illuminated CCD in Kovar tub package (see Fig. 4).
- Backside illuminated CCD on Invar substrate (see Fig. 5).
- Backside illuminated CCD in ceramic PGA package (see Fig. 6).

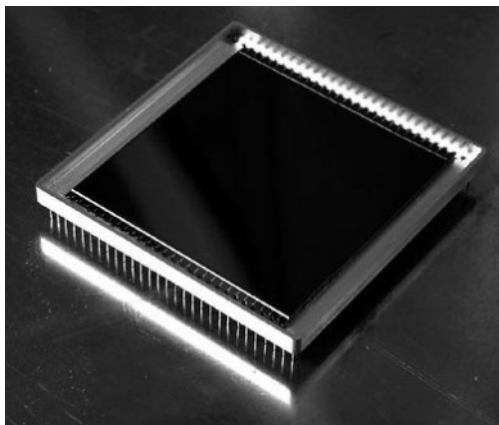


Figure 4. Backside-illuminated CCD486 in Kovar tub package.

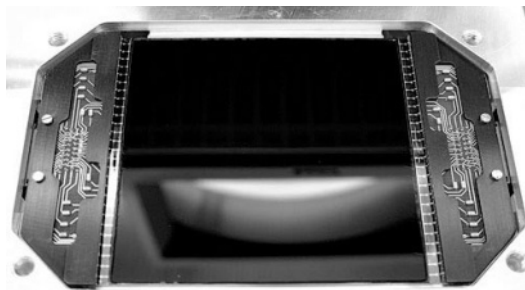


Figure 5. Backside illuminated CCD486 in Kovar tub package.

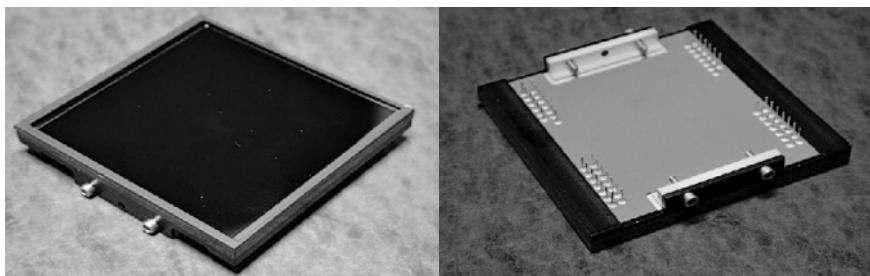


Figure 6. Backside-illuminated CCD486 in a ceramic PGA package.

4.2 CCD595

The CCD595 (see Fig. 7) was originally designed as a replacement for conventional film in airborne reconnaissance cameras. This application requires image sensors with high resolution and large field of view. There are clear benefits in using electronic image sensors to form electronic imagery and allow rapid access to information and the ability to distribute the data in real time to multiple observers. However, to date, few CCD manufacturers, other than Fairchild Imaging, have been able to demonstrate the ability to fabricate monolithic high resolution detector arrays of sufficient dimensions to compete with reconnaissance film.

4.2.1 CCD595 Device Architecture

The CCD595 is a 9216(H)×9216(V) full frame CCD image sensor with 8.75×8.75 μm sq. pix. The monolithic imaging area, 80.64×80.64 mm, is split into four vertical three-phase shift registers (each section is 2,304 pixel wide) which are connected at each end (top and bottom) with separate two-phase serial shift registers. A high speed output amplifier is attached to each serial register for a total of eight output ports. The 3 stage source follower amplifiers operate nominally at 25 MHz, yielding a data rate of 100 million pix/sec/side, using 4 outputs. The amplifiers can be clocked at up to 40

MHz. The vertical shift registers are clocked at 11 kHz, thus taking less than a second to read out an entire frame. The data throughput can be doubled by operating all eight outputs. The CCD is driven by 16 groups of 3 phase vertical clocks which are separately pinned out to effectively reduce the capacitive loading, and minimize the RC time constant. Figure 8 shows the 2 phase serial register of the CCD595.

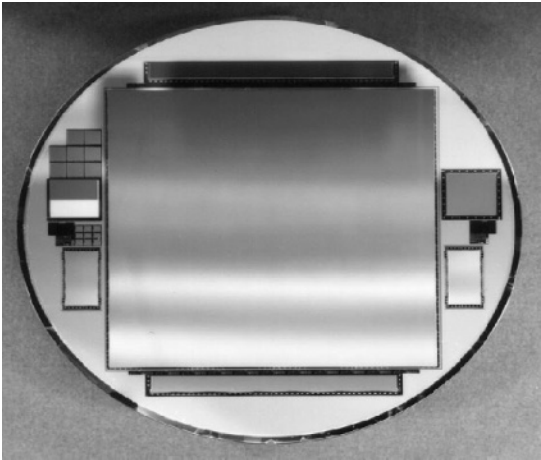


Figure 7. CCD595 on 125 mm wafer.

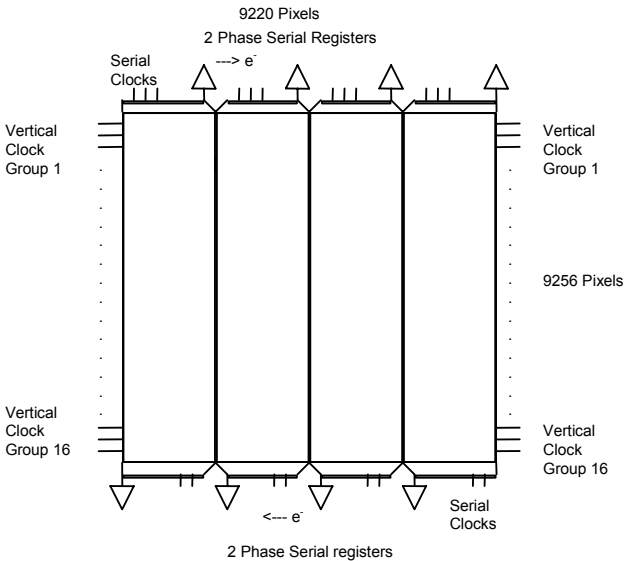


Figure 8. 2 Phase Serial Registers of the CCD595.

4.2.2 CCD595 Device Characteristics

The CCD595 characteristics are summarized in Table 1.

Table 1. CCD595 characteristics.

<i>Parameter</i>	<i>Measured Results</i>
Frame	81 mm×18 mm
Image	9216×9216
Pixel	8.75×8.75 μm
Architecture	Full Frame
Number of Outputs	8
Output Type	3 Stage Buried Channel
Integration Time	0.5 ms to 10.0 ms
Frame Rate	1 frame/sec
Pixel Full Well	>100,000 e^-
Vertical CTE	>0.999999
Horizontal CTE	>0.999995
Dark Current/non-MPP	$\leq 70 \text{ pA/cm}^2$
Pixel Readout Rate	>40 MHz
Readout Noise @ 25 MHz	<25 e^- rms
Conversion Gain	$\geq 9 \text{ } \mu\text{V/e}^-$
Operating Temperature	<-70 $^{\circ}\text{C}$
PRNU	$\leq 5\% \text{ V}_{\text{sat}}$
DSNU	$\leq 1 \text{ mV rms}$
Quantum Efficiency	$\geq 30\% \text{ } -(0.55\text{nm}-0.8\text{nm})$
MTF @ Nyquist	$\geq 50\%$
Vertical Transfer Time	<92 μsec
Array Transfer Gate Time	<10 $\mu \text{ sec}$

4.3 CCD424

The CCD424 (see Fig. 9) is a backside thinned split frame transfer CCD developed for the Deep Impact NASA mission scheduled to be launched in 2004 to study the internal composition of a comet for the first time. The CCD424 are the visible detectors on the High Resolution Instrument (HRI) and Medium Resolution Instrument (MRI) in the Flyby spacecraft. They are used to collect data for navigational purposes and to acquire scientific data following impact with the comet. The CCD424 is also used on the Impactor for guidance and for the collection of scientific information until the moment of impact.

Fairchild Imaging developed the image sensors in support of Ball Aerospace, the prime contractor for the instruments and the flight hardware.

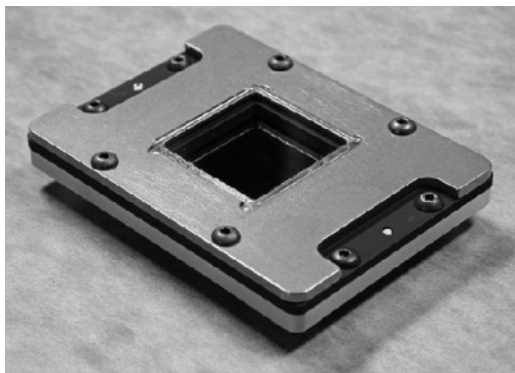


Figure 9. The CCD424 Deep Impact CCD in flight package.

4.3.1 CCD424 Device Architecture

The imaging area of the three-phase CCD is $1024(H) \times 1024(V)$, and the storage sections are each $1024(H) \times 512(V)$. The pixel size is $21 \mu\text{m sq}$. There are four output amplifiers, one at each end of the two serial shift registers. The serial registers are connected to gated fast dump drains for high speed flushing of charge in the serial registers. The polysilicon gates in the vertical registers and the channel stops are strapped to metal bus lines to accommodate high speed transport of the signal charge between the imaging area and the storage regions. The imaging area was selectively thinned, while doped bulk silicon was retained in the storage regions to improve grounding and permit high speed operation. Figure 10 shows the architecture of the CCD424.

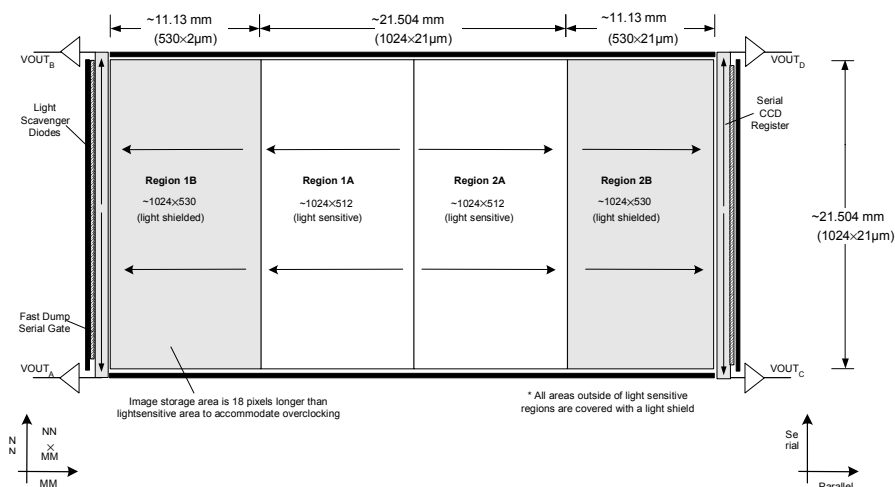


Figure 10. CCD424 device architecture.

4.3.2 CCD424 Device Characteristics

The CCD424 supports vertical transport frequency of 225 kHz for minimal image smear. The device was designed to operate in non-MPP mode to achieve better than 500,000 e⁻ full well charge capacity. Dark current is suppressed by cooling the device to -100 °C and operating the CCD in partial inversion using a special clock timing sequence which dithers the charge between phase 1 and phase 2, while phase 3 is kept in inversion to confine the charge. This technique lowers the dark current by 5 to 10 times. Peak QE measured 94% at 600 nm. Typical vertical CTE is 0.999999 and horizontal CTE is 0.999995.

5. FUTURE DEVELOPMENTS

Fairchild Imaging plans to continue to develop wafer-scale image sensors with unique capabilities. A number of new products are currently under development, with emphasis on improved sensitivity, lower noise, higher speed, and even larger active areas.

HgCdTe DETECTORS FOR THE HUBBLE SPACE TELESCOPE WIDE FIELD CAMERA 3 IR CHANNEL

Augustyn Waczynski¹, Terry Beck², Ray Boucarut³, Edward Cheng³, Dave Cottingham¹, Gregory Delo¹, Dale Fixsen⁴, Robert J. Hill⁴, Scott Johnson¹, Peter Kenny³, Wayne Landsman⁴, Eliot Malumuth⁴, Joel Offenberg⁴, Elizabeth Polidan¹, Anne Marie Russell¹, David Schlossberg², Elmer Sharp¹, Edward Wassell⁴, Yiting Wen⁴, John Yagelowich³

¹NASA GSFC/GST, ²NASA GSFC/Sigma, ³NASA GSFC, ⁴NASA GSFC/SSAI

Abstract: *Detector performance has been characterized for the HST WFC3 IR channel. This will be the first TEC cooled IR instrument on the Hubble Space Telescope (HST), which is made possible because of recent progress in HgCdTe technology. The original detector requirements are compared with the performance of the delivered devices. Achievements in quantum efficiency and dark current are described, as well as difficulties in meeting requirements for noise and dark stability. A special technique developed to illuminate a single pixel, which has demonstrated the excellent spatial resolution of the detectors is described.*

Key words: Hubble Space Telescope (HST), Wide Field Camera 3 (WFC3), HgCdTe, Infrared (IR), focal plane, multiplexer, Quantum Efficiency (QE), noise, dark current

1. INTRODUCTION

The HST Wide Field Camera 3 (WFC3) is a new instrument planned for deployment during Servicing Mission 4 in 2004. One of its key scientific goals is to provide panchromatic coverage from the near-UV through the near-IR. This is accomplished using two detector technologies: Marconi Applied Technologies back-thinned CCDs and Rockwell Scientific (RSC)

Mercury-Cadmium-Telluride (HgCdTe) IR focal planes. The instrument has separate channels for the near-UV/visible and near-IR parts of the spectrum. The key features of the IR channel are listed in Table 1.

Table 1. WFC3 Instrument Performance.

	IR Channel	CCD Channel	Units
Spectral Coverage	0.85 to 1.7	0.2 to 1.0	μm
Field of View	135 \times 135	160 \times 160	arcsec
Format	1024 \times 1024	2 \times (2048 \times 4096)	
Pixel Size	18 \times 18	15 \times 15	μm
Operating temperature	150 K	-83 $^{\circ}\text{C}$	

The performance of Marconi devices is exceptionally good, and will provide a new wide-field, near-UV capability for the observatory. These detectors are designed for space application and are radiation hardened.

The WFC3 IR channel has been made possible by recent advancements in HgCdTe technology and the flexibility offered by this material to trade off between spectral coverage and dark current. Devices processed with molecular beam epitaxy (MBE) offer dark current low enough to build a IR instrument based on thermoelectric cooling (TEC) with background limited performance.

The IR channel has a spectral range of 0.85 μm to 1.7 μm . In this range the zodiacal background seen by the instrument amounts to 0.4 $\text{e}^-/\text{sec}/\text{pix}$. In order to be background limited, we have required that the instrumental contribution to the background be less than 0.4 $\text{e}^-/\text{sec}/\text{pix}$, of which 0.2 $\text{e}^-/\text{sec}/\text{pix}$ has been allotted to detector dark current. Present thermoelectric coolers cannot achieve temperatures much lower than 150 K, hence this temperature was chosen as an operating point. A special, six stage TEC was developed and careful thermal shielding applied to implement this design.

The WFC3 detectors are a continuation of the Hawaii series of RSC products and they benefit from that experience. A new multiplexer has been designed for WFC3 to cope with the shortcomings of previous designs. For the first time (with IR detectors) this multiplexer has implemented reference pixels to track baseline drifts and to reduce any 1/f noise component. In addition, the multiplexer readout scheme has been modified to improve image uniformity and a number of design modifications were introduced to minimize the glow of the readout electronics. Another new feature in the multiplexer design is the presence of four temperature sensors. Placed close to the top of the multiplexer, they provide very accurate measurements of the array temperature. Figure 1 describes the detector layout, multiplexer readout and location of the reference pixels (rows and columns indicated).

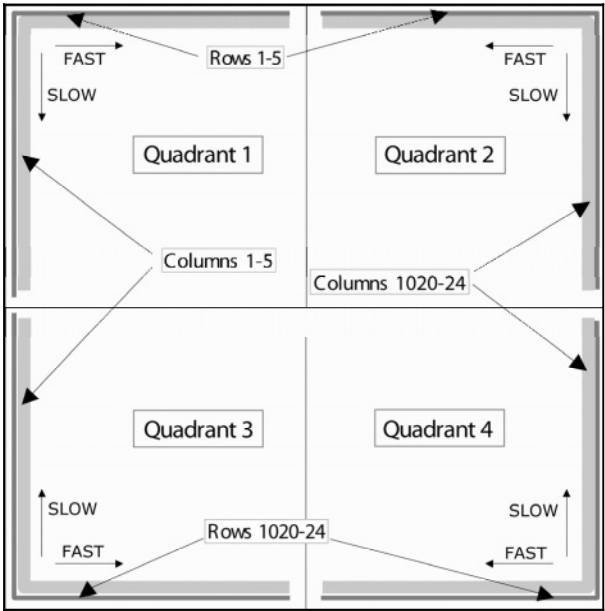


Figure1. WFC3 multiplexer organization. Reference pixels and readout direction.

Table 2 summarizes the detector performance requirements. Quantum efficiency (QE), read noise and dark current are the most important of these and are discussed in more detail below.

Table 2. IR Detector Requirements.		
Spectral Range	0.85 to 1.7	μm
Format	1024 \times 1024	
Pixel Size	18 \times 18	μm
Dark Current	< 0.2	e ⁻ /sec/pix
Quantum Efficiency	> 0.6	e ⁻ /photon
Read Noise	< 15	e ⁻ rms per read at 100 kHz
Full Well	> 70,000	e ⁻
Operability	> 97	%
Operation Temperature	150 K	

2. IR DETECTOR PERFORMANCE

2.1 Quantum Efficiency

Preliminary QE results obtained from the earliest fabricated detectors indicated that significant improvements were needed in order to meet expectations. The QE was good at the long wavelength peak but it deteriorated quickly toward shorter wavelengths, possibly due to absorption in the back surface layers. The long wavelength cutoff was well defined and met the design goal within an accuracy of a few nanometers. However, overall the initial QE results were not satisfactory, and subsequent flight devices showed a significant improvement.

Figure 2 compares the QE for an engineering sample device fabricated at the beginning of the project with that of a later flight-grade device and demonstrates impressive progress in material processing at RSC.

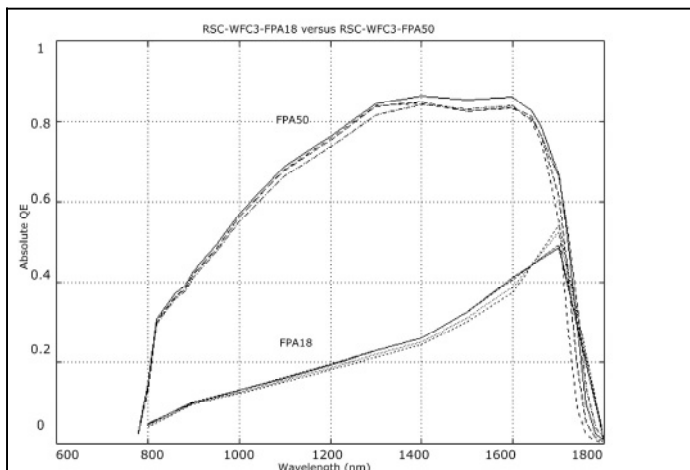


Figure 2. Comparison of QE between engineering and flight detectors (4 quadrants per device).

2.2 Dark current

Low defect density and better process control made possible with MBE resulted in a significant reduction in dark current compared to earlier PACE detectors. Some of the WFC3 detectors exhibit a dark current as low as 0.02 e⁻/sec/pix and the requirement for dark current specification (0.2 e⁻/sec/pix) has easily been met in almost all manufactured arrays. However, some of the

detectors show an abnormal dark current behavior. The dark current in these devices responds to perturbations of the diode biasing voltage. This may occur due to a change of operating condition, power-down and power-up of the instrument, or due to illumination of the pixel (as a charge accumulates on the diode capacitance, bias voltage changes). As a result, the dark current may temporarily increase (or even change direction) and will eventually return to its original value in up to a few hours (this effect is often called persistence). The physics of dark current instability is not well understood. Finally, it should be noted that only some devices show this behavior, and therefore it does not appear to be a fundamental characteristic of this material.

Figure 3 illustrates the use of reference pixels to correct dark current measurements for systematic multiplexer effects.

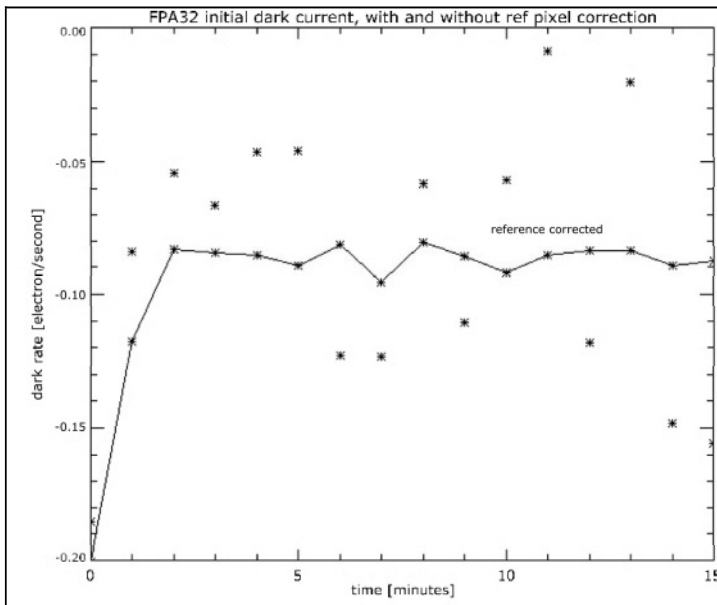


Figure 3. Dark current with and without reference pixel correction.

2.3 Noise

The detector read noise can be separated into two components: multiplexer noise and HgCdTe diode noise. The multiplexer noise has been measured using the reference pixels and by application of a permanent reset voltage to the input of the unit cell transistor for the length of readout. These measurements consistently yield a multiplexer read noise of 9 e^- rms

measured as a standard deviation of the difference of two frames (Correlated Double Sample (CDS) pair). The noise of the diode is significantly higher and at this point the detector does not meet the read noise requirement. The measured noise is in the range of 30 e^- to 45 e^- /CDS pair and its value varies from device to device. A Fourier transform of single pixel readout data indicates that the noise has a significant $1/f$ component. However, the data is not fully conclusive due to glow associated with continuous sampling of the same pixel. When measured as in the expected instrumental application, the noise increases with exposure time, providing yet another indication of a $1/f$ component. It is possible that the increase in noise and its $1/f$ character are driven by the presence of surface states.

2.4 Glow

The WFC3 IR detector operates with an external amplifier to minimize glow and thermal load to the focal plane. In this configuration, no glow has been observed. During continuous readout of a single pixel, glow has been observed, probably caused by the unit cell electronics. From that experiment, the unit cell glow was estimated as less than 0.0002 e^- /read (for a $10\text{ }\mu\text{s}$ readout time per pixel).

2.5 Spatial Resolution

Preliminary measurements have been made of the uniformity of a single pixel response of the WFC3 detectors. In order to do this, a special test setup was established as illustrated in Fig. 4.

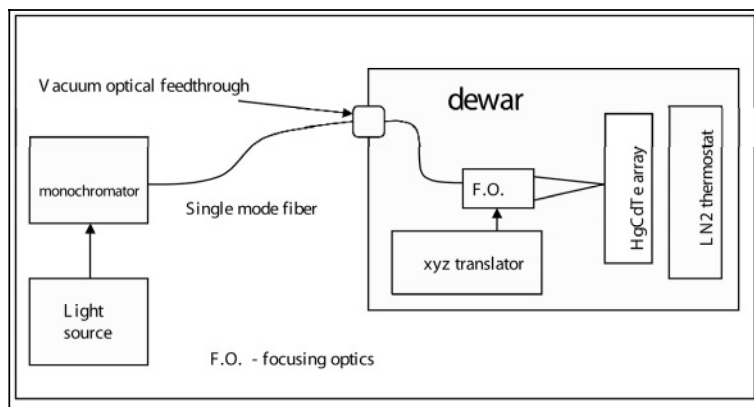


Figure 4. Test setup for single pixel illumination

The output from a monochromator is coupled to a single mode fiber. The optical signal is delivered through a vacuum tight optical connector to an illuminator positioned on a three-stage translator. The illuminator is placed in front of the focal plane and focuses the output of the fiber on the detector with a spot diameter less than $10\text{ }\mu\text{m}$ (measured as $1/(e^-)^2$ at 1310 nm). It is expected that for an $18\times 18\text{ }\mu\text{m}$ pixel size, most of the energy would be contained within a single pixel. The input beam was stepped in both the vertical and horizontal directions and the signal distribution recorded at each step.

Figure 5 shows the case where the beam was centered on a single pixel. The response of this pixel and its immediate neighbors is shown as a line plot. It confirms that essentially the entire beam energy is contained in this pixel and no crosstalk to other pixels takes place. This demonstrates that the device spatial resolution is determined by pixel size and is not degraded by inter-pixel crosstalk.

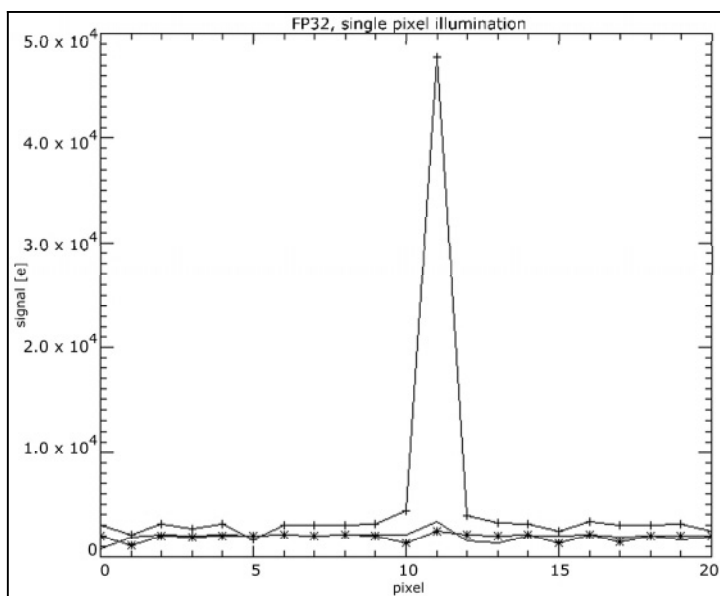


Figure 5. Detector response to single pixel illumination – line plots of the row containing the illuminated pixel, the row before, and the row after demonstrate the detector response to single pixel illumination.

3. CONCLUSIONS

Rapid progress in HgCdTe detector technology will permit a great improvement in HST's near-IR capabilities with the WFC3 instrument. The unique flexibility of this material makes it possible to trade long wavelength cutoff for lower dark current and opens the road for TEC based IR instruments. Implementation of reference pixels in a new multiplexer minimizes sensitivity to baseline drifts and other instabilities of the processing electronics. The focal plane design demonstrates excellent spatial resolution, as specified by the array format. The WFC3 detectors offer background limited IR performance with a convenient cooling system (eliminating the need for cryogenics) and economical packaging.



John Tonry, Mario Gai and Gerry Luppino meditate during one of the roundtables.

CMOS ACTIVE PIXEL SENSOR DEVELOPMENTS AT THE RUTHERFORD APPLETON LABORATORY

Guy F.W. Woodhouse, Nicholas R. Waltham, Marcus J. French, Mark L. Prydderch, Quentin R. Morrissey, Renato Turchetta, Andy J. Marshall, James M. King.

Rutherford Appleton Laboratory

Abstract: *This paper reports on an on-going research programme at the Rutherford Appleton Laboratory (RAL) to develop science-grade CMOS Active Pixel Sensors for space science missions in which compactness, low-mass, low-power, and greater radiation tolerance are advantageous.*

Key words: *Complementary Metal-Oxide Semiconductor (CMOS), Active Pixel Sensor (APS), detector, space science, solar orbiter, Earth observation.*

1. INTRODUCTION

The CCD is currently the image sensor of choice for nearly all space science, Earth remote sensing and ground-based astronomical visible light imaging systems. However, in the space environment CCD technology also has inherent weaknesses:

1. The requirements of compact, low mass, low power, and space-qualified CCD drive and video signal processing electronics.
2. The susceptibility of both the CCD and drive electronics to radiation damage.

The emergence of CMOS Active Pixel Sensors (APS) promises solutions to these issues, and is arguably the most important development in solid-state imaging technology since the invention of the CCD in 1969.

Although still in its infancy, and so far targeting the cost-sensitive commercial camera markets, APS technology is already promising significant advantages over CCDs for many space science applications. APS detectors are fabricated on low voltage CMOS processes that allow all necessary drive electronics to be incorporated on-chip, thus offering significant advantages in functional integration, readout speed, compactness, mass and power consumption [1-6].

However, one of the most important advantages is arguably the promise of higher radiation tolerance in the space environment. Although application and orbit dependent, the susceptibility of CCDs to radiation damage, and in particular the loss of charge transfer efficiency (CTE) is well known and reported [7-9]. Degradation of CTE is avoided in APS because the signal charge collected within a pixel is sensed within the pixel.

In this paper, we address our development of science-grade CMOS APS technology as an alternative to the CCD for space applications.

2. RAL SCIENCE-GRADE APS DEVELOPMENT

Our programme to develop science-grade APS technology began in 1999. Milestones of the programme over the intervening years are listed in Table 1.

Table 1. RAL Science-grade APS Development Programme

1999	Design and modeling of pixel test structures (in 0.5 and 0.7 μm CMOS).
2000	Fabrication and testing of pixel test structures. Collaboration established with E2V (formerly Marconi Applied Technologies and EEV) to exchange designs, expertise, packaging, testing, and back-thinning technology. Design of a 512 \times 512 pixel sensor with on-chip ADC (in 0.5 μm CMOS) as a replacement for the CCD in a wide-field star tracker.
2001	Fabrication of the 512 \times 512 pixel sensor. Collaboration extended to the University of Birmingham to participate in the test programme. Thinning of original pixel test structures by E2V to develop CMOS thinning technology. Planning for future designs in 0.25 μm CMOS.
2002	Design of a 4K \times 3K pixel sensor in 0.25 μm CMOS for ESA's Solar Orbiter. Design of a 4K pixel linear array with 3 μm pixels for Earth observation. Thinning of sample 512 \times 512 pixel sensors by E2V.

Our major achievements have been the design, fabrication, and testing of various pixel test structures, and a prototype 512×512 pixel image sensor with integral on-chip readout control circuitry and a 10-bit analogue-to-digital converter.

We have also formed a collaboration with E2V (formerly Marconi Applied Technologies and EEV). The scope of the collaboration includes an exchange of designs, expertise, and assistance with chip packaging and testing; and most importantly the development of CMOS thinning technology to allow backside illumination. The Astrophysics and Space Research Group at the University of Birmingham has also joined us to participate in the test programme.

3. TEST STRUCTURES

The first steps in our development programme were to design a series of test structures to evaluate the relative performance of varying pixel designs. We designed four pixel types, illustrated in Fig. 1, each with $25 \mu\text{m} \times 25 \mu\text{m}$ pixel pitch, and each in both 0.5 and $0.7 \mu\text{m}$ CMOS technology:

1. N-type diffusion on a p-type substrate (ndps pixel).
2. P-type diffusion in an n-type well on a p-type substrate (pdnwps pixel).
3. Polysilicon photogate over an n-type well on a p-type substrate.
4. Quadradot: four small interconnected n-type wells on a $12.5 \mu\text{m}$ pitch, on a p-type substrate.

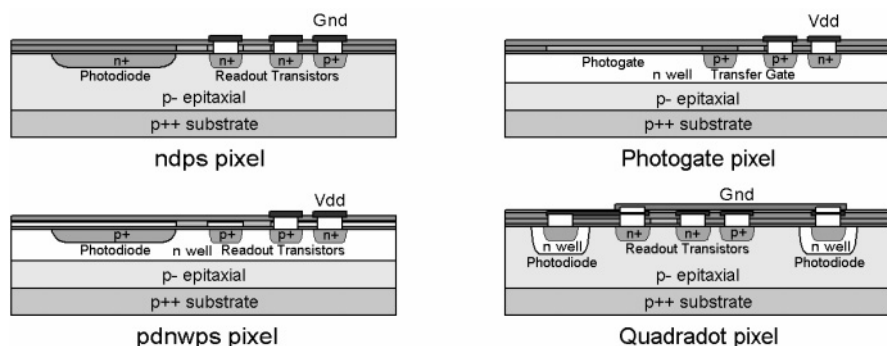


Figure 1. Four pixel test structures

The four pixel types were each expanded to arrays of 16×16 pixels, all driven from a common digital control bus. Photographs of the test structure array and a packaged chip are reproduced in Fig. 2.

The first two pixel types are arguably the most classical form of APS pixel design, consisting of a photodiode and a 3-transistor readout circuit. They differ in the nature of their photodiode construction and polarity. Both photodiodes are designed to be as large as possible to maximise fill-factor (*i.e.*, the proportion of the pixel sensitive to light), achieving $\sim 50\%$ within the $25\text{ }\mu\text{m}$ pixel. Large photodiodes have high capacitance and thus high charge capacity, but the disadvantage of low charge-to-voltage conversion sensitivity.

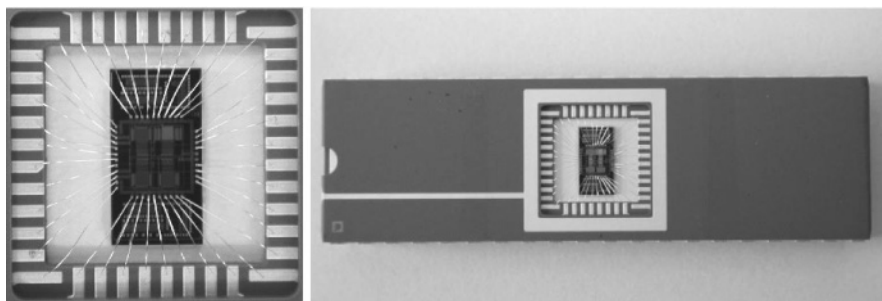


Figure 2. Pixel test-structure array and packaged chip

The photogate pixel follows the CCD concept, consisting of a polysilicon electrode overlying an n-type well on a p-type substrate. Applying a bias to the photogate induces a depletion region for collecting charge. A fourth transistor is added to the normal 3-transistor readout circuit to provide a transfer-gate, and thus a means of applying correlated double sampling (CDS) during the readout to cancel kTC noise. The node capacitance after the transfer-gate dictates the charge-to-voltage conversion sensitivity and can thus be minimised to ensure high gain and low readout noise. The advantages of high sensitivity and low noise are to some extent offset by lower fill-factor due to the fourth transistor.

The Quadradot pixel consists of four small interconnected n-well photodiodes spaced within the pixel on a $12.5\text{ }\mu\text{m}$ pitch, and a 3-transistor readout circuit. The four diodes collect charge created anywhere within the epitaxial layer and so the effective fill-factor is close to a theoretical maximum, in principle limited only by the overlying shielding of the readout transistors and aluminium tracks. A similar design has also been described in [10]. The spacing of the four diodes is intended to maximise the modulation transfer function (or resolution) of the sensor by trying to enhance the probability that charge created beneath a particular pixel is then collected by one of its four diodes.

Even before the completion of the detailed design work, we identified the Quadradot pixel as the most promising for our next objective of developing a

512×512 pixel image sensor. Results for the Quadradot pixel are listed in Table 2. The spectral response as measured by R Bell (E2V) is shown in Fig. 3.

Table 2. Quadradot pixel test results

QE	35% peak (absolute)
Noise	< 50 e ⁻ rms
Node capacitance	18 fF
Overall responsivity	8.9 μV/e ⁻
Peak output signal	1 V (167 Ke ⁻)
Dark signal	140 mV/sec (0.6 nA/sq cm) at room temperature
Fixed pattern noise	10 mV peak-to-peak

The peak QE is 35%. Readout noise is dominated by the kTC noise in the photodiode reset. Overall, the results are in close agreement with the characteristics predicted by our simulation and modelling.

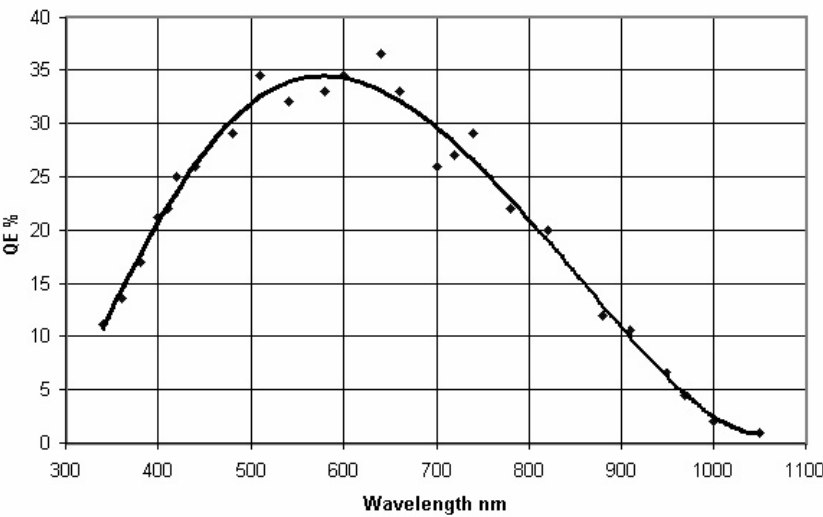


Figure 3. Spectra response from the Quadradot pixel test structure

4. 512×512 PIXEL PROTOTYPE SENSORS

Encouraged by the results from our pixel test-structures, we undertook the development of a 512×512 pixel image sensor [11] with an integral

analogue-to-digital converter (ADC). The sensor was originally conceived as a replacement for the CCD detector within a wide-field star tracker for satellite attitude reconstruction and navigation. Design specifications are listed in Table 3.

Table 3. 512×512 pixel star tracker APS

Array format	512×512 active pixels
Pixel size	25 μm ×25 μm
Pixel type	Quadrant: four interconnected n-type photodiodes on a 12.5 μm pitch, on a p-type substrate.
Well capacity	200 $\text{K}e^-$
Readout noise	$\leq 50 e^-$ rms
Frame rate	10 frames/sec
On-chip ADC	10-bit column-parallel
Gain adjust	Programmable: 1, 2, 4, 8
Outputs	1 V analogue and 10-bit digital
Control interface	I ² C serial bus
Technology	0.5 μm CMOS
Operating voltage	3.3 V
Radiation protection	triple-voting logic

The sensor consists of 512×512 Quadrant pixels with 25 μm pixel pitch. Each pixel incorporates the four photodiodes and three transistors for charge sensing, reset, and pixel selection. The diode capacitance is ~ 18 fF giving a charge to voltage conversion of $\sim 8.9 \mu\text{V}/e^-$. Readout noise of $\sim 50 e^-$ rms is dominated by the kTC noise from the photodiode reset.

The chip includes all necessary readout control logic and an integral 10-bit ADC, delivering an overall frame rate of 10 frames/sec. The control logic is designed with triple-voting registers to enhance tolerance to single-event-upsets (SEUs) from radiation within the space environment.

The ADC is implemented in a column-parallel architecture (*i.e.*, there is effectively one ADC per column). Video gain can be set to 1, 2, 4, or 8. Analogue bias supplies are generated on-chip, and programmed via a serial interface conforming to the Philips I²C protocol.

The chip is implemented in a 0.5 μm CMOS process. It is powered from a 3.3 V supply and dissipates less than 300 mW. The overall die size is 16.7 mm×19.9 mm including the associated readout and ADC circuitry. Figure 4 shows a 6-inch wafer containing 29 sensors and an individual die after being cut from the wafer. One of our first test images is reproduced in Fig. 5.

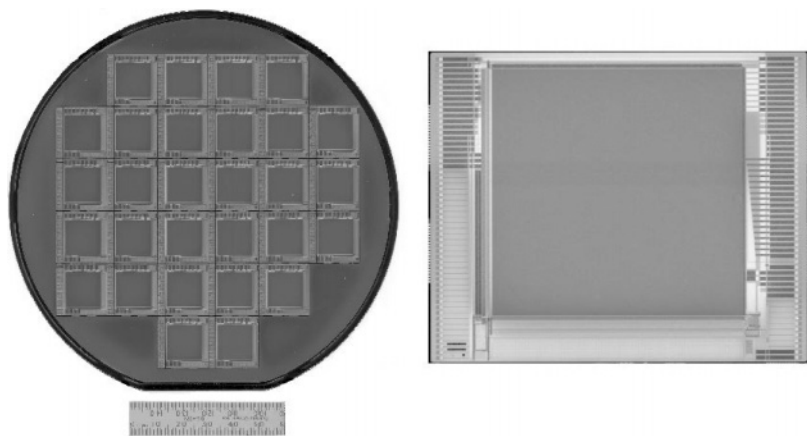


Figure 4. 6-inch wafer of 512×512 pixel sensors and an individual die.

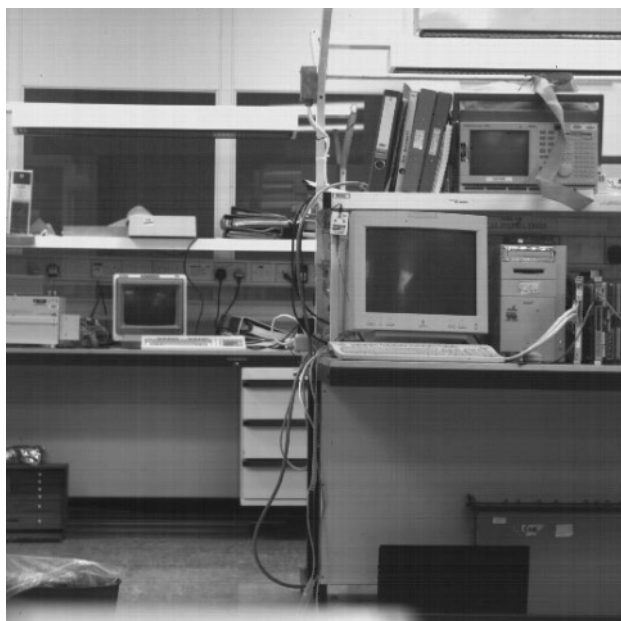


Figure 5. 512×512 pixel APS test image obtained at 10 Hz frame rate.

5. CURRENT PROGRAMME

For our new sensors we are switching to a 0.25 μm CMOS technology that will allow us to design smaller pixels and thus larger format arrays, and which promises even better radiation tolerance than the 0.7 and 0.5 μm processes.

The main features of our current programme are listed below:

1. Design of a 4K \times 3K pixel sensor with 5 μm pixels, primarily for future solar physics missions.
2. Design of a 4K pixel linear sensor with 3 μm pixels for future high-resolution Earth observation cameras.
3. Further testing of our 512 \times 512 pixel sensor, and in particular of samples that have been thinned by E2V.
4. Development of techniques to enhance sensitivity in the extreme ultra-violet (EUV) band, again primarily intended for solar physics missions.

With our 4K \times 3K pixel sensor, we are aiming to design a large-format science-grade APS, primarily for future solar physics missions. Our objectives are to minimise readout noise, and to maximise linearity and dynamic range with a target of 12 to 14-bits precision. To minimise the readout noise, we have added a fourth transistor to the basic 3-transistor pixel design as shown in Fig. 6. The fourth transistor provides a transfer-gate that isolates the output capacitance from the photodiode. CDS can be used to eliminate the kTC noise imposed on the output after reset, leaving the transistor noise which our modelling predicts to be $\sim 10\text{ e}^-$ rms.

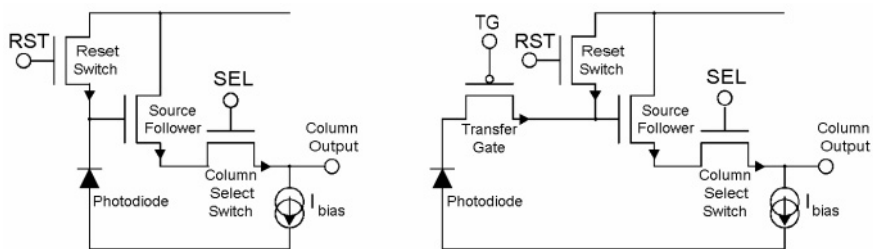


Figure 6. Common 3-transistor pixel and the new 4-transistor pixel

A block diagram of the 4K \times 3K pixel APS is shown in Fig. 7. The pixel size is 5 μm , giving an array of 20.5 mm \times 15.4 mm. The readout circuitry employs a minimum of output multiplexer stages to maintain maximum signal-to-noise, and provides a single differential analogue video output. The

chip is to be manufactured on a $0.25\ \mu\text{m}$ CMOS process that is specifically adapted for image sensors.

The $4\text{K}\times 3\text{K}$ sensor is a first step towards the development of a $4\text{K}\times 4\text{K}$ pixel APS for future solar physics missions, and in particular a spectrograph on ESA's Solar Orbiter [12]. In order to cope with the particle environment, with the bright solar sources, and to keep mass and power to a minimum, CMOS APS detectors rather than CCDs are proposed for many of the instruments on Solar Orbiter. Smaller pixels will also allow the design of shorter camera optics, and thus more compact and lower mass instruments.

In solar physics, imaging and spectroscopy in the EUV band are key to the study of chemical element abundances, temperature profiles, and activity in the solar corona and transition region. E2V have developed thinned CCDs with very respectable EUV sensitivity, and our hope is to transfer this technology to our APS programme. The first steps have been for E2V to thin samples of the 512×512 pixel arrays, and these are to undergo testing imminently. A key issue is the thickness of the epitaxial layer in the silicon. This is only $3\ \mu\text{m}$ in the case of our 512×512 pixel sensors, and too shallow to allow optimal thinning. In contrast, the $0.25\ \mu\text{m}$ process for our forthcoming $4\text{K}\times 3\text{K}$ pixel sensors starts with $8\ \mu\text{m}$ epitaxial silicon and is thus a more practical proposition for optimal back-thinning.

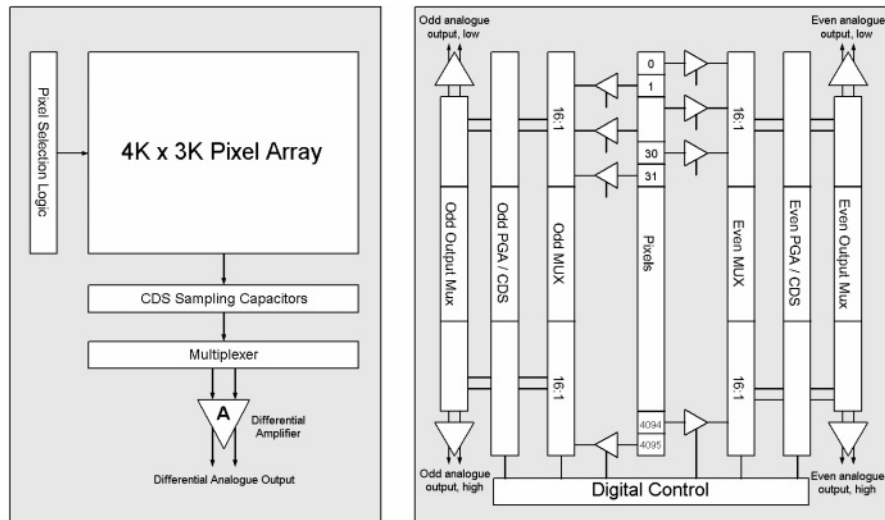


Figure 7. $4\text{K}\times 3\text{K}$ pixel APS and 4K pixel linear APS block diagrams

The second sensor in our current development programme is a 4K pixel linear array intended for high-resolution push-broom Earth observation (EO).

An underlying objective of the high-resolution EO industry is to deliver more competitively priced images, with higher re-visit frequency achieved through the deployment of satellite constellations rather than single units. Systems offering 1 m/pix ground-sampling already exist, and sub-metre pixel resolution is the next major challenge.

However, high-resolution cameras of this class are necessarily large and require appropriately sized spacecraft vehicles; both aspects incurring exceptionally high unit-cost. Ground resolution is ultimately governed by simple geometry relating detector pixel size, orbit altitude and the focal length of the camera optics. Accepting the physical constraints of low altitude orbits (*i.e.*, orbit decay and hence reduced mission lifetime), the most practical solution to shortening the camera optics, and hence reducing the instrument size and cost, is to reduce the detector pixel size.

Push-broom EO cameras currently employ one or more linear CCD arrays that are read out as the satellite tracks over the Earth's surface to build up a two-dimensional image. It follows that the better the ground resolution required, the less time there is available for the array readout which makes up each line of the final image.

The smallest pixel size and maximum readout rate of current commercial CCD technology compromises progress towards smaller EO cameras. However, APS technology promises both smaller pixels and higher readout rates. We are therefore looking to CMOS for our future EO cameras, and developing a prototype sensor [13].

A block diagram of the array is included in Fig. 7. The prototype will have 4K pixels with 3 μm pitch. Like many linear CCD arrays, the readout circuitry for odd and even pixels is placed on either side of the photodiodes. The benefit of this layout is that it increases the pitch of the readout electronics to twice that of the pixels.

An advantage of a linear array is that the pixel readout electronics can be located outside the pixel so that the majority of the 3 \times 3 μm pixel site can be occupied by the photodiode. Each pixel has its own reset transistor, and charge sensing and buffering circuitry. Signals from the pixel electronics are sampled through a fully differential 16:1 multiplexer with sampling capacitors to allow on-chip CDS, a programmable gain amplifier with range 1-8, and a final 64:1 multiplexer. Four outputs are provided in total. Modelling predicts a pixel gain of 7.7 $\mu\text{V}/\text{e}^-$, a full-well capacity of 250k e^- , and a readout noise of 66 electrons rms at the frame readout rate of 6.25 kHz (an effective pixel readout rate of ~ 6.25 MHz in each quadrant). The chip is to be manufactured on the same 0.25 μm process as the 4K \times 3K pixel sensor.

In the future, we intend to increase the array length to 8K pixels, to add on-chip ADCs, and to incorporate up to four adjacent arrays on the same die to allow imaging in different colour bands.

6. SUMMARY

RAL is developing science-grade CMOS APS technology for applications in space science and Earth observation. CMOS allows all necessary drive electronics to be incorporated on-chip, thus offering significant advantages in functional integration, readout speed, compactness, mass and power consumption. APS technology also promises greater radiation tolerance in the space environment than CCDs. To date, we have designed, manufactured and tested various pixel test structures and a 512×512 pixel sensor for satellite star trackers. We have also designed a $4K \times 3K$ pixel sensor for future solar physics missions, and a $4K$ pixel linear sensor for push-broom Earth observation cameras. We are also collaborating with E2V to develop CMOS thinning technology to allow backside illumination.

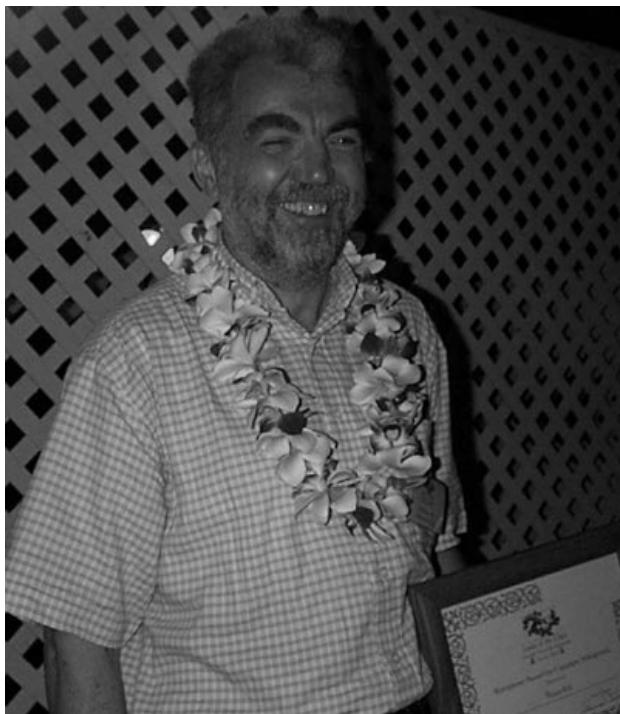
7. ACKNOWLEDGEMENTS

Our work has been funded from various sources including the UK's Particle Physics and Astronomy Research Council, Natural Environment Research Council, the Rutherford Appleton Laboratory of the Central Laboratory of the Research Councils, and the British National Space Centre (BNSC). A. Fant is acknowledged for his help with the detailed design and simulation of the amplifier circuitry. R. Holt, R. Bell (E2V), and H. Mapson-Menard (University of Birmingham) are acknowledged for the test work. Peter Pool and D. Burt (E2V) are thanked for their help, many fruitful discussions, and progress towards the realisation of thinned, back-illuminated sensors.

8. REFERENCES

- [1] Fossum, E.R., 1993, *Active Pixel Sensors - Are CCDs Dinosaurs?*, Proc. SPIE, Vol. **1900**.
- [2] Mendis, S., Kemeny, S.E., Gee, R., Pain, B., Kim, Q. and Fossum, E.R., 1994, *Progress in CMOS active pixel sensors*, Proc. SPIE Vol. **2172**.
- [3] Fossum, E.R., 1994, *Assessment of Image Sensor Technology for future NASA Missions*, Proc. SPIE Vol. **2172**.
- [4] Ricquier, N. and Dierickx, B., 1995, *Active Pixel CMOS image sensor with on-chip non-uniformity correction*, IEEE Workshop on Charge-Coupled Devices and Advanced Image Sensors.
- [5] Fossum, E.R., 1997, *CMOS Image Sensors: Electronic Camera-On-A-Chip*, IEEE Transactions on Electron Devices, **44**, p. 10.

- [6] Saint-Pé, O., Davancens, R., Tulet, M., Magnan, P., Cavadore, C., Gautrand, A., Degerli, Y., Lavernhe, F. and Farré, J., 1998, *Development and characterisation of Active Pixel Sensors for Space Applications*, Proc. SPIE Vol. **3440**.
- [7] Hopkinson, G.R., 1992, *Radiation effects on CCD's for spaceborne acquisition and tracking applications*, RADECS 91, Proc. IEEE.
- [8] Hopkinson, G.R., 1992, *Cobalt60 and proton radiation effects on large format, 2-D, CCD arrays for an earth imaging application*, IEEE Transactions on Nuclear Science, **39**, p. 6.
- [9] Hopkinson, G.R., Dale, C.J. and Marshall, P.W., 1996, *Proton Effects in Charge-Coupled Devices*, IEEE Transactions on Nuclear Science, **43**, p. 2.
- [10] Dierickx, B., Meynants, G. and Scheffer, D., 1997, *Near 100% fill factor CMOS Active Pixels*, IEEE Workshop on Charge-Coupled Devices and Advanced Image Sensors.
- [11] Prydderch, M., French, M., Holt, R., Marshall, A., Turchetta, R., Waltham, N., Eyles, C., Mapson-Menard, H., Burt, D., Bell, R., and Pool, P., 2002, *A 512x512 CMOS Monolithic Active Pixel Sensor with Integrated ADCs for Space Science*, Nuclear Instruments and Methods in Physics Research - Section A, in press.
- [12] Solar Orbiter - *A High Resolution Mission to the Sun and Heliosphere*, Assessment Study Report, 2000, ESA SCI (2000)6.
- [13] Morrissey, Q., Waltham, N., Turchetta, R., French, M., Bagnall, D., and Al-Hashimi, B., 2002, *Design of a 3 μm pixel linear CMOS sensor for Earth Observation*, Nuclear Instruments and Methods in Physics Research - Section A, in press.



*Klaus Reif was awarded the “Robespierre” award for his shutter project.
(See pages 367 and 378.)*

SECTION II:

OBSERVATORY STATUS/PLANS

ESO'S OPTICAL DETECTOR SYSTEMS IN THE VLT OPERATIONS ERA

Dietrich Baade

European Southern Observatory

Abstract: *A brief overview of the detector systems finished by ESO's Optical Detector Team (ODT) since 2000 is followed by a preview of forthcoming deliveries. Emerging trends are analyzed, and resulting actions and strategies are described.*

Key words: *Charge-Coupled Devices (CCDs), CCD controllers, detector systems*

1. INTRODUCTION

The pre-2000 development work for and status quo of the CCD systems in use at ESO's La Silla and Paranal observatories were described by Beletic in 2000 [1]. The most important achievements were the design of the FIERA controller (Beletic, Gerdes, and DuVarney in 1998 [2]), the PULPO house-keeping unit (Haddad and Sinclair in 1998 [3]), and the associated control software and their establishment as ESO's standard CCD control environment. By the year 2000, more than a dozen such systems had been deployed and were operating in Chile. Since then, six more systems have been completed. After a few decades of total system operating time it can now be safely said that, following the elimination of some initial dewar cleanliness problems, the reliability is excellent with downtimes of 0.5% or less. In fact, this performance poses a new kind of a challenge: the limited hands-on experience of the operations staff with trouble shooting is becoming a concern.

The six new systems and the three currently in preparation are briefly described in Sec. 2. On average, they are more complex and/or ambitious

than the earlier ones, and the VLT instrumentation plan has been expanded following a call for proposals for 2nd generation instruments. The associated trends are analyzed in Sec. 3; and Sec. 4 describes how ESO's Optical Detector Team (ODT) is responding to these and other challenges.

The corresponding summary of ESO's work on IR detectors is provided by Finger in 2002 [4].

2. RECENTLY DELIVERED AND FORTHCOMING CCD SYSTEMS

The available space permits each system to be described only briefly. The ODT Web site (www.eso.org/projects/odt) provides more in depth information or will soon do so.

2.1 Upgrades of FORS2 and EMMI (red arm)

FORS2 and EMMI are multi-mode, focal-reducer instruments at the VLT and the New Technology Telescope, respectively. They were initially equipped with one Tektronix TK2048 chip each with 2K32K 24 μm pixels. In 2001 (FORS2) and 2002 (EMMI) these detectors were replaced with 231 mosaics of 2K34K MIT/LL CCID-20 high-resistivity devices with 15 μm pixels. This increased the sky coverage by 50%. However, the improved red sensitivity was at least as strong a driver (see also [5]).

2.2 Optical wavefront sensor for NAOS/CONICA

The near-IR multimode instrument CONICA receives the telescope beam via the adaptive optics system NAOS, which features both an optical and an IR wavefront sensor. The former is described in detail by Feautrier et al. [6], and is based on a Marconi CCD-55 detector. Other ODT work on wavefront sensor systems is presented by Dorn [7] and Dorn et al. [8].

2.3 Giraffe

The high and medium resolution spectrograph Giraffe is a joint French/Suisse/ESO project. It can receive light through up to 130 fibers, which the FLAMES positioner can place anywhere in the 30' field of view of the VLT (using 8 more fibers FLAMES can simultaneously feed the UVES echelle spectrograph as well). The Giraffe detector system is built around one Marconi CCD44-82 chip (2K34K, 15 μm pixels; for ODT test results for this type of device see [5]).

2.4 VIMOS

Built by a French/Italian consortium, this multi-object spectrograph amplifies the data-taking power of the VLT even more massively than Giraffe by supporting the collection of up to 750 spectra simultaneously, depending on spectral resolution. The field of view of about $22'$ diagonal is divided into 4 quadrants and optical trains, each of which is equipped with a separate detector head mounting one Marconi CCD44-82 device. Two FIERA units control 2 detectors each.

2.5 HARPS

Late in 2002, the High-Accuracy Radial Velocity Planetary Search (HARPS) project will start its hunt for extra-solar planetary systems. This project is being realized by a Suisse/French/ESO collaboration. The detector system supplied by the ODT is comprised of a 231 mosaic of 2K34K chips with $15\text{ }\mu\text{m}$ pixels (Marconi CCD44-82).

2.6 MAD

The Multi-conjugate Adaptive optics Demonstrator (MAD) will test enabling technology for ELTs and the OWL 100-m telescope in particular. It is based on Marconi CCD-50 split frame-transfer devices with 1283128 light-sensitive pixels, but only one quadrant each will be used. Up to 3 separate detector heads (out of a total of 5) need to be operated at frame rates up to several 100 Hz and with various synchronization patterns. A big challenge lies also in the combination of the specified low read noise and the requirements with regard to weight, space, and position ability, which excludes LN2 cooling. Since delivery for system integration is foreseen for the end of Q1/2003, maximum use will be made of proven solutions adopted for the wavefront sensor of NAOS/CONICA. For a more comprehensive description see [9].

2.7 OmegaCAM

In collaboration with the Osservatorio Astronomico di Capodimonte, ESO will erect the 2.6-m VLT Survey Telescope (VST) at the Paranal Observatory. The only instrument of the VST will be the UV-optimized wide-angle imager OmegaCAM, which is a joint German/Dutch/Italian/ESO enterprise. An 834 mosaic of 2K34K Marconi CCD44-82 devices will fill the field of view (1.4° diagonal). Under the control of 2 FIERAs in a master/slave configuration, the total overhead per exposure will be 45 sec (using one port per chip). A third FIERA will control 4 auxiliary CCDs of the same type, of which 2 will be employed for autoguiding and the other 2

for curvature wavefront sensing to enable the closed loop operation of the telescope's active optics system.

2.8 MUSE

The Multi-Unit Spectroscopic Explorer (MUSE) was proposed by a multi-national consortium as a VLT 2nd generation instrument and recently selected for a Phase A study. It focuses on objects at redshifts, where their area density is so large that selective observations by means of positionable slits or fibers become very inefficient in sampling the required information. Therefore, the objective of MUSE is the complete stock taking over areas of $1' \times 3 \ 1'$. Adaptive optics will enable a spatial sampling of $0.2''$ so that every observation will result in 90,000 spectra. The current optical design foresees splitting the field into 24 beams, each of which would feature its own detector head with a 2K34K CCD. The detectors will need to have a red-optimized sensitivity to match the scientific high z requirement.

3. TRENDS

There are strong tendencies toward:

- Fully paving the focal plane with silicon.
- Ever more complex instruments with larger and larger wavelength coverage.
- Sensing very weak and rapidly variable optical signals in (closed) control loops.

FIERA has coped remarkably well with these challenges, which at the time of its conceptual design did not figure nearly as prominently as they do now. However, concern results from the weight, volume, and cooling requirements, which reach uncomfortable dimensions in systems with many channels. The priceless advantage of being able to implement and operate all optical detector systems of ESO's observatories in one and only one environment (including a standard dewar) was, therefore, not abandoned. Continuous investments have been, and also in the future will be, necessary to maintain the full power of this approach, which is integral part of the very successful VLT standardization strategy at large.

There is undoubtedly a need to further reduce all possible non-photon noise sources, especially for adaptive optics, scanning, and high-resolution spectroscopy applications. However, there appears to be another, speculative dimension, which, if unfolded, would bear much bigger promise for astronomy at large: detectors with intrinsic wavelength resolution. A picture, that is, *e.g.*, sometimes used in connection with adaptive optics, is the following: suppose that a photon was emitted billions and billions of years

ago, traveled over billions and billions of parsecs, hits M1, but bounces off M2 – just missing the slit. In imaging instruments, things are actually much worse. Chances are uncomfortably large that a filter discriminates against the impinging photon on account of its color although the detector could register it. This does not really appear scientifically or technically correct.

4. ACTIONS AND INITIATIVES

ESO's and the ODT's perception of the requirements to be met in the next couple of years have led to a number of activities, which are briefly enumerated in the following. For many of them, more comprehensive information is accessible from the ODT Web pages (www.eso.org/projects/odt).

Part of the FIERA concept is an LCU, which receives and orders the data during readout. The initially utilized SPARC20 computer is no longer manufactured and will be replaced by an UltraSPARC, which requires an upgrade to a PCI bus (cf. Reyes Moreno et al. [10]). Studies to eventually move to a Linux box are underway.

The 36 CCDs of OmegaCAM require more temperature sensors and heaters than a current single PULPO can handle. PULPO is therefore being upgraded and will incorporate a small PC running Linux (see [10]). The software will be ported to C.

OmegaCAM (and the contractual agreement with the supplier of the CCDs, which foresees that all 40+ devices are tested by ESO) was also the main driver for a comprehensive streamlining of both the control and the data reduction software of the ODT test bench [11]. This now supports the largely unsupervised acquisition and analysis of comprehensive data sets (cf. Christen et al. [12]). Discussions are ongoing about the benefits of converting the test bench to a fully VLT-like instrument, possibly with a VLT-like pipeline.

Following some unexpected problems, rigorous cleanliness standards were introduced for the CCD dewars, and numerous materials were studied for their suitability under vacuum and cryogenic conditions (cf. Deiries et al. [13]). Especially with the large OmegaCAM mosaic in mind, a class 100 clean room was furnished.

The VLT Control Software (VCS) at large has reached a level of robustness and stability that permitted the length of release cycles to be increased from half a year to one year. This frees capacities for development work and reducing the maintenance load on the operations staff. The FIERA software is integral part of the VCS and therefore followed this lead.

ESO just recently placed a contract for the production of 2nd generation technical CCDs. Part of the responsibility for these systems now rests with

the ODT, which thereby acquired a welcome direct contact with industrial systems.

In order to actively participate in the collection of experience with LLL CCDs, ESO and the Observatoire de Marseille have engaged in a joint evaluation project of a Marconi CCD65 device. First results are reported by Gach et al. [14].

The usage of liquid nitrogen poses a permanent safety hazard to personnel and equipment (although careful safety standards have so far permitted any serious incident to be avoided at ESO) and requires significant operations and/or maintenance efforts. As a potential alternative, a Cryotiger™ system will be tested.

As part of its strategic planning to be prepared for all future challenges, also with a view toward OWL readiness, ESO will conduct a study of the specific benefits that could be expected from a generic, wavelength-independent detector control and data acquisition environment. It will enable the ESO management to decide whether to go ahead with such a project and, if yes, to establish cutting edge, yet realistic requirements.

5. ACKNOWLEDGEMENTS

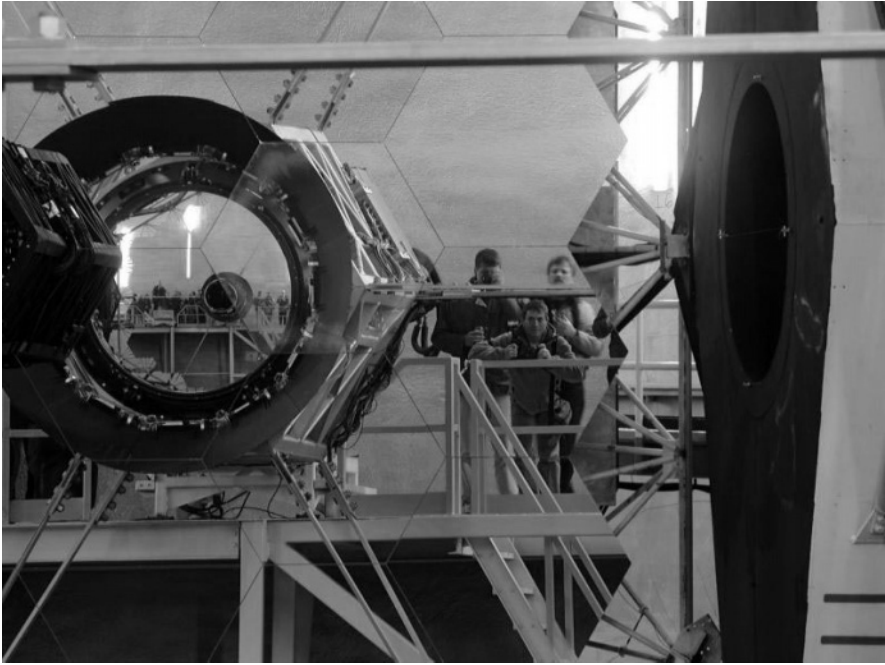
The author acknowledges that he has written the above paper. However, the actual work mentioned therein was performed by Andrea Balestra, Cyril Cavadore, Fabrice Christen, Claudio Cumani, Stéphane Darbon, Sebastian Deiries, Sandro D'Odorico, Reinhold Dorn, Christophe Dupuy, Jane Eskdale, Boris Gaillard, Christoph Geimer, Rolf Gerdes, Nicolas Haddad, Guy Hess, Joachim Hess, Evi Hummel, Olaf Iwert, Jean Louis Lizon, Robert Niemeczek, Gustavo Rahmer, Roland Reiss, Javier Reyes, Armin Silber, Peter Sinclaire, and others. Many of them also provided helpful comments on the manuscript.

The ESO participants in the SDW2002 workshop are grateful for the firework of Hawaiian hospitality and would be ready to host another workshop in the series; in any event: *Auf Wiedersehen!*

6. REFERENCES

- [1] Beletic, J.W., 2000, *Mission accomplished – ESO's optical detector systems come of age*, Optical Detectors for Astronomy II, eds. P. Amico and J.W. Beletic, Astrophys. Space Sciences Lib., vol. **252**, Kluwer, Dordrecht, p. 15.
- [2] Beletic, J.W., Gerdes, R., DuVarney, R.C., 1998, *FIERA: ESO's New Generation CCD Controller*, Optical Detectors for Astronomy, eds. J.W. Beletic and P. Amico, Astrophys. Space Sciences Lib., vol. **228**, Kluwer, Dordrecht, p. 103.

- [3] Haddad, N., Sinclair, P., 1998, *PULPO: Temperature, Vacuum, Shutter, LN₂ Level, All in One Box*, *Optical Detectors for Astronomy*, eds. J.W. Beletic and P. Amico, Astrophys. Space Sciences Lib., vol. **228**, Kluwer, Dordrecht, p. 131.
- [4] Finger, G., 2002, *Readout Techniques for Drift and Low Frequency Noise Rejection in Infrared Arrays*, these proceedings, pg. 435
- [5] Cavadore, C., Dorn, R.J., 2000, *Charge coupled devices at ESO – Performances and results*, in *Optical Detectors for Astronomy II*, eds. P. Amico and J.W. Beletic, Astrophys. Space Sciences Lib., vol. **252**, Kluwer, Dordrecht, p. 25.
- [6] Feautrier, Ph., Dorn, R.J., Rousset, G., Cavadore, C., Cumani, C., Hubin, N., 2002, *Performance and results of the NAOS visible wavefront sensor*, these proceedings, pg. 325
- [7] Dorn, R.J., 2001, PhD thesis, Ruprecht-Karls-Universität, Heidelberg.
- [8] Dorn, R.J., Burke, B.E., Beletic, J.W., 2002, *A CCD-Based Curvature Wavefront Sensor for Adaptive Optics in Astronomy*, these proceedings, pg. 319
- [9] Cavadore, C., Cumani, C., Marchetti, E., Franza, F., 2002, *CCD Wavefront Sensing System for the ESO Multi-Conjugate Adaptive Optics Demonstrator (MAD)*, these proceedings, pg. 283
- [10] Reyes-Moreno, J., Balestra, A., Geimer, C., Haddad, N., 2002, *Upgrade of ESO's FIERA CCD Controller and PULPO Subsystem*, these proceedings, pg. 449
- [11] Amico, P., Böhm, T., 1998, *ESO's New CCD Testbench*, *Optical Detectors for Astronomy*, eds. J.W. Beletic and P. Amico, Astrophys. Space Sciences Lib., vol. **228**, Kluwer, Dordrecht, p. 95.
- [12] Christen, F., Cavadore, C., Baade, D., Iwert, O., Kuijken, K., Gaillard, B., Darbon, S., 2002, *Characterizing the CCDs of the OmegaCam wide-angle camera*, these proceedings, pg. 485
- [13] Deiries, S., Iwert, O., Cavadore, C., Geimer, C., Hummel, E., 2002, *Ultra-clean CCD cryostats*, these proceedings, pg. 305
- [14] Gach, J.L., Guillaume, C., Cavadore, C., Boissin, O., 2002, *First Results of an L3CCD in Photon Counting Mode*, these proceedings, pg. 611



*Nothing like a 10-meter mirror to check for food stuck in your teeth.
(Courtesy P. Sinclair)*



*Nerds Conch-ert
From left to right: J. Beletic, C. Cavadore, J. Janesick, A. Janesick, ½ Fred Harris.*

THE DETECTOR SYSTEMS OF THE KECK OBSERVATORY: UV TO 25 MICRONS

Status, Plans and Dreams

James W. Beletic, Paola Amico, Randall Campbell, Robert Goodrich
W.M. Keck Observatory, Mauna Kea, Hawaii USA

Abstract: *We provide an overview of the Keck Observatory, its instrumentation, detector systems, and plans for new instruments and detector upgrades. Even though the Keck instrumentation is older than that of the new 8 meter telescopes, in several cases the Keck detector systems are leaders in their class. However, in winning the race for the first very large telescope, the Keck Observatory has paid a price in terms of performance, lack of standardization and difficulty in maintenance. We discuss these challenges and our plans and dreams for ensuring that the Keck Observatory has the detector systems needed to stay at the forefront of astronomy.*

Key words: *optical detectors, infrared detectors, Keck Observatory, instrumentation plan, E-Bay.*

1. INTRODUCTION

The W.M. Keck Observatory (WMKO) has been a world leader in astronomy for a decade. Since first light of the Keck I telescope in 1992, and first light on Keck II in 1996, WMKO has paved the way in spectroscopy and high resolution imaging, fostering some of the most significant advancements in astronomy, such as observational cosmology and extra-solar planet hunting. Part of the leadership has been due to being first and having at least 6 years head start in operations. Other telescopes in the 8-10 meter class have only recently come on-line: VLT (1998), Subaru and Gemini (1999). Now, Keck has to work much harder to keep an edge over its many exceptional “competitors”, which profit from newer technologies and richer budgets.

In this article we provide an overview of the Keck instruments and detector systems, two key aspects in the life of any observatory, and our plans and dreams for improving these systems so that the Keck Observatory remains at the forefront of astronomy.

2. THE KECK OBSERVATORY

The Keck Observatory is operated by a non profit entity entitled CARA, the California Association for Research in Astronomy. Founded by the University of California and the California Institute of Technology in 1985, CARA added a minor partner in 1996 when NASA joined to help fund the expansion of the Observatory for interferometry. The W.M. Keck Foundation has graciously supported the development of the Keck Observatory with donations totaling \$117 million, and thus the Observatory bears the "Keck" moniker. The Keck Observatory primarily serves the California astronomical community, arguably one of the strongest in the world, but it is also used by a much broader clientele. NASA receives one-sixth of the observing time, and the University of Hawaii receives observing time due to its stewardship of Mauna Kea. In addition, the U.S. national community has access to the Keck Observatory through the Telescope System Instrumentation Program (TSIP) which is funded by the National Science Foundation. TSIP presently has access to 24 Keck nights per year (12 per telescope).

The Observatory consists of two 10-meter telescopes. Actually each mirror is hexagonal in shape with the shortest dimension across the aperture being 9 meters, and the longest dimension equal to 11 meters: 10 meters is the effective light collecting diameter. The primary mirrors are composed of 36 hexagon "segments", each 1.8 m in diameter, as shown in Fig. 1. There are multiple secondary mirrors available: f/15 and f/25 for both telescopes, and an f/40 for Keck II. The f/15 is an aluminized secondary, while the f/25 and f/40 modules are gold-coated chopping secondaries designed for use with infrared detectors. The telescopes are azimuth-elevation design with four main locations for instruments: two Nasmyth foci, a Cassegrain focus and a forward Cassegrain focus. In addition, there are four "bent Cassegrain" foci on each telescope, located on the elevation ring, which can hold small instruments.

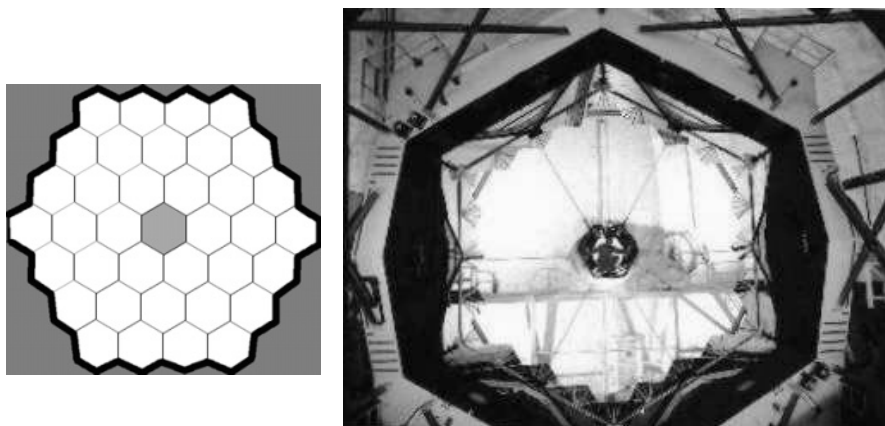


Figure 1. The segmented Keck Primary mirror. Schematic (left) and photo. In the photo, a technician is visible inside the Cassegrain tube.

Figure 2 shows a schematic diagram of the telescope and a photograph of the image of the Moon at Nasmyth focus. With a plate scale of 0.727 mm per arc sec, the 20 arcmin corrected field of view of the f/15 focus is 0.87 meters wide (just a shade under 3 feet).

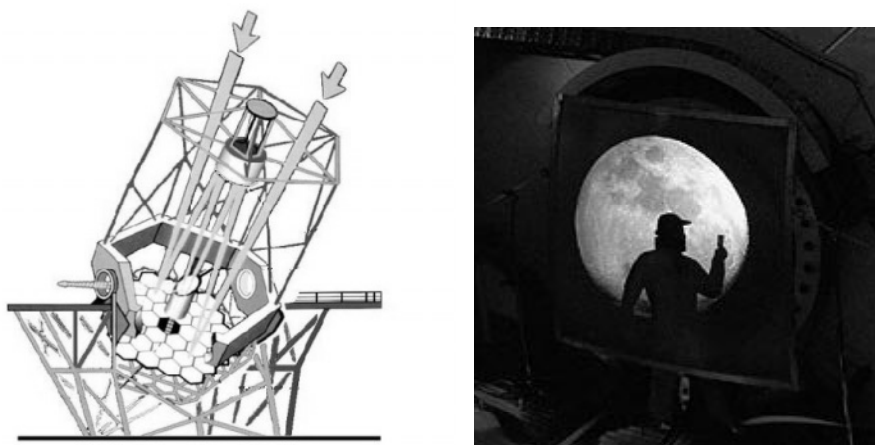


Figure 2. Schematic diagram of a 10-meter Keck telescope and the image of the Moon at Nasmyth focus. Each telescope weighs 300 tons. The Nasmyth foci are named “left” and “right” from the point of view of a person located at the center of the primary mirror, facing the sky.

3. THE INSTRUMENTS OF THE KECK OBSERVATORY

The Keck Observatory Science Steering Committee (SSC) guides the development of instrumentation at the Observatory. The SSC has espoused the philosophy that the Observatory should provide a broad range of instrumentation so that all astronomers have the facilities needed for their science. Thus, all wavelengths accessible from the ground in the optical / infrared regime are observed, from 310 nm in the ultraviolet to 25 μ m in the infrared. The Keck Observatory is presently the only large telescope facility that serves this large bandpass. The instrumentation of the Keck Observatory, in Table 1, shows the breadth of interests of the Keck astronomical community [2 and references therein].

Table 1. Single aperture instruments of the Keck Observatory.

		Instrument	Location	Ops Start Date	Wavelength (microns)	Image FOV (arc min)	Spectral Resolution	Nights per year
Keck I	Present	NIRC	} Forward Cass	1994	1 - 5	0.63 \times 0.63	100	40
		LWS		1999	3 - 25	0.17 \times 0.17	100 & 1400	30
		LRIS	Cassegrain	1994	0.3 - 1	6 \times 8	300 - 5000	160
		HIRES	Right Nas.	1994	0.3 - 1	N.A.	39,000-67,000	100
	Future	NIRES	Bent. Cass.	2005	1 - 2.5	0.67 \times 0.67	2500	100
Keck II	Present	ESI	Cassegrain	1999	0.39- 1	2 \times 8	1000-6000 & 20,000	100
		NIRSPEC	Right Nas.	1999	1 - 5	0.77 \times 0.77	2000 & 25,000	100
		NIRC2	Left Nas. (AO)	2001	1 - 5	0.67 \times 0.67	500-9000	30
		DEIMOS	Right Nas.	2002	0.39 - 1	5 \times 17	6000	100
	Future	OSIRIS	Left Nas. (AO)	2004	1 - 2.5	0.11 \times 0.11	4000	100
		KIRMOS	Right Nas.	2008	1 - 2.5	11 \times 11	5000	100

The Keck Observatory has also taken an aggressive approach in Adaptive Optics (AO), dedicating the left Nasmyth platform on each telescope to a high order Shack-Hartmann AO system. The AO systems, which have 20 subapertures across the 11-meter maximum diameter of the pupil, have been designed with laser guide star AO in mind, and thus their faint magnitude limit on natural stars is 14th magnitude. The Keck II AO system is used

with three of the science instruments (NIRC2, NIRSPEC and OSIRIS). The Keck I & II AO systems are used for the interferometer that combines light from both Keck telescopes. The combination of AO at two Nasmyth foci and a large instrumentation suite has resulted in the Keck Observatory having more instruments than it has foci, so several of the instruments are exchanged at some of the foci. The flexibility of instrument exchanges has added capability, but also has led to increased maintenance costs, and a higher incidence of instrument failure. The wavelength-spectral resolution plot of Keck instrumentation is shown in Fig. 3. Future instruments that are in development are shown in the figure as dashed lines.

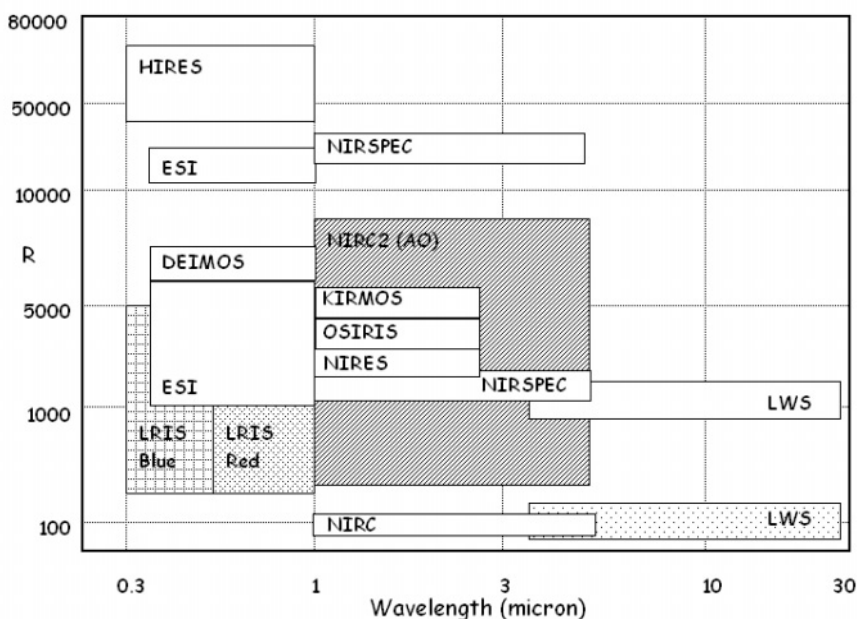


Figure 3. Wavelength - spectral resolution diagram for Keck instruments

The emphasis of Keck instrumentation has been on spectroscopy and not imaging. Even those instruments that have an imaging capability find most of their time dedicated to spectroscopy. Keck is not a place that produces a lot of pretty images to hang on the wall. (*Drive 500 meters down the road to CFHT to get pretty posters and calendars! Ask for Jean-Charles.*) However, when images are made, they are usually made with resolution that used to be sole purview of space missions. The Keck Observatory AO systems are now routinely producing 4 times higher resolution than the Hubble Space Telescope in the near infrared (J, H and K bands), sometimes with Strehl in excess of 60% (at L band) (see Fig. 4).

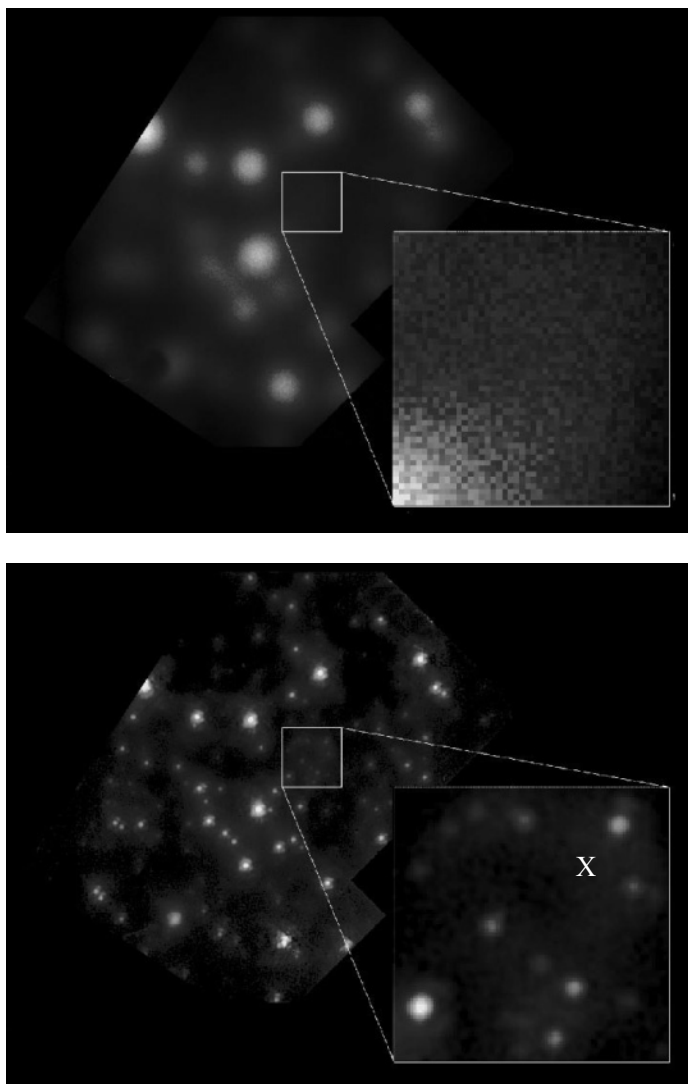


Figure. 4. Image of the galactic center, with adaptive optics off and on taken at $2.5\ \mu\text{m}$ with guidestar $30''$ away. Images such as these have been used to follow the motion of stars over a 7-year period to determine the location and mass of the black hole in the center of the galaxy. The black hole, marked with an X symbol, has a mass of 3 millions suns [1].

The Keck Observatory is also pushing the technology of interferometry, achieving "first fringes" with the two Keck telescopes on March 12, 2001. The interferometer is funded by the NASA Origins theme, which is concentrated on finding the conditions that would support the development of life. (*Other Origins programs are the Space Interferometer Mission, SIM, and the Terrestrial Planet Finder, TPF.*) The Keck interferometer is now being used for "visibility science" (at H and K bands), and will expand in 2004 to include the capabilities of nulling and differential phase.

4. THE DETECTORS OF THE KECK OBSERVATORY

The scientific detectors that are used in the single aperture (noninterferometry) instruments are shown in Table 2.

Table 2. Scientific detectors of the Keck Observatory

Instrument	Detector			Instrument type
	Wavelength (micron)	Format	Manufacturer	
LRIS - blue arm - red arm	0.3 - 0.6	two 2k x 4k	Marconi	Imager / Spectrograph
	0.39 - 1	2k x 2k	Tektronix	
HIRES	0.3 - 1	2k x 2k	Tektronix	Spectrograph
ESI	0.39 - 1	2k x 4k	MIT/LL	Imager / Spectrograph
DEIMOS	0.39 - 1.1	eight 2k x 4k	MIT/LL	Imager / Spectrograph
NIRC	1.0 - 5.0	256 x 256	Hughes / SBRC	Imager / Spectrograph
NIRC2 (AO)	1.0 - 5.0	1k x 1k	SBRC	Imager / Spectrograph
NIRSPEC (AO)	1.0 - 5.0	1k x 1k	SBRC	Imager / Spectrograph
OSIRIS (AO)	1 - 2.5	2k x 2k	Rockwell	IFU Spectrograph
NIRES	1 - 2.5	1k x 2k	Rockwell	Imager / Spectrograph
KIRMOS	1 - 2.5	4k x 4k	Rockwell or Boeing	Imager / Spectrograph
LWS	3. - 25	128 x 128	Boeing	Imager / Spectrograph

The range of quality does not befit a leading astronomical observatory. The two most striking deficiencies are the 1980's vintage Tektronix devices in the red arm of LRIS and in HIRES. Especially disconcerting is the "engineering grade" device that was "temporarily" installed in the red arm of HIRES. This device, which Tektronix branded with a pen spot at the center of the chip, has modest quantum efficiency (peak 70%) and poor readout noise (6.5 e⁻ at a 25 kHz pixel rate). In addition, the ancient readout electronics take 160 seconds to read out all pixels from one port (80 seconds out of 2 ports).

On the other hand, some of the detector systems at Keck are leaders in their class. The 8K×8K mosaic of eight MIT/LL 2K×4K CCDs on DEIMOS is the largest mosaic in any optical spectrograph in the world. These red-sensitive devices are one of the reasons that the DEEP2 [3] survey of the

distant universe will be the best map of cosmological structure yet made. DEEP2 is mapping galaxies with redshift 0.7 to 1.4, about half the age of the universe, at spectral resolving power of 5000, enough to measure both redshift and internal dynamics. The DEIMOS detector array takes spectra of up to 150 galaxies simultaneously down to magnitude 24 (m_R) in a 1-hour exposure. Figure 5 shows the excellent multiplexing capability of DEIMOS. This 1250×555 pixel image shows only 1% of the field of view of the detector mosaic! The spectra have been sky subtracted and wavelength aligned for about 8 slits of the DEIMOS mask (which had 100 slits in this case). Blue is on the left and red to the right. The center of the image shows a gravitationally bound group of 4 galaxies at redshift of 1.02. The 4 galaxies in the middle, plus the two others at slightly lower redshift, show the resolved pair of closely spaced emission lines due to singly-ionized oxygen [OII], the so-called “forbidden transition” lines at rest wavelengths 3726 and 3729 Å. Resolving these closely-spaced lines testifies to the quality of the instrument and detectors.

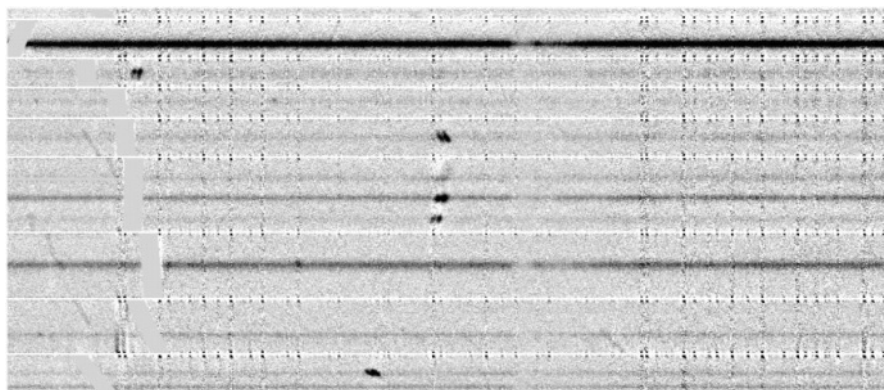


Figure 5. This negative image (dark is higher intensity) shows a 1250×555 pixel portion of the 8K×8K focal plane of DEIMOS, demonstrating the multiplexing capability of the largest focal plane in any optical spectrograph. Up to 150 galaxies are measured at one time. (See text above for details about this image.)

In the area of infrared detectors, the Keck Observatory has been the world leader in the use of InSb detectors sensitive to 1-5 microns. There are two Aladdin 1K×1K devices presently in use at the Observatory: NIRSPEC and NIRC2. At longer wavelengths, the Keck Observatory has been the only large telescope with 5-25 micron capability, although the LWS instrument and its Boeing 128×128 pixel detector are aging.

Lastly, the Keck Observatory has recently received delivery of three MIT/LL 2K×4K CCDs that set an entirely new standard for high quantum

efficiency in an optical spectrograph. The detectors, whose QE is shown in Fig. 6, are all thick (45 micron), high resistivity CCID-20 design. The two blue optimized CCDs have the Lesser backside process and single layer hafnium oxide AR coating optimized for peak QE at 320 nm. The red optimized device is from a boron implant laser anneal process with a two-layer AR coating (hafnium oxide over silicon dioxide). These CCDs will be used to upgrade the HIRES spectrograph in January 2004. This detector upgrade will make HIRES, once again, the most efficient high resolution spectrograph on the planet.

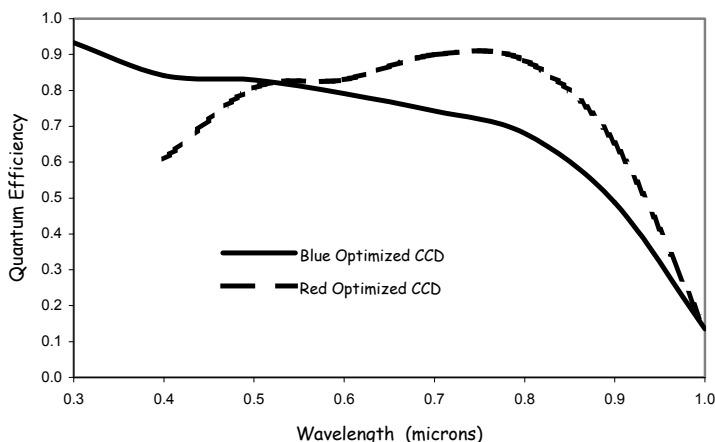


Figure 6. The QE curves for the CCDs that will be used in the HIRES upgrade.

5. THE PRICE OF RUNNING FAST TO BE FIRST

In the 1970's and early 1980s, a big debate was active in the astronomical community: what was the best way to build the next generation of 8-10 meter telescopes? Would it be possible to manufacture a piece of glass 8 meters wide with the required precision? Or is it better to make a set of smaller segments and phase them to operate as one large piece of glass? The answer, as we all know, is that both approaches have worked. However, the segmented mirror approach of the Keck Observatory won the race by 5 to 7 years, and the Keck community has greatly benefited from the opportunity to "skim the cream" in many areas of astronomical research.

However, during the construction of the Keck Observatory, time was critical and many systems were put together in the quickest way possible in order to win the race and to "own" the large telescope arena for as long as

possible. The detector systems are especially symptomatic of the problems that result from this "build it fast at all cost" approach.

The first casualty was system standardization. For nearly every instrument, it has always been easier to take an "off the shelf" solution to detector electronics instead of developing the infrastructure of a common standardized system. Thus, the Keck Observatory now struggles to maintain at least 17 different versions of detector controllers, including transputers, all generations of Leach, custom infrared array electronics from Berkeley Camera Engineering (BCE) and even some of the original Photometrics designs. The result is that most systems do not have adequate spares, many are "black boxes" to the Observatory staff, the systems are not optimized or even completely characterized, and significant detector problems can persist for a long time without being noticed. With obsolete systems and inadequate spares, we have even taken to buying guider electronics off E-Bay. (*We would feel even worse, were it not for NASA doing the same for some of its ground systems that support the Space Shuttle.*)

Also, with a 10-m telescope in a world of 4-m competition, the Keck Observatory did not need to strive for the highest performance level; one example is duty cycle, i.e., fast readout. There has been no premium on readout time, and the LRIS and HIRES systems take 80 to 160 sec to read out. Even the relatively modern DEIMOS detector system requires 39 sec to read out, a specification that was acceptable because in comparison with LRIS and HIRES, reading out 16 times as many pixels in half the time seemed like a big step. However, an opportunity was missed since the DEIMOS detectors are capable of being read out in 5 seconds with noise performance that is adequate for slitmask alignment and many calibrations. Thus, the Keck Observatory now has the following challenges:

- No standardized detector electronics
- Slow and inflexible readout electronics
- Lack of spares and minimal knowledge by Observatory staff
- Some detectors that are 1980 vintage

We recognize these challenges and have some plans, and many dreams to remedy the situation.

6. PLANS FOR THE FUTURE

The first detectors that the Keck Observatory must upgrade are the ancient ones in HIRES and the red arm of LRIS. Fortunately, the HIRES detector upgrade is underway and will be installed in January 2004. The new CCDs will bring several improvements to the HIRES instrument, including:

- Higher spectral resolution (due to reduced electron diffusion),
- Better spectral sampling (by virtue of the smaller pixel size),
- Superior charge-transfer efficiency,
- Flatter focal plane,
- Larger detector area,
- Higher quantum efficiency,
- Lower readout noise.

No firm schedule yet exists for the LRIS red detector upgrade, which is expected to be a 4K×4K, 15 micron pixel CCD mosaic. The favored option, at present, is the very thick (200 μm) LBNL p-channel CCD, which would greatly reduce the fringing that plagues this flexure-prone instrument that rotates at Cassegrain focus.

Two new instruments are expected to arrive at Keck in the next two years:

- **OSIRIS**, an AO-optimized integral field spectrograph featuring a 2K×2K Rockwell HgCdTe device for 1-2.5 μm operation. This instrument will arrive in mid-2004 and will commence science observations in early 2005.
- **NIRES**, a low resolution Cassegrain spectrograph that will provide simultaneous J, H, K spectral coverage and will be an excellent instrument for follow-up of targets identified by SIRTf (Space Infrared Telescope Facility) that will be launched in August, 2003. NIRIS will use a 1K×2K portion of a Rockwell HAWAII-2 array, and is expected to arrive at the telescope in the first half of 2005.

Presently in the preliminary design phase is the most ambitious infrared spectrograph yet proposed by any observatory: KIRMOS, a multi-object spectrograph and imager which will use a mosaic of four 2K×2K HgCdTe detectors (Rockwell or Raytheon) and could arrive at the telescope in 2008.

In parallel, the Keck community has pulled together to attack the problem of non-standardized detector systems. Caltech, UCLA, UC Santa Cruz and Observatory staff have formed a consortium to develop the next generation detector electronics - a system we call ASTEROID (A System To Efficiently Read Optical / Infrared Detectors). Unfortunately, we do not have the resources to properly pursue this effort, so we are being as inventive as possible to achieve our goal. We have divided the electronics control system into two pieces: hardware and software. We are concentrating on the software aspect at this time, and are investigating the ArcView software developed at CTIO to see if it can serve the purpose of the software backbone. In the meantime, we will wait to see whether the MONSOON

project at NOAO or other efforts will provide the hardware that is required for running optical and infrared detectors.

7. DREAMS FOR THE FUTURE

Beyond the plans listed above, we have many dreams and are seeking resources to make them come true.

We wish to develop the ASTEROID system, both software and hardware, as quickly as possible.

The Observatory desperately needs for a new generation of guiders. Besides having relatively poor performance, the obsolete Photometrics guiders cannot be purchased anymore and are an increasing maintenance headache. When developing a new guider, we would like to incorporate a low-order wavefront sensing capability - a feature that is part of the VLT and Gemini designs, and should be incorporated into the Keck system as soon as possible.

We also need to develop a detector team at the Observatory, and strengthen the detector laboratories at the University of California and Caltech.

8. PRESENCE IN THE WORLD DETECTOR COMMUNITY

We hope to also provide a continued presence in the worldwide detector community. We offer to work with others to ensure a smooth functioning of the 2005 version of this detector workshop. During the intervening time, we will support the SPIE telescope conference being held in June, 2004 at Glasgow, Scotland - James Beletic is detector track chair and co-chair with James Garnett (of Rockwell) of the Optical & Infrared detector conference.

We also are leading an effort to develop the next generation AO wavefront sensor CCDs. We plan to work with others to decrease the noise level of optical wavefront sensor detectors in 3 ways:

- Develop lower noise amplifiers
- Put more amplifiers on the CCD, thus reducing readout rate and readout noise
- Develop novel-geometry detector architectures, to maximize the information content of each pixel and minimize pixel count

The last bullet is important, since we feel that custom-designed CCDs are the next generation of detector development that will make a significant impact on instrument design. We should no longer think of detectors as simply a contiguous array of square pixels. One should be able to design the

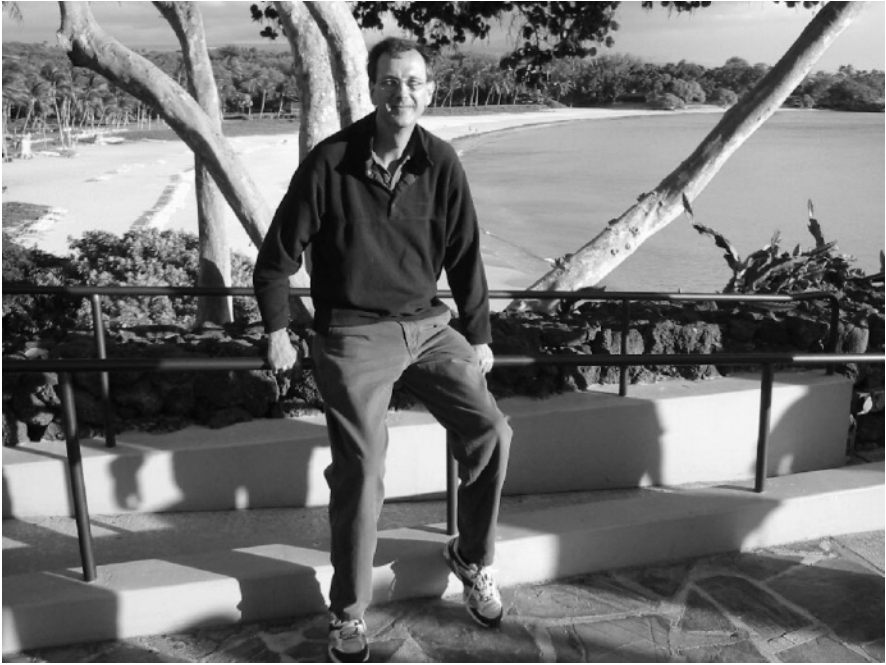
instrument and the detector pixel layout to optimize the use of a limited number of photons. These "designer detectors" will provide the best signal-to-noise ratio in photon-limited situations....which is most of astronomy!

9. REFERENCES

- [1] Ghez, A.M., Morris, M., Becklin, E.E., Tanner, A. & T. Kremenek, 2000, *The Accelerations of Stars Orbiting the Milky Way's Central Black Hole*, *Nature*, **407**, 349.
- [2] Ian S. McLean and David Sprayberry, 2003 *Instrumentation at the Keck Observatory*, Instrument Design and Performance for Optical/Infrared Ground-based Telescopes, Masanori Iye, Alan F. Moorwood Eds, Proceedings of SPIE Vol **4841**, pg.1
- [3] Marc Davis, Sandra Faber, Jeffrey Newman, Andrew Philips, Richard Ellis, et al., 2003, *Science Objectives and Early Results of the DEEP2 Redshift Survey* in "Discoveries and Research Prospects from 6- to 10-Meter-Class Telescopes II." Edited by Guhathakurta, Puragra. Proceedings of the SPIE, Volume **4834**, pg. 161



During Paniolo night, Mike Lesser and Fred Harris were amused by Gerry Luppino's reaction at discovering that there was going to be a compulsory line dancing lesson (see page 533)



*Moments before Greg Burley realizes that he has been superglued to the railing
(Courtesy G. Burley)*



The wonderful dancers from the Halau Hula Ka No'eau Halua enchanted the audience at the Mauna Kea Gala dinner. (Courtesy M. Downing)

IR DETECTOR DEVELOPMENTS AT ESO

Gert Finger, Reinhold J. Dorn, Hamid Mehrgan, Manfred Meyer, Alan F.M. Moorwood and Joerg Stegmeier
European Southern Observatory

Abstract: *New developments carried out for the next generation VLT instruments are discussed. Both HgCdTe and InSb large format arrays are used to cover the near infrared spectral region. A three-side buttable mosaic package for Aladdin InSb arrays will fill the focal plane of a high-resolution echelle spectrograph. Three instruments, a multi-object spectrograph, an integral field spectrograph and a test camera for multi-conjugate adaptive optics, will be equipped with HAWAII-II and HAWAII-II RG arrays. A fringe tracker of the VLT interferometer will use a PICNIC array which is optimized for use in an active control loop.*

Key words: infrared array, HgCdTe, noise, dark current, quantum efficiency

1. INTRODUCTION

Large format infrared arrays are now in routine operation at the 8-m VLT telescopes and have produced some spectacular results [1]. The advent of adaptive optics has improved the spatial resolution and now achieves almost diffraction limited images. The finer plate scales used with adaptive optics decrease the flux of thermal background photons and the associated photon shot noise. Hence, the readout noise of infrared arrays must be reduced to remain below the photon shot noise threshold. For wavefront sensors of adaptive optics systems and fringe trackers in interferometry, exposure times are less than 1 ms. The lowest readout noise has to be achieved at high speed. In order to sample a reasonable field with smaller plate scales, more pixels are required. Furthermore, the high spectral resolution of multi-object and integral field spectrographs as well as large survey telescopes are strong drivers for larger array formats. To fulfill all the requirements of 2nd

generation VLT infrared instruments, a large development effort needs to be made focal plane detector technology.

2. INSB 512×4086 MOSAIC

A 512×4086 pixel mosaic is under development to record simultaneously the maximum spectral range of a single order of the cryogenic echelle spectrograph CRIRES [2]. This instrument will provide a resolving power of 10^5 for wavelengths between 1 and 5 μm . As seen in Fig. 1, CRIRES has a curvature sensing adaptive optics system to minimize slit losses. The spectrograph has a prism pre-disperser for order sorting and thermal photon background suppression. The echelle grating provides the high-resolution spectra to be sampled by the detector mosaic in the useful optical field which extends 135 mm in the dispersion direction and 21 mm in the spatial direction at a plate scale of $0.1''/\text{pixel}$.

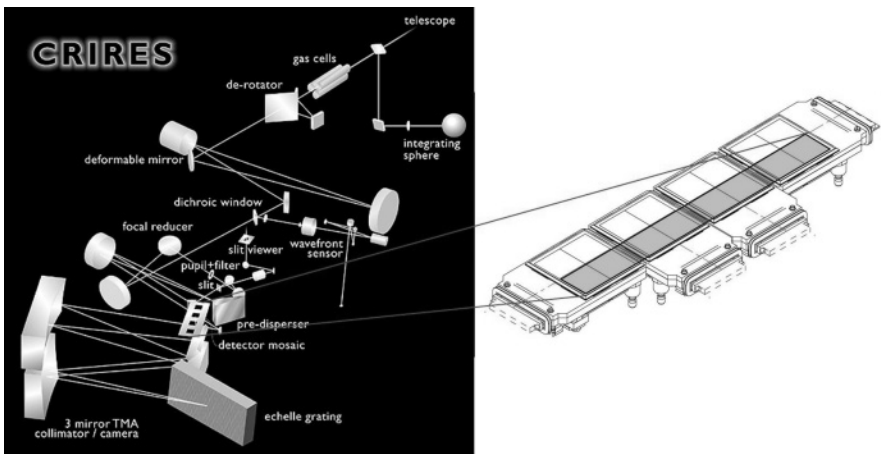


Figure 1. Optical layout of the cryogenic echelle spectrograph CRIRES and the 512×4086 pixels mosaic comprising four Aladdin 1K×1K InSb arrays.

A 3-side quasi-butttable ceramic package for Aladdin II and III arrays is being developed to minimize the spacing between arrays to < 283 pixels. Since only two quadrants of each array are used and the individual arrays have only two adjacent science grade quadrants, the arrays need to be mounted in different orientations. A short flexible manganin board interfaces each detector to a preamplifier board that is encapsulated in a light-tight box and also operates at cryogenic temperatures. More details are described elsewhere in these proceedings [3].

3. HGCDTE 2048×2048 ARRAYS

With the availability of large format IR arrays it is now possible to extend the multi-object spectrograph concept to the infrared. NIRMOS is an infrared instrument with capabilities of direct imaging, multi-object spectroscopy and integral field spectroscopy.

NIRMOS consists of four independent imaging spectrographs [4]. Each spectrograph has a resolution of $R \sim 2500$ and covers a field of $4 \times 6 \times 8$ arcmin². The four detector cryostats will be equipped with $2K \times 2K$ HAWAII-IIRG MBE arrays having a cut-off wavelength of $\lambda_c = 1.9 \mu\text{m}$ to cover the J and H bands. The four continuous-flow cryostats cool the detectors to a minimum temperature of 86 K and have cryogenic filter wheels including linear variable filters to reduce the thermal background for H band spectroscopy. The grism spectrographs are contained in an optical box which may be cooled to reduce the thermal flux in H band. The slit mask focal plane is at room temperature.

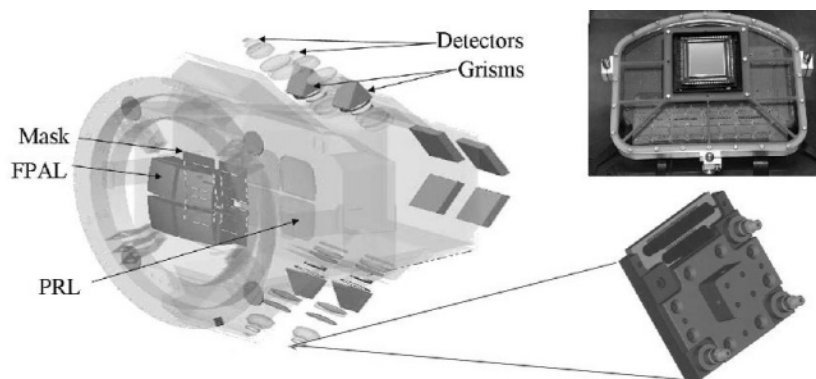


Figure 2. Layout of the NIRMOS multiobject spectrograph and HAWAII-II detector mount with 32 cryogenic amplifiers (*top*) and HAWAII-IIRG detector package (*bottom*).

The near-infrared ($1.0\text{--}2.5 \mu\text{m}$) integral field spectrograph SINFONI is based on an image-slicer and will be supported by adaptive optics [5]. The spectral resolution ranges from 1000 to 3000, and the 32×32 spatial pixels (of variable scales $250/100/25$ marcsec/pix) cover a field of view of either $8'' \times 8''$, $3'' \times 3''$ or $0.8'' \times 0.8''$ on the sky. Presently SINFONI is equipped with a Hawaii $1K \times 1K$ array but it will be upgraded to a HAWAII-IIRG array to allow Nyquist sampling of the spectra instead of spectral dithering required with the HAWAII $1K \times 1K$ array.

The HAWAII-IIRG arrays for both NIRMOS and SINFONI will be delivered in a 32 channel package without ASIC (Application Specific

Integrated Circuits). Because of schedule restraints, the ASIC will be implemented time.

To test the feasibility of multi-conjugate adaptive optics, which is a prerequisite for building the OWL 100-m telescope, an adaptive optics system known as MAD (Multi-conjugate Adaptive Optics) is under development. This has two deformable mirrors, one conjugated to the ground layer and one conjugated to the atmospheric layer at a height of 10 Km [6]. The goal is to demonstrate a Strehl ratio of $\sim 30\%$ over a field of $3'$ with 3 natural guide stars. The camera of MAD will be equipped with the HAWAII-II array which is discussed in more detail elsewhere in these proceedings [7].

4. SENSORS FOR ADAPTIVE OPTICS AND INTERFEROMETRY

At present the IR wavefront sensor of the Shack-Hartmann VLT adaptive optics system NAOS utilizes one quadrant of a HAWAII-I array [8]. The AO system delivers diffraction limited images for the science instrument CONICA, which is equipped with an Aladdin $1K \times 1K$ InSb array [9]. The Strehl ratio obtained in K is ~ 0.7 .

By combining light from two 8-m VLT telescopes, the commissioning instrument VINCI of the VLT interferometer obtained first fringes using one quadrant of a HAWAII-I array as well. A fringe tracker FINITO is being built to stabilize the fringes and allow long integrations with the science instruments [10]. If the beams of three telescopes are combined, this fringe tracker utilizes only seven pixels of the PICNIC 256×256 HgCdTe array, four pixels for the interferometric fiber outputs and three pixels for the photometric fiber outputs. These are imaged onto the detector as shown in Fig. 3. For the pixels, exactly the same positions are used in each quadrant to benefit from the multiplex advantage by reading out four pixels in each quadrant simultaneously.

Both AO sensors and fringe-trackers have integration times well below 1 ms. The readout noise of 10 to 20 e^- rms severely limits their performance. Further development is needed. A multiplexer having 256×256 pixels, a capacitive transimpedance amplifier in the unit cell, 32 parallel outputs, a frame rate of > 1 kHz and a readout noise of $\sim 1 e^-$ rms is envisaged.

5. CONCLUSION

Next generation instruments will be equipped with mosaics of large format arrays putting stringent requirements on the pixel performance. Adaptive optics systems and IR sensors used in active control loops require the development of special small format, high speed low noise detectors.

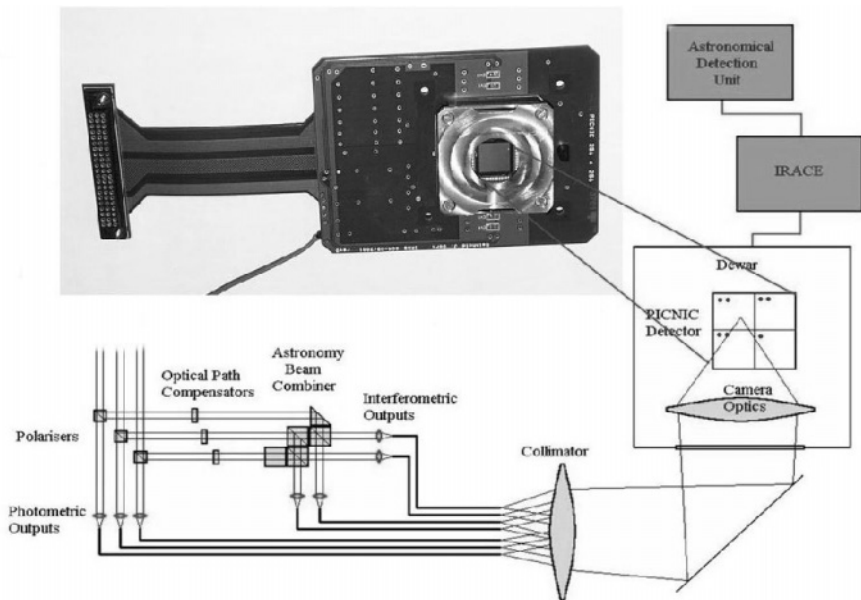


Figure 3. Layout of fringe-tracker FINITO with the combination of three telescopes.

6. REFERENCES

- [1] McCaughrean, M., 17 January 2001, *The Orion Nebula: The Jewel in the Sword*, <http://www.eso.org/outreach/press-rel/pr-2001/phot-03-01.html>.
- [2] Moorwood, A.F. M., et al., 2002, *CRIRES: a high resolution spectrograph for the VLT*, Proc. SPIE **4841**, to be published.
- [3] R. J. Dorn et al., 2002, *Design of the CRIRES 1024×4096 pixels Aladdin InSb focal plane array detector mosaic*, these proceedings, pg. 523.
- [4] LeFevre, O., Saisse, M., Mancini, D., Vettolani, G., Maccagni, D., Picat, J., Mellier, Y., Mazure, A., Cuby, J., Delabre, B., Garilli, B., Hill, L., Prieto, E., Voet, C., Arnold, L., Brau-Nogue, S., Cascone, Enrico, Conconi, P., Fiinger, G., Huster, G., Laloge, A., Lucuix, C., Mattaini, E., Schipani, P., Waultier, G., Zerbi, F., Avila, G., Beletic, J., D'Odorico, S., Moorwood, A., Monnet, G. Reyes Moreno, J., 2000, *The VIMOS and NIRMOS multi-object spectrographs for the ESO VLT*, Proc. SPIE vol. **4008**, p. 546.
- [5] Eisenhauer, F., Tecza, M., Mengel, S., Thatte, N., Roehlerle, C., Bickert, K., Schreiber, J., 2000, *Imaging the Universe in 3D with the VLT: The Next Generation Field Spectrometer SPIFFI*, Proc. SPIE vol. **4008**, pp 289.
- [6] Viard, E., Hubin, N., Le Louarn, M., Delabre, B., Monnet, G., Tokovinin, A., 2000, *Concept and performance of multiple laser guide stars for 8 m class telescope*, Proc. SPIE, vol. **4007**, p. 94.
- [7] Finger, G., et al., 2002, *Readout Techniques for drift and low frequency noise rejection in infrared arrays*, these proceedings, pg. 435

- [8] Feautrier, P., Dorn, R., Rousset, G., Cavadore, C., Charton, J., Cumani, C., Fusco, T., Hubin, N., Kern, P., Lizon, J., Magnard, Y., Puget, P., Rabaud, D., Rabou, P., Stadler, E., 2002, *Performance and results of the NAOS visible wavefront sensor*, these proceedings, pg. 325.
- [9] Hartung, M., et al., 2002, *CONICA design, performance, and final laboratory tests*, Proc. SPIE **4841**, to be published.
- [10] Gai, M., et al., 2002, *Near IR fringe tracking for the VLTI: the FINITO detection system*, these proceedings, pg. 341



*One of these nerds is not like the others
One of these nerds just isn't the same[Sesame Street]*

CONTROLLER DEVELOPMENTS

at the Anglo-Australian Observatory

Jason Griesbach

Anglo-Australian Observatory

Abstract: *The Anglo-Australian Observatory (AAO) has a history of developing CCD controllers which are high performance, low noise, and very adaptable to new applications and technologies. A brief history of the original AAO controllers is given, followed by the design and performance of the new generation AAO controller.*

Key words: *controller, Anglo-Australian Observatory (AAO), Charge-Coupled Device (CCD) controller, Complementary Metal Oxide Semiconductor (CMOS) array controller*

1. HISTORY OF THE AAO-1 CONTROLLER

The Anglo-Australian Observatory entered the world of CCD controller design in the early 1980's when John Barton led a team in the design and construction of AAO-1. The AAO prided itself in low noise performance, stability, and flexibility of design.

The flexibility of the AAO-1 became evident as astronomers took advantage of various clocking schemes that had been invented. The uniqueness of the AAO-1 was that it had the capacity for such clocking methods from the beginning. One such method is charge shuffling [1, 2], by which an image or spectra can be shuffled up and down synchronously while tuning or switching a filter. A similar clocking method is known as nod-shuffle [3]. Figure 1 illustrates this concept. As can be seen in Fig. 1(a), initially the middle third of the detector is used for spectra. In Fig. 1(b), the spectra are shuffled up and the telescope is 'noddied' off the object of interest. New spectra of the background sky are acquired. The spectra and telescope are synchronously noddied/shuffled to minimise the time dependence of the background sky, as shown in Fig. 1(c) and Fig. 1(d). The

sky spectra can ultimately be subtracted from the object spectra for enhanced signal/noise. The AAO, using the AAO-1 controller, was the first observatory to make this and similar novel clocking schemes available to the general astronomical community.

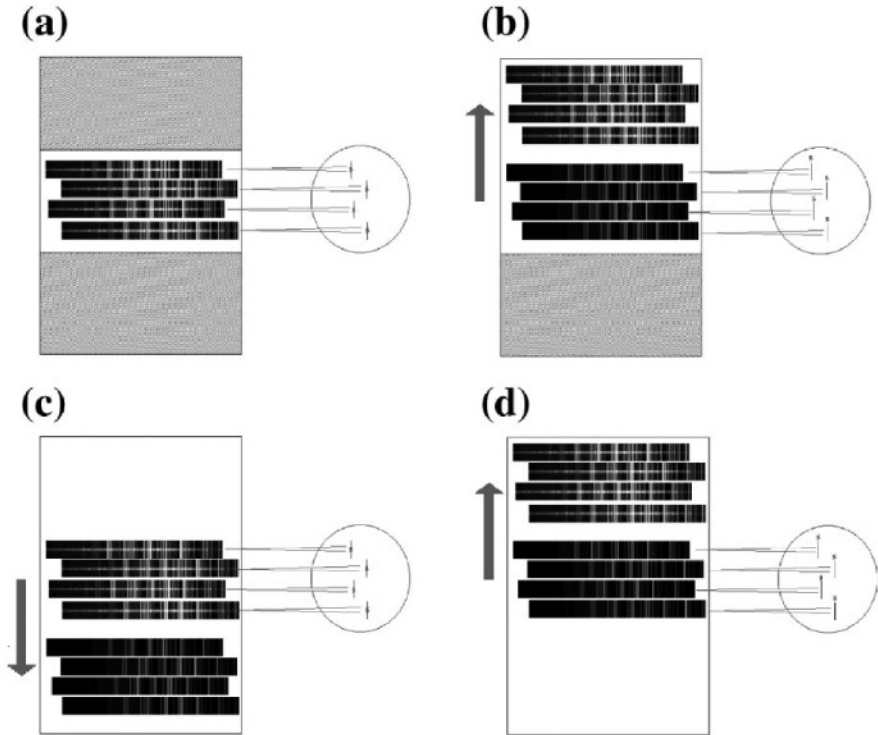


Figure 1. Illustration of Nod and Shuffle technique (from [3]).

Another proud moment of the AAO-1 was when the MIT/LL CCID-20 detectors were made available. These detectors, which were 2K×4K format, were much larger than any that had been seen previously. In fact, it was thought that such large CCD's would never be produced since the industry was not driving their development. When the CCID-20 devices became available, the AAO responded by commissioning the MIT/LL2 in October of 1997, six months before any other observatory. Equally as impressive, the MIT/LL2 was commissioned with 2 e^- read noise at 20 $\mu s/pix$ and only 1.3 e^- noise at 100 $\mu s/pix$. This success is attributed to the foresight in the design of the AAO-1, and the flexibility of operation that resulted.

2. THE AAO-2 CONTROLLER

Work began in the early 1990's on a new controller. This work was primarily led by John Barton and Lew Waller of the AAO. This new controller, the AAO-2, was to have the same flexibility and low noise performance as its predecessor while becoming faster and more compact. A version of the AAO-2 which is optimised for CMOS multiplexed arrays, has already been completed and commissioned. The AAO-2 for CCDs is in the design phase.

A block diagram of the general AAO-2 is shown in Fig. 2. This controller has up to four video boards with one input per board, and two clock boards for every four detectors or readout amplifiers. Also central to the controller are a power conditioning board and a utilities board. The latter handles various functions such as detector temperature control, input/output synchronisation, and shutter control. These boards are connected by separate digital and analog backplanes, where the digital backplane is connected to the sequencer and system control and the analog backplane is connected to the dewar.

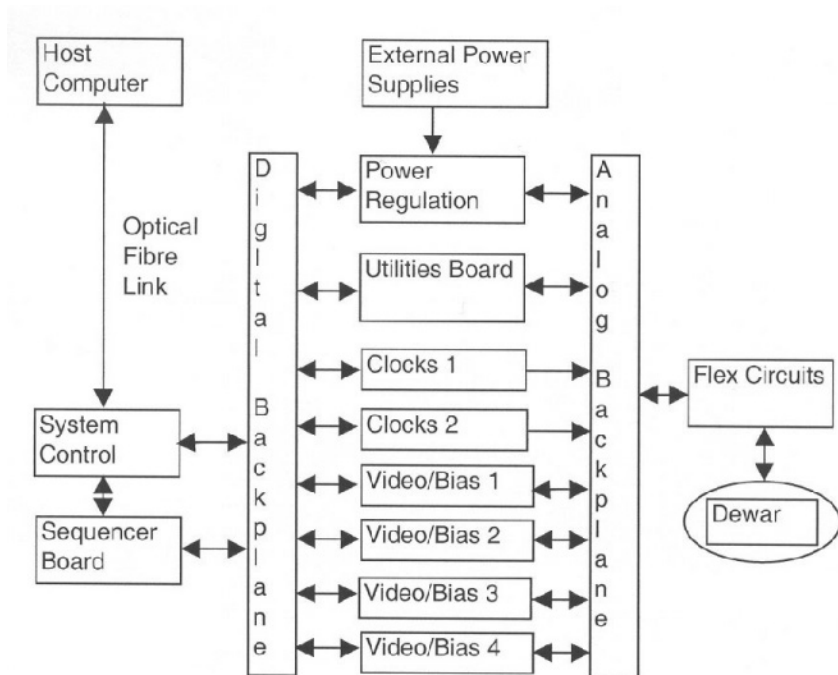


Figure 2. Block diagram of the AAO-2 controller.

The AAO-2 CMOS array controller has been commissioned with a Hawaii-1 array in the IRIS2 instrument at the Anglo-Australian Telescope. It is showing remarkable stability and low noise performance. Specifically, it can read the Hawaii-1 array using all four quadrant readouts in only 0.6 sec with 10 e^- of read noise. The images have been very clean and flat-fieldable.

Table 1. AAO-2 Controller Specifications.

Parameter	CMOS Array Controller	CCD Controller
Video		
Number of channels	4	4
Video processor type	CDS or Clamp/Sample	CDS or Clamp/Sample
ADC resolution	16 bit	16 bit
Max pixel rate per channel	2 MHz	1 MHz estimated
Read noise	10 e^- rms on Hawaii-1	2 e^- at 50k pix/sec est.
Biases		
Number of biases	24	48
Voltage range	0 to 10V, 0 to -10V, 0 to 5V	0 to 30 V, -12 to +12 V
Vertical Clocks*		
Number of clocks	20	20
Voltage range	0 to 5 V	-15 to +10 V
Max update rate	5 MHz	5 MHz
Min rise/fall time	2-3 μs (5 V step)	2-3 μs (10 V step)
Peak output current	100 mA	100 mA
Horizontal clocks		
Number of clocks	0	16
Voltage range	-	-10 to +15 V
Transition type	-	Programmable slope
Rise/fall time	-	100 ns to 2 μs (10 V step)
Peak output current	-	100 mA
Fast Clocks		
Number of clocks	16	12
Voltage range	0 to 5 V	-10 to +15 V
Rise/fall time	50 ns (5 V step)	50 ns (10 V step)
Peak output current	100mA	30 mA
Host Computer		
250 Mbps full duplex optical fibre interface	Yes	Yes
VMEBus architecture	Yes	Yes
Real time VXWorks	Yes	Yes

* In the CMOS controller, the vertical clocks have been heavily filtered and used as precision biases. The update rate and rise/fall time specifications for this controller only hold relevance if these filter stages are removed.

The design of the AAO-2 CMOS array controller is now being modified to be a general, high performance CCD controller. This work is primarily being carried out by the author (Jason Griesbach). One of the features that makes the AAO-2 CCD controller unique is the flexible clocking. There are

three kinds of clocks available in the controller—vertical (image) clocks, horizontal (register) clocks, and fast readout clocks. The vertical clocks are defined by fast parallel-loaded DACs. These DACs can be updated every 200 ns to create custom wave shapes. The horizontal clocks are bi-level clocks with programmable slope rise and fall times. The rising slope, falling slope, upper level, and lower level are all independently programmable. Finally, the fast clocks are designed for the summing well and reset gate, with provision for a spare clock as well. These clocks are fast to lend more time to the video processor between pixels, and they are very low noise since they are so close to the sense node. The fast clocks are also bi-level clocks, with independently programmable levels.

3. FUTURE PLANS

The first prototype of the AAO-2 CCD controller is scheduled to be operational later in 2002. In 2003, the AAO-2 will replace the AAO-1 on existing systems of the Anglo-Australian Observatory. The possibility of making the AAO-2 controllers externally available has been considered and may be pursued if the interest is there. For more information contact the author at jsg@aaoepp.aao.gov.au, or Lew Waller at lgw@aaoepp.aao.gov.au.

4. REFERENCES

- [1] Bland-Hawthorn, J., Barton J.R, 1995, AAO Newsletter **74**, p. 10.
- [2] Bland-Hawthorn, J., Jones, D.H., 1998, *TTF: a flexible approach to narrowband imaging*, Proc. SPIE, **3355**, p. 855.
- [3] Glazebrook, K., Bland-Hawthorn, J., 2001, *Microslit Nod-Shuffle Spectroscopy: A Technique for Achieving Very High Densities of Spectra*, Publications of the Astronomical Society of the Pacific; **113**, 780, p. 197.



Be careful what you say! Fred Harris is typing it all into his laptop! For the 4th workshop in a row he has transcribed in real time all of the presentations, questions and discussions. Thank you! Fred's notes for SDW2002 can be found at <http://www.not.iac.es/CCD-world/Workshop02.txt>. Sitting next to Fred, is Peter Sinclair, who is ready to help translate any Spanish words.

DETECTOR WORK AT THE UKATC

The optical to the sub-millimetre

Derek Ives, Nagaraja Bezawada and Maureen Ellis

United Kingdom Astronomy Technology Centre

Abstract: *The UK Astronomy Technology Centre (UKATC) is a UK facility for designing and building world class astronomical instrumentation covering spectra from the optical to the sub-mm. Most recently we have delivered a common user adaptive optics system fitted with optical CCDs and a mid-IR imager/spectrometer built with a Raytheon IBC Si:As detector implementing non destructive readout. We are in the process of designing and building an optical 3-channel fast photometer using CCDs, a 1-5 μm imager/spectrometer which uses an InSb array, two wide field NIR cameras based on MCT detectors and a wide field sub-mm camera which will use the latest SQUID / bolometer technology.*

We give an overview of some of these instruments and their performance with particular regard to their detectors, the problems associated with running them and the experience gained in their characterisation. We use in-house designed controllers and third party systems. We describe the reasons for choosing these particular controller types, the lessons learnt and ideas for the future.

Key words: *HAWAII-2, Raytheon Infrared Operations (RIO), CRC-774, Non Destructive Readout, Transition Edge Sensors (TES).*

1. INTRODUCTION

The UKATC is a new centre of excellence established at the Royal Observatory Edinburgh with an amalgamation of staff from both Edinburgh and the Royal Greenwich Observatory. It combines all expertise in telescope design and astronomical instrumentation, covering wavebands from the optical to the sub-millimetre in one establishment. Recently, the UKATC has

been very active in all these areas of work. However this paper will concentrate on the detector specifics of the recent work at the UKATC.

2. THE OPTICAL

The optical detector work has been wide ranging, from simple 4K×4K CCD cameras to auto-guiding systems. A more recent project has been the design and building of a 3-colour CCD photometer, ULTRACAM, for the University of Sheffield.

2.1 ULTRACAM

This is a simple 3 colour photometer which uses 3 Marconi MAT47-20 CCDs. These are AIMO (Advanced Inverted Mode Operation) devices with enhanced QE processes and are thermoelectrically cooled with an external 2 stage Peltier to operate at -45 °C. This ensures dark current rates less than 0.1 e⁻/pix/sec. We use the storage area as a pipeline to ensure high speed windowed readout in the order of 100 Hz. The CCDs readout from both outputs and in parallel using a single SDSU2 controller. We use the PCI interface in a PC running RTLinux. Each windowed frame is absolute time stamped using a commercial GPS system interfaced to the PC.

3. THE NEAR INFRARED

3.1 WFCAM

We are at present designing and building a new wide field Near Infrared mosaic camera for UKIRT in Hawaii. This is a fully funded project (partially funded by SUBARU) to build the widest field IR camera ever attempted, for delivery by the end of 2003.

Its key features are:

- (z) & 1-2.4 μm broad and narrow band
- 0.4'' pixels micro-stepping for PSF sampling (c.f. 2MASS)
- fast tip-tilt guiding (focal plane CCD)
- PACE/ZIF socketed HAWAII-2 detectors, 90% spacing of 4 detectors
- 4 parallel processing pipelines
- four exposures give filled 0.865° square (0.75 sq.°)

It is a very novel design with the main camera cryostat body mounted in front of the primary mirror fixed to the mirror plug hole.

The focal plane layout is shown below in Fig. 1. A point of interest is our plan to mount an optical CCD (the MAT47-10) at the focal plane, but position it a few millimeters above the IR active area. The main IR detectors will be readout synchronously. However it is impossible to readout the CCD synchronously with the HAWAII-2 devices. Thus there are great concerns about the CCD clocks coupling into the outputs of the IR detectors. To minimise this potential problem we have designed the layout so the CCD is mounted in its own electromagnetically shielded enclosure. This includes the window, which has a special coating to reduce electromagnetic interference.

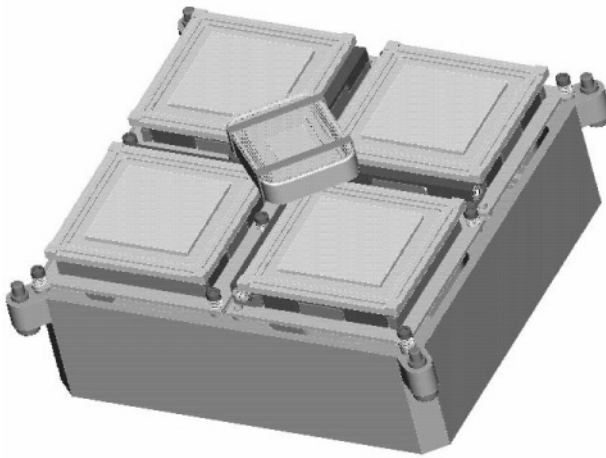


Figure 1. WFCAM Focal Plane Mosaic

Figure 2 shows more detail of the EMI enclosure for the autoguider CCD. The coating of the window makes electrical contact with a gasket which is in contact with the metal housing. We have already completed preliminary tests in the lab using tests probes and a spectrum analyser and have shown the enclosure to be effective at the frequencies of concern for our instrument. We also plan to run the CCD clocks at reduced voltages to reduce their radiative emissions.

If we do not get the required performance from the IR detector in terms of its noise due to the coupling of the CCD clocks to the IR array outputs, we then plan to implement a scheme of interleaved readout. As a last resort we can, of course, switch the auto-guiding CCD off during the IR mosaic readout.



Figure 2. WFCAM autoguider CCD shielding.

3.2 WFCAM Data Acquisition System

We plan to use the SDSU2 controller in its IR format to read out the HAWAII-2 detectors. Each controller will use four of the new 8 channel IR video boards from SDSU to readout from the 32 outputs of each detector. The controller will then feed the 16 bit pixel data down the new 250 MHz fibre link into a PCI board inserted into a PC running RTLinux as for the ULTRACAM system. We will implement a Master Controller/3 Slave Controller system to ensure that all the four arrays are clocked and readout synchronously to within a few 10 ns and to ensure no clock coupling between arrays.

3.3 VISTA IR camera

Our second more ambitious Infrared mosaic project is to build a camera with an array of 16 IR detectors for use on the VISTA telescope. The detectors will be HgCdTe $2K \times 2K$ detectors from Raytheon Infrared Operations (RIO). For this project we will use 3 edge buttable packages that are similar to those supplied by the CCD manufacturers in style. This should ensure that we meet our array co-planarity specifications much easier than we would with the “ZIF” socket detectors. In the minimum configuration RIO detectors, which have sixteen outputs each, we will have to build an acquisition system capable of dealing with 256 output channels. Our agreement with ESO means we must ensure that VISTA can easily be supported by ESO staff at Paranal. This means that we try to ensure commonality of as many systems as possible. We are therefore planning to use a suite of four of ESO’s IRACE controllers to drive the 16 arrays synchronously. The focal plane will also be populated with 6 CCD detectors which will be used for autoguiding, as Shack-Hartmann sensors and as curvature wavefront sensors. Figure 3 shows the focal plane layout.

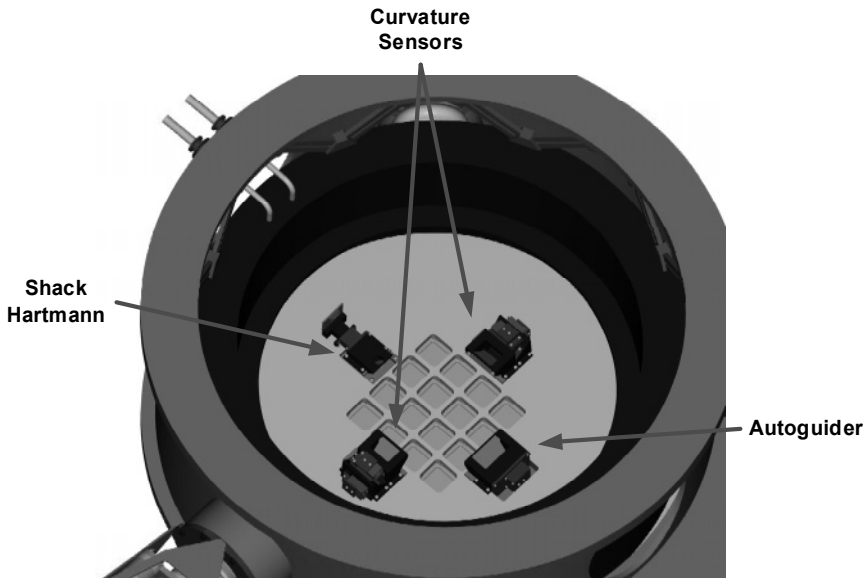


Figure 3. VISTA Focal Plane Array

3.4 UIST

The UKATC has recently been involved in the complete design, development and integration of an imager and spectrometer (UIST) to be delivered to UKIRT. UIST is a 1–5 μm imager and spectrometer with a cryogenically deployable Integral Field Unit (image slicer). It uses the ALADDIN 1K \times 1K InSb detector from Raytheon, operated using 32 outputs, with frames rates > 5 Hz, with Non Destructive Readout/Slope fitting and a digital over-sampler implemented in real time.

4. THE MID INFRARED

The UKATC has recently delivered to UKIRT, MICHELLE, an Echelle based imager and spectrometer. MICHELLE operates in the 8–28 μm wavelength range, has 5 different gratings, a resolving power of $R=100\text{--}30000$ and is interchangeable between UKIRT and GEMINI. The detector is from Raytheon and is the CRC-774 device, which is described below.

4.1 CRC-774 mid IR detector specification

- Si :As device - Impurity Band Conduction
- 320 \times 240 pixels (50 μm)
- <10 K operation

- >100 Hz frame rate
- Switchable wells from $6 \cdot 10^6$ – $25 \cdot 10^6$ e⁻
- Gated Pixels
- QE> 40%
- On board CDS circuitry, non destructive readout also possible

There are two very important features of this device. The first is switchable wells that allow the user to operate in the low background, array read noise limited regime and in the high background noise limited regime, all from the switch of a bias voltage. The second is that the gated pixel function also allows very short exposure times, which are only limited by the controller clock tick period.

The array has on board circuitry to allow removal of the “kTC” noise by performing a correlated double sample, controlled by the clocking. Non Destructive Readout can also be implemented as is described below.

4.2 CRC-774 Non Destructive Readout

In stare mode, each pixel in the array is multiplexed together with the other pixels in the same column. When a row is selected, the output from each pixel is connected to the other side of a clamp capacitor. The other side is fixed at a clamp bias voltage. When clamp is removed it leaves a difference between the signal and clamp on the capacitor. There is one clamp per column; and this clamping action happens in parallel for every column. The pixel is then reset. This brings the pixel output to the reset voltage. However the other side of the capacitor is floated to a voltage set by the reset voltage, minus the signal. This inverts the signal and also subtracts the reset voltage from the signal, thus removing the reset “kTC” noise.

The resetting of the pixels is an integral part of the conversion of the signal from the pixel to the outside world. However, this is not compatible with the method of non destructive reading in which we do not want to reset them each time we read them. The solution to this conundrum is to sacrifice the first row. On every frame, the first row is reset. Then, by manipulating the clocks it is possible to put a clamp voltage across the capacitor on the first row and then retain it for the remaining rows (see Fig. 4 for more detail). This has three main effects:

- The first row has to be sacrificed in the reset process.
- There is a level shift across the array as the voltage on the clamp capacitor slowly leaks away. This effect is small and the slope is removed in the slope fitting process.
- The signal is inverted with respect to the stare mode, that is, the array signal integrates down away from zero volts. The software

must take this into account when switching between stare and non-destructive readout.

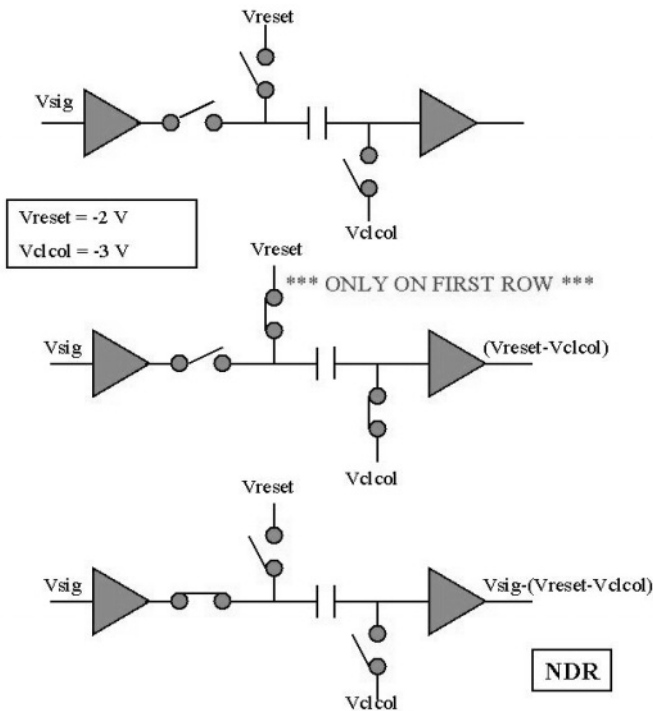


Figure 4. CRC-774 Non Destructive Readout Scheme.

4.3 Characteristics of the CRC-774 Detector

Our device was one of the very first devices produced by Raytheon and hence suffered from problems which we hope are not evident in later devices. These problems are too complex to describe in complete and are only to summarized.

We had problems with the array stability, thus taking many hundreds of frames to settle the array. We also had an "excess noise" problem that was a function of signal on the array and in excess of the signal shot noise. This was associated with resetting the array, as the excess noise was less of a problem in the non destructive read out mode of operation.

5. THE SUB-MILLIMETRE.

We are building a replacement for SCUBA at the JCMT (James Clerk Maxwell Telescope) that will use arrays of Transition Edge Sensors (TES) instead of the more commonly used feed horn and NTD bolometer configuration. The number of pixels will rise from approximately 120 to 12000. This is only possible because the TES devices can be made using micro-machined silicon structures. The TES pixels will be hybridised to a SQUID multiplexer. This work is being done in partnership with NIST, Boulder, Colorado and the Universities of Edinburgh and Cardiff.

6. REFERENCES

- [1] <http://www.roe.ac.uk/atc/projects/>
- [2] Henry, D.M., Atad-Ettdgui, E., Casali, M.M., Bennett, R.J., Bridger, A., Ives, D.J., Rae, R.G., Hawarden, T.G., 2000, *Wide field camera for the United Kingdom Infrared Telescope*, Proc. SPIE **4008**, p. 1325.



Happy and well-fed Paniolos smile at the camera.

CCD CAMERA SYSTEMS FOR THE GTC

Ralf Kohley¹, Marcos Suárez¹, Juan Manuel Martín¹, Greg Burley², Lluís Cavaller¹ and Rafael Vilela¹

¹*Gran Telescopio Canarias Project Office, Instituto de Astrofísica de Canarias (IAC)*

²*Observatories of the Carnegie Institute of Washington (OCIW)*

Abstract: *The construction of the GTC (Gran Telescopio Canarias) on La Palma, Canary Islands, is well under way with first light planned for October 2003. All subsystems are developed and are now in the fabrication or commissioning phase. Apart from the suite of instruments, this paper discusses the design and procurement of the CCD camera systems, which are designed for the close-loop active optics and the acquisition and guiding purposes of the telescope (wavefront sensors and guiding cameras) and for in-house developed scientific instrumentation. Furthermore, we describe our test bench facility for CCD evaluation up to surface sizes equivalent to a 4K×4K, 15 μm detector.*

Key words: *Gran Telescopio Canarias (GTC), Charge-Coupled Device (CCD), guiding, instrumentation, controller*

1. INTRODUCTION

The Gran Telescopio Canarias (GTC) is a 10.4-m telescope with 36 individually controlled primary mirror segments. It is equipped with 8 focal stations, of which the 2 Nasmyth foci will first come into operation.

Construction work on the telescope and the observatory facilities on La Palma started in 1999 and is progressing well. First light is planned for October 2003, followed by a one year period of telescope commissioning. Scientific operations will start in October 2004 (Day 1) with a range of instruments coming on-line, spanning the wavelength range from visible to the mid-IR. The instruments are designed as multi-purpose imaging

spectrographs to be able to cover a broad range of observing programs and to maximize the scientific return of the telescope from the beginning.

The GTC will, furthermore, be equipped with a powerful yet compact acquisition, guiding and wavefront sensing system, called GUACAMOLE (described in detail in [1]), to be installed as a module at each focal station.

In 1999, the Instrumentation Group at the GTC Project Office, hereafter PO, started with the design, procurement and fabrication of the CCD camera systems for the GTC, including the installation of a CCD test bench facility as the test bed for detector evaluation and the performance of the final systems.

2. GTC INSTRUMENTATION

Preliminary designs for the scientific instrumentation were carried out in 1999, just in the time to write an article for the last ESO Detector Workshop [2]. Initially three scientific instruments, OSIRIS, CanariCam and EMIR, were funded to be built by external research institutions. More detailed information about the different instruments can be found in several SPIE publications [3, 4, 5]. In October 2000, the GTC Project Board approved an additional instrument, ELMER, as a contingency action to be developed in-house. This instrument follows a low risk, low budget concept to have a simple but highly efficient instrument with a guaranteed delivery date to be put into operation in case of arrival delays of the more complex instruments. A detailed description of ELMER can be found in [6]. Table 1 gives a short overview of the currently funded instrumentation.

Table 1. GTC instrumentation overview.

Scheduled for	Instrument	Leading Institution	Design	Range [μm]	Detector
First Light: October 2003	A&G system (GUACAMOLE)	GTC PO (Spain)	Imaging, Wavefront Sensing	VIS, 0.38-1	Marconi 47-20, FT 1K×1K, 13μm, and Marconi 39-01, FT 80×80, 24 μm
	Commissioning Instrument	IA-UNAM (Mexico)	Imaging, Wavefront Sensing	VIS, 0.38-1	Marconi 47-20, FT 1K×1K, 13 μm
Day 1: October 2004	ELMER	GTC PO (Spain)	Imaging, Spectrograph	VIS, 0.36-1	Marconi 44-82, 2K×4K, 15 μm
	OSIRIS	IAC (Spain)	Imaging, Spectrograph	VIS, 0.36-1	Marconi 44-82 or MIT/LL CCID-20, Two 2K×4K, 15 μm
	CanariCam	Univ. of Florida (USA)	Imaging, Spectrograph	mid-IR, 8-24	Raytheon Si:As IBC array, 320×240, 50 μm
Day 2: July 2006	EMIR	IAC (Spain)	Imaging, Spectrograph	IR, 0.9-2.5	Rockwell Hawaii-2 FPA, 2K×2K, 18μm, HgCdTe

Table 2 compares the main characteristics of each scientific instrument.

Table 2. Main characteristics of scientific instruments.

ELMER	Imaging spectrograph, Visible (0.365 - 1.000 μm)
Features:	broad and narrow band Imaging; long slit, slit-less and Multi-Object Spectroscopy; Fast Photometry & Spectroscopy; Charge Shuffling
Pixel FOV:	0.195'' (square)
max. FOV:	3.0' \times 3.0' (4.2 arcmin circular)
Resolution:	200 - 1500
OSIRIS	Imaging Spectrograph, Visible (0.365 - 1.000 μm)
Features:	broad and narrow band Imaging; long slit and Multi-Object Spectroscopy; Fast Photometry & Spectroscopy; Charge Shuffling & Tunable Filters
Pixel FOV:	0.125'' (square)
max. FOV:	8.5' \times 8.5' (Imaging), 8.0' \times 5.2' (Spectroscopy)
Resolution:	250 - 2500
CanariCam	Imaging Spectrograph, mid-IR (8 - 24 μm)
Features:	diffraction limited Imaging; long slit Spectroscopy; Coronagraphy; Polarimetry
Pixel FOV:	0.095'' (square)
max. FOV:	0.42' \times 0.32'
Resolution:	60 - 1300
EMIR	Imaging Spectrograph, IR (0.9 - 2.5 μm)
Features:	broad and narrow band Imaging; long slit and multi-slit Spectroscopy; Fast Photometry & Spectroscopy
Pixel FOV:	0.2'' (square)
max. FOV:	6.0' \times 6.0' (Imaging), 6.0' \times 4.0' (Spectroscopy)
Resolution:	1300 - 4250

3. DETECTOR SYSTEM DESIGNS AND PROCUREMENT

In 1999 the GTC PO had already started the procurement of the scientific detectors and controllers for instrumentation and acquisition and guiding (A&G) purposes to ensure the scheduled availability of the detector systems to the instruments and avoid putting the systems onto a critical path due to delivery delays.

We envisioned a single standard controller which would interface to our control system to cover the detector system needs from the visible to the infrared. These intentions failed, and due to the different requirements of

each sub-system we ended up with currently three different controller systems to maintain.

3.1 CCDs and CCD Controllers

CCDs are used as detectors in two of the scientific instruments and for all the A&G cameras.

3.1.1 Optical Instruments

The main requirements for the first optical instrument, OSIRIS, had been:

- High speed, very low noise amplifiers
- Large form factor (4K×4K, 15 μm)
- Very good cosmetic quality
- High overall quantum efficiency with optimization in the red
- Low fringing
- Very good flatness
- Frame-transfer capability
- High line shift rates
- Very good transfer efficiency

To fulfill the requirements without too many compromises, the PO decided to obtain a mosaic of 2K×4K, 15 μm CCDs built on high-resistivity silicon (high red response, low fringing) with about 40 μm thickness for the instrument. Due to availability we chose two main suppliers for these detectors, MIT Lincoln Laboratory (via the University of Hawaii consortium) and Marconi Applied Technologies, hereafter Marconi (formerly EEV, now E2V Technologies).

Initial problems with the detector development at MIT/LL seem to have been resolved, and we are hopeful, after the delivery of a single engineering grade CCID-20, to receive our first science grade devices soon.

The contract with Marconi has suffered slight delays, but nevertheless we are very satisfied with the momentary delivery status having received the first two science grade CCD44-82 devices early this year and expecting the final delivery in August. These detectors will be tested soon, and we are trustful that they will fully comply with the specifications.

The in-house instrument, ELMER, as the second instrument operating in the visible range, will be equipped with a single Marconi CCD44-82 as a result of availability and simplicity. The cooling system is a LN₂ bath cryostat built by the French company SNLS under license from ESO (cryostat design by Jean-Louis Lizon, ESO). Both optical instruments will use a San Diego State University Generation II controller (SDSU-II) with a parallel timing board interfacing over a RS-422 cable to a commercial frame grabber. An article of the OSIRIS team within this publication [7] describes

this particular data acquisition system in more detail. DSP programming of the observing modes is done by Francis Beigbeder (Observatoire Midi-Pyrénées).

3.1.2 Acquisition and Guiding System

The A&G system of the GTC has to fulfill four different purposes: (1) object acquisition, (2) slow and fast guiding, (3) wavefront sensing for open and close loop active optics, and (4) seeing monitoring. These functionalities were grouped into three different CCD camera systems mounted on two articulated arms, which are versatile throughout the telescope focal plane. For the camera systems we needed two types of detectors, one with a reasonable area and resolution, and one with a relatively small area but high frame rates. Constraints were: electronic shuttering, fast readout, high quantum efficiency, low noise and low dark current. After a market survey we finally decided on Marconi as the provider and ordered several CCD39-01 (80×80, 24 μm pixels, SFT, four outputs, thinned, NIMO, broadband coating) and CCD47-20 (1K×1K, 13 μm pixels, FT, four outputs, thinned, AIMO, midband coating) detectors mounted in the Marconi 2-stage Peltier package. All detectors are delivered now and undergoing testing at the PO. Initial results show a good match to the manufacturer's specifications.

Since mechanical constraints required a very compact and light weight controller system with even smaller, remote CCD heads able to operate in changing ambient conditions ($T_{\text{amb}} = -2\text{ }^{\circ}\text{C}$ to $19\text{ }^{\circ}\text{C}$, $\text{RH} = 2\%$ to 87%), the initial idea of copying the A&G controller system developed for Gemini was replaced by a proper design, more adapted to our needs. Our A&G controller is now based on the Guider Camera for Magellan (see [8]) with upgrades made at the PO (see [9]). The controller weights 3 kg including a heat exchanger and measures 270 mm×120 mm×115 mm in size. It can operate up to four channels simultaneously with max. 400 Kpix/sec and 14-bit A/D conversion. The controller is connected to the Control System by a 30 m, 25 Mbits/sec, serial LVDS link to a PCI interface board. Anticipated frame rates are about 200 Hz for the CCD39-01 and 1 Hz for the CCD47-20. Eleven units of the controller are now in the last stages of manufacturing at the IAC workshop and are partly already under test at the PO. The remote CCD heads are able to operate the detectors at a fixed temperature of about $-35\text{ }^{\circ}\text{C}$ and are separated from the controller by 1.5 m. They are fabricated at the Spanish company NTE, S.A. and are being finished now too.

3.2 IR array detectors and controllers

There are two instruments for the GTC operating in the infrared wavelength range, CanariCam in the mid-IR (8–24 μm) and EMIR in the IR (0.9–2.5 μm). Management, procurement and testing of the mid-IR detector

system (array and controller) are being handled directly by the CanariCam team of the University of Florida. A Raytheon Si:As BIB array (320×240, 50 μm pixels) has been obtained for the instrument and will be operated by an MCE-4 designed by Kevin Hanna (University of Florida).

For EMIR, the Project Office ordered at an early stage a Hawaii-2 FPA from Rockwell foreseeing the delivery delay. Nevertheless, the multiplexer, engineering and science grade detectors have now arrived and are under test by the EMIR team at the IAC [10].

4. CCD TEST BENCH FACILITY

Our CCD test bench was designed as a multi-purpose facility fulfilling the following requirements:

- Peltier and cryogenically cooled detector systems
- Stabilized light source (good short and long term stability)
- High throughput from UV to NIR
- Homogeneous illumination over at least 90 mm diameter circular FOV (detector sizes up to 4K×4K, 15 μm including mosaics)
- Target imaging with pure reflective optics (no chromatic aberrations) for MTF measurements
- For visual inspections
- Test procedures fully automated

The requirements let to a simple and compact design using an arc lamp (Xenon or Mercury) with a close loop intensity control as illumination source. Choosing one of 12 interference filters with 10 nm bandwidth in a 14 position filter wheel does the wavelength selection. The current filter set covers the visible wavelength range from 350 nm to 990 nm. To reduce stray light blocking filters precede these filters. The color beam enters a 12 in integrating sphere, which produces a 4 in (101.6 mm) diameter monochromatic flat field at its output. A motorized diaphragm and iris shutter controls illumination flux and exposure times, respectively. Throughput is also high at the UV and NIR end of the spectrum due to the availability of lines in the arc lamp spectrum. Figure 1 shows a photo of the whole system.

All components are under PC control operated via RS-232 with National Instrument's LabVIEW™ drivers. Automated test procedures for all standard CCD tests such as QE, dark current, linearity, read out noise, full well, transfer efficiency, etc., are currently being written. The transfer optics for target imaging have been developed and will be added to the facility soon. Plans are to add a Fe^{55} source in the future to be able to accurately determine system gain and CTE defects.

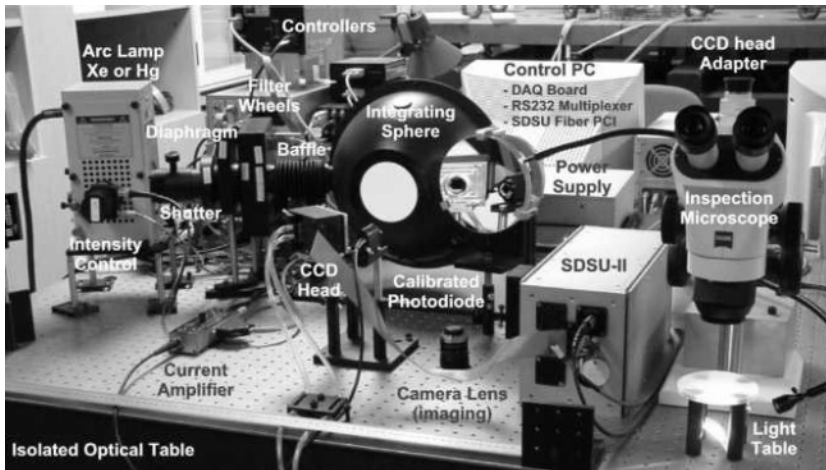


Figure 1. CCD test bench at GTC Project Office Laboratory.

5. REFERENCES

- [1] Devaney, N., Cavaller, L., Jochum, L., Bello, C.D., Castro, J., 2000, *GUACAMOLE: the GTC guiding, acquisition, and calibration module*, SPIE Conf. Proc., Vol. **4003**, p.146.
- [2] Kohley, R., 2000, *GTC - Present status and future plans*, Astr. and Space Sci. Lib., Vol. **252**, Kluwer Acad. Pub., p.51.
- [3] García-Vargas, M.L., 2000, *First generation of instruments for the GTC (Gran Telescopio Canarias)*, SPIE Conf. Proc., Vol. **4008**, p.62.
- [4] Cepa, J., Aguiar, M., Escalera, V., Gonzalez-Serrano, I., Joven-Alvarez, E., Peraza, L., Rasilla, J. Rodriguez-Ramos, L., Gonzalez, J.J., Cobos Duenas, F., Sanchez, B., Tejada, C., Bland-Hawthorn, J., Militello, C., Rosa, F., 2000, *OSIRIS tunable imager and spectrograph*, SPIE Conf. Proc., Vol. **4008**, p. 237.
- [5] Balcells, M., Guzman, R., Patron, J., Aragon-Salamanca, A., Azcue, J., Ballester Lluch, J.A., Barroso, M.T., Beigbeder, F., Brau-Nogue, S., Cardiel, N., Carter, D., Diaz-Garcia, J.J., de la Fuente, E., Fuentes, F.J., Frago-so-Lopez, A.B., Gago, F., Gallego, J., Gomez-Elvira, J., Heredero, J.C., Jones, Damien, J., Lopez, J.C., Luke, P., Manescau, Antonio, Munoz, T., Peletier, R.F., Pello, R., Picat, J.P., Robertson, D.J., Rodriguez, J.A., Serrano, A., Sharples, R.M., Zamorano, J., 2000, *EMIR: cryogenic NIR multi-object spectrograph for GTC*, SPIE Conf. Proc., Vol. **4008**, p.797.
- [6] García-Vargas, M.L. et al., 2002, *Status of ELMER, an instrument for the GTC 10-m Telescope*, SPIE Conf. Proc., Vol. **4841-191**.
- [7] Joven, E. , Gigante, J., Beigbeder, F., 2002, *OSIRIS detectors: first tests and control system*, this publication, these proceedings, pg 345.
- [8] Burley, G., Thompson, I., Hull, C., 2002, *Compact CCD guider camera for Magellan*, these proceedings, pg 431.
- [9] Suárez, M., Kohley, R., Burley, G., Cavaller, L., Vilela, R., Tomas, A., 2002, *GTC Acquisition Cameras and Wavefront Sensors*, these proceedings, pg 459.
- [10] Diaz, J., Gago, F., Beigbeder, F., Garzon, F., Patron, J., 2002, *EMIR Hawaii-2 first test results*, these proceedings, pg. 493



Fernando Pedichini won the prize "Most ingenious presentation" for his spherical cryostat project. Moments after this picture was taken, the cheering crowd also nominated him "Mr. Alternative Elegance"

DETECTORS AT CTIO: PRESENT STATUS AND FUTURE PLANS.

Ricardo E. Schmidt

Cerro Tololo Inter-American Observatory¹

Abstract: *Visible and IR detector systems in use are reviewed. In progress are a wide field 2K×2K IR Imager for the 4m Blanco telescope and a 4K×4K CCD Mosaic for the new 4-m SOAR telescope. New projects include exploring visible-range AO options for SOAR and active collaboration with NOAO/Tucson in the development of the next-generation Image Acquisition System.*

Key words: *detectors, optical, Infrared (IR), imager, SOAR, Infrared Side Port Imager (ISPI), MONSOON, Adaptive Optics (AO)*

1. PRESENT STATUS

1.1 Optical detectors in use at CTIO

Optical detectors in use at CTIO and their applications [1] are summarized in Table 1. All scientific CCDs in use are thinned and all are still operated by Arcon controllers developed at CTIO.

1.2 IR detectors in use at CTIO.

The IR detector in use at CTIO [1] is the Rockwell HAWAII-1. It is used on two Ohio State Instruments: the OSIRIS Imaging Spectrometer used

¹ CTIO is a division of the National Optical Astronomy Observatories, operated by AURA Inc., under cooperative agreement with the National Science Foundation (NSF).

on the Blanco 4-m telescope and the Andicam Optical/IR Imager at the 1-m Yalo telescope.

The HAWAII-1 HgCdTe focal plane array covers the 1-2.4 μm wavelength range. It is operated near 77 K and some of its specifications are as follows:

- 1024 \times 1024 format.
- Array has 4 output amplifiers, each reads out one quadrant.
- 18.5 μm square pixels
- Readout noise is 15 e^-

Table 1. A summary of the optical detectors currently in use at CTIO.

	SITe ST002A	SITe S1424AB/ TK2048EB	Loral 3K	Loral 1K	Loral 2K
Format	2K \times 2K	2K \times 2K	3K \times 1K	1200 \times 800	2K \times 2K
Pixel Size	15 $\mu\text{m}\times$ 15 μm	24 $\mu\text{m}\times$ 24 μm	15 $\mu\text{m}\times$ 15 μm	15 $\mu\text{m}\times$ 15 μm	15 $\mu\text{m}\times$ 15 μm
Amplifiers Used	2 (Mosaic) or 1 (Hydra)	2 (S1424AB) or 4 (TK2048EB)	1	1	2
Readout Noise	5 e^- -8 e^-	3 e^- -5 e^-	7 e^-	6 e^-	11 e^-
Comments	3-side- abutable 85% QE, 6000 \AA	MPP-mode used	UV flooded for high QE	UV flooded for high QE	Used on Andicam (optical and IR imager made by OSU)
	Hydra: 6 e^- RON @ 60 Ke \cdot FW or 3 e^- RON @ 15 Ke \cdot FW	S1424AB: 80 pins TK2048EB: 68 pins	75% QE at 3500 \AA	93% QE at 6000 \AA	
Applications	8K \times 8K Mosaic PF Imager	Imaging and Spectroscopy	Spectroscopy at 4-m telescope CF	Spectroscopy at 1.5-m telescope CF	Imaging (1-m Yalo telescope)
	Hydra fiber fed MOS				

2. PROJECTS IN PROGRESS

2.1 The SOAR Optical Imager.

A high resolution Optical Imager (see Fig. 1) [1-3] is being developed at CTIO as the commissioning instrument for the 4.2-m SOAR telescope on Cerro Pachon, a 2700 m high mountain sited 10 km eastwards from Cerro Tololo. The SOAR telescope is designed for high-resolution imaging and moderate field imaging spectroscopy. Tip-tilt-corrected best image sizes of $0.24''$ are expected over its 6×6 arcmin field.

SOAR Optical Imager.

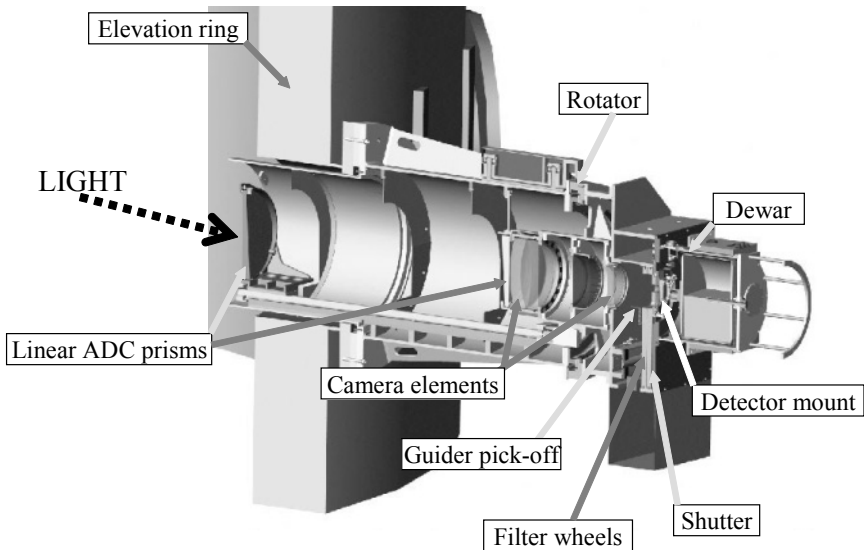


Figure 1. The SOAR Optical Imager

The Imager will be mounted at one of three bent Cassegrain ports on the telescope elevation ring. The light beam is sent to the Imager by the tertiary mirror, which directs an $f/16$ beam to either of two Nasmyth or three bent-Cassegrain foci. The Imager optics is designed to work down to atmospheric cutoff and incorporates a Linear Atmospheric Dispersion Corrector (ADC) and an $f/16$ to $f/9$ focal reducer to generate a $0.08''/\text{pix}$ scale for $15\text{ }\mu\text{m}$ CCD pixels.

The Imager incorporates its own instrument rotator: two filter wheels with five positions each and a shutter. A pick-off mirror is included to allow light to be fed to an external tip-tilt guide camera. Two Lincoln Labs CCID-

20 detectors configured as a $4K \times 4K$ minimosaic are housed in a dewar which can store 6 liters of LN₂. The dewar has a hold time of near fifty hours and weighs 24.5 kg filled with LN₂. The two CCID-20 CCDs will include the MBE backside treatment and a two layer AR coating for high QE. The minimosaic CCDs are operated by a SDSU-2 controller, which includes two video boards, one clock board, one timing board and one utility board. The controller is connected via a 0.5 m shielded cable to the hermetic connectors on the dewar. Similarly a SDSU-3 controller will operate the tip-tilt guider sensor, a CCD39-01 made by Marconi. Each controller uses a heat exchanger fitted with two glycol lines for cooling.

The general specifications for the CCID20 detectors are:

- Format: 2048 4096, 3-side-abutable
- Pixel size: $15 \mu\text{m} \times 15 \mu\text{m}$
- Full well 150 Ke^-
- 2 channels, output responsivity $10\text{-}15 \mu\text{V/e}^-$
- $\text{RON} = 2\text{-}2.5 \text{ e}^- @ 100 \text{ Kpix/sec.}$
- High resistivity bulk silicon ($7000 \Omega\text{-cm}$) thinned to $40 \mu\text{m}$
- Red QE boost and less fringing due to larger thickness
- Back-illuminated but not MPP
- AR coated (blue optimized), backside treated with MBE process
- CCD is epoxy glued on top of a stack of three slabs of aluminum nitride which get clamped onto a molybdenum mount

Each of the CCID-20s is epoxy bonded to a sandwich of three slabs of aluminum nitride – with excellent thermal conductivity and good CTE match to Silicon- which get clamped onto a molybdenum piece machined to ensure co-planarity of the two CCDs. The nominal separation between the two CCDs of the mini-mosaic is 0.5 millimeters. Signals from each CCID-20 are brought out by way of a flex circuit to a 37 pin micro-D-connector and then wired to two 41 pin hermetic connectors.

The Imager uses the ArcVIEW software package [4]. This is a LabVIEW based instrument control system originally developed under a contract with Imaginatics. The LabVIEW graphical user interface runs in a Linux environment on a PC. The ArcVIEW structure is based on a Client/Server scheme. Instrument control or observing scripts can be written in almost any scripting language including IRAF cl, UNIX csh, tcl, etc.

SilvermaxTM motors are used to move all the mechanisms except for the two filter wheels. SilvermaxTM motors are smart, are fed high level commands over an RS-485 link and are also controlled by a LabVIEW program. The shutter is a special design that includes a blade that closes in the same direction as it opens. The shutter is fast and has a very low profile design that fits in a space of only five mm. Minimum exposure time is 108

msec and the exposure time error over the whole detector field is less than 1 msec.

2.2 An IR Imager for the 4-m Blanco telescope.

The Infrared Side Port Imager, ISPI (eye-spy, see Fig. 2), provides wide field, moderate spatial resolution imaging at the Blanco 4-m telescope and will fit at F/8 focus on a sideport [1,3,5]. It is one component of a fixed instrument complement for future Blanco operations. The others are the Prime Focus MOSAIC for optical imaging, and Hydra for multiobject optical spectroscopy.

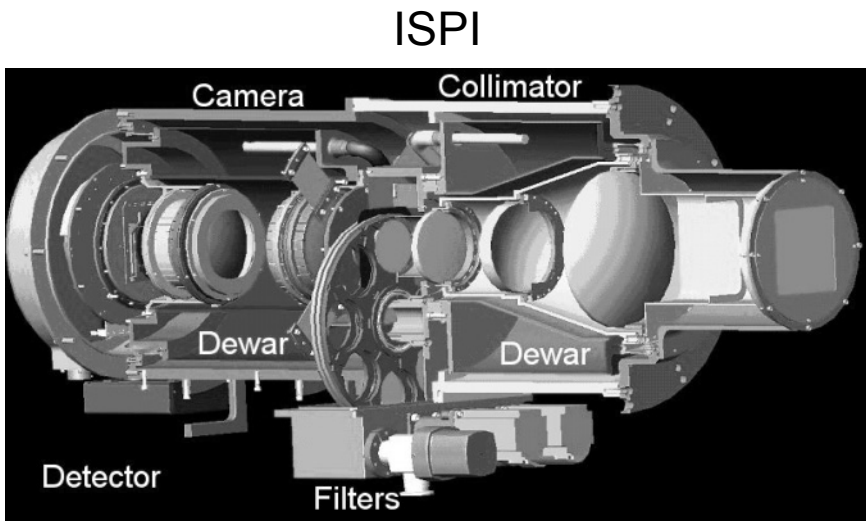


Figure 2. The configuration of the ISPI.

ISPI provides 1-2.5 μm imaging with a LN2 cooled 2K \times 2K HAWAII-2 HgCdTe array from Rockwell Scientific. With 0.6'' two-pixel sampling matched to f/8 IR image quality, ISPI covers a 10' \times 10' field. Like the SOAR Imager, ISPI will use a Leach SDSU-2 controller with software written in the LabVIEW environment, under LINUX.

The design separates into two halves with separate cryogen tanks that surround the optical path. The fore dewar has the entrance window, collimator, and filter wheel assemblies. The aft dewar holds the camera and detector assemblies. The dewars join to form a common vacuum envelope.

Some of the HAWAII-2 specifications are as follows:

- 2048 \times 2048 HgCdTe.
- Spectral response from 0.9-2.5 μm .
- 18 μm Pixel Pitch.

- Four independent quadrants, each read out by way of one or eight outputs.
- Signal conversion gain 3–6 mV/e⁻
- RON = 15 e⁻ nominally.
- Full well 100 Ke⁻.

The decision to implement the option of reading each quadrant through only one output amplifier was adopted after deciding that in this operation mode dark current, read noise and well capacity are all satisfactory for our imaging application.

The software design for ISPI is adapted from the vendor-supplied ArcVIEW [4] software package for the SOAR Optical Imager. Since ISPI will operate on the Blanco 4-m telescope, large pieces of software already exist for telescope communication and motor control.

3. FUTURE PROJECTS

3.1 Monsoon

As part of a collaborative effort to develop Monsoon [6], the new Image Acquisition System for NOAO, CTIO is handling the design of the IR Clock and Bias board. This board will generate a minimum of 32 bi-level clocks, with a 12 V to -12 V output amplitude and a slew rate no less than 20 V/msec. Also, 36 bias normal plus 8 fast varying bias voltages will be generated by this board. The fast bias voltages provide a DC voltage that can be modified in a way similar to clocks. Clocks, biases and fast biases are generated with 8-bit serial DACs. The output voltage range for all IR biases is +10 V to -10 V. 12-bit ADCs will be employed to provide telemetry of signals right before they leave the board: the clock and bias voltages as well as the current level for each of the bias signals. Each signal leaving the board is preceded by an analog switch in series with it, so signals to be fed to the detector are only enabled if the telemetry confirms that they are within the specified voltage range. As an additional convenience the clock signals will also be made available for oscilloscope inspection via a connection.

3.2 SOAR AO.

A concept study of an Adaptive Optics (AO) implementation for the SOAR 4.2-m telescope is in progress [7]. The 8-m Gemini-South telescope operates next to the SOAR telescope site. If both 4-m and 8-m telescopes are equipped with AO systems, diffraction-limited resolution at the 8-m would be 2 times higher, and sensitivity 4 times better than at SOAR.

Gemini AO will be only available in the near IR. SOAR will have a unique scientific niche in the visible-range AO.

Optical AO possibilities for SOAR are being studied. Two cases are being analyzed. The first option converts nights of average seeing into nights of excellent seeing by using UV-Rayleigh laser guide stars to get seeing improvement over a moderate 3' field of view. The second option is to use bright natural guide stars –and at a later date possibly Na laser guide stars- to attain diffraction limited imaging over a small field of view.

The basic AO configuration includes a deformable mirror that is employed to correct the deformations detected by a wavefront sensor. Detector options -with low readout noise, 64×64 to 128×128 formats and frame transfer capability- to implement a wavefront sensor with a capability to read out up to 1000 frames/sec for bright stars are being explored.

4. REFERENCES

- [1] Schmidt, R., 1999, *Optical Detectors for Astronomy II*, Kluwer Academic Publishers, pp. 71-75
- [2] Walker, A. et al., 2002, *The SOAR Optical Imager*, Proc. SPIE **4848**, to be published.
- [3] <http://www.ctio.noao.edu>
- [4] Ashe M.C. et al, 2002, *ArcVIEW: A LabVIEW-based Astronomical Instrument Control System*, Proc. SPIE **4848**, to be published.
- [5] Probst, R. et al., 2002, *ISPI: the Infrared Side Port Imager for the CTIO 4-m telescope*, Proc. SPIE **4848**, to be published.
- [6] <http://www.noao.edu/ets/monsoon/>
- [7] <http://www.ctio.noao.edu/~atokovin/soar/index.html>



Gerry Luppino pays in cash and asks all his customers to do the same.



*Speak no evil, see no evil, hear no evil.
(We are counting on these guys to keep Keck at the forefront of Astronomy.
From Left to Right: Al Honey, Jason Chin and Bob Goodrich.)*

STRANGE HAPPENINGS IN THE DUNGEONS

A new detector group at Caltech

Roger Smith

Department of Astronomy, California Institute of Technology (Caltech)

Abstract: *In anticipation of the 30-m California Extremely Large Telescope (CELT), Caltech is increasing its depth of expertise in instrumentation, adaptive optics and detectors, to a level not seen for many decades. A single detector group will address both optical and IR needs for science and wavefront sensors with common technology wherever possible. The team is deploying several cameras on Palomar Mountain, and is beginning work on the Keck IR Multi-object Spectrograph. Development projects include testing low-noise amplifiers for IR adaptive optics and testing the 32-channel ASIC for the Rockwell Hawaii-2RG.*

Key words: astronomical detectors, CELT

1. THE CALTECH YOU KNOW

The California Institute of Technology is a small university with a comparatively large budget, which focuses on research, while cultivating the next generation of leading researchers. It was founded by an astronomer (Hale), a physicist (Millikan), and a chemist (Noyes). Each left his mark on the direction of research, though the university has diversified and excelled in molecular biology, geology, medicine and engineering. It is the parent institution for NASA's Jet Propulsion Laboratory.

In 2002, 15% of the 3365 applicants were accepted as undergraduates. The student population is very small, 900 undergraduates and 1100 graduates, especially in relation to the 350 faculty, who in turn are supported by 2,580 staff. The 29 Nobel prizes awarded to Caltech graduates and faculty attest to the success of this mix.

Apart from cultivating researchers, a high priority has always been the funding of state-of-the-art research equipment, made possible through very generous donations. In the late 1930's and 40's the 5-m Palomar Telescope was constructed without the aid of computers or many other modern technologies, yet it remains a competitive facility today, thanks to a continuing investment in instrumentation, detectors and adaptive optics.

Caltech has provided half of the funding for the Keck 10-m telescopes, and has built several heavily used instruments for Keck, which include two Near IR Cameras and the (optical) Low Resolution Imaging Spectrograph.

The Caltech board of trustees not only wishes to continue the tradition of big science on big telescopes, but they believe they can raise the money for (a significant share of) a 30-m telescope dubbed the "California Extremely Large Telescope" (see Fig. 1). A team of experts drawn from Caltech and UCLA has prepared a design study for CELT called "The Green Book." This has been favorably reviewed by an external committee of experts, so that funding for the preliminary design review level is now possible. Estimates for the DPR (Design Phase Run) to approximately \$60M.



Figure 1. The California Extra Large Telescope, to scale.

2. NEW CREATURES IN THE DUNGEONS

Caltech's level of technical involvement in the development of the Keck telescopes was insufficient to build the standing army of technologists needed to initiate such a project like the CELT 30-m. Caltech did successfully build a number of major instruments for Keck which are very heavily used, such as the Near IR Cameras I and II, and the Low Resolution Imaging Spectrograph and its various upgrades. However this was done by a small band of hardy engineers directed by astronomers who visited from the upper floors and then continued their research. The emphasis was on building particular instruments rather than the acquiring infrastructure and cultivating the pool of expertise necessary to take on larger projects.

Nothing much appears to have changed above ground. This sensation is enhanced by the old bronze lanterns, medieval vaulted ceilings and exquisite drawings of the Palomar 200-inch by Russell Porter, which date back to the 1930's.

However, at the instigation of the Division Chair and the new Palomar Director, key technical staff have been hired with experience in telescope design (Steve Padin) and control systems (Doug McMartin), adaptive optics (Richard Dekany), instrumentation (Keith Taylor), and detectors (the author). The most recent additions to the instrumentation group are a programmer (Marco Bonati), electronics engineer (Dani Guzmán), a contract optical designer, and administrator/web-master. Positions are open for an instrument scientist, several mechanical engineers and an optical engineer. In total, fifteen new positions are to be filled in the next 12 months.

To accommodate this growth, the lower levels of the Robinson Building are being refurbished. The basement is already full with postdocs, graduate students, and Palomar administration, so the engineering group is being housed in the sub-basement, while 20,700 photographic plates are being moved to Palomar Mountain to make room for laboratories in the sub-sub-basement. As yet, no one occupies "the pit" which extends 3 or 4 floors further down, beneath the solar telescope. This ensures that there will be no shortage of dark rooms for detector testing.

3. THE DETECTOR GROUP

The detector group has very wide ranging goals, including the consolidation of technology and sharing of expertise between optical and IR detectors, both for scientific and wavefront sensors. The group will undertake the procurement, characterization, and detector deployment for Palomar, Keck and CELT

3.1 Projects Near Completion

3.1.1 Keck I: LRIS – New Blue Camera

The blue arm of the Low Resolution Imaging Spectrograph was recently upgraded with a 4K×4K mosaic of blue-optimized Marconi CCD44-82 CCD's and Leach-2 controller, offering not only a large increase in blue response but faster readout and lower noise. (May 2002)

3.1.2 Hale 200-inch: Double Beam Spectrograph upgrade

Blue optimized Loral 2688×512 CCD, Lesser thinned, UV-flooded. Fred Harris' CCD controller circa 1985. (Sep 2002)

3.1.3 Hale 200-inch: Wide-Field Infrared Camera (WIRC)

Deploy a HAWAII-2 array in this prime focus IR imager built by Cornell. Leach-2 controller, ArcView software. (Sep 2002)

3.2 New Instrumentation Projects

3.2.1 Keck IR Multi-Object Spectrograph

The most significant new instrumentation project at COO is the Keck IR Multi-Object Spectrograph (KIRMOS). This \$12M, six-year project will deliver a fully cryogenic imaging spectrograph to Keck with interchangeable cold slit masks, mapping a 4K×4K Rockwell HgCdTe mosaic into an 11' field. The detector component of this project will be a collaborative effort, with UCLA procuring and characterizing the detector, while Caltech will supply the 128-channel electronics and software, most probably in the form of fully characterized ASIC's. (PDR 2004)

3.2.2 Hale 200-inch: PISCO

Detector electronics and software for the Palomar Infrared Spectrograph with Cross-dispersed Optics (PISCO). A HAWAII 1K×2K detector will be used for the science channel and a HAWAII-1K for imaging and guiding. Leach-2 + ArcView. (in planning)

3.2.3 Hale 200-inch: Large Format Camera Upgrade

Upgrade software (to ArcView) and attend to some noise and reliability issues in the 6-CCD prime-focus mosaic camera.

3.2.4 Palomar 60-inch: Multi-Band Camera

Simultaneous G, R, I and Z band imager for remote observing of transient phenomena, particularly Gamma Ray Bursts detected by the

SWIFT satellite. SITe 2K×2K CCD, Leach-2 electronics + ArcView software. (in planning)

3.3 Development Projects

3.3.1 Controller development

We are participating in the ASTERIOD consortium and collaborating with the Monsoon project at NOAO to develop flexible and scalable detector control electronics and software. Maximum commonality is sought between the full range of IR, optical scientific and technical detector systems. We are likely to contribute mainly to software while providing review and testing of hardware.

3.3.2 Controller ASIC evaluation

Integrated circuits incorporating the entire electronics for operating detectors not only promises to save commissioning costs and simplify maintenance, but can offer new speed-performance options through highly parallel readout, with important implications for large IR focal planes, ultra-low-noise spectroscopic detectors and very low-noise high-speed adaptive optics sensors. These are all very relevant issues for CELT, so we will be evaluating controller ASIC's as they become available. Caltech has contracted Rockwell to package the 32-channel ASIC separately from the HAWAII-2RG, and will begin testing samples in conjunction with a science-grade H2-RG multiplexer at the end of 2002. Related integrated circuits such as clock buffers and amplifiers will be tested for cryogenic performance.

3.3.3 AO sensor evaluation

Caltech has contracted with Rockwell to develop very low-noise amplifiers for IR sensors which could be used for adaptive optics. The detector group will be testing these when they become available late this year.

3.3.4 New laboratories

About 1200 sq.ft. of the sub-sub-basement is being fitted out as electronics and detector labs, including clean room, cryogenic and vacuum support and dark rooms. Work is planned to improve detector characterization facilities such as an automated QE tester for optical and IR, automation of linearity, variance and ADC DNL tests, laser profilometer for measuring focal plane flatness, spot scanner to measure intra-pixel response and CCD alignment, large format projectors and so on.



The friends of the Keauhou Canoe Club offered to bring all the daring nerds for a ride on the Hawaiian outrigger canoes.



The participants could visit Captain Cook's monument on British soil!

NOAO OBSERVATORY PLANS

Barry M. Starr

National Optical Astronomical Observatory

Abstract: *The National Optical Astronomical Observatory (NOAO) has an ambitious long-range plan to support US astronomical research efforts. This plan includes large-scale new facilities such as LSST, GSMT, and NVO, as well as instrumentation development programs, and continuing efforts in detector research and development. This paper serves to provide a brief overview of the NOAO observatory plans.*

Key words: *Charge-Coupled Device (CCD), Infrared (IR), Focal Plane Assembly (FPA), mosaic, data acquisition, imager, MONSOON, Large Synoptic Survey Telescope (LSST), One Degree Imager (ODI), NOAO Extremely Wide-Field Infrared Imager (NEWFIRM), ORION, observatory.*

1. INTRODUCTION

The stated mission of NOAO is “to enable research and discovery in U.S. ground-based astronomy and promote public education, understanding, and support of astronomy and related sciences.”[1] The current long-range plan states that NOAO will: 1) support the use of state-of-the-art facilities, such as Gemini; 2) undertake the next generation of forefront facilities; 3) develop an integrated national observing system and work with the community to achieve a robust instrumentation capability; and 4) foster an environment in which the integration of astronomical research with public outreach and education is a routine part of daily activities and staff responsibilities. NOAO is strongly influenced by the recent Astronomy and Astrophysics Survey Committee (AASC) report [2], often referred to as the Decadal Survey. In the Decadal Survey are detailed a range of new initiatives such as the LSST, GSMT, TSIP, NVO and other efforts. NOAO is to play a key role in all these efforts.

2. DETECTOR RESEARCH AND DEVELOPMENT

NOAO is continuing its long-standing role as a center for detector research and development. One of the ongoing efforts is the development of a next-generation $2K \times 2K \times 1-5 \mu m$ InSb focal plane assembly (FPA) known as ORION (see Fig. 1). ORION is an extension of the successful Aladdin $1K \times 1K$ program with Raytheon Infrared Operations (RIO) in Santa Barbara, formerly known as SBRC (Santa Barbara Research Center). ORION is a collaborative effort amongst NOAO, the U.S. Naval Observatory, and NASA Ames Research Center.

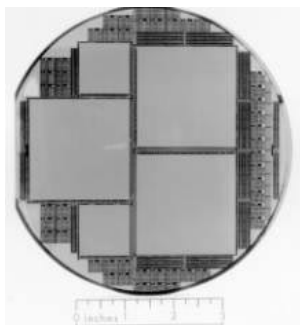


Figure 1. The ORION focal plane assembly.

Efforts are also on going in the OUV where NOAO is collaborating with the Lawrence Berkeley National Laboratories (LBNL) and Lick Observatory in the evaluation of high-resistivity deep depletion CCDs.

NOAO, in collaboration with Steward Observatory and Lucent Technologies/Bell Labs, is in the process of specifying and evaluating optical detector technologies for the LSST [3,4] project detailed later in this paper. These include high-resistivity back-illuminated CCDs, orthogonal transfer CCDs, silicon PIN diodes on CMOS multiplexor readouts, and monolithic CMOS devices.

All of these detector technologies and research efforts are discussed in more detail in other papers in these proceedings.

The MONSOON Image Acquisition System is a scalable, high-performance, multi-channel data acquisition system designed to provide “detector-limited” performance for all imaging devices needed for the next-generation of systems under development at NOAO and the astronomical community. It is being developed in collaboration with a number of external institutions and is a full “open-source” development effort for the astronomical community. MONSOON is designed to support all imaging system needs: single OUV or IR detector to large-scale mosaics, technical as well as scientific applications. For more information, MONSOON is detailed in a paper in these proceedings [5], or visit www.noao.edu/ets/monsoon/.

3. U.S. GEMINI PROGRAM

NOAO is tasked with acting as the interface of the U.S. astronomical research community to the twin 8-m telescopes of the International Gemini Project. To this end NOAO has created the NOAO Gemini Science Center, which provides remote operations from Tucson to both Mauna Kea and Cerro Pachon (see Fig. 2). In addition, NOAO will continue to develop and support OUV and IR instrumentation and detector technology for Gemini [6].



Figure 2. “Gemini South”- The Gemini Observatory’s telescope in Cerro Pachon, Chile

Currently, Phoenix, a high-resolution $1K \times 1K$ $1-5 \mu m$ imaging spectrometer, and ABU, a $1K \times 1K$ IR Imager are operating at Gemini South with GNIRS, a $1-5 \mu m$ Near Infrared Long-Slit Spectrometer to be in commissioning later this year. The Gemini Array Controller at Gemini North is part of the NIRI instrument developed at UH. NOAO has collaborated on the GMOS and bHROS optical instrumentation efforts as well. NOAO has just completed a design study for the GSAOI $4K \times 4K$ $1-2.5 \mu m$ NIR Imager for the Gemini MCAO system. The NOAO Data Products Program is working to strengthen data reduction, pipelining and analysis tasks for the Gemini data products.

4. KPNO AND CTIO

NEWFIRM (see Fig. 3) [7] is a $4K \times 4K$ $1-2.5 \mu m$ IR wide-field imager currently under design for both the Mayall and Blanco 4-m telescopes at Kitt Peak and Cerro Tololo, respectively. NEWFIRM will have an array of four $2K \times 2K$ butttable focal plane array (FPAs). These FPAs are the ORION $2K \times 2K$ InSb described in the Detector Research and Development section of this paper. Goddard Space Flight Center and the Space Telescope Science

Institute are developing an NGST prototype multi-object NIR spectrograph called IRMOS for use at KPNO.

Ricardo Schmidt describes the instrumentation efforts at CTIO in a paper also in these proceedings [8].

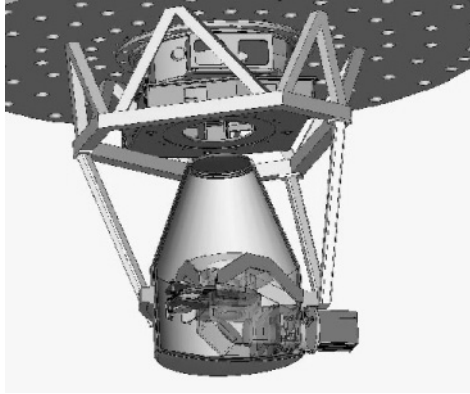


Figure 3. The NEWFIRM imager.

QUOTA is an $8K \times 8K$ optical imager based on a mosaic of four $4K \times 4K$ orthogonal transfer arrays (OTAs) designed for the WIYN 3.5-m telescope. QUOTA, which stands for “QUad OTA,” is intended as a scalable design component for the follow-on One Degree Imager (ODI) project, which is a $32K \times 32K$ mosaic imager. ODI will effectively be 16 QUOTAs in a single focal plane [9].

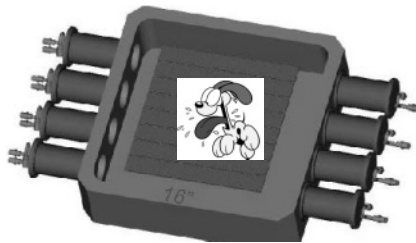


Figure 4. The QUOTA optical imager.

5. NVO

The National Virtual Observatory (NVO) is a development effort to establish a federated system of astronomical databases spanning the electromagnetic spectrum. NVO is a project of national scale requiring partnerships of many institutions and organizations spanning the range of national centers, universities, and the private sector. NOAO's role will be to function as a focal point for assembling the core scientific, technical, and

management skills for development of the NVO, to serve as an Optical/IR node, and lead the development of the data management system. For more information visit <http://www.us-vo.org/>.

6. LSST

The Large-aperture Synoptic Survey Telescope (LSST) (see Fig. 5) is an 8.4-m telescope with a 3-degree field and better than 0.2" pixel sampling. The telescope is a 3-mirror design with an f-ratio of 1.25, designed to "go faint, fast."

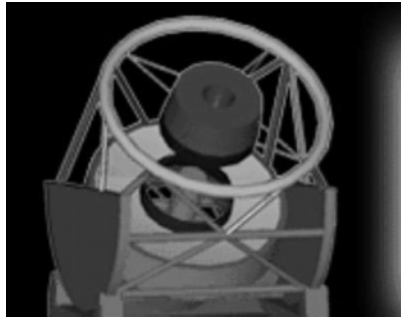


Figure 5. The LSST telescope.

LSST is estimated to provide a digital survey of the entire visible sky every few weeks to a deep limiting magnitude (~ 24 magnitude), LSST will fulfill a broad range of science goals such as: detection of near-earth objects, supernovae research, study of variable objects, gravitational lensing, etc. The LSST will have a single optical instrument (0.3 to 1 μm) which will be a 55 cm focal plane fully-filled with a close-butted mosaic of 10 μm pixel devices. The current design employs 568 2K \times 2K devices, over 2.2 Gigapixels (see Fig. 6), and would translate in size to a 47K \times 47K square focal plane. The typical integration time of LSST is anticipated to be 10 sec with a maximum 2 sec read time and better than 5 e^- readnoise. The MONSOON Image Acquisition System has been designed to address the needs of the LSST camera.

NOAO plans to facilitate the community-based effort to construct the LSST with the project proceeding in four phases: 1) generate fully-coasted proposal for construction, 2) during proposal evaluation, continue to develop the plan especially in the areas of evaluating detector design, data acquisition, and data management, 3) construction, 4) operation and distribution of data. The nucleus of the project will be Steward Observatory, Lucent Technologies/Bell Labs, LBNL, NOAO, as well as other institutions. For more information visit <http://www.noao.edu/lsst/>.

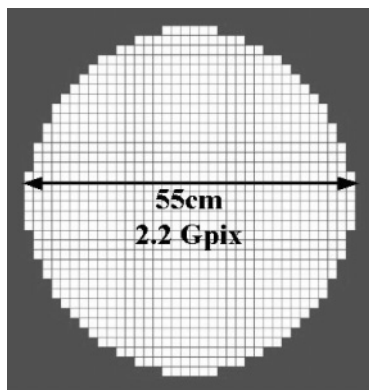


Figure 6. The LSST 47K×47K square focal plane.

7. GSMT

The Giant Segmented Mirror Telescope (see Fig. 7) is a proposed 30-m optical/infrared ground-based telescope.

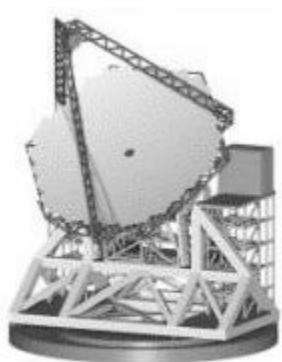


Figure 7. The GSMT telescope.

NOAO was charged with the essential roles of involving and representing the U.S. community in all phases of GSMT development and operation. The AURA (Association of Universities for Research in Astronomy) New Initiatives Office is leading this effort. Near-term goals are a summary of key design issues, initial trade studies of key technologies, development of cost and performance models, and a proposal for a preliminary GSMT design study. For more information visit <http://www.aura-nio.noao.edu/>.

8. TSIP

The Telescope System Instrumentation Program (TSIP) is a 5 million dollar per year program to fund the development of instruments for the independent observatories and provide time on these telescopes to the community. NOAO role will largely be management and administrative support. For more information visit <http://www.noao.edu/system/tsip/>.

9. CONCLUSION

NOAO has a wide-ranging plan for a mixture of science support, next-generation observatory facilities design, OUV and IR instrumentation and detector research and development, as well as educational outreach. The LSST effort and GSMT efforts are of an impressive scale and will obviously be accomplished through collaborative efforts with many institutions. The instrumentation development efforts focus primarily on large mosaics of both IR FPAs and CCDs, with a defined focus to push new limits in performance both in data rates and quality.

10. REFERENCES

- [1] NOAO Long-Range Plan: FY 2002-2006, www.noao.edu
- [2] National Research Council Astronomy and Astrophysics Survey Committee, 2000, *Astronomy and Astrophysics in the New Millennium*, National Academy Press.
- [3] Starr, B.M. Claver, C. Wolff, S., Tyson, J.A., Lesser, M.P., Daggert, L., Dominguez, R., Gomez, R.R., Jr., Muller, G., 2002, *LSST Instrument Concept*, SPIE Conf. Proceedings, vol. **4836**, p. 228.
- [4] Lesser, M.P., Tyson, J.A., 2002, *Focal plane technologies for LSST*, SPIE Conf. Proceedings, vol. **4836**, p. 240.
- [5] Barry M. Starr, Nicholas Buchholz, Gustavo Rahmer, Jerry Penegor, Ricardo Schmidt, Michael Warner, K. Michael Merrill, Charles F. Claver, Y. Ho, Kaviraj Chopra, Eduardo Mondaca, Chirag Shroff, D. Shroff
- [6] Simons, D.A., Gillet, F., Oschmann, J., Mountain, M., Nolan, R., 2000, *Gemini instrument program*, SPIE Conf. Proceedings, vol. **4008**, p. 28.
- [7] Autry, R., Probst, R., Starr, B.M., Abdel-Gawad, K., Blakley, R., Daly, P., Dominguez, R., Hileman, E., Liang, M., Pearson, E.T., Shaw, R., Tody, A., 2002, *NEWFIRM: The Widefield IR Imager for NOAO 4-m Telescopes*, SPIE Conf. Proceedings, vol. **4841**, p. 525.
- [8] Schmidt, R., 2002, *Detectors at CTIO: Present Status and Future Plans*, these proceedings, pg. 247.
- [9] Jacoby, G.H., Tonry, J., Burke, B., Claver, C., Starr, B.M., Saha, A., Luppino, G., Harmer, C.F.W., 2002, *WIYN one degree imager (ODI)*, SPIE Conf. Proceedings, vol. **4841**, p. 217.



A nice portrait of Giovanni and Giovanna Bonanno. In the back Barry Starr, Roger Smith, Bonner Denton, Peter Fochi, Peggy and Peggy.



Nobody got burned during this typical Hawaiian sunset! (Courtesy P. Sinclair)

MONSOON IMAGE ACQUISITION SYSTEM

Barry M. Starr, Nicholas Buchholz, Gustavo Rahmer, Jerry Penegor, Ricardo Schmidt, Michael Warner, K. Michael Merrill, Charles F. Claver, Y. Ho, Kaviraj Chopra, Eduardo Mondaca, Chirag Shroff, D. Shroff
National Optical Astronomical Observatory (NOAO)

Abstract: *The MONSOON Image Acquisition System is a scalable, multichannel, high-speed data acquisition system designed for the next-generation optical/infrared detectors and mosaic projects currently under development at NOAO. MONSOON is more than a controller; rather it is new image acquisition architecture, providing a total solution to “detector-limited” image acquisition for all astronomical detectors, scientific and technical, OUV to IR. MONSOON addresses detector-interface as well as the significant data flow and processing issues large-scale imaging systems require. The Monsoon effort is a full-disclosure “open-source” development effort by NOAO in collaboration with the CARA ASTEROID project for the benefit of the astronomical community.*

Key words: *Charge-Coupled Device (CCD) controller, Infrared (IR) controller, mosaic, data acquisition, imager, pixel server, Large-aperture Synoptic Survey Telescope (LSST), One Degree Imager (ODI), NOAO Wide-Field Infrared Imager (NEWFIRM), ORION*

1. INTRODUCTION

The MONSOON Image Acquisition System has been designed to address the needs of the next-generation NOAO imaging projects, which include:

- ORION (2K×2K) 1-5 μm InSb development [1]
- NEWFIRM (4K×4K) 1-2.5 μm imager for KPNO and CTIO [2]
- QUOTA (8K×8K) orthogonal transfer optical imager for WIYN [3]
- ODI (32K×32K) orthogonal transfer optical imager for WIYN [3]
- LSST (47K×47K) instrument [4,5]

MONSOON focuses on all the issues associated with “detector-limited” data acquisition. In MONSOON parlance, “detector-limited” encompasses all the requirements related to detector interface including noise, linearity, dynamic range, readout rates, readout modes, etc. Concerns in previously neglected areas of controller design have been addressed, such as physical size, form factor issues, power dissipation, and excess heat near the telescope. Total cost of ownership is a fundamental design criteria, which includes system assembly, test, and integration time, along with long-term reliability and the on-going cost of operation. Finally, quality of the image data is paramount. This includes strategies to insure data integrity, stability, calibration, and verification.

In reference to the torrential summer rains of Tucson, and the flood of pixel data produced by these large-scale next-generation imaging systems, this system is named MONSOON. MONSOON is a proper name, not an acronym, and is inspired by the classic model developed by Kristian and Blouke of the CCD as an array of buckets catching raindrops [6].

It is apparent that the future of imaging devices will eventually become “photons in bits out.” One implication of this is that system designers will no longer need to provide an “analog interface” (clocks, biases and digitization), but rather simply a “digital interface.” Anticipating this evolution in focal plane technology, the MONSOON architecture partitions the system into two fundamental subsystems: the image data acquisition system (digital domain, non-sensor specific) and the detector interface. MONSOON is designed to support digitizing focal planes as well as conventional analog interface devices. The system has a modular software and hardware architecture composed of separable elements, which can then be configured to form the appropriate and cost-effective system for a wide range of applications

The fundamental MONSOON vision is that any new image acquisition system design should: 1) provide detector-limited performance; 2) embrace all the relevant imaging devices and systems currently existing, in the planning stages, or on the visible horizon; 3) consider the “total” view of the observatory as an integrated system where the output is high-quality science data ready to fuel the production of scientific papers and the advancement of astronomy; and 4) maximize “open-shutter” integration time, by minimizing losses due to overheads and downtime due to system failures, thereby maximizing observing time.

2. SYSTEM ARCHITECTURE

MONSOON is based on a scalable network of powerful yet low-cost of LINUX-based PC's, each supporting a commercial 1 Gb/sec (or 2.4 Gb/sec)

fiber-optic link. This architecture, shown in Fig. 1, yields an attractive digital communications and processing platform for large imaging systems.

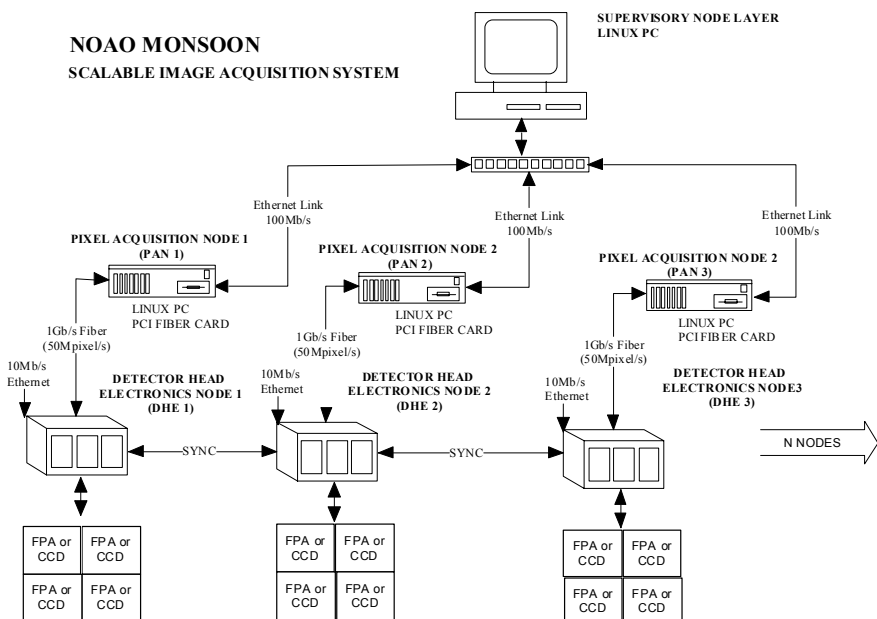


Figure 1. MONSOON Scalable Image Acquisition System Architecture. Illustrates a possible N node implementation. Nodes are added to the system as needed and/or as costs permit.

There are three primary layers in the system: the Supervisory Node layer, the Pixel Acquisition Node (PAN) layer, and the Detector Head Electronics (DHE) layer. These are logical partitions that usually map to a physical partition but not always. For example, in the case of a single Detector Head Electronics system as used for ORION, NEWFIRM, or QUOTA, the Supervisor Layer and the PAN Layer will likely be on the same physical PC.

Within the system there will only be one Supervisor Node, orchestrating the entire system and providing a single point interface to MONSOON, hiding the details of how many PANs are present to external systems. With regard to the PAN and DHE there are two fundamental “operating states”: Master and Slave. Within a multiple node implementation there can be at most one Master Node Pair, all others must be configured as Slave Node Pairs. A Master Node controls the triggering of an exposure and exposure timing. Each Slave Node Pair is “armed” and waiting for an exposure trigger that comes from a single Master, then all nodes run in synch. The entire N node system can be configured as Slave Nodes with the logical Master Node being an external system such as an AO system, chopper signal, time

sequencer, etc. The DHEs are hard synched together by a distributed clock and serial sync (control) line.

The Supervisor Layer handles all interfaces to the external systems and entities. This is the only layer that has knowledge of the total system configuration (how many PAN/DHE Node Pairs are present). It handles system security, data and error logging and system error recovery functions.

The PAN Layer handles all interfaces to the DHE. Each PAN knows only about itself and its DHE. It performs all exposure sequencing and data processing related to multiple reads of the detector associated with image co-additions and performs all image de-scrambling of pixel data. It is responsible for maintaining system diagnostics, error detection and recovery for the associated DHE. System status and details of these functions are passed to the supervisor for “system” logging and interface functions.

The DHE will provide the lowest-level sequence control, readout patterns for the detector, exposure integration timing, and shutter control. All primary communications, both command/response and pixel data, is over the fiber interface. The optional Ethernet interface is used for secondary diagnostics, system configuration, and error recovery if the fiber interface is disabled. The system will run fully without the Ethernet connection.

Three communication links should be detailed: the fiber-optic link, the synchronization link, and the Ethernet link. The bi-directional 1 Gb/sec or 2.4 Gb/sec fiber-optic links are commercially available standard products from Systran Corp [7]. These links provide high-speed full-duplex bi-directional communication both from the DHE to the PAN. The bi-directional nature of these links can be significant for some applications such as QUOTA and ODI [3], where the PAN will be doing centroid calculation and determining the required image shifts in the OTACCD cells. The second communication link connects multiple DHE nodes and is used for synchronization purposes. To support low-noise performance, all clocks for all imaging devices must be synchronized to avoid crosstalk and clock coupling. A low-voltage differential-signaling (LVDS) clock pair distribution network with skew control is provided to tie all system components together into a single synchronized whole. The third communication network is ground-isolated 10-base-T Ethernet. Each DHE node has an option for an embedded micro-controller with Ethernet and TCP/IP network support. This link is for system configuration and diagnostic/error recovery only. It is not part of the system “pixel” path, and is provided for system support only.

The MONSOON architecture is scalable at multiple levels:

- the DHE level, where boards can be added as needed
- the fiber-optic link level, which can be scaled from 1 to 2.4 Gb/s
- the PAN PC level, faster CPU more memory as needed

- the data processing/fiber network level, where the fiber can broadcast from 1 DHE to multiple PCs
- the system level, where PAN-DHE node-pairs can be added to an arbitrarily large number

2.1 Detector Head Electronics

The DHE nodes shown in Fig. 2 will typically be comprised of three types of boards: 1) Master Control Board, 2) Clock and Bias Board, and 3) Video Acquisition Board.

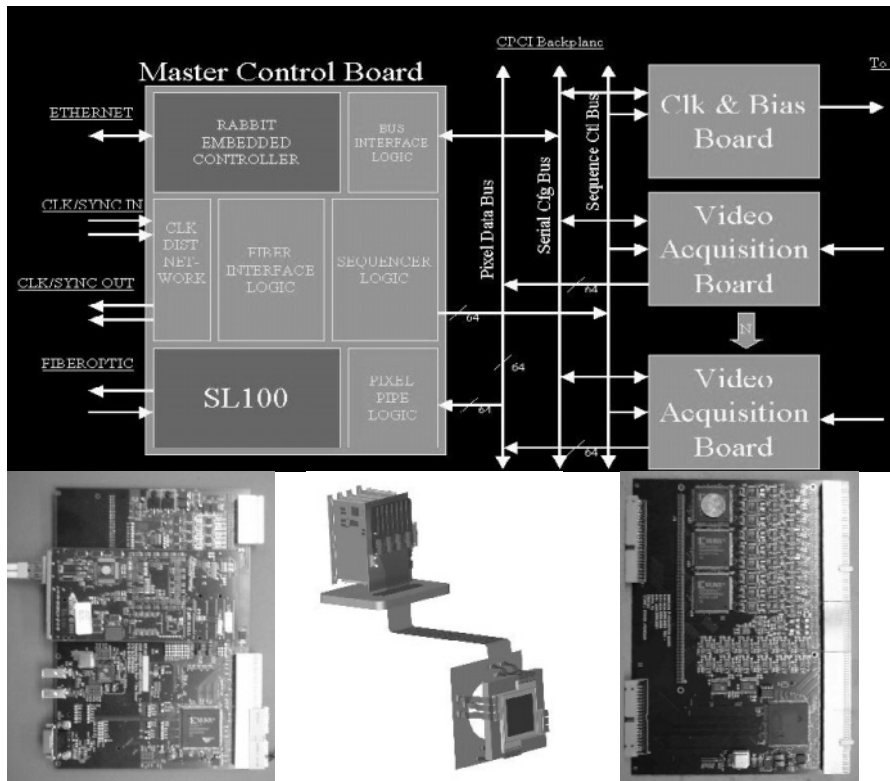


Figure 2. MONSOON DHE Architecture. (top) The three main components of the system and interconnection. (bottom-left) Master Control Board. (bottom-center) DHE to focal plane interface-center. (bottom-right) 36-Channel IR Acquisition Board.

The Master Control Board constitutes the “digital domain” boundary of the system that will be common to all systems, and independent of detector technology. The analog portions of the system are best served with a variety of boards that can be used as needed, tailored and/or even repackaged for individual project needs.

The DHE is designed to be extremely modular and very simple to assemble, configure, test, and support. Standard configuration will be a 6U Eurocard format. It will employ two backplanes for signal distribution: a standard Compact PCI backplane for digital signal and digital DC power distribution, with a custom analog backplane for analog power and interface to the focal plane. This backplane is fully specified in the MONSOON ICD 7.0 [8]. The digital backplane will follow CPCI signal integrity standards but not the CPCI signal timing protocol in order to maximize system performance for our application. The analog backplane will incorporate all necessary overvoltage and static protection circuitry for the focal plane, and will be an integral part of the dewar assembly and focal plane interconnect through the use of rigid-flex technology.

2.2 Software Architecture

MONSOON is an image acquisition system or “pixel server.” Basically, within a classic client-server architecture model of an observatory, the “pixel server” is the system that provides image data when requested by some general “client.” This client can be an instrument control system, and observatory control system, or some other external entity. Figure 3 is a context level dataflow diagram illustrating this.

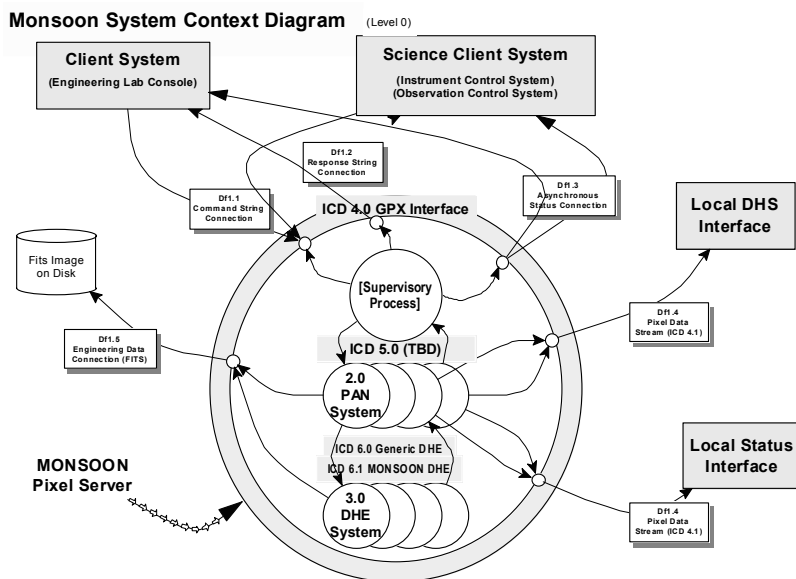


Figure 3. MONSOON System Data Flow Diagram. This shows the major data flows into and out of the MONSOON.

The interface definition to MONSOON is described in the Generic Pixel Server Interface Control Document [9]. This is a proposed astronomy-wide

standard for defining the interface to a “generic pixel server,” which may be a system other than MONSOON.

The MONSOON software has strong interface control definition (ICD) and will enforce modular design. The implementation is shown in Fig. 4. The PAN software will support multiple DHE implementations including the Lick Guider and SDSU Controller, in addition to the MONSOON DHE. This is to increase flexibility and provide for backward compatibility to existing systems. It should be emphasized that the system design stresses that all components, hardware and software, are modular and separable and thus can be easily upgraded.

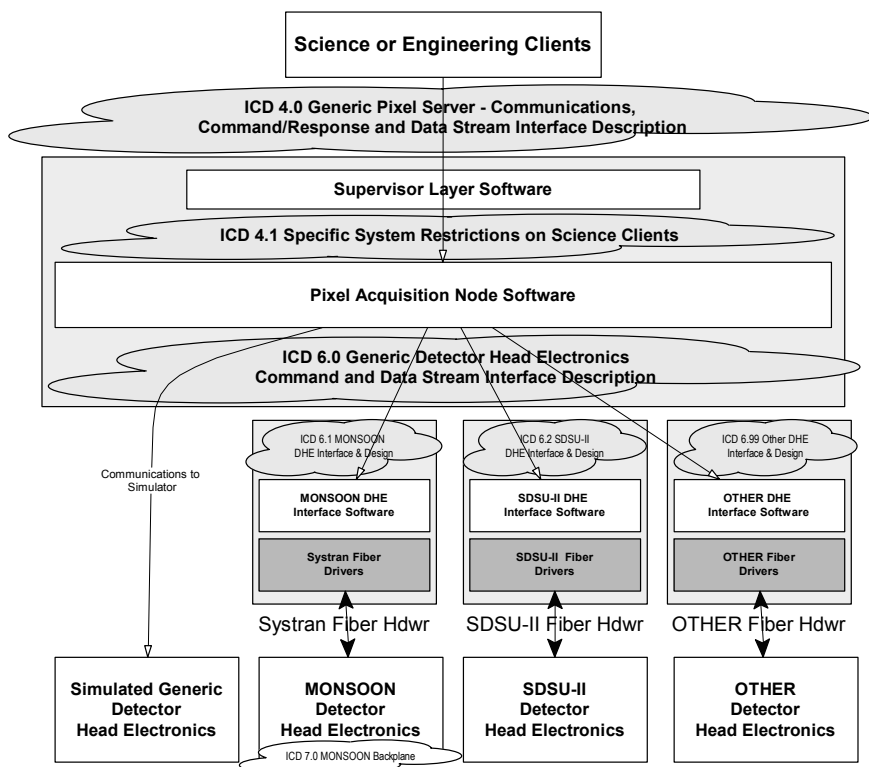


Figure 4. MONSOON Interface Control Layers. This illustrates the ICD layers within MONSOON and support for multiple DHEs.

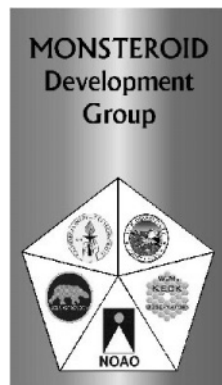
3. CONCLUSION

MONSOON is a forward-looking solution to the needs for next-generation astronomical imaging. The design is high-performance, scalable and cost-effective. MONSOON is more than a controller, but rather an

image acquisition system or “pixel-server” providing a total integrated solution to imaging needs ranging from science observing to laboratory research and development. MONSOON is a full “open-source” cross-institutional development effort for the entire astronomical community.

4. ACKNOWLEDGEMENTS

MONSOON has benefited greatly by the support and interaction of the ASTERIOD development group. NOAO looks forward to the formal collaboration of the MONSOON and ASTERIOD efforts into a single “MONSTEROID” project (see the figure at right).



5. REFERENCES

- [1] Fowler, A., Merrill, M., Ball, W., Henden, A., Vrba, F., McCreight, C., 2002, *The Largest Infrared Hybrid Focal Plane in Production*, SPIE Conf. Proceedings, vol. **4841**, p. 853.
- [2] Autry, R., Probst, R., Starr, B.M., Abdel-Gawad, K., Blakley, R., Daly, P., Dominguez, R., Hileman, E., Liang, M., Pearson, E.T., Shaw, R., Tody, A., 2002, *NEWFIRM: The Widefield IR Imager for NOAO 4-m Telescopes*, SPIE Conf. Proceedings, vol. **4841**, p. 525.
- [3] Jacoby, G.H., Tonry, J., Burke, B., Claver, C., Starr, B.M., Saha, A., Luppino, G., Harmer, C.F.W., 2002, *WIYN one degree imager (ODI)*, SPIE Conf. Proceedings, vol. **4841**, p. 217.
- [4] Starr, B.M. Claver, C. Wolff, S., Tyson, J.A., Lesser, M.P., Daggert, L., Dominguez, R., Gomez, R.R., Jr., Muller, G., 2002, *LSST Instrument Concept*, SPIE Conf. Proceedings, vol. **4836**, p. 228.
- [5] Lesser, M.P., Tyson, J.A., 2002, *Focal plane technologies for LSST*, SPIE Conf. Proceedings, vol. **4836**, p. 240.
- [6] Janesick, J., 2001, *Scientific Charge-Coupled Devices*, SPIE Optical Engineering Press, xvi, p.23, SPIE Press monograph PM83.
- [7] Systran Corporation, <http://www.systran.com>
- [8] Rahmer, G., 2002, *NOAO Document - Interface Control Document 7.0 DRAFT – MONSOON Detector Head Electronics (DHE) Backplane Specification*, <http://www.noao.edu/ets/monsoon/>
- [9] Buchholz, N., Daly, P., Starr, B., 2002, *NOAO Document - Interface Control Document 4.0 - Generic Pixel Server Communications, Command/Response and Data Stream Interface Description*, <http://www.noao.edu/ets/monsoon/>

SECTION III:

INSTRUMENTATION

IMPROVED CCD DETECTORS FOR HIGH SPEED, CHARGE EXCHANGE SPECTROSCOPY STUDIES ON THE DIII-D TOKAMAK

Keith H. Burrell¹, Punit Gohil¹, Richard J. Groebner¹, David H. Kaplan¹, John I. Robinson¹, Daniel M. Thomas¹, and David G. Nilson²

¹General Atomics, ²Lawrence Livermore National Laboratory

Abstract: *Charge exchange spectroscopy allows the determination of ion temperature, poloidal and toroidal velocity, impurity density and radial electric field, E_r , in high temperature tokamak plasmas. Charge exchange spectroscopy has been one of the workhouse diagnostics of the Doublet III and DIII-D tokamaks since 1983. The ability to determine the E_r , for example, has been essential in testing the model of $E \times B$ shear expression of turbulence. For the 2000 experimental campaign, we have replaced the intensified photodiode array detectors on the edge portion of the system with advanced CCD detectors mounted on faster (f/4.7) spectrometers. This combination has improved the photoelectron signal level by approximately a factor of 20 and the signal to noise by a factor of 2 to 8, depending on the absolute signal level. A major portion of the signal level improvement comes from the improved quantum efficiency of the back-illuminated, thinned CCD detectors (70- 85% for the CCD versus 10-20% for the image intensifier) with the remainder resulting from faster spectrometers. The CCD camera also allows shorter minimum integration times: 320 μ s while archiving to PC memory and 150 μ s using temporary storage on the CCD chip. The PC memory option allows up to 4096 spectra per tokamak shot, which is only limited by available memory. The faster on-chip storage is limited to 254 spectra. Results from tokamak plasma shots will also be discussed.*

Key words: *tokamak plasma, Charge-Coupled Device (CCD) detectors, charge exchange spectroscopy*

1. INTRODUCTION

The tokamak plasmas utilized in magnetic fusion research provide access to some of the longest duration, highest temperature plasmas on earth. For example, on the DIII-D tokamak, plasmas lasting up to 10 sec have been produced with ion temperatures up to 27 keV and electron temperatures up to 15 keV in toroidal plasmas with 1.7 m major radius, 0.65 m half width and 2.5 m vertical height. Typical particle densities of these plasmas range from $2.0 \times 10^{19} \text{ m}^{-3}$ to $2.0 \times 10^{20} \text{ m}^{-3}$. Spectroscopic measurements of line radiation from highly ionized atoms provide one of the key techniques for determining the plasma parameters in tokamak discharges.

2. CHARGE EXCHANGE SPECTROSCOPY

Charge exchange spectroscopy [1] allows the determination of ion temperature, poloidal and toroidal velocity, ion density and radial electric field, E_r , in high temperature tokamak plasmas. This technique is based on the excitation of visible and near UV radiation from hydrogen-like and lithium-like ions via charge exchange with high energy (80 keV) neutral deuterium beams injected into the plasma. Spectroscopic lines used for these measurements include He II (468.6 nm), C IV (465.83, 772.62 nm), B V (494.47 nm), C VI (343.37, 529.05, 771.68 nm), O VIII (297.57, 434.04 nm), F IX (342.9, 479.4 nm), Ne X (524.90 nm), Ar XVI (346.3 nm), Ar XVIII (344.9 nm), Ca XXVIII (344.9 nm) and Ca XX (346.3 nm). Charge exchange spectroscopy has been one of the workhorse diagnostics on the Doublet III and DIII-D tokamaks since 1983 [2]. The ability to determine E_r , for example, has been essential in testing the model of $E \times B$ shear suppression of turbulence [3], which has revolutionized our understanding of turbulence in magnetized plasmas.

A key issue for charge exchange spectroscopy is the need for multiple spatial views, demanding the detection of multiple spectra, while simultaneously obtaining millisecond time resolution. Our present system acquires spectra simultaneously from 40 different spatial locations across the plasma at 750 different times during the discharge. Our initial spectroscopic system utilized intensified linear photodiode array detectors [4,5]. For the 2000 experimental campaign on DIII-D, we replaced the intensified photodiode array detectors on a portion of our system with advanced CCD cameras [6] mounted on faster (f/4.7) spectrometers [7]. The 16 spatial locations in this portion of the system are concentrated on the edge of the tokamak plasma, which exhibits some of the steepest spatial gradients and the most rapid changes in temperature, rotation speed and E_r . These cameras utilize a 652x488 pixel Pluto chip from SITE [8]. We are now in the midst of a similar upgrade on the portion of the system that views the plasma core.

Relative to the intensified diode system, the new spectroscopic system has improved the photoelectron signal level by approximately a factor of 20 and the signal to noise by a factor of 2 to 8, depending on the absolute signal level. A major portion of the signal level improvement comes from the improved quantum efficiency of the back-illuminated, thinned CCD detector (70-85 % for the CCD versus 10-20% for the image intensifier) with the remainder coming from the faster spectrometer. The CCD cameras also allow shorter minimum integration times: 320 μ sec while archiving to PC memory and 150 μ sec while using temporary storage on the CCD chip. The PC memory option allows up to 8192 spectra per camera per tokamak shot, limited only by available memory, while the faster on-chip storage is limited to 254 spectra.

2.1 The Design

A detailed description of the design of the spectroscopic system and the detectors developed for the 2000 campaign has been published previously [9]. A key design feature is use of the split frame architecture of the CCD chip to measure two spectra per chip while maintaining high-speed readout. A simple optical coupling system utilizing two planar mirrors allows the use of two CCD cameras per spectrometer, thus reducing the number of spectrometers required by a factor of two.

2.2 Results

An example of the high-speed spectroscopic results produced by the upgraded CCD system is shown in Fig. 1. This shows the line brightness, Doppler temperature and toroidal velocity for several points near the plasma edge while the plasma is undergoing repetitive bursts of Magneto-hydrodynamic (MHD) oscillations called Edge Localized Modes (ELM). These MHD modes periodically reduce the confinement in the edge plasma, causing the reductions in temperature and rotation shown in the figure. One of these ELM bursts is shown in Fig. 1. Also shown in Fig. 1 is the D_α brightness from another diagnostic. D_α change is used as a marker for the onset of the ELM. The CCD data for this figure was taken at 0.332 ms integration time as part of a detailed study of the ELM dynamics. The distinct changes seen in rotation and temperature in 0.332 ms demonstrate the excellent time resolution of the CCD cameras.

3. ACKNOWLEDGEMENTS

This work was supported by the U.S. Department of Energy under Contract Nos. DE-AC03-99ER54463 and W-7405-ENG-48.

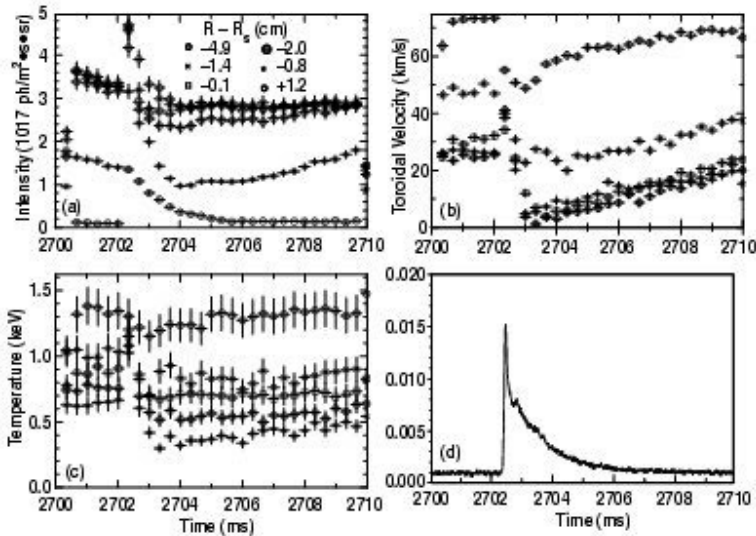


Figure 1. Plot of (a) edge C VI 529.05 nm line brightness, (b) toroidal rotation determined from C VI Doppler shift, (c) ion temperature determined from C VI Doppler line broadening and (d) D_{α} brightness from the divertor region of the D III-D tokamak. The measurements in (a-c) are made at the locations indicated. These locations (in cm) are relative to the magnetic separatrix, which marks the edge of the plasma as defined by the location of the last closed magnetic flux surface. The time range shown includes the time when an edge MHD instability (Edge Localized Mode) occurs, which rapidly alters the brightness of the C VI and D_{α} lines, and quickly changes the rotation and ion temperature. The measurements in (a-c) are made at 0.332 ms intervals by the CCD cameras discussed in the main text. Note that on the locations closer to the plasma edge, the rotation and ion temperature first increase right after the ELM before decreasing again. The behavior would not have been detectable without the excellent time resolution of the CCD camera and the high quantum efficiency, which allows gathering sufficient amount of photons to make good measurements in short time intervals.

4. REFERENCES

- [1] R.C. Isler, 1994, Plasma Physics and Controlled Fusion, **36**, p. 171.
- [2] R.J. Groebner, et al., 1983, Appl. Phys. Lett., **43**, p. 920.
- [3] K.H. Burrell, 1997, Phys. Plasmas, **4**, p. 1499.
- [4] R.P. Seraydarian, K.H. Burrell, N.H. Brooks, R.J. Groebner, and C. Kahn, 1986, Rev. Sci. Instrum., **57**, p. 155..
- [5] R.P. Seraydarian, K.H. Burrell, and R.J. Groebner, 1988, Rev. Sci. Instrum., **59**, p. 1530.
- [6] PixelVision, Tigard, Oregon.
- [7] Acton Research Corp., Acton, Massachusetts.
- [8] Scientific Imaging Technologies, Inc. Tigard, Oregon.
- [9] K.H. Burrell, D.H. Kaplan, P. Gohil, D.G. Nilson, R.J. Groebner, and D.M. Thomas, 2001, Rev. Sci. Instrum., **72**, p. 1028.

A CCD WAVEFRONT SENSING SYSTEM FOR THE ESO MULTI-CONJUGATE ADAPTIVE OPTICS DEMONSTRATOR (MAD)

Cyril Cavadore, Claudio Cumani, Francis Franza and Enrico Marchetti
European Southern Observatory

Abstract: *MAD's mission is to demonstrate the feasibility of Multi-Conjugate Adaptive Optics (MCAO) as a prerequisite for the 100-m OWL telescope, as well as several 2nd Generation VLT Instruments. It aims at comparing the relative merits of different methods and, therefore, alternatively employs multiple Shack-Hartmann and layer-oriented wavefront sensors requiring 3 and 2 detector units respectively. The 5 detector heads will be identical and equipped with CCD50 devices from Marconi, which have already been successfully tested with the VLT AO instrument NAOS-CONICA. ESO's standard CCD controller FIERA will be utilized in its new version, upgraded to a PCI bus board.*

Major challenges are the space restriction for the detector heads, the low weight allowance in mobile probes, the opto-mechanical coupling, the stringent noise requirements in the presence of limited options for cooling and high demands on the frame rates, and the high data transfer rates to the real-time computer. At the same time, as for all VLT instruments, a maximum compatibility with existing hardware and software standards must be maintained. The adopted solutions are described and discussed.

Key words: wavefront sensing, Shack Hartmann sensing adaptive optics, Multi-Conjugate Adaptive Optics (MCAO), fast readout Charge-Couple Device (CCD)

1. INTRODUCTION

The MAD project aims at demonstrating Multi-Conjugate Adaptive Optics (MCAO) capabilities by building a prototype to be tested on the VLT visitor focus (UT3). The instrument will use 3-8 natural guide stars and a laser guide star to achieve more than 60% Strehl ratio point spread function

over a field of view of $2'$ in the K band. Two concepts will be tested with this prototype. The first is the Shack Hartmann MCAO, which uses an asterism of 3 stars in the visible domain. Each star's wavefront is measured independently with the Shack Hartmann method by a high-speed CCD camera coupled with an array of microlenses. A global wavefront reconstruction scheme is applied to deformable mirrors. The correction across the field of view can be optimized for specific directions. The second scheme is called the layer-oriented approach: The wavefront is reconstructed at each altitude independently. Each wavefront CCD sensor is optically coupled to the others. The pyramid wavefront sensor conceived in 1995 offers a practical and compact solution to the optical design. Layer-oriented adaptive optics can also be coupled to laser guide stars.

The goal of the MAD instrument is to determine which method of layer-oriented MCAO (LOWFS) and Shack-Hartmann MCAO (SHWFS) is best suited for use with future MCAO systems. MAD is the ESO laboratory and sky tool for MCAO techniques. It is also an important milestone for the design of VLT 2nd generation instruments, and especially the OWL instruments.

2. THE CCD SYSTEM CONCEPT AND THE DETECTORS

As a fast track project, MAD needs to utilize as many parts and sub-systems that were used for other instruments, such as NAOS [1] (wavefront sensors) and SINFONI (optics and deformable mirrors), as possible.

There are 59 different parts needed for the CCD system. The optical setup is mounted on a table on the VLT Nasmyth platform. The 3 heads for the SHWFS move on a XY table to locate a star in a $2'$ field of view. In contrast, the LOWFS CCD systems are attached to their dedicated optics. The CCD heads require flexible cables for clocks, bias and video that are attached to the FIERA controller. Since CCD procurement could lead to time overhead that does not comply with this project, it has been decided, as the best trade-off, to use a CCD that ESO knows very well: the Marconi AO CCD50. ESO has several of these CCDs in stock. This device has already been used for the NAOS [1] project as a wavefront sensor and has delivered satisfactory performance therein. This is a CCD with a split frame transfer architecture featuring 16 output ports and 128×128 pixels. The CCD is a $24 \mu\text{m}$ sq., backside illuminated device. The quantum efficiency is comparable to a standard backside illuminated device from Marconi. Only 4 of the 16 ports are going to be used. So $\frac{1}{4}$ of the useful sensitive surface will be digitized, whereas the rest of the area is just clocked out to avoid charge contamination.

3. THE HEADS AND THE CCD COOLING

The head design must be compact (90×60 mm) because of the limited space available for the head inside the focal plane. This poses difficulties because the CCD package itself is not compact (*i.e.*, 30×60 mm). The heads will be vacuum tight and include the cooling system and temperature sensors. Micro sub-D connectors will be welded to the box to ensure its tightness with respect to moisture.

The following points summarize the design constraints:

- Liquid nitrogen (LN₂) cannot be used to cool the CCD because of the head compactness requirement.
- The CCD is a non-MPP CCD, thus producing a large amount of dark current (~ 500 pA/cm² at room temperature).
- The noise performance can not be jeopardized by additional dark current shot noise.
- The maximum exposure time is only 40 ms using 4×4 binning mode.
- It leads us to consider an efficient triple-stage thermoelectric Peltier cooler. The thermal load has been estimated at 1 W and requires an open loop Peltier controller able to provide up to 4/5 A per head. The heat from the hot Peltier side will be extracted by a cold water heat sink exchanger. Thus, the CCD temperature will depend mainly on the cold water temperature. The water circuit will be provided either by a closed cycle chiller or by the VLT service connection point.

The requirement for dark current is less than 500 e⁻/pix/sec with 1×1 binning, which is reached at -27 °C. However, our goal is ~ 250 e⁻/pix/sec, which is achieved between -32 °C and -45 °C. The temperature range requires a moderate vacuum inside the head (0.1–0.01 mb)

If the intrinsic system readout noise is 4 e⁻ at 50 Hz frame rate and 2×2 binning, an operating CCD temperature of -35 °C is required to prevent dark shot noise from becoming dominant. The temperature needs to be -50 °C for a 25 Hz readout rate and 4×4 binning. The increase in system noise has a direct impact on the ability to see fainter stars and/or achieve acceptable Strehl ratios. Therefore, the operating CCD temperature should be as low as possible.

4. THE READOUT MODES AND THE EXPECTED SYSTEM PERFORMANCE

Due to the CCD frame transfer architecture, the exposure time is defined by the frame rate. The later is set via a software parameter that is entered by the user. Nevertheless, for the highest frame rates, this is limited by the

readout time of a given sub frame at a given binning. A trade-off has to be found between the readout noise, binning, frame rate and pixel frequency as shown in Table 1.

Table 1. Frame rates vs. readout noise

500 Hz	400 Hz	200 Hz	100 Hz	50 Hz	25 Hz	Frame rate
< 7 e ⁻ 600 Kpix/sec	< 6.5 e ⁻ 600 Kpix/sec	< 4.5 e ⁻ 300 Kpix/sec	< 4.5 e ⁻ 300 Kpix/sec	< 4.5 e ⁻ 300 Kpix/sec	N/A	Binning 1×1
< 4.5 e ⁻ 300 Kpix/sec	< 4.5 e ⁻ 300 Kpix/sec	< 4.5 e ⁻ 300 Kpix/sec	< 4.5 e ⁻ 300 Kpix/sec	< 4.5 e ⁻ 300 Kpix/sec	N/A	Binning 2×2
N/A	< 3.5 e ⁻ 50 Kpix/sec	< 3.5 e ⁻ 50 Kpix/sec	< 3.5 e ⁻ 50 Kpix/sec	< 3.5 e ⁻ 50 Kpix/sec	< 3.5 e ⁻ 50 Kpix/sec	Binning 4×4

It must be noted that, without binning, 1068 pixels must be read out per port, using 2×2 binning, 272 pixels and 68 pixels with 4×4 binning. The frame shift frequency is 6250 Hz (160 ms).

The noise figures are based on experiences with the NAOS CCD system. This means that three readout frequencies will be used to satisfy the requirements: 50 Kpix/sec, 300 Kpix/sec and 600 Kpix/sec. The frame rate is defined as a combination of frame shift, pixel readout time and idle time defined by the user. This scheme permits a synchronous readout of the 3 SHWFS CCDs. Like the SHWFS, the readout scheme will also be synchronous for the LOWFS CCDs. However, to overcome large brightness differences of stars on CCD1 and CCD2, the frame rate of CCD1 can be a multiple of CCD2, with a ratio of 1 (synchronous), 2 or 4. Minor FIERA software modifications must be undertaken to handle this specific new readout mode.

The plan is to deliver this system for integration in Q2 2003. First light at the telescope should occur in Q4 2002.

5. ACKNOWLEDGEMENTS

The authors would like to thank ESO's ODT and AO teams for their help in making this paper a reality, and for performing the preliminary studies for this project.

6. REFERENCES

- [1] P. Feautrier et al, *Performances and results of the NAOS visible wavefront sensor*, these proceedings, pg. 325
- [2] Dorn et al., *A CCD based curvature wavefront sensor for adaptive optics in astronomy*, these proceedings, pg. 319

CFHT'S SKYPROBE: TRUE ATMOSPHERIC ATTENUATION MEASUREMENT IN THE TELESCOPE FIELD

Jean-Charles Cuillandre, Eugene A. Magnier, Sidik Isani, Dan Sabin, Wiley Knight, Simon Kras and Kamson Lai
Canada France Hawaii Telescope

Abstract: *Developed at the Canada France Hawaii Telescope (CFHT), SkyProbe is a system that allows the direct measurement of the true attenuation by clouds. This measurement is performed approximately once per min, directly on the field viewed by the telescope. It has been possible to make this system relatively inexpensively due to low cost CCD cameras available on the amateur market. A crucial addition to this hardware is the recent availability of a full-sky photometry catalog at the appropriate depth: the Tycho catalog from the Hipparcos mission. A very important element in the SkyProbe data set creation is the automatic data analysis pipeline, Elixir, developed at CFHT for the improved operation of the CFHT wide-field imagers CFH12K and MegaCam. SkyProbe's FITS images are processed in real time, and the pipeline output (a zero point attenuation) provides the current sky transmission to the observers and aids immediate decision making. These measurements are also attached to the archived data, adding a key tool for future use by other astronomers. Specific features of the detector, such as intra pixel quantum efficiency variations, must be taken into consideration since the data are strongly undersampled.*

Key words: SkyProbe, camera, photometry, attenuation, Elixir

1. INTRODUCTION

The validity of scientific data collected by ground-based telescopes can be strongly compromised by the undetected effects of variable atmospheric transmission caused by passing clouds during the exposures. While the

presence of big fluffy clouds is a sign that the night may be lost all together (guide stars are lost resulting in many interrupted exposures), observations can still take place in the presence of thin to semi-thick cirrus. However, the major drawback that the stellar flux will be difficult to calibrate remains. Still worse, cirrus can sometimes come and go undetected during the night, especially on moonless nights if the dusk and dawn skies look clear, which causes the night to be stamped as photometric.

Infrared satellite imaging is a tremendous help in the detection of clouds over the observatory areas, but they can not determine the effect on the observed fields. Various other approaches have been investigated, all focused on all-sky monitoring using either 10 μm infrared systems [1] or wide-format scientific LN2 cooled CCDs [2]. However, none of these approaches is helpful on the tiny patches of sky viewed by the telescope.

To make the best out of a cloudy night, a system that follows the absolute atmospheric transmission in real time is needed, in addition to an all-sky monitor (used to help define a clear patch of sky). This system would define if a night is photometric, hence allowing key decisions concerning observing strategy to be made. This is extremely relevant to the fast expanding queued observing mode flourishing around the world (see [3] for an example at CFHT).

This will save telescope time, because photometric field observations will not be necessary. It will also allow real-time decisions, such as expanding the exposure time on a given field to achieve the desired signal-to-noise ratio for the conduction of scientific programs. In addition, attaching absorption data benefits future users.

The concept for SkyProbe arose from the following conditions: to derive absolute photometric measurements in real time on the field viewed by the telescope (including the science field) using photometry on the set of available stars.

The specifications for such on-field monitor are:

- A camera working in the visible, as absorption is stronger at visible wavelengths and large precise photometric catalogs exist in this domain.
- A large field of view to collect many stars per exposure (better statistics).
- A field of view that includes the science field.
- A fast system allowing frequent measurements, *e.g.*, 1/min, of sky transmission.
- A maintenance free camera system, since it is meant to operate as an observatory facility, available all year round.

- A reliable data processing pipeline, because downtime is unacceptable for a crucial element in the chain of observing strategy decisions.

Recent technological developments in several unrelated fields have allowed us to design and build such a system:

- The availability of low-cost high reliability CCD cameras from the amateur market.
- The availability of an all-sky photometry catalog at the appropriate depth (Tycho catalog [4]).
- The development at CFHT of an automatic analysis system (Elixir [5]) at CFHT.

This article presents a complete overview of the SkyProbe system.

2. HARDWARE

2.1 CCD camera and lens

SkyProbe utilizes a Santa Barbara Instrument Group (SBIG) ST-7E camera which contains two CCD detectors. Only the principal detector is used for direct imaging (the second one is a small guiding unit). The detector is a Kodak KAF-0401E, a frontside illuminated array of 765×510 , $9 \mu\text{m}$ sq. pixels with enhanced quantum efficiency in the blue. To achieve proper photometry, the pixel fill factor must equal 100%, hence antiblooming protection must be dismissed. This comes as an option (CCD replacement) when ordering the system.

The CCD is cooled by a single thermoelectric stage, which allows the detector to function anywhere from -25°C to ambient temperature. With a frequent sub-zero temperature at night on Mauna Kea, rarely rising above $+5^\circ\text{C}$, the running temperature is set at -20°C . (stable within $\pm 0.1^\circ\text{C}$). The dark current is negligible on 30 sec exposures taken by SkyProbe. The analog to digital converter encodes the data on 16 bits with a gain of $2.3 \text{ e}^-/\text{ADU}$. The read noise is 15 e^- and the full well capacity is approximately $100,000 \text{ e}^-$. The charge transfer efficiency has not been measured, but trends in our data analysis indicate that a higher sky background level helps increase the quality of the photometry, such a “fat-zero” level is provided naturally by the moon or twilight. Keeping the dark current higher could help to increase the charge transfer efficiency.

The detector size is 6.9×4.6 sq. mm, a surface much smaller than the nominal field of view of 36×24 sq. mm film for which the Nikon 50 mm lens (open at $f/1.8$) was designed. This lens collects a lot of light and provides a field of view large enough (7×5 sq. deg.!) to collect at least 100 stars in each

image from the Tycho catalog at the depth reached in 30 sec exposures. The pixel scale is $35''/\text{pix}$ (see Sec. 4.1).

2.2 Shutter

With a system that takes an exposure every minute throughout the entire night all year, in a single year the number of shutter cycles surpasses 200,000! The only moving part in the system, usually the weak point of cameras, must be designed for such stress. The SBIG ST-7E comes with a shutter that can tolerate such stress. It is a double aperture light disk driven by a stepper motor (see Fig. 1) producing little if no mechanical stress. The exposure time can be as short as 0.1 sec with a resolution of 10 msec. With such control, a given exposure is guaranteed to be repeatable within a fraction of a percent (max 0.3% with the provided specifications), which is an important point when one is trying to derive the absolute sky transmission to the one percent level.

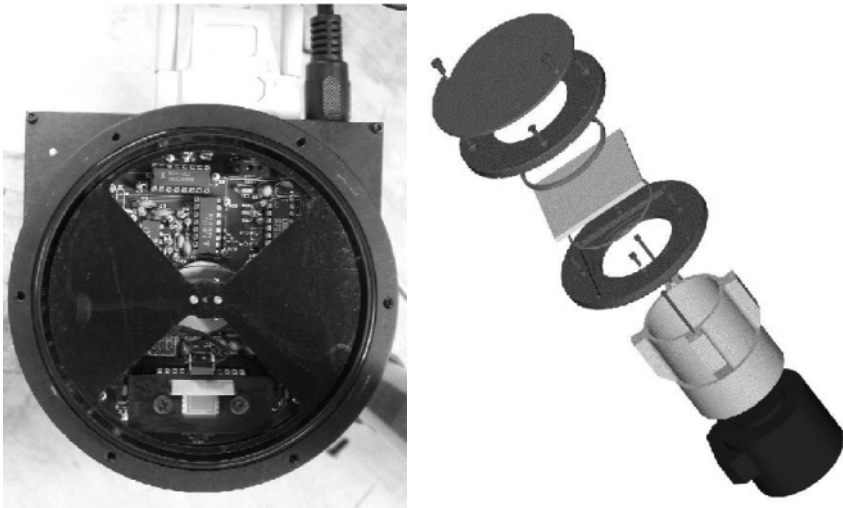


Figure 1. (left) View of the SBIG ST-7E shutter, a blade driven by a stepper motor taking two exposures to complete a full cycle. (right) An enlarged rendering of the mechanical elements holding the filter and the various protections (cover, gutters). The Nikon 50 mm lens is not shown here.

2.3 Housing

The Tycho catalog provides the photometry in two colors: B and V bands. We chose the V band since CCD quantum efficiency peaks in that domain. We designed a camera head bolting on the body of the CCD camera to safely hold the large V band Johnson filter just above the lens. A safety

cover can be pulled over the filter to protect it if telescope operations have moving parts nearby (Fig. 1).

Although not shown in Fig. 1, there is a small endless screw that touches the focus ring of the Nikon lens. We found the focus to be critical to achieve proper behavior of the entire system. This means that there will be a few manual iterations on the telescope when the camera is installed for the first time.

Due to SkyProbe's location on the telescope (a place where there can be water leaks from the dome), we added some internal gutters so water would not collect on the filter. There is also a leash attached to the camera to keep the whole camera from rolling onto the mirror if, *e.g.*, the main support failed.

The whole structure is approximately 25 cm tall, 9 cm wide and weights less than 2 kg (not including the acquisition system).

2.4 Acquisition system

The camera is connected to a small PC via a parallel port, reading out in approximately 25 sec using an interface developed under Linux. CFHT is currently using an i-Opener by Home Appliances adapted in-house to run Linux and connected to the network via a USB-ethernet adapter. However, virtually any PC with a parallel port is fit to run such camera, but the i-Opener has the advantage of no moving parts (no hard drive).

The camera connects to the PC via a 15 ft (~4.55 m) long cable allowing the computer to be placed further away in a protected environment (the camera power supply comes through the parallel port too).

2.5 Location on the telescope

With a telescope as versatile as CFHT, top-end exchange between the prime focus and the cassegrain foci are frequent. Initially installed on top of the prime focus cage, SkyProbe quickly gained popularity and was requested to be transformed into a full-time observatory facility. This implied moving SkyProbe down near the mirror cell outside the struts with enough clearance so that the top ring does not enter the field of view of the camera (see Fig. 2(left)). The drawback is that on rare occasions about 20% of the field of view gets occulted by the dome as the telescope points North of zenith and the dome slit passes North (see Fig. 2(right)). This situation has no effect on SkyProbe's performance since stars get occulted and are not detected at all.

For other telescopes working only with a cassegrain and/or nasmysth focus, the location will not be an issue since SkyProbe can simply sit on the top ring.



Figure 2. (left) SkyProbe, in the foreground, is mounted near the mirror cell at the feet of the telescope struts. An unobstructed view of the sky viewed by the telescope is available by setting SkyProbe at the edge of the telescope structure. (right) A typical SkyProbe image, 30 sec exposure of the Galactic bulge. Notice the slight occultation by the dome on the top left corner.

2.6 Performance

The Tycho catalog [4] from the Hipparcos mission provides more than 2 million stars up to 11.5 magnitude in the V band over the entire sky (completeness limit = 10.5 mag). With a 35 sq. deg. field of view and 30 sec exposures in the V band, SkyProbe easily reaches 11 magnitude. It gathers approximately 400 of the Tycho stars near the galactic plane, and approximately 100 near the galactic pole. As discussed below in Sec. 3.2, increased statistics with many stars is the key to reach precise photometry accuracy on such undersampled data.

3. SOFTWARE

3.1 Data pre-reduction and field preview

Data that are taken by SkyProbe are processed automatically in a analysis system [5], Elixir, developed at CFHT for the improved operation of the wide-field imager CFH12K [6]. The first step of the data analysis is typical

pre-reduction with the additive and multiplicative effects removed (bias/dark/flat-field). The detector response does not appear to change with time, hence the pipeline uses single master detrend frames constructed at the time the camera was first installed.

The first element provided to the observer (within 15 sec after the exposure is taken) is a JPEG format greyscale image of the processed image directed the web page to assess the overall quality of the field (*i.e.*, are there any stars visible?). A small rectangle indicates the camera's field of view and allows the location of nearby bright stars, the worst contaminant of wide-field imaging data.

3.2 Data analyses

The next steps continue to follow the procedure developed at CFHT to analyze and track data from the large mosaic cameras. The first is the detection (position and photometry extraction) of all the objects in the image. The pixel coordinates are converted to celestial coordinates using the Tycho catalog as astrometric reference. The measurements for each star are added to the Elixir photometry internal database where each star is identified by its position in the sky. Elixir immediately provides the association between the SkyProbe measurement and the stellar magnitude from the Tycho catalog. The average zeropoint offset is calculated using as many Tycho stars as are in the image to reduce the noise.

A significant scatter is present when plotting the SkyProbe measurement versus the Tycho measurement. This is due to the coarse pixel scale, $35''/\text{pixel}$ (with a median seeing of $0.7''$ on Mauna Kea!), which causes issues in terms of photometry (see Sec. 4). This is why SkyProbe's large field of view is the perfect compromise, since a system providing a finer scale while preserving a reasonable field of view for increased statistics would be too large to be easily installed on the telescope. With a typical scatter of 10% based on at least 100 stars/image, a final accuracy of less than 1% is achieved, well within our initial specification for the system performance.

The per-image zeropoint offsets represent the attenuation by the sky in magnitudes, and are stored in the database along with a set of other per-image information.

3.3 Real time plots

With a sky transparency measurement available every minute, it is possible to build statistics and provide plots on the evolution of the sky transmission for the observer over the course of the night. Such a plot is

showed in Fig. 3, which displays a night with a significant amount of cirrus clouds in the second part of the night.

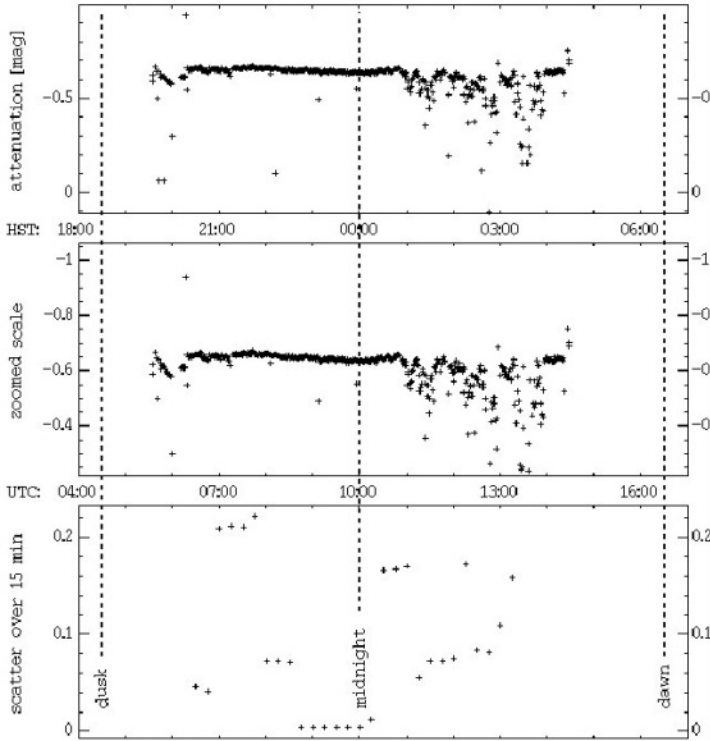


Figure 3. SkyProbe plot on a night photometric during the first half, and then with moving clouds on the second half (erratum: scale in attenuation are offset by 0.6 mag - the flat part of the plot lies at an attenuation of 0.0 mag).

3.4 Observing efficiency

As scientific data are collected throughout the night, each frame can be directly compared with a collection of SkyProbe measurements. Though these scientific data are collected in various bands (and even in the infrared as SkyProbe is now a full time facility), the V band data provide the key information if a night is photometric. With the CFHT wide-field imagers essentially operating in queued observing mode [3], SkyProbe has proven to be a key element of the chain as scientific programs requiring photometric conditions. When the nights are not photometric, the exposures get tagged and will have a short exposure taken to bootstrap the photometry.

Since SkyProbe provides true attenuation in the V band, it is also now possible to derive the signal to noise ratio in real time on scientific frames using the image quality and sky background level measurements, which

result from the main Elixir process. Comparing these three parameters indicates how much the exposure should be extended in order to achieve the intended signal to noise ratio on the final data. However, further investigations need to be pursued to determine how absorption detected in the V band can be scaled up and down to other filters in the visible. Due to observing time ratio balancing issues, this has not yet been implemented in queued mode, but only as a standalone program (the “classical” mode) where the PI (Principal Investigator) is in charge of managing his/her time budget. This possibility will come very useful in ensuring the scientific success of the observing program.

3.5 Archiving

A second group that uses CFHT data are archive users (data handled by the Canadian Astronomy Data Center), without any knowledge of the sky transparency, ground based telescope archived data can appear dubious to potential users. The addition of the SkyProbe measurements to each scientific frame (indicating whether the night was photometric, and if not, the average transmission in the V band in the course of the exposure) will greatly increase the level of confidence for the potential archive users.

4. DETECTOR ISSUES

Anti-blooming structures and pixel fill-factor physical anti-blooming structures are popular in the amateur community due to the natural aesthetic value they bring to the raw image by stopping bright objects from saturating onto neighboring pixels. However they have a major disadvantage: they use a fraction of the pixel that does not contribute in collecting photons. They represent dead spots within the pixel, typically less than 10%. However, for undersampled data, this can be a real puzzle as stars will appear on and off depending on the slight movement of the telescope on the field viewed (which is common when running some dithering patterns, for example).

The first incarnation of SkyProbe is a SBIG ST-237 that utilizes a TC237 chip by Texas Instrument. Strong jumps (10%) in the photometry plots appeared as set of stars disappeared in the blind spots. The TC237 was then replaced by the Kodak KAF-0401E because of its 100% fill factor, a common specification for any scientific oriented detector.

4.1 Undersampled data and frontside illuminated CCDs

The KAF-0401E is a frontside illuminated CCD with increased sensitivity in the blue, as stated by the manufacturer. This is achieved by replacing a typical polysilicon gate with a gate that uses a conductive

transparent material made of indium-tin-oxide or ITO [7,8]. The quantum efficiency increases from 2% to 30% at 400 nm and the peak efficiency at approximately 600 nm jumps from 40% to 63%.

These numbers are misleading since it is an integrated sensitivity over the pixel. It is well known that intra-pixel sensitivity variations exist and must be taken into account, especially when dealing with undersampled data [9].

Based on the literature available from Kodak [9], we built a model of the pixel. Figure 3(right) shows the evolution of the quantum efficiency along the pixel height. With the KAF-0401E, the difference within the pixel is as large as 40%! The full line describes the expected QE following the physical structure of the gates; the dashed and dotted lines are probably more realistic representations of the actual QE as the light hits the detector at a pretty steep angle on SkyProbe with uses the 50 mm lens open at f/1.8.

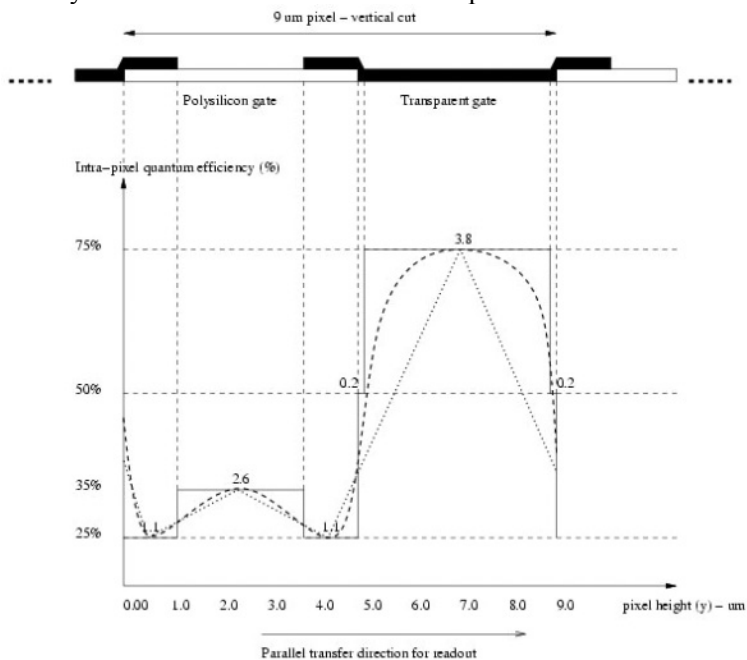


Figure 4. Kodak KAF-0401E large intra-pixel quantum efficiency variation due to the use of a polysilicon gate on one half and an indium-tin-oxide transparent gate on the other half.

We decreased the intrinsic effect of the intra-pixel quantum efficiency variations by slightly defocusing the camera while making sure the depth of each single exposure was still high enough to reach the Tycho's limit of 11 magnitude.

This effect is corrected on a per star basis in Elixir, by correcting its flux based on its position within the pixel. Since Elixir can define a very precise

astrometric solution over the whole field of view using the 100 plus stars, their position can be in return pinned down to a 1/20 of a pixel. Knowing the structure of the pixel in terms of sensitivity variation, Elixir then adjusts the flux for all the stars. This decreases the initial scatter by a factor of three.

5. CONCLUSIONS AND FUTURE PLANS

CFHT has developed an efficient and reliable system capable of deriving the absolute sky transmission at a one minute resolution over entire nights. SkyProbe has been in operation since Fall 2000 and has become a facility observers can not live without after they have experienced this valuable addition. This is especially true in the newly implemented queued observing mode at CFHT, a common trend to most ground-based telescopes today. Most large facilities will probably take some effort to duplicate SkyProbe soon, since the cost is fairly low for the benefits.

The V band, however, limits our knowledge of the nature of the absorption. We plan on adding a B band channel (the second color provided in the Tycho catalog) and investigate the effect of cirrus versus more fluffy clouds or even volcano haze that sometimes reaches the summit.

At the dawn of the new wide-wield imaging era starting at CFHT with the new 1 sq. deg. wide-field imager MegaCam [10] and its infrared counterpart WIRCAM (20'×20'), which are mainly focused on large surveys of the sky over several years, SkyProbe will prove to be a crucial element in the global observing strategy.

6. REFERENCES

- [1] C.L. Hull, S. Limmongkol, W.A. Siegmund, 1994, *Sloan Digital Sky Survey cloud scanner*, Proc. of S.P.I.E **2199**, p. 852.
- [2] R. Smith, 2002, *Cloud Monitoring with CCDs*, Optical detectors for astronomy II, Kluwer Academic Publishers, Astrophysics and Space science library, **252**, p. 345.
- [3] P. Martin, R. Savalle, T. Vermeulen, J. Shapiro, 2002, *Queued Service Observing (QSO) project at CFHT*, Proc. of S.P.I.E **4844**.
- [4] E. Hog, C. Fabricius, V.V. Makarov, S. Urban, T. Corbin, G. Wycoff, U. Bastian, P. Schwekendiek, A. Wicenec, 2000, *The Tycho-2 catalogue of the 2.5 million brightest stars*, Astronomy & Astrophysics **335**, L27.
- [5] E. Magnier, J.-C. Cuillandre, 2002, *Elixir - how to handle 2 trillion pixels*, Proc. of S.P.I.E **4844**.
- [6] J.-C. Cuillandre, B. Starr, S. Isani, G. Luppino, 2000, *CFH12K: Optimizing 12 MIT/LL CCID20 CCDs for a Direct Imaging Application*, Optical Detectors for Astronomy II, Kluwer Academic Publishers, Astrophysics and Space science library, **252**, p. 93.

- [7] E.G. Stevens, S.L. Kosman, J.C. Cassidy, W.C. Chang, W.A. Miller, 1991, *A large format 1280×1024 full-frame CCD image sensor with a lateral overflow drain and transparent gate electrode*, Proc. of S.P.I.E **1447**, p. 274.
- [8] W. Des Jardin, S.L. Kosman, 1999, *True two-phase CCD image sensors employing a transparent gate*, Proc. of S.P.I.E **3649**, p. 74.
- [9] T.R. Lauer, 1999, *The Photometry of Undersampled Point-Spread Functions*, PASP **111**, p. 1434.
- [10] O. Boulade, L. Vigroux, X. Charlot, P. Borgeaud, P.H. Carton, J. de Kat, J.Y. Rousse, Y. Mellier, P. Gigan, D. Crampton, C. Morbey, 1998, *MegaCam, the next generation wide-field camera for CFHT*, Proc. of S.P.I.E **3355**, p. 614.



Continues from page 102: Barry Burke, with a sentimental gleam in his eye, belts out “My old MOSFET design” while Garnett (left) pensively awaits his turn at the karaoke mike. The other singers: Peter Pool (extreme left), Paul Vu (right), Lester Kozlowski and ¼Ken Ando.

CFHT'S FLYEYES: ASSESSING ON-SKY PERFORMANCE OF THE NEW MIT/LL CCID-35 CCD CURVATURE WAVEFRONT SENSOR

Jean-Charles Cuillandre¹, James Beletic², Reinhold Dorn³, James Beletic², Gerard Luppino⁴, Sidik Isani¹, Nicolas Gorceix¹, Olivier Lai¹, Thomas Craven-Bartle⁵, Barry Burke⁶, François Mênard⁷

¹Canada-France-Hawaii Telescope (CFHT), ²W.M. Keck Observatory, ³European Southern Observatory, ⁴Institute for Astronomy, University of Hawaii, ⁵Anoto Group, ⁶MIT Lincoln Laboratory, ⁷Laboratoire d'Astrophysique de l'Observatoire de Grenoble.

Abstract: *Due to strict requirements of a very short integration time and very low readout noise, Avalanche Photodiodes (APDs) are the only detectors that have been used for curvature wavefront sensors in astronomy thus far. In 1999, Beletic et al. [1] presented a new CCD design that achieves the same performance as APDs, but with higher reliability and lower cost. In addition, this CCD has a higher quantum efficiency than APD modules and a larger dynamic range, eliminating the need for neutral density filters when viewing bright objects. In close collaboration with ESO and IfA, MIT Lincoln Laboratory designed and fabricated the device, the CCID-35. R. Dorn [2] tested the CCD in the laboratory at ESO extensively and proved that it achieves the predicted performance. CFHT is currently implementing this CCD on the PUEO Adaptive Optics system, to assess its performance on the sky for the first time, and for a direct comparison with the current 19 APD detector system. In this overview we present the current implementation scheme and discuss the upgrade we foresee for PUEO NUI, a 104 element high-order curvature AO system envisaged to replace the current AO system at CFHT [3,4].*

Key words: *Avalanche Photodiode (APD), Charge-Coupled Device (CCD), detector, Adaptive Optics (AO), PUEO, PUEO NUI, PUEO-FlyEyes, cryostat, controller*

1. INTRODUCTION

We present a CFHT/UH-IfA collaboration to integrate a newly designed CCD based curvature wavefront sensor on PUEO, the CFHT adaptive optics system. The CCID-35 detector was designed by MIT Lincoln Laboratory, ESO and UH between 1999 and 2000 [1], with the first front illuminated devices successfully integrated and tested in the ESO laboratory in 2001 [2]. ESO will not have an opportunity to test the CCID-35 on the sky before 2004, despite it being more cost effective. Hence, there was no immediate opportunity to prove that CCDs can do as well, in terms of sensing, as APDs in real observing conditions.

For CFHT's PUEO NUI project, a proposal to upgrade PUEO into a 104 actuator system [3,4] using APDs as wavefront sensors is not possible due to budget limitations (one APD costs about \$3K). This paper proposes a project called PUEO FlyEyes, which suggests temporarily substituting the APDs with the CCID-35 for a few engineering nights. A direct comparison between the performance of PUEO using APDs and using a CCD wavefront sensor system offers CFHT a unique opportunity to participate in an effort that could greatly benefit the future of AO curvature systems.

The PUEO-FlyEyes project can be split in seven distinct parts:

1. Integration of two detectors in a dewar [IfA]
2. SDSUII Controller & DSP code (CCD control + membrane synchronization) [CFHT]
3. CCD selection and optimization [MIT/LL & CFHT]
4. Coupling of the fibers to the CCD cells [CFHT & IfA]
5. Feeding the pixel intensities into the existing RT (Real Time) computer [CFHT]
6. Mechanical integration on the outside skin of PUEO [CFHT]
7. On-sky performance evaluation [CFHT]

PUEO-FlyEyes is a fairly straightforward project with a potentially large return, as it provides a fully integrated and operational 160 cell system for wavefront analysis on PUEO NUI. A test on the sky in Spring 2002 is our current goal.

Integrating two CCID-35s into a single dewar requires almost the same amount of effort as integrating a single detector. To produce a system that is fully scaled for PUEO NUI, we plan to integrate two back-illuminated CCDs in a dewar designed by G. Luppino [5]. This will provide two "eyes", each with 80 cells, whose light will be analyzed by a computer to reconstruct a coherent image of what is happening in the pupil. This is very similar to actual fly eyes, which are made of many facets and lenses working together to produce a single image. In actual fly eyes this is made possible by a highly ordered process of organized neurons that identify specific regions of

space in the visual field, which is very similar to our design. Hence the name of the project - FlyEyes.

2. PUEO OVERVIEW

The CFHT Adaptive Optics Bonnette (AOB), also called PUEO (Hawaiian owl), is based on the curvature concept. First light for the system was in Fall 1996. Extensive documentation and information exists for this instrument adaptor, which is mounted at the f/8 Cassegrain focus [6,7]. It has been used with a variety of instruments, including KIR (1K×1K infrared direct imaging camera), FOCAM (2K×2K optical direct imaging camera) and OASIS (integral field spectrograph).

PUEO uses a 19 element deformable mirror requiring 19 APDs. Another issue related to the FlyEyes project is the real time computer (dual processor) that not only makes the real time calculation, but does it with optimization and modal control. The machine used is a Sparc5 (few tens of MHz dual CPU). See Fig. 1 for an overview of the new elements.

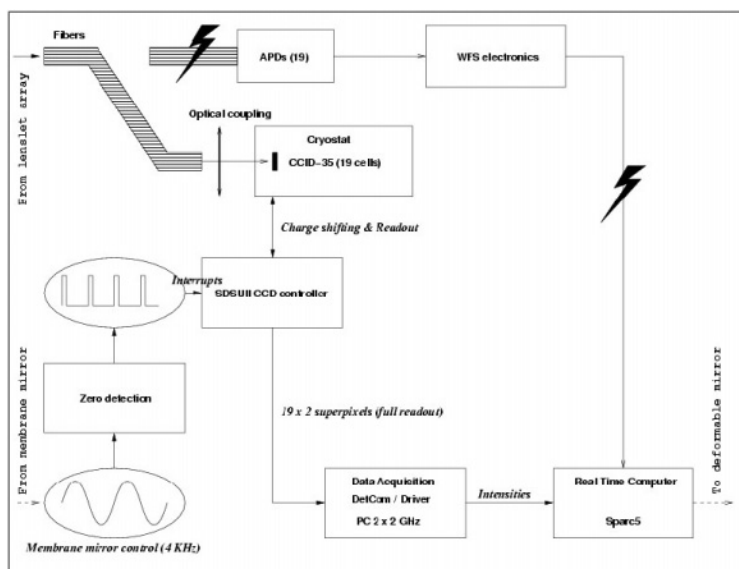


Figure 1. FlyEyes: overview of the new elements.

3. CCID-35 OVERVIEW

In 1999, ESO and UH-IfA funded the development of a detector by the MIT Lincoln Laboratory to address a major drawback of curvature systems: the highly expensive Avalanche Photo Diodes (APDs). APDs cost

approximately \$3K per unit and are only available from a single manufacturer. There have also been reports within the AO community that the failure rate of these actively quenched APDs is quite high. At that time ESO was launching the AO project MACAO, a multi purpose 60 element curvature system developed for the Very Large Telescope (VLT), and in particular for the VLT Interferometer (VLTI) which required four identical systems.

The nature and working principles of the detector are extensively covered in Beletic et al. [1]. The CCD has been successfully produced and subsequently tested on an optical bench at ESO, which allowed a complete evaluation of the detector to build predicted comparisons with APDs [2].

An extensive computer simulation comparison of CCDs and APDs for curvature wavefront sensing was also conducted by T. Craven-Bartle at ESO [8]. The simulated AO-system was the MACAO 60 elements curvature system, and the results indicated a difference in performance of 5% Strehl in K-band for a 15th magnitude guide star, 2% Strehl for a 16th magnitude star, and less than 0.6% Strehl for all other magnitude guide stars.

Unfortunately, due to some delay in the production of this new detector, the CCID-35 could not be considered as WFS for the MACAO systems due to time constraints. However, as of January 2002, the CCID-35 is available in the backside illuminated version and the only prospect of testing it in real conditions is on CFHT's PUEO.

PUEO uses passively quenched APDs which are more robust than the actively quenched ones (known for their higher failure rate due to extreme sensitivity to over illumination) but present a quantum efficiency lower by a factor of two (40% versus 80%). The thinned version of the CCID-35 should have a QE peaking in the red at 95%. This should overcome some of the penalty induced by the readout noise and reduce the relative time lag due to the readout time by reducing the exposure time when using faint guide stars.

4. WORK PACKAGES

4.1 CCD cryostat

These CCDs need to be cooled at cryogenic temperatures in order to remove the dark current component from the noise. A standard dewar designed by G. Luppino [5] will be used.

The camera head wiring has 18 outputs in total: 8 per CCD for the cells and 2 for the tip-tilt arrays that, although they will not be used on PUEO-FlyEyes, represent an added benefit for PUEO NUI. Although the PUEO-FlyEyes experiment requires only 4 outputs (see Sec. 4.2), all 18 outputs will

be wired out to the main cryostat connector. Using this camera head on PUEO NUI will imply the connection of a single controller, because our current plan is to use a SDSU-II system with limited ultra-fast parallel readout capabilities.

4.2 CCD controller

The SDSU-II CCD controller will be used to run the two devices. Each readout will consist of $19 \times 2 = 38$ superpixels from the camera. If the 19 light beams can not be arranged on a single CCD due to the physical crowding of the optical design, they can be split between the two CCDs. There will be a total of 160 cells available in FlyEyes — 80 cells per CCD! To keep the readout time as low as possible, parallelism is a requisite. The default controller box provided in a SDSU-II system has six slots. Of the six slots one is for the timing board, one for the utility board and one for the clocking board. This leaves room for up to three video boards, each with two video channels, though we will limit the FlyEyes system to four video channels. Each of the four video channels will deal with 5 cells from a row, *i.e.* 20 pixels per output per dual-readout (in and out of the pupil plane).

Using the performance numbers established by R. Dorn at ESO [2], *e.g.*, a 250 μsec readout time when using 6 rows of 10 cells each, and scaling it down to using only 5 cells in 4 rows (a total of 20, with one empty cell), the predicted readout time is about 150 μsec (including pre-scan pixels and other overheads). This results in a $1.5\ e^-$ readout noise with front illuminated CCDs. However, the SDSU-II controller has a different architecture than the ESO CCD controller (CDS vs. clamp and sample). Only testing will reveal the noise level we will achieve with the SDSU-II.

The maximum sampling/command frequency of PUEO is 1 kHz, or a cycle time of 1 ms. The lag induced by the 150 μsec CCD readout is only 15%. Note that the lag is important to the correction only at the highest frame rate - on bright objects - when the correction is already very good. As the flux decreases and the frame rate is adjusted to increase the exposure time, the relative contribution of the readout delay becomes less and less important in the loop.

We will "plug" the readout values into the RTC to get an exact simulation (signal and timing) of the information it is passed in the current APD based system. This will require the development of an interface electronic board connecting the CCD acquisition host (running real-time Linux) to the RTC.

A crucial part of the operation of this new WFS device is perfect synchronization between the membrane vibration in and out of the pupil plane (4 kHz) and the shifting of the charges on the CCD, in order to achieve symmetric integration timing for both sides. The SDSU-II controller will

easily satisfy this requirement since it can operate in an interrupt mode based on an external signal. The membrane sinusoidal signal simply needs to pass through a zero crossing circuitry that will generate a pulse. Each pulse will trigger an immediate shift of the charges in the storage areas. This interruption of SDSU-II has been tuned and was used for the first time within the SDSU community in 1998 at CFHT to synchronize the readout of both CFH12K controllers within 6 ns.

4.3 Optical coupling

We first investigated a coupling through the silicate cryostat window, but the optical losses appeared to be too high. It is, however, possible to produce a 1 to 1 optical coupling through the window that would preserve a decent image quality without any overlap between the fibers' signal on the CCD. A new design is currently being developed by G. Luppino and CFHT to allow the fibers to go through a front plate and come within 200 μm of the CCD surface.

5. REFERENCES

- [1] R. Dorn, 2001, *A CCD based curvature wavefront sensor for adaptive optics in Astronomy*, PhD thesis.
- [2] O. Lai, T. Craven-Bartle, 2002, *High contrast imaging using curvature adaptive optics*, Proc. of the S.P.I.E., **4860**, 2002, in press.
- [3] G. Luppino, K. Miller, 1992, *A modular dewar design and detector mounting strategy for large-format, astronomical CCD mosaics*, PASP, **104**, p. 215.
- [4] R. Arsenault, D. Salmon, J. Kerr, F. Rigaut, 1994, *PUEO: the Canada-France-Hawaii Telescope adaptive optics bonnette I: system description*, Proc. of the S.P.I.E., **2201**, p. 833.
- [5] F. Rigaut, D. Salmon, R. Arsenault, J. Thomas, O. Lai, D. Rouan, J.P. Véran, P. Gigan, D. Crampton, J.M. Fletcher, J. Stilburn, C. Boyer, P. Jagourel, 1998, *Performance of the Canada-France-Hawaii Telescope Adaptive Optics Bonnette*, PASP, **110**, p. 152.
- [6] J. Beletic, R. Dorn, T. Craven-Bartle, B. Burke, 2000, *A new CCD designed for curvature wavefront sensing*, Optical Detectors for Astronomy II, Kluwer Academic Publishers, p. 283.
- [7] T. Craven-Bartle, R. Dorn, J. Beletic, 2000, *Computer simulation comparison of CCDs and APDs for curvature wavefront sensing*, Proc. of the S.P.I.E., **4007**, p. 444.
- [8] O. Lai, F. Ménard, J.-C. Cuillandre, 2002, *PUEO NUI: a feasible AND fast upgrade of the CFHT adaptive optics system for high dynamic range imaging*, Proc. of the S.P.I.E., **4839**.

ULTRA-CLEAN CCD CRYOSTATS

CCD contamination can be kept under control

Sebastian Deiries, Olaf Iwert, Cyril Cavadore, Christian Geimer, and
Evi Hummel

European Southern Observatory (ESO)

Abstract: *A reproducible method to achieve ultra-clean CCD cryostats is presented, including a list of suitable materials and necessary treatments. In addition, proper handling under clean-room conditions and suitable molecular sieves to eliminate contamination on the detector surface in cold cryostats for years are described.*

Key words: *contamination, cleaning, Charge-Coupled Device (CCD), cryostat, charcoal, clean-room, out-gassing, zeolith*

1. INTRODUCTION

Over the last few years, ESO's Optical Detector Team (ODT) has developed a comprehensive method to achieve ultra-clean CCD cryostats, because scientific results are insecure if obtained with unclean systems. Usually, contamination (see Fig. 1) first decreases the ultraviolet and blue spectral response of a CCD sensor. In this phase contamination is invisible to the naked eye. If contamination features become visible, the resulting effect is much greater and, obviously, affects the visible spectral range as well. In order to measure the probable effects of contamination on Quantum Efficiency (QE) at the telescope, the ODT developed a portable test bench. In order to be able to quantify this critical problem, a procedure was developed for the ODT test bench in Garching to measure the exact degree of contamination on detectors. Contamination occurs under vacuum conditions due to the out-gassing of unsuitable materials. If this occurs near the CCD detector, which has the lowest surface temperature, unwanted

condensation forms at its surface. The graphs shown in Fig. 2 illustrate the corresponding QE decrease.

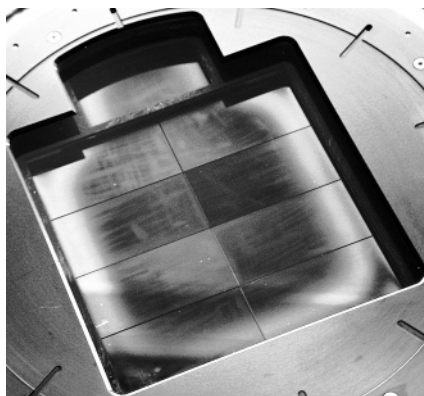


Figure 1. Contaminated CCDs.

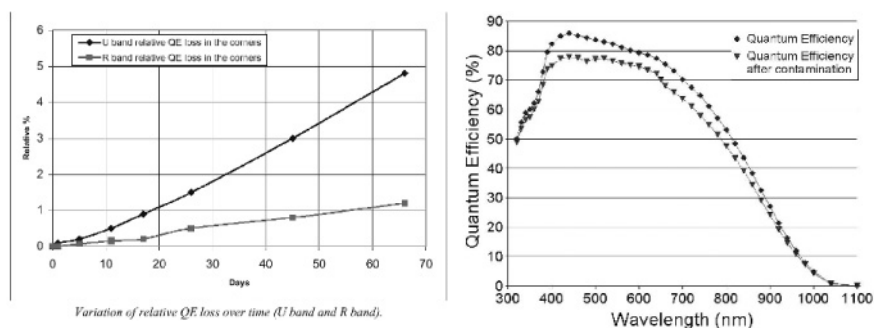


Figure 2. QE decrease on CCD due to contamination.

2. RECIPE AGAINST CONTAMINATION

A reproducible method to avoid QE decrease due to contamination is now available [1]. A list of materials used in ESO's cryostats is given in Table 1. Suitable and unsuitable materials alike have been obtained as a result of ESO's program of categorizing samples with a mass-spectrometer [3] and from a NASA list [2]. The procedure used to achieve the components of ultra-clean cryostats is given in Table 2. First, all components are hand cleaned with paper and a suitable solvent. Then they are washed twice in an ultrasonic bath, eventually dried with pressurized nitrogen or paper and later baked in a vacuum oven at the maximum possible temperature. Lastly, the CCD cryostat is assembled with gloves under clean-room conditions (see Fig. 3).



Figure 3. Cryostat assembly in clean room.

Table 1. Materials used for ultra-clean cryostats in addition to stainless steel, aluminum, glass, INVAR, gold coating, oxygen free copper and electronic SMD components.

	Material, manufacturer	Curing in vacuum	Max. service temperature
Cleaning agents	Ethanol, propanol, acetone, any	-	40 °C
	Tickopur-soap, Bandelin	-	85 °C
Fiberglass	HGW 2372, Ferrozell	-	130 °C
Glue	EP21TCHT-1, Master Bond	1-2 h/93 °C	-269 to +204 °C
Heating resistors	MP821, TO-220 power package, 20 W, Caddock	-	175 °C
Internal connectors	Glass-filled polyester UL94V-0, Harwin	-	85 °C
O-ring	Viton 70A/80A, Busak & Shamban	-	200 °C
PCBs	Kapton with copper, any	4 h/120 °C	130 °C (250 °C)
Ultra high vacuum grease	Fluorinated Fomblin grease, FM 090, Pfeiffer	-	100 °C
Vacuum connectors	Hermetic connect., Hirelco Intern. connectors, Microdot	-	95 °C
Sorption pumps	Zeolith, any	18 h/200 °C	350 °C
	Coconut active charcoal, any	18 h/20 °C	> 100 °C
Thermal fuse	R&S, 176-9148, any	-	75 °C
ZIF-Socket	Glass-filled polyphenylene sulfide (PPS), 3M, any	18 h/105 °C	105 °C

Table 2. Treatment of components.

Material		Washing				Vacuum baking (10 ⁻² mBar)	
		Possible solvent	Hand cleaning	1. Ultrasonic water bath with Tickopur detergent at 80 °C	2. Ultrasonic bath with water (80 °C) or non ultrasonic bath with solvent	Maximum temp.	Min. duration
Modified epoxy material		Acetone	no	30 min	30 min.	120 °C	16 h
Metals parts (Al and steel)		Acetone	yes	30 min.	30 min	180 °C	16 h
Electronic boards	ZIF-sockets	Alcohol	no	30 min	30 min	150 °C	72 h
	Raw boards	Alcohol	no	30 min	30 min	120 °C	72 h
	Soldered PCB	Alcohol	yes	Not Performed	Not Performed	85 °C	72 h
CCDs	EEV	None	yes	Not Performed	Not Performed	80 °C	72 h
	Tektronix	None	no	Not Performed	Not Performed	55 °C	72 h
	MIT/LL	None	yes	Not Performed	Not Performed	60 °C	72 h
Vacuum connectors		Alcohol	no	30 min	30 min	85 °C	16 h
Welded inner tank		Acetone	yes	30 min	30 min	85 °C	72 h
CFC inner tank structure		Alcohol	yes	30 min	30 min	85 °C	72 h
Painted shields		None	no	Not Performed	Not Performed	120 °C	72 h
Glued components		Alcohol	yes	Not Performed	Not Performed	120 °C	72 h
VITON O-rings		Alcohol	yes	30 min	30 min	120 °C	16 h
Zeolith (sorption pump)		-	no	-	-	>180°C	16 h
Active charcoal		Alcohol	no	-	-	100 °C	16 h
Vacuum pipes		Acetone	yes	30 min	30 min	180 °C	16 h
Fittings	Vacuum valve	Alcohol	yes	-	-	120 °C	16 h
	Vacuum gauge	Alcohol	yes	-	-	85 °C	16 h

Further investigations comparing zeolith and charcoal, used in the cryostat's molecular sieve, have been done. Coconut charcoal was found to

be the best material to prevent organic contamination. Regenerated zeolith absorbs water better. It is only if the geometry of the cryostat is unfavorable that water ice contamination on the CCD is unavoidable. This results from a large warm surface “looking” directly at the CCD detector. Lastly, a specially designed clean room was built for the proper handling and assembly of the cleaned parts to ensure very clean CCD cryostat. With all these measures, we have been able to avoid contamination at the telescopes for several years in all the CCD cryostats that are kept cold.

3. REFERENCES

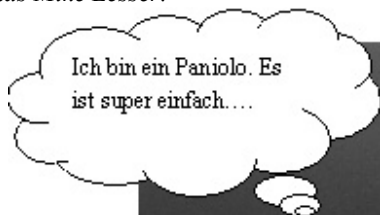
- [1] Deiries, S., Hummel, E., 2002, *How ESO achieves ultra-clean cryostats*, <http://www.eso.org/projects/odt/contamination/clean.html>.
- [2] NASA, *Materials and Processes Technical Information System*, <http://map3.msfc.nasa.gov/mapweb/page7.html>.
- [3] Schütz, O., Deiries, S., 2002, *Out-gassing of CCD components in the vacuum*, <http://www.eso.org/projects/odt/contamination/msreport/index.html>.



Sebastian Deiries, moments before measuring the temperature of molten lava. For the experiment he used a specially engineered PULPO system. The temperature was exactly 1234.2998 °C, averaged over 50 simultaneous measurements. (Courtesy P. Sinclair)



"Why can't we all just get along and use my process for backside passivation?" pleads Mike Lesser.



Ich bin ein Paniolo. Es
ist super einfach....



Gert Finger fulfills his lifetime dream of riding a "wild" bull.

THE IMPACT OF ASTRONOMY TECHNOLOGIES ON CHEMICAL ANALYSIS

M. Bonner Denton¹, Andrew K. Knight², Stephen C. Denson², Roger P. Sperline¹, Erick T. Young¹, James H. Barnes³, Gary M. Heiftje^{3,2}, Mahadeva Sinha², Mark Wadsworth², David W. Koppenaal⁴, Charles J. Barinaga⁴, Christopher A. Gresham⁵

¹University of Arizona, ²Jet Propulsion Laboratory, ³Indiana University, ⁴Battelle Pacific Northwest National Laboratory, ⁵Sandia National Laboratory

Abstract: *The chemical sciences have been profoundly influenced by the development of advanced focal plane array detectors. The incorporation of existing technologies developed for infrared multiplexers has already had a positive effect on the fields of isotope ratio mass spectrometry and ion mobility spectrometry. Multiplexer based ion detectors have improved detection limits by several orders of magnitude over conventional Faraday cups while maintaining a high degree of stability.*

Key words: *InfraRed (IR) multiplexers, Charge-Coupled Device (CCD), Charge-Injection Device (CID), ion detection, Ion Mobility Spectrometry (IMS), mass spectrometry, focal plane array*

1. INTRODUCTION

1.1 Use of Charge-Transfer Detectors in Analytical Chemistry

Technologies originally developed by the astronomy community have had a great effect on the field of chemical spectroscopy. Scientific Charge-Coupled Devices (CCDs) and Charge-Injection Devices (CIDs) are the detectors of choice for many areas of optical spectroscopy. The use of specialized formats and operating modes custom-tailored for spectroscopy, coupled with optimized optical trains, has resulted in a major increase in

performance. The high quantum efficiency, low read-noise, and multiplex advantage offered by modern focal plane arrays yield improved sensitivity, increased linear dynamic range, higher accuracy, and shorter analysis time. Recently, high performance charge read-out multiplexers designed for IR arrays have been utilized to detect ions in both mass spectrometry and Ion Mobility Spectrometry (IMS). The initial results have been spectacular.

1.2 Ion Detection

Detector technology employed in modern mass spectrometers and other instruments, such as ion mobility spectrometers, has remained virtually unchanged for the past thirty years. Two approaches are usually employed [1].

The more common method of ion detection uses an electron multiplier. Most instruments currently using electron multipliers have either a discrete dynode multiplier or a continuous dynode multiplier. These ion detectors operate when an ion crashes into a conversion dynode. Impact causes the emission of an electron subsequently amplified by a dynode structure similar to that found in a photomultiplier. This approach suffers from gain drift and from conversion efficiencies that degrade with use and are dependent on ion mass, ion energy, and ion conformation. Aging caused by contamination of the conversion dynode and subsequent multiplier dynodes further contributes to operational instability.

When stable measurements involving ion detection are required, such as in isotope ratio mass spectrometry, the next most common detector—the Faraday cup—is used. The classic Faraday cup consists of a conducting electrode surrounded by a conducting cup to contain secondary electrons. The ion beam is intercepted by the Faraday cup opening, and the discharge current is determined via a picoammeter. This method of direct current detection offers very high stability but suffers from lack of sensitivity. State-of-the-art Faraday cup detectors require 6000 ions/sec to produce a detectable signal [2,3]. Most instruments require a current several orders of magnitude higher (up to one million ions/sec) under normal operating conditions.

Professor M. B. Denton [1,4] suggested the use of a modified IR focal plane multiplexer to read out an array of micro-Faraday cup ion interceptors. The IR multiplexer was modified by removing the IR active photolayer and wire-bonding the Faraday fingers to the multiplexer input pads. Experimental characterization of this innovative approach is presented here, as are the first experimental results using this technology in conjunction with ion mobility spectrometry.

2. RESULTS

2.1 Micro-Faraday Finger Ion Detector Characterization

The first-generation micro-Faraday finger array ion detector consisted of 32 flat, gold, finger-shaped electrodes used as individual ion detector pixels, wire-bonded to a Capacitive Trans-Impedance Amplifier (CTIA) [4]. The CTIA was developed by E. T. Young of Steward Observatory for use on the multi-band imaging spectrometer (MIPS) to be deployed on the space infrared telescope facility project (SIRTF) [5]. The equivalent circuit for the detector is shown in Fig. 1. Each amplifier in the array employs a 36 fF capacitor in the feedback loop to produce an output of 4.4 mV per charge intercepted by the collecting electrode. The detector elements are 145 μm wide and follow a repeat pattern of a full pixel (5.0 mm), $\frac{1}{2}$ pixel (2.45 mm), a full pixel, and $\frac{1}{3}$ pixel (1.60 mm). The fingers are separated by a 10 μm gap, a 10 μm guard electrode to suppress secondary electron emission from spreading between pixels, and another 10 μm gap. This configuration was chosen to evaluate the effect of the finger capacitance on performance.

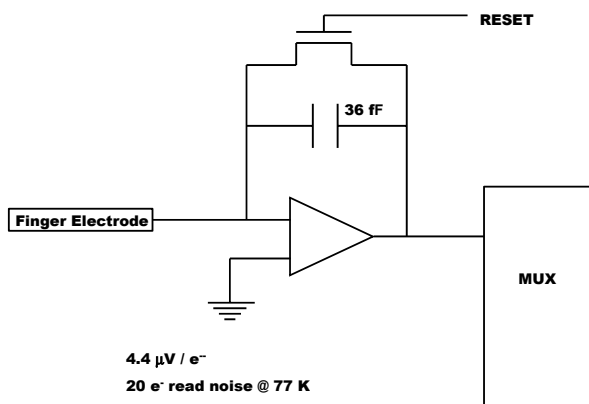


Figure 1. Effective circuit of an individual detector element.

Unlike traditional Faraday cup operation, the CTIA integrates charge from incident ions, enabling a few ions to be detected over an extended integration time. As a consequence, very few ions are required to produce a detectable signal while maintaining the high degree of stability associated with Faraday cup detection. The bipolar charge integration circuit allows the device to detect either positive or negative charged ions. The finger and multiplexer array are incorporated into a modified Spectral Instruments series 500 camera electronics package. The multiplex advantage of an array detector is realized because the spectrum does not need to be scanned. The increased sensitivity demonstrated thus far is phenomenal. Figure 2 shows the

detection of an Ar^+ beam by the micro-Faraday finger array, with 100 ions incident during an exposure time of 1.0 sec.

Ion Exposure : 100 Ions / sec in 1.0 sec

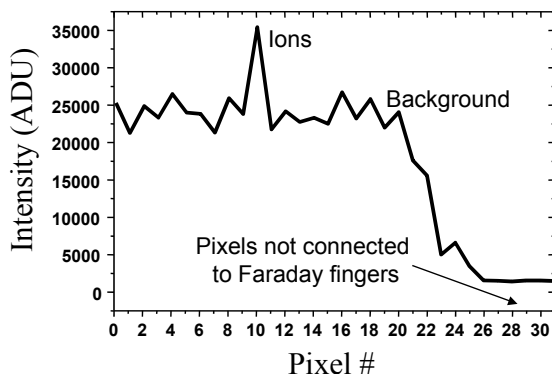


Figure 2. Detection of 100 Ar^+ ions by the micro-Faraday finger array.

The device readout architecture supports the ability to perform non-destructive readouts. This allows the expansion of the linear dynamic range from five orders of magnitude using destructive reads, as in a CCD, to over nine orders of magnitude using Random Access Integration (RAI). In RAI, the time between destructive read-outs is varied from pixel to pixel so that the detector elements receiving low ion fluxes are integrated for longer periods than those receiving a high ion flux. Detection limits can be further reduced through ensemble averaging, by using multiple non-destructive readouts. Read-noise decreases by the square root of the number of rereads. The overall detection limit is therefore reduced from thousands of ions/sec, as in a Faraday cup, to less than fifty ions.

2.2 Micro-Faraday Detector on a Mattauch-Herzog Mass Spectrometer

The micro-Faraday array was coupled to a Mattauch-Herzog geometry mass spectrometer and operated without the need to scan the magnetic field. The initial results of this union are presented by Barnes, et al. [6]. In this work, the resulting detection limit of the device when coupled to the mass spectrometer was studied, as were the isotope ratio accuracy, the % RSD, the linear dynamic range, and the effect of ensemble averaging on the % RSD by increasing the integration time. This spectrometer employed a DC glow discharge as the ion source with a steel sample (NIST SRM 443) serving as the cathode. The mass spectrometer was composed of an entrance slit and electric and magnetic sectors at angles of curvature of 31.8° and 90° ,

respectively. In a mass spectrometer of this geometry, the ions are focused onto a flat focal plane, suitable for an array detector.

The micro-Faraday array detector was placed at the center of the focal plane and was cooled to 233 K by a Peltier cooler. The range detected by the focal plane detector depended upon the mass-to-charge ratio setting of the mass analyzer. On this instrument, the 32 pixel device typically covered a range of 8 m/z units: future larger arrays could easily be made to encompass the entire m/z range of all elements on the periodic table. A mass spectrum containing several isotopes of Sn from a steel sample is shown in Fig. 3.

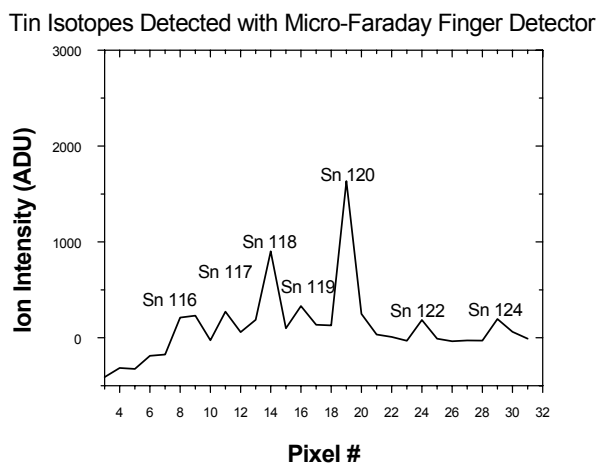


Figure 3. Mass spectrum of Sn isotopes using micro-Faraday finger array detector.

Detection limits for several isotopes comparable to those of the electron multiplier, previously employed as a single channel detector, were obtained for many elements in the ppb or ng/g range. In some cases, detection limits using the micro-Faraday array were superior to those of the electron multiplier, and in all cases, detection limits were improved three orders of magnitude over those observed with an electro-optical imaging (array) detector utilizing a CCD [7]. For ^{49}Ti , the detection limit using the micro-Faraday finger array was 5 ng/g (ppb). Ti from the steel sample was used to determine isotope ratio accuracy and precision. The average determined error in accuracy was 1-3%. At the longest integration time then possible with the camera read-out system, the % RSD for $^{46}\text{Ti}/^{47}\text{Ti}$ and $^{49}\text{Ti}/^{50}\text{Ti}$ was 0.2%. A decrease in % RSD was demonstrated with increased integration time from 2 msec to the limit of 100 sec. This decrease in % RSD is due to ensemble averaging. Longer integration times are expected to further improve isotope ratio precision.

Initial studies using this un-optimized focal plane detector are promising because the figures of merit are already comparable to those of established

technologies. The low detection limits can be further improved with advanced readout modes and specialized architecture to minimize read-noise. Isotope ratio precision is expected to increase as integration time is increased. Even un-optimized, the micro-Faraday array has a dynamic range of six orders of magnitude [6]. This new technology holds great potential for the advancement of detectors in mass spectrometry.

The micro-Faraday array currently has limitations when used in this particular mass spectrometer. At the moment, resolution is limited by physical pixel size. Future generations of this technology will employ smaller pixels, on the order of tens of microns, and optimized electronics.

2.3 Charge Detection in Ion Mobility Spectrometry

Ion mobility spectrometry relies on the differential times of flight between large and small ions in a viscous gas at or near atmospheric pressure. Ions are identified by their relative arrival times. IMS normally uses direct current Faraday plate detection [8] often requiring 10^6 ions for a detectable signal. The success of IMS has been severely limited by the large number of ions present in the mobility spectrometer that are required for detection. The presence of so many ions causes poor dynamic range (two orders of magnitude) and low resolution, which results in false positive responses for chemical warfare agent monitoring and detection limits too poor to be useful for certain compounds. Employing the micro-Faraday array on IMS instrumentation promises to improve linear response, eliminate false positives, and improve detection limits.

The micro-Faraday array detector was coupled to a PheMto-Chem PC-110 ion mobility spectrometer to determine the applicability of this new detector to IMS. Although the multi-channel capability of the array detector is not crucial in IMS, the detector's extreme sensitivity is a considerable advantage. The sample used in this study introduced a total of 100 femtograms of the explosive HMX in an acetonitrile solution. For each experiment, the micro-Faraday array was held at $-19\text{ }^{\circ}\text{C}$ and the IMS was heated to $80\text{ }^{\circ}\text{C}$ (a larger temperature differential rendered the multiplexer inoperable). Spectra were acquired at 8 Hz using a 2 msec shutter pulse and 1300 V applied to the drift rings. The average of 5 spectra of HMX is shown using the micro-Faraday array, along with the average of 10 background spectra, in Fig. 4.

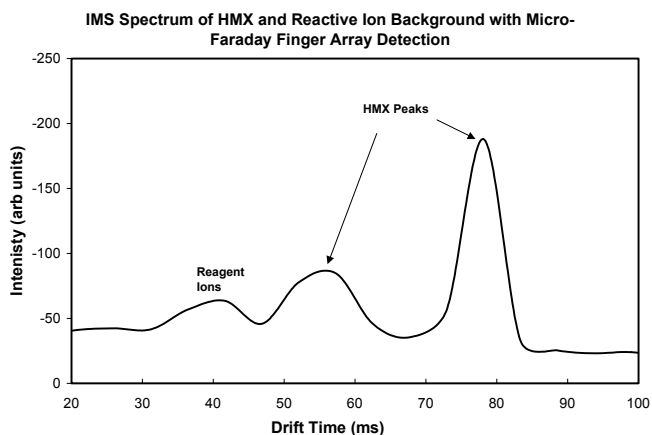


Figure 4. Ion mobility of HMX and reactive ions.

These preliminary data showed that the most significant advantage of the micro-Faraday array technology was a marked increase in sensitivity over that of conventional direct ion current detection. This sensitivity was tested by comparing HMX spectra acquired with the modified PC-110 IMS with those acquired on an unmodified PC-110. Two hundred averaged spectra with the direct current detection system were required to achieve the signal-to-noise ratio obtained from five averaged spectra with the micro-Faraday array detector. Additionally, the micro-Faraday array fingers used in this study intercepted only one-third of the area of the IMS ion beam. Had the full area been detected, sensitivity would have increased overall by two orders of magnitude over that of Faraday plates.

3. DISCUSSION

Although the micro-Faraday finger array detector has been shown to work in mass and ion mobility spectrometries with acceptable results, these two types of detectors have yet to be optimized. These studies indicate that technologies developed for IR focal plane detectors can be adapted to create improved ion detectors for chemical analyses.

Ion detectors for various applications require significantly different operating characteristics. Isotope ratio studies require long integration periods to achieve high precision (the 0.01% RSD design goal of the DOE). Ion mobility experiments, on the other hand, require high speed because full spectra must be acquired on the ms time scale—charge measurement precision is not as important as time resolution. Other parameters, including

operating temperature and pressure, detector-element geometry, stability requirements, and dynamic range, must be optimized for each application.

4. CONCLUSION

Results obtained using ion detector arrays based upon IR focal plane multiplexers are comparable to those obtained with single channel electron multipliers and are superior to those of traditional Faraday cups while also offering a significant multiplex advantage. Optimized micro-Faraday array detectors for ion detection have the potential to revolutionize chemical techniques, such as mass spectrometry and ion mobility spectrometry. Development of multiplexers and readout systems specifically for ion detection in chemical fields will greatly improve the capabilities of modern analytical instruments.

5. ACKNOWLEDGEMENTS

The authors would like to acknowledge support for this work provided by the DOE, Office of Nonproliferation Research and Engineering, under contract DE-AC06-76RLO-1830.

6. REFERENCES

- [1] Denton, M. B., 1998, *Spectroscopic Instrumentation in the 21st Century: Excitement at the Horizon*, Plenary Lecture, Winter Conference on Plasma Spectrochemistry (Scottsdale, AZ).
- [2] Evans, S., 1990, *Detectors*, Meth Enzymol **193**, p. 61.
- [3] Geno P.W., 1992; *Ion Detection in Mass Spectrometry*, NATO ASI Ser., Ser. C, (Mass Spectrom. Biol. Sci.: Tutorial), **353**, p. 133.
- [4] Knight A.K., Sperline R.P., Hieftje G.M., Young E., Barinaga C.J., Koppenaal D.W., Denton M.B., 2002, *The development of a micro-Faraday array for ion detection* Int J Mass Spectrom; **215**, p. 131.
- [5] Young, E. T., Scutero, M., Rieke, G. H. , Davis, J., 1995, *Construction of the large-format far-infrared array for SIRTf*, Infrared Detectors and Instrumentation for Astronomy, ed. A.M. Fowler, SPIE **2475**, p. 441.
- [6] Barnes J.H., Sperline R.P., Denton M.B., Barinaga C.J., Koppenaal D.W., Hieftje G.M., 2002, *Characterization of a new focal plane camera fitted to a Mattauch-Herzog geometry mass spectrograph. I. Use with glow discharge source*. submitted to Anal. Chem.
- [7] Solyom, D. A.; Burgoyne, T. W.; Hieftje, G. M., 1999, *Plasma-source sector mass spectrometry with array detection*, J. Anal. At. Spectrom. **14**, p. 1101.
- [8] Eiceman G.A., Karpas Z., 1994, *Ion Mobility Spectrometry* CRC, Boca Raton, FL.

A CCD-BASED CURVATURE WAVEFRONT SENSOR FOR ADAPTIVE OPTICS IN ASTRONOMY

Reinhold J. Dorn¹, Barry E. Burke² and James W. Beletic³

¹European Southern Observatory, ²MIT Lincoln Laboratory, ³W.M.Keck Observatory

Abstract: *Advances in Charge-Coupled Device (CCD) technology motivated an investigation of the use of a specially designed CCD as the wavefront sensor detector in a 60 element curvature AO system. A CCD has never been used before as the wavefront sensor in a low light level curvature adaptive optics system. A CCD can achieve nearly the same performance as APDs at a fraction of the cost and with reduced complexity for high order wavefront correction. Moreover the CCD has higher quantum efficiency and a greater dynamic range than an APD. A readout noise of less than $1.5 e^-$ at 4000 frames/sec was achieved. A back-illuminated thinned version of this CCD can replace APDs as the best detector for high order curvature wavefront sensing.*

Key words: *Charge-Coupled Device (CCD), Avalanche Photo Diode (APD), curvature sensing, Adaptive Optics (AO), detectors*

1. INTRODUCTION

Curvature AO systems have traditionally used Avalanche Photo Diodes (APDs) as detectors. APDs are photon counting devices that produce a pulse on their output whenever a photon is detected. APDs have no readout noise and readout is almost instantaneous. However, they have some serious drawbacks compared to Charge-Coupled Devices (CCDs):

- ***A Small dynamic range.*** This calls for the use of neutral density filters to adapt the incident photon flux to the dynamic range of the APD. CCDs, on the other hand, have an enormous dynamic range and thus require no filters.

- **Low quantum efficiency.** APDs typically have a peak quantum efficiency of 70% at 700 nm, while the same number for CCDs is over 90%.
- **High dark current.** APDs generate dark current, or false photon counts, of 100 to 250 counts/sec depending on the cost of the APDs, while a well-cooled CCD generates a negligible amount of dark current.
- **High cost.** A 60 element AO system using APDs is significantly more expensive than one using a CCD.

2. ARCHITECTURE AND FUNCTIONALITY OF THE CURVATURE CCD

To summarize the design [1, 2], the curvature CCD (see Fig. 1) consists of 80 integration areas (superpixels). Each superpixel consists of 20×20 pixels, where a pixel is $18 \times 18 \mu\text{m}$ in size. The total height of each column is 10 superpixels or 200 pixels. There are 8 columns for a total of 80 superpixels and an independent tip/tilt sensor array. Very short exposure times (250 μsec) with “long” integration times (1 to 20 msec, 2 to 40 cycles of a 2 KHz membrane) are possible with the ability to switch between half-cycle integrations within 10 μsec and to store half-cycle frames on-chip while integrating other half-cycle frames. The read out time of all pixels is 250 μsec with the use of multiple readout ports to have slower readout rates and lower readout noise. BI (Back-Illuminated) devices will have high quantum efficiency (peak greater 80%).

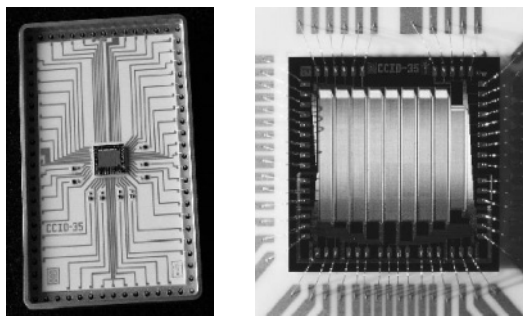


Figure 1. Pictures of the curvature CCD

3. PROTOTYPE SYSTEM AND CCD TEST RESULTS

To test the performance and the functionality of the curvature CCD, a laboratory system (see Fig. 2) has been built to allow independent testing without the need to interface to a full adaptive optics system. An integrating sphere and a stable light source were used to simulate the membrane movement and providing the light signal for CCD characterization. An Oeffner relay optics was designed (consisting of two spherical, reflecting surfaces) to re-image the light of the fibers 1:1 onto the superpixels) and a fiberfeed with 60 individual fibers plus 4 additional fibers for the tip/tilt sensor to feed the subapertures of the CCD with light.

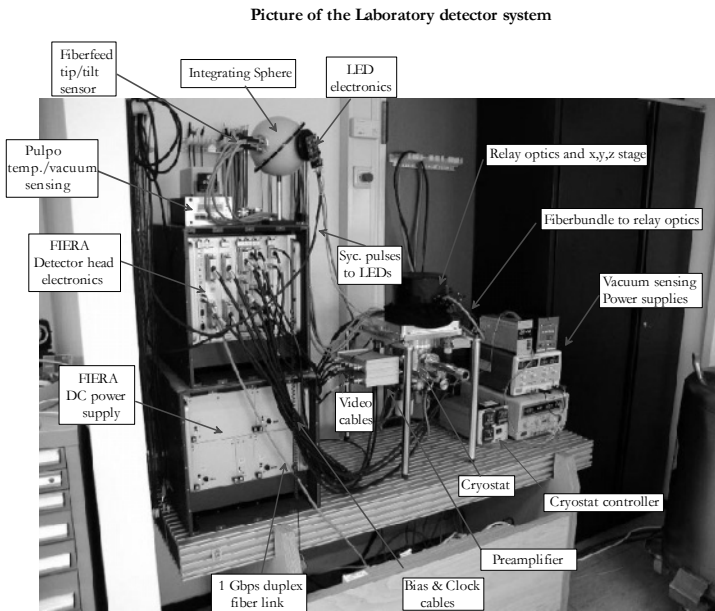


Figure 2. Prototype system of the CCD based curvature wavefront sensor

A readout noise of less than $1.5 e^-$ was achieved for all readout ports including the tip/tilt sensor at a readout speed of 4000 frames/sec [1]. With all pixels per readout port binned into 12 superpixels, it was possible to read the serial register relatively slowly at 50 Kpix/sec. Vertical and horizontal CTE is better than 0.99999 down to lowest light levels. Residual non-linearity better than 0.5% / -0.5%. (peak to peak). Negligible amount of dark current at 197 K ($0.25 e^-$ per subaperture at 50 Hz frame rate).

4. CCD PERFORMANCE COMPARED TO APDS

A common measure used to quantify the performance of an AO-system is the *Strehl ratio* of the corrected Point Spread Function (PSF). To compare the performance of the CCD and APDs, a computer model of the atmosphere, telescope and AO-system was developed in MatLab. Using the computer model [1,3], the Strehl ratio in K band was measured for guide stars of magnitude 10 to 18 and compared for the different detectors. The CCD performs as well as APDs over the entire range of magnitudes down to very faint guide stars at magnitude 18. Figure 3 and Table 1 show a small difference in the performance of the CCD of 3% at magnitude 15 compared to APDs

Table 1. Parameters for the Simulation

Property	APD	CCD
Sky background magnitude	19.0	19.0
Field of view diameter	2"	2"
Quantum efficiency	70%	80%
Dark current [e ⁻ /sec]	250	0
Read-out noise [e ⁻ RMS]	0	1.5
Read-out delay [μs]	0	250
Seeing [arcsec]	0.65	0.65

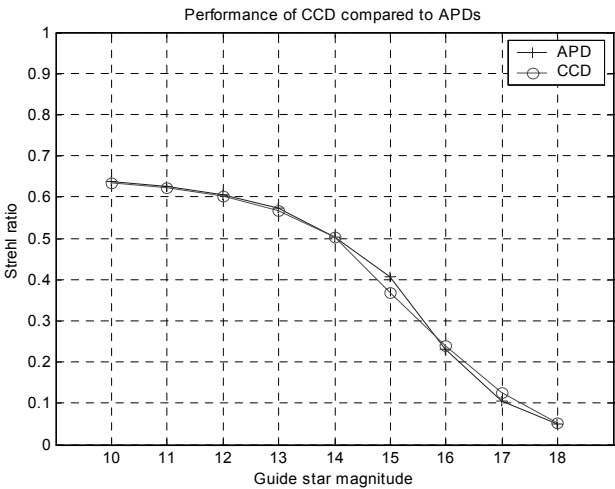


Figure 3. CCD performance compared to APDs

5. CONCLUSION

It can be concluded that the CCD achieves nearly the same performance as APDs. Thinned versions have the potential to work as well as APDs with reduced cost and reduced complexity. No neutral density filters are needed (simpler) and the CCD provides a much greater integration area per subaperture (360 μm by 360 μm). Moreover, the CCD has a higher quantum efficiency and a greater dynamic range (factor 1000) than APDs. A readout noise of less than 1.5 e^- at 4000 frames/sec has been demonstrated with the laboratory system. The curvature CCD combines high order curvature sensing with the possibility of separate tip/tilt sensing in one sensor and will be tested in the future at the CFHT telescope in the mainframe of the CFHT's FlyEyes project [4].

6. REFERENCES

- [1] Dorn, R.J., 2001, *A CCD based curvature wavefront sensor for Adaptive Optics in Astronomy*; Ph.D. thesis; University of Heidelberg/Germany.
- [2] Beletic, J. W., Dorn, R. J., Craven-Bartle, T., Burke, B., 2000, *A new CCD for curvature wavefront sensing*, Optical Detectors for Astronomy II, eds. Amico, P. and Beletic, J.W., Kluwer Academic Publishers, pp. 283-309.
- [3] Craven-Bartle, T. V., Dorn, R. J. and Beletic, J. W., 2000, *Computer simulation of CCDs and APDs for curvature wavefront sensing*, SPIE's International Symposium on Astronomical Telescopes and Instrumentation 2000, Munich, March 27-31, 2000.
- [4] Cuillandre, J.-C., Beletic, J.W., Dorn, R.J., Beletic, J.W., Luppino, G.A., Burke, B., Gorceix, N., Isani, S., Thomas, J., Lai, O., Craven-Bartle, T, *CFHT's FlyEyes: Assessing on-sky performance of the new MIT/LL CCID35 CCD curvature wavefront sensor*, these proceedings, pg. 299



*The audience listens intently.
All the talks were held at the Hawaii Preparatory Academy (HPA) theater.*

PERFORMANCE AND RESULTS OF THE NAOS VISIBLE WAVEFRONT SENSOR

Philippe Feautrier¹, Reinhold J. Dorn², Gérard Rousset³, Cyril Cavadore², Julien Charton¹, Claudio Cumani², Thierry Fusco³, Norbert Hubin², Pierre Kern¹, Jean-Louis Lizon², Yves Magnard¹, Pascal Puget¹, Didier Rabaud³, Patrick Rabou¹ and Eric Stadler¹

¹Laboratoire d'Astrophysique de Grenoble (LAOG), ²European Southern Observatory (ESO),

³Office National d'Etudes et de Recherches Aéronautiques (ONERA)

Abstract: *The Nasmyth Adaptive Optics System (NAOS) was installed in December 2001 on the Nasmyth focus of the ESO Very Large Telescope (VLT). It includes two wavefront sensors: one operates at IR wavelengths, the other at visible wavelengths. This paper describes the NAOS visible wavefront sensor based on a Shack-Hartmann principle. This wavefront sensor unit includes: 1) A continuous flow liquid nitrogen cryostat and a low noise fast readout CCD camera controlled by the ESO new generation CCD system FIERA using a fast frame rate EEV/Marconi CCD-50. This 128×128 pixels split frame transfer device has a readout noise of 3 e⁻ at 50 Kpix/sec/port. FIERA provides remotely controlled readout modes with optional binning, windowing and flexible integration time. 2) Two remotely exchangeable micro-lens arrays (14×14 and 7×7 micro-lenses) cooled to the CCD temperature (-100 °C). The CCD array is directly located in the micro lenses focal plane, only a few millimeters apart without any relay optics. Additional opto-mechanical functions are also provided (atmospheric dispersion compensator, flux level control, field of view limitation). On-sky performances of the wavefront sensor are presented. Adaptive optics corrections were obtained with a reference star as faint as visible magnitude 17. The maximum achievable band-pass is 35 Hz at 0 dB for the open loop transfer function.*

Key words: *Charge-Coupled Device (CCD), low noise, camera, Adaptive Optics (AO) system, wavefront sensor, Strehl Ratio, microlenses, cryostat.*

1. INTRODUCTION

NAOS, fully described in [1] and [2], is the Adaptive Optics (AO) system of the ESO Very Large Telescope (see Fig. 1). Installed at the Nasmyth focus of the VLT, NAOS is the AO system for CONICA (see [3]), the science infrared camera. NAOS will provide diffraction-limited images in the 1-5 μm wavelength range. NAOS was designed and manufactured by a French consortium (ONERA, LAOG and Observatoire de Paris).

The deformable mirror with 185 useful actuators compensates for the atmospheric disturbance measured by two Shack Hartmann WaveFront Sensors (WFS), one covering the visible wavelengths and the other covering the infrared. This paper describes the visible wavefront sensor and its CCD camera. NAOS is mounted on the telescope adapter rotator and rotates with the telescope field rotation. Therefore, the structure stiffness of the whole instrument is critical for the final performance of the instrument. The opto-mechanical path of the wavefront sensing channel requires special care to avoid flexure which may highly contribute to an image quality degradation.



Figure 1. NAOS-CONICA mounted on the Yepun telescope (left) and the VLT Platform at Paranal just before the NAOS first light in November 2001 (right).

The sensitivity of the whole NAOS instrument is highly dependent on the wavefront sensor performance. The visible WFS for NAOS uses a 128×128 pixels low noise CCD fabricated by EEV/Marconi with 16 output ports to allow a high frame rate (up to 500 frames/sec) and low noise ($3 e^-$).

2. NAOS AND VISIBLE WAVEFRONT SENSOR PRESENTATION

A set of dichroic beam splitters allow the sharing of the NAOS incoming light between the scientific path (CONICA) and the wavefront sensing path. The reflected part of the light is redirected to the wavefront sensors.

A field selector, composed of two parallel mirrors placed in the f/15 beam, chooses the reference star for wavefront sensing separately from the scientific observed object. The description of the field selector is given in [4]. Then a mirror selects the required Shack-Hartmann wavefront sensor, either IR or visible WFS.

The visible wavefront sensor is basically comprised of a cooled CCD camera, including 2 lenslet arrays that can be remotely exchanged and one opto-mechanical bench located at the cryostat outside. The different elements of the visible wavefront sensor are shown in Fig. 2.

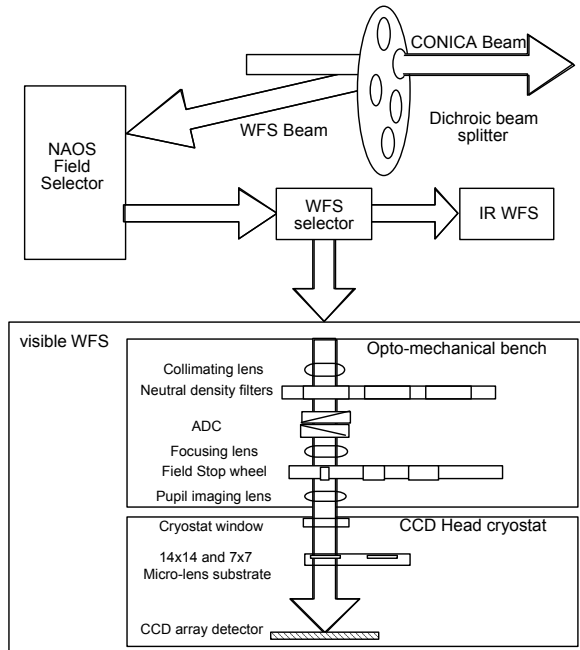


Figure 2. Block diagram of NAOS and of the visible wavefront sensor.

3. THE LOW NOISE READOUT CAMERA

The Visible WFS Detector System (see [5,6]) is split into three main parts: the CCD detector, the cryostat and the CCD controller.

3.1 The EEV/Marconi CCD-50 description and architecture

The CCD used in the NAOS project was manufactured by EEV/Marconi based on a contract with ESO.

This CCD is a split frame transfer CCD with a light sensitive area of 128×128 pixels and a pixel size of $24 \mu\text{m}$. The 2 storage sections are light shielded. If the light shield is misaligned an additional 4 rows on each storage section will compensate. The charge is shifted to each 8 output amplifiers on the bottom and top side. Therefore, the CCD is partitioned into 16 sections with one amplifier per section (see Fig. 3).

A subsection of the CCD with 16×64 pixels of the image zone, the corresponding storage section and the serial register are also shown in this Fig. 3. All of these sections of the CCD are clocked in exactly the same way. Due to the lenslet array configuration (14×14 or 7×7 sub-apertures), only 14 of the 16 CCD outputs are used for NAOS.

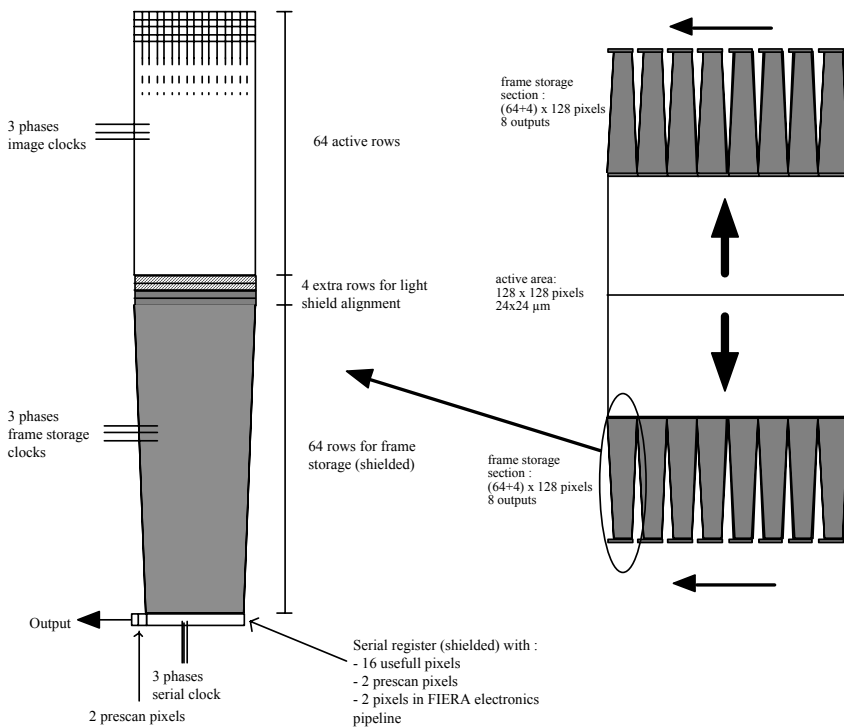


Figure 3. Detector architecture of the 128×128 CCD.

3.2 The FIERA CCD Controller

3.2.1 Presentation

ESO has built a universal CCD controller able to drive a variety of "new generation" CCDs. This system is called FIERA (Fast Imager Electronic

Readout Assembly). The requirements for the FIERA CCD Controller are briefly summarized hereafter:

- System noise negligible compared to the readout noise of the CCD amplifier.
- $\times 2$ and $\times 4$ binning capability, windowing capability
- Up to 2 Mpix/sec operation
- 16 simultaneous video outputs can be managed (on NAOS, we use 14 A/D converters 16 bits/1 MHz)
- Cross-talk between channels of the CCD controller must be negligible – less than 1 bit or less than the CCD readout noise.

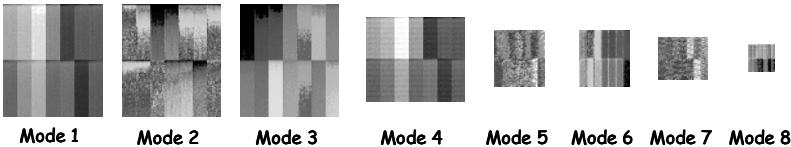
3.2.2 The CCD readout modes and noise performances

Each readout mode defines the following parameters: windowing, binning, conversion gain (in e^-/ADU) and frame rate. We need several readout modes for the following reasons:

- we have to match the readout mode with the micro-lens array configuration (7×7 or 14×14 microlenses).
- the readout noise has a strong impact on the NAOS performance in terms of sky coverage. Because the readout noise decreases with the pixel frequency, the CCD readout is designed to skip the unused pixel, either by binning or by windowing. The pixel frequency can then be reduced. Table 1 shows the list of readout modes that are effectively used in NAOS. Also shown in this table is the noise performance of the CCD camera measured on the VLT telescope, demonstrating the very low noise with this system.

Table 1. List of readout modes for the NAOS visible wave-front sensor and readout noise performance measured on the VLT telescope. CCD dark images are also shown.

Mode Number	Pixel rate (Kpix/sec)	Gain (ADU/ e^-)	Measured Noise (e^-)	Binning	Windowing	Max Frame Rate (Hz)
1	280	0.34	3.9	1 \times 1	No	209
2	635	0.33	5.4	1 \times 1	No	444
3	635	2.1	6.9	1 \times 1	No	444
4	280	0.35	3.9	1 \times 1	6 \times 6	277
5	50	0.34	2.9	2 \times 2	No	136
6	280	0.36	4.3	2 \times 2	No	587
7	50	0.34	2.98	2 \times 2	6 \times 6	133
8	50	0.34	2.92	4 \times 4	No	383



3.3 Cryostat flexures

The specifications concerning the cryostat flexures when the system is rotated are very strict. Flexure tests were performed using a rotating table allowing a full 360° rotation to simulate the NAOS adapter rotation during the astronomical observations on the telescope.

Cryostat flexures as low as $2\text{ }\mu\text{m}$ (peak to peak for one complete turn) of the inner part of the cryostat compared to the outer part was measured and $0.1\text{ }\mu\text{m}$ in the same conditions for the microlenses displacement compared to the CCD. These demonstrated a remarkable stiffness of the cryostat and of the micro-lens arrays exchange mechanism (see [6]).

3.4 Lenslet array alignment

The two lenslet arrays are aligned with respect to the CCD and the following specifications :

- X and Y lenslet location (CCD) accuracy : $2\text{ }\mu\text{m}$
- parallelism CCD/lenslet array : $2\text{ }\mu\text{m}$ from one side of the lenslet to the other

An image of the aligned spots obtained at cold temperature with the two lenslet arrays is shown in Fig. 4. From these images, we computed the location of each spot by measuring the centroid of each spot and, hence, we deduced the overall lenslet alignment accuracy in location and parallelism.

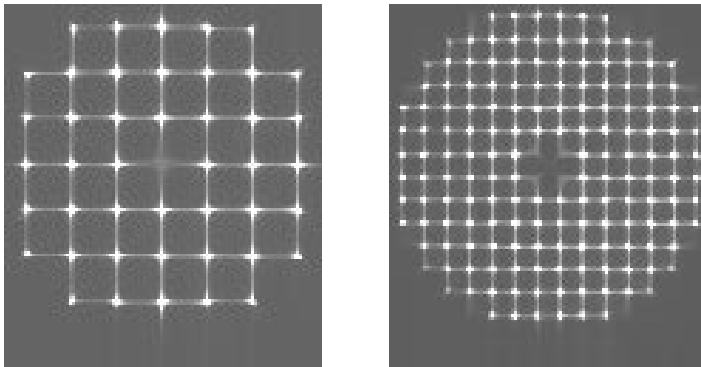


Figure 4. (left) Image of the spots with the 7×7 lenslet array at cold temperature, micro-lenses aligned; (right) same image with the 14×14 lenslet array.

The two lenslet arrays can be exchanged at cold temperature with a re-positioning precision of $2\text{ }\mu\text{m}$ (RMS).

4. RESULTS ON THE VLT TELESCOPE

NAOS, including all its subsystems such as the visible wavefront sensor, was installed on the VLT *Yepun* telescope unit in mid-November 2001, as well as the scientific infrared camera CONICA. NAOS and CONICA obtained their first light on the VLT November 25th 2001 during the first commissioning period. The excellent performance of NAOS and the visible wavefront sensor allows very high Strehl ratio as shown in Fig. 5.

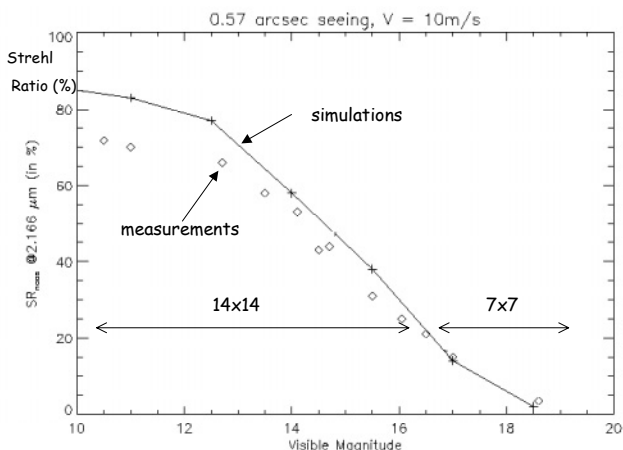


Figure 5. Strehl Ratio of NAOS and CONICA using the visible wavefront sensor. Simulations and measurement in the laboratory are shown at the same time in the figure, as well as the micro-lenses configuration (7×7 or 14×14). The seeing was 0.57 arcsec, the wind speed 10 m/s, and the Strehl Ratio is measured using a narrow band filter at 2.166 μm with the CONICA science camera.

At low visible magnitude, a Strehl Ratio of up to 70% can be obtained, whereas closed-loop AO operation was demonstrated with a natural guide star as faint as magnitude 17, as shown in Fig. 6. These two properties (high Strehl ratio and closed-loop with very faint stars) demonstrate the remarkable qualities of the NAOS visible wavefront sensor and of its CCD camera. The maximum achievable band-path is 35 Hz at 0 db for the open loop transfer function. This was measured in the laboratory using readout modes at 444 Hz corresponding to the lowest magnitudes of Fig. 5.

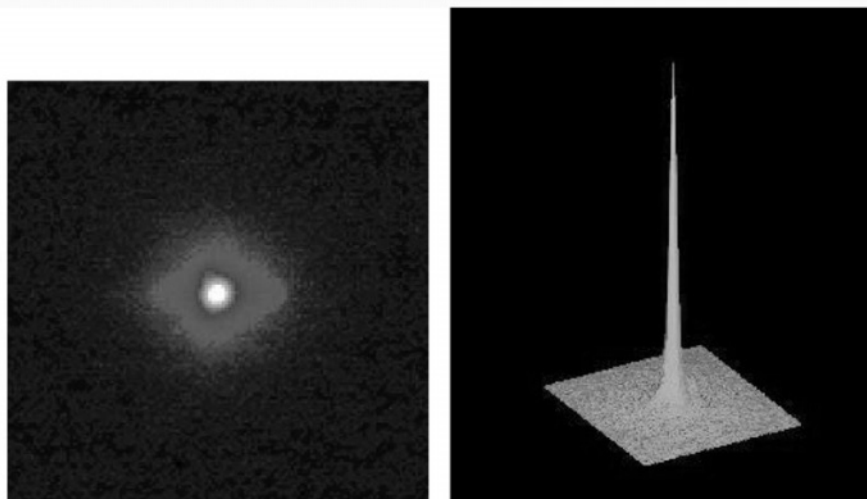


Figure 6. With the visible wavefront sensor, NAOS was able to close the loop using a 17-magnitude reference star just one week after the NAOS first light on the VLT (November 25, 2001).

5. CONCLUSION

The NAOS visible wavefront sensor, based on the Shack-Hartmann principle, was a collaborative effort between the ESO Optical Detector Team, the Observatory of Grenoble and ONERA. It demonstrated excellent performance due to the quality of the EEV/Marconi CCD chip, of the ESO/FIERA camera and the mechanical stiffness. Despite the possibility to remotely exchange the two lenslet arrays on the sky inside the cryostat at cold temperature, the mechanical properties of the wavefront sensor in terms of stiffness and re-positioning accuracy are remarkable. Also the possibility to obtain very low readout noise with fast frame rates gives the NAOS AO system the possibility to have high Strehl ratios and close the loop with very faint reference stars, thereby increasing the sky coverage with visible natural guide stars. NAOS will be offered to the astronomical community by autumn 2002.

6. ACKNOWLEDGMENTS

These developments are funded by ESO under contract number 49632/ESO/INS/95/7454/GWI. Additional funds are provided in France by INSU/CNRS and ONERA. The authors are grateful to all the colleagues involved in that project at LAOG (Grenoble), Observatoire de Paris/Meudon, ONERA and ESO.

7. REFERENCES

- [1] Rousset, G., Lacombe, F., Puget, P., Gendron, E., Arsenault, R., Kern, P. Y., Rabaud, D., Madec, P., Hubin, N., Zins, G., Stadler, E., Charton, J., Gigan, P., Feautrier, P., 2000, *Status of the VLT Nasmyth Adaptive Optics System (NAOS)*, Proc. SPIE Vol. **4007**, p. 72.
- [2] Rousset, G., et al., 2002, *The first AO system of the VLT: on-sky performance*, SPIE proceedings, Astronomical Telescope and Instrumentation, 22-28 August 2002, Waikoloa, Hawaii, USA.
- [3] Lenzen, R., Hofmann, R., Bizenberger, P., 1998, *CONICA: the high resolution NIR camera for the ESO VLT*, Proc. SPIE Vol. **3354**, p. 606.
- [4] Spanoudakis, P., Zago, L., Chetelat, O., Gentsch, R., Mato Mira, F., 2000, *NAOS Field Selector*, Proc. SPIE Vol. **4007**, p. 408.
- [5] Cavadore, C., Dorn, R.J., 2000, *Charged Coupled Devices at the European Southern Observatory Performances and results*, Optical Detectors for Astronomy II: State-of-the-Art at the Turn of the Millenium, 4th ESO CCD Workshop, 1999, Garching, Germany, eds P. Amico and J. Beletic, p. 25.
- [6] Feautrier, P., Kern, P., Dorn, R. J., Rabou, P., Laurent, S., Lizon, J., Stadler, E., Magnard, Y., Rondeaux, O., Cochard, M., Rabaud, D., Delboulbe, A., Puget, P., Hubin, N., 2000, *The NAOS visible wavefront sensor*, Proc. SPIE Vol. **4007**, p. 396.



Giovanni Bonanno, moments before strangling himself with the lasso. Behind him, unaware of the danger, is Dietrich Baade.

FABRY PEROT OBSERVATIONS USING A NEW GaAs PHOTON COUNTING SYSTEM

Jean-Luc Gach¹, Olivier Hernandez^{1,2}, Jacques Boulesteix¹ and Claude Carignan²

¹Observatoire de Marseille, ²Laboratoire d'Astrophysique Expérimentale, Université de Montréal

Abstract: *We present a third generation Image Photon Counting System (IPCS) based on an GaAs photo cathode that can achieve quantum efficiency up to 28%, comparable to a thick CCD, but without readout noise. This system is 10 times more sensitive at H_α wavelength than previous photon counting cameras. In terms of S/N ratio, the system outperforms the CCD for extremely faint fluxes, including anti-reflective coated low noise thin CCDs.*

This system offers up to $1K \times 1K$ pixel, which is the largest monolithic IPCS. An original cooling system based on a Ranque-Hilsh vortex tube is used on this camera. The real-time centering is done by a scalable DSP board. Preliminary results obtained with this new camera coupled with a scanning Fabry-Perot at the Cassegrain focus of the 3.6-m ESO telescope, the 1.93-m Observatoire de Haute Provence (OHP) telescope, and 1.6-m mont Mégantic OmM (Québec) telescope are presented.

Key words: *Image Photon Counting System (IPCS), photon counting detectors, Fabry Perot, galaxies, radial velocities, integral field spectroscopy*

1. INTRODUCTION

In the last two decades, several multiplex scanning instruments, e.g., Fourier Transform Spectrographs (FTS) [1], scanning Fabry-Perot integral field spectrometers such as TAURUS [2], CIGALE [3], HIFI [4], and PYTHEAS [5], have been developed and tested at the foci of 2-6-m class telescopes. At the same time, since the last development achieved in the 80's

(see [6-8]), it is only recently that image photon counting systems (IPCS) have opened new perspectives to the full exploitation of multiplex scanning instruments. Indeed, a new generation of GaAs and GaAsP photocathodes have appeared. They have high quantum efficiency (QE), proximity focused image intensifier, without image distortion, associated high frame rate and large format CCDs that can be used as detectors behind the image intensifier leading to large format IPCS.

The paper presents the study and the application of a third generation of IPCS based on a GaAs photo cathode that can achieve a quantum efficiency up to 23 %, which is comparable to a thick CCD, but without readout noise.

2. CCD vs IPCS

One remarkable sign of progress with this new generation of GaAs electron tubes (GaAs photo cathode, 2 MCPs and the phosphor screen) is that their quantum efficiency is more than 5 times higher than the previous electron tubes in the visible. Twenty-eight percent of RQE is now achieved over a broadband range of wavelength (500-850 nm see Fig.1)

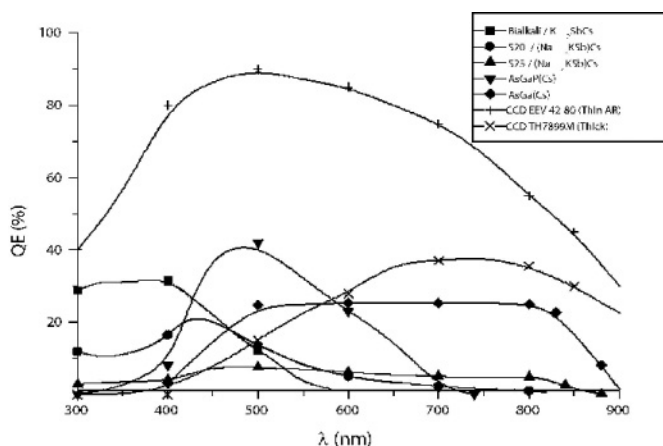


Figure 1: Quantum efficiency of different types of photo cathodes compared to CCDs.

IPCS do not have readout noise and are less affected by cosmic rays, since one event is seen as one photon only, a decisive advantage with respect to CCDs when long exposures are required as in the case of faint object investigation. Although first generation IPCSs offer poorer quantum efficiency with respect to CCDs and are affected by image distortion, they are still competitive with the latter in multiplex instruments or in speckle interferometry.

Because of the very small readout time (25 ms in our case) of an IPCS, it is possible to observe each channel several times during the multiplex observation, averaging then all these variations. Typically, each channel is observed for 5-15 sec, and when the last channel has been integrated, the first is observed again. Each set of n channels is called a cycle which has a typical duration of 3-10 min (depending on the exposure time per channel and the number of channels) and a total observation of several cycles. Technically, it is possible to make one whole cycle within a few seconds, taking only one 25 ms exposure per channel, but we found this unnecessary and instead preferred instrument stability. Since there is no readout noise, it is then possible to sum up each i^{th} channel of all the cycles without losing any SNR. Obviously, adapting this observing technique to CCDs would considerably degrade the SNR due to the large number of images produced. This has been largely discussed in Gach et al. [9].

3. SYSTEM OVERVIEW¹

The camera head (see Fig. 2) is composed of a GaAs proximity focused 2-stage MCP image intensifier tube fiber-coupled to a 1K×1K 40 frame/sec (fps) CCD. The cathode is cooled down to -25 °C with a cold air flow in the cold finger. Vacuum is done between the cathode and the input window to avoid thermal losses or condensation and ice on the window. The CCD can work in 1K×1K mode (12 μm pixel) at 40 fps or in hard binned mode

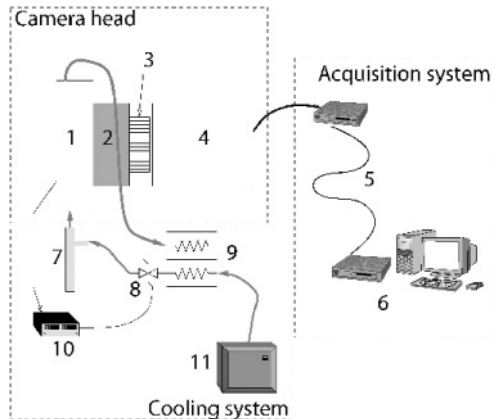


Figure 2. Overview of the system: (1) Cold finger, (2) Image intensifier, (3) Fiber bundle, (4) 1K×1K CCD, (5) 1.5 Gbits/s fiber link, (6) Host centering computer, (7) Vortex tube, (8) Proportioning valve, (9) Heat exchanger, (10) Temperature controller, (11) Air compressor.

¹ (See [10] for a complete description)

512×512 pixels at 80 fps (24 μm pixel). Each photon interacting with the photo cathode is amplified up to 10^6 to 10^7 times by the image intensifier producing a signal much larger than the internal noise of the CCD. In previous IPCSs, the centering of the spot produced by amplified photons was done by a hardwired system. Here, the camera is connected to a scalable DSP board based on the TMS 320C80 MVP chip consisting of 4 DSP cores working in Multiple Instruction Multiple Data scheme (MIMD). This board acquires data from the camera into a buffer and centers each spot. This allows more versatility and even would permit the centering of events at a better resolution than the physical pixel of the readout CCD by fitting a Gaussian on the event spot. The acquisition and centering of the events is done in real time by the ADHOCw software developed by Jacques Boulesteix (see [11]).

4. RESULTS

The new IPCS camera has been tested coupled with the scanning Fabry-Perot CIGALE at the Cassegrain focus of the 3.6-m ESO telescope (La Silla: September 2000), on the 1.93-m OHP telescope (October 2000 and May 2001), and with the scanning Fabry-Perot in the PANORAMIX focal reducer of the 1.6-m OMM telescope (March 2001). The observations are parts of different scientific projects addressed to studies going from gas rich, late-type galaxies (GHASP project, [12]) to gas poor early-type systems [13].

Figure 3 shows raw comparison between CCD and the new IPCS system. The CCD data were obtained at the 3.6-m CFH telescope with an exposure of 3 hours. The IPCS data were obtained on the 1.6-m Observatoire du mont Mégantic Telescope (OmM) with only a 1 hour exposure.



Figure 3. (left) NGC 2403 velocity field using the MOS/FP at CFHT. (right) NGC 2403 velocity field using FaNTOmM IPCS at OmM.

5. ACKNOWLEDGEMENTS

We would like to thank the ESO (La Silla), the OHP, and the OmM staff for their assistance during the commissioning of the new camera, Olivier Boissin for his technical help and Mathieu Ouellet for the mechanical design. Many thanks also to our collaborators Chantal Balkowski, Nils Bergvall, Sébastien Blais-Ouellette, Isabel Marquez, Josefa Masegosa, Claudia Mendes de Oliveira. Special thanks to Philippe Amram, Olivia Garrido, Michel Marcelin, Goran Östlin, Henri Plana and Roberto Rampazzo for their reduced data [14].

6. REFERENCES

- [1] Maillard, J.P., Simons, D., 1992, *Spectro-Imaging Mode of the CFHT-FTS with a NICMOS Camera: First Results*, ESO Conf. on Progress in Telescope and Instrumentation Technologies, p. 733.
- [2] Atherton, P.D., Taylor, K., Pike, C.D., Harmer, C.F.W., Parker, N.M., Hook, R.N., 1982, *TAURUS: A wide-field imaging Fabry-Perot spectrometer for astronomy*, MNRAS, **201**, p. 661.
- [3] Boulesteix, J., Georgelin, Y.P., Marcelin, M., Monnet, G., 1984, *First results from CIGALE scanning Perot-Fabry interferometer*, Proc. SPIE, **445**, p. 37.
- [4] Bland, J., Tully, B. 1989, *The Hawaii imaging Fabry-Perot interferometer (HIFI)*, AJ, **98**, p. 723.
- [5] Le Coarer, E., Bensammar, S., Comte, G., Gach, J.L., Georgelin, Y., 1995, *PYTHEAS: A multi-channel Fabry-Perot spectrometer for astronomical imaging*, A&AS, **111**, p. 359.
- [6] Boulesteix, J., Marcelin, M., 1980, *Marseille Observatory IPCS – Image Photon Counting System*, ESO: Two-dimens. Photom., p. 119.
- [7] Blazit, A., 1985, *The intensified multi CCD camera*, ESA Colloq. on Kilometric Opt. Arrays in Space, p. 155.
- [8] Foy, R., 1988, *The Photon Counting Camera CP40*, 9th Santa Cruz Summer Workshop in Astronomy and Astrophysics, p. 589.
- [9] Gach J.L., Hernandez O., Boulesteix J., Amram P., Boissin O., Carignan C., Garrido O., Marcelin M., Ostlin G., Plana H., Rampazzo R., 2002, *Fabry-Perot Observations Using a New GaAs Photon-counting System*, PASP **114**, p. 1043.
- [10] www.astro.umontreal.ca/fantommm
- [11] <http://www-obs.cnrs-mrs.fr/adhoc/adhoc.html>
- [12] Garrido, O., Marcelin, M., Amram, P., Boulesteix, J., 2002, *GHASP: An Halpha kinematic survey of spiral and irregular galaxies. I. Velocity fields and rotation curves of 23 galaxies*, A&A, **387**, p. 821.
- [13] Rampazzo, R.; Amram, P.; Boulesteix, J.; Bressan, A.; Gach, J. L.; Longhetti, M.; Padoan, F.; Plana, H.; Zeilinger, W, 2002, *Warm Gas and Stars in Shell Galaxies: The Third Dimension*, ASP Conference Proceedings, Vol. **282**, San Francisco: Astronomical Society of the Pacific, 2002., p.284
- [14] Östlin, G., Amram, P., Masegosa, J., Bergvall, N., Boulesteix, J., Márquez, I. 2001, A&A, pp. 374, 800.



Jean-Charles Cuillandre and Sidik Isani were surprised by the photographer

NEAR IR FRINGE TRACKING FOR VLTI: THE FINITO DETECTION SYSTEM

Mario Gai, Leonardo Corcione, and Giuseppe Massone

Istituto Nazionale di Astrofisica (INAF) - Osservatorio Astronomico di Torino

Abstract: *ESO and the Osservatorio Astronomico di Torino (INAF-OATo) are engaged in a collaboration to implement the first generation fringe sensor for VLTI: FINITO. Only seven individual pixels are required for interferometric measurements; however, the instrument sensitivity is greatly improved by an array detector. We describe the FINITO concept and operation, the expected performances, and the detection system, which is based on a Rockwell PICNIC array.*

Key words: *interferometry, infrared (IR) detectors*

1. INTRODUCTION: VLTI AND FRINGE SENSING

The FINITO project is a collaboration between the European Southern Observatory (ESO) and the Italian Istituto Nazionale di AstroFisica – Osservatorio Astronomico di Torino (INAF-OATo) for implementation of a 2/3 beam Fringe Sensor Unit (FSU) for the Very Large Telescope Interferometer (VLTI). The structure and operation of VLTI and current instruments are described in literature [1] and on the ESO Web pages [2]. FINITO (Fringe-tracking Instrument of Nice and Torino) is based on a previous prototype from the Observatoire de la Côte d’Azur (France), completely rebuilt according to current VLTI specifications and requirements on optical layout, electronics and software. The main improvement for the telescope unit, operating in H band ($\lambda \approx 1.5 - 1.8 \mu\text{m}$), is due to use of an array detector in lieu of the IR photodiodes of the laboratory unit. FINITO supports *closure phase* measurements: high spatial resolution measurement of the target

structure, on two independent directions, can be performed simultaneously. Three-beam operation and wavelength difference with respect to the instruments can also be exploited to perform *baseline* and *wavelength bootstrapping*. The detection scheme is discussed below. The concept and operations are briefly recalled, a more detailed description is available in Gai et al. [3].

VLTI instruments (VINCI, MIDI, AMBER) measure the degree of coherence among two or more optical beams, collected by individual telescopes (8-m Unit Telescopes or 1.8-m Auxiliary Telescopes), and transferred to the combination laboratory by the Delay Line (DL) system. From the fringe visibility in different directions, the light distribution of the target can be reconstructed, as in the radio case. For simple geometries, few measurements are sufficient to reconstruct the high angular resolution information.

The wavefront is corrected by adaptive optics on each telescope, but the Optical Path Difference (OPD) between beams is perturbed by atmospheric turbulence, *i.e.*, *piston noise*, on a time scale similar to adaptive optics. Interferometric measurement is potentially limited by atmospheric coherence time (10-100 ms) to short snapshots (like speckle observations). To perform longer exposures, a control system must be included in the interferometer; the actuator is the DL, whereas the sensor is the FSU. Increasing exposure time from 10 ms to 100 sec, the sensitivity improves by 5 magnitudes.

2. FINITO: CONCEPT AND DETECTION SYSTEM

FINITO measures the OPD variation on the beams from 2 or 3 telescopes, pair-wise. Temporal modulation is applied to internal OPD; the interferometric signal is demodulated to deduce the external OPD variation. The nominal control loop bandwidth assumed for VLTI is 40 Hz; internal OPD modulation is in the 200 Hz – 4 kHz range, to allow effective identification of the external disturbances.

The VLTI beams are fed to FINITO by the Alignment and Compensation Unit (ACU). At the start of observation, longitudinal and lateral beam positions are set by ACU to the selected initial offset; then they are progressively adjusted for tracking. The ACU allows compensation of the mismatch between the FSU and a scientific instrument operating in a different band. It also supports the capability for off-axis tracking, *i.e.*, a small separation (0.5" radius) between reference source and scientific target. The beams are superposed to a reference laser beam at wavelength 1310 nm, used for internal metrology and closed loop control of the OPD modulation, and injected in the fiber modulators, piezoelectric drums stretching a few fiber coils accordingly to a triangular law. The metrology component is then

extracted for independent combination to get the internal OPD signal for the modulation control loop, detected by individual photo-diodes. The H band beams are divided by polarization; one component is used for interferometric combination, whereas the complementary one is used for photometric normalization. In the beam combiner, the reference beam is split in two, and each half is separately mixed with one of the other beams, by amplitude combination. The three photometric and four interferometric outputs are fed to the array detector by a fiber optics link.

The four metrological signals are detected on InGaAs photodiodes, but this is not optimal for the seven astronomical outputs: in H band, mercury cadmium telluride (MCT or HgCdTe) is an adequate sensitive material, but the performance of an array detector is required. Although the quantum efficiency of photodiodes is comparable to that of arrays (*e.g.*, 70%), their noise figure is worse. For example, the Hamamatsu Peltier-cooled G8605-21 has $NEP = 3.e - 15 \text{ W} / \sqrt{\text{Hz}}$ (typical), and, for operation up to a few kHz, the corresponding noise level is of order of 1000 e^- ; even at liquid nitrogen temperature, the noise is large. Detection performance is thus significantly improved even by a device without extremely good readout noise. The choice can be restricted between the HAWAII ($1k \times 1k$, $RON = 10e^-$) and PICNIC (256×256 , $RON = 20e^-$) devices.

Detection performance is also affected by the MTF. The photon distribution resolution is degraded by conversion into electrons, because of charge spreading within the sensitive material [4]. According to the literature data and simple geometric models, it can be shown that a comparable amount of signal is detected either on a single PICNIC pixel, or on a 2×2 window on the HAWAII. Their readout noise performance is thus equalized by the different MTF. The PICNIC is preferable, because at equal QE and effective RON the requirements on the imaging optics are more relaxed due to the smaller chip size; also the device cost is lower.

Performance is maximized by allocation of the seven pixels over all four quadrants, in corresponding positions, so that they are read in parallel; the higher readout rate provides further reduction of the effective RON, by Non-Destructive ReadOut (NDRO).

3. STATUS, PERFORMANCE AND THE NEXT STEPS

Procurement of the FINITO components is in progress; several critical parts are already available, and the instrument opto-mechanics will be assembled in Torino during Autumn 2002. Integration with the detector in Garching and shipment to Paranal is planned for the first months of 2003.

The OPD measurement noise depends upon target magnitude, exposure time and observing conditions. It is advisable to set progressively increasing

integration time for fainter magnitudes; up to ~ 10 ms, the DL loop is dominated by the sensor noise. Using this smooth regulation, the limiting magnitude for $10 \mu\text{s}$ astrometry (with OPD noise below 30 nm) is $H \cong 12.5 \text{ mag}$, whereas for $\lambda/20$ imaging it ranges from $H \cong 14.5 \text{ mag}$ in K band to $H \cong 16.5 \text{ mag}$ for the thermal infrared ($10 \mu\text{m}$).

ESO awarded the contract for manufacturing of the FSU for the Phase-referenced Imaging and Micro-arcsecond Astrometry facility (PRIMA) of VLTI to a team led by Alenia Spazio and including the FINITO team as responsible for support to detailed design and test, performance analysis, measurement algorithms, and detection system. The detection system is based on the concept used in FINITO, i.e., imaging of a fiber array on the four quadrants of a PICNIC detector. The first implementation of the PRIMA FSU is in K band ($\lambda \approx 2 - 2.5 \mu\text{m}$).

4. ACKNOWLEDGEMENTS

FINITO is supported by funding from OATo, ESO, and Italian National Council for Astronomy and Astrophysics (CNAA ref. 17/T 2000 and 2001). The detection system design benefits from contributions by Gert Finger.

5. REFERENCES

- [1] Finger, G., Biereichel, P., Mehrgan, H., Meyer, M., Moorwood, A.F., Nicolini, G., Stegmeier, J., 1998, *Infrared detector development programs for the VLT instruments at the European Southern Observatory*, SPIE Proc. **3354**, p. 87.
- [2] <http://www.eso.org/projects/vlti>
- [3] Gai, M., Bonino, D., Corcione, L., Gardiol, D., Gennai, A., Lattanzi, M.G., Loreggia, D., Massone, G., Ménardi, S., 2001, *FINITO: a fringe tracker for VLTI in two and three beam configuration*, Proc. of the Workshop Scientific Drivers for ESO Future VLT / VLTI Instrumentation, XL VI C.N. SAlt.
- [4] Glindemann, A., Abuter, R., Carbognani, F., Delplancke, F., Derie, F., Gennai, A., Gitton, P.B., Kervella, P., Koehler, B., Lévêque, S.A., Menardi, S., Michel, A., Paresce, F., Duc, T.P., Richichi, A., Schöller, M., Tarenghi, M., Wallander, A., Wilhelm, R., 2000, *VLT interferometer: a unique instrument for high-resolution astronomy*, SPIE Proc. **4006**, p. 2.

OSIRIS DETECTORS

First tests and control system

Enrique Joven¹, José V. Gigante¹ and Francis Beigbeder²

¹*Instituto de Astrofísica de Canarias (IAC),* ²*Observatoire Midi-Pyrénées*

Abstract: *OSIRIS (Optical System for Imaging and Low-Resolution Integrated Spectroscopy) is an instrument designed to obtain images and low-resolution spectra of astronomical objects in the optical domain (from 365-1000 nm). It will be installed on Day One (2004) in the Nasmyth focus of the 10-m Spanish GTC Telescope. The mosaic is composed of two abutable 2K×4K CCDs to yield a total of 4K×4K pixels, 15 $\mu\text{m}/\text{pixel}$, 0.125" plate scale. The arrangement allows the linking of a classical ARC-GenII controller to a PMC frame-grabber, plugged into a VME-CPU card, where a RTOS (VxWorks from Wind River) is running. Some tests and results, carried out with a couple of MAT44-82 engineering grade devices at room temperature, are given.*

Key words: *MAT44-82; ARC-GenII; VxWorks*

1. THE OSIRIS DAS: OVERVIEW

The OSIRIS Data Acquisition System (DAS, see Fig. 1) is based on an ARC-GenII-controller, using a timing board with parallel cable linked to a digital PMC-type frame grabber plugged into a VME-crate running VxWorks OS. The main change to typical ARC-GenII controller configurations is the different timing board. This parallel cable version of the timing board is similar to the fiber optic version, but instead has support for a 16-bit parallel image data link that transmits over a commercially available SCSI-3 cable to a host computer interface card for PCI buses. The cable supports very high data rates and is presently implemented at 6.25 Mpix/sec. To do this, some specific programming and minor hardware modifications, different from the original ARC's one, have been done into the controller. It must be noted that the bandwidth (6.25 MHz - the timing board, 20 MHz -

the frame grabber) far exceeds the requested OSIRIS needs (4 MHz maximum, running the four outputs at 1 MHz). Commands are sent via RS-232 serial communication to the ARC-Utility Board. On the other side, there is a mandatory design about the so-called Local Control Units (LCU), where instruments have to be connected to. Basically, they are VME crates connected by ATM communication (155 Mbps) to the GTC Control System. The crates also support a 10/100 Mbps Ethernet, a serial port and a CAN-bus communication. They are controlled by PowerPC-based CPU cards running embedded VxWorks Real-Time Operating System (RTOS), from Wind-River. The main advantage of this type of CPU cards is that their internal PCI bus is far faster than external VME. The software architecture allows the user to run any of the complex “Observing Modes” (*Direct or Tunable Imaging, Long-Slit Spectroscopy, Multiple-Object Spectroscopy, Long-Slit-Fast Photometry or Fast Spectroscopy*) that involves coordination and synchronization of critical operations (as charge shuffling and wavelength tuning) with real time constraints.

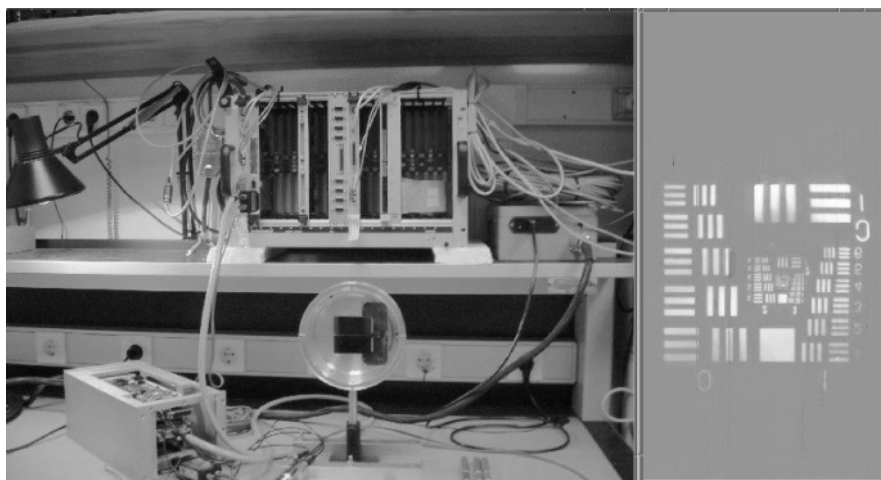


Figure 1. OSIRIS-Data Acquisition System. Each module of the Local Control Unit (*left*) is handled by a Motorola MVME-2430 CPU-card. They contain an internal 64-bit PCI Local Bus, with four 32/64-bit PMC expansion slots (using the PMC-span module). The ARC-GenII interface is implemented using a frame-grabber card (SNP-PMC-DIG16 from Datacell, programmable up to 16-bit digital data in RS-422 format, 40MB/s). A Technobox 2901-PMC-Serial Port Adapter Card controls the shutter configuration and the ARC-commanding. Fiber-optics transceivers (as the 9PFLST model from B&B Electronics) are used to connect the serial ports from the crate to the controllers. Net controller cards are Thales CPMC-ATM2-115MMF. VME-crate is a two-backplane, CAN-bus remote control available, 20-slot, from Wiener. (*right*) Full image (2Kx4K) taken with a MAT44-82 engineering grade array working fast at room temperature (800 kHz). A dark image has been subtracted.

2. TESTING THE OSIRIS MOSAIC

The mosaic is composed of two abutable $2K \times 4K$ CCDs which yields a total of $4K \times 4K$ pixels, $15 \mu\text{m}/\text{pixel}$, $0.125''$ plate scale. Day One arrays will be MAT-44-82 from Marconi (2 channel each, Frame-Transfer type, 20-1000 kHz readout rate), although they will be probably upgraded to MIT-LL CCID-20 blue-enhanced CCDs. The mosaic tested (see Fig. 2) in the prototype is comprised of two MAT44-82 engineering grade arrays. The basic operations of the *Observing Modes* have been programmed into the controller (as “sequences” and “cycles,” each one including operations such as: “idle,” “clear,” “shift the charge up or down,” “exposure,” “read inside/outside the loop” or specific readout modes such as frame-transfer, windowing and binning). This software allows driving one or two MAT44-82 CCDs, by one or two outputs. It is also possible to modify parameters in order to change, for example, the video integration time, or the reset or settle times. We can read out the array from 20 kHz per channel up to the CCD readout limit of 1 MHz.

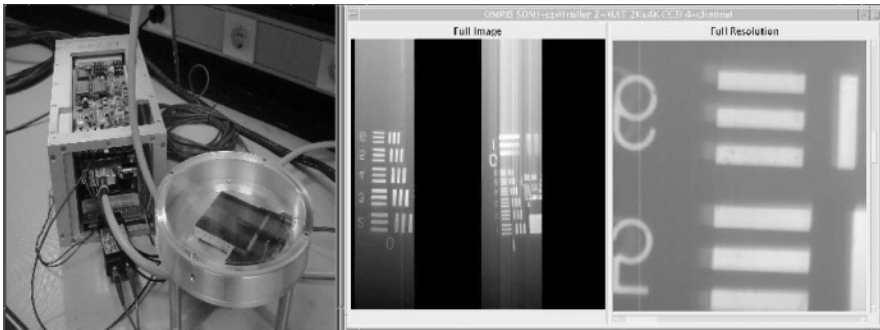


Figure 2. (left) OSIRIS Test-bench mosaic. In this arrangement a MAT44-82 grade-6 (not operative) has been mounted together with a MAT44-82 grade-5 (engineering). The modified ARC-GenII controller is also shown. Two standard 11×11 grid ZIF sockets from 3M have been used to plug the arrays. Four-layer PCB card has been designed at IAC. Connectors are on the backside. (right) Full image ($4K \times 4K$) of the Test Bench Graphic User Interface, showing the four-channel output of the mosaic acquired with the mentioned arrangement. The raw image is intentionally defocused.



One of many intense moments during the finals of the Taka-Taka competition.

THE OPTIMIZED CRYOSTAT FOR THE LBC CAMERA

Fernando Pedichini and Roberto Speziali

Istituto Nazionale di Astrofisica, Osservatorio Astronomico Roma

Abstract: *The Large Binocular Camera (LBC) is the double optical imager that will be installed at the prime foci of the Large Binocular Telescope (2m×8.4m). Three Italian observatories are cooperating in this project: Rome (CCD Camera), Arcetri-Padua (Optical Corrector) and Trieste (Software). LBC is comprised of two separate large field (27' FOV with a sampling of 0.23"/pix) 6 lense optical correctors, one optimized for the UVB bands and the second for the V, R, I, and Z bands. The two focal plane cameras use each one an array of four 42-90 chips (4.5K×2K) provided by Marconi and optimized for the maximum quantum efficiency (85%) in the blue or red end of the optical spectrum, that can be read with a speed is of 4 Mpix/sec using an Elettromare CCD controller. The arrays are cooled by peculiar LN2 cryostats that can assure more than 24 hours of continuous operation with 8 liters of LN2. Here we present an overview of the project and a description of the CCD cameras mainly describing the cryogenic project and the laboratory tests. This instrument is planned to be the first light instrument of LBT.*

Keywords: *cryogenics, imager, Charge-Coupled Device (CCD), wide field, Large Binocular Telescope (LBT).*

1. LBC PRIME FOCI OVERVIEW

The main architecture of the LBT (Fig. 1 and 2) telescope will be governed by the LBC cameras: two mirrors will mean two different prime focus correctors one optimized for the UBV bands and another for the VRIZ bands working together for multi color imaging on the same sky area. Using this technique, it is possible to acquire multi wavelength data with a large efficiency covering the large field of 27 arcmin. The optical correctors,

derived by a modification of the Wynne approach (Fig. 3) [1], balance the aberrations induced by the fast ($f/1.14$) parabolic primary mirrors. Each corrector uses six lenses, the first having a diameter of 80 cm and the third with an aspherical ellipsoid surface assure that 80% of the Point Spread Function (PSF) encircled energy falls inside one pixel for more than 90% of the field (Fig. 4 and 5). The two channels have similar optical designs satisfying the same requirements, but differ in the lens glasses: fused Silica for the "blue" arm and BK7 for the "red" one. The two cameras are also each equipped with a set of eight filters.

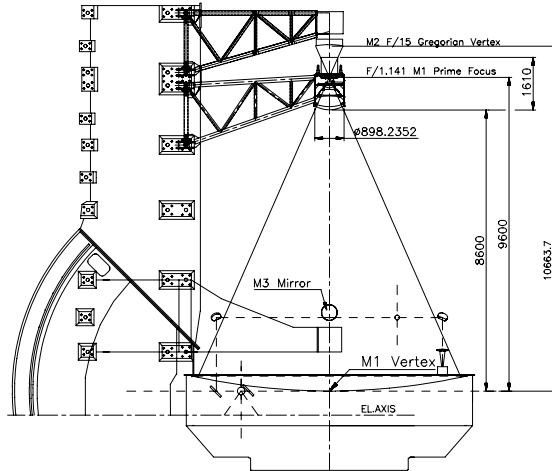


Figure 1. The LBC position within the LBT optical layout.



Figure 2. The LBT telescope in the workshop.

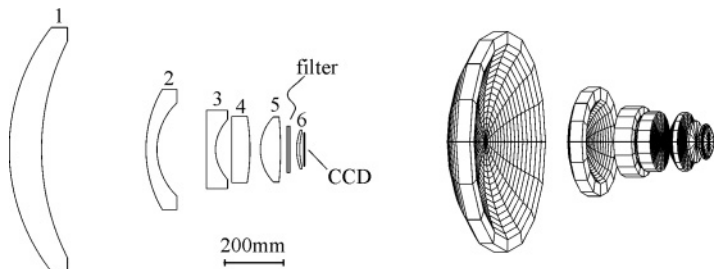


Figure 3. Prime focus corrector optical design (2D layout and solid model)

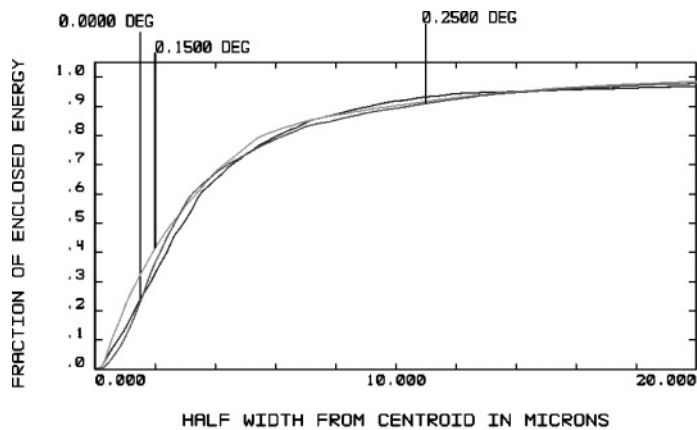


Figure 4. Optical performance of prime focus corrector. (top) Polychromatic ensquared energy plot.

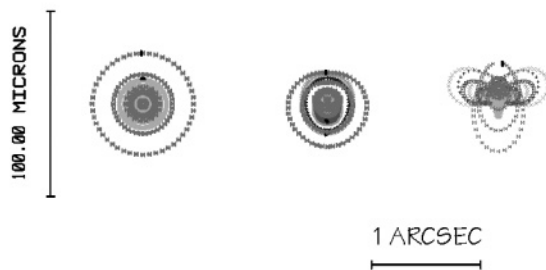


Figure 5. Optical performance of prime focus corrector. Polychromatic spot diagrams for different field angles (0°, 0.15°, 0.25°); the spot size is roughly 10 times larger than the Airy disk, indicating that the optics are not diffraction limited.

The mechanical design of the prime focus consists of two main parts: the hub that mounts the fixed lenses and the derotator, which holds the filters wheels and the cryostat. Each one of the five fixed lenses is cinematically

mounted into an INVAR frame, which is then connected to the steel hub through some flexure elements to accommodate the differential thermal expansion of the two materials. For the same reason, the two main lenses, which are 810 mm and 400 mm large, are mounted into their INVAR frames by means of special RTV pads that are tailored to compensate for the differential thermal expansion of the glass and the INVAR.

The derotator decouples the CCD imager from the corrector lenses and hosts two filter wheels, the shutter, the cryostat and all the control electronics including two CCD controllers. The mechanical design of the prime focus hub is shown in the following Fig. 6. The derotator module assures the control of the parallactic angle on the detector focal plane by means of a dual motor driving and an absolute encoder. The two 200 W brushless motors will work in closed loop with the encoder, in a push-pull configuration to reduce any backlash of the system. The on axis resolution of 18" will assure sub pixel accuracy up to the edge of the focal plane. For further details about the optomechanics of both channels see [2].

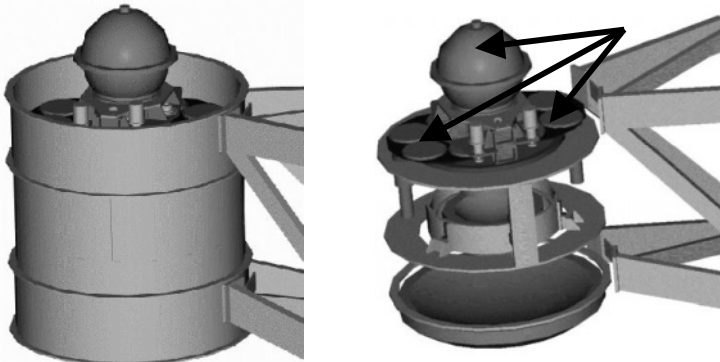


Figure 6. (left) CAD view of the hub with the camera. (right) CAD view of the LBC's interiors where the arrows show the derotated components

2. CRYOGENICS

The cryostat for the CCD camera of the double prime focus imager was designed to cool the four EEV 42-90 chips down to their best operative temperature of 170 K. Contrary to the designs of other large field imagers [5,6], we decided to use a standard cryogenic solution. This method adopts a LN₂ bath instead of more expensive and not deep tested cryocoolers. The experience with the small cameras built for the prime focus at the Schmidt telescope of Campo Imperatore [3-5] based on a LN₂ bath, led us to design a cryostat consisting of three independent modules: the stainless steel interface flange, the bimetallic nitrogen vessel and the housing sphere made of

aluminum. This solution (Fig.7) allows an easy separation of the array part (flange with CCD, wavefront sensors, cables, etc) from the cryogenic part.

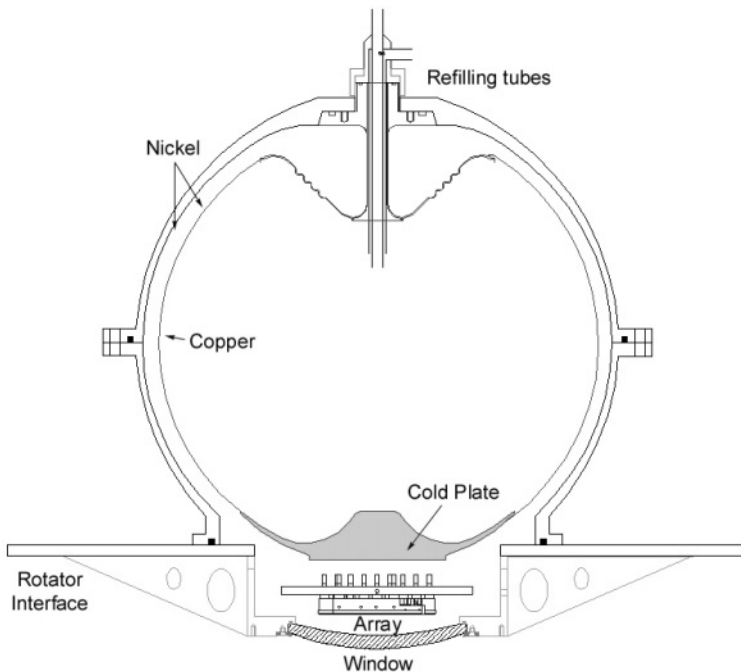


Figure 7. The cryostat

2.1 The vessel

The unique component of this cryostat is its spherical bimetallic monolithic vessel. It was designed as a sphere to both minimize the radiative thermal inlet and to make it a compact instrument, even for a wide field camera. This geometry guarantees the best *volume to tank surface ratio*, minimizing the radiative thermal input with respect to the available volume of LN₂. Moreover, we have tested new mechanical technologies based on electroforming processes producing a monolithic, bimetallic vessel without any welding (Fig. 8). This reduces the risk of leaks during the thermal cycles. The inner part of the vessel is made up of a 1.5 mm copper layer to ensure high thermal conductivity, covered by a layer of 2 mm Nickel that is polished to reach high reflectivity. On the bottom of the inner copper sphere there is a large copper flange, which is always in thermal contact with the LN₂. This ensures a uniform smooth cooling of the CCD sensors' baseplate. A cylindrical cryosorption pump is applied on this flange to keep the vacuum level below 10^{-5} mbar. On the opposite side of the vessel there is a

standard refilling system based on cryogenic coaxial tubes to minimize the thermal inlet by conduction.

2.2 The spherical case

The spherical case is made of aluminum and consists of two halves of a sphere with a diameter about 10 mm larger than the vessel's and with a thickness of 3 mm. The two halves are joined by an O-ring and are covered by a few μm layer of Nickel to reduce degassing and to ensure a high reflectivity of the inner surfaces after polishing. Two standard KF ISO flanges are soldered on the upper half for evacuation and vacuum sensors.



Figure 8. The vessel and its housing during the construction phases

2.3 The interface flange

This flange is made of stainless steel (AISI 4130) and fulfills two tasks: to hold the baseplate with the sensors and to interface the cryostat with the derotator of the prime focus. Ten Fischer vacuum connectors are used to connect the sensors to the outer read-out electronics. The numerical simulation of the 3D model confirms a very low deformation ($2\ \mu\text{m}$) even with the telescope in the horizontal position (Fig. 9 and 10).

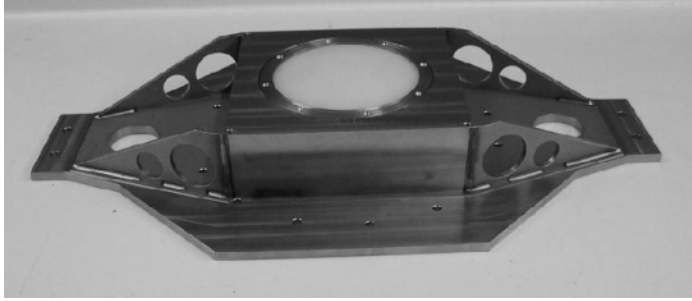


Figure 9. The AISI 4130 interface. (Courtesy ADS)

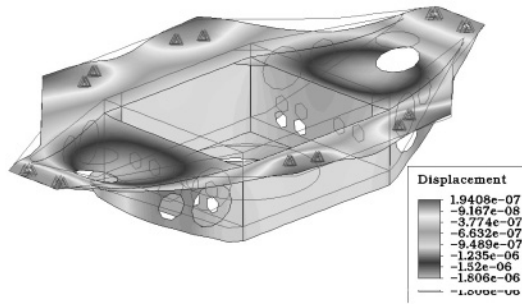


Figure 10. The numerical simulation of the displacement of the flange. (Courtesy ADS)

2.4 Cryogenic estimated performances

The cryostat is designed to keep the sensors at the operating temperature for at least one day without refilling. To estimate a lower limit for the holding time of the cryostat we have considered a reservoir of liquid nitrogen equal to the half of the tank volume (8.5 lt). This situation guarantees no LN2 spill out even with the telescope working in the worst condition, *i.e.*, in horizontal position. We derived the thermal radiative input on the vessel using the formula for the radiative exchange [8] between $T_{\text{hot}} = 300 \text{ K}$ and $T_{\text{cold}} = 77 \text{ K}$.

$$\dot{Q}_{\text{rad}} = \sigma (T_{\text{hot}}^4 - T_{\text{cold}}^4) \frac{\epsilon_{\text{cold}} \epsilon_{\text{hot}}}{\epsilon_{\text{cold}} + \frac{A_1}{A_2} (1 - \epsilon_{\text{cold}}) \epsilon_{\text{hot}}} \quad (1)$$

Assuming that the nickel on the surfaces of the vessel and cryostat is highly polished with an emissivity of $\epsilon_{300\text{K}} = 0.2$ and $\epsilon_{77\text{K}} = 0.1$. and having

the two surfaces an area of $A_1=3761 \text{ cm}^2$ and $A_2=3257 \text{ cm}^2$, we obtained a value of

$$\dot{Q}_{rad} \approx 11 W \quad (2)$$

More radiative input has to be added due to the optical window of the cryostat. Assuming an emissivity of 1 for the atmosphere and 0.5 for the chip we estimate an extra radiative input of about

$$\dot{Q}_{window} \approx 2.5 W \quad (3)$$

Heat transfer by conduction is due to the stainless steel tube of the vessel and from about 100 constantan wires 10 cm long, and the fiberglass support of the baseplate. The diameter of these wires is 0.1 mm.

Applying the simple formula

$$\dot{Q}_{cond} = \frac{A}{l} \bar{\lambda}_{T_2-T_1} (T_2 - T_1) \quad (4)$$

we obtain

$$\dot{Q}_{cond} = 1.3 W \quad (5)$$

An additional watt can be considered from the power consumption of the sensors on the baseplate. In our calculation we have assumed heat transfer by convection is negligible, being sure that, after pumping, the large cryopump provides an insulation vacuum of $10^{-5} \div 10^{-6}$ mbar. Therefore the overall heat inlet should be about:

$$\boxed{\dot{Q}_{total} \approx 16 W} \quad (6)$$

giving the expected holding time of **one day**.

2.5 First cryogenic tests

The first cryogenic tests were performed in March 2001 at the Rome Observatory Labs. No leaks were detected after the construction of the cryostat. The vacuum was obtained and kept during the tests (the cryopump was not yet available) by two turbomolecular pumps in series. Pirani and Penning heads provided by Alcatel were used to measure the vacuum. The acquisition of the data was performed by a PC that was simply connected

with the sensors by means of the RS-232 serial ports. A gas-meter was also used to record the evaporation of LN_2 . The first cryogenic test was performed with the cryostat closed by a “dummy” aluminum flange, without window and baseplate, just to verify the pure radiative input of the vessel and the conduction by the stainless steel tube (Fig. 11).

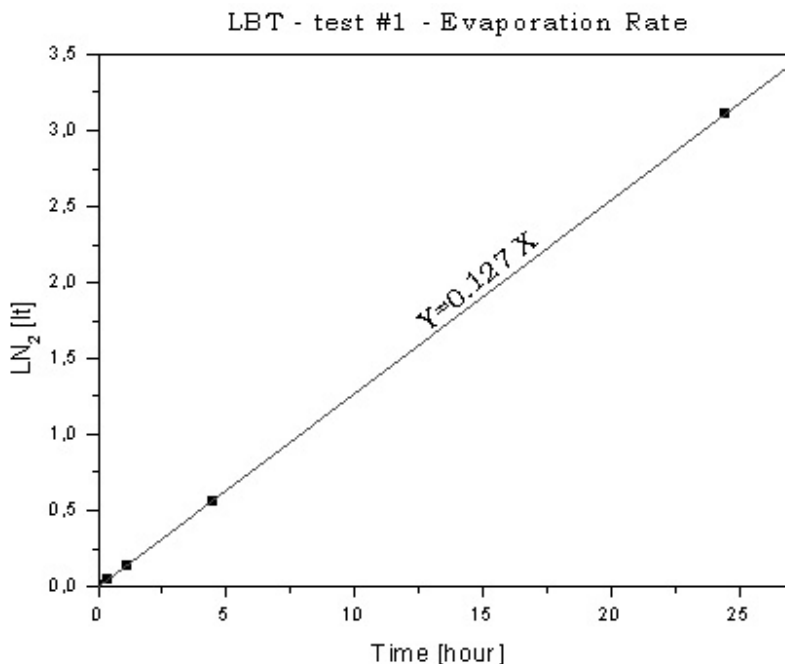


Figure 11. First evaporation test.

From the evaporation test we derived a mainly radiative thermal inlet of about 6W, nearly the half of what we estimated in our calculation may be due to the good polishing of the nickel surfaces.

2.6 Cooling the array

To cool the detectors we have developed a thermal link between the detectors flange and the vessel, fulfilling the following requirements:

- operative temperature of 170 ± 2 K
- cooling speed below 5 K/min, that is the maximum rate allowed by MAT(Marconi Applied Technologies, now E2V)
- temperature stability of 3 K
- no active temperature control to avoid LN_2 extra consuming

At the operative temperature of 170 K, suggested by MAT, the best compromise between a low dark current ($\ll 1$ e⁻/min) and a high quantum efficiency and charge transfer efficiency is achieved. Even a fluctuation of ± 5 K does not produce a significant change in the performances. The sensor flange is stainless steel made (INVAR type) and has been provided directly by MAT. It is attached to the dummy head of the cryostat by means of three stiff fiberglass standings to reduce any tilting of the sensor array induced by the telescope movements during the pointing and tracking operations. Indeed due to the very fast Focal Ratio of 1.41 and to the pixel size of only $13.5 \mu\text{m}$ we can accept a maximal displacement at the edge of the array of only 0.004 mm to maintain the optical quality inside the specifications. On this flange 10 holes were provided to connect a second flange, made by aluminum, where the thermal links are mounted on. These links consist of three springs having two copper pads at the two ends (Fig. 12 and 13).

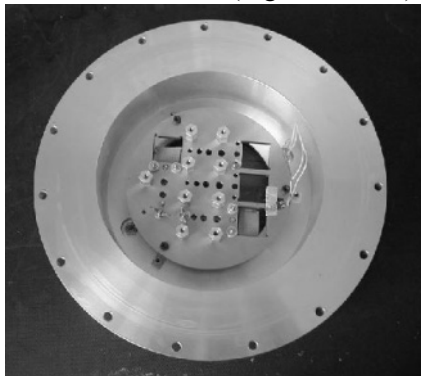


Figure 12. The dummy flange with the baseplate mounted

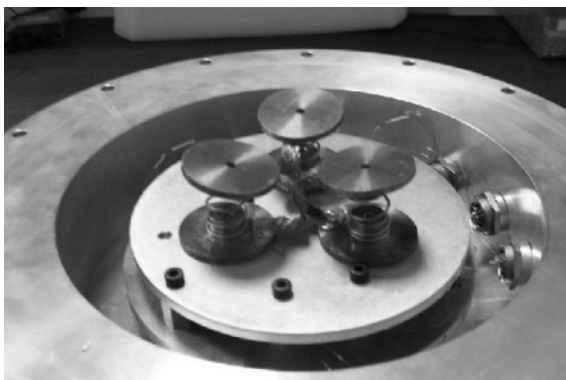


Figure 13. The thermal links.

The springs push the pads to the copper flange of the vessel when the cryostat is closed, making a good thermal contact. Three copper wires were soldered connecting the two pads, and it is possible to adjust the operative

temperature and, therefore, the cooling speed by simply varying the diameter and the length of the copper wires. This system allows us to achieve good temperature control and stability below 1 K without any active heater. A test was done with a Lake Shore DT-470 silicon sensor used to acquire the temperature on the baseplate. The results are shown in Fig. 14 and 15.

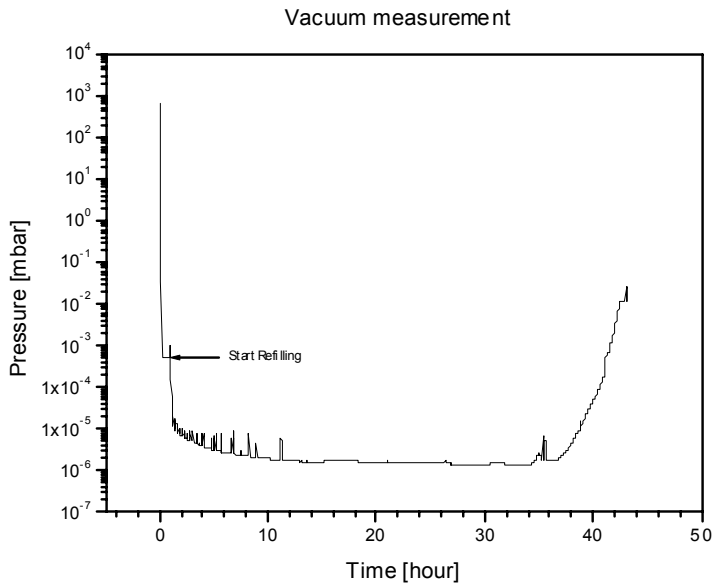


Figure 14. Vacuum level vs. time.

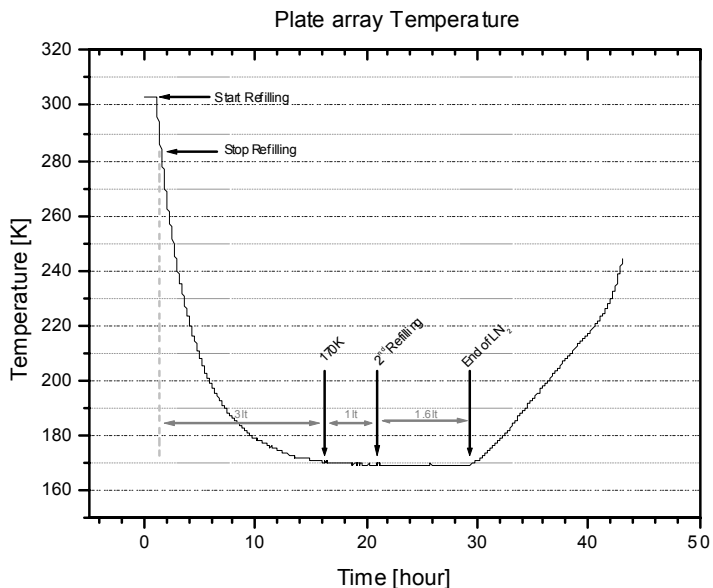


Figure 15. Temperature of the plate array vs time

As shown in Fig. 15 and 16, the time needed to cool down the baseplate with the sensors was about 15 hours and the consumption of LN₂ was 3 liters. The maximum cooling rate at the beginning of the refilling was of 1.3 K/min well below the maximum cooling rate of 5 K/min suggested by EEV. In regime conditions we measured an evaporation rate of 0.2 lt/hour. Further tests have been performed in the laboratory of the Rome Observatory between April 2001 and April 2002 to optimize the performances of the cryostat. In the last one (Fig. 16 and 17) we simulated the movements of the camera of the telescope tilting the cryostat up to 60°.

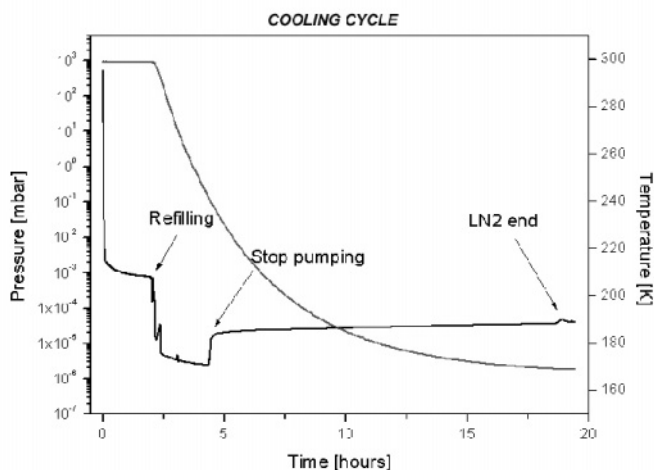


Figure 16. Cooling test of the cryostat.

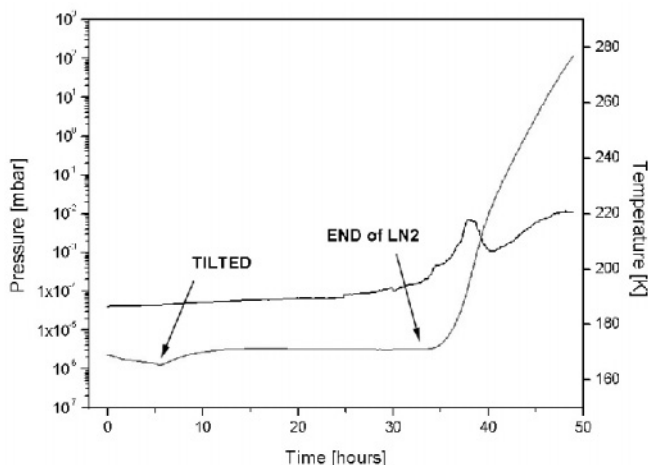


Figure 17. Temperature and pressure time plot after tilting the cryostat

As shown in Fig. 16, the operative temperature was 170 K. After having reached this temperature the cryostat was refilled with about six liters of LN_2 . Five hours later the temperature reached 168 K and, after tilting the cryostat, the temperature reached 170 K until the end of the cycle 30 hours later (Fig. 17). During the test the static vacuum changed from 4×10^{-5} to 8×10^{-5} until reaching 1×10^{-2} after complete heating. It took about 14 hours to reach room temperature. From these tests we have verified that the cryostat of the blue camera fulfills all the requirements of operative temperature and holding time. With this experience we are going to build the second cryostat for the red channel with a few modifications. We will make the vessel core from a single block of aluminum vessel using a CNC milling machine. We are developing, together with Forestal s.r.l., a new process to weld the stainless steel refilling system to the aluminum vessel. This approach of using Al instead of Cu for the core of the cryogenic vessel will reduce the weight of the component and increase its stiffness. Figures 18 and 19 show the original cryostat assembled and its main components.

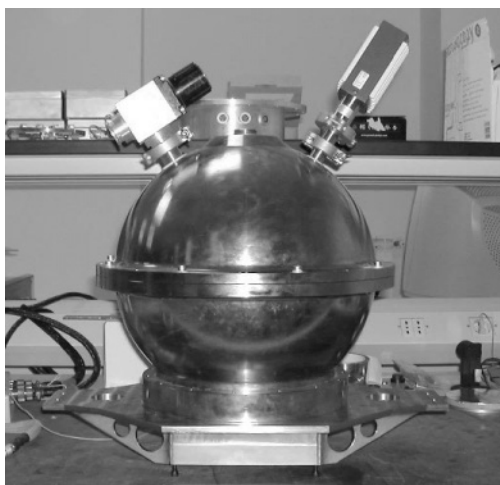


Figure 18. The assembled cryostat.



Figure 19. The main components of the cryostat.

3. FOCAL PLANE CCD ARRAY

Two types of MAT detectors have been chosen to allow both the scientific data acquisition and the control of the instrument: an array of four MAT 42-90 (4.6K×2.5K) chips cover the corrected field ($\varnothing = 27'$) with a sampling of $0.23''/\text{pix}$ providing the scientific image, while two MAT 42-10 will be used to acquire short exposure images for tracking and wavefront control. The four scientific MAT 42-90 chips are mounted on an invar plate as shown in Fig. 13. This plate has been directly machined by MAT, with the holes for the electrical connectors and for the orientation registers needed to align the detectors. The corrected fields have a diameter of 110 mm and 108.2 mm for the blue and red channel respectively and the four MAT42-90 chips cover about the 75% of these useful areas. Figure 20 shows that there is a 5% of energy loss in the blue channel at the edge of the corrected field, while in the red channel this percentage of vignetting is well outside from the corrected area. The two MAT 42-10 chips will be placed at the two sides of the scientific array, mostly inside the corrected field .

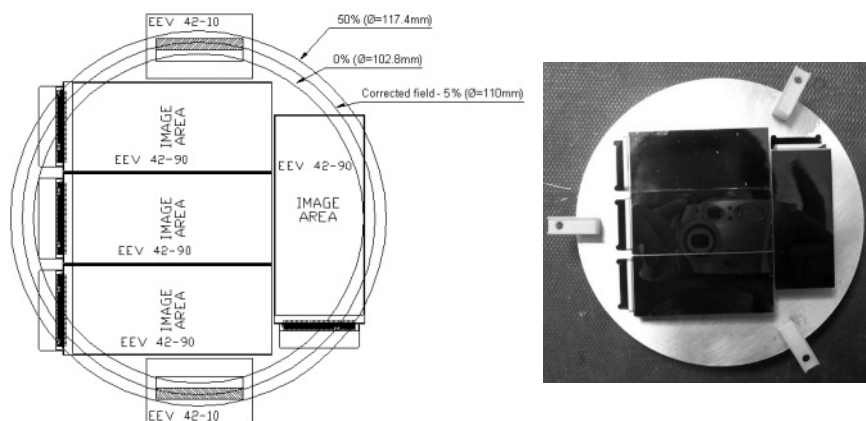


Figure 20. The array arrangement of the focal plane.

3.1 The MAT 42-90 detector

Two sets of four 42-90 grade-1 detectors (Fig. 21) were ordered following these requirements:

- QE > 85% at peak
- Charge Transfer Efficiency > 99.999%
- Read Out Noise < $5 e^-$ at 1MHz
- Dead Pixels < 1350
- Column Defects < 6
- Surface roughness < $7 \mu\text{m}$ peak to valley

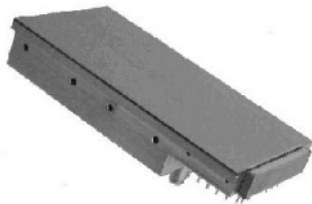


Figure 21. The EEV 42-90 chip.

The last requirement is imposed by the very fast focal ratio of the camera (f/1.41) and is needed to keep the nominal optical quality (80% of the energy in one pixel) of the image all over the focal plane. We have received all the eight 42-90 chips for both channels. The electrical and mechanical samples have been used to make the preliminary tests and set up of the blue channel camera. In the Table 1 the QEs of the chips we have received are listed as reported by MAT datasheets:

Table 1. Quantum Efficiency of the scientific sensors.

CCD sn	350 nm	400 nm	500 nm	650 nm	900 nm	1000 nm
Blue channel array (thin silicon)						
8341-16-3	53.8	81.3	85.4	78.8	28.3	-
8351-18-4	56.1	83.7	88.2	80.1	27.3	-
9283-4-5	53.8	81.1	83.8	76.8	27.4	-
9283-1-4	56.3	77.7	80.5	75.0	28.3	-
Red channel array (thick deep depletion silicon)						
9434-17-3	-	-	95.1	96.7	57.0	13.2
9434-16-5	-	-	82.8	90.2	53.2	11.8
9434-15-3	-	-	84.3	90.6	51.5	11.2
9434-15-4	-	-	87.4	95.7	54.4	12.2

3.2 The MAT 42-10 chips

This chip is a frame transfer CCD with 2048×256 13.5 μm useful pixels which will be used for guiding, real-time focusing and high order wavefront analysis. The refresh time of this system will be about 1 Hz. We performed a simulation of the images given by the 42-10 chips to evaluate the sampling time needed to track a field star. Conservatively, we considered 1'' of seeing, and we requested a centroid determination accuracy better than 0.02''. Due to the position of the trackers on the same focal plane of the science array, the attenuations and bandwidths of the science filters have been considered. Taking into account the CCD Q.E. response we ran the simulation using stars with a magnitude range from 15 to 20 and the results are exposure

times always below 2-3 seconds. The total sky coverage of the 2 trackers is about $4.5'$ sq. Therefore combining the chip performance, the area and the number of star in one squared degree following the Bahcall model, we expect to find at least one reference star with $M_V = 19$ or $M_B = 20$ at high galactic latitude. In the U band, due to the low surface density of bright stars, we may consider to slightly modifying the pointing by changing the paraxial angle if a very fast tracking loop is needed.

3.3 The Wavefront analysis

Two different accuracy wavefront analysis modes are planned for the LBC to best exploit the performances of the active primary mirror of the LBT. These will be performed by one of the two 42-10 chips placed in a slight out of focus position at the edge of the corrected field. Thanks to a peculiar staired glass plate attached to this one it will be possible to acquire IN and OUT of focus star images [8-10] for the optical aberrations computation (Fig. 22).

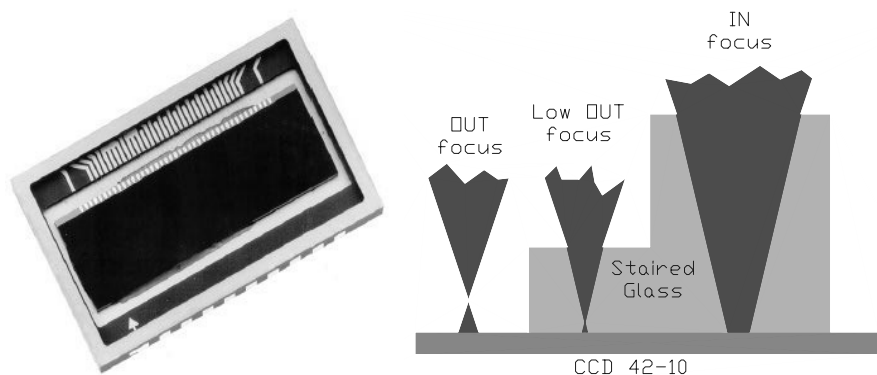


Figure 22. (left) The MAT 42-10 chip. (right) The staired glass with in and out of focus images schematic

3.4 CCD controller

The CCD controller selected for the LBC camera is produced by the Italian firm Elettromare and has been developed with contributions from the Italian astronomical community. Indeed it is an evolution of the new CCD controller for the instrumentation of the National Galileo TNG telescope in La Palma Canarian [11]. Three boards compose the whole system. A PCI interface board, that hosts a DSP MOTOROLA 56301, provides all the clocks and control signals by means of a high speed fiber link (1.2 Gbit/sec)

transferring all the data patterns in real time to a re-synchronizing and parallelizing gate array placed on the SEQUENCER BOARD in the camera head. An ANALOG BOARD provides 8 programmable biases and acquires four video channels. This architecture allows a reduced heat dissipation in the camera head electronics and a very compact housing can be built around the three boards (VME format) needed to drive the chip array. The incoming data rate is 4 Mpix/sec and Win NT – WIN 2000 driver has been developed to store the data in the control PC memory. Standard aux. digital and analog I/O are provided in the camera head to perform system telemetry and the read-out of temperatures, voltages, vacuum levels and logic lines. Two dedicated output lines are provided to drive a standard iris shutter with its holding current and a small heater to lock the temperature of the CCD array with a 12-bit resolution via a simple PID. filter. A general description of the architecture and philosophy of this system can be found in Bonanno [11]. The actual performances are a readout time of less than 15 sec for the full array and a RON of about 10-12 e^- . The final version of the CCD controller, due to a large use of VLSI gate arrays and the removing of the DSP, will have a different layout to be hosted in a small housing to better comply with the weight and dimensional constraints of the LBC cameras at its installation on the prime focus derotator. This version will be assembled using only 2½ eurocard format card and hosting the preamplifiers on the analog video board. A reduced version of this controller with only 2 video channels will be used to drive the 42-10 chips for tracking and WF sensing.

3.5 Shutter

Previous experiences [12,13] and three main constraints guided the shutter design for this camera. These constraints are:

- 1) A wide unvignetted shutterable aperture greater than 12 cm×12 cm
- 2) Maximum thickness of 17 mm and less of 8 mm in the central parts
- 3) Exposure uniformity on the whole field better than 1/100 mag at 1 sec exposure time

Optical tests (Fig. 23) of the first prototype show an exposition accuracy of 0.56 msec RMS at an exposure time of 460 msec well below the maximum error, which is 4.6 msec. RMS.

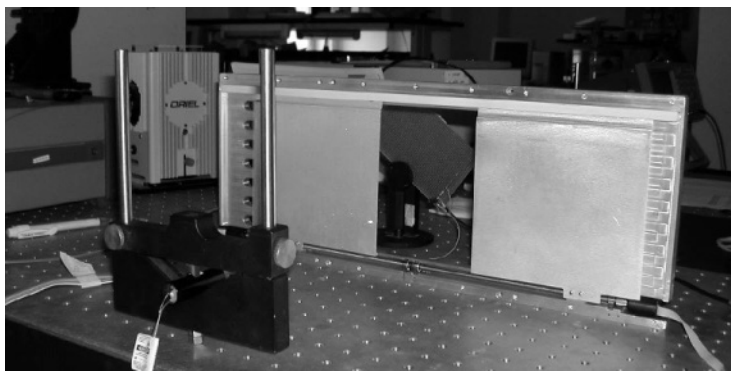


Figure 23. The shutter during the laboratory tests.

4. REFERENCES

- [1] R. Ragazzoni, E. Giallongo, et al., 2000, *Double prime focus camera for the F/1.14 binocular telescope*, Proc. SPIE **4008**, pp. 439-446.
- [2] Diolaiti et al., 2002, *Blue and Red channel of LBC: a status report on the optics and mechanics*, Proc. SPIE, in press.
- [3] R. Speziali, F. Pedichini, 1997, *Design of a new cryostat for the Schmidt Telescope at Campo Imperatore*, Internal Report, OAR/97/IR 2.
- [4] F. Pedichini, R. Speziali, F. D'Alessio, A. Di Paola, 2000, *ROSI: a compact 2kx2k CCD imager for the Schmidt telescope*, Proc. SPIE **4008**, pp. 389-396.
- [5] Natali G., Pedichini F., 1990 Rev. Sci. Instrum. **61**, 7, 1839
- [6] O. Baulade, et al., 2000, *Development of MegaCam, the next generation wide field imaging camera for the 3.6-m Canada-France-Hawaii Telescope*, Proc. SPIE **4008**, pp. 657-668.
- [7] B. A. McLeod, M. Conroy, T. M. Gauron, J. C. Geary and M. P. Ordway, 1998, *MegaCam: paving the focal plane of the MMT with silicon*, Proc SPIE **3355**, pp. 447-486.
- [8] White, 1979, Cryogenics.
- [9] P. Hickson, 1994, *Wave-front curvature sensing from a single defocused image*, JOSA A **11**, pp. 1667-1673.
- [10] P. Hickson and G. Burley, 1994, *Single-image wavefront curvature sensing*, Proc. SPIE **2201**, pp. 549-554.
- [11] Bonanno et al., 2000, *TNG new generation CCD controller*, Optical detectors for Astronomy II- Kluwer Academic Publishers, J.W. Beletic & P. Amico eds.
- [12] Pedichini F., Comari M., Cosentino R., Farisato G., De Baco W., Sandre G., 1998, *High precision shutter for the TNG CCD Camera*, Optical detectors for Astronomy, Kluwer Academic Publishers, J.W. Beletic & P. Amico eds.
- [13] D'Odorico S., Beletic J.W., Amico P., Hook I., Marconi G., Pedichini F., 1998, *Commissioning of a 4Kx4K CCD mosaic and the new ESO FIERA CCD controller at the SUSI-2 imager of the NTT*, Proceedings SPIE, vol. **3355**, p. 507.

THE OMEGACAM SHUTTER

A low-acceleration impact-free device for large CCD mosaics

Klaus Reif¹, Günter Klink¹, Phillip Müller² and Henning Poschmann¹

¹*Sternwarte of the University. of Bonn,* ²*Radio Astronomy Institute of the University of Bonn*

Abstract: *The shutter for OmegaCam - the 16K×16K CCD mosaic camera for the 2.6-m ESO VLT Survey Telescope (VST) - is described. The OmegaCam is a high precision photometric slit type shutter with an aperture of 370 mm×292 mm. The device was designed and built at the University of Bonn. Performance measurements show that the shortest exposure time is less than 1 msec and that 100 msec exposures are homogeneous to within $\pm 0.3\%$.*

Key words: *shutter, Charge-Coupled Device (CCD) mosaic*

1. SHUTTER DESCRIPTION

The OmegaCam shutter consists of three main components, which work together to achieve the expected shutter performance: timing accuracy of better than 1 msec at any position across the aperture. The three components are:

1. Shutter mechanical unit
2. Shutter control unit
3. Shutter control firmware

1.1 Shutter Mechanical Unit

The mechanical design is point symmetric with respect to the optical axis (see Fig. 1) and does not have a preferred direction of movement. Consequently, the shutter blades move first from left to right and then from right to left for consecutive exposures. Everything is mounted on a single aluminum base plate with a rectangular aperture in the center:

- Two carbon fiber blades move on two linear ball bearings

- Two microswitches are used for position reference, one for each blade.
- Stepper motors in micro stepping mode drive the blades by means of toothed belts (1600 microsteps per revolution). The whole blade movement takes about 16000 microsteps.
- Incremental encoders (1600 increments per revolution) are mounted on the motor shafts.

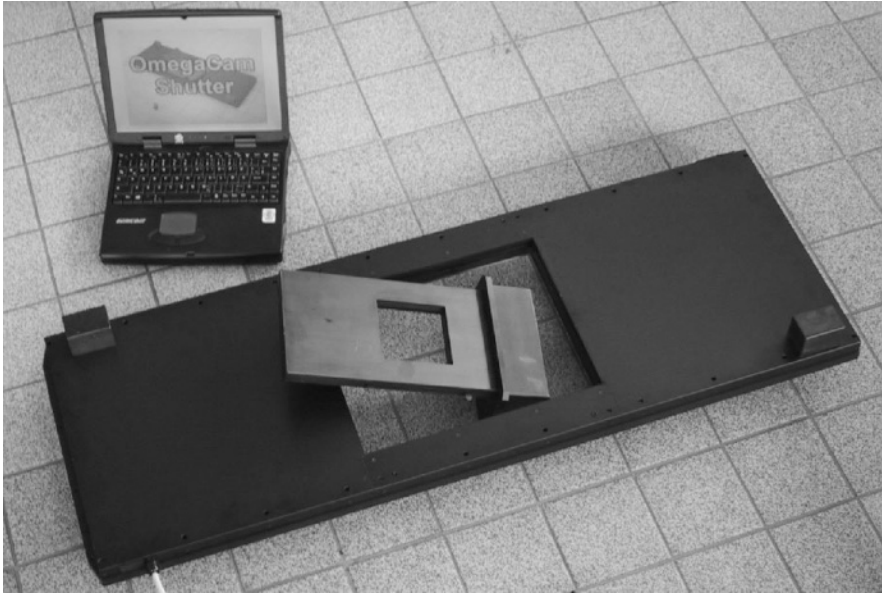


Figure 1. The OmegaCam shutter, together with the much smaller BUSCA shutter - the first shutter of this type [1].

A comparison of the number of commanded motor steps with the counted encoder increments provides the primary check of proper shutter operation. This check is done after each blade movement. If the position mismatch exceeds a given (programmable) threshold an error signal is generated.

1.2 Shutter Control Unit

The control electronics hardware design is symmetric as well. Two identical control modules exist - one for each shutter blade - plus a third one for host communication. Additional hardware status lines are provided.

Each module (160 mm × 100 mm Eurocard format) is built around an Infineon C515C microcontroller. Parameters defining the shutter operation (e.g., velocity profile) are stored in non-volatile serial EEPROM (I2C). A microstep driver for the stepper motors and an integrated encoder/counter allow motor control. The modules communicate with each other through the

CAN serial bus and a few status lines. An RS232 interface to the instrument workstation is used for monitoring and parameter programming.

1.3 Shutter firmware and movement control

The ShutterCU firmware is first component responsible for the blade movement control after an exposure control signal (open/close) is received and for the detection of a mismatch between the commanded motor position and the actual encoder position. The shutter blade movements follow a trapezoidal velocity profile which is identical for both blades and directions. It is characterized by four parameters: start velocity, acceleration, maximum velocity and blade travel distance.

2. PERFORMANCE

Basic parameters are listed in Table 1. One of the key parameters is the exposure uniformity. Non-uniform exposures occur if the movements of both shutter blades are not exactly identical. Limitations are due to the stepper motor resolution and the tolerances of the mechanics. The effect becomes more and more important for shorter exposures. Uniformity can be checked by comparison of flat-field exposures with different exposure times. The long exposure will serve as a reference while the short exposure will be affected most. We find that at the exposure time of 0.1 sec the residual nonuniformity is within $\pm 0.3\%$ or 0.3 msec, respectively (see Fig. 2).

Table 2. Shutter data.

Aperture size	370 mm \times 292 mm
Type	Slit
Blade material	Carbon fibre
Drive mechanism	Linear ball bearings, toothed belts, stepper motors, incr. encoders
Movement control	Microcontroller system, software programmable velocity profile
Exposure control	External (internal exposure timing provided)
Control interfaces	RS232 line, control and status lines
Dead time	0.9 sec (<i>i.e.</i> , blade travel time)
Shortest exposure time	< 1 msec
Exposure homogeneity	Deviations $< \pm 0.3\%$ at 100 msec exposure time
Exposure time accuracy	About 0.3 msec
Expected lifetime	>1 million operations (Endurance test with 10^7 ops. passed)

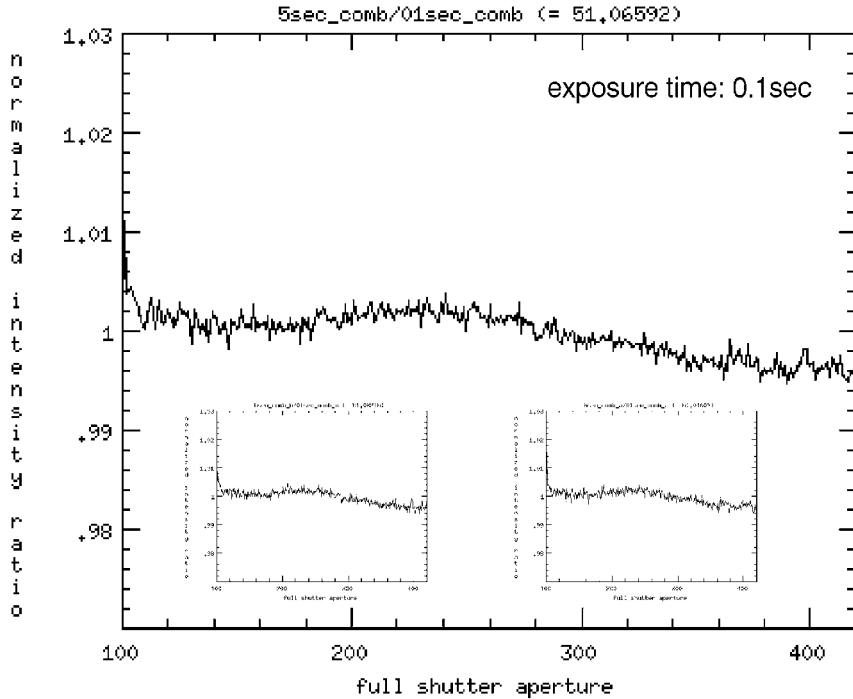


Figure 2. Shutter exposure homogeneity. Two flat fields were taken with 0.1 sec and 5 sec exposure times, divided by each other and the results were normalized. The diagram shows the intensity ratio along the shutter blade movement direction. The two small diagrams inside are for the two opposite shutter blade movement directions. No significant differences are found.

3. ACKNOWLEDGEMENTS

OmegaCam is realized with financial support by the German Federal Ministry of Education and Research (BMBF) through grants 05AV9MG1/7 and 05AV2WM1/2.

4. REFERENCES

- [1] Reif K., Bagschik K., de Boer K.S., Schmoll J., Müller P., Poschmann H., Klink G., Kohley R., Heber U., Mebold U. 1999, *BUSCA: a telescope instrumentation for simultaneous imaging in four optical bands*, Proc. SPIE Vol. **3649**, p. 109.

ULTRA-DEEP OPTICAL SPECTROSCOPY WITH PMAS

Using the Nod-and-Shuffle Technique

Martin M. Roth, Thomas Fechner, Dieter Wolter, Andreas Kelz, Thomas
Becker

Astrophysikalisches Institut Potsdam

Abstract: *PMAS, the Potsdam Multi-Aperture Spectrophotometer, is a new integral field spectrograph in the optical, which is optimized for good transmission and high image quality from 350 nm to 1 μ m. We present our plan to implement a CCD charge-shuffle mode to allow for beam switching with a very high degree of sky subtraction accuracy for faint object 3-D spectroscopy.*

Key words: *integral field spectroscopy, faint object spectroscopy, beam switching*

1. INTRODUCTION

The exploration of the high-redshift universe is certainly among the most exciting topics of modern astrophysics, both on the grounds of advances with numerical simulations in theoretical cosmology, as well as observationally with the light collecting power of 8–10-m class telescopes. While HST has provided us with images of galaxies up to a redshift of $z \approx 5$, ground-based imaging and spectroscopy even with the largest available telescopes is embarrassingly difficult and expensive in terms of observing time.

The intrinsic faintness of high-redshift galaxies is only one of the reasons for the problem. Ground-based observations are confronted with the fact that these objects are much fainter than the surface brightness of the sky, typically 1% the brightness of the sky or less. Therefore, the detection limit for low- and medium-resolution spectroscopy is dominated by the limited accuracy in subtracting the bright and variable sky background. As an

instructive example, Fig. 1 shows images and a spectrum of a galaxy at redshift 6.56 (pictures taken from a press release of the IfA, Univ. of Hawaii), obtained as part of a total of ~ 24 hours of multi-wavelength broad- and narrow-band imaging at the Keck and SUBARU telescopes, and with 4 hours worth of integration using Keck and the LRIS spectrograph [1].

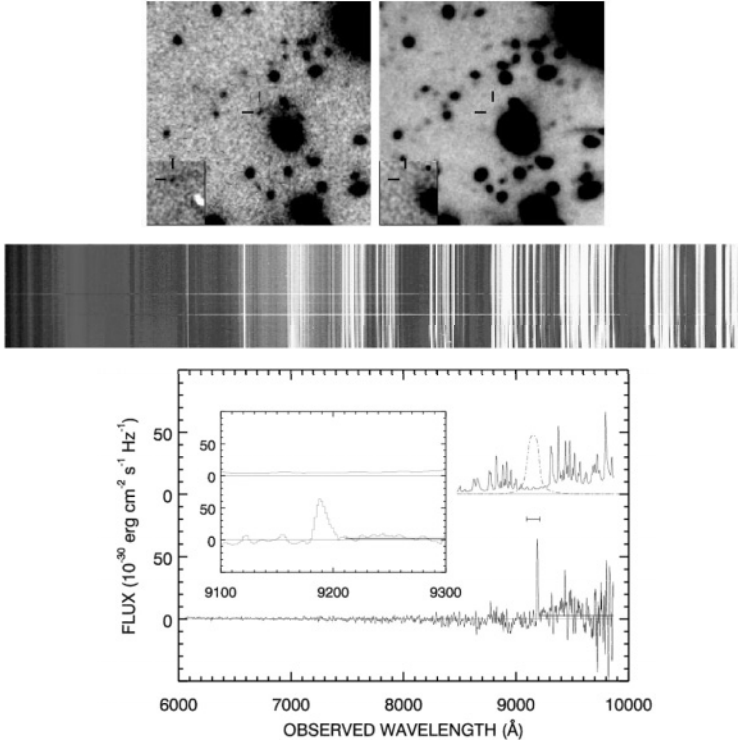


Figure 1. Ly_α emission at $z=6.56$, detected with an onband/offband imaging technique. The narrow-band filter transmission curve (insert) has been strategically chosen to fall in a gap between two strong OH night sky emission bands (note that the sky lines have been scaled down by a factor of 100). The strong residuals redward of the redshifted Ly_α line (near 9200 Å) are typical for the problem of low/medium resolution spectroscopy in the red. The ~ 10 Å resolution LRIS spectrum on the top (taken from another source) demonstrates that more than half of the available wavelength range is contaminated by the disturbingly bright OH emission bands (pictures from IfA press release by Hu [1] and I. Lehmann, AIP).

2. BEAM SWITCHING TECHNIQUES

The spectacular images of the Hubble Deep Fields, obtained with integration times on the order of 100 hours, may seem to suggest that it is merely a matter of allocating sufficiently long observing time at 8–10-m

class telescopes to also obtain good quality *spectra* of the most distant galaxies of the universe. It has been known for some time that this is not true, and is, rather, due to the presence of the bright night sky [2]. Chiefly, the limited accuracy of a conventional slit spectrograph in subtracting the sky contribution from a spectrum containing (object + sky) flux results in systematic errors which propagate *multiplicatively*. Contrary to photon shot noise and others sources of random error the resulting signal-to-noise ratio cannot be reduced by increasing the observing time. Instead, the S/N is saturating at some limiting value, no matter how large the telescope is, or how long we expose our spectra. The effect is particularly worrisome near bright night sky lines, dominating the sky spectrum at wavelengths above 6000 Å (for spectrophotometric data, see [3]).

Cuillandre et al. [2] proposed a method to overcome this limitation, called “*va-et-vient*,” which is essentially an adaptation of the familiar beam-switching technique, known from IR astronomy, to CCDs. Like in many other measurement problems, regardless of any specific technical domain, small signals affected by temporarily varying bias or gain can be determined more accurately by rapidly switching between the signal of interest and a reference (chopping). The problem for CCDs in adopting this scheme, however, has been the prohibitively long readout-time required for low read-noise operation of the detector. “*Va-et-vient*” makes use of the fact that in frame transfer mode charge can be clocked in *two* directions, thus allowing the user to consecutively obtain (sky + object) and (sky) exposures on the same frame without having to read out each sample immediately. This scheme requires provision on the CCD for one active zone (exposure) plus two masked areas (storage), and to parallel-clock two thirds of the resulting charge image back and forth. This must be synchronized with the telescope, which has to alternate between the object and a sky pointing accordingly. The important thing is that both (object + sky) and (sky reference) are always observed quasi-simultaneously through the identical optical train, with identical slit/aberration/distortion/flexure/... properties, and with identical CCD pixels, which exhibit essentially the same flatfield and fringing behaviour.

A more recent paper by Glazebrook and Bland-Hawthorn [4] describes the method which they dubbed “*Nod- Shuffle-Spectroscopy*,” and a practical implementation with the LDSS spectrograph at the Anglo-American Telescope. Based on a wealth of test data, the authors claim that, in principle, nod-shuffle should be able to reach a limiting flux level of 10^{-4} of the sky brightness — provided one can spend enough observing time.

3. PMAS

PMAS, the Potsdam Multi-Aperture Spectrophotometer, is a new integral field spectrograph, which was designed as a flexible traveling instrument, and which has seen first light at the Calar Alto 3.5-m Telescope in May 2001 [5]. The instrument was developed at the Astrophysical Institute Potsdam [6-10].

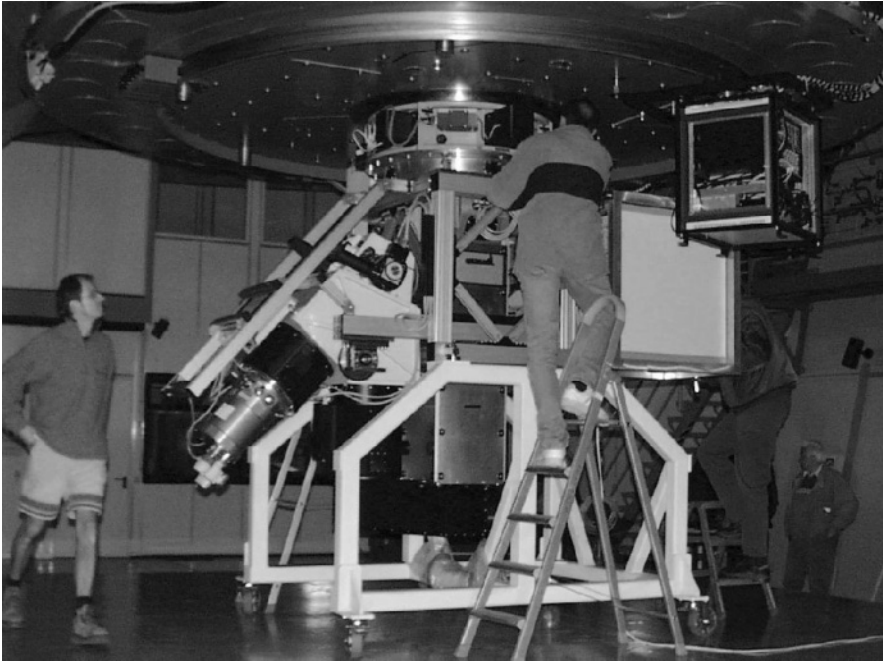


Figure 2: PMAS during the process of mounting to the Calar Alto 3.5-m Telescope Cassegrain flange for first light on May 28, 2001.

A major motivation for this development has been the goal to use the advantages of integral field spectroscopy (IFS) for the difficult observation of individual sources in crowded fields, e.g., resolved stars and nebulae in nearby galaxies, analogous to the development of crowded field photometry after the advent of CCDs in astronomy. We have also considered the benefits and limitations of IFS for *faint object spectroscopy* [9] which can be summarized as follows:

- absence of slit losses (there is no slit), image slicer effect for extended sources
- sky background estimate can be derived more reliably from an annulus or an extended region around the target rather than from interpolation along a slit

- uncritical telescope pointing for faint targets due to extended 2-dimensional FOV
- differential atmospheric refraction and associated slit losses are irrelevant for IFS

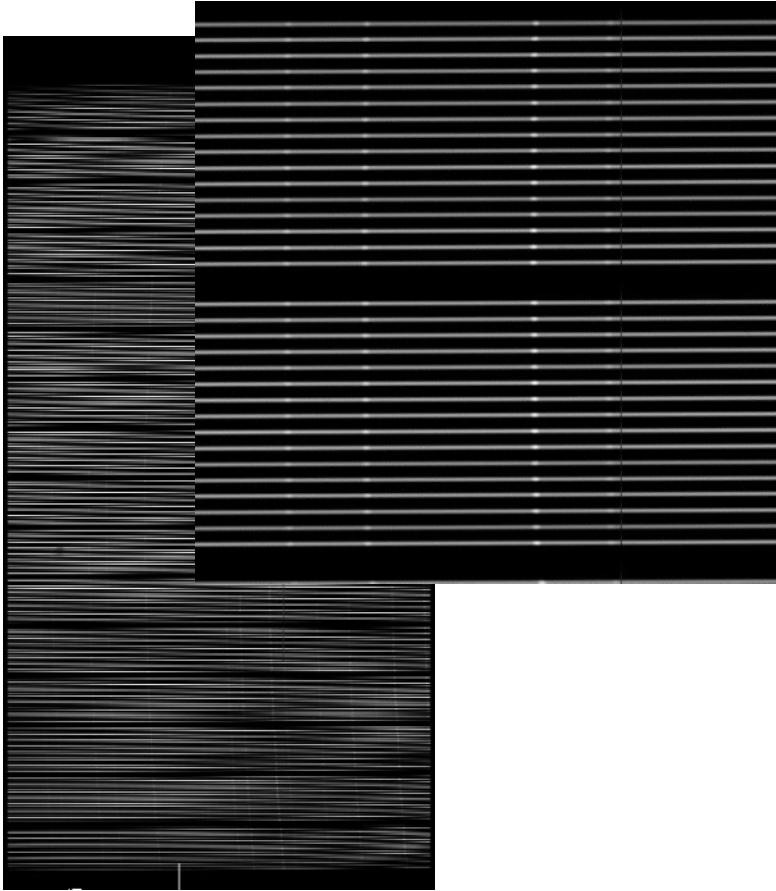


Figure 3: Single 2Kx4K CCD frame of PMAS fiber spectrograph internal calibration exposure (continuum+spectral line lamp). The magnified insert shows two groups of 16 well-separated spectra, corresponding to two rows of 16 spatial elements of the lens array.

4. NOD-AND-SHUFFLE WITH PMAS

With funding from the Verbundforschung of the German BMBF, and in collaboration with Lutz Wisotzki and Joachim Wambsganss, University of Potsdam, in April 2002 we started the “ULTROS” project, which is intended to implement a variant of the nod-and-shuffle technique in PMAS.

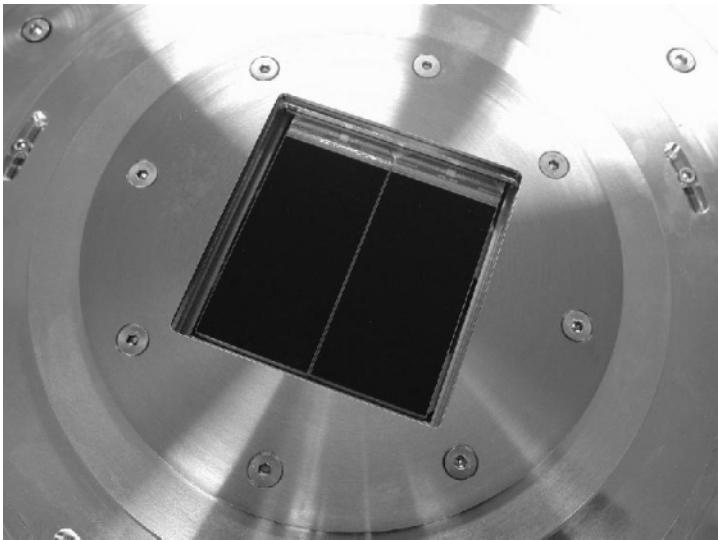


Figure 4: The PMAS fiber spectrograph supports a large spectroscopic field of view: 4K×4K with 15μm pixels, corresponding to 3200 Å coverage at 3 Å resolution (600 l/mm grating).

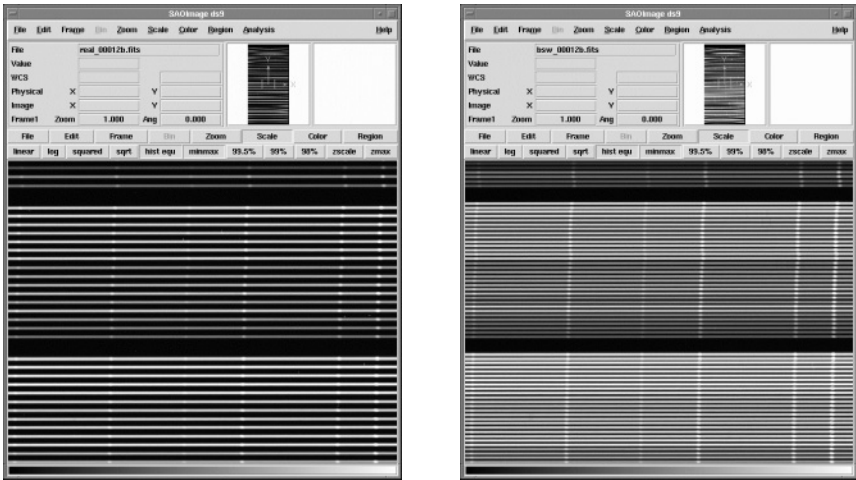


Figure 5: PMAS charge-shuffle mode experimentally implemented in the lab.

The idea is to use the strips of free space between neighbouring spectra as storage areas for the shuffling process rather than masked storage space at the edges of the chip. Figure 5 demonstrates how this mode has been implemented in the lab: while the left frame shows a normal calibration frame, the right frame has twice the number of spectra—generated by

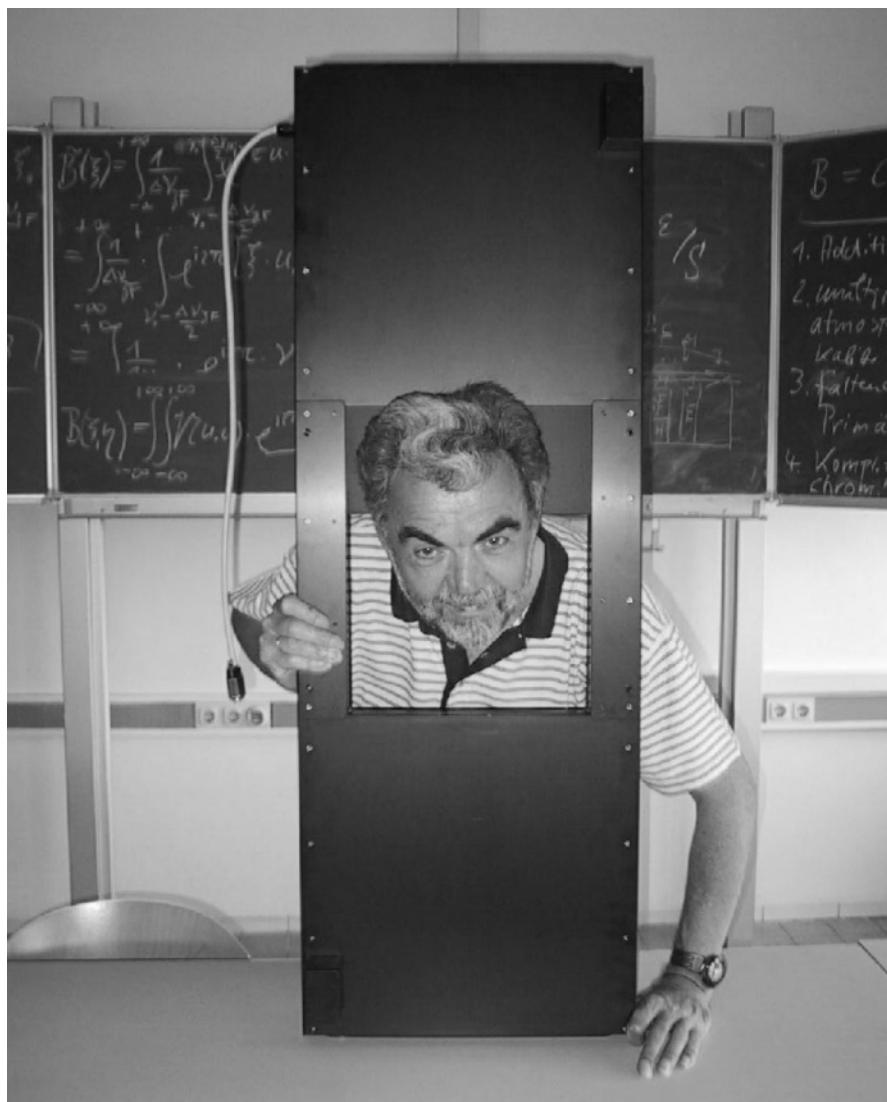
clocking charge 7 pixels (half the average vertical distance between spectra) back and forth, synchronized with the shutter.

5. ACKNOWLEDGEMENTS

The PMAS project has received financial support from the German BMBF under Verbundforschung grants 05 3PA414/1 and 05 AL9BA1/9. The ULTROS project is funded under grant 05AE2BAA/4. TB acknowledges support from the DFG grant HA1850/10. We wish to thank our colleagues of the ESO ODT and their former team leader Jim Beletic for allowing us to copy the ESO design VLT detector head, the ACE CCD controller, developed by Roland Reiss, and generous support and advice throughout, without which the project would not have become a success. Thanks also to Ingo Lehmann for providing us with the LRIS frame (Fig. 1).

6. REFERENCES

- [1] Hu, E.M., Cowie, L.L., McMahon, R.G., Capak, P., Iwamuro, F., Kneib, J.-P., Maihara, T., Motohara, K. 2002, *A Redshift $z=6.56$ Galaxy behind the Cluster Abell 370*, *ApJ* **568**, L75.
- [2] Cuillandre, J.C., Fort, B., Picat, J.P., Soucail, G., Altieri, B., Beigbeder, F., Dupin, J.P., Pourthie, T., Ratier, G. 1994, *'Va-et-Vient' spectroscopy: A new mode for faint object CCD spectroscopy with very large telescopes*, *A&A* **281**, p. 603.
- [3] Massey, P., Foltz, C.B. 2000, *The Spectrum of the Night Sky over Mount Hopkins and Kitt Peak: Changes after a Decade*, *PASP* **112**, p. 566.
- [4] Glazebrook, K., Bland-Hawthorn, J. 2001, *Microslit Nod-Shuffle Spectroscopy: A Technique for Achieving Very High Densities of Spectra*, *PASP* **113**, p. 197.
- [5] Roth, M.M., Becker, T., Böhm, P., Kelz, A. 2002, *Galaxies - The Third Dimension*, in Proc., ASP Conf. Ser., eds. Margarita Rosado, Luc Binette, Lorena Arias.
- [6] Roth, M.M., Seydack, M., Bauer, S.M., Laux, U. 1997, *Design study for the Potsdam Multiaperture Spectrophotometer (PMAS)*, in Proc. SPIE **2871**, p. 1235.
- [7] Roth, M.M., Laux, U. 1998, *The PMAS Fiber Spectrograph*, in Proc., Fiber Optics in Astronomy III, ASP Conf. Ser. **152**.
- [8] Roth, M.M., Bauer, S.M., Dionies, F., Fechner, T., Hahn, T., Laux, U., Nickel, U., Popow, E., Schmoll, J., Wolter, D. 1998, *PMAS – the Potsdam multiaperture spectrophotometer: a progress report*, in Proc. SPIE **3355**, p. 798.
- [9] Roth, M.M., Becker, T., Schmoll, J. 2000, *Faint Object 2-D Spectroscopy: Promise and Limitations*, in Proc., 3D - Imaging the Universe in Three Dimensions, ASP Conf. Ser. **195**, p. 122.
- [10] Fechner, T., Wolter, D., Roth, M.M. 2000, *CCD systems for PMAS – A new optical integral field spectrophotometer for the Calar Alto Observatory 3.5-m telescope*, in Proc., Optical Detectors For Astronomy II, Kluwer Dordrecht, p. 153.



Klaus Reif, following Robespierre's footsteps, shows one of the many practical ways to use the OmegaCam shutter. (paper on page 367. See also page 194). Courtesy K. Reif.

THE TOLOLO ALL SKY CAMERA

TASCA

Roger Smith, David Walker and Hugo E. Schwarz
Caltech Optical Observatories, Cerro Tololo Inter-American Observatory

Abstract: *An all sky camera using commercial parts has been assembled at Cerro Tololo Inter-American Observatory to monitor a wide range of atmospheric effects of interest to astronomers, including thin cirrus and contrails which are otherwise invisible on moonless nights, air glow variations, light pollution in the Sodium and Mercury bands, and aircraft lights. To enhance the visibility of clouds, raw images are divided by the corresponding clear sky image, inferred from images taken at the corresponding sidereal time on previous nights. Frames are taken every 30 seconds so that subsequent animation is smooth enough for the eye to pick out motion of clouds at or below the noise floor.*

Key words: all sky camera, cloud camera, air glow, light pollution

1. INTRODUCTION

The principal goal of the Tololo All Sky Camera (TASCA) is to provide the astronomer with a tool for continuous qualitative assessment of clouds over the entire sky, with particular emphasis on detecting thin cirrus on moonless nights, since this is invisible even to the dark-adapted eye. In addition the camera has to be robust, and require little labor to construct, using all commercial parts costing \$20K or less.

1.1 Why not use a thermal imager?

A thermal imaging camera would be an excellent solution since the clear sky appears smooth under starlight, moonlight and even sunlight, with

clouds introducing changes in emissivity and temperature. The principal difficulty is that the capital cost approaches \$100K when one takes into account the specialized silicon fish eye lens required, and sensitivity is reduced for cold (high) clouds such as cirrus. Microbolometer arrays are only available at 320×240 pixels, providing rather coarse 0.75 deg resolution. While a scanning IR photometer can provide better spatial resolution, the frame rate is low and it would not meet the requirements for mechanical simplicity or commercial availability.

1.2 Optimizing a CCD to detect clouds

TASCA is based on a CCD primarily because of the large price advantage. It is simply a commercial thermo-electrically cooled CCD camera, Nikon fish eye lens, Linux/PCI computer, in a custom weatherproof housing, with custom acquisition and image processing software.

Other all-sky CCD cameras have been constructed, but are either not optimized for the detection of clouds or for operation under starlight. For example, ConCam [1] seeks economies by compromising optical quality, lens aperture and CCD sensitivity, which require exposures of several minutes. During this time, clouds move across many pixels causing contrast to be lost, and the sample rate becomes too coarse for animation.

Clouds are seen by a CCD primarily through extinction of starlight, combined with some scattering from bright sources such as planets, the Milky Way, and light pollution. The detection limit is ultimately set by the photon statistics.

Sufficient resolution is needed to maintain contrast on fine cloud structure. However, as pixel scale is made finer, not only must the optics be improved, but exposures must also be made shorter so that image motion doesn't negate the contrast gained. Thus signal-to-noise ratio scales as the pixel size to the power of 1.5, provided that photon shot noise dominates read noise and dark current noise.

Air glow due to atmospheric emission longward of 700 nm, exhibits strong spatial variations which change significantly on a timescale of a few seconds, and can thus be confused with clouds, so a suitable blocking filter must be used.

The need for short high-resolution exposures and spectral filtering conspire to reduce the signal. Yet with a backside illuminated CCD and a fast fish eye lens it is still possible to detect extinction of less than 10 % over 0.2 deg.

To see extinction near the noise floor, the inherent structure in the night sky must first be removed, so that display contrast is limited only by photon shot noise. Finally, by displaying the images as short movie sequences the

pattern recognition ability of the eye is harnessed to extract correlated motions from the noise. Smaller extinctions can be detected on larger spatial scales. For the eye to successfully extract weak patterns from noise, the acquisition frame rate must be high enough to allow smooth animation. Replay rate must be greater than ten hertz, *without pauses or decompression artifacts*.

2. THE CAMERA

A Nikon 8mm f/2.8 lens was chosen for its fast f-ratio, high optical quality and reasonable price (\$2500). Although it is no longer in production, it makes regular appearances on eBay. The only 8mm f/2.8 currently in production, is sold by Coastal Optical at ~4 times the price [2]

An 8 mm fish eye lens produces a 23 mm image circle, which maps to a 960 pixels on a SITe 1K CCD with 24 μm pixels. A 16 mm f/2.8 fish eye, which would collect more light per square deg, is available, but requires a larger and prohibitively expensive CCD.

Any more resolution would soon exceed that of the display monitor. Any less would sacrifice contrast on wisps of cirrus. To verify this, compare cirrus with the diameter of the moon (2.6 pixels at $180^\circ/960 = 11'/\text{pixel}$).

The thermo-electrically cooled CCD camera is an IMG1024S, manufactured by Finger Lakes Instruments [3] currently costing \$13K. It interfaces through a serial cable to a parallel port adapter to achieve about 25 second readout time.

A filter wheel, also manufactured by FLI places the following 1" circular filters close to the back of the fish eye lens: BG38 (Edmund Scientific L46-433) for clouds [4]; RG695 (Edmund L32-756) for airglow; 589/10 nm (Edmund L43-129) for sodium; 546/10 nm (Edmund L43-125) for mercury. Optical flats have been added to make the filters parfocal.

The cylindrical housing is constructed from 12" PVC pipe, with smaller PVC elbows providing rainproof inlets and outlets for the cooling fan. The camera power supply is mounted on the filter wheel where it warms the optics and interior of the window to prevent condensation.

An inexpensive and easily replaced 8" diameter acrylic hemisphere (Edmund Scientific #L53-997) was found to make a satisfactory entrance window, even with no antireflection coating. The housing is mounted on a steel pillar 3 m high and 30 cm in diameter at the western edge of the summit where it has a clear view of the approaching weather and potential sources of light pollution. It is high enough to be protected from curious tourists by day and stray flashlights by night.

3. IMAGE ACQUISITION

Image acquisition is controlled by software written (by David Walker) in C running under Linux on a PCI bus computer [ASL 900Mhz Pentium, 512MB PC133 RAM] using drivers based on code samples supplied by FLI. The ephemeris program by John.Thorstensen@dartmouth.edu was adapted and embedded in the acquisition routine. This schedules exposures only when the sky is dark and moonless since the moon produces considerable scattered light from the window and optics, and clouds can be easily seen by eye when the moon is up anyway.

Three second exposures are scheduled every 30 sidereal sec after zero Greenwich Mean Sidereal Time, so that images can be exactly registered from night to night. Cumulative errors are avoided by slaving the Unix clock to a local GPS clock (TrueTime NTS200) using the Network Time Protocol [5] to achieve millisecond accuracy. Erasure during the two second idle time is not deemed necessary.

Choosing Greenwich Sidereal Time over Local Sidereal Time assures that cameras in different locations take simultaneous exposures, which can be used for stereoscopic imaging of airglow, meteors, or aircraft traffic, or for verifying a transient astronomical event.

Images through shortpass and longpass filters are alternated so that both clouds and airglow are continuously monitored. Light pollution is recorded in narrow Sodium and Mercury bands [6] several times per night to determine whether regulations for shutting down commercial lighting late at night are being adhered to.

4. IMAGE PROCESSING

Images of the clear sky are constructed during the daytime by calculating the median of images taken at the same sidereal time on previous nights. Incoming are divided by the corresponding median image (see Fig. 1 and 2). Since a clear sky produces a flat ratio, any atmospheric phenomena greater than the noise are easily identified [7]. This contrast enhancement technique is robust, self-calibrating and completely automatic, but typically it takes a month or two after the camera has been installed to build up good medians due to the requirement for stable registration.

A web interface has been provided, which presents the latest images in each filter, plus animations of recent frames and of the whole night. Still images (PNG format) and moving GIF animations are binned 2×2 to reduce network bandwidth requirements.

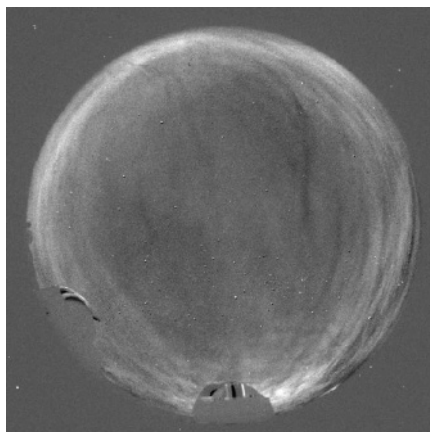


Figure 1. Direct image showing some thin cloud. Display contrast is limited by astronomical sources of light.

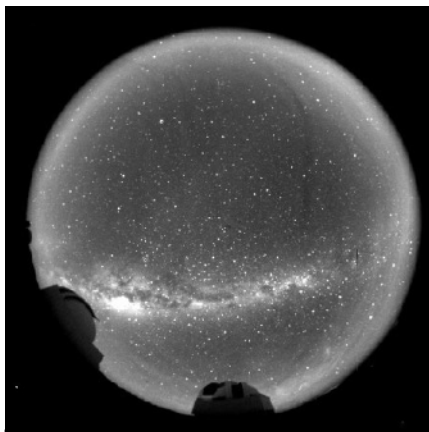


Figure 2. The same image after division by median of corresponding frames from previous nights. Residual image structure is due only to atmospheric effects.

Full resolution images will also be made available on the web in compressed FITS format (gzipped). A year of data occupies about 150 GB. At least this much will be held on disk. A progressive deletion scheme will be adopted which retains some images from every night, but with temporal coverage decreasing with age. Backups will be copied to 120 GB removable disks for ease of retrieval.

A separate interface is planned for full resolution movie replay on local computers (e.g. telescope consoles). A script on the local machine will poll the TASCA disk, then update a movie loop holding the last N frames. The TASCA software is not involved in this process. ImageMagick is currently the best candidate for full resolution replay, since it first builds the individual bitmap frames in memory, then copies them to the video buffer at full bus speed to produce a short but smooth full resolution animation.

TASCA was released for public preview in late July 2002, at <http://www.ctio.noao.edu/~david/tasca.htm>. At that date only blue images were offered since optical flats had not yet been added to make filters parfocal. A revised version of the shutter had been installed in the hope of achieving longer life. The web interface to the archive was still under development, but the basic cloud detection functionality was in place.

5. REFERENCES

- [1] www.concam.com
- [2] http://www.coastalopt.com/prod_a04.htm
- [3] www.fli-cam.com

- [5] <http://www.eecis.udel.edu/~ntp/>
- [4] Roger Smith, 2000, *Cloud monitoring with CCDs*, Optical Detectors for Astronomy II, P. Amico & J. W. Beletic (eds), p. 345-350
- [6] <http://www.ctio.noao.edu/~emond/lpc/lpc-presentations.html>
- [7] <http://www.ctio.noao.edu/sitetests/WorkShop2002/meeting.html>



*Paul Jorden and Peter Sinclair show us the spirit of Aloha.
In the back Mark Downing and wife Diana.*

THE ORTHOGONAL PARALLEL IMAGING TRANSFER CAMERA

John L. Tonry¹, Barry Burke², Gerald Luppino¹, Nicholas Kaiser¹

¹*Institute for Astronomy, University of Hawaii*, ²*Lincoln Laboratory, Massachusetts Institute of Technology*

Abstract: *The Orthogonal Parallel Transfer Imaging Camera (OPTIC) is a recently constructed camera designed to remove image motion from optical images. It has 4K×4K pixels, subtending about 10' at the UH 2.2-m telescope. It is capable of removing image motion at rates up to 100 kHz and recording guide stars at rates up to 100 Hz. It will be permanently mounted at a bent-Cassegrain port on the UH 2.2-m and used for follow-up observations of transients such as supernovae, Gamma Ray Bursts (GRBs), and gravitational lenses as well as general purpose imaging. It is also extremely useful for monitoring the atmosphere and telescope performance.*

Key words: *Charge-Coupled Device (CCD), Orthogonal Parallel Transfer Camera (OPTIC), image motion, turbulence*

1. THE CAMERA AND CONTROLLER

The heart of the OPTIC camera is the MIT Lincoln Laboratory (MIT-LL) CCID28 (see Fig. 1). This is a CCD designed by the authors using funding from MIT-LL as well as the National Science Foundation (NSF). The CCID28 has 2K×4K 15 μm pixels, with serial registers at both 2K ends and amplifiers at each corner. The CCD is mirror symmetric around the 4K centerline, and each of the 2K×2K halves have separate clocks for the “lower” 512 rows closest to the serial registers and the “upper” 1536 rows closest to the centerline. The CCD, therefore, has effectively four “cells” which can be clocked independently. The CCID28 sits on a molybdenum

package and is buttable to <0.5 mm on the 4K sides, and buttable to within 5 mm on the 2K sides. Figure 1 shows the CCID28 on its package.

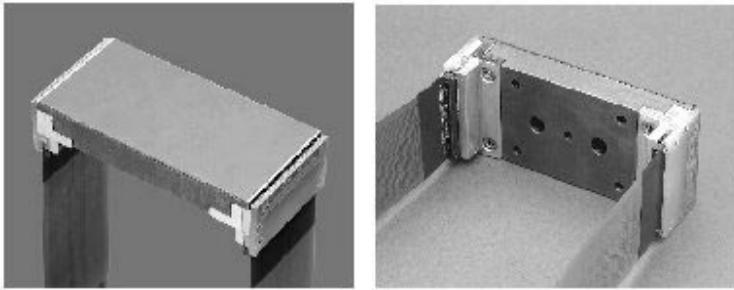


Figure 1. The CCID28 sits on a molybdenum package and is buttable to <0.5 mm on the 4K sides, and buttable to within 5 mm on the 2K sides.

The bond wires from the CCD go to a piece of AlN which has traces running around to load resistors, follower JFETs, and a Nanonics connector all lying underneath the footprint of the CCD.

Each serial register is read out of one amplifier, for a total of four video outputs from the focal plane. We use SDSU-2 electronics for readout, with 3 clock boards providing the 32 parallel clock signals, 20 serial clocks, 4 reset gates and 4 serial dump gates. Two video boards handle the four outputs, a utility board operates the shutter, filter wheel, temperature control, pre-flash LEDs, and a timing board carries the DSP which runs the whole operation. We currently run with a CDS with 1usec integration on signal and reset for a net pixel rate of 125 kpix/sec at $4 e^-$ read noise.

1.1 Orthogonal Transfer

The unique feature of the CCID28 is the structure of the pixels. These are laid out in as an “orthogonal transfer” design, as described by [1]. Figure 2 illustrates how the gate layout permits charge movement in all directions.

Therefore the developing electronic image within the silicon can be clocked during exposure to follow an optical image which may be dancing around on the detector.

This process can cause blurring, but since the offset between photons and electrons never needs to be larger than 0.5 pixel, this blurring is equivalent to convolution with a 1 pixel PSF. Non-perfect charge transfer efficiency (CTE) can also cause blurring, but with a CTE of more than 0.99999 and typical exposures of a few thousand shifts. This creates a very small skirt (few percent at most) of charge around a given charge packet, which is lost in the optical PSF.

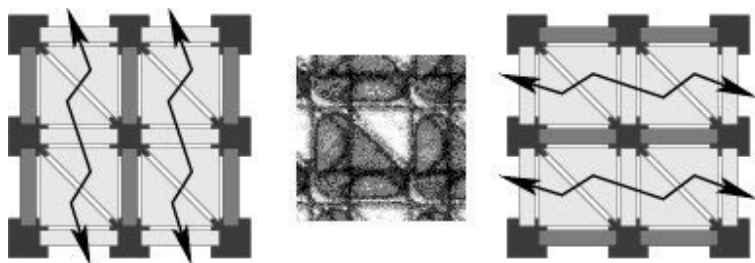


Figure 2. The layout of the orthogonal transfer gates is symmetric to 90° rotations, and so the charge can be 3-phase parallel clocked in the vertical direction or the horizontal direction by setting the appropriate vertical or horizontal gates negative to act as a barrier. The center image is a photomicrograph of the gates of a single pixel.

OT clocking can also create spurious charge if clock voltages are excessive, but since a normal readout involves 2K shifts anyway, it is not significant. The advantages conferred by OT clocking include some amount of clocked anti-blooming (saturated stars tend to create a mesa of charge which never overflows the pixel boundaries), and automatic dithering of CCD defects or obscuring particles. Figure 3 shows how two CCID28 devices have been deployed in a cryostat.

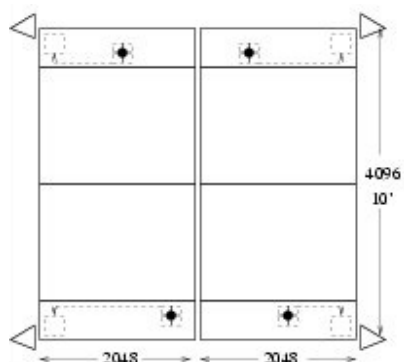


Figure 3. The OPTIC camera consists of two CCID28s next to each other in a cryostat. These two devices therefore offer $4K \times 4K$ pixels, and the plate scale at the UH 2.2-m is $0.138''/\text{pixel}$ so the camera subtends about $10'$ on the sky. The four “lower” regions of $0.5K \times 2K$ are designated as “guide regions”, and the four “upper” regions of $1.5K \times 2K$ are designated as “science regions”.

1.2 Operation

Operation of OPTIC first requires a quick snapshot of the four guide regions in order to locate guide stars. The observer is presented with an image and selects zero or one guide star in each of the guide regions for a

total of 1–4 guide stars. The shutter is then reopened, a few video frames are taken of the stars, the precise centroid of each is determined, and then the shutter is reclosed and the arrays are cleared. The observation then commences when the shutter is reopened, and OPTIC goes into its basic video loop.

The first stage of the video loop consists of a “shutterless video” readout of a small region around the 1–4 guide stars, typically 32×32 pixels binned 2×2. This is done simultaneously for up to four stars, with a horizontal and vertical parallel transfer to quickly bring each of the 1–4 regions down to the amplifier, and then a standard subarray readout of 1–4 guide regions. The science regions and any guide areas which are not currently being used for guiding are left quiescent. Although the shutter is open throughout this process, the speed of the parallel transfer and readout, and the preeminence of the guide stars virtually guarantees that the guide star images will be uncontaminated by other stars in the field. This process is reasonably fast, requiring up to 1–10 msec for parallel transfer depending on whether guide stars are close to or on the opposite side of the CCD from an amplifier, and 2–5 msec for the readout.

The guide star images are then analyzed by the host computer for centroid, FWHM, and flux. The time sequence of each guide star’s position is analyzed to predict where it will be at the next iteration. We have found that an algorithm which finds coefficients which predict observation N in terms of a weighted sum of observation $N-1$, $N-2$, etc. works well. The coefficients are periodically determined from the earlier observations, and a three coefficient algorithm performs well, even on periodic motions with only a few samples per period.

Once the host computer has determined the predictions of the guide stars, it rejects bad predictions based on discordant offsets from multiple guide stars (if there is more than one) or on recent positions of a single guide star. The offsets are then used to update the location of the guide box for each guide star.

The offsets of the guide stars are then used to make a prediction of how the next iteration’s optical image will differ from the accumulating image in each of the science (or unused guide) regions. Various algorithms are used here: the closest guide star, various averages of the guide stars, based on their distance from the center of the science region, or use time-lagged averages of the guide stars. These predicted shifts are then applied to the science regions by performing orthogonal transfer shifts to bring the accumulating image into registration with the optical image.

Telescope guiding is also carried out by periodically applying a leaky average of the average offsets of the guide stars to the telescope drives. The host and DSP then pause for some number of msec to fill out the guide star

exposure time and the process iterates. The rate at which we guide depends on the brightness of the guide stars and the signal to noise ratio that we want for the guide stars, however the rate is typically ranges between 30 and 5 Hz. It is possible to run as fast as 100 Hz with guide stars near the amplifier.

When the desired exposure time has elapsed, the shutter is closed and the is CCD read out. There are four basic files saved: the science observation, all of the video frames of the guide stars as a 3-D FITS file, a table of all the guide star analysis, and a table of all the OT shifts applied to the science regions. The only complication in subsequent reduction is that each observation has undergone a unique pattern of OT shifts. We have a utility that will convolve an unshifted flatfield with the shift pattern from the shift table of a given observation. This does a very good job of flattening, but obviously causes problems for creating a “superflat” out of the sky from all of the observations during a night. OPTIC requires that high signal to noise flats (*e.g.*, dome flats) be used to remove the pixel-to-pixel and OT shift pattern from all images. They can then be shifted into pixel registration, a superflat process applied, and a second round of flattening performed if necessary.

We have not yet pressed OPTIC to see how faint it can stably carry out operations, but scaling from present performance we expect to be able to work usefully to $m=18$ on the UH 2.2-m telescope. At these magnitudes, the probability of finding a guide star within one of the four $1'\times 4'$ guide regions is very high, even at the galactic pole.

During the exposure, the observer is presented with a video display which shows the image of each guide star in its box, a “radar” display which shows how the images are moving around on the CCD (even though the readout boxes are adaptively following the stars), a leaky average, a strip chart of the image FWHM, and a strip chart of the magnitude of the stars. The latter two are particularly useful for monitoring the quality of the seeing, transparency, and telescope focus.

2. IMAGE MOTION

We expected that tracking image motion at modest rates (5-10 Hz) would lead to a significant improvement in image quality, and indeed found that the motion compensated images were approximately 80% the width of images with telescope guiding at about 0.5 Hz. It was not uncommon to approach or hit the optical floor of the UH 2.2-m telescope (0.4", mostly triangular astigmatism). We were surprised, however, to find that the image quality did *not* vary appreciably with distance from the guide star. Previous observations at MDM observatory (TBS 97) had hinted at this, but had only demonstrated it to a modest separation of $2'$. This camera is capable of

covering a full $10'$ separation between guide stars, and we never saw the characteristic radial elongation of image motion, which heralds the edge of the isokinetic patch.

In order to investigate the degree to which motions of distant stars are correlated, we searched the USNO-A2 catalog for all constellations of bright stars where all four guide regions would have a star. At $m < 12$ these constellations are rare, but for $m < 13$ they are plentiful. A good example is fl 121-0852, which has two pairs of stars separated by about $2'$, and about $8'$ separation between the pairs.

Over the course of nine nights throughout the Spring semester of 2002 we imaged these constellations and recorded the image motion at typical rates of 15–30 Hz. We analyzed these videos to look for correlations between the image motion of the various pairs, the angle at which the motions decorrelate (isokinetic angle), and for correlations with non-zero time lag.

It was immediately obvious that the images *always* show a striking degree of correlation in their motion, regardless of separation up to $12'$ or so. Of course, any flaw in the telescope pointing from bad tracking, wind or dome shake will give us a correlated motion in all the stars imaged, so this result is not very significant of itself. However, the *differential* image motion comes purely from atmospheric distortion.

It was immediately obvious that the images *always* show a striking degree of correlation in their motion, regardless of separation up to $12'$ or so. Figure 4 shows typical motion of the stars in the fl 121-0852 field.

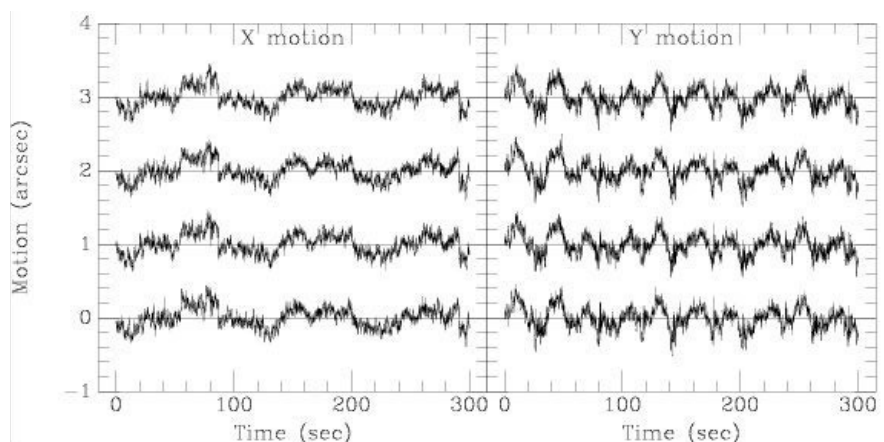


Figure 4. Image motion of $0.32''$ and $0.38''$ FWHM in x and y seen between stars at separations of $8'$, $2'$, and $8'$ (top to bottom with respect to star on the bottom). The overall image size during this exposure was $0.5''$, or $0.4''$ with image motion removed.

Of course, any flaw in the telescope pointing from bad tracking, wind or dome shake will give us a correlated motion in all stars imaged, so this result is not very significant of itself. However, the *differential* image motion comes purely from atmospheric distortion. Figure 5 illustrates this differential motion of the stars relative to the first one.

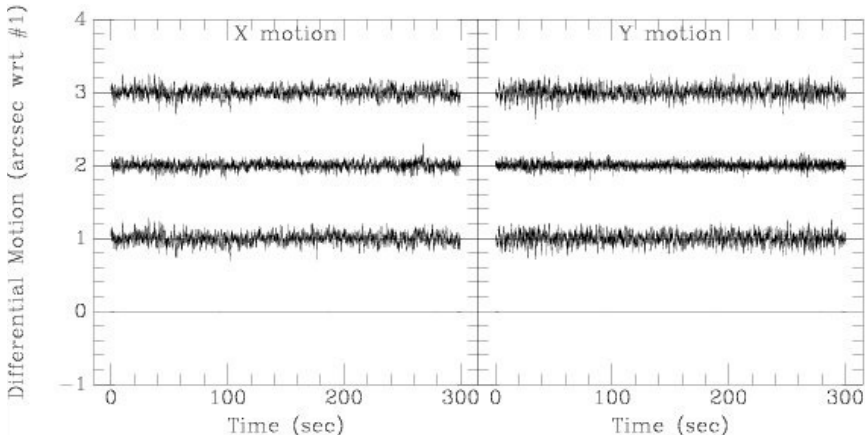


Figure 5. Differential motion of 0.17" FWHM (stars at 8' separation) and 0.11" (stars at 2').

There is a modest amount of decorrelation at 8' relative to 2', but the overall amount of image motion is quite small. Even at 8' the differential image motion is less than 0.18" FWHM, which will degrade 0.4" seeing by only 10%, whereas with no correction the seeing would degrade by about 20%. At 2' the degradation is only 4%.

3. TURBULENCE

Kolmogorov turbulence has a structure function that causes density and index variations whose variance scales as $r^{2/3}$ and wavefront phase variations which vary as $r^{5/3}$ [2]. The mean tilt of the phase variation that this causes across a telescope pupil gives rise to the coherent image motion, and the higher order components cause other distortions whose integrated effect can be conceptualized as an image with a certain width which dances around the focal plane with a characteristic amplitude.

If we calculate the amount of the image motion (as a FWHM), the intrinsic FWHM from the higher order wavefront distortions, and the net image size for 800 nm, 0.7" seeing, and a 2.5-m telescope diameter we find that for Kolmogorov turbulence these three quantities form a 3-4-5 right triangle, i.e. 3 units of image motion and 4 of intrinsic size combine to make 5 units of net (uncorrected) image size. Although this exact ratio does

depend on wavelength, r_0 , and telescope diameter, it is valid to the $1/6$ power. Thus this rule of thumb is accurate for practically all circumstances.

If we look at all pairs of stars in all constellations observed throughout the nine nights spread through the semester, we find that the median seeing was about $0.7''$, as is commonly reported at Mauna Kea. Figure 6 shows the seeing and differential motion from all the observations this Spring at the UH 2.2-m telescope.

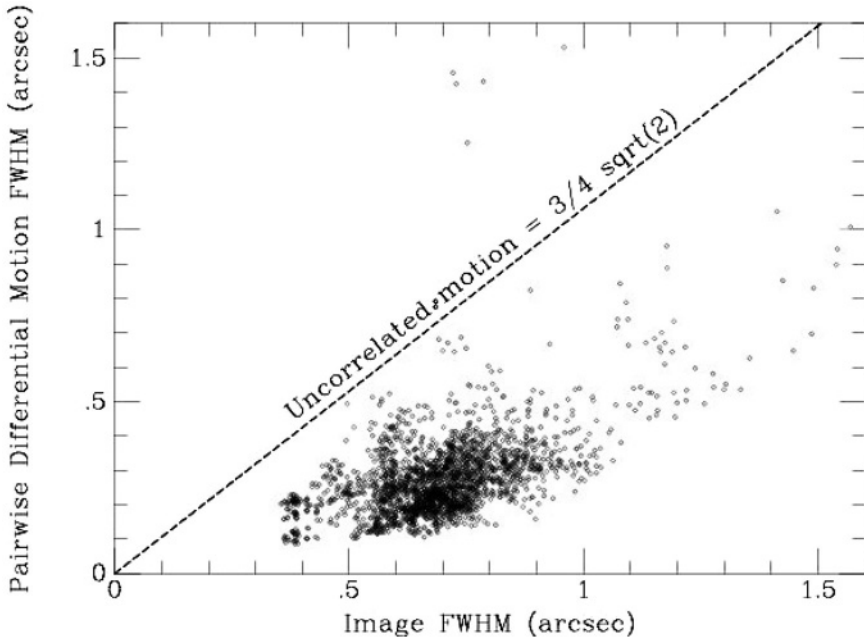


Figure 6. Sample of seeing and pairwise differential image motion over nine nights at the UH2.2-m.

However, the differential image motion was far less than what we would have expected if the star pairs were undergoing independent Kolmogorov turbulence. In that case we would expect the differential image motion to be something like $(3\sqrt{2})/4$ times the intrinsic image size. In fact, given the amount of differential motion, if we could somehow remove the image size which occurs because of correlated wavefront distortion, the median seeing at the UH 2.2-m would be about $0.3''$, not $0.7''$.

What is going on? We expect the wavefronts of guide stars to become uncorrelated when the telescope pupil to each passes through different regions of turbulence, i.e. in the simple case that a single layer of turbulence exists at a height h , the star motions should decorrelate at an angle D/h , where D is the telescope diameter [3]. The high degree of correlation at greater than $10'$ means that the height of the majority of the turbulence is

very much less than 500 m altitude. It is possible that we are seeing a boundary layer at a few 100 m altitude, but it seems more likely the problem is local to the telescope and is related to the thermal environment in the dome. Presently the 2.2-m mirror typically has a temperature of $T \sim 1^\circ\text{C}$, the closed tube $\sim 2^\circ\text{C}$, and the ambient air $\sim 1^\circ\text{C}$, which is a certain recipe for generating plumes of rising air. Ventilating the tube with a fan, and the short period at the start of a night when the tube has not cooled below the mirror helps the seeing. The seeing does seem to show some sensitivity to the orientation of the dome with respect to the wind. These suggest that the UH 2.2-m has a very bad thermal environment and that the seeing is primarily generated in the dome or the telescope tube. The newer generation of telescopes on Mauna Kea such as Subaru and Gemini are starting to report much better median seeing than is supposed to be possible on the older telescopes.

The Kolmogorov turbulence model and the supposition of thermal problems at the UH 2.2-m may or may not be correct. What is undeniable, however, is that images become much sharper when their motion is corrected according to a guide star as distant as $12'$.

Typically, a 20% improvement in image size accompanies the application of reasonably rapid image motion correction (see Fig. 7).

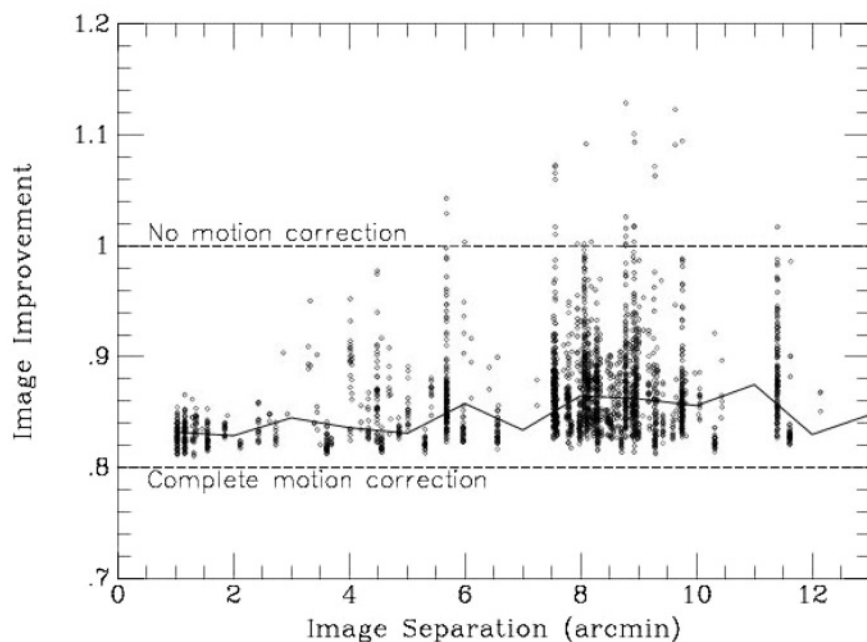


Figure 7. The image improvement as a function of guide star separation.

This may seem like a modest gain, but making the point spread function (PSF) 20% smaller corresponds to the signal to noise ratio increasing the quantum efficiency or throughput of the system by 50%, and the gains are even larger in crowded fields. Image motion compensation is very beneficial if the cost does not exceed 50% the cost of the system with it.

4. SUMMARY

The median seeing at MK generated at high altitude appears to be about 0.3", and the expectation is that this cannot be improved beyond about 1' (depending on altitude) from a guide star. However, image sizes in excess of 0.3" appear to be almost always caused by turbulence generated in the telescope or dome, and the image motion is highly correlated over very large angles, certainly well in excess of 12'. Even when higher order AO corrections are not possible (e.g., with wide field imaging), removal of image motion is extremely worthwhile. At least On Mauna Kea it seems that, one is either enjoying 0.3" median seeing or else one can expect to improve the PSF by about 20% using guide stars at angular separations of 10' at rates of 5–10 Hz.

5. ACKNOWLEDGEMENTS

We acknowledge support for this work from NSF grant AST97-96150.

6. REFERENCES

- [1] Tonry, J.L., Burke, B., & Schechter, P.L. 1997, *PASP*, **109**, p. 1154.
- [2] Tatarski, V.I., 1961, *Wave Propagation in a Turbulent Medium*, Dover: New York.
- [3] Kaiser, N., Tonry, J.L., & Luppino, G.A. 2000, *A New Strategy for Deep Wide-Field High-Resolution Optical Imaging*, Publications of the Astronomical Society of the Pacific, **112**, pp. 768-800.

GIGA-PIXELS AND SKY SURVEYS

John L. Tonry¹, Gerald A Luppino¹, Nicholas Kaiser¹, Barry Burke², George H. Jacoby³

¹*Institute for Astronomy, University of Hawaii*, ²*Lincoln Laboratory, Massachusetts Institute of Technology*, ³*WIYN Observatory*

Abstract: *We describe a project to build a new type of astronomical CCD that should significantly decrease the cost per pixel of detectors. This device should also provide very fast readout, autoguiding capability, image motion compensation, and good red sensitivity.*

Key words: Charge-Coupled Device (CCD), Panoramic Survey Telescope and Rapid Response System (PanSTARRS), pixel, Orthogonal Transfer Array (OTA)

1. INTRODUCTION

We anticipate funding to build a telescope facility known as the Panoramic Survey Telescope and Rapid Response System (PanSTARRS). This will be a four telescope array, each of aperture 1.5–2-m and equipped with a Gpix focal plane, which will survey the entire visible sky approximately every week. We will build a software pipeline that will monitor the data in real-time for everything which moves—near Earth “killer” asteroids (NEOs), comets, other asteroids, KBOs, or blinks—supernovae, variable stars, gravitational lenses. We will also build an image of the sky of unprecedented quality which can be used for the study of weak lensing, counts of stars and galaxies, discovery of exotic classes of objects, etc. The first year will be spent carrying out design studies and building prototypes, the second and third years will be telescope and detector construction, the fourth year will be integration, and we expect to commence routine science by the fifth year. Many of the ideas concerning this project are described by Kaiser et al. [1], however, they lay out a more ambitious project than the one envisioned here.

Our scientific interests have been endorsed by the Astronomy and Astrophysics Decadal Survey, which calls for a “Large Synoptic Survey Telescope” (LSST) which has a 6-8-m effective aperture, 7–9 sq. deg. field-of-view, and a 1–3 Gpix detector. Our PanSTARRS project will build a system with an effective aperture of 3–4-m, and as such is *not* intended to be the full LSST. However, should we prove successful, it is possible to build more telescope/detector units to achieve the full aperture desired at a very predictable cost and schedule.

2. DETECTOR ECONOMICS

It is a very sobering prospect to build four focal planes, each with ~ 1 Gpixs. Currently CCD detectors cost approximately 1 cent per pixel (thinned, science grade $2K \times 4K$ devices can be bought for $\sim \$80k$). Infrared arrays hybridized to a silicon readout multiplexer are at least a factor of 10 more expensive per pixel (the Rockwell $2K \times 2K$ HgCdTe devices are sold for $\sim \$500k$). In addition, the total cost of the current crop of “megacams” which offer 0.3 Gpixs is 2-3 cents per pixel partly because of the cost of engineering and controller electronics. Even at 1 cent per pixel for a detector, the cost of 4 Gpix is $\$40M$, which is prohibitively high for the system we envision.

Our proposed detector should permit us to reduce the detector cost to approximately 0.1 cents per pixel, offering $4K \times 4K$ pixels at a cost of $\sim \$20k$. The total cost of each of our Gpix focal planes would then be $\sim \$2M$ when cryostat, shutter, filters, controller, and assembly are added in, and we expect an additional $\sim \$2M$ of non-redundant engineering (NRE) cost.

3. PROPOSED IMPROVEMENTS

There are a number of areas where we expect to improve the detector cost to performance ratio. First and foremost, we expect to improve the yield of workable detectors, since the cost per detector is inversely proportional to the yield. We will decrease the pixel size as much as possible, since the cost of CCDs is roughly proportional to the area of silicon, not to the number of pixels. We will remove image motion, since a 20% improvement in PSF width improves signal to noise as much as a 50% improvement in quantum efficiency. We will reduce the readout time to approximately 2 sec, so that the duty cycle of the detector will be nearly unity. Finally we have the luxury of designing the telescope, the CCDs, the package, the cryostat, the readout

electronics, and the host computer all at the same time, so we will pay close attention to the costs and scalability of our total system.

3.1 Yield

The probability that a CCD from a given silicon wafer will turn out to be operable depends in large part on the absence of very localized, catastrophic defects such as gate to substrate shorts or bad amplifiers. For example, the “engineering grade” CCID28’s from the U. Hawaii OPTIC camera are poor detectors for science because of three tiny gate-to-gate shorts, which cause massive bright defects. In order to operate these devices half of the array has to be “turned off” by reducing the gate-to-gate voltages below the point where the device can be clocked effectively.

It is possible, of course, to make very small devices (*e.g.*, 1K×1K) and then reject the ones with defects, but this leads to very rapidly rising packaging and focal plane costs, and the metrology of the focal plane also becomes highly unstable. Current CCD foundries do a very good job on yield of 2K×4K parts, typically achieving yields of 25% which means ~ 0.1 defect cm^{-2} . To increase yield we need a way to isolate defects without losing the entire device.

3.2 Pixel Size

Given the freedom to design the optical telescope, we can push the size of a pixel that samples the PSF quite small, perhaps as small as 5 μm . However, we want to have thick devices for good performance in the near IR (800-1000 nm). Ideally we would like to 40–50 μm thick, fully depleted, high-resistivity silicon. However, on such devices charge diffusion may negate the value of small pixels. Experiments by UH, ESO, MIT-LL, and others find charge diffusion of $\sim 5\mu\text{m}$ rms. In addition, small pixels and standard NMOS lithography increase the probability of design traps or yield problems. At present we know that 12–15 μm pixels yield well, we think that 8–10 μm pixels may be possible, and we believe that less than 8 μm pixels are unlikely in a thick, deep depletion CCD. Other technologies such as CMOS have little difficulty with smaller pixels, and use of a vertical electric field can improve charge diffusion, but we do not believe that these technologies are mature enough to provide detectors on the 1–2 year time scale necessary for PanSTARRS.

3.3 Motion Compensation

Image motion compensation is extremely important, since approximately 20% of the blur in uncompensated image comes from motions that are coherent over cycles that are as large as $10'$. Various schemes have been used to remove image motion optically, including small field of view cameras with tip-tilt mirrors, but the most ambitious to date is the transmissive tip-tilt plate for the 1 degree FOV CFHT Megacam. It remains to be seen how well the CFHT system works, but one major limitation is that it can only correct the entire field of view at once. No one expects image motion from the atmosphere to be coherent across 1 degree, much less the 3 degrees planned for PanSTARRS. Instead what we need is a “rubber focal plane” which can effectively stretch and move to follow differential image motion across an arbitrary field of view.

We believe that the orthogonal transfer technology [3,4] can be used to create a rubber focal plane. It is a very fast way to shift charge to follow a moving optical image, and if the focal plane is divided into individual cells that are smaller than the isokinetic angle we can follow image motion over an arbitrarily large field of view.

3.4 Readout Speed

Fast readout is essential. With the SUPRIME camera on Subaru, for example, the total readout time of 100 sec is nearly equal to the time it takes the detector to saturate in the Z band, so the 8.2-m telescope is reduced to less than 6-m effective aperture because of readout overheads. Telescope time is simply too expensive to waste with a closed shutter. In addition, a large part of the rationale for LSST and PanSTARRS is to find NEOs, which move quite rapidly.

Once a moving object has moved more than one point spread function (PSF) width the detection signal to noise does not improve with exposure time. For NEOs this can happen in as little as 20 sec. We therefore feel that a readout in ~ 2 sec is essential. This requires us to have many signal chains. We are willing to tolerate $4e^-$ of read noise, but cannot accept much more without becoming dominated by read noise instead of sky noise in a 20 sec exposure. It is possible to run a single amplifier at 1 Mpix/sec with $4e^-$ noise, but it is unlikely to be able to run much faster. Therefore reading out 1 Gpix in 2 sec at 1 Mpix/sec requires 500 amplifiers and signal chains, or one amplifier per 2 million pixels. As a benchmark, the CFHT Megacam reads out in about 20 sec using 80 amplifiers, so we need nearly an order of magnitude more readout channels and faster readout.

4. THE ORTHOGONAL TRANSFER ARRAY

We believe we can achieve these goals by building monolithic devices, which are broken into an 8×8 chessboard of independent orthogonal transfer CCDs (OTCCDs). A given device might have $4K \times 4K$ pixels total, and be comprised of 64 OTCCDs that are each 512×512 pixels. We call this device the Orthogonal Transfer Array (OTA). Figure 1 illustrates the composition of an OTA in terms of cells, and cells in terms of Orthogonal Transfer (OT) pixels.

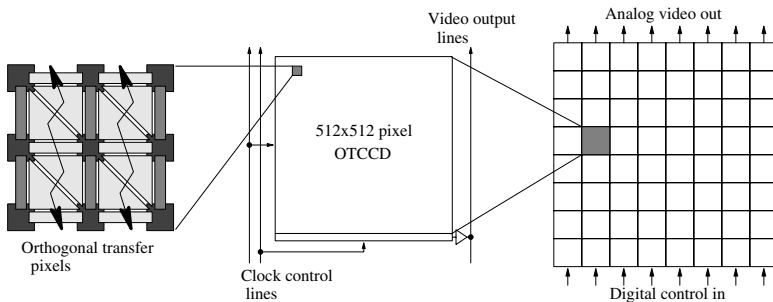


Figure 1. Layout of the OTA, showing OT pixels, which can clock charge horizontally or vertically, a single CCD cell with its addressing and clock lines, and a full OTA of 64 OTCCD cells.

Each cell in this device shares common serial clocks and biases (appropriately buffered for isolation), but there are two independent sets of parallel clock lines – active and standby. Row and column addressing lines determine which set of parallel clocks a cell is connected to (see Fig 2). When connected to standby, the charge does not move in a cell. When connected to active, the charge can be clocked for readout or for OT shifting to follow image motion. Likewise, the cell addressing also determines whether a cell is connected to an output bus line or not. Readout of the entire array would normally proceed row by row, with each cell in a row connected to the column video bus line for readout. The connections to these cells are via metal lines, which run in $100\ \mu\text{m}$ gaps between the devices or over the gates.

As with any device of this size, we expect catastrophic defects in these OTAs, but we can isolate the defects to individual cells. With a typical defect rate of $0.1\ \text{cm}^{-2}$, a $5 \times 5\ \text{cm}$ OTA would have 2–3 dead cells on average. The gaps between the cells and these dead cells would simply be accepted as dead area, and dithered away by the four telescopes of PanSTARRS and/or multiple observations with small telescope shifts.

We therefore expect the yield of these devices to be significantly greater than 50%, and we expect to obtain 30–40 per lot run, which is how we hope to achieve our goal of less than \$20k per device. We note also that bad columns are confined to a cell. In addition the OT pixel structure does not bloom for bright stars as much as three phase CCDs, and that the OT shifting which is a normal component of observation does quite a bit of clocked antiblooming.

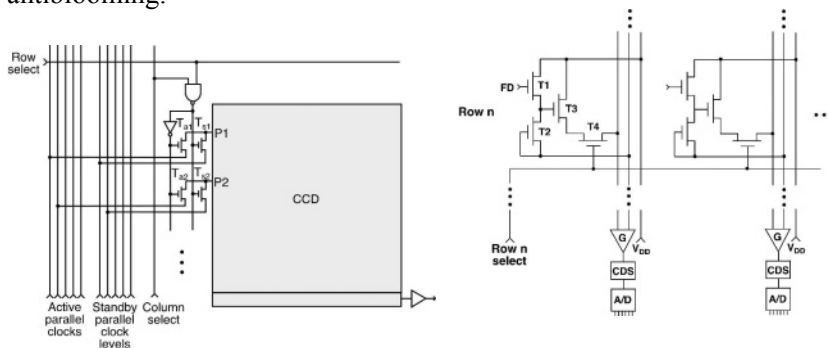


Figure 2. Sketch of how the OTA cells can be connected to active or standby clocks and output buffer lines.

Nevertheless, there will be very bright stars on the array (a given PanSTARRS field will have a magnitude 6 star and many magnitude 10 stars). Our plan is to write off these cells for science and instead rapidly read out a little patch around these bright stars and use them for guiding. We therefore simultaneously dispense with the enormous bleeding of charge from bright stars and acquire a distributed guide signal over the focal plane. These cells will subtend 1–3' on the sky, depending on our precise choices of pixel size and focal length, and independent OT shifting of each cell provides a rubber focal plane. Figure 3 sketches out how one of these OTAs might look and suggests a typical dispensation of cells.

The readout time of this device should meet our goal of 2 sec, since we can use 8 amplifiers simultaneously (one per column). We can wrap the serial register around underneath each device to the output amplifier structure, and add a follower JFET for buffering onto the output bus and addressing logic. We expect to keep the gaps between the cells to <100 μm , which means that we will have a fill factor in the focal plane of close to 97%. We have experimented with some NMOS structures to carry out NAND and NOT functions, and it appears to be practicable.

Use of orthogonal transfer shifting to remove image motion is a very attractive option (see the article on the OPTIC camera in this volume), since it allows us to remove image motion from atmosphere and telescope, and

substantially reduces the tolerances on telescope tracking. Even if the OT pixel topology has a lower yield than three-phase (our most current CCID28 lot suggests that this is not the case), the defects would not cause a problem with an OTA since they would simply lower the number of operable cells slightly.

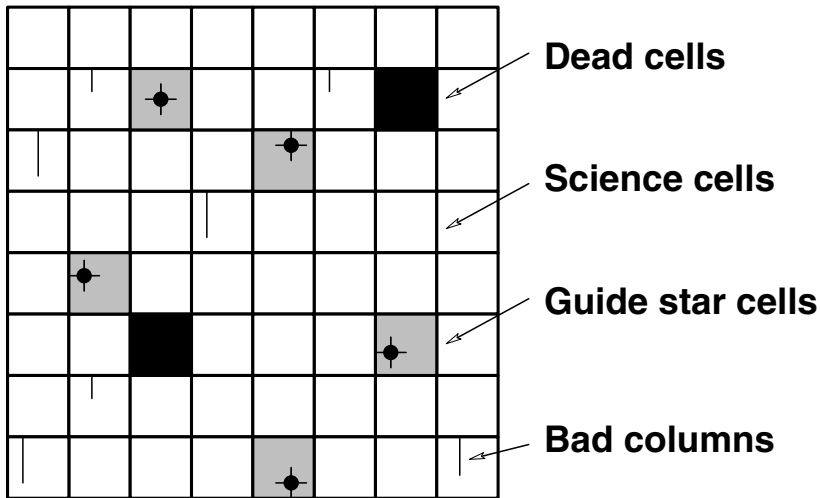


Figure 3. Typical use of an OTA, showing dead cells, cells devoted to guide stars, cells devoted to science, and bad columns.

The OTA package must be four-side buttable, for which we have designed a custom multi-layer AlN substrate that brings the bond pads to a pair of Nanonics connectors or a pin grid array underneath. The package sits on a 3-point pseudo-kinematic mount, which can accept precision spacers to adjust the device to a desired focal plane. We will use flex circuits to attach to the package and provide thermal isolation. We have also had success in passing the flex circuits through the cryostat wall and potting the gap to maintain vacuum integrity.

The large number of video channels for the PanSTARRS focal planes requires a new generation of controller, but fortunately the electronics and computer industry has advanced well beyond the state of the art of current astronomical controllers. For example, the SDSU-2 video board has two channels, is capable of up to 500 Kpix/sec with a correlated double sample and a 16-bit A/D, and consumes about 15 W of power. In contrast, the Analog Devices 9826 part, which is designed for HDTV and has three channels (nominally RGB), manages 15 Mpix/sec with a CDS and 16 bit A/D. The power consumption is 250 mW, and it is more than two orders of magnitude smaller than an SDSU-2 video board. The possibility of using an

ASIC for some or all of the device control and interface is extremely attractive, and we recognize that this is probably going to be the way things are done in the future, but we do not believe that ASICs will be available early enough or at a low enough development cost for PanSTARRS.

Barry Starr has spoken during this conference about his plans for a “Monsteroid” controller [2], which has an open and scalable architecture. Under this scenario, four OTA’s (an 8K×8K portion of the focal plane) would be run by a quad interface unit, which in turn communicate with a host computer via a Gbit fiber. Any number of these Quad OTA (QUOTA) units can be chained together, with a synchronization connection keeping readouts in lockstep.

The final Gpix imager we envision (PanSTARRSCam) has 64 OTAs, making a 32K×32K focal plane spanning 16 in (40 cm) on a side and covering 8 sq. degrees. The system will have 512 signal chains, a cluster of host computers, and a data processing pipeline. Each of four telescopes will have a PanSTARRSCam, and the data from each will be brought together for the following processing steps: flat-fielded, registered onto a common coordinate system, combined with cosmic ray rejection, and then analyzed to find objects with parallax (things in Earth orbit), objects which move, objects which blink relative to a growing master image of the sky, etc. We hope to see a first deployment of one of these cameras and telescopes in 2005, and routine science operations in 2006-7.

The OTA is a realizable and cost effective solution for very large focal planes. Other advantages include the fact that bright stars become guide stars, a rubber focal plane compensates for image motion, and very fast readout. We do not know of any other technology which is likely to be able to fill our need, including large monolithic CCDs (too expensive and readout too slow), small individual CCDs (packaging and electronics become overwhelming and no image motion compensation), monolithic CMOS (poor red QE and non-filled pixels are problematic for marginally sampled PSFs), and hybrid CMOS (still too expensive). We are confident that the next decade will see great strides in imaging technology, and we believe that our proposed device has the right combination of conservatism and audacity to carry out its science mission.

5. REFERENCES

- [1] Kaiser, N., Tonry, J.L., & Luppino, G.A. 2002, *PASP*, pgs. 112, 768
- [2] Starr, B.L., et al., 2002, *NOAO Observatory plan*, these proceedings, pg. 261.
- [3] Tonry, J.L., Burke, B., & Schechter, P.L. 1997, *PASP*, pgs 109, 1154
- [4] Tonry, J.L., Luppino, G.A., Kaiser, N. & Burke, B. 2002, *The Orthogonal Parallel Imaging Transfer Camera*, these proceedings, pg. 385

THE HUBBLE SPACE TELESCOPE WIDE FIELD CAMERA 3 INSTRUMENT CHARGE-COUPLED DEVICE DETECTORS

CTE Performance and Mitigation

Augustyn Waczynski¹, Terry Beck², Ray Boucarut³, Edward Cheng³, Dave Cottingham¹, Gregory Delo¹, Dale Fixsen⁴, Robert J. Hill⁴, Scott Johnson¹, Peter Kenny³, Wayne Landsman⁴, Eliot Malumuth⁴, Joel Offenberg⁴, Elizabeth Polidan¹, Anne Marie Russell¹, David Schlossberg², Elmer Sharp¹, Edward Wassell⁴, Yiting Wen⁴, John Yagelowich³

¹NASA GSFC/GST, ²NASA GSFC/Sigma, ³NASA GSFC, ⁴NASA GSFC/SSAI

Abstract: *The Hubble Space Telescope Wide Field Camera 3 (WFC3) is a new instrument planned for deployment during Servicing Mission 4 in 2004. One of its key scientific goals is to provide panchromatic coverage from the near-UV through the near-IR. This is accomplished using two detector technologies, Marconi Applied Technologies back-thinned CCDs and Rockwell Scientific Mercury-Cadmium-Telluride (HgCdTe) IR focal planes. The Marconi CCDs have been delivered and characterized. The performance of these devices is exceptionally good, and will provide a new wide-field, near-UV capability for the observatory. Several notable advances are described.*

Key words: *Hubble Space Telescope (HST), Wide Field Camera 3 (WFC3), Charge-Coupled Device (CCD), Charge Transfer Efficiency (CTE), Charge Transfer Inefficiency (CTI), charge injection*

1. MARCONI CCD PERFORMANCE

The WFC3 CCDs are based on the Marconi Applied Technologies commercial CCD44 (4K×2K) devices. For the WFC3 application, Marconi has modified the device design to create the CCD43 model, which has parallel register in the short direction (2K×4K operation). This device

includes a mini-channel (or supplementary buried channel), MPP mode of operation, and provide a charge injection feature at the top of the device. The modifications are for the purpose of mitigating the effects of radiation damage: primarily charge transfer efficiency (CTE) degradation and an increase in hot pixels.

2. CTE PERFORMANCE & CHARGE INJECTION

An extensive program of CTE characterization has been completed for the commercial CCD44 devices and radiation testing of the flight CCD43 devices is almost complete. Initial results show that the Marconi CCDs perform very well in an ionizing radiation environment.

The Detector Characterization Laboratory (DCL) tests include careful characterization of the CTE using ^{55}Fe , Extended Pixel Edge Response (EPER), and First Pixel Response (FPR) methods. Independent of the method, the CTE has a unique meaning only when operational conditions are specified because it depends on many factors, such as detector temperature, readout rate and the size and distribution of the charge packets. For example, figure 1 shows how the charge transfer inefficiency ($\text{CTI} = 1 - \text{CTE}$) for a device with the equivalent of 2.5 years on-orbit radiation damage can vary by a factor of two depending on the number of detected x-ray photons per column.

The Marconi CCD43s implement a charge injection feature that is being investigating for on-orbit CTE degradation mitigation. This method has the advantage of being essentially noise-free compared to optical bias techniques. Initial results are very promising.

A comparison was made of optical bias and charge injection techniques for mitigating CTE degradation. Figure 2 shows the effect of an optical bias on the performance of a CCD exposed to the equivalent of 2.5 years of on-orbit radiation damage (2.5×10^9 protons/cm² at a single energy of 63.3 MeV). As the bias signal level is increased the CTE improves such that at a level of $\sim 200\text{ e}^-$ the CTE of the detector is equivalent to that of a detector which has only been exposed to a 1-year dose of radiation damage. The penalty associated with this improvement in CTE is that each pixel has a shot noise of $\sim 14\text{ e}^-$, thus reducing the ability to detect faint sources.

The CTE of a detector can also be improved by injecting rows of charge into the detector prior to the exposure. The charge in the injected rows fills up many of the charge traps in advance of the ^{55}Fe signal packets, resulting in improved CTE for these packets. Figure 3 shows the improvement in CTE for a device exposed to a 2.5 years dose of radiation damage, for different intervals of the injected lines. For a device with charge injected once every

50th row, the CTE is improved to that of a device with only a 1 year dose of radiation damage.

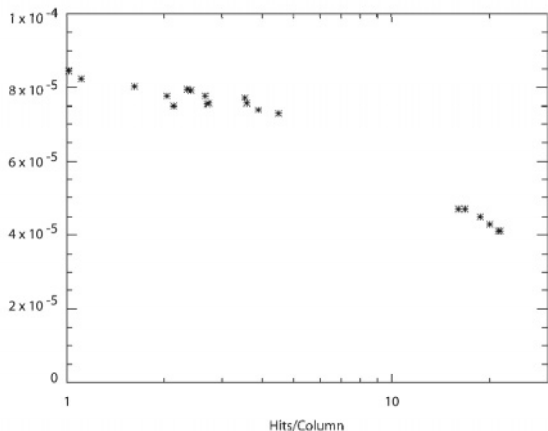


Figure 1. The measured CTI depends on the density of the ⁵⁵Fe x-ray events. An increase density of ⁵⁵Fe events results in as much as a factor of two improvement in CTI.

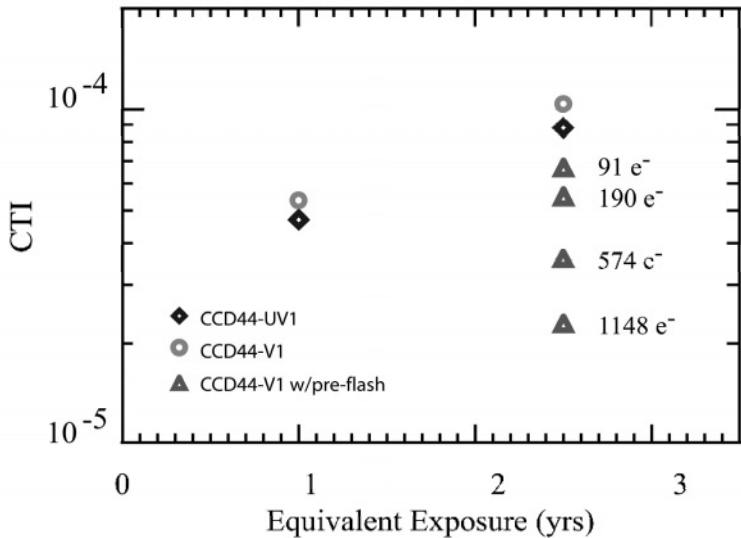


Figure 2. An optical bias level of ~200 e⁻ on a device with the equivalent of 2.5 years on-orbit radiation damage results in CTE performance similar to a device with only 1-year of radiation damage.

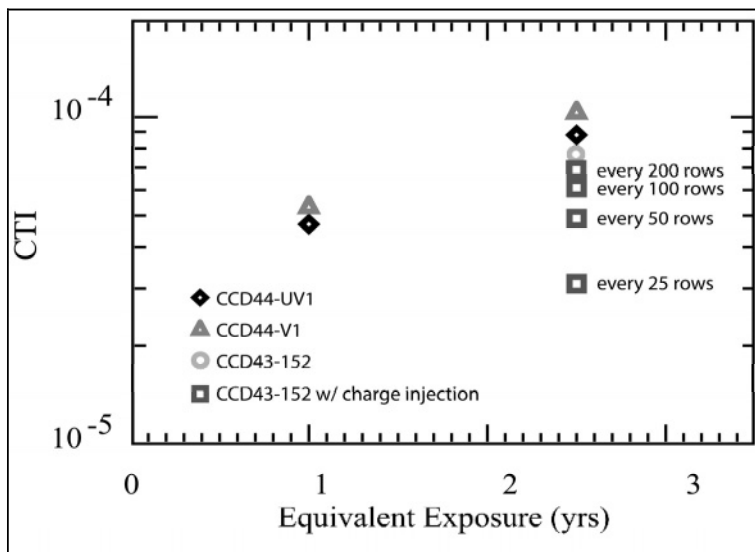


Figure 3. When charge injection is employed, device CTE improves. For example, a device with the equivalent of 2.5 years on-orbit radiation damage shows a CTE similar to a device with only 1-year of radiation damage after charge is injected every 50 rows.

The effect on the scientific capability of the detector is quite different in the presence of charge injection than for an optical bias. In the case of charge injection, the injected rows might not be useful for science. The rows immediately trailing the injected rows will also have an increased signal and hence increased noise. However, most of the non-injected rows will suffer only a slight increase in noise. This technique thus offers the potential of improving the CTE while still being background or read noise limited in the detection of faint sources.

Further work is currently being undertaken to characterize the noise associated with the charge trails from the injected rows. In particular, the amount of noise, along with its repeatability must be determined in order to assess the usefulness of charge injection in mitigating CTE degradation.

This work is being performed at the NASA Goddard Space Flight Center Detector Characterization Laboratory. For general information on the DCL please visit <http://dcl.gsfc.nasa.gov>.

CAMERA AND DETECTOR DEVELOPMENT IN THE SPACE SCIENCE AND TECHNOLOGY DEPARTMENT OF THE RUTHERFORD APPLETON LABORATORY

Guy F.W. Woodhouse, Nicholas R. Waltham, James M. King, Gary R. Burton, Duncan L. Drummond, Andy J. Marshall, John A. Rainnie, Marcus J. French.

Rutherford Appleton Laboratory

Abstract: *This paper reports on detector and camera developments in the Space Science and Technology Department of the Rutherford Appleton Laboratory. In recent years, we have been developing CCD-based cameras for, amongst others, solar physics research, and high resolution Earth observation from space. More recently, we have diversified into the development of both CCD and IR detector systems for ground-based astronomy. This paper summarises our project work and on-going development programmes.*

Key words: *Charge-Coupled Device (CCD), Active Pixel Sensor (APS), Complementary Metal-Oxide Semiconductor (CMOS) Active Pixel Sensor, camera, detector, infrared, focal plane array, astronomy, earth observation.*

1. INTRODUCTION

The development of CCD instrumentation within the Space Science and Technology Department (SSTD) at the Rutherford Appleton Laboratory (RAL) began in earnest in 1990. Our programme has consisted of project work for several space science and Earth observation missions, and a smaller element of underpinning research and development. Recently, we have diversified into the development of CCD and IR systems for ground-based astronomy. This paper provides a brief description of our recent project work and our research interests.

2. SPACE PROGRAMME

The development of CCD instrumentation for the space environment poses a number of challenges due to requirements to minimise size, mass and power, and the susceptibility of CCDs and electronics to radiation damage. Our programme has combined project work with two primary themes of research and development (R&D):

1. The development of radiation-tolerant ASICs for space-borne CCD camera instrumentation [1].
2. The development of science-grade CMOS Active Pixel Sensors (APS) as an alternative image sensor to the CCD [2].

Our CCD camera programme was initiated in 1990. The first cameras to be developed were:

1. Star trackers for the SPECTRUM-RG/JET-X X-ray telescope [3], and the LEGRI gamma-ray telescope on the Spanish Minisat mission [4].
2. Earth Observation cameras for the Pakistan BADR-B and Moroccan MAROC-TUBSAT micro-satellites [5].

Building on these first projects, we have expanded both our project and R&D activities. Our R&D has been strategic in that we have identified key requirements of future missions, and then developed 'enabling' technologies common to as many future mission requirements as possible, thus aiming to maximise the return on the non-recurring R&D investment.

Our current project programme is outlined below.

2.1 SMEI (Solar Mass Ejection Imager)

SMEI [6] is a heliospheric imager designed for the study of coronal mass ejections and 'space weather', comprising three CCD cameras to image transient heliospheric features from Earth orbit over the entire sky every 90 minutes. The project is in collaboration with the University of Birmingham, the US Air Force Research Laboratory (AFRL), and the University of California San Diego. Our role has been to design the CCD camera electronics, the challenging requirements being for low readout noise and wide dynamic range. The CCD used is a Marconi Applied Technologies (formerly EEV, and now E2V) CCD05-30. We use the Inverted-Mode variant for low dark current and enhanced tolerance to ionizing radiation effects. The camera is designed to run at 100 Kpix/sec with 16-bit digitisation.

2.2 DCIXS X-ray spectrometer

DCIXS (Demonstrator Compact Imaging X-ray Spectrometer) [7,8] exploits novel CCD-based technology in an X-ray fluorescent spectrometer to fly on the ESA SMART-1 technology demonstrator mission to the Moon. DCIXS works by the detection and spectral energy resolution of X-ray fluorescence from the lunar surface mineralogy, and is intended to provide the first complete survey and material analysis of the Moon's surface composition in X-rays. The novel aspect of DCIXS is the exploitation of the newly developed Marconi Applied Technologies Swept Charge Device (SCD). The SCD exploits the same basic technology as an imaging CCD, but its high effective frame rate yields X-ray detection and spectroscopic measurement capabilities while running at a significantly higher operating temperature. This enables a compact instrument that avoids the need for a large cooling radiator.

2.3 TOPSAT

A major goal in Earth observation has been to develop more compact and affordable high-resolution camera systems, 1 m/pixel ground-sampling being a primary aspiration of the industry. Traditionally, camera systems of this capability have been large and required substantial spacecraft vehicles; both aspects leading to high unit cost. Our SURCIS (Sub-one-metre Resolution Compact Imaging System) programme [9] aims to develop more compact affordable solutions. We have designed modular and scalable cameras based on the concept of an off-axis 3 mirror telescope with integral 'push-broom' linear CCD detectors. The culmination of this work is the TOPSAT programme [10], which aims to provide 2.5 m/pix panchromatic and 5 m/pix 3 colour ground-sampling from a micro-satellite on a 600 km altitude orbit. RAL are providing the camera within the TOPSAT consortium with QinetiQ, Surrey Satellite Technology Limited (SSTL), and InfoTerra.

2.4 STEREO/SECCHI

We are designing the CCD cameras for the SECCHI (Sun Earth Connection Coronal and Heliospheric Investigation) [11] remote sensing instrumentation of NASA's STEREO (Solar Terrestrial Relations Observatory) mission. SECCHI will observe coronal mass ejections from their birth at the Sun, through the corona to their impact at Earth. There are four instruments: two white light coronagraphs, an extreme ultraviolet imager, and a dual-head heliospheric imager. There are thus five CCDs, all of which are thinned, back-illuminated Marconi Applied Technologies 2K x 2K pixel CCD42-40s. The camera electronics makes extensive use of our ASIC technology [1], aiming for 1 Mpix/sec readout with 14-bit dynamic range.

3. GROUND BASED ASTRONOMY PROJECTS

In the early 1990's a Transputer-based CCD controller [12] was developed for general-purpose laboratory R&D, and which ultimately provided the design of the Earth Observation cameras for the Pakistan BADR-B and Moroccan MAROC-TUBSAT micro-satellites [5]. The Transputer controller was also successfully exploited in a variety of projects at the South African Astronomical Observatory [13].

Three ground based astronomy detector projects are currently in progress, and these are described in the following sub-sections:

3.1 VISTA Infrared Camera

VISTA (Visible and Infrared Telescope for Astronomy) [14] is a 4-m wide-field survey telescope, currently under development, for operation at ESO's Cerro Paranal Observatory. VISTA has been designed to feed either an IR or an optical wide-field camera.

RAL, UKATC and the University of Durham are designing VISTA's IR camera. The focal plane will employ 16 Raytheon 2K×2K VIRGO HgCdTe detectors, controlled by ESO IRACE controllers [15].

3.2 FMOS (Fiber Multi-Object Spectrograph) camera

FMOS [16] is a fiber-fed, OH suppression, near-infrared spectrograph for the SUBARU telescope, which is being developed in conjunction with Oxford University and the University of Durham. RAL is undertaking the optical design of both spectrograph and camera, and the design and construction of the camera. The camera will use a HAWAII-2 infrared array, controlled with an SDSU infrared controller [17].

3.3 SUBARU fast photometer

A frame-transfer CCD camera has been designed as a high-speed alternative to the camera normally used on the SUBARU telescope FOCAS [18] instrument. A Marconi CCD47-20 with integral Peltier cooler is used, with an SDSU-II CCD controller and LINUX PC. The flexibility exists to read out either the full CCD frame (1K×1K pixels) or just small regions of interest (windows) to enable high frame-rate operation.

FOCAS may be used in both imaging and spectrographic modes and the fast camera will enable progress, for example, in the spectroscopic study of short period binaries.

3.4 Summary

We have described the current CCD project activities in the Space Science and Technology Department of the Rutherford Appleton Laboratory.

4. ACKNOWLEDGMENTS

Our work has been funded from various sources including the UK's Particle Physics and Astronomy Research Council, Natural Environment Research Council, the Rutherford Appleton Laboratory of the Central Laboratory of the Research Councils, the British National Space Centre (BNSC), and the European Space Agency (ESA). The University of Birmingham and the USAF have funded SMEI.

5. REFERENCES

- [1] Woodhouse, G.F.W. et al., 2002, *The use of ASIC technology in the development of compact, low power CCD cameras*, these proceedings, pg. 467
- [2] Woodhouse, G.F.W. et al., 2002, *CMOS Active Pixel Sensor developments at the Rutherford Appleton Laboratory*, these proceedings, pg. 183
- [3] Curtis, W.J., Waltham, N.R. and Eyles, C.J., 1993, *JET-X attitude monitor for the Spectrum-RG mission*, Proc. SPIE Vol. **1950**.
- [4] Gimenez, A., 1998, *EUV and hard x-ray instruments on board the Spanish Minisat 01 mission*, Proc. SPIE Vol. **3445**.
- [5] Waltham N.R., Newton, G.M., Lidiard, K.A., Paynter, P. and King, J., 1995, *Development of a compact low-mass wide angle CCD camera for Earth Observation*, Proc. SPIE Vol. **2583**.
- [6] Jackson B.V. et al., 1994, *A spaceborne near-Earth asteroid detection system*, Astronomy Astrophysics Supplement Series 108.
- [7] Dunkin S.K et al., 2001, *The D-CIXS X-ray spectrometer on ESA's SMART-1 mission to the Moon*, Lunar and Planetary Science **XXXII**.
- [8] Grande M., et al., 2001, *The D-CIXS X-ray mapping spectrometer on SMART-1*, Planetary and Space Science, in press.
- [9] Waltham, N.R., Gray P.F., Morris, N., and Holdaway, R., 1999, *A compact, High Resolution, Remote Sensing Camera System*, Proc. IAF, Netherlands.
- [10] Brooks P. et al., 2001, *TOPSAT – A Small Satellite Approach to High Resolution Remote Sensing Missions*, 52nd International Astronautical Congress, Toulouse, France.
- [11] Howard, R.A., Moses, J.D., and Socker, D.G., 2000, *Sun Earth Connection Coronal and Heliospheric Investigation (SECCHI)*, Proc. SPIE Vol. **4139**.
- [12] Waltham, N.R., van Breda, I.G. and Newton, G.M., 1990, *A simple Transputer-based CCD camera controller*, Proc. SPIE Vol. **1235**.
- [13] Glass I.S. et al., 1995, *The Rutherford-SAAO CCD Controllers and their Applications*, IAU Symposium 167, New Developments in Array Technologies and Applications.
- [14] Fisher, M. et al., 2000, *Status of VISTA systems and and engineering design*, Proc SPIE Vol. **4004**.

- [15] Meyer, M. et al., 1998, *ESO infrared detector high-speed array control and processing electronic IRACE*, Proc. SPIE Vol **3354**.
- [16] Maihara, T. et al., 2000, *FMOS Fiber-multi-object spectrograph (FMOS) for Subaru Telescope*, Proc. SPIE Vol. **4008**.
- [17] Leach, R., Beale, F. and Eriksen, J., 1998, *New generation CCD controller requirements and an example: the San Diego State University generation II controller*, Proc. SPIE Vol. **3355**.
- [18] Kashikawa, N., et al., 2000, *FOCAS: Faint Object Camera and Spectrograph for the Subaru Telescope*, Proc. SPIE Vol. **4008**.

COMPACT CCD CAMERA

Zhaowang Zhao and Binxun Ye

Research Labs for Astronomy, National Astronomical Observatory, Chinese Academy of Science

Abstract: *We have produced a compact, high performance CCD camera which utilizes a TH7899 $2K \times 2K$ chip cooled by thermo-modules functioning in both the frame transfer and drift scan (TDI) modes. The maximum readout speed is 4 MHz. The readout noise is $20 e^-$ at a readout rate of 1 MHz. The full well capacity of the CCD in MPP mode is over $260K e^-$. The composition and performance of the camera are discussed in this paper.*

Key words: *Charge-Coupled Device (CCD), camera, Erasable Programmable Logic Device (EPLD), signal processor, readout*

1. INTRODUCTION

The CCD camera discussed (see Fig. 1) was purposely built for astronomical observations at Beijing Observatory. High-speed readout and compactness are the desired characteristics for our new camera. These will increase efficiency and make new applications available. The compact controller we designed and built is an attempt to synthesize the key components into one design. A high level of integration was achieved by a programmable logic device (EPLD) for generating CCD clocks and a CCD Signal Processor for readout.

2. EPLD CLOCK GENERATION

The versatility of the compact controller stems from the use of an Altera's EPLD, EPM7256AETC100-7, without any other counters, memories, latches etc. The EPLD is a high performance, EEPROM-based programmable logic device and has 68 user I/O pins with 2500 gates. The in-system programmability via standard JTAG interface allows unlimited design

modifications. The maximum speed is 150 MHz. The EPLD generates the sequences to drive the charge transfer on the serial and parallel CCD directly. We selected the most efficient tool, VHDL, to design all of the logic circuit. A programmable logic device-based controller delivers the flexibility to upgrade with no limit and the easiness to add new special functions.

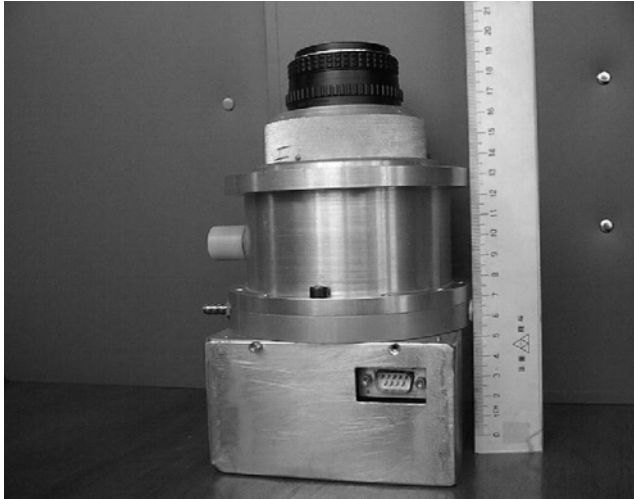


Figure 1. Camera outline with its small dewar and circuit box. The size of the camera is about 100mm×58mm; its weight is about 1.5 kg.

3. CCD SIGNAL PROCESSOR

The analog circuit in most CCD controllers uses a separate amplifier, dual slope integrator and AD converter. Thus the circuit size and power consumption is obviously larger. We employed the CCD signal processor, AD9826, to reduce space and power consumption. The single device contains a programmable gain amplifier, offset DAC, double correlated sampling circuit and 16 bit AD converter. The operation speed is >15 MHz. The AD9826 features a 3-channel architecture designed for the color CCD camera. The internal registers are programmable through a 3-wire serial interface. The power supply is a single 5 V, 3 V/5 V digital I/O compatible, which is packaged in a 28-lead SSOP. The size of the AD9826 is about 10 mm×5 mm. The power consumption of the AD9826 is less than 100 mW at the clock rate of 4 MHz in our camera. We suffered from external noise and possible cross talk at a vacuum connector when we initially placed the ADC outside the CCD dewar. After installing all the analog amplifier chains and the AD9826 in the dewar, we successfully eliminated the noise. As a bonus, we reduced the space too.

After testing, the CCD signal processor shows excellent performance. Although the read-out noise does not satisfy our final requirement, the signal processor is still, potentially, a competitive device in scientific applications.

4. SYSTEM PERFORMANCE

Thomson's MPP mode CCD, TH7899 2K×2K, 14 μm pixel size, is employed in our system. The CCD is thermoelectrically cooled within a small dewar. Our camera offers 3 modes of CCD operation: full frame, drift scan and frame transfer. Computer software also captures images in 3 modes: single frame, continuously scan and selected frames. A MicroConverter MCU-AduC812 selects the operations. It is controlled by a host computer via RS-232.

5. TEST RESULTS

The camera's electronics require +18V, +8V and -15V of power. The total power consumption is about 5 W. The frame rate is 2 frames/sec when operated in 2K×1K frame transfer mode. The readout noise is 5 ADU and the gain is about 4.0 e^-/ADU when operating at a 1 MHz pixel rate (see Fig. 2). The read out pixel rate can be up to 4 MHz. The full well is more than 260K e^- , in spite of the MPP mode CCD. The charge transfer efficiency (see Fig. 3) was derived using the residual signal in the overscan area on variety. The best result was obtained at a high light level, *i.e.* CTE >0.99999, along the horizontal direction. The linearity is better than 0.99997 (see Fig. 4). The dark current was 0.4 $\text{e}^-/\text{sec}/\text{pixel}$ at -20 $^{\circ}\text{C}$.

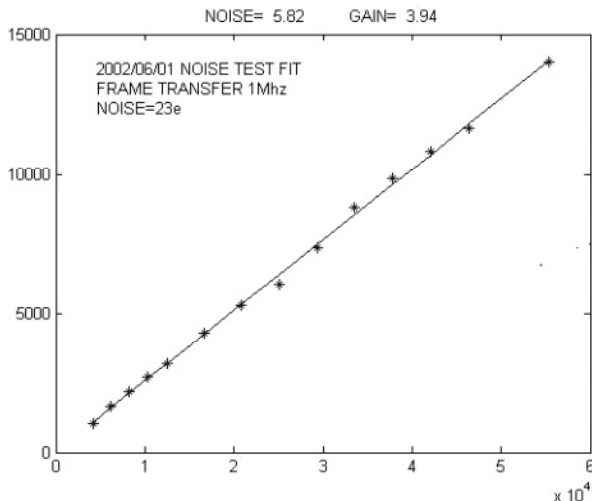


Figure 2. Photon transfer curve. The X-axis is the CCD output (ADU) and the Y-axis is the noise squared. The gain is 4 e^-/ADU , and the read out noise is about 20 e^- operating at a 1 MHz pixel rate.

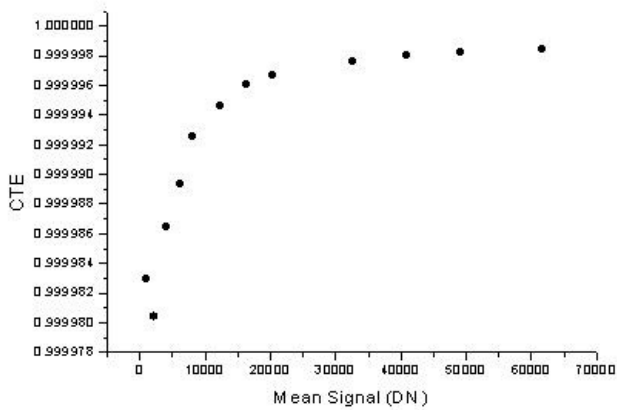


Figure 3. Charge Transfer Efficiency (CTE) characteristics. The X-axis is the CCD output (ADU) and the Y-axis is the charge transfer efficiency. At the lowest level of the CCD output the CTE is about 0.999978. When the CCD output is more than 30000 ADU the CTE reaches 0.999998.

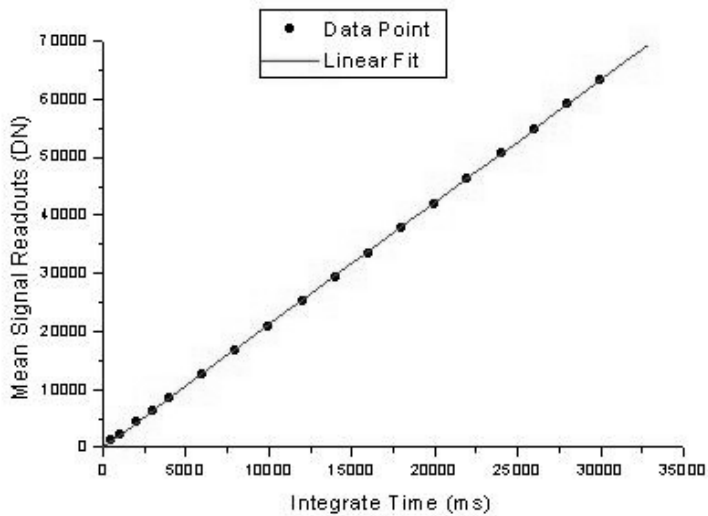


Figure 4. Linearity Characteristics. The X-axis is the integration time (ms) and the Y-axis is the CCD output (ADU). The linearity is better than 0.99997. The CCD output at 65000 ADU shows good linearity and gives the full well more than 260 K e⁻ when the read out speed is 1 Mhz pixel rate.

SECTION IV:

ELECTRONICS

THE DESIGN AND TESTING OF A CRYOGENIC PRE-AMPLIFIER FOR THE ROCKWELL HAWAII AND HAWAII-II DETECTOR ARRAYS

Paul D. Berry, Rene Doyon, Philippe Vallée, Daniel Nadeau
Laboratoire d'Astrophysique Expérimentale, Université de Montréal

Abstract: *In order to reduce electronic noise to a minimum, it is desirable to include gain early in the electronic chain. A cryogenic pre-amplification stage situated on the fanout board provides this as well as reducing external electronic complexity. This paper presents the results of cryogenic tests on pre-amplifier components to be used on HAWAII and HAWAII-II fanout boards. The OPA×I34 and AD851× are both good candidates for low noise, high speed (1 μ s/pixel) applications.*

Key words: detector, readout electronics, HAWAII, HAWAII-II, pre-amplifier

1. INTRODUCTION

In order to produce an astronomical instrument with limited detector noise, it is necessary to keep electronic noise to a minimum. A cryogenic pre-amplification stage offers significant performance advantages due to the reduced effect of noise pick-up on the sensitive output connections. It also allows the simplification of the electronics outside the cryostat, which is becoming more relevant with the ever increasing size of detectors and mosaics.

At the Laboratoire d'Astrophysique Expérimentale, two separate cryogenic fanout boards are under design for two infrared instruments; one for TRIDENT (TRIPLE Imager for Detecting Earth Near T-dwarfs), a high-speed camera capable of near-simultaneous readout in three wavelength bands; and one for CPAPIR (Camera PANoramic Proche Infra-Rouge), a

panoramic camera to be used to search for brown dwarfs. TRIDENT currently uses a HAWAII detector array with a warm pre-amplification stage. CPAPIR is under construction and will use the HAWAII-II detector in the eight outputs per quadrant mode.

2. READOUT ELECTRONICS

The readout circuit and connections for CPAPIR are shown in Fig. 1.

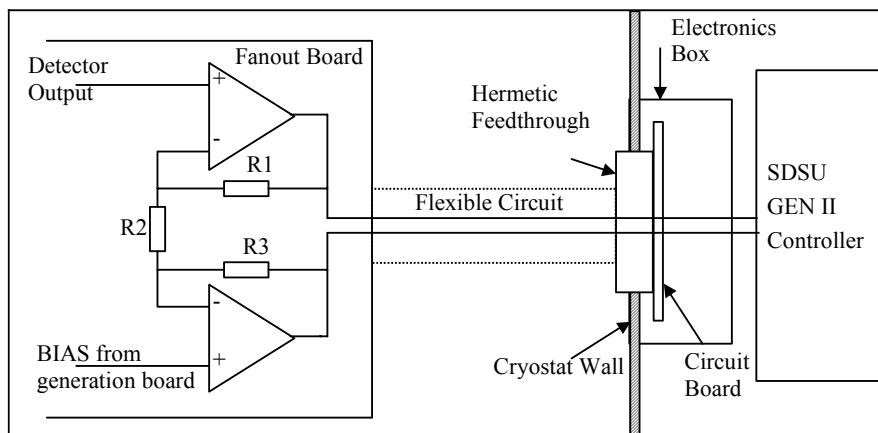


Figure 1. Readout electronics for CPAPIR.

Each of the 32 HAWAII-II outputs together with a user-generated BIAS signal are the inputs to two operational amplifiers that are configured as the front end of an instrumentation amplifier. The difference between these signals is amplified by a gain determined by the ratio of the resistors shown on the fanout board.

Two flexible circuit boards, one for analogue and one for digital signals, connect between Micro-D connectors on the fanout board and D-type hermetic feedthroughs in the cryostat wall. This modular approach reduces the complexity of the individual components inside the cryostat allowing easier handling, insertion and removal of the connections during any work required inside the cryostat.

Attached to the outside of the cryostat and to the feedthrough connectors, circuit boards generate the bias signals required inside the cryostat. Boxes are used to shield the boards, which are connected to an SDSU Gen II controller.

The electronics differ slightly in TRIDENT, as the use of a cryogenic preamplifier was not originally included in the design. This has resulted in only analogue +5 V and ground power supplies being available on the fanout

board. This imposes an additional constraint on the component selection for the differential amplifier as it must be capable of operating with low voltage single supplies.

3. OPERATIONAL AMPLIFIER SELECTION

The op-amps required for a cryogenic pre-amplifier must have several characteristics: ability to operate at cryogenic temperatures, a high slew rate, low settling time and low noise. It was already known that the TLC2272 from Texas Instruments is suitable due to their use by ESO in ISAAC. TRIDENT can operate with readout speeds of up to $1 \mu\text{s}/\text{pix}$ but the TLC2272's small bandwidth and slew rate suggested it might not be able to meet this specification. A list of the alternatives found is shown in table 1.

Table 1. Selected characteristics of op-amps under test.

Name	BW (MHz)	Noise Density at 1kHz (nV/ $\sqrt{\text{Hz}}$)	Slew Rate (V/ μs)	Settling Time to 0.1% (ns)	Power Supply
TLC2272	1	9	3.6	2600	Both
AD8512	7.5	8	20	1000	Dual
OPA2134	8	8	20	700	Dual
OPA2228	8	3	2.3	5000	Dual
AD8062	300	11	800	35	Single
OPA2353	44	10	22	220	Single

The amplifiers were first placed on small circuit boards to see if they could still perform as specified at 77 K as well as withstand repeated thermal cycles. If the results were satisfactory they were to be tested on a TRIDENT fanout board to allow an accurate comparison of the system gain and the noise of each op-amp. The amplifier showing the best results would then be used in CPAPIR.

All the amplifiers have been tested at 77 K and showed no adverse affect due to the low temperatures. The results obtained suggested that all the alternatives found offered better performance than the TLC2272, with the AD8512 showing the fastest response. It was also confirmed to us that the response of the TLC2272 at high frequencies was too slow, and thus, it is of little use at the speeds required by TRIDENT.

TRIDENT was tested using the TLC2272 on the fanout board and an engineering-grade HAWAII detector was read at a speed of $10 \mu\text{s}/\text{pix}$. The results showed very low noise of less than $10 e^-$ and demonstrated that the system had limited detector noise.

4. CONCLUSION

The inclusion of the pre-amplifier in TRIDENT has greatly reduced system noise to less than 10 e^- . The component testing is currently ongoing, but has shown a need to replace the TLC2272 due to its poor high frequency performance. The AD8512 has provided the best initial results, but remains to be tested in a complete system.



Crouching nerd hidden crowd.

Jenda Johnson, the geologist who accompanied us to visit the Volcanoes National Park, is talking to a hidden crowd (left out in this photo). She is unaware of the dangerous crouching nerd behind her. Fernando Pedichini (left) urges Jim Beletic to jump.

THE NEW GENERATION CCD CONTROLLER: FIRST RESULTS

Giovanni Bonanno¹, Rosario Cosentino^{1,2}, Massimiliano Belluso¹, Pietro Bruno¹, Fabio Bortoletto³, Maurizio D'Alessandro³, Daniela Fantinel³, Enrico Giro³, Leonardo Corcione⁴, Alessandro Carbone⁵, Gioacchino Evola⁵

¹Osservatorio Astrofisico di Catania, ²Telescopio Nazionale Galileo (TNG),

³Osservatorio Astronomico di Padova, ⁴Osservatorio Astronomico di Torino,

⁵Elettromare La Spezia

Abstract: *The new generation CCD controller, developed by the Italian Detector Working Group (DWG), is an improvement on the CCD controller in use at TNG. A new interface with the host computer, based on a high-speed link and PCI board, able to sustain high data transfer rate has been designed and built. The sequencer has been modified in order to improve high-speed clocks and different reading modes. A new analogue board based on a fast ADC's and new signal processing has been designed. The board is able to process four channels simultaneously allowing high acquisition rates. Preliminary tests demonstrating the improved performances of the controller are shown.*

Key words: *Charge-Coupled Device (CCD), CCD controller*

1. CCD CONTROLLER IMPROVEMENTS

The new generation CCD controller is an improvement on the controller in use at TNG and at local Italian telescopes. The same philosophy in conjunction with technological improvements guarantees an increase in performance and a full compatibility with the previous version. Changes involved the host interface, the communication link,

the sequencer, the bias generator, the clock generator, the preamplifier and the signal processing. In Table 1 the main differences between the two controllers are listed.

The main differences consist of changes in the architecture of the system. Basically the system can be divided in two parts: close to the control computer (local), and close to the detector (remote). In the new CCD controller the preamplifier is integrated into the analogue board mounted close to the detector, and the sequence generation is located in the host computer, far from the detector. This is possible due to the capability of the high speed links to serialize and de-serialize the sequence with a resolution of 50 ns.

Table 1. Main differences between the two controllers

CCDC MODEL	TNG CCDC-I 1994	TNG CCDC-II 2000
SEQUENCER	DSP 56001 RESOL.: 100 ns	DSP 56301 RESOL.: 50 ns
DATA LINK	FIBER TRANSPUTER LINK 20 MBaud	FIBER GIGALINK 1.2 GBaud
CLOCK	LOCAL	HOST
DATA HANDLING	TRANSPUTER	HOST PROCESSOR
CHANNELS (16 bit ADC)	4x2 boards	4x8 boards
ADC speed	10 μ s	2 μ s
PIXEL PROCESSING	CORRELATED DUAL SLOPE	CORRELATED DUAL SAMPLING SINGLE SAMPLING
PROGRAMMABLE BIASES	8(14 bit DAC)x2 boards	16(14 bit DAC)x8 boards
PROGRAMMABLE CLOCKS	8(8 bit DAC)x2 boards	8+8+8 (10 bit DAC)
ADJ. OFF-SET	ONLY OUT-OFF/SET	IN and OUT OFF/SET
PROGRAMABLE GAIN	NO	15, 75, 150
PROGRAMABLE FILTER	NO	NONE, 234 KHz, 3.4 MHz
AMPLIFIER NOISE	4.5 μ V (OPA627 @ 1MHz)	1+2 μ V (THS4061 @ 1MHz)
READOUT TIME	17 μ s/pix	2.7 μ s/pix

1.1 Host interface and communication link

The new host interface is a PCI based board, equipped with a full-duplex optical link, operating at 1.2 GBauds. It allows data and telemetry communication (remote to local), and commands and clocks sending (local to remote). Communication with high-level languages is guaranteed by low level drivers (Windows NT, 2000 and XP) and a DLL.

The architecture evolution of the new CCD controller with respect to the old version is shown in Fig. 1. Thanks to the high-speed link the phases are generated in the host computer and are rebuilt by the sequencer. All the TTL control signals are generated on the PCI board (far from the CCD head), while the analogue circuits are next to the CCD head. This guarantees a high performance in terms of noise immunity.

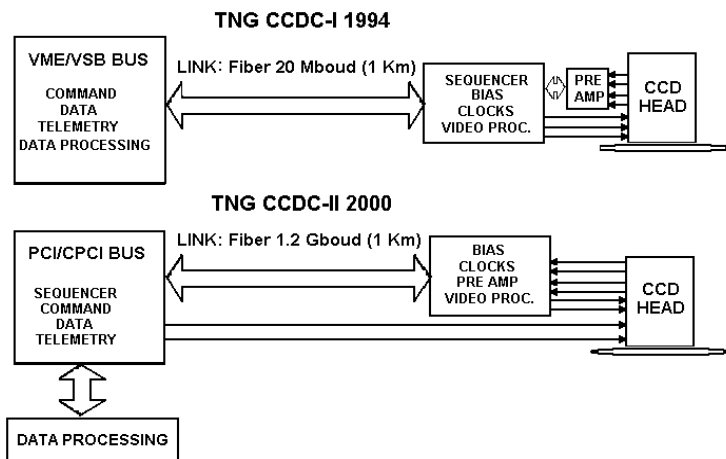


Figure 1. Block diagram of the two CCD controller.

1.2 Sequencer

The sequencer board mounts a MOTOROLA DSP 56301 and allows a minimum tick of 50 ns (in the previous controller it was 100 ns). This solution guarantees a full compatibility with already developed software for sequence generation (Waveform Editor). Moreover, the clock levels are generated in this board (in the previous version they were generated in the analogue board). This minimizes a possible cause of cross talk.

1.3 Analogue board

The analogue board consists of three main parts: the preamplifier, the correlated dual sampler and the bias generator. The preamplifier (see Fig. 2) is based on the low noise operational Amplifier THS4061. This configuration allows 4 gain selections (G-SEL), band pass filter selection (B-SEL) and input offset programmability. The Signal Processing (see Fig. 3) is carried out by using the Correlated Double Sampling (CDS) technique (single sampling is also allowed). The output offset can be adjusted through the 14-bit D/A Converter (AD7834) and the A/D Converter is the LTC1608 that has 16 bits of resolution and a conversion time of 2 μ s.

In summary, the analogue board allows: four selectable input gains and four selectable bandwidths to work at different readout speeds, and the possibility to program the offsets before and after the CDS stage, to adapt the signal to the A/D converter and the choice of different references for the dummy input. The bias generator allows 16 programmable bias voltages with different ranges, which are divided in four groups. The voltage ranges are: from 15 to 30 V, from 5 to 15 V, from -5 to 5 V, and from -10 to 10 V.

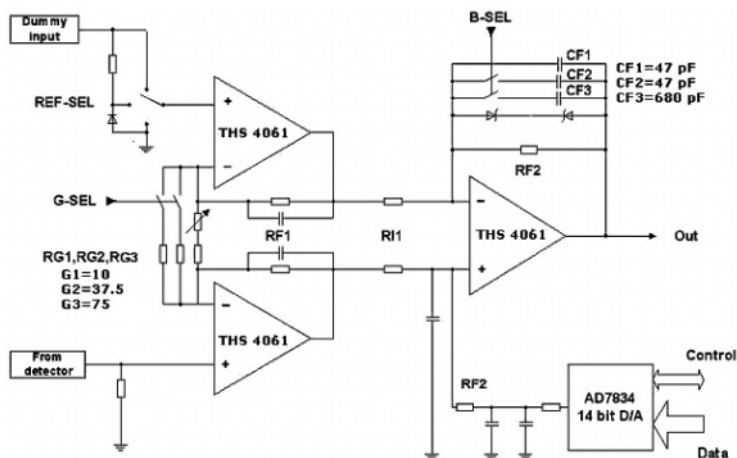


Figure 2. Preamplifier (one channel).

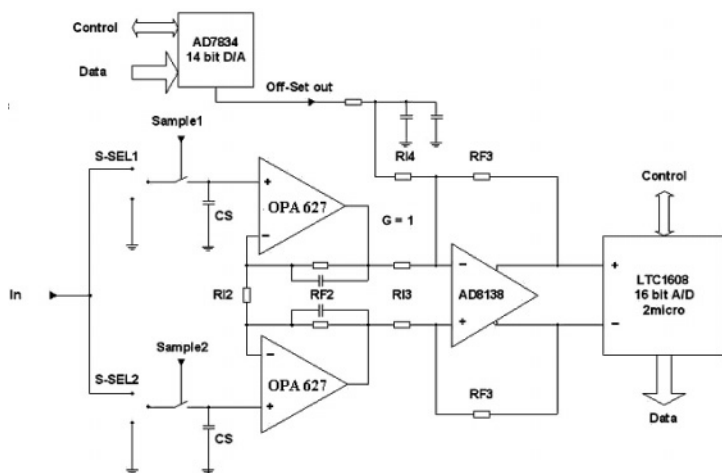


Figure 3. Signal Processing (one channel).

2. RESULTS

The new generation CCD controller lives up to expectations. The data acquisition rate is increased, the reliability is high and the readout noise is acceptable. The typical readout noise at different gain is showed in Table 2.

Table 2. Readout noise at different gains.

GAIN	NOISE (DN)	NOISE (e-) for sens. $3\mu\text{V}/e^-$
20	3	4.45 e ⁻ rms
75	4	1.36 e ⁻ rms
150	4.5	0.76 e ⁻ rms

ISPI SOFTWARE

An Infrared Application of the ArcVIEW System

Marco Bonati¹ and Michael Ashe²

¹Caltech-CTIO, ²SOAR-Imaginatics

Abstract: *The Infrared SidePort Imager (ISPI) being used on Cerro Tololo's 4-m telescope, uses Labview-based software, known as ArcView, to control the detector, acquire images, and interface to the Telescope Control System and instrument. The software architecture described is also being applied to Cornell's Widefield InfraRed Camera (WIRC) on the Hale 200" on Palomar Mountain, and optical imager on the SOAR telescope (Cerro Pachon). In order to achieve maximum flexibility and functionality, we decided to implement the software as a collection of independent modules. These modules can be classified as: modules for specific hardware (or transmission media), modules specific to a logic process, and completely generic modules. As we have the ability to load and unload any of these modules dynamically from memory, we have great flexibility, with the advantage that controlling new hardware, or adding new preprocessing methods does not imply increasing the complexity of the system, or even recompiling it. Instead, one just builds a new module with very specific and well-determined functionality. The generic modules serve any type of detector system; current examples are ISPI and the SOAR Optical Imager (a CCD mosaic).*

Key words: infrared imaging, instrument software, detector software, ArcVIEW

1. ABOUT ARCVIEW

ArcVIEW is a Labview-based control system designed for use as a general-purpose controller software. It consists of a Server which receives commands through the network, and external clients which connect to it, requesting tasks/actions to be performed (see Fig. 1).

The mechanism for performing the required actions is based on the "modularity" concept; the Server calls (loads dynamically) a specific module for performing some specific type of actions, passing the command received

to it. This module is a "standalone" piece of software which knows what to do with the received command; it will perform what is requested and will return a response through the Server.

The scope of the commands depends completely on the client which connects and the module which perform the action; this means that ArcVIEW can be used in a wide range of areas (detector data and command handling, mechanisms, TCS communications, etc.), depending on the type of modules which are available to the Server.

The modular architecture allows a very "easy growing" of the capabilities without increasing the complexity of the system; new features will imply only to write well-defined and specific modules for adding such capabilities, without affecting the rest of the system.

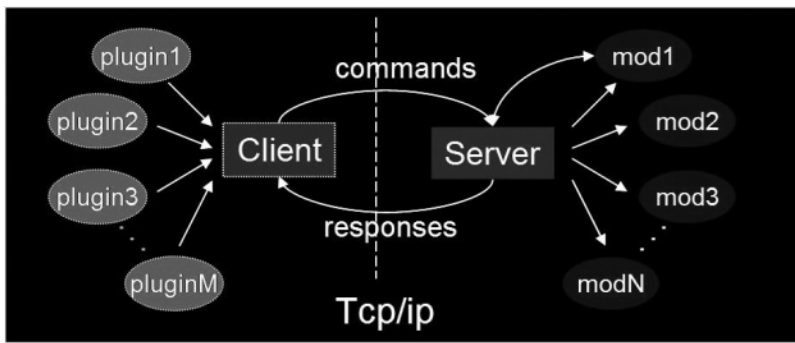


Figure 1: ArcVIEW Architecture.

2. SPECIFIC ISPI SOFTWARE ARCHITECTURE

Goals: Detector controlling (data and commands), TCS and Filter wheel control, scripting capabilities.

Since this is an application of ArcVIEW, it's an intrinsically modular system. We created a series of specific modules in order to perform the required goals, separating these modules into three basic types:

- **Hardware-dependent:** Correspond to those modules which depend exclusively on the hardware being controlled. These are similar to a modular driver on a UNIX system (driver for a specific card). Included in these categories are: SDSU-II (performs all the actions related to the actual detector controller), TCSBLANCO (communication with the Telescope Control System in the 4-m Blanco telescope), FILTERISPI (controls the ISPI Filter wheel, consistent with two serial line motors).

- **General-purpose (independent):** The modules which perform generic functions that will be always done in the same way, independently of the rest of the system. We identified and isolated such functions (that may be performed in any acquisition system): FITS (write images to disk and/or memory from a memory buffer), UNSCRAMBLE (takes an image from a buffer and, according to some directives, unscrambles it and writes it to another buffer), BUFFERMGR (acquiring buffers), RTD (Real Time Display: takes data from a memory buffer and displays it on some image displayer such as Ximtool, DS9 or SAO image).
- **Process-dependent:** Correspond to those modules that depend exclusively on the logic of the process to be performed. These modules are the ones which handle the flow of the information for a determined process; they are the "brain of the process." For example, a Correlated Double Sampling (CDS) module may ask the controller module to take two frames, then subtract those frames in memory, send the result to the Unscrambler, and then finally ask the FITS Writer module to format the resultant image. Depending on the complexity of the process, these modules can be quite simple or fairly complex, but they should be always limited to some very specific and well-delimited process. Modules done on this category: CDS (performs a Double Correlated Sample), FOWLER (coadds N-images that were K-times Fowler sampled).

Note that the above classification is **completely generic**, and it is useful for any type of process (including optical and IR processing). Figure 2 shows the ISPI architecture.

About the scripting, we are able to accept commands generated by any external client. This implies that any scripting/language that is able to open a socket or write to a file can handle the complete system (CL, Csh, TCL, Python, etc.). Currently there are in use many scripts for communicating with the filter wheels or TCS, for taking images, etc. Most of these scripts are written using CL (Iraf) or Csh.

3. OTHER APPLICATIONS

All the software described above is being or will be used at least in another two applications:

SOAR imager (Cerro Pachon): This is an optical application. The system is exactly the same, however, different modules are involved (TCS, filter wheel). The process-dependent module here is specific for an optical application. It also uses an SDSU-II controller.

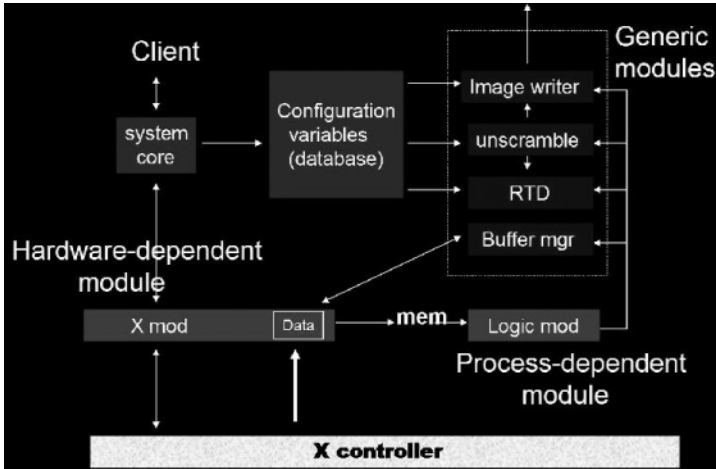


Figure 2: ISPI architecture.

- **Wide Field Infrared Camera -WIRC- (Palomar Mountain):**
This is an infrared application, too. Almost all the modules are the same, except the hardware-dependent one for the TCS and filter wheel. It also uses an SDSU-II controller.

4. ACKNOWLEDGEMENTS

Manuel Martinez (CTIO) contributed with all the drivers for the ISPI filter wheels as well as part of the drivers for the WIRC filter wheels. Rolando Cantarutti (CTIO) helped us in developing the Labview-MPG router interface needed for implementing the interface to the Blanco telescope. Michael Warner and Ricardo Schmidt (CTIO) helped us with testing and giving feedback and thoughts about the behavior of the system. Dani Guzman (Caltech) helped with the WIRC filter wheels drivers and hardware.

5. REFERENCES

- [1] http://www.ctio.noao.edu/instruments/ir_instruments/ispi/
- [2] <http://www.soartelescope.org/sac/OpticalImagerDesignReview/OpticalImager.html>
- [3] <http://www.imaginatrics.net/sys-tmpl/door/>

COMPACT CCD GUIDER CAMERA FOR MAGELLAN

Greg Burley, Ian Thompson and Charlie Hull

Observatories of the Carnegie Institution of Washington (OCIW)

Abstract: *The Magellan guider camera uses a low-noise frame transfer CCD with a digital signal processor based controller. The electronics feature a compact, simple design, optimized for fast settling times and rapid readout rate. The camera operates (nominally) at -20°C with thermoelectric cooling. Multiple operating modes are supported, with software selectable binning, exposure times, and subrastering.*

Key words: *guider camera*

1. INTRODUCTION

The design objective for the Magellan guider camera was to build simple, low-power hardware with enough flexibility to operate in full-frame imaging mode, subrastered guiding mode, and Shack-Hartmann wavefront sensing mode.

2. THE CCD

The guider camera uses a Marconi CCD47-20 $1\text{K}\times 1\text{K}\times 13\text{ }\mu\text{m}$ pixel, low-noise, back-illuminated, frame transfer CCD with a Digital Signal Processor (DSP) based CCD controller. For reduced complexity, most of the digital logic functions are concentrated in the DSP and its internal peripherals, and a programmable logic chip (EPLD). A block diagram of the CCD camera is shown in Fig. 1. Table 1 shows the detector and readout specifications.

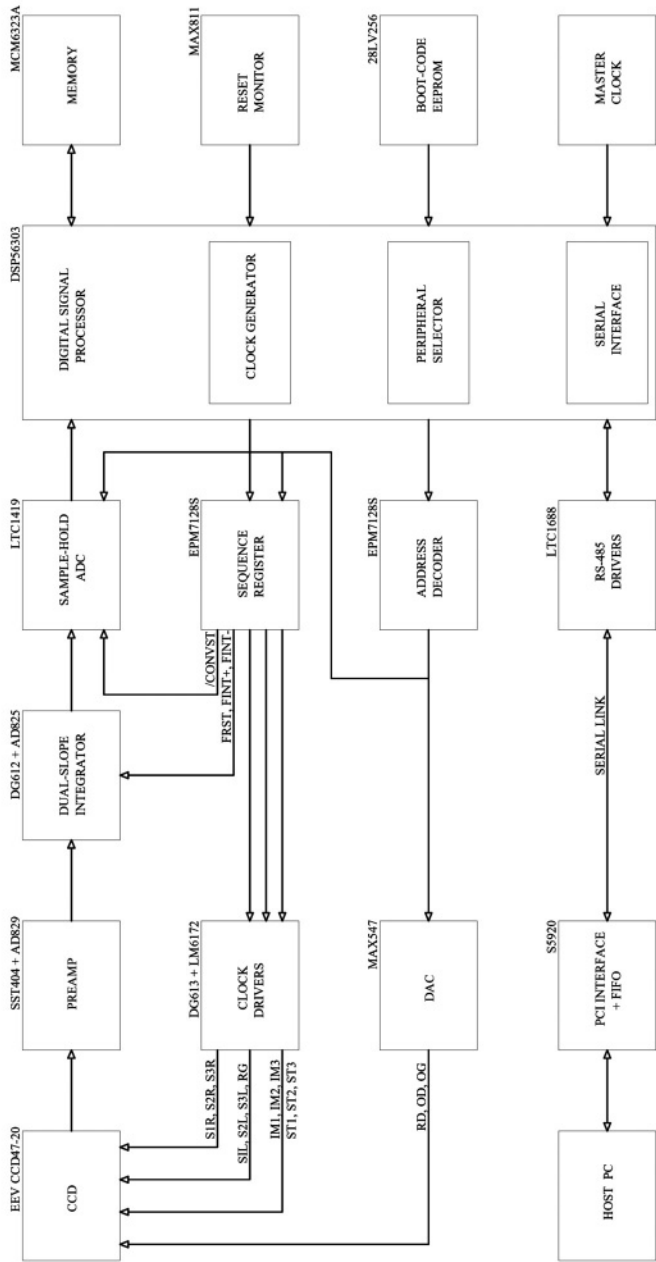


Figure 1. Magellan guider camera block diagram.

Table 1. Detector and readout specifications.

Property	Value	Units
Image size	1024×1024	Pixels
Pixel size	13	μm
Read noise	5	e ⁻ (slow scan)
Readout rate (slow)	5.0	μs/pix
Readout rate (fast)	2.5	μs/pix
Dark current (-20 °C)	2	e ⁻ /pix/sec
Frame rate (binned 4×4)	4	fps
Subraster rate (32×32 pixels)	40	fps

3. THE CONTROLLER

The CCD controller for the guider camera has a number of interesting properties. It features a programmable DSP56303 digital signal processor, which allows for software control of image size, subraster, binning, clock voltages, dual-slope signal processing, and exposure times. The circuit designs use simple op-amps and analog switch components for the clock driver and signal processing circuits [1]. The preamplifier [2] and signal processing circuits are optimized for fast settling times (less than 100 ns) to maximize the pixel readout rate. The design has dual signal processing channels with 14 bit, 1.2 μs conversion time analog-to-digital converters. Clock and bias voltages are set by Digital-to-Analog Converters (DAC). The controller features temperature monitoring of the CCD, and digital control of Thermo-Electric (TE) cooler current. The on-board DC-DC converters (with heavily filtered outputs) generate +3.3 V, ±5 V, ±12 V and +28 V from the 48 V DC input. Table 2 shows the estimated power of the system.

Table 2. Power estimate.

Circuit block	Value [W]
Digital electronics	1.05
Clock drivers	1.60
Signal processing	2.50
Preamplifiers	0.35
TE cooler	6.50
TOTAL	12.0

In operation, the CCD system is controlled by commands and program code sent over the data link. The DSP is fast enough to directly generate the sequences used for the CCD parallel and serial transfers from on-chip memory [3], and write them to the sequence register. Each bit controls one of the CCD clock lines, with a clock driver that translates to CCD-level voltages. The DSP controls the dual-slope integrators and Analog-to-Digital Conversion (ADC), extracts the signal pixel-by-pixel and multiplexes the digitized data onto an RS-485 serial link at 20 Mbps for up to 100 m. Each

of the ADCs, DACs, sequence register, and data link peripherals are memory mapped in the DSP to simplify the software design.

The basic sequence patterns programmed into the DSP memory (serial shift, parallel shift, read pixel, flush pixel) are combined to read out the array. With the appropriate sequences the CCD can be read out through one or both output amplifiers.

Physically, the guider camera consists of six circuit boards (DSP timing generator, signal processing, clock driver, power supply, backplane, and CCD header boards), and occupies a volume of less than $3.75 \times 3.5 \times 6.0$ in. An additional PCI interface board is used in the host computer.

The CCD is enclosed in a sealed, dry gas filled housing with an off-the-shelf two-stage Thermo-Electric (TE) cooler. The CCD temperature is monitored with an off-chip sensor (AD590) mounted inside the housing. An adjustable current source provides up to 3 A to the TE cooler, which is rated for $\Delta T = 83^\circ\text{C}$ under ideal no-load conditions. In practice, a $\Delta T \approx 40^\circ\text{C}$ is achievable with a TE current of about 2 A.

A liquid-cooled heat sink removed heat from the TE cooler hot side. Even at low flow rates (a few lt/min), the entire CCD housing can be rapidly chilled to the fluid temperature (nominally 10°C at the telescope). The TE drive transistor is mounted on the heatsink as well, to prevent it overheating.

4. CONCLUSION

OCIW has open-sourced the design information for the guider camera, which is available at www.ociw.edu/~burley/ccd/guider.html. The on-line information contains a complete design description, including all schematics, pcb layouts, EPLD code, dsp source code, C subroutine library, and test results.

The guider cameras are in regular use on the two Magellan 6.5-m telescopes at Las Campanas Observatory.

5. REFERENCES

- [1] Gunn, J.E., Emory, E.B., Harris, F.H., Oke, J.B., 1987, *Palomar Observatoy CCD camera*, PASP **99**, p. 518.
- [2] Geary, J. and Amato, S., 1998, *Camera electronics for the SAO Megacam*, SPIE **3355**, Optical Astronomical Instrumentation.
- [3] Burley, G.S., Walker, G.A.H., Johnson, R., 1998, *A versatile CCD wavefront curvature sensor*, PASP **110**, p. 330.

READOUT TECHNIQUES FOR DRIFT AND LOW FREQUENCY NOISE REJECTION IN INFRARED ARRAYS

Gert Finger¹, Reinhold J. Dorn¹, Alan W. Hoffman², Hamid Mehrgan¹, Manfred Meyer¹, Alan F.M. Moorwood¹ and Joerg Stegmeier¹

¹European Southern Observatory, ²Raytheon Infrared Operations

Abstract: *Three different methods are presented to subtract thermal drifts and low-frequency noise from the signal of infrared array. The first is dead pixels with open Indium bumps, the second is reference output as implemented on the Hawaii2 multiplexer, and the third is dark pixels to emulate reference cells having a capacity connected to the gate of the unit cell field-effect transistor (FET). The third method is the most effective and yields a reduction in readout noise from 15.4-9.4 erms. A novel method will be described to extend this readout technique to the Aladdin 1K×1K InSb array.*

Key words: *infrared detector, readout techniques, HgCdTe, InSb, reference cell, noise*

1. INTRODUCTION

Contrary to CCDs, the video output of infrared arrays is DC coupled. The time interval between the two samples of a double correlated clamp may be several thousand seconds instead of microseconds typical for CCDs. Due to these long exposures, IR arrays are extremely susceptible to drifts and low-frequency noise pickup down to the MHz regime.

In an ongoing effort to reduce noise pickup and thermal drifts of the video signal of IR arrays we have tried different readout schemes. The best configuration tested thus far is a symmetrical amplifier located as close as possible to the detector as shown in Fig. 1. It consists of two linear CMOS operational amplifiers and is cooled to cryogenic temperatures as it is placed on the detector board next to the detector [1]. It constitutes the front part of a differential signal chain. The amplifier requires two input signals and

generates two antisymmetric output signals: Signalout+ and Signalout- for the differential input of the ADC located at a distance of a few meters outside the instrument. One input is reserved for the video signal and the second input is a reference which has two functions. First, it is used to shift the DC offset of the outputs. Second, the reference helps to cancel thermal drifts and low-frequency noise pickup, since only the difference between reference and video input contributes to a signal change. The topic of this paper is the discussion of different options for the reference input to achieve this goal in an optimum way.

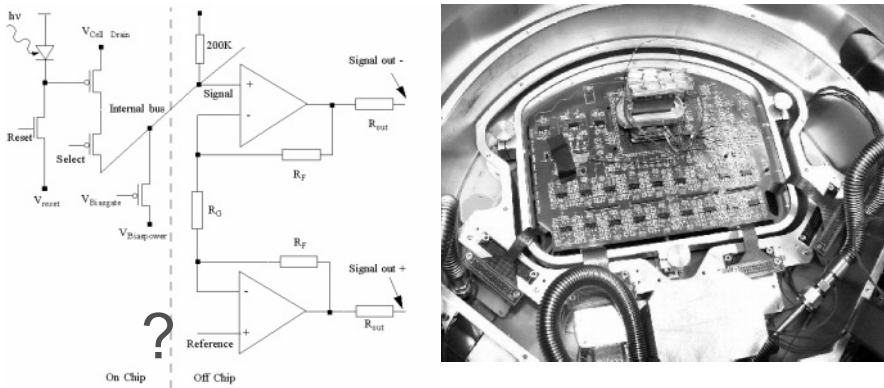


Figure 1. Cryogenic preamplifiers. (left) Schematics of symmetric amplifier with video and reference input. (right) Backside of detector board for Rockwell Hawaii2 2Kx2K HgCdTe array with 36 preamplifiers, 32 for video outputs and 4 for reference outputs. The cold finger is above the amplifiers and cools the detector via the central pins of the PGA package.

2. DEAD PIXELS AS REFERENCE

A standard technique to reduce the readout noise of deep exposures with long integration times is to apply multiple nondestructive readouts. This technique is affected by the thermal drifts of the detector, as can be seen in the plot of Fig. 2. This shows the nondestructive readouts of the integration ramp of a dark exposure taken with an engineering grade Aladdin 1Kx1K InSb array. The raw signal is represented by triangles and exhibits an irregular time evolution reflecting thermal drifts. The cosmetics of the engineering grade array, shown by the flat field on the right side of Fig. 2, is degraded and has cracks and dead pixels in the upper right corner. These are unit cells containing open Indium bumps. The gate of the unit cell source follower is not connected to the infrared diode, but is floating. However, it can be used as a reference to monitor the thermal drifts. The signal of dead pixels is represented by diamonds in Fig. 2, and closely follows the irregular

pattern of the video signal. For the Aladdin array, the temperature drift of the DC level of the video signal was measured at $1700 \text{ e}^-/\text{K}$ at a temperature of 27 K. Subtracting the dead pixel signal from the video signal results in a compensated video signal, which is represented by squares. For demonstrative purposes, the measurement in Fig. 2 has been carried out without active temperature stabilization. It yields a dark current of $2.7 \cdot 10^{-2} \text{ e}^-/\text{sec}$. Of course, temperature stabilization is the best way to eliminate drifts. However, even with an active detector temperature control loop, extremely low dark currents are masked by thermal drifts. Stabilizing the detector temperature was necessary to apply this monitoring technique to measure the dark current of $4 \cdot 10^{-3} \text{ e}^-/\text{sec}$. This is the lowest value reported for InSb [1].

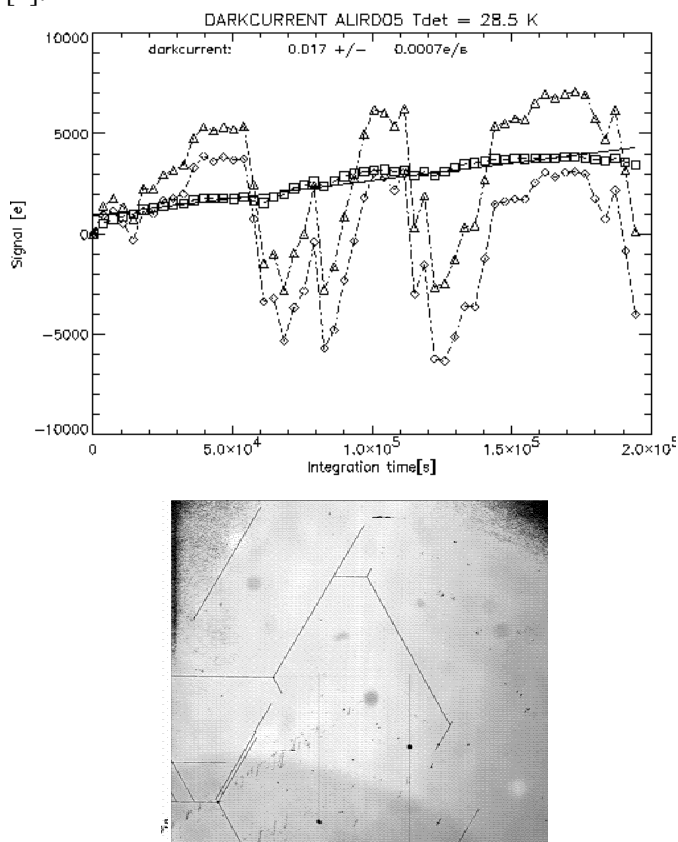


Figure 2. (top) Integration ramp of dark exposure with multiple nondestructive readouts. Triangles denote raw detector output. Diamonds denote dead pixel output. Squares denote compensated detector signal by subtracting the signal of dead pixels from detector signal. (bottom) Cosmetics of Aladdin 1Kx1K InSb engineering grade array. Dead pixels for monitoring thermal drift are taken in upper right corner.

3. HAWAII2 MULTIPLEXER REFERENCE

The first infrared array providing an on-chip reference cell is the Hawaii2 2K×2K HgCdTe array from Rockwell. Unfortunately, the reference output is implemented as an additional output for each quadrant and requires four channels in addition to the 32 channels for the video signal if the subtraction is to be done in the real-time processor of the data acquisition system. The reference output is activated as the 129th pixel at the end of each row, which is comprised of 128 pixels if 32 outputs are used. Since the reference output is not available while the detector pixels are being read, a cryogenic clamp is needed on the detector board. First, the multiplexer must be clocked to the reference pixel. Then the reference output is clamped and fed as reference input into the symmetric preamplifier while the same row is clocked again to read the detector pixels. On our detector board we have implemented four additional channels for digitizing the reference output as well as a cryogenic clamp to make an analog subtraction of the reference.

The temperature dependence of the video signal and the reference outputs of the Hawaii2 array are shown in Fig. 3. The rate at which the DC level of the video and reference output drifts is 327 e⁻/K and 338 e⁻/K, respectively.

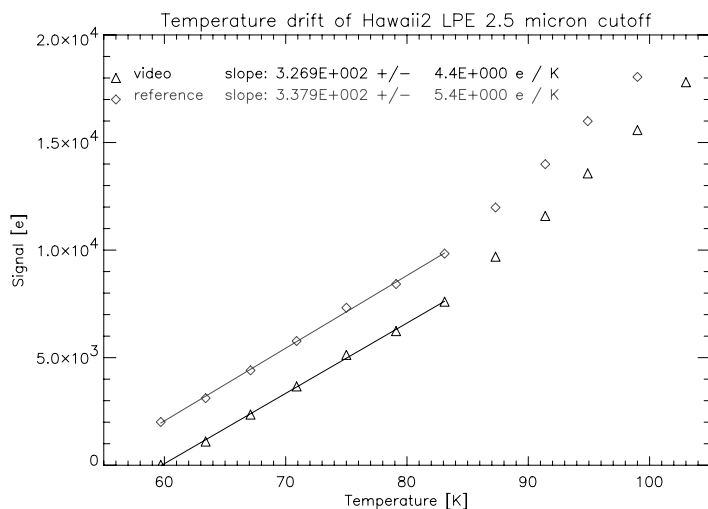


Figure 3. Temperature drift of Hawaii2 array. Triangles denote video signal shift 327 e⁻/K. Diamonds denote reference signal shift 338 e⁻/K.

Hence, the reference output is well suited to track the temperature drifts of the video signal as demonstrated by the 46-hour integration shown in Fig. 4. This shows the deviation of the uncorrected (squares) and the corrected (triangles) nondestructive readouts from a least squares fit to the measured

integration ramp of the detector signal. The standard deviation of the uncorrected readouts is 9.0 e^- rms. The standard deviation of the readouts from which the reference output has been subtracted is 4.1 e^- rms.

The reference output on the Hawaii 2 multiplexer does not work in the unbuffered mode, which bypasses the second stage on-chip source follower having the current source of the internal bus switched off. This is the standard way we operate the Hawaii2 array. The gate of the Hawaii2 reference output source follower is tied to V_{reset} . If the internal current source is switched on by changing the bias power from 5 V to 3.4 V the reference output follows V_{reset} even if the second stage source follower is still bypassed ($V_{\text{drain}} = 5\text{ V}$). However, good thermal monitoring of drifts is only achieved in the buffered mode ($V_{\text{drain}} = 0\text{ V}$). First measurements of thermal drifts did not take this fact into account and were misleading.

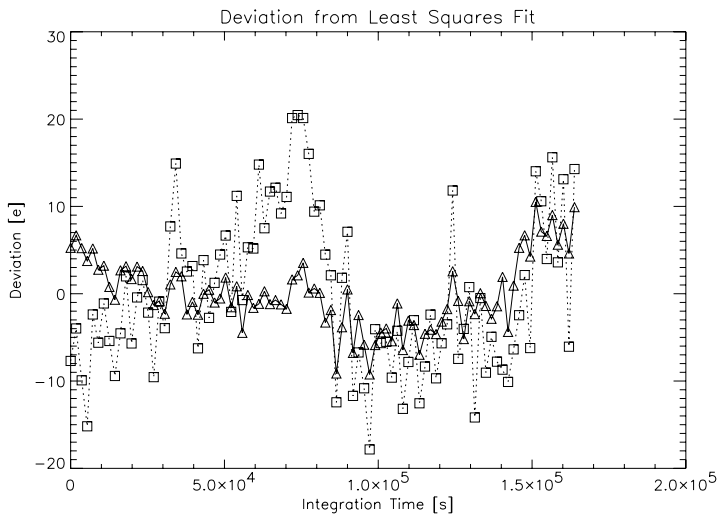


Figure 4. Deviation of uncorrected (squares) and corrected (triangles) nondestructive readouts from least squares fit to measured integration ramp. Standard deviation uncorrected: 9.0 e^- rms. Standard deviation corrected with Hawaii 2 reference output: 4.1 e^- rms.

The efficiency of the reference output to suppress low-frequency noise and pickup has also been investigated. The difference of two subsequent 5 sec dark exposures is shown in Fig. 5. The left image is the raw, unsubtracted difference and shows some low-frequency stripes. The high-frequency stripes are due to 50 Hz pickup. The different orientation of the stripes in the four different quadrants is due to the readout topology of the multiplexer. The stripes are parallel to the direction of the fast shift register. The histogram of the readout noise is shown by the dotted line in Fig. 6. The mean readout noise is 19.4 e^- rms. This is partly increased by quantization

noise of the ADC since the conversion factor had to be increased from $3.7 \text{ e}^-/\text{ADU}$ to $9.7 \text{ e}^-/\text{ADU}$ to cope with the higher DC level when switching from unbuffered to buffered mode of operation.

The difference image in the middle of Fig. 5 has been corrected with the reference output. The intensity of the stripes is slightly reduced and the histogram of the readout noise is shown by the dash dotted line in Fig. 6. The mean noise is 16.7 erms. The time to read out a row of 128 pixels is $t_s = 586 \mu\text{s}$. The squared transfer function of a double correlated clamp is $2-2\cos(2\pi f t_s)$. For a pickup frequency of 50 Hz, the sampling interval t_s between reading the pixel and reading the reference will be $586 \mu\text{s}$ in the worst case with the transfer function being 0.185, which is the suppression factor for 50 Hz pickup [2].

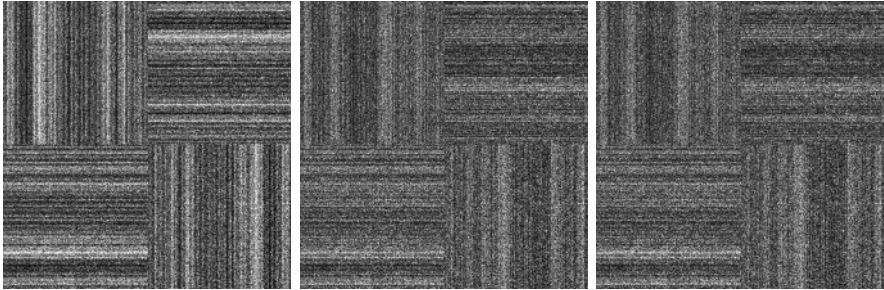


Figure 5. Difference images of double correlated clamps corrected with the reference output of a Hawaii 2 multiplexer. (left) Uncorrected. (middle) Corrected with single readout of reference output after reading row. (right) Corrected with two readouts of reference output before and after reading row using linear interpolation.

To explore the possibilities to further reduce t_s the reference output was read out twice, once by clocking to the end of the row and reading the reference before reading the row and a second time after reading the row. The reference is sampled 16 times and the average is taken to minimize the noise increase induced by the subtraction. For each pixel the reference signal is linearly interpolated from the two readings of the reference output. The result is shown in the right image of Fig. 5 and in the noise histogram represented by the solid line in Fig. 6. The mean readout noise is 16.2 erms, a marginal improvement. The Hawaii2 reference output only partially suppresses low-frequency noise components.

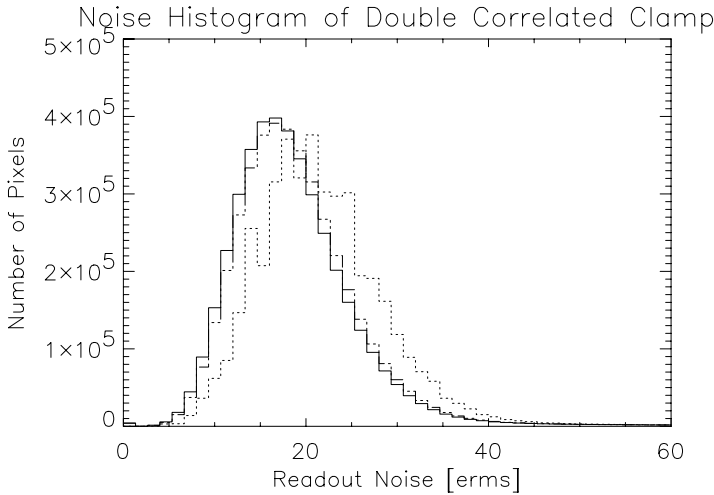


Figure 6. Noise histogram of a double correlated clamp corrected with the reference output of a Hawaii 2 multiplexer. (*dotted line*) Uncorrected, mean noise 19.4 e^- rms. (*dash dotted line*) Corrected with single readout of reference output after reading row, mean noise 16.7 e^- rms. (*solid line*) Corrected with two readouts of reference.

4. DARK PIXELS AS REFERENCE

Since tying the gate of an on-chip reference's source follower to a fixed voltage is insufficient at reducing drift and noise, we tried to use reference cells with gates connected to a capacity. We chose this method because it should closely parallel the effects on actual pixel. As such a reference is not available on the Hawaii2 multiplexer, dark pixels have been used instead. They are located in the lower left quadrant on the left edge and are shaded in the left image of Fig. 7. The pixels on the left edge of channel 1 are used to correct the complete array. The noise histogram of the uncorrected image is shown by the dotted line in Fig. 8. The mean noise is 15.4 e^- rms. Subtraction of dark pixels, as shown by the middle image in Fig. 7 and the dash dotted line in Fig. 8, is very effective in removing low-frequency noise components, reducing the read noise to 10.4 e^- rms. Linear interpolation of two readings of the dark pixels before and after reading the row further improves the removal of pickup components and yields almost perfect images. The mean readout noise is reduced to 9.4 e^- rms, as displayed by the solid line in Fig. 8. Most of the low-frequency noise sources V_i are capacitively coupled into the integrating node capacity C , which is assumed to be large in comparison to the coupling capacities C_i . In this case the coupling constant of noise source V_i is C/C_i , and the capacity connected to the gate of the reference cell field-effect transistor (FET) should be equal to C for the best noise rejection.



Figure 7. Difference images of double-correlated clamps corrected with dark pixels indicated by the shaded area in the lower left quadrant of the left image which is uncorrected. (middle) Corrected with single readout of dark pixels. (right) Corrected with two readouts of dark pixels before and after reading row using linear interpolation.

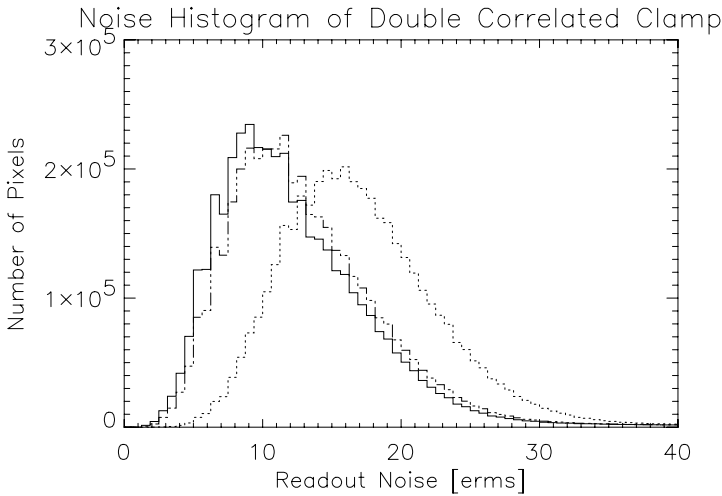


Figure 8. Noise histogram of double correlated clamp corrected with reference output of Hawaii 2 multiplexer. (dotted line) Uncorrected, mean noise 15.4 e^- rms. (dash dotted line) Corrected with single readout of reference output after reading row, mean noise 10.4 e^- rms. (solid line) Corrected with two readouts of reference output before and after reading row using linear interpolation, mean noise 9.4 e^- rms.

5. COLUMN CLAMP OF ALADDIN MULTIPLEXER AS REFERENCE

Taking into consideration the attractive features of reference cells not only to monitor thermal drifts but also to remove all noise pickup components and get clean and low-noise images, we searched for ways to

implement an on-chip reference for the CRIRES mosaic focal plane, which consists of four Aladdin $1K \times 1K$ InSb arrays. The column clamp circuit of this array seems to be well matched to function as a reference cell [3]. Its geometry and layout is identical to the unit cell source follower connected to the detector pixel. If V_{ddCl} is tied to V_{ddUc} and V_{ggCl} to V_{detCom} the clamp circuit emulates a saturated pixel during row transitions when the row enable switch disconnects all unit cells from the column bus (see Fig. 9). We have both simulated and measured that gain is not affected by keeping V_{ggCl} at V_{detcom} during readout of the detector pixels. The effectiveness in suppressing noise by utilizing the clamp FET as a reference cell still remains to be tested with the Aladdin array. It is planned to evaluate this technique by both connecting V_{detcom} to the clamp gate and by connecting a capacity to the gate reset together with detector pixels, but left floating while reading out the array and the reference.

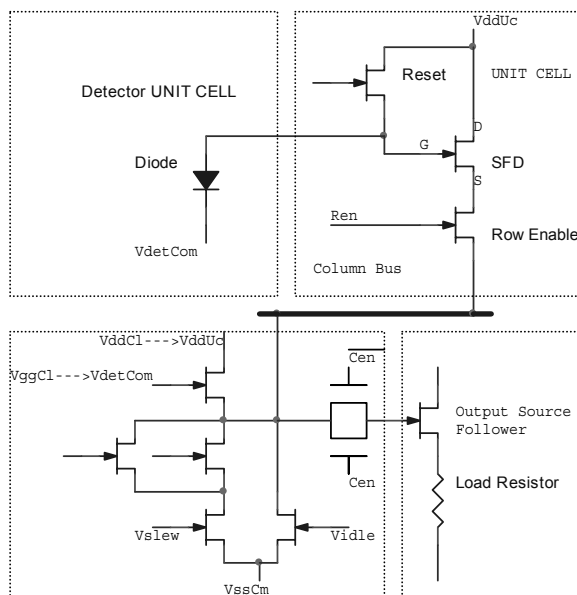


Figure 9. Column clamp circuit used as reference cell by replacing V_{ddCl} with V_{ddUc} and V_{ggCl} by V_{detCom} . Reference is sampled during row transitions when row enable switch is open.

6. CONCLUSION

Reference cells are indispensable in the elimination of thermal drifts during long integrations and in obtaining images untainted by low-frequency

noise pickup on IR arrays. Dead pixels not hybridized to the unit cell can be used to eliminate thermal drifts. The reference cell of the Hawaii2 multiplexer reduces thermal drifts but does not reject low-frequency pickup very well. Dark pixels have been used to demonstrate that connecting a capacity to the gate of a reference FET achieves clean images free of noise pickup. By employing this technique, the readout noise of a double-correlated clamp on a Hawaii2 array could be reduced from 15.4 erms to 9.4 erms. In next-generation multiplexers, such as the Hawaii-2RG, reference cells will be implemented with capacities. A method to use the clamp circuit of the Aladdin 1K \times 1K InSb array as reference pixel is under development.

7. REFERENCES

- [1] Finger, G., Mehrgan, H., Meyer, M., Moorwood, A.F.M., Nicolini, G., Stegmeier, J., 2000, *Performance of large format HgCdTe and InSb arrays for low background applications*, Proc SPIE **4008**, p. 1280.
- [2] Janesick, J. R., 2001, *Scientific Charge Coupled Devices*, SPIE Press, p. 564.
- [3] Hoffman, A. W., 2001, private communications, Raytheon Infrared Operations.



Gert Finger won two awards: “Best paper” (you just read it!) and “Meister Procrastinator”. Guess whose Mauna Kea-size nose is peeking from the left?

AZCAM: A WINDOWS-BASED CCD/CMOS CLIENT/SERVER DATA ACQUISITION SYSTEM

Michael Lesser and Madhuvanesh Parthasarathy
University of Arizona (UA)

Abstract: *AzCam is a software package developed to utilize a common architecture for the characterization of CCD and CMOS imagers in both laboratory and astronomical observatory environments. It follows a standard client/server model in which the server runs on a PC under the Microsoft Windows operating system to allow easy integration with the many CMOS imager cameras.*

Key words: *Charge-Coupled Device (CCD), Complementary Metal-Oxide Semiconductor (CMOS) imagers, software, computer, data acquisition*

1. INTRODUCTION

AzCam is a software package and data acquisition architecture developed at the University of Arizona Imaging Technology Laboratory (ITL) as an interface to image acquisition hardware. It has been developed primarily to create a common user interface and software toolset for both CCD and CMOS cameras. The Windows operating system was chosen because most CMOS imager hardware uses proprietary drivers that are not available under Linux or Solaris. *AzCam* follows a standard client/server model, allowing hardware running on the server machine to be completely isolated from user clients. This enables the development of common clients which are reusable among different imaging systems, as well as easy debugging since all commands are simple strings passed over sockets.

The structure of AzCam is based on levels, each with independent code. These levels consist of a generic *server*, system-dependent *libraries*, and hardware-dependent *drivers*. User *clients* are located on either remote or local machines and provide the user interface. These software components are described below.

2. SERVER

The server handles only high level tasks such as network communication, security, and command parsing. Dynamic Link Libraries (DLLs) at the library and driver levels contain all hardware-dependent code and camera-specific commands.

AzCamServer is a Windows executable program (written in C) which handles these server functions. It is executed before any other AzCam operations (usually at boot-up of the server PC). At startup the program opens a socket port and waits for incoming client connections. It has the option of opening one or more interface cards. The server waits on all connected client sockets for incoming commands. After client commands are executed (by calling a library interface function) a status value is returned in the format “OK message” or “ERROR message” where “message” is data, an error message, or is not used.

3. LIBRARIES/DRIVERS

AzCam has been used with Astronomical Research Cameras, Inc., Generation 2 CCD controllers and CMOS cameras from Rockwell and Epix. An SDSU Generation 1 controller interface is under development as an upgrade for older Steward Observatory systems now using VME interfaces. Each of these systems has a library associated with it. These libraries contain functions which are specific to each camera. Each library has a single interface function which parses client commands from strings into numerics as needed and calls the appropriate functions. These may be internal C functions or external functions from proprietary vendor-supplied libraries. New commands are added by adding the corresponding parsing function to the interface function. As an example, *ARCLibrary.dll* is a run-time library containing C functions which perform the basic operations required to run the ARC CCD controller. Typical functions are *Reset_Controller* and *Start_Exposure*. Example commands issued by clients for the SDSU/ARC system are shown in Table 1.

The library functions call the driver level functions to perform actual hardware I/O. Normally written as DLLs, drivers usually contain just a few calls which open, read/write, and close a device. As an example, the

ARCdriver.dll run-time library contains low-level C functions which interface directly with the ARC PCI card.

Table 1. Example AzCam commands issued by clients.

Command(s)	Parameters	Return	Description
RunScript	<i>Filename</i>	OK	Executes a script file containing commands
ResetController		OK	Resets the camera to a known state
PowerOn, PowerOff		OK	Turns camera power on/off
OpenShutter, CloseShutter		OK	Opens/closes camera shutter
Expose	<i>time filename</i>	OK	Takes an image exposure and saves it to disk
GetTemp		OK CamTemp DewTemp	Reads the current detector and dewar temperatures
DataClient		OK	Identifies the client as a DataClient to receive image data
CloseConnection		OK	Closes the client's socket connection to the server

In order to support many hardware systems as simply as possible, AzCam takes advantage of a driver toolkit called WinDriver from Jungo, Inc. [www.jungo.com]. This toolkit, which is only required when interfacing custom hardware for which there are no drivers, simply allows hardware driver development under Windows without kernel level programming. Because it is source compatible with WinDriver versions for Linux, Solaris, and other operating systems, the AzCam package is, in fact, not directly tied to Windows. We expect to test a Linux version of AzCam in the near future for those traveling applications which need a one-computer acquisition system and also require the image processing functions of a Linux environment.

4. CLIENTS

Clients can be written in any language or platform which supports sockets, and are typically graphical user interfaces (GUIs) or command line interfaces running on a machine with image processing capabilities. Clients have been developed for Steward's "90Prime" 8K×8K CCD mosaic, for detector characterization at IITL, for control of telescope guide cameras, and as a command line interface in IRAF (Image Reduction and Analysis Facility, distributed by the National Optical Astronomy Observatory) for powerful scripting capabilities.

Our main user interface to AzCam is currently a GUI written in National Instruments LabView called *AzCamTool* (see Fig. 1). Buttons are used to pop up windows which select parameters and allow user input. AzCamTool

has been tested under Windows and Linux, and can be distributed as a stand-alone executable which does not require a LabView installation. It is also used at ITL for detector characterization. Waveforms and voltages can be downloaded (if supported by the hardware system) and temperature sensors and heaters manipulated. LabView allows quick and simple user interfacing for these and other hardware oriented tasks.



Figure 1. Screenshot of AzCamTool.

The use of standard sockets allows many different programs and platforms to interface with the AzCam server. As an example, Dr. Gary Schmidt has written a Tcl/Tk interface for the new Steward Observatory guiders. The guiders use 512×1024 back-illuminated, frame transfer CCDs in custom TEC dewars (both developed at the UA). The current system uses an ARC Gen 2 CCD controller. The camera can be controlled by AzCamTool (or other clients) for direct imaging or debugging and by the Tcl/Tk GUI when autoguiding.

5. ACKNOWLEDGEMENTS

This work has been supported by National Science Foundation Grant AST-9876630. We thank Dr. Gary Schmidt (University of Arizona, Steward Observatory) for developing the Tcl/Tk telescope guider client.

UPGRADE OF ESO'S FIERA CCD CONTROLLER AND PULPO SUBSYSTEM

Javier Reyes-Moreno, Christoph Geimer, Andrea Balestra, Nicolas Haddad
European Southern Observatory

Abstract: *An overview of FIERA is presented with emphasis on its recent upgrade to PCI. The PCI board hosts two DSPs, one for real time control of the camera and another for on-the-fly processing of the incoming video data. In addition, the board is able to make DMA transfers, to synchronize to other boards alike, to be synchronized by a TIM bus and to control PULPO via RS232. The design is based on the IOP480 chip from PLX, for which we have developed a device driver for both Solaris and Linux. One computer is able to host more than one board and therefore can control an array of FIERA detector electronics. PULPO is a multifunctional subsystem widely used at ESO for the housekeeping of CCD cryostat heads and for shutter control. The upgrade of PULPO is based on an embedded PC running Linux. The upgraded PULPO is able to handle 29 temperature sensors, control 8 heaters and one shutter, read out one vacuum sensor and log any combination of parameters.*

Key words: *Charge-Coupled Devices (CCDs), CCD controllers, DSP, PCI*

1. INTRODUCTION

ESO's Optical Detector Team has developed a new-generation CCD controller -FIERA- for the Very Large Telescope (VLT) facility on Cerro Paranal and for the observatory at Cerro La Silla, Chile [1].

FIERA's excellent design, performance and flexibility have been proven extensively in more than fifteen detector systems by mid-2002 [2]. However, the rapid evolution of electronic components and computer platforms have made it necessary to take prompt action to redesign and upgrade FIERA in order to be able to deliver the upcoming systems.

The redesigning and upgrading of FIERA's serves to improve the performance and availability of new detector systems like GIRAFFE, HARPS, and OmegaCAM.

2. MOTIVATION FOR THE UPGRADE OF THE HARDWARE OF FIERA

The core of the upgrade is a change on the platform of the SLCU (SPARC Local Control Unit) and is motivated to overcome the unavailability of SPARC20s on VME and with S-bus. The SPARCs used up until now have become obsolete. Their unavailability prevented us from delivering further systems with the current configuration. This situation could not have been foreseen when FIERA's design was initiated in 1995. The new platform for the SLCU is a UltraSPARC with an universal PCI bus.

In addition to the change of the SLCU platform, FIERA's upgrade consists of a new analog bias board, the upgrade of PULPO, improvements to the video board and an increase in the number of channels on the clock driver board.

One of the design requirements on this upgrade is its transparency to the user and its backward compatibility. It means that any of the instruments already deployed can benefit from this new design in case of an upgrade or refurbishment.

3. FIERA PCI-BUS UPGRADE

The upgrade involved the design of a PCI board which integrated the functionality of the VME I/F board, DSP board, video capture board and TIM (Time Interface Module) board along with the PULPO optical transceiver and the cables for the interconnection of all the boards. As mentioned before, the main motivation to migrate to an SLCU on PCI-bus is to overcome the unavailability of SPARCs on VME and with S-bus. However, this migration in the platform is also accompanied by the following advantages:

- Shorter CCD read-out time due to higher data transfer rate of the PCI-bus. In multiport and fast read-out modes, the performance is better by a factor of three.
- Possibility to control not only a mosaic of CCDs but also a set of controllers with only one SPARC (one SLCU will be able to control up to six controllers).
- Significant SLCU cost reduction, by a factor of five.

- Much higher physical compactness. Only one board is needed to set up the SLCU. This improves reliability.
- Possibility of faster on-the-fly pixel re-ordering (very important for large CCD mosaics).
- Platform independency.
- Integrated DMA engine.
- 32-bit interface to Real Time Computer (RTC).
- Synchronization lines for event triggering.

An increase in versatility is also achieved along with a reduction in weight, volume and heat dissipation.

4. FIERA BIAS BOARD UPGRADE

The number of bias channels was doubled from 16 to 32 per board, maintaining the same dimensions of the board. Therefore, this upgrade provides:

- more bias channels to cope with the upcoming systems, especially big CCD mosaics such as OmegaCAM,
- a more compact detector electronics system (by a factor of two) on each bias board.

5. FIERA VIDEO BOARD

This upgrade is still in progress and the new video board will feature:

- a minimum of 8 channels per board, previously: 4.
- use of inexpensive 16-bit ADCs (cost reduction by a factor of 40).
- lower power consumption and heat dissipation.

6. FIERA CLOCK DRIVER BOARD

As with the video board, this upgrade is still in progress and will feature:

- 16 clock lines with +/-14 V swing and 20 MHz, previously: 14 clocks.
- half the mechanical size.
- lower power consumption and heat dissipation.

7. PULPO UPGRADE

This upgrade has been carried out in cooperation with Paranal. The motivation for the upgrade was to allow for:

- the control of 8 heater control circuits and the monitoring of 29 temperature sensing circuits (PT100) on the cryostat head.
- vacuum monitoring.
- better alarm signaling to the IWS (Instrument Work Station) in case of a cryostat failure, i.e. loss of vacuum or nitrogen.
- telemetry of the continuous flow cryostat sub-systems.
- standard software maintenance, since it is based on an embedded PC running Linux.
- optical serial interface to the SLCU.
- flexible interface to a wide range of shutters.
- deeper data logging capability.
- Ethernet connection.

The new PULPO also features a display to show the data to the user locally and an Ethernet connection to check the status remotely. This upgrade also satisfies the complex requirements of the OmegaCAM 16K×16K mosaic camera.

8. ACKNOWLEDGEMENTS

The authors wish to acknowledge helpful comments on the manuscript received from Dietrich Baade, Cyril Cavadore, Fabrice Christen, Claudio Cumani, Sebastian Deiries, Reinhold Dorn, Jane Eskdale, Rolf Gerdes, Olaf Iwert, Gustavo Rahmer, Roland Reiss and others.

9. REFERENCES

- [1] Beletic, J.W., Gerdes, R., DuVarney, R. C., 1998, www.eso.org/odt/Fiera/index.html
- [2] Baade, D., 2002, *Optical detectors in the VLT operations era*, these proceedings, pg. 197

AN OPTIMIZED DATA ACQUISITION SYSTEM WITHOUT RESET ANOMALY FOR THE HAWAII AND HAWAII-2 ARRAYS

Martin Riopel, René Doyon, Daniel Nadeau and Christian Marois
Laboratoire d'Astrophysique Expérimentale, Université de Montréal

Abstract: *This paper presents the data acquisition software system used for controlling near-infrared cameras/spectrometers designed and built by the Laboratoire d'Astrophysique Expérimentale of the Université de Montréal. These instruments are used on the 1.6-m Mont Mégantic Observatory and/or the 3.6-m Canada-France-Hawaii Telescope (CFHT). The system features a modified DS9 imaging display with custom user interface functions written in Tcl/Tk. It includes standard coadd and multi-sample readout modes with pixel rates up to 1 MHz (demonstrated on HAWAII array with a SDSU-II coadders board). Its fast readout mode coupled with other efficient data management functions yield very high observing efficiencies virtually unlimited by the array controller speed. This feature is particularly crucial for applications requiring very short exposures on bright objects such as searching faint companions close to nearby bright stars. The system also features a unique clocking pattern that eliminates the reset anomaly effect of the HAWAII and the HAWAII-2 arrays without penalizing observing efficiency, and reduces temperature drifts of the arrays.*

Key words: *infrared, controller, software, clocking, HAWAII, HAWAII-2*

1. INTRODUCTION

In the last few years, great efforts have been made to find faint companions to stars. In the near-infrared, this kind of observation often requires very short exposures to avoid saturation by the nearby bright star. Short exposures usually imply low efficiency (efficiency being defined as the ratio of time elapsed collecting photons divided by the total time for acquiring and displaying the image). This paper presents data acquisition

software, developed by the Laboratoire d'Astrophysique Expérimentale of the Université de Montréal, that can read a HAWAII array [1] in about a third of a second with an efficiency of 90% for an exposure time of 15 sec. The acquisition system is designed to maximize speed, observing efficiency and reliability.

2. GENERAL DESIGN

The acquisition software is written in C for the Unix/Solaris/Linux environment while the display and user interface software is written in Tcl/Tk. Its main characteristic is the use of shared memory calls to manipulate data. Shared memory has the advantage of being persistent (it is not freed at the end of a program) and can be accessed by more than one program simultaneously. These features greatly facilitate multi-language, multi-tasking software development and maintenance. For maximum flexibility, the image is stored in shared memory in FITS format.

To maximize efficiency, the acquisition software uses the exposure time to update parameters and write previous images to disk. In a typical acquisition sequence, the Tcl/Tk interface software will tell the C program what the user wants. The C program will then launch the acquisition, write the previous image to disk, prepare the next header while exposing, and read the actual image directly in shared memory space. The display software will begin to show the image as soon as the image is in shared memory, before it is written to disk.

The display software is a modified version of SAOIMAGE DS9 [2]. This application is written in Tcl/Tk and the source code is public. Since Tcl/Tk is essentially an interpreted language, it is possible to add lines of source code directly at run time without pre-compilation. In order to display the FITS image stored in shared memory space, the LoadFitsShared function from the SAOTk package [3] is used. SAOIMAGE can also be used to transmit information to the acquisition software, such as coordinates, by modifying header parameters stored in shared memory. Since no compilation is necessary, upgrading to new versions of DS9 can be easily done by downloading new executables from official site.

3. READOUT SOFTWARE

The readout is controlled by a SDSU II controller [4] with an infrared coadders board. The coadders board has the ability to keep an image in board memory. This enables the controller to manage multi-sample read and

coaddition without the external intervention of the main computer, thus increasing efficiency. The 1 MHz clocking is essentially the clocking proposed in the Rockwell datasheet, with a 1 μ s delay between successive changes in the pixel clock state. Typical clocking with delays is shown in Fig. 1. We have observed that some of the clocks need to be slower to maximize image quality.

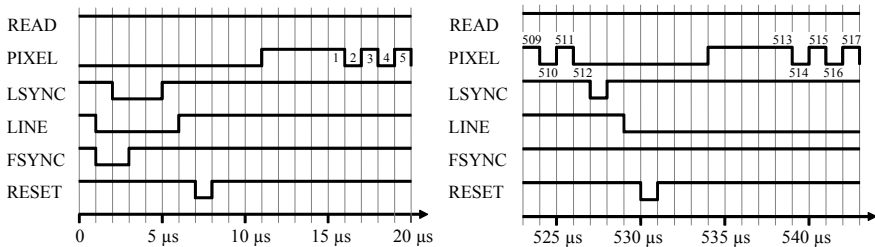


Figure 1. Pattern for clocking the HAWAII array at 1 MHz, showing the readout of the beginning of the first and second lines.

Note that the reset clock must be kept up to actually read the array. Note also that a 3.6 ms delay must be inserted just after the read clock is raised. A slower readout can be achieved by simply slowing down the pixel clock. For speeds higher than about 0.3 MHz, each pixel value is correlated with few precedent pixel values on the same line, thus reducing the sharpness of image and the statistical noise. This is to be taken into consideration when observing astronomical phenomena with spatial dimension close to the pixel size. For larger phenomena, a little blur in the image can be acceptable, considering the reduced statistical noise and the gain in efficiency.

The readout software uses highly synchronized read patterns and no-pause sequencing to eliminate the reset anomaly effect associated with the HAWAII and HAWAII-2 arrays. This effect is described in [5] and is caused by the nonlinearity of the signal for about 10 s after reset. Figure 2 shows typical images with and without the effect. To achieve this kind of flatness (for the difference of two reads), we have taken advantage of two observed characteristics of the anomaly with our system :

- The anomaly is a decreasing function of time since the last read on the same pixel.
- The anomaly has some kind of persistence from one read to another.

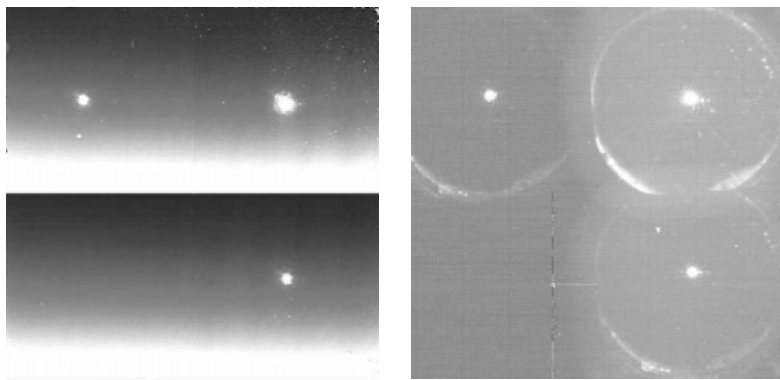


Figure 2. Images with and without the reset anomaly affect for reset-read-expose-read with exposure time of about 5 sec. It should be noted that the experimental setup is responsible for the circles on the right image.

In order for the anomaly to have a constant value for a given pixel, one has to make sure that pixels are read on a strictly regular basis, whatever the observing sequence requested. As an example, when exposing, the array must be continually read, even if the result is to be thrown away. The reset must also be done at exactly the same rate as the read (and with the same clocks), and continually when the array is in idle mode. A typical sequence of acquisition is shown in Fig. 3. On our system, it is necessary to synchronize everything to a 10 μ s precision (integrated over the entire sequence, including commands processing time) to reduce the anomaly variability to a non-detectable level.

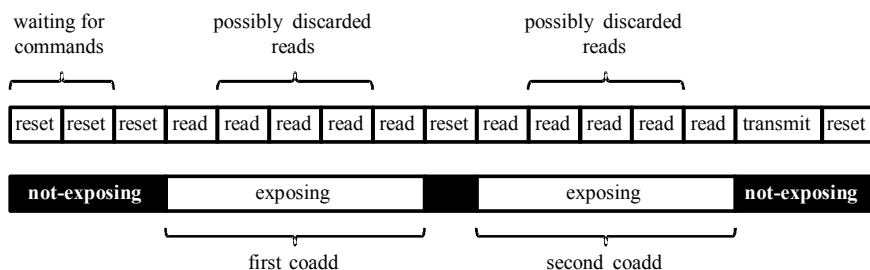


Figure 3. A typical multi-sample, multi-coadd sequence to remove reset anomaly effect.

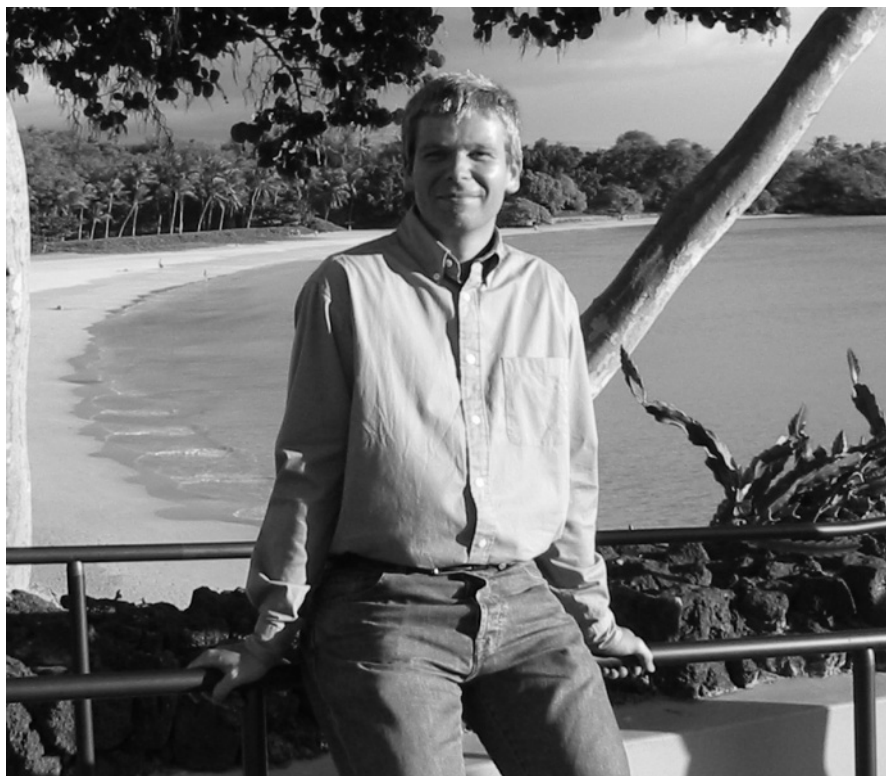
We have observed that this sequence had a real effect in stabilizing the array temperature, thus reducing the noise caused by temperature drifts. It should also be noted that this sequence will increase the glow for long exposures. However, for a given exposure time, the glow can be reduced by slowing down the read and the reset clocking rates.

4. CONCLUSION

In this paper, we have presented an acquisition system that is fast, efficient and reliable. For a reset-read-read sequence, the image doesn't show the reset anomaly effect usually associated with the HAWAII and HAWAII-2 arrays. In real time observing, these qualities can have a crucial influence on the quality of data whenever short exposures are required.

5. REFERENCES

- [1] Kozlowski, L.J., Montroy, J.T., Cabelli, C.A., Cooper, D.E., Chen, A.C., Bostrup, G.L., Bai, Y., Vural, K., Hodapp, K.-W., Hall, D.N., 2000, *Visible and infrared detectors at Rockwell Science Center*, Optical and IR Telescope Instrumentation and Detectors, M. Iye & A. F. Moorwood Eds, Proc. SPIE, Vol. **4008**, p. 1240-1253.
- [2] Mandel, E., 1997, *The SAOTng Programming Interface*, Astronomical Data Analysis Software and Systems VI, G. Hunt & H. E. Payne Eds, ASP Conference Series, Vol. **125**.
- [3] Joye, W., Mandel, E., 1999, *SAOTk: Tcl/Tk Widgets for Imaging and Data Visualization*, Astronomical Data Analysis Software and Systems VIII, D. M. Mehringer, R. L. Plante, & D. A. Roberts Eds, Vol. **172**, p.429-432.
- [4] Leach, R.W.; Low, F.J., 2000, *CCD and IR array controllers*, Optical and IR Telescope Instrumentation and Detectors, M. Iye & A. F. Moorwood Eds, Proc. SPIE, Vol. **4008**, p. 337-343.
- [5] Finger, G., Mehrgan, H., Meyer, M., Moorwood, A.F., Nicolini, G., Stegmeier, J., 2000, *Performance of large-format HgCdTe and InSb arrays for low-background applications*, Optical and IR Telescope Instrumentation and Detectors, M. Iye & A. F. Moorwood Eds, Proc. SPIE Vol. **4008**, p. 1280-1297.



Another nerd (Ralf Kohley) falls for the superglue trick.....
(Courtesy G. Burley)

GTC ACQUISITION CAMERAS AND WAVEFRONT SENSORS

Marcos Suárez¹, Ralf Kohley¹, Greg Burley², Lluís Cavaller¹, Rafael Vilela¹ and Albert Tomás³

¹Gran Telescopio Canarias Project Office, Instituto de Astrofísica de Canarias (IAC);

²Carnegie Observatories (OCIW); ³Nuevas Tecnologías Espaciales, S.A. (NTE, S.A.)

Abstract: *The GTC (Gran Telescopio Canarias) employs an Acquisition and Slow Guiding Sensor based on a Marconi CCD47-20. This chip is also the core sensor for the telescope Segment Figure Sensor. A third sensor, based on a Marconi CCD39-01 implements Fast Guiding and is also used for Wavefront Sensing under continuous rotation. 1 Hz full-frame readouts and 10 Hz window readouts are performed onto the slow guiding sensor, whereas 200 Hz full-frame readouts are required for the fast guiding sensor in binning modes. GTC sensors are low-profile, lightweight, individual CCD heads with integral low-noise preamplifier stages and Peltier cooling electronics. These CCD heads are liquid-cooled and include forced, dry air circulation. Besides, high noise immunity, proper shielding and grounding and impedance matching of the cabled links have been major design concerns. Sensor readout is performed by a Magellan CCD Controller (Greg Burley - OCIW), which has undergone modification at GTC in order to include additional analog input channels and to provide support for off-board, cable-linked sensors. The sensor's built-in electronics are also derived from the original Magellan design. We describe the detailed design of the GTC sensors and the modifications carried out in the Magellan controller.*

Key words: *Acquisition and Guiding (A&G), guiding camera, wavefront sensor, Charge-Coupled Device (CCD) detector, CCD head, CCD controller*

1. GTC ACQUISITION AND GUIDING INSTRUMENTS

The GTC Acquisition and Guiding (A&G) system [1] consists of the instruments listed in Table 1, which are distributed over two articulated guiding arms that can be positioned anywhere in the field of view.

Table 1. Description of the GTC A&G instruments

<i>Instrument</i>	<i>Purpose</i>	<i>Detector</i>	<i>Readout Specifications</i>
ASG (Arm#1)	Acquisition and Slow Guider - Acquisition of scientific targets - Slow guiding	Marconi CCD47-20	10 Hz, two-window readout over two channels
SFS (Arm#1)	Segment Figure Sensor - Shack-Hartmann wavefront sensing for closing primary mirror active optics loop in parallel with scientific observations	Marconi CCD47-20	
STS-FGC (Arm#2)	Segment Tilt Sensor – Fast Guider Camera STS configuration: - Primary mirror segment tilt sensing (SFS backup) - Correction of low-order global telescope errors using secondary mirror - “Fast seeing” monitor FGC configuration: - Fast guiding for image motion correction using secondary mirror - Slow guiding using a low-pass filter (ASG backup)	Marconi CCD39-01	200 Hz, full-frame readout over four channels (FGC mode)

1.1 CCD Detector Characteristics

The Marconi CCD 47-20 is a 2-channel, 13 μm pixel size, AIMO chip with midband coating, whereas the Marconi CCD39-01 is a 4-channel, 24 μm pixel size, non-AIMO chip with broadband coating.

All CCD detectors in the GTC A&G instruments are mounted in the Marconi, two-stage Peltier package.

2. CCD HEADS

Custom CCD heads have been developed to encapsulate each GTC detector type. Heads are integrated in the A&G instruments and cabled to the CCD controllers. Table 2 and Fig. 1 describe the CCD head design.

The preliminary design of the heads was produced by the GTC Project Office. The detailed design and manufacturing has been carried out by NTE, S.A. The head electronics are based on Magellan controller design [2].

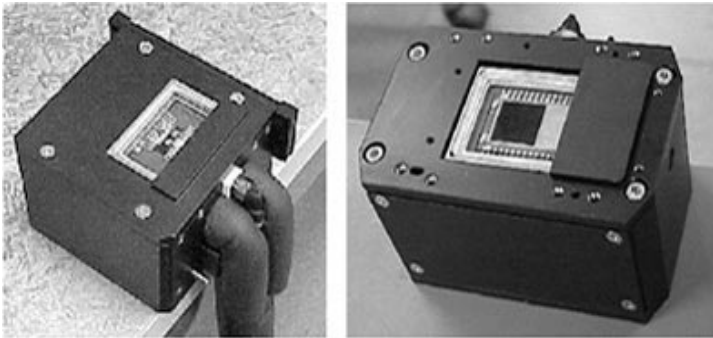


Figure 1. CCD39-01 head (left) and CCD47-20 head (right)

Table 2. Description of GTC CCD heads

Mechanical Characteristics	Electrical Characteristics
Material:	Low-noise, JFET-buffered Preamplifier [3]:
- Metal parts in aluminium (painted black for improved optical performance)	- 2 video channel (CCD47-20 head)
- Isolating parts in DELRIN	- 4 video channels (CCD39-01 head)
Dimensions/Weight:	Peltier Drive Electronics:
- 63×86×54mm / 450 g (CCD47-20 head)	- Linear PI current regulator
- 96×84×54mm / 510 g (CCD39-01 head)	- Output capability: 3.3 V/3 A
CCD Positioning Tolerance:	Temperature Sensing Electronics:
- Centering in the optical path: ±0.2 mm	- Redundant on-package thermistors
- Tilt in respect to optical plane: ±2.5mrad	- I-to-V amplifier for NTC sensing
Thermal Control:	Cabling:
- Head operation range: -2 °C to +19 °C; 2% to 87%RH	- Separate cabling for video lines, clock lines and bias+power lines
- Peltier hot side cooling by integrated heat exchanger operated with water (35% glycol) at -6 °C	- Miniature individually shielded, twisted pairs for video lines
- Dry air outlet over detector window	- Miniature coaxial cables for clock lines
- Heater resistors	Controlled Grounding:
Cable Harnessing:	- Galvanic isolation from support structure
- Low torque: lower than 0.25 Nm	- Head grounded to CCD controller case
- High flexibility	Enhanced Shielding:
	- Double shielding of video and clock lines

3. CCD CONTROLLER

The Magellan controller design [2] has been adapted to meet the GTC needs and is used in conjunction with the GTC CCD heads. Table 3 describes the CCD controller board design.

Major modifications of the original design include support for off-board CCD heads as well as an additional signal processing board for the operation of the CCD39-01 over four channels. Minor modifications include the availability of a TTL signal for shutter operation.

The GTC Project Office has produced the design modifications. The manufacturing has been realised by the IAC workshop.

Table 3. Description of GTC CCD controller boards

Controller Board	Characteristics
Timing Board	100 MHz DSP frequency: <ul style="list-style-type: none"> - 10 ns clock signal resolution - 25 Mbps LVDS serial link data rate
Clock Driver Board	15 usable clock lines: <ul style="list-style-type: none"> - +/-12 V voltage swing - 20 MHz bandwidth - 100 mA output capability
Signal Processing Board	2 usable, low-noise video channels: <ul style="list-style-type: none"> - CDS analogue chains - 14-bit, 800 kHz A/D converters 6 usable bias lines: <ul style="list-style-type: none"> - +/-15 V voltage swing (4 lines) - 0-30 V voltage swing (2 lines) Off-line CCD temperature readout
Power Board	Unique 48 V/1 A external supply On-board 5 V, +/-15 V, 30 V and 3.3 V supply: <ul style="list-style-type: none"> - LC+ferrite filtering of on-board supplies - Linear post-regulation of the on-board 30V supply
PCI Interface Board	PCI to PMC adapter for operation from a VME CPU board VxWorks driver under development at GTC Project Office

4. REFERENCES

- [1] Devaney, N. et al., 2000, *GUACAMOLE: the GTC Guiding, Acquisition and Calibration Module*, SPIE Conf. Proc., vol. **4003**, p.146,
- [2] Burley, G., 2002, *Compact CCD Guider Camera for Magellan*, these proceedings, pg. 431.
- [3] Geary, J.C. et al., 1998, *Camera Electronics for the 72-channels S.A.O Megacam*, SPIE Conf. Proc., vol. **3355**.

A NEW CCD CONTROLLER AT UCO/LICK OBSERVATORY

Mingzhi Wei and Richard Stover

University of California Observatories/Lick Observatory, University of California, Santa Cruz

Abstract: *We have developed a new CCD controller for Lick Observatory. Although the controller was developed for the new generation of guide cameras at Lick, it is still a versatile, high-performance, general purpose CCD controller for single-CCD applications.*

Key words: *Charge-Coupled Device (CCD), controller, guide camera, Lick Observatory*

1. INTRODUCTION

This project began as an effort to develop an inexpensive, compact CCD controller that would be part of the replacement for Lick Observatory's present guide cameras. The requirements for a high performance guide camera are no less stringent than for any other astronomical imaging system and the controller was incorporated into several science cameras even before being used in a guider.

Five guide cameras are presently under construction and we plan to install these at Lick Observatory on Mt. Hamilton, California during the second half of 2002.

2. CONTROLLER DESCRIPTION

The controller consists of a timing card, a clock driver card, a bias voltage, analog processing cards (one for each channel), and a dual-ADC converter plus optical fiber interface card. A 6U VME-style connector is used as a system backplane.

With two video channels the controller can operate a single CCD at a data rate of almost 4-Mbit/sec (1 μ s per 16-bit pixel/channel). Data is

transmitted over a fiber link to a PCI bus interface. An RS232 link is used for command and status I/O.

At the heart of the camera design is the Xilinx XC4000 family of programmable logic devices. The use of programmable logic devices combines the best of hardware speed and parallel operation with the ease of programmable modifications and enhancements. A small microprocessor is used for commands and status. The microprocessor is turned off during image readout to avoid noise from asynchronous operation.

The camera hardware supports a large number of programmable parameters, designed to satisfy nearly every possible CCD control function we have used in the entire two decades of CCD testing and operation.

PC software developed for the camera runs under the Linux operating system and consists of a Linux device driver in C, low-level C code that handles communications and initial image processing, and a user interface written in tcl/tk. The use of a Postgres database to store camera parameters and user-defined setups is being explored. We plan to use this camera as a test bed for the development of ASTEROID pixel server software [1].

We have achieved 4 e^- read-noise performance in tests with a SITe SI-424AB $2\text{K}\times 2\text{K}$ CCD. This is the same performance achieved with an SDSU controller or our old Lick CCD controllers.

Table 1 lists some of the controller characteristics and Fig. 1 illustrates some controller applications.

Table 1. Camera Components and Characteristics

Item	Description
Voltages	All programmable with 12-bit DACs
Clocks	Generated by setting rails and switching between rails. Clock frequencies for serial and parallel clocks are settable and independent of waveforms.
CCD Isolation	Bias and clocks can be isolated from the CCD by a bank of analog switches.
Waveforms	MPP/nonMPP parallels, binning by 1, 2, 4, or 8. All stored in nonvolatile memory
Windowing	A single readout window is supported. Subwindows within the readout window are handled by higher level software.
Frame transfer	Frame transfer and full CCD parallel clocking is possible
Exposure	16-bit counter with 0.01 sec timebase.
Video	Conventional CDS, 4 selectable gains, CDS times from 50 ns to 25.5 μs .
ADC	ADS-937 16-bit 1 MHz
MPU	AT89LS8252
Xilinx	XC4028EX-HQ208 (28K logic gates, 2560 flip-flops, 208 pins)
Fiber Optics	HFBR-1119T/2119T transmitter/receiver, 266 Mbit
PCI	Custom board with Cypress Semiconductor CY7C09449PV PCI Bus Controller and a Xilinx XC4010E-PQ208

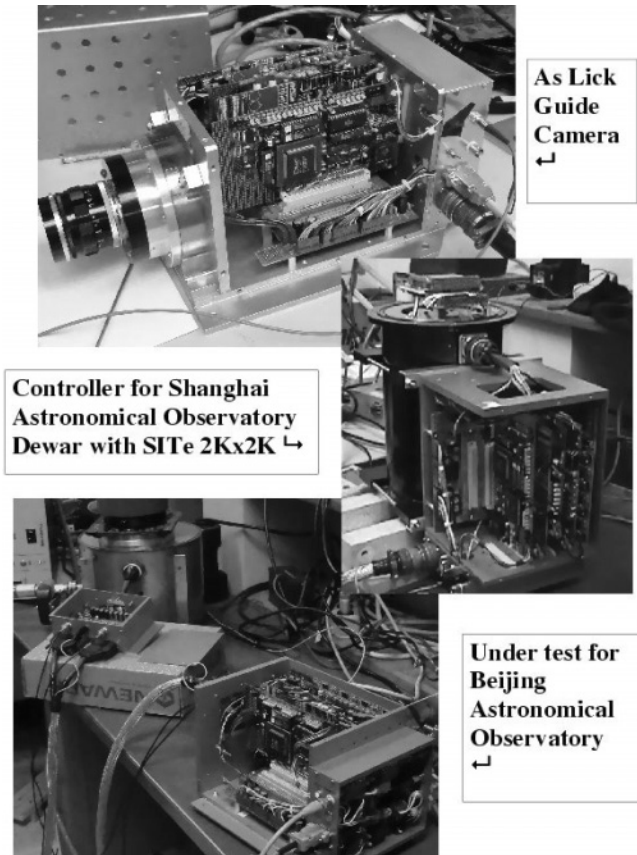


Figure 1. Three examples of controller applications. The BAO controller uses an external preamplifier.

3. ACKNOWLEDGEMENTS

We would like to thank Lloyd Robinson, who designed and built the original Lick guide cameras, for his valuable advice and assistance. William Brown did a superb job ordering and tracking all of the parts that went into the new cameras. Carol Harper did excellent work in assembling the camera electronics. The Beijing Astronomical Observatory (BAO) supplied all of the printed circuit boards. For more details see [2].

4. REFERENCES

- [1] Starr, B.M., et al., 2003, *MONSOON Image Acquisition System*, these proceedings, pg. 269
- [2] <http://www.ccd.ucolick.org>.



*Peter Love moments before he realizes that the boat has come to dock...
but at least he's going out in style in his Speedo.*

(Courtesy G. Woodhouse)

THE USE OF ASIC TECHNOLOGY IN THE DEVELOPMENT OF COMPACT, LOW-POWER CCD CAMERAS

Guy F.W. Woodhouse, Nicholas R. Waltham, Marcus J. French, Lawrence L. Jones

Rutherford Appleton Laboratory

Abstract: *This paper reports on a research programme at the Rutherford Appleton Laboratory to develop radiation-tolerant ASICs for space-borne CCD instrumentation. We have developed three CCD camera ASICs. The first is a programmable CCD waveform generator and sequencer for providing the digital timing signals needed to read out a CCD, and to control the video sampling and digitisation electronics. Our second ASIC is a single-chip CCD preamplifier, correlated double sampling, and 16-bit analogue-to-digital conversion video signal processor. Finally, our third ASIC is an eight-channel digital-to-analogue converter for providing software-programmable CCD bias and clock voltages. All three ASICs are intended to operate in the space environment, and are therefore designed for high total-dose radiation tolerance, and incorporate protection against single-event upset.*

Key words: *Charge-Coupled Device (CCD), camera, Application Specific Integrated Circuit (ASIC), Correlated Double Sampling (CDS), space, astronomy, Earth observation.*

1. INTRODUCTION

The CCD is currently the image sensor of choice for nearly all space-science, Earth remote sensing and ground-based astronomical visible light imaging systems. Large-format sensors with many millions of pixels, low readout noise, good pixel-to-pixel uniformity, and low dark current are readily available. However, for space-science missions, CCD technology also has inherent weaknesses:

- The requirement for compact, low mass, low power, and space-qualified CCD drive and video signal processing electronics.
- The susceptibility of both the CCD and the drive electronics to radiation damage.

This paper addresses the issues of the off-chip CCD drive and video processing electronics.

In designing electronics for space environments, there are strong initiatives to minimise size, mass, and power dissipation, and yet work from just a small catalogue of high-reliability space-qualified components. These requirements place severe constraints upon the CCD camera designer, particularly in the area of the analogue video signal processing and digitisation electronics. These problems are amplified with the ever increasing aspirations of the space science community, which calls for larger focal plane arrays of multiple CCDs, reading out at increasingly higher pixel readout rates, and through multiple CCD output amplifiers. Collectively, these requirements demand a continuous and strategic programme in the development of space-qualified CCD readout electronics. Our research aims to address these issues through the development of radiation-tolerant ASIC technology. To date, we have developed three CCD camera ASICs:

1. A programmable CCD waveform generator and sequencer for providing all the digital timing signals needed to read out a CCD, and to control the video sampling and digitisation electronics.
2. A single-chip CCD preamplifier, correlated double sampling (CDS), and 16-bit analogue-to-digital conversion (ADC) video signal processor.
3. An eight-channel digital-to-analogue converter (DAC) for providing software-programmable CCD bias and clock voltages.

All three ASICs are designed to operate in space environments, and are thus designed for high total-dose radiation tolerance, and incorporate protection against single-event upset (SEU).

2. WAVEFORM GENERATOR & SEQUENCER ASIC

Our Waveform Generator ASIC [1] has been designed to provide all the timing signals needed to read out a CCD and to control the video sampling and digitisation electronics. A block diagram of the ASIC is shown in Fig. 1. The heart of the design is an internal memory (RAM) that is partitioned into two independently addressed blocks which we refer to as the WAVE memory and the TABLE memory. The memory is 16 bits wide and permits 16 independent hardware control lines to the CCD clock drivers, video

signal processing, and digitisation electronics. The WAVE memory can store up to ten individual waveform patterns. Examples include:

- A ‘pixel’ waveform to generate all the clocks associated with reading out and digitising a single CCD pixel.
- A ‘line-transfer’ waveform to shift an image down the CCD array by one line element.

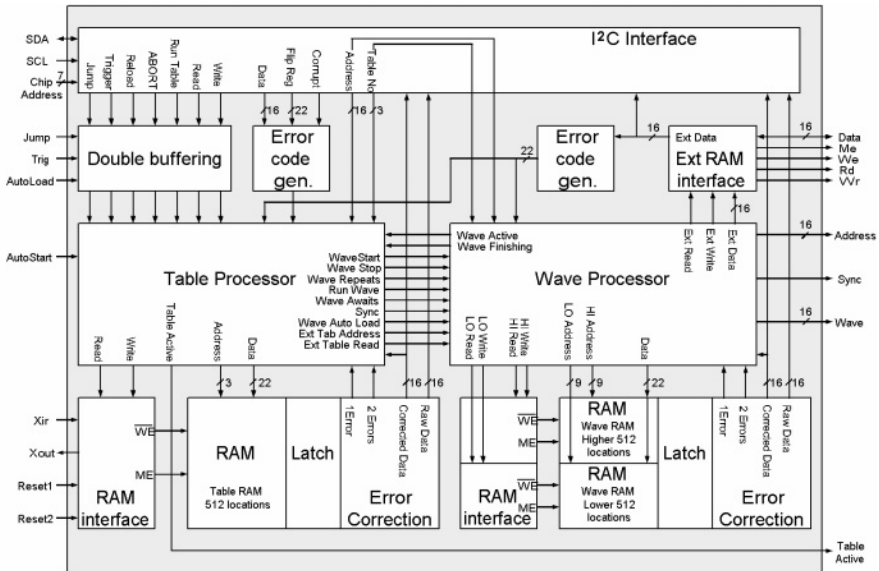


Figure 1. Block diagram of Waveform Generator ASIC.

The ASIC and its internal memory can sustain waveform state changes at a clock rate of 40 MHz. Waveform patterns are clocked-out of the ASIC under the control of high-level instructions stored within the TABLE memory. These instructions are contained within programs which we refer to as ‘readout tables’, and up to eight of these tables may be programmed into the TABLE memory at any one time. The most basic instruction defines a waveform ‘number’ and a ‘loop count’ parameter, and commands the sequencer logic to clock the specified waveform pattern out of the ASIC and repeat this for the number of times specified by the loop count parameter. Other instructions are concerned with defining the beginning, end, and loop count of loop-type operations, which may in turn be stacked to a depth of six nested-loops. A complete list of the instruction set is given in Table 1.

The WAVE memory is 1024 words long, and the TABLE memory is 512 words long. Waveform patterns and readout tables may be programmed anywhere within their specified memory blocks, but their ‘start’ and ‘stop’

addresses must be programmed into reserved registers at the bottom of the TABLE memory. A key feature of our design is that the WAVE and TABLE memories are addressed independently by the internal controlling logic. This allows TABLE instructions to be processed whilst the WAVE processor outputs WAVE data, resulting in a seamless output of WAVES with no software-looping delays between successive waveform patterns.

Although in practice we have never needed to exploit the capability, an external memory port on the ASIC allows the WAVE memory to be expanded with the addition of external memory components so as to provide a total memory depth of 64 kwords.

Table 1. Waveform Generator ASIC Instruction Set.

Repeat	Keyword	Code	Comment
n	WAVE <i>i</i>	0000- <i>i</i>	Output Wave <i>i</i> n times, endlessly if n=0 (<i>i</i> = 0-9)
-	TRIG	1010	Stop and wait for external trigger
-	SYNC	1011	Output a pulse on "Sync" output
n	BOL	1100	Start loop, repeat loop n times, endlessly if n=0
-	EOL	1101	End of loop
n	JUMP	1110	Jump to line n in the table on "Jump" instruction/external trigger
-	EOR	1111	End of table (hold outputs at last logic state)

The ASIC is programmed and controlled over a serial interface that follows the Philips I²C standard. A list of programming commands is given in Table 2. The first byte of a command defines the command type, and subsequent bytes specify the address/data of memory read/write operations. Two bytes specify the address and data for each memory location. For read operations only the pointer is written, and data are then read with a separate read transfer.

Table 2. Waveform Generator ASIC Programming Commands.

Command Byte	Definition
b00000000	Write Data (2-bytes address + 2-bytes data)
b00000001	Read Data (2-bytes of data from the pointer address)
b0 -- <i>j</i> 0010	Run TABLE <i>j</i> (<i>j</i> = 0-7)
b00001111	Abort
b00000100	Trigger
b00000101	JUMP
b00000110	Read ASIC Status Register

Programming the ASIC is best illustrated by the example shown in Table 3, which assumes the readout of an 800×600 pixel frame-transfer CCD. In this example, three different waveform patterns (WAVES) are used. WAVE0 executes a single frame-transfer line shift in the CCD's imaging and storage

areas, WAVE1 shifts the image in the CCD's storage area down the array by one line element, and the bottom-most line into the CCD output register, and WAVE2 reads a single pixel. The loop causes the line-readout to be repeated 600 times.

Table 3. Readout Table Example.

Line	Repeat	Keyword	Comment
0	600	WAVE0	Executes 600 frame-transfer line shifts
1	600	BOL	Start a loop for each of 600 lines
2	1	WAVE1	Shift image down the CCD storage area by one line
3	800	WAVE2	Read 800 pixels out of the CCD's output register
4		EOL	Close line readout loop
5		EOR	Stop

Each line in a TABLE is a 16 bit number for which the first 12 bits define a repeat qualifier, and the remaining 4 bits specify a keyword (as listed in Table 1). The repeat qualifier for loops and WAVES may therefore be set from 0 to 4095. If '0' is specified, then that item is repeated endlessly and may only be stopped by sending an ABORT command or resetting the chip.

An internal stack allows six levels of nested looping. A simple branch instruction (JUMP) acts as a GOTO statement that, on the assertion of an external pulse on a dedicated input pin, or a serial command via the I²C interface, switches TABLE execution to the line specified in the qualifier. The SYNC command produces a pulse of one clock cycle duration on a dedicated output pin at the transition between consecutive WAVES, and thus provides a trigger function for external synchronisation purposes.

Because TABLEs control the number and order of the WAVE data blocks, efficient changes to the overall readout patterns are realised by simple changes to the TABLE data. Multiple TABLEs may be called in succession which permits fast switching between programs for alternative readout modes, *e.g.*, switching between a full-frame readout mode, and a windowed readout mode.

To enhance the ASIC's immunity to single-event upsets, the internal memory contains error detection and correction logic. The error check codes are designed for single error correction and double error detection, and are created/tested by this block each time data is written/accessed. The system is based on a 5bit hamming code with an additional parity bit. The hamming code detects and corrects the single bit errors, and the parity bit is used to test the presence of two bit errors.

The ASIC is manufactured on a radiation-hard 0.8 μm BiCMOS process, and packaged in a 132 pin CQFP. To date, the ASIC is being used in five space missions, and proposed for two additional opportunities.

3. CCD PREAMPLIFIER/CDS/16 BIT ADC ASIC

One of the most challenging problems facing the designer of space-qualified CCD camera electronics lies in the video processing chain. With many applications now wishing to exploit the low-noise MHz-rate capabilities of current CCDs, the camera designer is faced with the problem of finding high-speed, low-noise op-amps, analogue-switches and analogue-to-digital converters that are radiation tolerant, and that can be procured with the appropriate levels of high-reliability component screening and space qualification.

One possibility is to upgrade and space-qualify one of the high-speed single-chip CCD video processors that have emerged for document scanners and digital cameras. Their attraction is the integration of a complete CDS/ADC video processor with programmable gain and offset adjustment, all in a single monolithic chip, and with low power consumption. However, while these new chips overcome many of the problems associated with high-speed analogue signal design using discrete components, there remain other issues to consider, particularly for space applications:

- Limited dynamic range: Only a few of the available ICs claim 14-16 bits precision, and the 16 bit parts typically disclose input referred noise of several LSBs rms, and thus questionable dynamic range. We have evaluated most of the current offerings and obtained our best results from the Analog Devices 14 bit AD9814 for which we measured a noise floor of 0.85 LSB rms.
- Large signal input requirement: The 14-16 bit ICs assume that the CCD will present several volts of input signal to achieve full dynamic range. We found that we had to operate the AD9814 with a 4 V signal input range to achieve the noise floor of 0.85 LSBs rms. We therefore need to add a low-noise preamplifier for use with the $\sim 4.5 \mu\text{V}/e^-$ output of our science-grade CCDs.
- Space qualification: Quite understandably, the commercial manufacturers are not attempting to meet the typical requirements of space-qualification and high-reliability component screening.
- Radiation tolerance: Again, the commercial manufacturers are not interested in radiation tolerance or single-event upset.

Noting these limitations, we therefore decided to develop and space-qualify our own CCD preamplifier/CDS/ADC video processing ASIC. A block diagram of our chip is shown in Fig. 2 and the main design features are listed in Table 4.

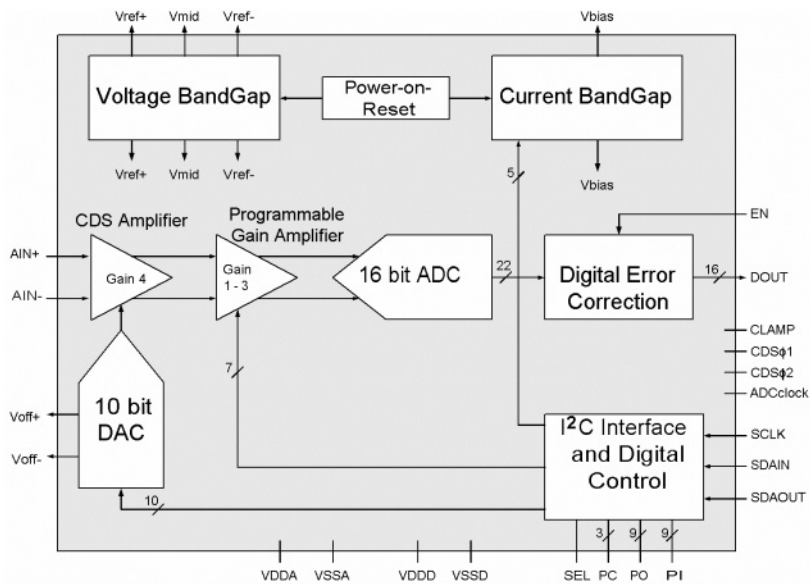


Figure 2. CCD Preamplifier/CDS/ADC Video Processor ASIC.

Table 4. CDS/ADC Video Processor ASIC.

Design Features
Differential input preamplifier, gain 4.0, optimized for a 1 V CCD signal input.
Fully differential CDS processor, optimized for 1 Mpix/sec CCD readout.
Programmable video offset, 10 bits, +/- 500 mV.
Programmable gain amplifier, 7 bits, gain 1-3.
Fully differential pipelined 16 bit ADC.
Input noise 0.5 LSB at 14 bits precision.
Differential Non-Linearity (DNL) 0.5 LSB at 14 bits precision.
I ² C interface for programmable gain and offset.
Triple-voting logic in digital interface and DAC registers for enhanced SEU immunity.
Radiation tolerant 0.35 μm CMOS process.

A key feature of our design is the incorporation of a preamplifier with a signal gain of 4, thus eliminating the need for an external preamplifier. The CCD need only present a 1 V signal to achieve full swing in the ADC with unity gain set in the programmable gain amplifier. The preamplifier has differential inputs for the cancellation of any common-mode interference that may arise between the CCD and the ASIC. The inputs are AC-coupled from the CCD in order to isolate the ASIC from the typically high CCD output voltage. An internal pixel-rate clamp switch is used to restore the input signals to optimal bias values.

CDS is performed within the preamplifier circuitry using switched-capacitors. A schematic is shown in Fig. 3. The design is again fully differential for enhanced rejection of common-mode noise and ground-bounce. A 10 bit DAC allows ± 500 mV of programmable DC offset to be introduced into the video signal. The bandwidth of the preamplifier/CDS circuitry is optimized for a CCD readout rate of 1 Mpix/sec.

A 7 bit programmable gain amplifier with a gain of 1-3 enables the CCD output voltage swing to be matched to the signal input range of the ADC. The ADC is a 16 bit fully differential pipelined converter using feedback capacitor switching in the amplifier stages, and over-ranging at intervals in order to minimise Differential Non-Linearity (DNL) due to capacitor mismatching and amplifier gain errors. A block diagram is shown in Fig. 3. The codes generated by each pipeline stage are fed into a delay block to ensure that all data appears at the output on the same clock cycle. Digital error correction adjusts for amplifier and comparator offsets.

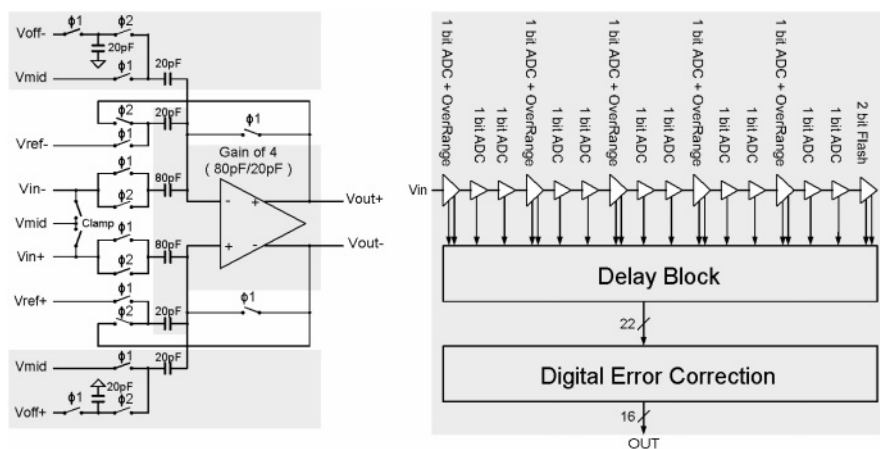


Figure 3. Preamplifier/CDS and ADC.

Our ASIC achieves a noise figure of 0.5 LSBs rms in 14 bits, equivalent to an input referred noise of 30 μ V rms within the 1 V signal input range. The digital dynamic range is therefore similar to the AD9814's, but our ASIC achieves this with a four-fold reduction in input signal range, thus eliminating the need for a preamplifier in our application.

It follows that the input referred noise of our ASIC is four times less than the AD9814's. We have achieved this by minimizing noise contributions while optimizing the design for our required 1 Mpix/sec bandwidth. In particular, we have employed significantly larger switched input capacitors within the preamplifier/CDS in order to minimise kT/C noise contributions.

Overall, we have been careful to balance the noise contributions from the kT/C input noise, the preamplifier itself, and the internal band-gap voltage references.

There are two band-gap references to generate the various bias voltages and the bias current required by the amplifiers and comparators. The bias points are connected to output pins to allow for external decoupling.

The ASIC is programmed through an I²C compatible interface, similar to that used in the Waveform Generator ASIC. Triple-voting logic is employed to enhance its SEU tolerance.

The ASIC is manufactured on a radiation tolerant 0.35 μm 3.3 V CMOS process, and packaged in an 84 pin CQFP.

4. 8 CHANNEL DAC ASIC

Our most recent ASIC development is an 8 channel DAC, intended to allow software programming of CCD bias and clock voltages. The arguments for its development are the same as for the CDS/ADC ASIC, namely a lack of suitable radiation-tolerant space-qualified multi-channel DAC ICs.

A block diagram of our ASIC is shown in Fig. 4. It contains eight 10 bit voltage-output DACs. Each DAC consists of an input register, a DAC register, a resistor ladder, and a multiplexer connecting the appropriate tap from the resistor ladder to an output amplifier.

The input registers and DAC registers provide double buffering. Data programmed into the input registers can be transferred into the DAC registers independently or collectively under the control of an external load-enabling clock.

Each DAC contains a resistor ladder of 1023 series-connected 100 Ω resistors. The 10 bit DAC code determines which tap from the resistor ladder is fed through to the output amplifier. The design is guaranteed to be monotonic.

Each DAC has independently controlled voltage reference inputs on both the top and the bottom of its resistor ladder for added flexibility in output range programming. An output-enabling function allows all DACs to be enabled or disabled collectively. Power-on-reset ensures that all DACs are initialized to zero.

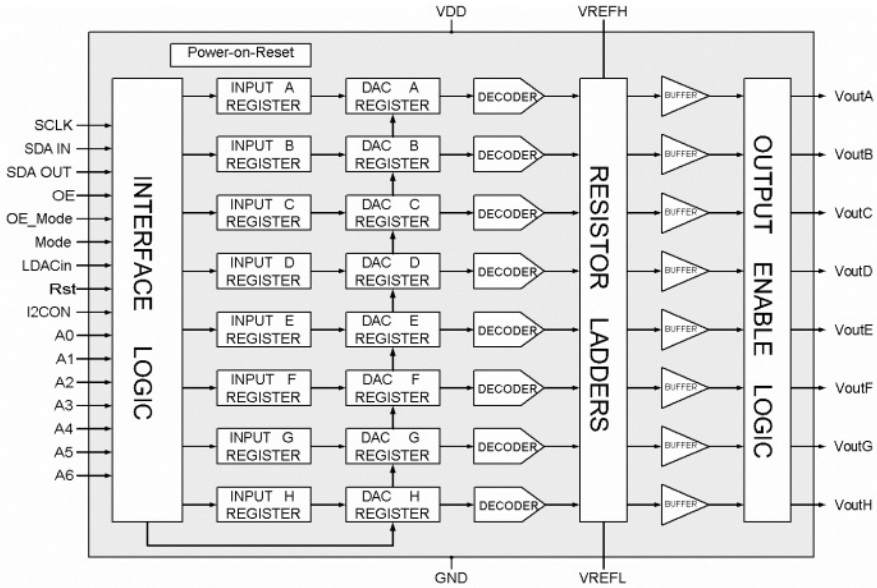


Figure 4. 8 channel DAC ASIC.

The ASIC is programmed through an I²C compatible interface like the Waveform Generator and CDS/ADC ASICs. Triple-voting logic is again incorporated to enhance SEU tolerance.

The ASIC is manufactured on the same radiation tolerant 0.35 μm 3.3 V CMOS process, and packaged in the same 84 pin CQFP as the CDS/ADC ASIC.

5. SUMMARY AND FUTURE DEVELOPMENTS

We have developed three ASICs aimed at reducing the size, mass and power requirements of space-borne CCD instrumentation that was initiated by the lack of appropriate commercially available space-qualified components. All three ASICs address the special requirements of radiation tolerance and protection against single-event upset in the space environment.

Our Waveform Generator ASIC is being used in five space missions, and proposed for two additional opportunities. We are planning to use our CDS/ADC ASIC in the SECCHI [2] CCD camera remote sensing instrumentation of NASA's Solar Terrestrial Relations Observatory (STEREO) mission.

The question of future developments now arises. Our medium term plans are as follows:

- We plan to upgrade the Waveform Generator ASIC with increased output channels, and an ability to extend waveform states by a predefined number of clock cycles. We are also planning to translate the design to a radiation hard 0.25 μm CMOS process and employ LVDS compatible inputs and outputs.
- A new version of the CDS/ADC ASIC will be optimized for 2 Mpix/sec CCD readout, and translated to a radiation hard 0.25 μm CMOS process.
- The DAC ASIC will be increased to 16 channels and also translated to the 0.25 μm CMOS process.

6. ACKNOWLEDGEMENTS

Our work has been funded from various sources including the UK's Particle Physics and Astronomy Research Council, Natural Environment Research Council, the Rutherford Appleton Laboratory of the Central Laboratory of the Research Councils, and the British National Space Centre (BNSC). Lawrence Jones, Bill Gannon, Andrea Fant and Quentin Morrissey are acknowledged for the detailed design and simulation of the ASICs. James King, Andrew Marshall and Duncan Drummond are acknowledged for much of the test work.

7. REFERENCES

- [1] French, M.J., Waltham N.R., Newton, G.M., and Wade, R., 1998, *A Single-chip CCD waveform generator and sequencer*, Proc. SPIE Vol. **3355**, p. 547-559.
- [2] Howard, R.A., Moses, J.D., and Socker, D.G., 2000, *Sun Earth Connection Coronal and Heliospheric Investigation (SECCHI)*, Proc. SPIE Vol. **4139**, p. 259-283.



"Why does the workshop have to end? I could stay here forever"
(Courtesy G. Burley)

SECTION V:

**DETECTOR TESTING AND
CHARACTERIZATION**

CHARACTERIZATION OF THE SI:AS BLOCKED IMPURITY BAND (BIB) DETECTOR IN KECK'S LONG WAVELENGTH SPECTROMETER (LWS)

Randall D. Campbell
W. M. Keck Observatory

Abstract: *Keck's Long Wavelength Spectrometer (LWS), is the facility instrument used for imaging and spectroscopy in the wavelength range of 3-28 μm at the Keck Observatory. LWS uses an 128×128 Si:As blocked impurity band (BIB) array manufactured by the Boeing Corporation. This paper discusses the method used for optimizing the detector's operating parameters at a temperature of 8.5 K and bias voltage of 1.2 V. A process for characterizing detective quantum efficiency of BIB detectors is also presented.*

Key Words: *Long Wavelength Spectrometer (LWS), Blocked Impurity Band (BIB) detectors, quantum yield, gain dispersion, detective quantum efficiency*

1. INTRODUCTION

The Long Wave Spectrometer, LWS, [1] is the W. M. Keck Observatory's mid-infrared facility instrument. The LWS detector is a Boeing 128×128 blocked impurity band (BIB) Si:As moderate flux array. The sensitive bandwidth of the array is approximately 3-28 μm . The detector was installed as an upgrade to the existing instrument and was restricted to minimal changes to the hardware and software, which narrowed the parameter space of detector operability (i.e., number of readout channels, pixel scale, physical envelope, etc.). The moderate-flux 4-channel readout device was chosen because its well depth and dark current properties matched the high to moderate background application of the instrument, which operates in imaging and low-resolution spectroscopy modes. The

operating parameters of the device were optimized during the upgrade and it has proven to be robust, reliable and relatively easy to operate. The detector and instrument have performed well and as anticipated, have produced many scientific results.

2. TEMPERATURE AND BIAS

The responsivity of BIB detectors is a strong function of temperature and bias, which is made evident by the data in Fig. 1. Measuring the signal to noise ratio over a range of operating temperatures and detector bias voltages was used to optimize these two parameters. A relatively high operating temperature of 8.5 K is preferred for LWS because of cryostat properties. 8.5 K is maintained with a heater control servo to compensate for the changing thermal coupling properties caused by dewar attitude. A higher bias voltage is also preferred because of the 12-bit ADCs in the readout electronics. Higher bias voltages used in BIB detectors increase the gain region and lead to higher signal amplification. The larger signal is advantageous for the LWS system in overcoming read noise and quantization noise of the 12-bit ADC sample.

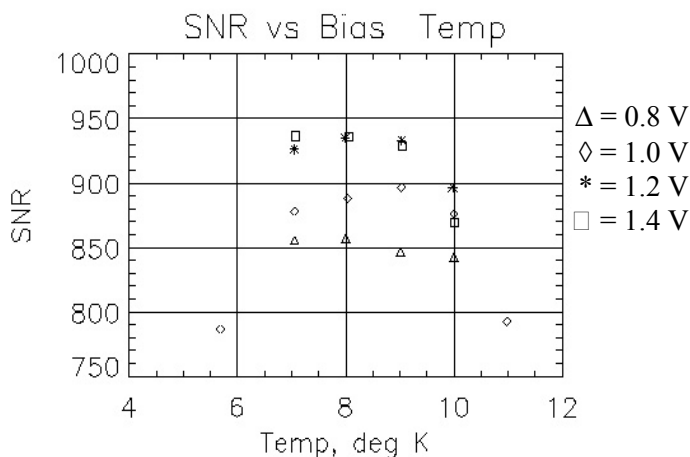


Figure 1. Detectivity as a function of bias voltage and temperature.

3. QUANTUM YIELD, GAIN DISPERSION, AND DETECTIVE QUANTUM EFFICIENCY

BIB detectors have signal amplification or gain that occurs at the interface of the blocking layer and the infrared active region [2]. Gain can

increase the quantum yield, ηG , but introduces an additional source of noise, denoted β . The β noise degrades the detective quantum efficiency (DQE) [2].

$$DQE = \frac{\eta G}{\beta G} \quad (1)$$

Figure 2 plots the quantity of measured electrons as a function of incident photons with the data used for measuring ηG [3]. The detector readout electronics conversion from electrons to DN can be determined using measurements of the readout electronics only. The number of incident photons was computed assuming an ideal radiator (black body). The slope of a linear fit to the data in Fig. 2 yields a value for $\eta G = 0.9 \pm 0.3$ if the instrument optical throughput, ϵ , is assumed to be 60%.

$$N_e = \epsilon \eta G N_{ph} \quad (2)$$

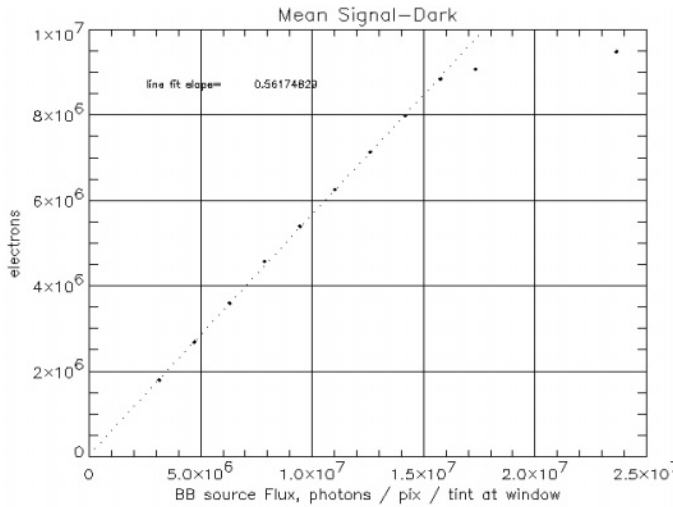


Figure 2. Characterization of the quantum yield of the detector.

To determine gain dispersion, βG , we plot the measured signal-to-noise ratio (SNR) vs. the ideal SNR, which is the square root of the measured signal (electrons) assuming read noise is negligible. Using the DQE relation,

$$SNR = \sqrt{N_{ph} \frac{\eta G}{\beta G}} \quad (3)$$

It can be shown that the slope difference from an ideal photon noise limited system is a measure of the gain dispersion, βG .

$$SNR = \frac{1}{\sqrt{\beta G}} \sqrt{N_e} \quad (4)$$

The slope of the linear fit in Fig. 3 is used to determine a value of $\beta G = 1.760.1$. Each of the measurements for ηG and βG yields a value for the detective quantum efficiency, DQE of

$$\frac{\eta}{\beta} = 0.5 \pm 0.15 \quad (5)$$

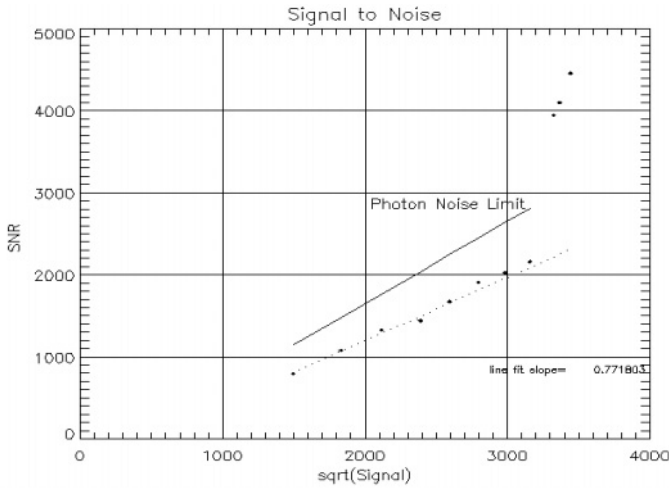


Figure 3. Characterization of gain dispersion.

4. ACKNOWLEDGEMENTS

I wish to thank Barbara Jones and Robert Piña for sharing their knowledge of mid-IR instruments. I also wish to thank Richard Matsuda and Ed Wishnow for laboratory help, and Robert Goodrich for editing the text.

5. REFERENCES

- [1] Jones, B. and Puetter, R. C., 1993, *Keck long-wavelength spectrometer*, Proc SPIE **1946**, p. 620.
- [2] Rieke, G.H., 1994, *Detection of light from the ultraviolet to the submillimeter*, ed. Visnovsky, K., Cambridge, UK: Cambridge University Press.
- [3] Piña, R. K. and Hanna, K. T., private communication.

CHARACTERIZING THE CCDS OF THE OMEGACAM WIDE-ANGLE CAMERA

Fabrice Christen¹, Cyril Cavadore², Dietrich Baade², Olaf Iwert², Konrad Kuijken¹, Boris Gaillard², Stéphane Darbon².

¹Kapteyn Instituut (Groningen), ²European Southern Observatory.

Abstract: *The OmegaCAM will cover the $1 \text{ deg} \times 1 \text{ deg}$ field of view of the ESO VLT Survey Telescope with thirty two $2K \times 4K$ pixels CCDs. Since the replacement of a unit detector or a rearrangement of the mosaic after commissioning is not an option, every detector needs to be fully characterized in advance. These chips need to be tested under astronomical operating conditions, which differ from average CCD manufacturer procedures. The changes realized in the testbench and the results of the measurements are described below.*

Key words: Charge-Coupled Devices (CCDs), CCD testing, CCD characterization

1. OMEGACAM CCD CAMERA

The OmegaCAM is a consortium composed of NOVA (The Netherlands Research School for Astronomy), Kapteyn Instituut, Leiden, Universitäts-Sternwarte München, Göttingen, Osservatori Astronomici di Padova e Capodimonte and the European Southern Observatory (ESO). The consortium is responsible for the development of the OmegaCAM instrument.

The instrument is a mosaic of 32 Marconi chips (CCD44-82 1-A57). It covers a field of view of $1 \text{ deg} \times 1 \text{ deg}$. (mosaic filling factor: 93%) with a sampling of $0.23''/\text{pixel}$. Forty science grade and sixteen engineering grade CCDs have been ordered and are being tested by the Optical Detector Team (ODT) with the ESO test bench.

The CCD44-82 1-A57 is a thinned, backside illuminated device with $2K \times 4K$ pixels of $15 \mu m$. Two serial readout registers are available. A Pt100 temperature sensor is provided on the chip. A single-layer HfO_2 anti-reflective coating ensures optimal sensitivity in the blue and the near UV. The invar package provides a high flatness level of $\pm 10 \mu m$.

2. THE TEST BENCH

In 1996, Amico and Böhm [1] designed the new ESO test bench. Several improvements were realized to optimize the turnaround time and the precision of individual CCD characterization. Two new detector heads, each accommodating two CCDs, have been manufactured and put into use. Scripts for a largely autonomous acquisition and data reduction have been written. Measurements of Quantum Efficiency (QE), Photon-Response Non-Uniformity (PRNU), dark current (short and long exposures), bias, readout noise, conversion factor, linearity, Charge Transfer Efficiency (CTE) and cosmetic defects (hot pixels, very bright pixels, dark pixels, traps, very large traps, bad columns, and coating blemishes) are routinely performed.

The primary capabilities of the test bench are long dark exposure times (up to several hours), configurable modes and readout speeds supported by the FIERA CCD controller, uniform illumination up to a field of 20 cm diameter provided by the integrating sphere, large wavelength coverage (300-1100 nm), good spectral sampling (1 nm) and remote control of all functions by software.

3. QUANTUM EFFICIENCY (QE) AND PHOTON-RESPONSE NON-UNIFORMITY (PRNU)

Quantum efficiency and photon-response non-uniformity are measured at an operating temperature of $-120^\circ C$. The repeatability is very good (error: $\pm 0.2\%$ max). The QE dispersion from device to device is increasing toward shorter wavelengths. The QE figures in the range of 300-400 nm are higher than the minimum specification (see Table 1 for mean values).

Table 1. Mean and standard deviation of the QE for 19 science grade devices.

Wav.[nm]	350	400	500	600	700	850	1000
QE [%]	62.5	82.9	83.7	79.1	69.9	39.9	4.5
rms [%]	8.7	4	3.8	3.7	3	1.9	0.2

PRNU is increasing at near-IR wavelength due to fringing effects (see Fig. 1(c)), and at near UV wavelength due to the backside laser annealing (“diamond pattern”), see Fig. 1(a).

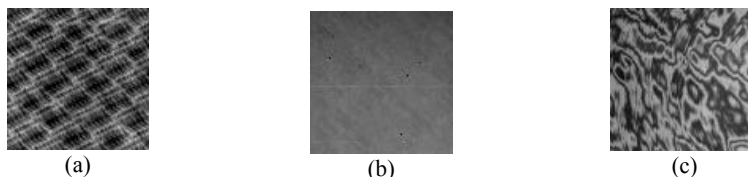


Figure 1. Example of flat field patterns at 350 nm (a), 600 nm (b) and 900 nm (c).

Between 420 and 870 nm the PRNU is photon noise limited (see Table 2 for mean values).

Table 2. Mean and standard deviation of the PRNU of 19 science grade devices.

Wav. [nm]	350	400	500	600	700	850	1000
PRNU [%]	3.5	1.6	1.2	1.2	1.3	2	8.3
rms [%]	0.8	0.3	0.3	0.3	0.4	0.8	2

4. COSMETICS AND COSMETIC DEFECTS

The general appearance of the images is inspected to search for anomalies (bright spot, patterns, 512×1K block stitching, scratches, parasitic light injected by on-chip ESD protection diodes (Fig. 2.) and inky pattern (Fig. 3.), six specific kinds of cosmetic defects are checked: hot and dark pixels (mean per CCD: 66, rms: 72), very bright pixels (mean per CCD: 5, rms: 4), traps (mean per CCD: 3, rms: 3), very large traps (mean per CCD: 1, rms: 2), and bad columns (mean per CCD: 2, rms: 2). The overall cosmetic quality of the OmegaCAM devices is very well within specifications.

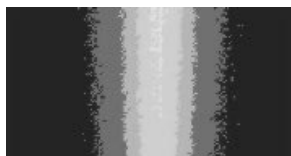


Figure 2. Part of a bias at 50 Kpix/sec, binning 15×15, 6ADU of difference between the center and the sides, gain= 0.55e-/ADU.

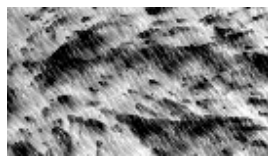


Figure 3. Part of a flat at 350nm, 50Kpix/sec, binning 15×15.

5. LINEARITY

The method consists of reading the CCD while it is illuminated with a light source (assumed to be constant on such short time scales). After flat fielding (the test is performed at 600 nm where PRNU effects are the lowest), the columns are averaged, applying a median filter. The residuals from a linear least-squares fit to the signal as a function of row number represents the non-linearity. Non-linearities are typically less than $\pm 0.3\%$.

6. ELECTRICAL PARAMETERS

- Conversion Factor (Gain): derived from the measurement of the mean signal on a flat field exposure and its variance (for 17 CCDs at -120 °C: $0.53 \pm 0.03\text{e}^-/\text{ADU}$ at 50 Kpix/sec).
- Readout Noise: spatial rms of the bias measured (for 19 CCDs at 50 Kpix/sec: $2.9 \pm 0.4\text{e}^-$, at 225 Kpix/sec: $4.4 \pm 0.7\text{e}^-$).
- Conversion factor and read-out noise are measured for both ports and at two speeds (50 and 225 Kpix/sec). The test bench is not read-out noise optimized because the main objective is to measure relative differences only.
- Dark Current: A median-filtered stack of five 1 hour dark frames is used (temperature: -120 °C, read out speed: 50 Kpix/sec, high gain mode: $\sim 0.55\text{e}^-/\text{ADU}$) is computed. The horizontal and vertical over scan pixels are used to determine the dark current. It is mostly less than $1\text{e}^-/\text{pix/h}$ (for 17 CCDs at -120 °C: $0.7 \pm 0.6\text{e}^-/\text{pix/h}$).
- Charge Transfer Efficiency: Two methods are used: one is based on the extended pixel response through the image over scan area (EPER), the other uses the standard Fe55 method (for 17 CCDs at -120 °C: horizontal CTE: $0.999997 \pm 3 \cdot 10^{-6}$, vertical CTE: $0.9999995 \pm 2 \cdot 10^{-7}$).

7. SUMMARY

For the OmegaCAM project 88 CCDs have been ordered (40 science grade, 16 engineering grade and 32 mechanical sample CCDs). 29 science grade and the entire engineering and mechanical sample have been delivered. All CCDs have been characterized according to the function of their group. To realise these tests, the CCD evaluation procedure was streamlined, the reliability improved and the accuracies were assessed. The results are generally satisfactory.

8. REFERENCES

- [1] Amico, P., Böhn, T., 1997, *ESO's New CCD testbench*, In J. W. Beletic and P. Amico (eds): Optical detectors for astronomy, Astrophysics and space science library, vol. 228, Kluwer Academic Publishers, Dordrecht, pp. 95-114.
- [2] <http://www.eso.org/~ccavador/testbench/Prism/CCDtest-US.html>

EMIR HAWAII-2 DETECTOR TEST BENCH

José J. Díaz¹, Fernando Gago¹, Francis Beigbeder², Francisco Garzón^{1,3} and Jesús Patrón¹

Instituto de Astrofísica de Canarias (IAC), ²Observatoire des Midi-Pyrénées, ³Departamento de Astrofísica, Universidad de La Laguna

Abstract: *EMIR is a multiobject intermediate resolution near infrared (1.0-2.5 μm) spectrograph with image capabilities to be mounted on the 10-m Gran Telescopio Canarias (GTC) as one of the first common user instruments. The GTC, located on the Spanish island of La Palma, is due for first light in early 2003. EMIR is being built by a consortium of Spanish, French and British institutions, led by the Instituto de Astrofísica de Canarias. The current development of EMIR is funded by GRANTECAN and the Plan Nacional de Astronomía y Astrofísica.*

The EMIR Electronic Team is committed to provide the full characterization of its detector and associated controller well in advance of the Instrument completion. To carry out this task in parallel with the instrument development, a Detector Test System (DTS) has been designed and manufactured. This test system is described along this poster.

Key words: *Espectrógrafo Multiobjecto InfrarRojo (EMIR), test bench, HAWAII-II, InfraRed (IR)*

1. THE EMIR DETECTOR TEST BENCH OBJECTIVE

The EMIR detector test bench (see Fig. 1) has been developed to characterize a HAWAII-II detector planned for the instrument. Moreover, most of the work carried out for the test bench will be of interest for the final instrument configuration. As an example, the fan-out board configuration has shown its suitability for thermal control, mechanical fixing and early signal amplification of the array. The data acquisition system, in particular the detector controller configuration and its required capabilities have also

been explored. To fulfill the EMIR requirements on frame rate it is mandatory to read the detector in a 32 output mode. It implies a fairly complex controller configuration and the possibility of using channel multiplexing or a system with 32 channels end to end is still under consideration.



Figure 1. Detector test bench in the optical lab.

2. OPTO-MECHANICAL SET-UP

The system consists of a cryostat containing the detector, fan-out board and a filter wheel working at cryogenic temperatures. The cryostat has an inner shield and the light path is baffled to avoid spurious radiation coming from undesired sources.

The cooling system is based on a two-stage close cycle cooler. The most powerful stage is connected to the cold plate and is in charge of cooling the most massive elements as filter wheel, shield, optical baffle, etc. The second stage is connected directly to the back of the fan-out board using a multithread flexible cold finger. Temperature stability is assured using a PID control implemented with a resistor and a temperature sensor.

The optical path consists of a cryostat window whose cap acts as a pinhole, and a filter, open or blank depending on the filter wheel position. Projecting an image onto the full detector was not an objective and is not possible due to the reduced size of the filters. What is assured is uniform

illumination using the pinhole. Figure 2 shows the entire mechanical configuration of the system.

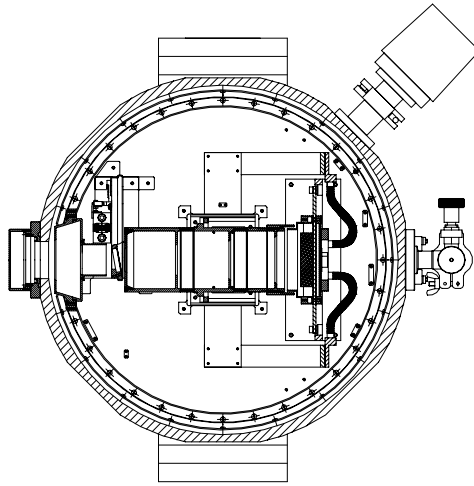


Figure 2. Mechanical configuration.

3. ELECTRONIC CONFIGURATION

The most remarkable electronic components are:

- The fan-out board: It includes the detector socket and the first amplification stage at cryogenic temperatures. It has been designed to support 32 parallel channel operation but is presently being used in a four channel mode.

We are using a single-supply (therefore, with low power consumption) rail-to-rail operational amplifier (Burr-Brown OPA350). It has shown a good behavior at cryogenic temperatures (77 K and even at 60 K) without appreciable loss of performance with respect to its nominal characteristics at room temperature.

Despite being of single-supply, this operational is faster (settling time around 500 ns to 0.01%) than others used in fan-out boards for the HAWAII-II so that the detector can be driven at its maximum readout rate without distorting the analog signal. Its internal noise and bandwidth make the noise added by the opamp negligible compared with the detector's noise.

The opamp is unity gain stable although it is currently being used with a greater gain (3.2). Care must be taken when loading the opamp with large capacitive loads (such as the capacitance of long

cables) in order to avoid unstable signals. However, this issue can be (and has been) worked out with an appropriate design.

As for the bias current, it is only about 1 pA. Together with a high input impedance (around $10^{13} \Omega$) it allows work with the detector when bypassing its internal amplifiers in order to reduce the glow.

- The detector controller: An ARC/IRL (Leach Gen-2) controller with 4 channels, a parallel data link and a serial command line has been used. The controller is also used in a four channel configuration. It is a critical part and its final configuration for the instrument is still under study.

Some modifications (gain and bandwidth changes) had to be made in the controller hardware to improve the analog chain performance. Furthermore, an external comparator (MAX961) had to be used to get much faster pixel clocks than the ones provided by the controller to properly drive the pixel clock signals.

The value of rising/falling times for CLK1, CLK2, CLKB1 and CLKB2 proved to be critical. We are now working with times less than 40 ns. CLK1 and CLK2 (the same for CLKB1 and CLKB2) must be complementary to each other within less than 25 ns (less than 15 ns in our case).

As can be seen, we are working with more restrictive time values than the ones suggested by Rockwell, which originally caused problems to drive the multiplexer and proved not to be suitable for our detector.

- The data storage and user interface: A PC with a frame grabber is used to acquire the detector data coming from the controller. A user interface based on Windows NT allows the user high flexibility in the definition of working parameters. Immediate visualization of the images and basic statistics are shown.
- Temperature control: Temperature control is carried out using a PID loop. Its parameters are remotely set from the computer and the temperature evolution is logged.
- Filter wheel control: The filter wheel is remotely operated through a serial line.

One important point to acknowledge is the ground and earth configuration, which is critical when trying to reduce noise. We are almost certain that we detector-limited regarding noise. After several tests, the final configuration (the one which proved to be the least noisy) coincides with the one suggested by theory. Noise contamination is clearly dependent on the ground/earth configuration and special care must be taken to properly design the system connections.

EMIR HAWAII-II FIRST TEST RESULTS

José J. Díaz¹, Fernando Gago¹, Francis Beigbeder², Francisco Garzón^{1,3},
Jesús Patrón¹

Instituto de Astrofísica de Canarias (IAC), ²Observatoire des Midi-Pyrénées, ³Departamento de Astrofísica, Universidad de La Laguna

Abstract: *EMIR is a multiobject intermediate resolution near infrared (1.0-2.5 μm) spectrograph with image capabilities to be mounted on the 10-m Gran Telescopio Canarias (GTC) as one of the first common user instruments. The GTC, located on the Spanish island of La Palma, is due for first light in early 2003. EMIR is being built by a consortium of Spanish, French and British institutions, led by the Instituto de Astrofísica de Canarias. The current development of EMIR is funded by GRANTECAN and the Plan Nacional de Astronomía y Astrofísica.*

The EMIR Electronic Team is committed to provide the full characterization of its detector and associated controller well in advance of the Instrument completion. A first run of tests have been performed on the engineering grade array. These tests facilitate to fine tune the test bench and to give a rough idea of the science grade detector behavior prior to its use.

Key words: Espectrógrafo Multiobjecto Infrarrojo (EMIR), test, HAWAII-II, infrared

1. THE OBJECTIVE OF THE TESTS

The main objective of the tests is to fully characterize the HAWAII-II detector to be used in EMIR. The final science-grade array tests are preceded by those of the engineering array. Even though this detector does not show the performance of a science grade device, its behavior in many aspects is comparable. The use of this device is really helpful to characterize and fine tune the detector test bench to set the correct parameters before plugging in the science grade detector. Moreover, some areas of the engineering grade

array show characteristics similar to a science grade array and thus the results will faithfully reflect what will be found with the final device.

2. TESTS PERFORMED TO THE ARRAY

Both qualitative and quantitative tests have been performed to the array. The most important qualitative test has been the detector behavior vs. clocking scheme (see Fig. 1). As a result, it has been obtained that the maximum readout speed is limited to 140 Kpix/channel. This will force the final EMIR system to a 32 channel configuration to assure a frame rate of at least 1 Hz.

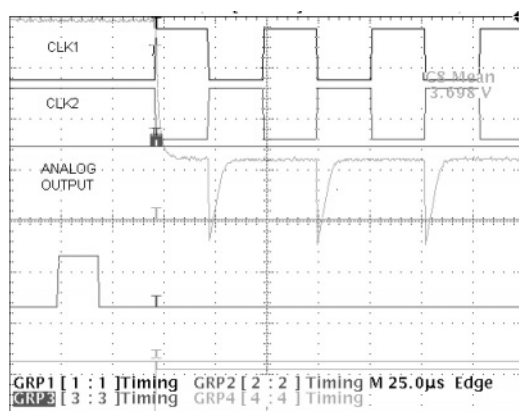


Figure 1. Timing pattern and output waveform

3. DETECTOR GAIN, WELL DEPTH

The detector gain has been calculated using the variance method. A series of images, with different integration time, or flux, is acquired and a signal-variance plot obtained. The resulting slope is $1/\text{gain}$ and intercepts the variance axis at $(\text{RON}/\text{gain})^2$. The resulting gain is $3 \text{ e}^-/\text{ADU}$ ($3.2 \text{ } \mu\text{V}/\text{e}^-$). To obtain a meaningful number, the pixel values have been filtered to consider only those with reasonable response and avoiding faulty pixels.

A mean value of 150 ke^- value has been obtained for the detector well depth. The linearity of the pixels varies from one to another but is similar for ‘science grade pixels.’ This points to a more uniform linearity among pixels for the science grade array.

4. DARK CURRENT

Dark current has been measured at 60 K and 77 K. The dark current is low, 75 e^- /hour @ 77 K (see Fig. 2) and 35 e^- /hour @ 60 K. As both values match with the instrument constraints, it will probably be used at 77 K to avoid the expected QE penalty for lower temperatures.

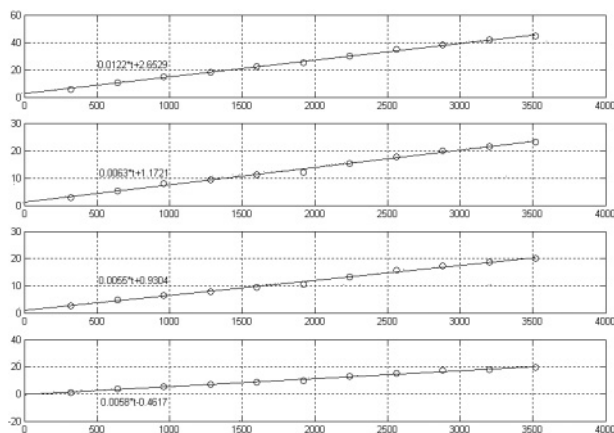


Figure 2. Dark current at 77 K.

Dark current measures give higher values for samples immediately after the reset cycle. The mean dark current diminishes with time. It has not been identified as the reason for this behavior; which is apparently different from what has been identified as reset anomaly. Further study is required to understand and calibrate or compensate this effect.

We have observed that a low frequency drift affects the results. It implies that a correction must be applied using the detector reference outputs or any other appropriate reference. The use of the reference outputs implies adding 4 extra AD channels to a fairly complex system with 32 outputs. Another possibility is to use a clamp circuitry to hold the reference and electronically compensate the drift. New methods are being explored to find a suitable method to correct the drift with no added electronics.

5. READOUT NOISE

The readout noise has been computed and, as a result, it has been obtained, for CDS, a mean value of 11 e^- . This magnitude is well within the expected performances and has been obtained by proper filtering of the faulty pixels. The Gaussian distributions obtained reflect the correct selection of the sample pixels. These graphics show the statistics obtained

for a window of 160k pix/quadrant where approximately a 0.0003% of the pixels, less than 50 pixels, have been excluded from the calculations.

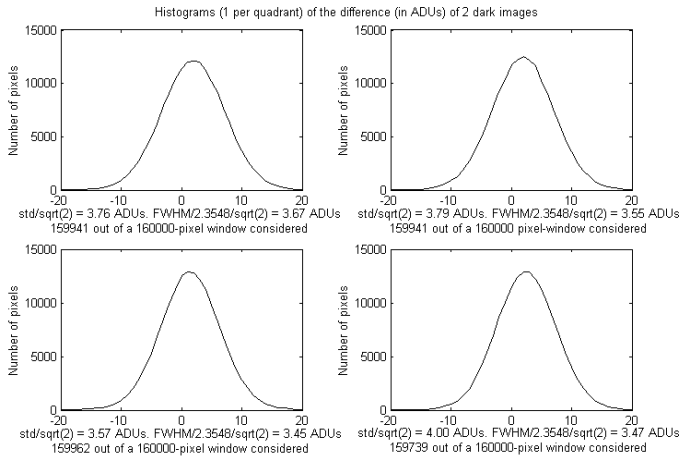


Figure 3. Read noise distribution.

6. CONCLUSION

As a result of the engineering grade array tests, a first adjust of the working parameters has been performed prior to the use of the scientific grade device. It is envisaged that pixel rate limitation will force the instrument to use a 32 channel configuration in its final system. The detector gain, read out noise, dark current and well capacity found for this device are promising and will hopefully be better for the scientific grade device. The low frequency drift found needs to be compensated, either analytically or by building a more complex system to avoid it electronically. Additional tests such as QE, crosstalk, image persistency, etc., need to be performed to complete the science grade detector.

TEST RESULTS WITH 2K×2K MCT ARRAYS

Gert Finger, Reinhold J. Dorn, Hamid Mehrgan, Manfred Meyer, Alan F.M. Moorwood and Joerg Stegmeier
European Southern Observatory

Abstract: *The performance of both an LPE 2K×2K engineering grade and a science grade array has been evaluated. Both arrays have a cut-off wavelength of $\lambda_c=2.6 \mu\text{m}$. At an operating temperature of 60 K, the dark current of the science grade array is $0.004 \text{ e}^-/\text{sec}$. The peak quantum efficiency of the science grade array is 84.4%. The readout noise is $14 \text{ e}^- \text{ rms}$ for a double correlated clamp and $5 \text{ e}^- \text{ rms}$ for readout with 16 Fowler pairs.*

Key words: *infrared array, HgCdTe, noise, dark current, quantum efficiency*

1. INTRODUCTION

In 1997 the University of Hawaii and ESO made a joint contribution to fund the HAWAII-II 2K×2K development. Within the framework of this contract two LPE 2K×2K HgCdTe arrays grown on a sapphire substrate have been delivered and evaluated. Both arrays have a cut-off wavelength of $\lambda_c=2.6 \mu\text{m}$.

2. MEASUREMENT SETUP

A prototype continuous flow test cryostat was built for the evaluation of the HAWAII-II arrays. The detector is cooled by a two-stage pulse tube closed-cycle cooler that has no moving cryogenic parts and is completely free of vibration. The second stage of the pulse-tube can reach a temperature of 21 K.

The arrays are read out by accessing the internal bus directly. All 32 analog outputs are used and fed into a symmetrical operational amplifier. It

is located near the focal plane on the fan-out board which is at cryogenic temperatures. In this configuration the on-chip output source followers are bypassed and switched off [1]. Hence, they do not glow when multiple sampling is applied to reduce the readout noise. This is an important advantage of using off-chip cryogenic amplifiers.

3. QUANTUM EFFICIENCY

The cut-off wavelength of the first engineering grade array was measured to be $\lambda_c = 2.58 \mu\text{m}$. The dark current of the engineering grade array was higher than expected and showed a temperature dependence yielding an effective temperature of one third of $T_{\text{eff}} = E_g/2Kb$, the typical temperature for a g-r conduction mechanism. Hence, the sensitivity of the array was investigated at wavelengths longer than λ_c . With a narrow band filter centered at $\lambda = 3.22 \mu\text{m}$ the quantum efficiency was determined to be 10^{-5} . Photon response at $\lambda = 3.22 \mu\text{m}$ was confirmed by measuring the transmission of the narrow band filter with a scanning grating monochromator. An extrinsic transition from impurity donors to the conduction band in either the multiplexer, the buffer layer, or the diode array could explain the excess dark current and the photon response at $\lambda = 3.22 \mu\text{m}$.

The quantum efficiency of the science grade array is above 0.68 over the whole spectral range of the detector and peaks in the K band at 0.84. The accuracy of the measurement shown in Fig. 1 is limited by the sensitivity of the pyroelectric detector used to calibrate the efficiency of the monochromator. The HAWAII-II science grade array has the highest QE of all LPE arrays ever evaluated at ESO.

4. DARK CURRENT

For the LPE science grade array the temperature dependence of the dark current yields the correct effective temperature $T_{\text{eff}} = 2360 \text{ K}$. The dark current is $0.004 \text{ e}^-/\text{sec}$ at 60 K and $0.20 \text{ e}^-/\text{sec}$ at 79.1 K . The cosmetic quality degrades substantially by raising the temperature from 60 K to 79 K .

Since the final arrays which will be installed in the NIRMOS multi-object spectrograph are MBE arrays grown on CdZnTe substrate with $\lambda_c = 1.9 \mu\text{m}$, a smaller format engineering array grown by using this technology was hybridized to a PICNIC 256×256 multiplexer. It has already been tested in order to validate the continuous flow concept for the NIRMOS cryostats. The MBE array shows excellent dark current performance. At a temperature of 100 K the dark current scaled to a pixel size of $18 \mu\text{m}$ is $0.008 \text{ e}^-/\text{sec}$. The persistence is strongly reduced in comparison to LPE grown MCT material, which demonstrates the potential of MBE on CdZnTe.

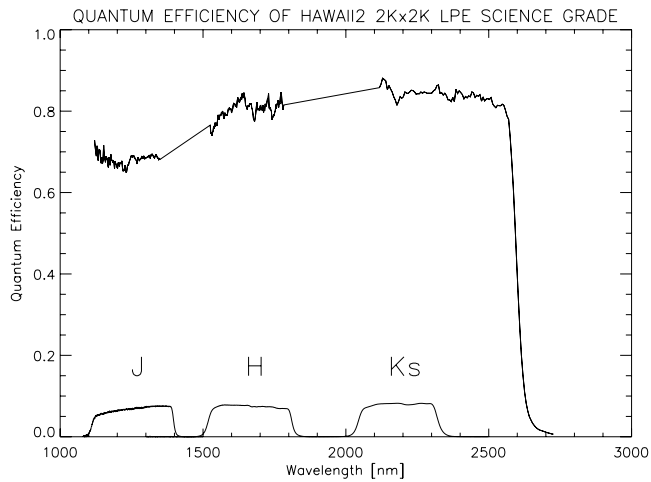


Figure 1. Quantum efficiency of LPE HAWAII-II 2K×2K HgCdTe science grade array.

The glow of the HAWAII-II multiplexer is substantially reduced in comparison to the HAWAII-I multiplexer. At the edges of the array the glow is 1.5 e⁻/frame and peaks to 3 e⁻/frame in the corners. The glow is negligible at a distance of 30 pixels from the edges.

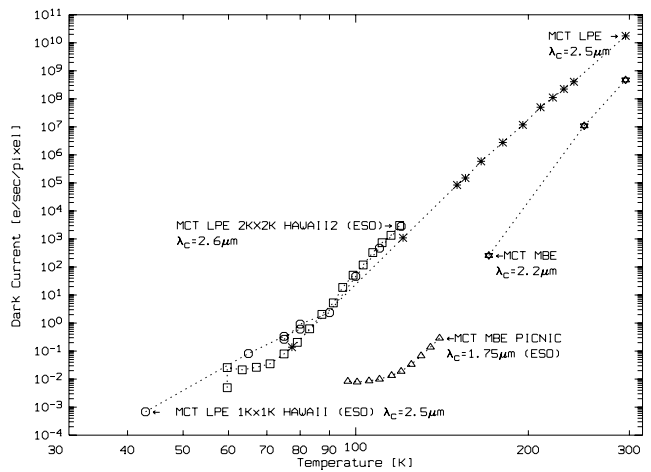


Figure 2. Dark current versus temperature for MCT LPE and MBE arrays and different λ_c .

5. READOUT NOISE

The readout noise has been measured with the unbuffered output reading out all 32 channels at a frame rate of 1.7 Hz. For a double correlated clamp it

is 12 e^- rms. With multiple nondestructive sampling using 16 Fowler pairs the readout noise can be reduced to 5.2 e^- rms. In the best quadrant the readout noise is as low as 4.4 e^- rms [2].

6. CONCLUSION

Although in most respects the HAWAII-II science grade array exhibits excellent performance, there are some problems associated with the HAWAII-II multiplexer such as rise times of < 50 nsec for clocks of the fast shift register and the complexity of using the reference output. Consequently, Rockwell redesigned the HAWAII-II multiplexer resulting in the new HAWAII-IIRG, which will be delivered with all MBE arrays presently on order by ESO.

7. REFERENCES

- [1] Finger, G., Mehrgan, H., Meyer, M., Moorwood, A., Nicolini, G., Stegmeier, J., 2000, *Performance of large format HgCdTe and InSb arrays for low background applications* Proc. SPIE vol. **4008**, p. 1280.
- [2] Finger, G., et al., *Readout Techniques for drift and low frequency noise rejection in infrared arrays*, these proceedings, pg. 435

THE HAWAII-2 2048×2048 HgCdTe DETECTOR ARRAYS

Klaus W. Hodapp¹, Jeff Kuhn¹, Robert Thornton¹, Everett Irwin¹, Hubert Yamada¹, Mark Waterson¹, Lester Kozlowski², John T. Montroy², Alan Haas², Kadri Vural², Craig Cabelli²

¹*Institute for Astronomy, University of Hawaii,* ²*Rockwell Scientific*

Abstract: *This paper discusses the design and testing of the new HAWAII-2 devices. The HAWAII-2 design is largely based on the very successful HAWAII-1 devices developed by Rockwell, but with an extended detector array size of 2048×2048. The device was designed for use in the AEOS spectrograph, a cross-dispersed spectrograph intended to cover a large spectral range in a single exposure, therefore, array size was of paramount importance.*

Key words: *HAWAII-2, detector array, multiplexes, pixel, reference signal, focal plane array, spectrograph*

1. INTRODUCTION

The development of the HAWAII-2 detector arrays was initiated by the Institute for Astronomy (IfA), under contract by the Air Force Research Laboratory, to develop a high-resolution optical and infrared spectrograph for the AEOS telescope. The European Southern Observatory and the Subaru Telescope Project joined the IfA in a consortium to have these devices developed at the Rockwell Science Center.

The HAWAII-2 devices are based on the successful HAWAII-1 devices developed by Rockwell in 1994. These devices have demonstrated the feasibility of fabricating large multiplexers with good fabrication yield and of fabricating reliable large format hybrid detector arrays [1]. The HAWAII-1 devices have shown very low dark current and low noise suitable for the low background conditions of high-resolution spectrographs.

The primary motivation for expanding the HAWAII-1 design was to build a cross-dispersed infrared echelle spectrograph with as much spectral coverage as possible in a single exposure. The design of this spectrograph has been described elsewhere [2] and the spectrograph is currently going through the commissioning phase.

2. DISCUSSION OF DESIGN TRADEOFFS FOR THE HAWAII-2 DEVICES

The HAWAII-2 devices introduced the opportunity for several design changes from the original HAWAII-1 detector arrays to address known shortcomings. A detailed technical review of some of these design features has been given by Vural et al. [3].

2.1 Packaging and Thermal Coupling

Thermal coupling of infrared detector arrays has traditionally relied on a "cold finger", a cooled metal surface pressed against the back of the ceramic chip carrier. The device was usually pressed against the cold finger by a frame that was spring-loaded against the front side of the chip carrier, in areas not covered by bond wires. This method can introduce bending forces into the chip carrier if the cold finger is not sufficiently large, and some HAWAII-1 devices have reportedly been cracked by excessive mechanical stresses.

For the much larger HAWAII-2 devices, we have searched for a package solution that eliminates the need for pressing the chip carrier against cold surfaces. Since our budget did not permit the development of a custom chip carrier and socket, we decided on a pin-grid array for the chip carrier (see Fig. 1) and the use of a Zero-Insertion-Force (ZIF) socket.

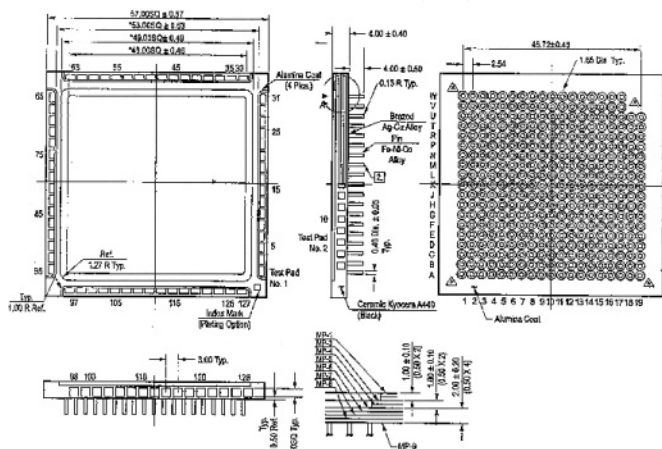


Figure 1. Drawing of the chip carrier used for the HAWAII-2 arrays.

Only the two outer rows of pins were needed for the electric contacts. The remaining pins on the pin grid could therefore be used to conduct heat out of the ceramic chip carrier through the ZIF socket into a thermal sink. This method of thermally connecting the device proved successful. We have not encountered any difficulties in achieving the proper operating conditions of the HAWAII-2 devices.

2.2 Multiplexer Layout

The pixel grid spacing in the HAWAII-2 devices is $18.0\ \mu\text{m}$, compared to $18.5\ \mu\text{m}$ for the HAWAII-1 hybrids. In the HAWAII-1 design, Rockwell had tried to maximize the unit cell size within the available maximum reticle size of the stepper aligner system. However, they later encountered some practical difficulties with assembling the hybrid, epoxy backfilling, and bonding of these devices, due to the tight space constraint imposed by this choice. For the HAWAII-2 multiplexers (see Fig. 2), a $18.0\ \mu\text{m}$ grid spacing was chosen to relax these constraints.

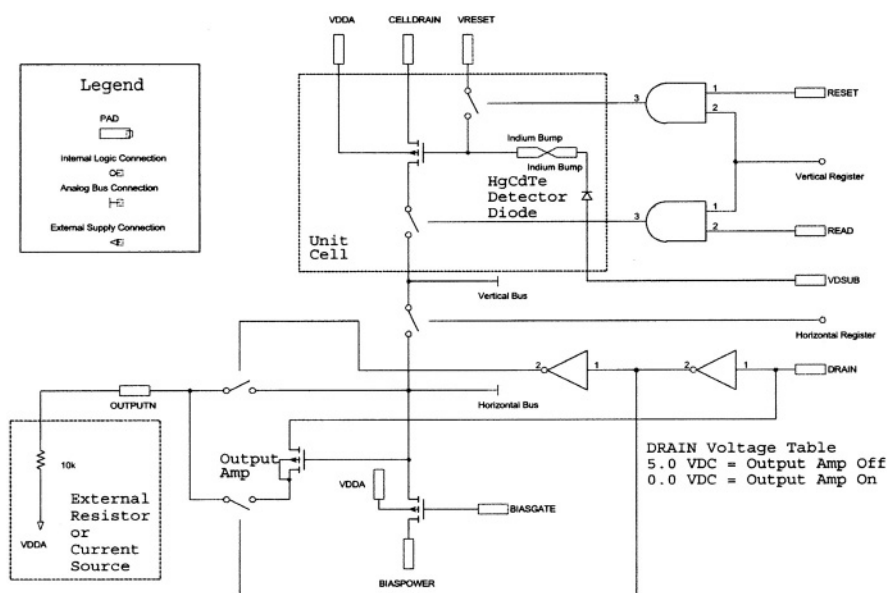


Figure 2. Simplified circuit diagram of the HAWAII-2 multiplexers.

The unit cell design is virtually identical to that used in the HAWAII-1 devices and uses 3 FETs per unit cell. Compared to the earlier NICMOS devices, this unit cell design does not allow individual pixels to be reset, rather, resetting is by column.

2.3 Reference Signal

The most common method of operating infrared detector arrays is to directly couple (DC couple) the signal of the output FET through a DC preamplifier to an analog-to-digital converter. Instabilities during the integration time of either the output amplifier operating point or other components in the signal chain directly translates into the signals. However, these are usually of little consequence, since astronomical measurements are taken in a differential manner. In ground-based imaging, data reduction procedures have to eliminate varying sky background flux anyway, and for most spectroscopic applications the signal is extracted by fitting and subtracting the residual sky background along the slit. Figure 3 shows a raw, *i.e.*, unsubtracted, data frame.

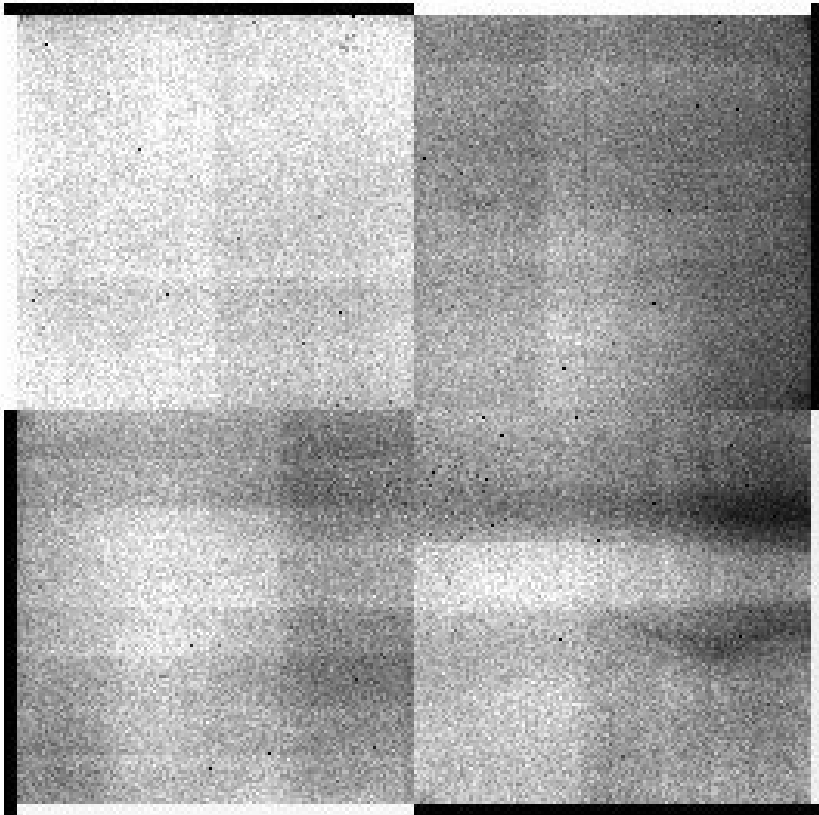


Figure 3. A HAWAII-2 raw, *i.e.*, unsubtracted, data frame, including the reference signal regions as we are using them for the AEOS spectrograph. At the end of each column, the reference signal is switched onto the signal chain and read 32 times and the resulting data are displayed as an additional 32 signal values per column.

Nonetheless, absolute measurements of dark current in switched-FET infrared detector arrays require extreme stability of the device temperature and of all voltages that couple into the signal. The temperature dependence of the output signal comes from the fact that the operating point of the output source follower is itself temperature dependent.

Since the HAWAII-2 devices were designed for a low-background spectrograph, we were motivated to implement a simple way of obtaining a signal level reference that is independent of photon flux or dark current, but is otherwise similar to the signal outputs in its dependence on temperature and voltages. The original design intent was to provide a reference signal output that is continually enabled while the device is being read out. However, due to a design problem, the reference signal output is now only active after the shift register has been clocked through all 1024 pixels in one quadrant. The reference signal now effectively functions in the same way as the overclocking in CCDs that is used to establish a signal level reference. While the reference signal in this form is useful for its original purpose of detecting very slow signal drifts, it cannot be used to calibrate out higher frequency pickup signals, like 60 Hz pickup noise.

2.4 Output Amplifier Options

The HAWAII-2 is organized as four electrically independent quadrants, fabricated from separate mask sets and with no stitching of electrical connections between them.

The lowest number of output amplifiers that can be used is four, one per quadrant. This gives similar output characteristics, which is important as the community is familiar with from the NICMOS and HAWAII-1 devices.

In order to facilitate faster readout options, the HAWAII-2 device also offers the option of reading the signal through a total of 32 outputs, 8 per quadrant. In this mode, the HAWAII-2 can be read out faster than the HAWAII-1, despite having a total pixel count which is four times as large.

In the simplest mode of operation, the signal of a group of 128 columns is read through a specific output amplifier. It is also possible to read the device in "shuffle mode", where the signals from a given group of 128 columns are successively read through each of the 8 amplifiers in a quadrant. This can be used to minimize fixed-pattern effects introduced by always reading through the same signal chain, and can be used to bypass defective signal chain channels.

2.5 Glow Minimization

Electroluminescence in CMOS components is the inevitable byproduct of operating them. These so called glow effects can, however, be minimized by

placing high current elements away from the photosensitive areas of the device.

Glow effects are an important limitation of the sensitivity of infrared detector arrays. Depending on the operating conditions, glow can be produced at any time during the integration and readout, but it is typically possible to turn off the output amplifiers and other major glow sources during the staring integration, outside of the device readout. When operated in this way, glow was only a minor nuisance in NICMOS and HAWAII-1 arrays in the double-correlated mode of operation. However, when multiple samples are used to further reduce the read-noise, glow is produced in each of these reads. After a number of reads, shot noise associated with glow dominates the total noise, thereby preventing further sensitivity gains from multi-sampling. Efforts were made to reduce the glow in the HAWAII-2 multiplexers compared with the HAWAII-1.

As a result of efforts to reduce the number of active components in the shift registers, the HAWAII-2 clocking is somewhat more complex than the HAWAII-1. Even when using the HAWAII-2 under low background conditions in the AEOS spectrograph, we find that glow is concentrated in a few locations on the perimeter of the array, which does not pose a problem in practice.

The HAWAII-2 multiplexers were fabricated using the same 0.8 μm design rule CMOS process that had been used for the HAWAII-1.

2.6 Detector Material

For the initial HAWAII-2 devices produced under this program, the detector diode arrays were fabricated in the PACE-1 process, the same that was used for the HAWAII-1 devices. In the PACE-1 process, the detector material (HgCdTe) is grown by liquid-phase epitaxy on a sapphire substrate with a vapor deposited CdTe interface layer. This production process is well understood and could be scaled up to 2048 format with little development cost. It was for these practical reasons that this process was chosen, despite its known disadvantages. None of the components involved in the PACE-1 process form matching crystal lattices, thus defects propagate into the PN junctions of the HgCdTe diodes. These defects manifest themselves as reduced quantum efficiency, higher dark current, and residual image effects.

2.7 Hybridization

One of the main technical challenges in fabricating the HAWAII-2 devices was the hybridization of the large focal plane array. However, after some initial experimentation, the first science-grade hybrids were produced with remarkably high interconnect yield. The first science-grade device delivered to the IFA (see Fig. 4) had 99.97 % operable pixels [4].

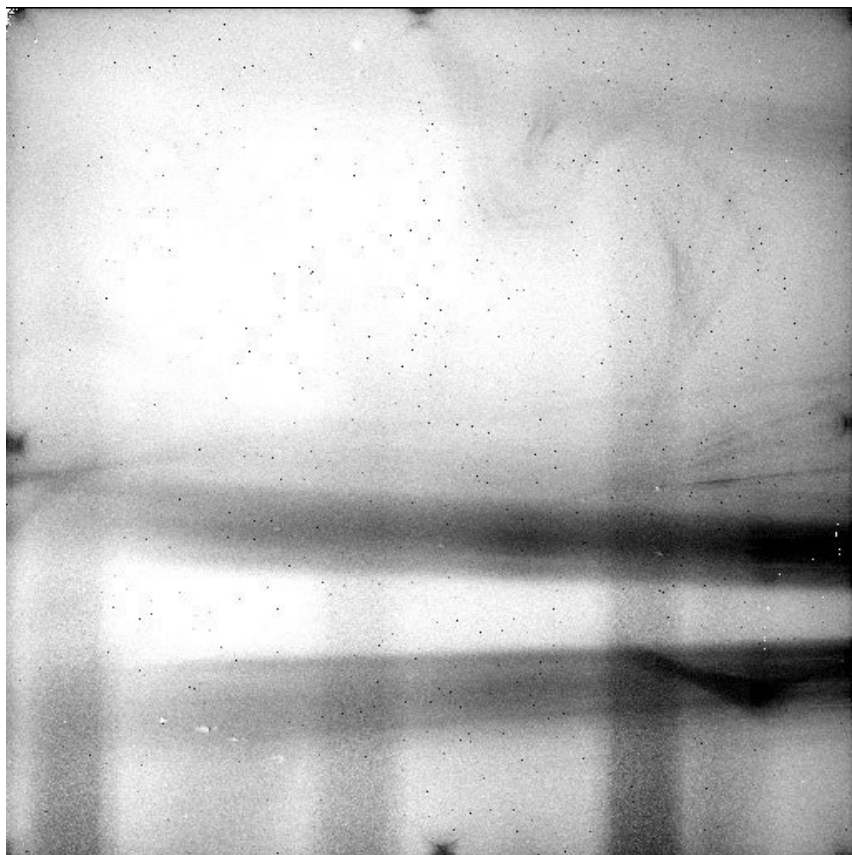


Figure 4. The result of a least-square linear fit through 99 reads of the HAWAII-2 device in the AEOS spectrograph, each read taking 21.6 sec. Glow from the output amplifiers and other multiplexer components is visible near the edges of the device, but most of the flux comes from stray light in the spectrograph that still needs to be eliminated.

3. DEVICE OPERATION FOR THE AEOS SPECTROGRAPH

For the AEOS spectrograph, long integration times are the norm and consequently, we have not gone through the extra effort and cost of using all the available 32 output amplifiers. Rather, the device is readout relatively slowly through one amplifier per quadrant. The HAWAII-2 is controlled by a San-Diego State (R. Leach) controller. We added a video switcher board to this system that allows switching from reading the output amplifier signal to reading the reference output. With this design, the detector signal and the reference signal share most of the signal chain components.

We have decided to use the internal output amplifiers of the HAWAII-2 multiplexer. The more complex alternative would have been to use the direct bus output and boost the signal with external JFETs. The glow effects produced even in the most demanding multi-sample operation of the array only affect small areas (about 50×50 pixel) near the glowing components at the edge of the detector array. These small areas of glow will not, in practice, affect the intended use of the HAWAII-2 array in our spectrograph.

As with all infrared arrays with DC coupling of the output signal, the thermal stability of the multiplexer during readout is important to assure a uniform, flat dark level. On long time constants, proper thermal control of the device will keep signal drifts at insignificant levels and remaining drifts can be measured and calibrated by use of the reference signal. However, internal heating effects on time constants of the order of the readout time are more difficult to control. In the simplest readout scheme, correlated double sampling, the device is reset (by column), followed by the first read of the correlated pair, then the integration time, and finally the second of the correlated reads. In this scheme, the second read is preceded by a long integration time during which the device is not being clocked, while the first of the correlated reads is preceded by the reset frame. Therefore, the thermal conditions in the multiplexer, in particular the output amplifiers, are not identical. When subtracting two CDS frames taken under these conditions, the amplifier instabilities do not subtract out perfectly. In practice, they do subtract out sufficiently well for direct imaging under moderate background levels, but for ultra-low background operation, the subtraction is often less than perfect.

One way of mitigating this problem is to introduce a waiting period between the reset frame and the first correlated read, so that the multiplexer can cool back to the cold-start condition. The other alternative is to precede both the correlated reads by readout activity for a sufficient time to stabilize the multiplexer in the continuous-operation condition. Both methods work well. In addition, the reference signal of the HAWAII-2 can be used to further calibrate the warm-up effects in the multiplexer.

A very advantageous mode of operation of infrared arrays is sampling-up-the-ramp, *i.e.*, resetting the device and then repeatedly reading the devices until the desired integration time has elapsed. For signals well below the saturation level it is sufficient to fit a straight line through the signals obtained in each frame. Beyond simple least-square line fitting, it is possible to allow for the detection of cosmic ray hits during the ramp and for the detection of saturating pixels.

4. CONCLUSIONS

The development of the HAWAII-2 detector array has been successful in providing a large format focal plane array for the AEOS spectrograph and other instruments. While the design is largely based upon the successful design of the HAWAII-1 devices, several incremental improvements were made. Our implementation of a reference signal proved the very useful and leads to the design of far more capable reference pixel and reference signal systems in future detector arrays.

5. REFERENCES

- [1] Hodapp, K.-W., et al., 1996, *New Astronomy*, **1**, p. 177
- [2] Hodapp, K. W., Mickey, D. L., Stockton, A. N., Luppino, G. A., Thornton, R. J., Waterson, M., Maberry, M., Irwin, E., Young, T., and Yamada, H., 2000, *SPIE* **4008**, p. 778.
- [3] Vural, K., Kozlowski, L. J., Cooper, D. E., Chern, C. A., Bostrup, G., Cabelli, C., Arias, J. M. Bajaj, J., Hodapp, K., Hall, D. B., 1999, *SPIE* **3698**.
- [4] Kowlowski, L. J., Montroy, J. T., Cabelli, C., Cooper, D. E., Chen, A., Bostrup, G. L., Bai, Y., Vural, K., Hodapp, K., and Hall, D. 2000, *SPIE* **4008**, p. 1240.



Paul Jorden (left) is amazed to hear that EEV has been once again renamed to Marconi, oops, make that E2V.



Despite the high security measures in place, an “unknown” detector salesman made it through. Notice the enlarged detail of the contract he is offering....



Dick Bredthauer is officially an asteroid.

HOW ACCURATE ARE QE MEASUREMENTS?

Binxun Ye and Qian Song

National Astronomy Observatories, Chinese Academy of Sciences (CAS)

Abstract: *The accuracy of the Quantum Efficiency (QE) test facility in NAOC (National Astronomical Observatory of China) is evaluated. After thorough testing an accuracy of 2.3% is reached.*

Key words: *Charge-Coupled Device (CCD), Quantum Efficiency (QE) evaluation*

1. MECHANISM

The signal intensity to obtain the measurements is acquired by exposing the camera to a uniform, calibrated monochromatic light field, of which the wavelength is tuneable [1]. Then, the QE is derived from the following equation:

$$QE = \frac{S \cdot G \cdot E_{\text{photon}}}{t \cdot W_m \cdot A} \quad (1)$$

where S is the averaged pixel output of the signal in ADU over the censored area (1.0 cm^2), G , the camera gain in e^-/ADU , E_{photon} , the energy of one photon of the testing wavelength in joule, t , the exposure time in sec, W_m the irradiance flux of the uniform illumination at the position of the CCD surface in w/cm^2 , and A , the area of a pixel in cm^2 .

2. EXPERIMENT SETUP

The uniform light field utilized is produced by an integrating sphere using a monochromator as a light source. The irradiance flux, W_m , is measured by two photodiodes: the standard probe and the monitoring probe. The standard probe is calibrated and can produce the power (W) of the incident light on 1 cm^2 area, the W_c . The monitoring probe is attached to a port on the integrating sphere to observe the intensity shift

of the light and give the readout of electricity I_c , when measuring W_c and I_m , while exposing the camera. W_m can be derived by [2]

$$W_m = \frac{I_m}{I_c} W_c \quad (2)$$

3. ACCURACY ANALYSIS

From the differential (3),

$$d(QE) = QE \cdot \left(\frac{dS}{S} + \frac{dG}{G} + \frac{dE_{photon}}{E_{photon}} - \frac{dt}{t} - \frac{dW_m}{W_m} - \frac{dA}{A} \right) \quad (3)$$

the variance of QE , δ_{QE}^2 , can be derived from

$$\left(\frac{\delta_{QE}}{QE} \right)^2 = \left(\frac{\delta_S}{S} \right)^2 + \left(\frac{\delta_G}{G} \right)^2 + \left(\frac{\delta_{E_{photon}}}{E_{photon}} \right)^2 + \left(\frac{\delta_t}{t} \right)^2 + \left(\frac{\delta_{W_m}}{W_m} \right)^2 + \left(\frac{\delta_A}{A} \right)^2 \quad (4)$$

W_m and $\delta_{W_m}^2$ can be derived the same way.

3.1 Measurement of W_m

The linear response of the standard probe and the monitoring probe was examined and found to have a correlation coefficient of 0.99992. Therefore, the nonlinearity of the two probes can be ignored. Using (2) the instability of the testing light can also be removed. The RMS of the readouts of the two probes remains 4 magnitudes lower than the readout values and can, thus, also be ignored. The calibration error of the standard probe is difficult to evaluate and, thereby, we decided not to include it in our discussion. However, when compared with a probe calibrated by the China Institute of National Standards, the difference between the two was rather small.

While measuring W_c , the standard probe cannot be placed at the same position as the CCD and which causes W_c error. The irradiance flux of the light field changes roughly with the inverse square of the distance from the outlet port of the integrating sphere. With the help of a distance-measuring microscope and a vernier caliper, the positioning error can be controlled to less than 0.5 mm accuracy. The CCD is purposely placed at least 60 mm away from the outlet port of the integrating sphere for this purpose. Due to these efforts, the error of the W_c induced by the positioning error can be controlled within 0.5%. The stray light, photons that are not testable in the test light flood cause W_c and S measurement errors. This is discussed in the next section.

3.2 Stray light

The stray light level of the monochromator, $Stray(\lambda)$, is obtained with an He-Ne laser source. Using this stray light calibration, the induced error can be computed. λ_l is the testing wavelength. $P(\lambda_l)$ is the number of photons of the wavelength λ_l that reach the sampled pixels while $Stray(\lambda)$ is of the stray light photons. QE is the actual quantum efficiency of the CCD and qe is the measured quantum efficiency. $\omega(\lambda)$ is the response of the standard probe. The measured number of photons that reach the CCD pixel is

$$P(\lambda_l) + \int Stray(\lambda) \frac{\omega(\lambda)}{\omega(\lambda_l)} d\lambda \quad (5)$$

The measured number of the induced photo-electrons in the CCD pixel is

$$P(\lambda_l) \cdot QE(\lambda_l) + \int Stray(\lambda) \cdot QE(\lambda) d\lambda \quad (6)$$

From (5) and (6) it can be derived that either,

$$qe = \frac{P(\lambda_l) \cdot QE(\lambda_l) + \int Stray(\lambda) \cdot QE(\lambda) d\lambda}{P(\lambda_l) + \int Stray(\lambda) \cdot \frac{\omega(\lambda)}{\omega(\lambda_l)} d\lambda}, \quad (7)$$

or

$$qe = QE(\lambda_l) \left\{ 1 + \frac{\int Stray(\lambda) \left[\frac{QE(\lambda)}{QE(\lambda_l)} - \frac{\omega(\lambda)}{\omega(\lambda_l)} \right] d\lambda}{P(\lambda_l) + \int Stray(\lambda) \cdot \frac{\omega(\lambda)}{\omega(\lambda_l)} d\lambda} \right\} \quad (8)$$

Then the QE curves with the QE for a typical frontside-illuminated CCD and a backside-illuminated are calculated. After comparison, the averaged error rate is around 2%.

3.3 Shutter timing

To accurately and repeatability obtain the timing of the shutter, it is put between a stably powered lamp and a fast-respond photodiode. The time in which the shutter is open is measured by an electronic counter with a nanosecond time resolution. With repeated testing it is found that when exposing time surpasses 500 ms the RMS/average is below 0.06%. Therefore, timing error can be neglected.

3.4 Measurement of S

In the illuminating light flood, the CCD area selected to perform the measurements is not exactly the same size of the standard probe [3]. Thus, if the light field is not perfectly uniform, it can cause measurement error. To evaluate such error, we assume that the non-uniformity of the illumination is 1%, that both of the selected CCD area and the sensitive area of the standard probe are 1 cm^2 , and that there is a 10% area in which the two do not overlap. The difference between the measured irradiance flux and the actual one illuminates on the selected CCD area is then within 0.01%. Therefore, the error caused by the ununiformity of the illumination can be ignored.

The noise readout values cause signal measurement error too. If we assume that the noise floor is 100 e^- , the averaged signal readout is $10,000 \text{ e}^-$ and the number of selected pixels is 500,000 (approximately 1 cm^2 with bad pixels removed), then the impact of the noise floor to the averaged signal is only 0.14 e^- and, at the signal level of $10,000 \text{ e}^-$, the shot noise will be 100 e^- . Therefore, noise can also be dismissed from our error count.

3.5 Measurement of camera gain

The photon-transfer technique adopted to measure the gain and the error can be controlled to approximately 1% accuracy.

4. CONCLUSION

The total effects of all the sources discussed above result in an error rate of 2.3% in our QE measuring.

5. REFERENCES

- [1] Amico, P. & Böhm, T., 1998, *ESO's New CCD Testbench*, Exp. Astr., **8**, pp. 1-8.
- [2] Tulloch, S., 1999, *The ATC QE Measuring System*, 1999 <http://www.ing.iac.es/~smt/publications/ATCqemeasurement.PDF>
- [3] ING Detector Group, 1999, *Quantum Efficiency Measurement Rig*, http://www.ing.iac.es/~eng/detectors/QC/qe_rig.htm

SECTION VI:

FOCAL PLANE MOSAICS

THE ELECTRONIC CONTROLLER OF THE 40 CCDS MEGACAM MOSAIC

Jean de Kat, Olivier Boulade, Xavier Charlot, Philippe Abbon, Stéphan Aune, Pierre Borgeaud, Pierre-Henri Carton, Dominique Eppelé, Pascal Gallais, Remy Granelli, Michel Gros, Jean Y. Roussé, Pierre Starzynski, Laurent Vigroux

Département d'Astrophysique, de physique des Particules, de physique Nucléaire et d'Instrumentation Associée (DAPNIA), Commissariat à l'Energie Atomique (CEA)

Abstract: *MegaCam is the last generation wide-field imaging camera, which is presently mounted at the prime focus of the Canada France Hawaii Telescope. It is based on a mosaic of 40 $2K \times 4.5K$ backthinned CCDs.*

Key words: *Charge-Coupled Device (CCD), MegaCam, CCD mosaic, cryostat, driver board, readout board, sharc board, power board*

1. THE CHALLENGE OF THE CONTROLLER

How is it possible to fully control a mosaic of 40 scientific CCDs of 10 Mpixels each, and achieve a readout of the 80 channels with less than 5 ϵ noise in 20 sec?

2. THE FINAL RESULT: ***THE MOST COMPACT CONTROLLER IN THE WORLD!***

To achieve the results mentioned above we connected 110 V to the optic fibers bundle on each crate. Crates are hermetically sealed to preserve boards against moisture or dust. We did not use a fan; the heat produced (75 W/crate) is extracted by a regulated glycol closed loop. Six LEDS on top give information about the status controller. Figure 1 shows the controller and the CCD mosaic used. Table 1 gives an overview of the MegaCam CCD Mosaic.

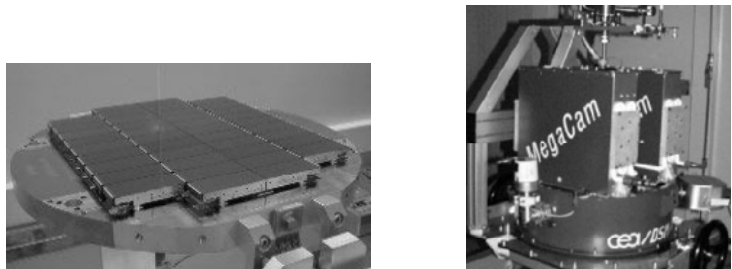


Figure 1. The CCD Mosaic (left) and the controller mounted on the cryostat (right) .

Table 1. The main characteristics of the MegaCam CCD mosaic.

Total FOV	$\Phi\ 1.4^\circ$	Mosaic filling factor	93 %
Focal plane size	313 mm×261 mm	Operating temperature	150 K
Array size	20K×18K	Spectral range	350 - 1000 nm
Number of CCDs	40	Minimum exposure time	1 sec
CCD type	Marconi 4290	Number of CCD amplifiers	2 (split register)
CCD size	2K×4.5K	Readout time	20 sec
Pixel FOV	0.18"×0.18"	Readout noise	<10 e ⁻
Pixel size	13.5 μ m ×13.5 μ m		

3. THE CRYOSTAT CONNECTORS

The custom through pass consists of a PCB glued on an aluminum flange with epoxy to achieve the required hermeticity (see Fig. 2).

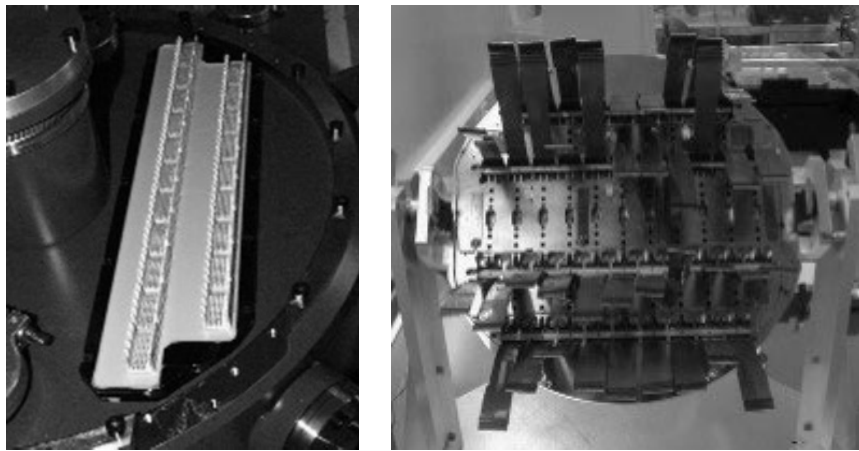


Figure 2. One of the two custom hermetic through pass (left) and the 40 internal flex circuits (right).

This results in large hermetic through pass (960 pins each one) at a reasonable cost, with the possibility of using two different connectors inside and outside the cryostat.

A metal layer enhances the electromagnetic protection. Different shorted caps are used to protect the CCDs against static discharge during the mounting, or when the controller is removed.

Each flex circuit consists of a folded kapton circuit with four layers of printed copper strips. One end of the zero insertion force connector delivered with the CCDs was welded, and a low profile socket was connected to the other end. This provides both the simplicity/reliability of a flat cable, the performance of a PCB and gives 15 cm identical paths between the output of the CCDs and the preamplifiers. There are no components on the flex in order to minimize out gassing and to facilitate maintenance.

4. THE ASSEMBLED SYSTEM

The components of the assembled system are listed in Table 2.

Table 2. The components of the assembled system.

528 Independent CCDs Biases
528 Independent CCDs Clocks Levels
704 Independent CCDs Clocks
1400 Amplifiers
80 DACs (8 bits/12 channels)
80 ADCs (16 bits)
2 Digital Signal Processors
16 Programmable Logic Devices
8 Fibers in 1 bundle
12 Boards in 2 crates
<150 W Dissipation (including power supply)

The high integration associated with the ‘natural’ architecture of the system allows minimum size, weight and dissipation, and results in a system with almost no connectors. This enhances reliability and makes management of the system easier. All the components have been chosen according to low size and low dissipation criteria. All the boards are designed to manage a strip of 11 CCDs. The driver board (see Fig. 3) is the main board, carrying the readout board as a mezzanine. The heat exchanger (made by AAVID) passes heat from crates to glycol loop. Inside the crate, natural convection is sufficient to cool the boards.

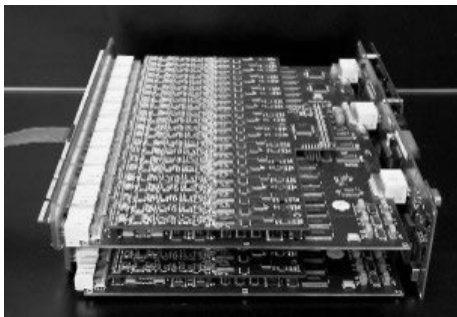


Figure 3. The boards assembled, which yields half of the controller.

5. THE FOUR CUSTOM BOARDS

There are four boards that were produced for the controller. These boards are shown in Fig. 4 and 5.

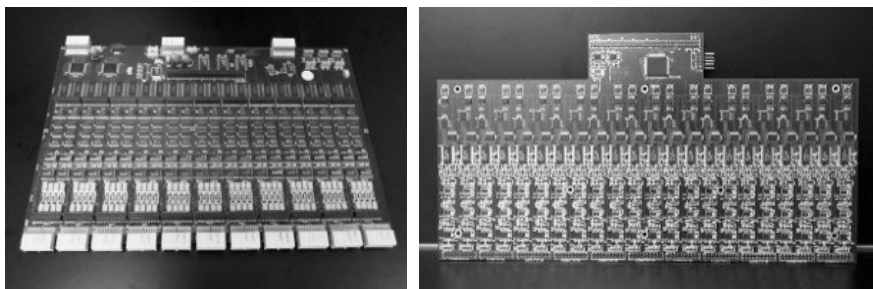


Figure 4. The driver board (*left*) and the readout board (*right*).

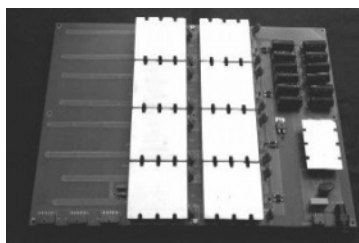
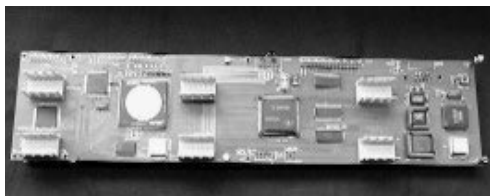


Figure 5. The sharc board (*left*) and the power board (*right*).

5.1 The Driver Board (10 layers)

The driver board (see Table 3) generates a battery of 12 independent bias voltages and 16 shifting clocks for each CCD connected. All voltages are downloadable from the user interface. Protection from over voltage is also provided. A network of analog multiplexes associated with 12 bits ADC allows us to monitor all the signals generated, and also to measure CCD and

board temperatures. Moreover, it is used to auto-calibrate the whole board at power up. The CCDs can be shifted either toward both their outputs or only toward one. In the latter case, CCDs are classified via software in two groups: the left output group and the right output group.

Table 3. The main components of the driver board.

DA Converters	Analog Devices AD8802 (12 outputs)
Range Amplifiers	Burr Brown OPA4234 & LM324 (36 V range)
Analog Switches	Maxim MAX333A (17 Ω , 145 ns, ± 20 V)
Voltage Reference	Maxim MAX6350
Analog Multiplexes	Maxim MAX306 (16 inputs)
Multiple AD Converters	Maxim MAX186 (8 inputs, 12 bits)
CCD Connectors	Berg METRAL (4 \times 12 pins)

5.2 The Readout Board (seven layers)

The main components of the readout board are listed in Table 4.

Table 4. The main components of the readout board.

Clamp Transistors	Fairchild FDV301N (4 Ω , 10 pF)
Preamplifiers	Burr Brown OPA627 (4.5 nV/ $\sqrt{\text{Hz}}$)
AD Converters	Linear LTC1604 (16 bits, 90 dB, 3 μs , 220 mW)
Voltage Reference	Maxim MAX6325

Twenty-two channels are implemented in parallel in a design that is as simple as possible: CCD load resistor, AC coupling, baseline management and CDS operation by clamping to ground once per pixel, only one IC for amplification and the ADC. Gains are about 2 e⁻/ADU depending on CCD responsivity, offsets are approximately 1000 ADU. Readout frequency is 166 Kpix/sec. RDB dissipation is only 7 W.

5.3 The Sharc Board (six layers)

The entire controller is built around the SHARC DSP (Table 5 shows its main components). Its numerous I/O capabilities with associated DMA are useful when writing the DACs, sequencing the CCDs, reading the ADCs and transferring the data. Its 4 Mbit double port internal memory allows to local descrambling of a super-row of 11 CCD rows.

An additional FIFO contains the elementary CCD sequences. All operations are pipelined. The SLink card resides on top as a daughter board to evacuate the pixels' data at high rate toward the PC. The SHARC Board interfaces with the MegaCam software via an RS232 link. The downloadable internal SHARC code is written in assembling language.

Table 5. The main components of the sharc board.

DSP	Analog Devices ADSP21060 SHARC (40 MIPS, 4 Mbits RAM)
FIFO	Texas Instruments ACT3631 (512×36bits)
PLDs	Lattice MACH131SP (64 I/O, 5 ns)

5.4 The Power Board

The main components of the power board are listed in Table 6.

Table 6. The main components of the power board.

AC/DC Converter	VICOR VI-ARM (110/220 V to 300 V, 500 W, 97%)
DC/DC Modules	VICOR VI-J00 (5 V/12 V/28 V, 25 W/100 W, 90%)
Filter Modules	VICOR VI-RAM (10 mVpp)

A local power supply eliminates the need for long, thick cables to carry low DC voltages. The DC/DC modules provide high power with high yield and small size. Additional modules filter the voltages to make them useful in the low noise acquisition system. The input module is 110/220 V auto adaptable.

6. THE LINKS TO THE COMPUTER

The SLink cards [1] are easy to implement in the controller due to the FIFO-like interface, the PMC form factor, and performing on the PC side due to the PCI interface. The data rate is up to 117 Mbit/sec. We developed the Linux driver to perform operations with two cards in the PC. The eight fibers bundle (made by Glenair) provides a simple way to connect/disconnect the Controller. An opto-RS232 module link (115 Kbitds) carries the slow control data between the PC and the controller. This optical link can be replaced by a standard serial cable in maintenance operation in the lab. In the last case, a PC laptop containing simple software from analog devices is enough to dialog with Sharc and, thus, to perform all the controller commands (except pixel data transfer).

7. REFERENCES

- [1] www.cern.ch/HSI/s-link

DESIGN OF THE CRIRES 512×4096 PIXEL ALADDIN INSB FOCAL PLANE ARRAY DETECTOR MOSAIC

Reinhold J. Dorn, Gert Finger, Gotthard Huster, Jean Louis Lizon, Hamid Mehrgan, Manfred Meyer, Joerg Stegmeier and Alan F.M. Moorwood

European Southern Observatory

Abstract: *Near infrared focal plane technology has developed rapidly during the past decade. The array format has increased exponentially and surpassed the megapixel threshold. For the high-resolution IR Echelle Spectrometer CRIRES (1-5 μm range), to be installed at the VLT in 2004, ESO is developing a 512×4096 pixels focal plane array mosaic based on Raytheon Aladdin II and III InSB detectors with a cutoff wavelength of 5.2 μm . To fill the useful field of 135 mm in the dispersion direction and 21 mm in the spatial direction and to maximize simultaneous spectral coverage, a mosaic solution similar to CCD mosaics has been envisioned. It allows a minimum spacing between the detectors of 264 pixels. ESO developed a 3-side buttable multilayer co-fired AlN ceramic chip carrier and package for both the Aladdin II and Aladdin III detectors. This paper presents the design of the CRIRES 512×4096 pixels Aladdin InSb focal plane array mosaic and the newly developed 3-side buttable package.*

Key words: *Infrared (IR) Detectors, Focal Plane Array (FPA), mosaics, Charge-Coupled Devices (CCDs), packages, AlN*

1. INTRODUCTION

Functionally, the CRIRES instrument can be divided into four units. A fore-optics section for field de-rotation, curvature sensing adaptive optics and slit viewing, cold pupil and field stops. This is followed by prism pre-disperser which isolates one echelle order and minimizes the total amount of light entering into the high-resolution section.

The high resolution section comprises a collimator, an echelle which is tilt-tuned for wavelength selection, a camera providing the 0.1"/pixel

plate scale, and the detectors. A calibration unit outside the cryogenic environment contains light sources for flux/wavelength calibration and detector flatfielding [1].

2. A NEW 3 SIDE BUTTABLE PACKAGE FOR THE ALADDIN II SBRC-152 AND ALADDIN III SBRC-206

ESO and Raytheon are collaborating to develop a new 3-side buttable package for the Aladdin II and III detectors to allow a minimum spacing between the *active* pixel areas of 264 pixels. ESO developed a 3-side buttable multilayer co-fired AlN ceramics carrier glued to an invar base plate. The detectors will be glued onto this ceramic. Detectors mounted in the standard leadless chip carrier will be removed from the LCC package prior to assembly on the new ceramic board. A two layer, flexible manganin board interfaces each detector to a preamplifier board equipped with 64 operational amplifiers operating at cryogenic temperatures.

The package (see Fig. 1) includes an invar package base, a copper block for braid connection, a 3-point kinematic mount, the AlN ceramic chip carrier, a NANONICS 65 pin miniature connectors and an integrated temperature sensor and heating resistor. Basic material properties are high thermal conductivity (160 W/mK) and excellent thermal coefficient of expansion to match silicon. Hot press technology with precision tolerances (0.1%) and a Tungsten ($0.15 \text{ } \Omega/\text{sq}$) metallization is used.

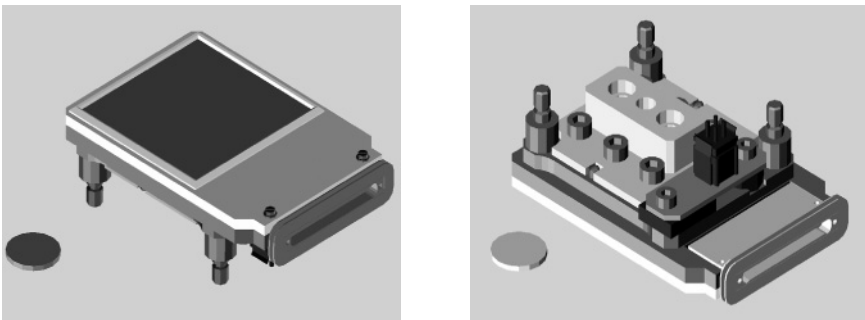


Figure 1. CRIRES 3 side buttable package design

3. DESIGN OF THE CRIRES FOCAL PLANE ARRAY MOSAIC

The CRIRES focal plane mosaic will consist of 3 Aladdin III arrays and one Aladdin II array. Two quadrants of each array are used to cover

the useful optical field indicated by the rectangle in Fig. 2. Since the individual arrays have only two adjacent science grade quadrants, the arrays need to be mounted in different orientations.

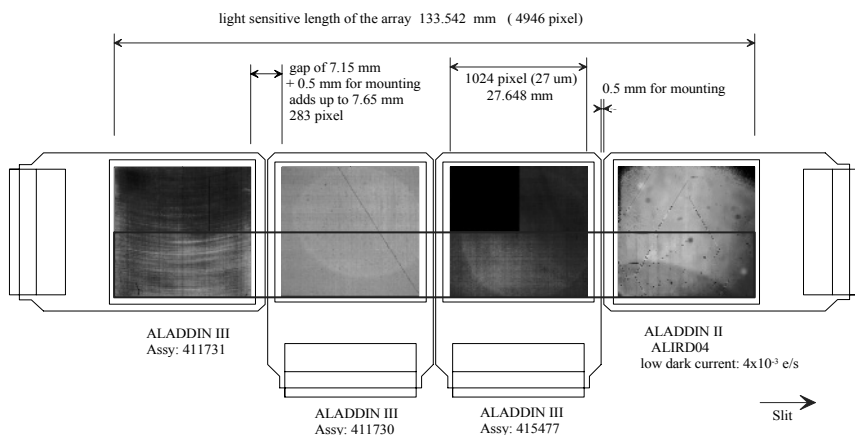


Figure 2. CRIRES focal plane mosaic.

In the vicinity of the detector, the detector board is also cooled to cryogenic temperatures. The amplifiers have to be at temperatures above 60 K but should be placed as closely as possible to the detector, which has to be cooled to 30 K. The detector is well baffled from thermal radiation emitted by the preamplifiers and load resistors on the daughter board in a light tight box. The flexible manganin board will maintain the temperature gradient between the detector and the preamplifiers.

4. DETECTOR CHARACTERISTICS

For the CRIRES detector system, two Aladdin II detectors, the ALIRD06 (to be used for the slit viewer) and the ALIRD04 have been evaluated so far.

- *Dark current:* With a special monitoring technique using dead pixels with open Indium bumps, a darkcurrent as low as 14 e⁻/hour has been measured at a detector temperature of 25 K. This is the lowest dark current ever reported on InSb with an Aladdin array (ALIRD04).
- *Temperature drift:* The temperature drift of the video signal for Aladdin arrays is 1700 e⁻/K. A temperature stability in the micro K range is required without drift compensation.
- *Readout noise:* With our versatile 32 channel high speed data acquisition system (IRACE) the readout noise of Aladdin arrays could be suppressed to below 10 e⁻rms by application of multiple nondestructive readouts and subpixel sampling of the analog signal. Double correlated: < 70 e⁻rms

- *Quantum efficiency*: QE has been measured to be in J=89%, H=73%, K=88%, L=68% and M=74 % bands [2,3].

5. DETECTOR CONTROLLER SYSTEM IRACE

The CRIRES detector mosaic will be read out by the ESO standard Infrared Detector High Speed Array Control Electronics, IRACE. IRACE is designed as a modular system and well suited to read out and process the 64 channels simultaneously needed for the CRIRES detector mosaic. A picture of an IRACE 128 channel prototype data acquisition system for reading up to 4 1K×1K InSb arrays each having 32 parallel video channels is shown in Fig. 3. Left rack: Interface to Sun Ultrasparc. Right rack: Front end electronics with 128 ADC channels, sequencer and clock drivers. Data transport (gigalink) and communication (TIF) to front end by fiber optic links. For more details see Meyer et al, 1996 [4].

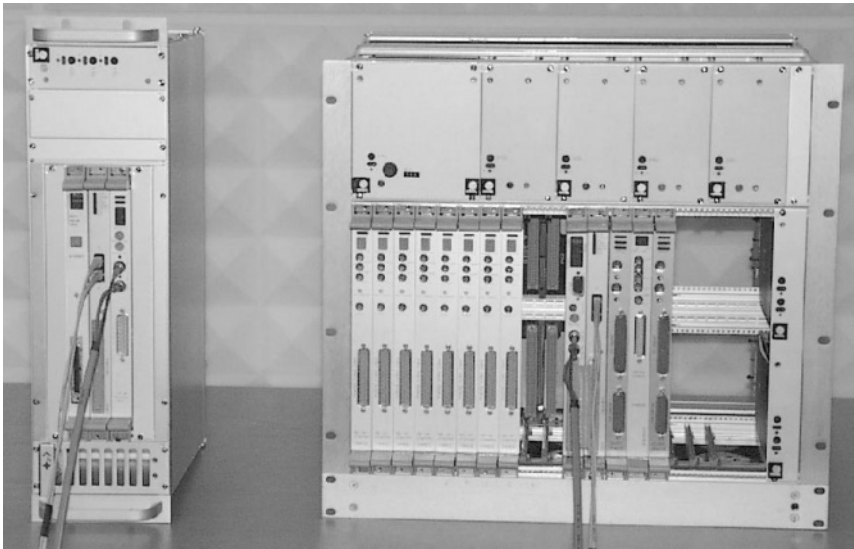


Figure 3. 32 channel IRACE system

6. REFERENCES

- [1] Moorwood, A.F.M. et al, 2002, *CRIRES: a high-resolution infrared spectrograph for the VLT*, In: *Instrument Design and Performance for Optical/Infrared Ground-Based Telescopes*, Waikoloa, Hawaii, August 2002, Proceedings of SPIE, vol. **4841**.
- [2] Finger, G., Dorn, R.J, Hoffman, A.W., Mehrgan, H., Meyer, M., Moorwood, A.F.M., Stegmeier, J., 2002, *Readout techniques for drift and low frequency noise rejection of infrared arrays*, these proceedings, pg. 435.

- [3] Finger, G., Dorn, R.J, Mehrgan, H., Meyer, M., Moorwood, A.F.M., Stegmeier, J., 2002, *Test results with 2K×2K MCT arrays*, these proceedings, pg. 497
- [4] Meyer, M., Finger, G., Mehrgan, H., Moorwood, A. F. M., Stegmeier, J., 1996, *The ESO Infrared Detector High-Speed Array Control and Processing Electronics IRACE*, In: The ESO messenger 86, pp.14-17



Cognitive dissonance on display by Al Fowler and Ian McLean



Linda Janesick (left), moments after realizing that Jim has forgotten his helmet. Amanda Janesick is dreaming of being on a beach, instead of at Subaru....



The "Pizza Hawaii" served at the Café' Pesto started several fierce disputes between the Italians, French and Germans (right) and the Chinese-American delegation. Guess who liked the pizza?

PERFORMANCE OF HAWAII-2 FPA FOR SUBARU MULTI-OBJECT NEAR-INFRARED CAMERA AND SPECTROGRAPH

Takashi Ichikawa¹, Yuka Katsuno¹, Ryuji Suzuki^{1,2}, Chihiro Tokoku^{1,2} and Tetsuo Nishimura²

¹*Astronomical Institute, Tohoku University,* ²*Subaru Telescope, National Astronomical Observatory of Japan*

Abstract: *MOIRCS (Multi-Object Infrared Camera and Spectrograph) is a new Cassegrain instrument for Subaru Telescope, which is designed for multi-slit spectroscopy and wide-field imaging in the near-infrared. The notable feature is the capability of multi-slit spectroscopy in K band with cooled slit masks. Twenty-three slit masks kept in a carousel at 150 K are interchangeable during observations. To cover a wide field of view with a Cassegrain focal plane, we adopt two-channel cooled optics which focuses the telescope field onto two HAWAII-2 FPAs. Array performances (read noise, dark current etc.) have been investigated under various operation conditions and detector bias voltages. We report the results of various tests for engineering the HAWAII-2 FPA.*

Key words: *near-infrared astronomy, HAWAII-2, Infrared Focal Plane Array (FPA), Wide-field Imaging, Multi-object Spectroscopy.*

1. INTRODUCTION

To profit from the development of large format arrays and the superb image quality of the Subaru telescope in the near-infrared, we are constructing a new facility instrument, the Multi-Object Infrared Camera and Spectrograph (MOIRCS) (see Fig. 1(left)).

One of the notable features is a wide field of view of $4' \times 7'$ with the high spatial resolution of $0.12''/\text{pix}$ ($18 \mu\text{m}$) in the wavelength range of $0.8\text{--}2.5 \mu\text{m}$. To achieve this field view, the field of Cassegrain focus is divided into two areas by a roof mirror and then re-focused onto two mosaic 2048×2048 HgCdTe (HAWAII-2) arrays through the two sets of identical optics (Fig. 1(right)), each of which covers $4' \times 3.5'$.

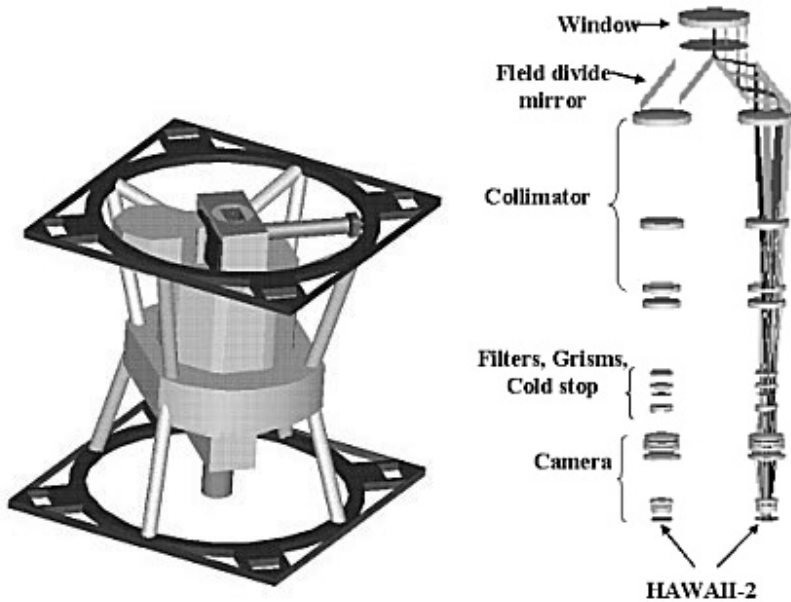


Figure 1. (left) The Schematic view of MOIRCS and (right) the optical system.

MOIRCS is capable of multi-object spectroscopy at near-infrared wavelengths with multi-slit masks cooled at 150 K, which is low enough for the spectroscopy in K band. We have developed a slit mask exchanger, which selects one from 24 slit masks housed in a vacuum carousel at cryo-temperature and places it at the proper position at the Cassegrain focus.

2. HAWAII-2 CONTROLLER

TUFPAC (Tohoku University Focal Plane Array Controller) is an array control system specifically designed for flexible control and efficient data acquisition of HAWAII-2 arrays. A personal computer with Linux OS controls two mosaic HAWAII-2s with the help of commercially available

DSP boards installed in the PCI bus. TUFPAc is capable of controlling a mosaic camera of 8 HAWAII-2 arrays at most. We used on-chip amplifiers in four output mode for the presented study. Since the readout from 32 outputs is more efficient in saving observation time, especially for imaging in high background, we are designing the system for 32 channel outputs.

The basic clocks for the horizontal register include CLK1, CLK2, CLKB1, CLKB2 (CLK1=CLKB2, CLK2=CLKB1). CLK1 is complementary to CLK2 within 25 ns. The two clock phases should overlap with a rise time of less than 100 ns, otherwise the pixel data cannot be read properly. The rise time of our controller is about 80 ns. CLK1 and CLKB2 are synchronous with CLK2 and CLKB1 with a rise time of 10 ns.

The PGA pins of the ceramic package that is not wired to the HAWAII-2 array are used for the heat sink. A copper plate, on which socket pins are adhered, is inserted into a ZIF socket (manufactured by 3M) of 21×21 PGA from the backside (Fig. 2). Two small Pt resistors of a surface mount type with size of 3.2 mm×1.6 mm are directly soldered to the ZIF pins for temperature monitor.

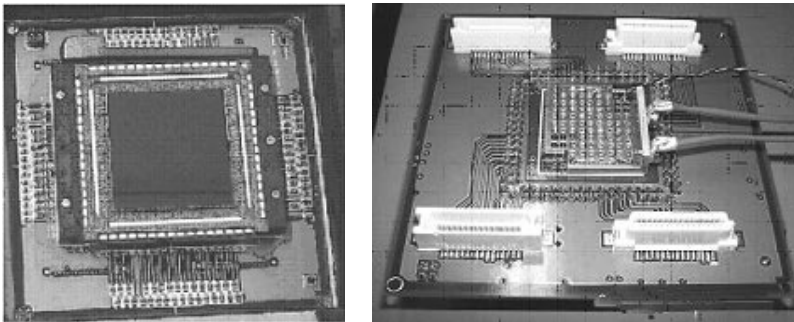


Figure 2. (left) HAWAII-2 on a ZIF socket and (right) the heat sink.

3. TEST RESULTS

Using TUFPAc, we have examined the performance of HAWAII-2 in the cryostat for array tests equipped with a mechanical cooler. The settling time of pixel output strongly depends on BIASGATE voltage. It is about 4-14 μ s for BIASGATE = 3.2–3.6 V. The array is operated with 3.4 V and pixel rate of 100 kHz for the following tests. The readout noise and the dark current of the engineering-grade HAWAII-2 is about 39 e^- and 0.27 e^- /sec/pix, respectively, which are much higher than those in the data sheet for the science grade array ($< 10 e^-$ and 0.03 e^- /sec).

We obtained the image data of the array illuminated by a black body source with various exposure times. The full integration capacity, which

depends on the reset voltage (VRESET), varies from $1.0^5 \times 10^5 \text{ e}^-$ to $1.8 \times 10^5 \text{ e}^-$ for VRESET = 0.5-1.0 V. The linearity is within 3-80 % of the full capacity for VRESET = 0.5 V (Fig. 3).

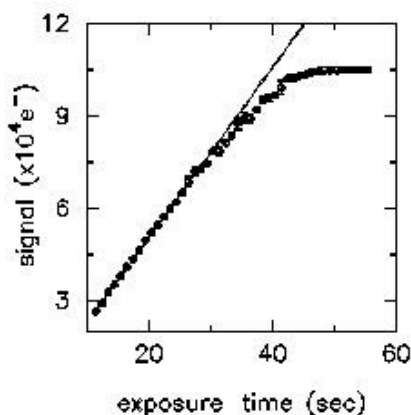


Figure 3. Linearity of HAWAII-2.

The glow emission from the on-chip amplifiers and the shift registers in the array is invisible or buried in the high dark current and readout noise of the engineering array. If the emission is serious for the science-grade array, we will use off-chip amps.

4. PROSPECTS

We have described the application of 2048×2048 HgCdTe (HAWAII-2) for the near-infrared camera and spectrograph (MOIRCS). The data acquisition and control system (TUFPA) shows good performance for the operation of the HAWAII-2 FPA (see Fig. 4).

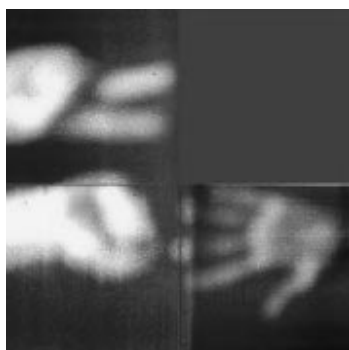


Figure 4. An image in H band.

The extensive assessment of the performance of the engineering-grade array has given us suggestions for operating the science-grade arrays in optimum conditions. The science-grade arrays will be installed in the summer of 2002. We will start assembling the optics, mechanics, and electronics in the fall of 2002, targeting first light in 2003.



“Gerry! This is not Rock & Roll, it’s line-dancing!”

Meanwhile, in front of Gerry Luppino, Roger Smith surrenders to the passion for line-dancing.



Elise Beletic (front right) leads the Hula class at the Keauhou Canoe Club during the “Barbie at the Beach” event.



The powerful swing of Sebastian Deiries blows away Giovanni Bonanno’s hat.

WIDE FIELD FOCAL PLANE ARRAYS FOR UKIRT AND VISTA

Derek J. Ives, Ken Laidlaw and Naidu N. Bezawada

United Kingdom Astronomy Technology Centre

Abstract: *This paper briefly describes the focal plane arrays of the UKIRT Wide Field Camera and the IR camera for the Visible and Infrared Survey Telescope for Astronomy (VISTA). Laboratory test results on the HAWAII-2 engineering grade detector are summarised. The interference problems resulting from the on-axis wavefront/autoguider sensors and their controllers (autoguider, wavefront sensor, etc.) are anticipated and possible options to eliminate or attenuate these effects are presented. Laboratory tests on the Electromagnetic Interference (EMI) issues are also reported.*

Key words: *Wide Field Camera (WFCAM), Visible and Infrared Survey Telescope for Astronomy (VISTA), HgCdTe, characterization*

1. INTRODUCTION

The infrared detector work at the UK Astronomy Technology Center has been reported elsewhere in these proceedings [1]. The current near IR work includes a mosaic of 4 HAWAII-2 detectors in a Wide Field CAMera (WFCAM) for the UK InfraRed Telescope (UKIRT) and detectors for the VISTA IR Camera. The initial testing and characterization of the VISTA IR detectors will be carried out at UKATC while the final mosaic focal plane assembly will be integrated with the rest of the IR camera at Rutherford Appleton Laboratories (RAL). We present the details of these focal planes, detectors, controllers, auxiliary units associated with these instruments and some test results obtained with the IR detectors.

2. FOCAL PLANE ARRAYS

The WFCAM [2] will become the most capable survey instrument in J, H and K bands in the world with four $2K \times 2K$ detectors in its focal plane. The instrument will use HAWAII-2 PACE detectors. Since these detectors are not close buttable, the four detectors are placed at 90% spacing of their active area for the most efficient survey speed that also allows sufficient field overlap to fill up the inter-gaps. Four similar exposures at different positions can be used to obtain a full image (filled square) of 0.75 sq. degrees with 0.4" pixel sampling while the instantaneous field coverage is $\sim 0.19'$. The WFCAM detectors will be operated synchronously by four SDSU-II controllers each catering for one device with 32 readout channels.

VISTA is a new 4-m class facility dedicated to astronomical survey, which will be added to ESO's Cerro Paranal site in 2006. In order to maximize the survey speed, the IR camera will utilize sixteen $2K \times 2K$ near IR detectors in its focal plane placed at 90% of the active area. The detectors will be either from Raytheon Infrared Operations or Rockwell Scientific. The IR camera also utilizes an innovative cold-baffle design instead of the conventional cold stop and re-imaging optics. The VISTA detectors will be operated synchronously with ESO's IRACE controllers.

3. DETECTORS AND MEASUREMENTS

UKATC has received one Hawaii-2 science grade and two engineering grade detectors along with a few bare multiplexers for the wide field camera. So far we have only performed a few tests on the multiplexers and engineering grade detectors. As the test cryostat needs to be cleaned thoroughly before integrating with the science detector, we have only been able to perform tests on the engineering detectors. On the engineering grade detector all four quadrants are functional except for a delamination of the detector and ROIC at one corner. The characterization tests performed include dark generation and its variance with pixel rest voltage, linearity and charge handling capacity with varying pixel reset, system gain calibrations, pixel settling time and some tests on image persistence.

The detector has been mounted in a test cryostat and operated at 77 K. The detector mount houses a flex-rigid PCB with a ZIF socket to hold the HAWAII-2 detector. For precise dark current measurements, the detector housing can be completely sealed while the detector observes a cold aluminum cover plate, which kept at 85 K. The detector PCB consists of detector protection circuitry and passive decoupling on the bias voltages. An SDSU generation-II controller with 4 analog signal processing channels is

being used to run the array at 250 kHz pixel. The controller interfaces to a host computer through a PCI board. Data acquisition software, VOODOO (ver. 1.7), is currently being used to direct the controller and perform data acquisition. An infrared LED is incorporated into the cold chamber to provide input flux to the detector. The LED is controlled using one of the spare clock lines in the controller that allows both programmable exposures and the adjusting of flux levels.

Table 1 summarizes the measurements of an engineering grade detector, while Table 2 shows test results from the manufacturer for the science detector.

Table 1. Test measurements on the engineering grade HAWAII-2 PACE detector

Parameter	Value	Notes
Sensitivity	3.5 $\mu\text{V}/\text{e}^-$	using the photon transfer technique
Read noise	12 e^- (rms)	using double correlated sampling
Full well	150 ke^- to 215 ke^-	obtained with reset from 0.55 V to 0.95 V
Non-linearity	$\sim 4\%$ peak to valley	from 5% to 80% full well capacity
Dark generation	$\sim 0.2 \text{ e}^-/\text{sec}/\text{pix}$	see text
Pixel settling time	1.5 μs to 4.0 μs	with bias gate from 3.2 V to 3.6 V

Table 2. Science grade test data

Parameter	Value
QE (J, H and K bands)	66%, 76% and 76%
QE Uniformity (J, H and K bands)	17.9%, 15.5% and 15.7%
Read noise	13.6 e^-
Charge handling capacity (0.55 V reset)	95 ke^-
Dark generation	0.05 e^-/sec

Series of dark frames using single correlated double sampling are obtained when the detector is completely sealed from any thermal leaks. Dark tests showed that the rate of dark current generation is very high immediately after the reset. The rate of dark generation is reduced to $< 0.2 \text{ e}^-/\text{sec}$ in ~ 10 minutes after reset.

HAWAII-2 devices with LPE (Liquid Phase Epitaxy) process are known to have image persistence. We have used a localized spot spread over a few tens of pixels to roughly estimate the persistence decay time. Once saturated with the spot, a series of dark frames were obtained at regular intervals and the persistence decay time was obtained. Tests showed that even if the detector is not saturated, it still has image persistence, but for a shorter period of time. The more the detector is saturated, the longer the decay time. The image persistence decays to below the dark limit in about 150 sec. Multiple resets had no effect on the decay time.

4. FOCAL PLANE ASSEMBLIES - AUTOGUIDER (AG) CCDs

Both WFCAM and VISTA focal plane assemblies will be integrated with AG CCDs. The AG for WFCAM requires acquisition of the guide window at 40 Hz and 10 Hz for VISTA. Since CCDs will run asynchronously close to the science devices, there is potential electromagnetic interference with the science readout. This interference may be primarily due to the radiated emission from the CCD clocking. Routing the AG wiring separately from the science detector will eliminate the interference or cross-talk due to the capacitive coupling from the clocks. A complete stainless steel enclosure for the AG mount and wiring with separate ground control will be used to minimize the inductively coupled interference. The radiation from the CCD electrode gate structure acts like radiating antenna with the ROIC of IR detectors acting as receivers. This radiated emission can be attenuated using special optical windows that are processed with Electromagnetic Compatibility (EMC) shielding and > 90% optical transparency. An EMC test was performed with simulated CCD clocks in a stainless steel sealed enclosure with the EMC window. The results show that the EMC window attenuates emissions to 9 dBV and is as good as stainless steel window.

If we are still left with interference in the above scheme, an interleaved readout can be implemented in which the autoguider CCD window (10×10 or 20×20 pixels) readout is performed after a certain number of rows are readout from the science array. This interleave will impose a certain amount of overhead on the total readout time of the science array, but effectively eliminates the radiated EMI problems.

5. REFERENCES

- [1] Ives, D., Bezawada, N. N., Ellis, M., 2002, *Detector work at UKATC - from optical to the sub-mm*, these proceedings, pg. 231.
- [2] Henry, D. M., Atad Ettedgui, E., Casali, M.M., Bennett, R., Bridger, A., Ives, D.J., Rae R.G, and Hawarden, T.G., 2000, *A Wide field camera for the United Kingdom infrared telescope*, SPIE Vol. **4008**, p. 1325-1333.

FULLY BUTTABLE IMAGERS

Michael Lesser and David Ouellette

University of Arizona

Abstract: *A new post-fabrication technique has been developed which allows charge coupled device wafers to be hybridized and then processed for backside illumination. This allows the creation of a fully buttable imager in which the electrical I/O from the device frontside is brought under the device rather than to its edge. This 3-D packaging allows extremely close spacing of imagers in a focal plane mosaic. It also allows standardized processing for wafers of the same size, which may lead to lower cost of back-illuminated detectors.*

Key words: *Charge-Coupled Device (CCD), detectors, imaging, focal plane mosaic*

1. INTRODUCTION

Very large focal planes are often required for modern astronomical imaging systems such as large telescopes and spectrographs. Because the physical size of Charge-Coupled Devices (CCDs) and CMOS imagers is limited by yield and ultimately silicon wafer size, modern very large area focal planes require mosaicing of detectors. The gaps between these detectors represent a dead region which is either ignored or removed in software through imaging processing. For many applications, these gaps represent an expensive loss of observing time and inefficient use of the optical system. To minimize these effects, most mosaics utilize “edge-butable” technology in which the detector pixels are placed as close as possible to device edges. These devices are in turn butted closely together. The logical extension of this technology is to develop new techniques to reduce gaps even further. We have recently developed such a process at the University of Arizona Imaging Technology Laboratory (ITL). This new 3-D backside process allows the dead gap region to be limited only by the edge

effects associated with dicing the individual detectors from their wafers and the detector layout itself.

In addition to allowing very closely spaced devices in focal plane mosaics, this new technique allows backside processing (hybridization, thinning, and coating) at the wafer level. Wafer processing has previously been unsuitable for devices which are hybridized or flip chip bonded because of I/O constraints which would require the devices to be widely spaced on the wafer during fabrication.

2. BACKSIDE PROCESSING

Our Fully Buttable Imager (FBI) process is based on hybridizing a silicon wafer to a ceramic substrate. This is a post-fabrication technique which utilizes silicon wafers that are produced using CCDs from any foundry. Once the wafers are received, they are cold probe-tested to determine which devices are shorted and the cosmetic quality of the unshorted parts. Because the wafer frontside will not be available for probing after hybridization, this screening process must be performed completely. All devices must be probed, not just those to be used as FBIs in a mosaic. After screening, the wafers are lapped to a thickness of 250 μm to reduce the time required for later chemical etching. This also improves the cosmetic quality of the final parts.

We use gold stud bumping to make electrical contact to the aluminum bond pads on the CCD. A stud bump is applied with a wire bonder that has a mode in which a gold ball is attached to the CCD bond pad and then terminated immediately above the ball. A tool is used to ultrasonically flatten the balls to a uniform height of 50-75 μm . We have developed a tool which flattens all bonds simultaneously, but this can also be easily done individually with the stud bump bonder. All bond pads on all devices on the wafer must be bumped at this time. A commonly used alternative technology for high volume processing is to electroplate bumps onto the bond pads. Solder is used for room temperature applications while indium works best for cooled detectors due to its malleability at low temperature.

The mating substrates consist of Aluminum Nitride (AlN) ceramic with indium bumps, 2-sided or multi-layer metal electrical traces, and electrically conductive filled vias. Substrates are typically square and 0.5 inch larger than the CCD wafer diameter. Our tests with 100 mm (4 inch) diameter wafers were made with 0.040" thick, 4.5" square AlN and alumina (Al_2O_3). Indium bumps are plated onto metal traces at the matching location to the CCD bond pads. The gold stud bumps of the CCD mates to these indium bumps. We are exploring alternatives to indium plating, including screened flexible epoxy. We are also considering the reverse process in which the

bumps are plated onto the CCD wafers and gold stud bumps are applied to the ceramic substrates. Metal traces on the top side (usually thin film TiW/Au) lead from the indium bumps to vias and from the vias to the package I/O pads on the bottom side. The vias are 200 μm in diameter and are laser drilled by a vendor. The package I/O pads are designed to mate to any of several package options.

The hybridization process itself consists of using a flip chip bonder (Research Devices M8A) with wafer-size chucks to mate the ceramic substrates and the CCD wafer. Alignment is made optically using a split field microscope. The wafer and substrate are pressed together and heated to 135 °C to fuse the indium and gold. This diffusion bond has been shown to be stronger than the adhesion force holding the gold ball to the aluminum CCD bond pad.

After bonding, a low viscosity epoxy is underfilled between the substrate and wafer. We use Epoxy Technologies 301-2 epoxy that has been outgassed to eliminate trapped air bubbles. Underfilling takes less than 10 min at 60 °C for a 100 mm diameter wafer. Voids in the epoxy, which can lead to blister-like distortions of the thinned device, can be eliminated with proper care of flow rate, outgassing, and temperature. We also utilize a custom vacuum tool to hold the wafer flat during the underflow and curing operations.

After the curing of the underfill epoxy, the hybrid (CCD wafer and substrate) is ready for thinning. A wax bead is placed around the wafer edge to protect against acid seeping into the underfill. The wafer is etched in a selective acid mixture in the same manner as our standard die process [1, 2]. Next, an epitaxial etch is used to remove residual p+ material and polish the surface. Following this etching, the hybrid is cleaned and then backside coated. We first grow a thin oxide on the backside to reduce the surface state density and then apply chemisorption charging and antireflection coatings [3].

All wafers of the same size are processed in the same manner during hybridization, thinning, oxidation, and backside coatings. This simplifies tooling and handling fixtures and may lead to lower device cost.

After coating, the devices must be diced into their individual die form. Photoresist is spun onto the wafer to protect the imaging surface from the swarf generated during the dicing operation. The dicing process is still under development as it is difficult to avoid edge chipping. Proper selection of the dicing blade is critical. The dicing blade must cut through the 250 μm unthinned silicon lip around the edge of the wafer, the 10-20 μm CCDs, the 50 μm underfill medium, and the 1500 μm ceramic substrate. The dicing is also done backside up, which means the dicing streets are not easily seen without an infrared camera. We have successfully diced this stack, but

continue to seek ways to reduce edge chipping. In Fig. 1 we show a demonstration 2K×2K FBI device processed as described above.

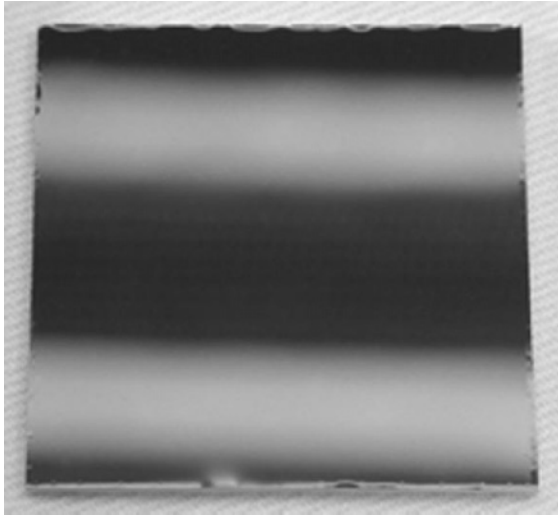


Figure 1. A 2K×2K 15 μm pixel fully buttable imager after backside processing and before packaging. Edge chipping created in the dicing process can be seen. The reflection from fluorescent lamps is also visible in the mirror-like imager surface.

3. PACKAGING

Packaging of an FBI is the last step before characterization and operation. We are still in the process of developing a final process for FBI packaging, however, our current technique is described here. A metal frame is attached to the bottom of the ceramic carrier with an adhesive to provide rigid support. This frame also provides the cooling path to the imager and thereby avoids stressing the ceramic with the direct attachment of a cold finger. The frames are machined aluminum or Invar-36. Electrical I/O to the bottom contact pads (metal traces) is provided by surface mount soldering an appropriate connector. The mating connector is typically on a flex or wire cable and leads to the dewar (hermetic) I/O connector or directly to the camera electronics. We prefer the use of a female connector on the carrier to eliminate pins that could promote electrostatic damage to the device. There are several suitable connectors for this purpose, one type being from Samtec [4]. However, one dominant challenge is to identify a connector that physically fits the die. Since the number of active I/O pads is not necessarily related to imager size, it is often easier to identify a suitable connector for

large imagers than the smaller ones. We are currently using 1 mm pitch connector technology (InterCon Systems) for FBI devices.

Once the frame and connector are bonded to the bottom of the carrier, the processing is complete and the device can be operated. The metal frame also allows for the attachment of various tools which are of great importance during handling, since FBI devices cannot, in practice, be touched from the top or sides without touching the imaging surface.

4. FULLY BUTTABLE TEST DETECTOR

As an experiment to understand the issues associated with producing fully buttable imagers, we developed a detector layout which is more buttable than normal edge-butable CCDs. Dr. Richard Bredthauer of Semiconductor Technology Associates, Inc., designed and added the STA0535 fully buttable detector to a University of Arizona CCD foundry run. This CCD is a $1K \times 1K$, $7.5 \mu\text{m}$ -pixel device with bonding pads ON TOP of the pixels instead of at the device periphery. The gap between the diced edge of the device and the first row or column of pixels is $100 \mu\text{m}$ on two sides and $250 \mu\text{m}$ on the other two sides. This distance can be reduced to about $50 \mu\text{m}$ per side plus the serial register width by building the metal busses on top of the pixels as well. A metal layer has been added between the pixels and the bonding pads to reduce reflection artifacts from near-IR light that travels through the CCD.

It is important to note that this device is a pathfinder only; it is not intended that FBI devices need to be custom designed. We show in Fig. 2 the STA0535 device after stud bumps have been applied.

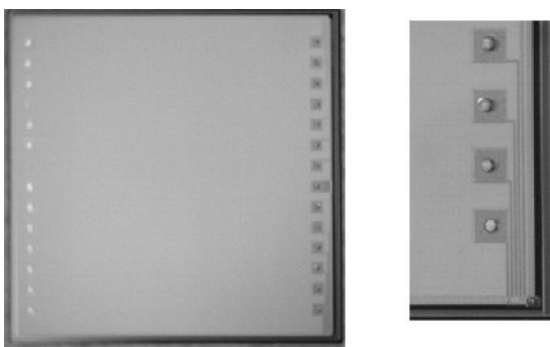


Figure 2. The STA0535 fully buttable CCD detector. The zoomed image on the right shows stud bumps applied to the aluminum bond pads.

Two such devices were thinned and backside processed. We found no unusual backside processing issues. We do, however, see the effect of the

bond pads in images. Interestingly, the pattern is visible in dark images as well as light, indicating that stress, and not reflected light, is most likely the cause. The devices we processed had poor CTE due to a fabrication problem unrelated to the FBI devices, and they were difficult to fully characterize. Similar devices will be fabricated in the future to continue this study.

5. SUMMARY

We have demonstrated a process to produce CCD devices which have 3-D I/O to create fully buttable imaging detectors. Focal plane coverage as great as 97% may be achieved with large mosaics and small inter-device gaps. Large-scale, closely butted mosaics will be especially useful for future projects such as the Large Synoptic Survey Telescope (LSST) which will repeatedly image a 3-degree-wide field-of-view with over a thousand detectors. The inter-device gaps for such a survey instrument represent true observing inefficiency and will lead to significant extra expense. The technology demonstrated here would be well suited for such a project, using either CCDs or CMOS imagers as detectors.

The hybridization technique described allows detectors from any fabrication facility to be processed as FBIs. The aluminum nitride ceramic substrates have good thermal properties for focal plane cooling and expansion matching of large area detectors. Ceramics also allow the utilization of commercial techniques such as laser drilling, filled vias, and thin- and thick-film metallization to reduce costs. We have also shown that CCDs can be fabricated with bonding pads and bus structures on top of the pixels to reduce the gaps between detectors even further when necessary. Additional work is ongoing to test the fundamental limits of such devices as well as to improve our techniques for dicing and packaging these hybridized fully buttable imagers.

6. ACKNOWLEDGEMENTS

The authors wish to thank David Baxter, Charles Bridges, Teresa Lappin, Joanne McGinnis, Dianne Sanders, and Lee Ulrickson of the University of Arizona Imaging Technology Laboratory for their support of this work. We thank Dr. Richard Bredthauer for his design of the STA0535 CCD.

7. REFERENCES

- [1] Lesser, M. P., 1996, *Back Illuminated CCD Processing at Steward Observatory*, Recent Developments in Scientific Optical Imaging, M. B. Denton, R. E. Fields, and Q. S. Hanley, eds., Royal Society of Chemistry, p. 62.

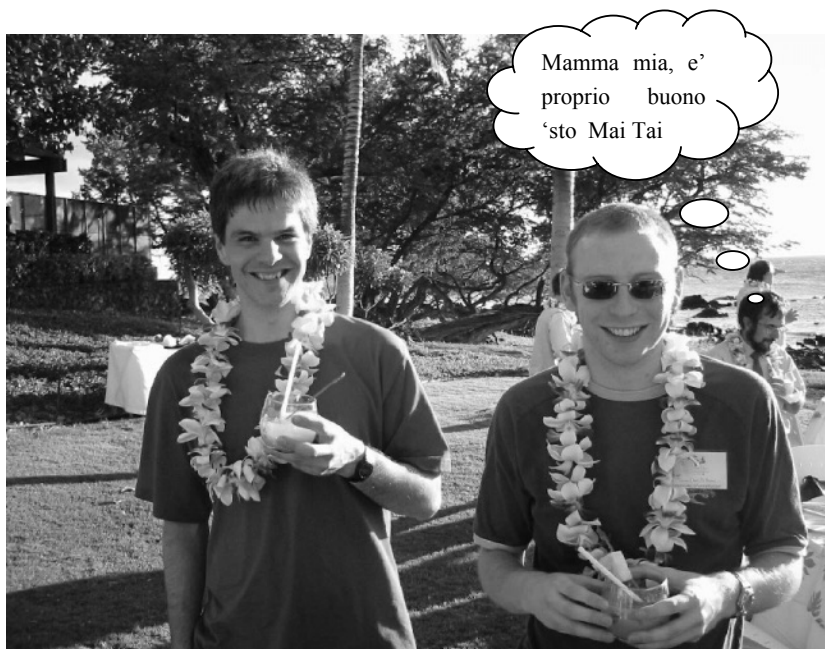
- [2] Lesser, M. P. and Ouellette, D. B., 1995, *Back Illuminated CCD Mosaics*, Proc. SPIE **2415**, p. 182.
- [3] Lesser, M. P. and Iyer, V., 1998, *Enhancing Back Illuminated Performance of Astronomical CCDs*, Proc. SPIE **3355**, p. 23.
- [4] www.samtec.com



The Scientific Organizing Committee (a few seen above, left to right, J. Tonry, J. Geary, R. Stover and P. Poole) had the auspicious duty of selecting the winners of coveted awards such as “Best paper”, “Most original presentation”, as well as the more dubious distinctions “Best sales pitch”, “Most loquacious”, etc... (Courtesy A.G.D. Philip)



The post-workshop survey revealed that 99.2% of the 125 participants found the poster sessions engaging and kept them on their feet. Sitting at the table is the disagreeing .8%. (Courtesy A.G.D.Philip)



Don't they look cute with the leis? The Mai Tais helped unleash the "romantic" side of all the nerds who attended the Gala Dinner. (Courtesy G. Burley)

MOSAIC FOCAL PLANE DEVELOPMENT

David Mason, Scott Horner, and Earl Aamodt

Lockheed Martin Advanced Technology Center

Abstract: *Advances in manufacturing and applied sciences have enabled the development of large ground and spaced based astronomical instruments having a Field of View (FOV) large enough to capture a large portion of the universe in a single image. A large FOV can be accomplished using light weighted optics, improved structures, and the development of mosaic Focal Plane Assemblies (mFPAs). A mFPA comprises multiple Charged Coupled Devices (CCD) mounted onto a single baseplate integrated at the focus plane of the instrument. Examples of current, or proposed, missions utilizing mFPA technology include FAME, GEST, Kepler, GAIA, LSST, and SNAP. The development of a mFPA mandates tight control on the design trades of component development, CCD definition and characterization, component integration, and performance verification testing. This paper addresses the results of the Lockheed Martin Space Systems Company (LMSSC), Advanced Technology Center (ATC) developed mFPA. The design trades and performance characterization are services provided by the LMSSC ATC but not detailed in this paper.*

Key words: *mosaic Focal Plane Assembly (mFPA) integration, Charge-Coupled Device (CCD) characterization, mosaic Focal Plane Assembly testing*

1. MFPA DEVELOPMENT SYSTEMS ENGINEERING

A mFPA development begins with a Systems Engineering (SE) approach to flow top level mission requirements to lower level subassemblies, assemblies, components, and into the verification processes. This approach identifies the interacting engineering sciences and initiates the trade studies required to optimize the science and engineering disciplines to achieve the mission objectives. These trade studies at the mFPA level

include the electrical interfaces with the first CCD electronics, the mechanical assembly processes and hardware interaction, the thermal stability at the operating temperature, and the integration sequence to formulate the mFPA. This paper will focus on the integration of the CCDs onto the baseplate and the resulting measurements.

2. CCD SURFACE INSPECTIONS

The first activity performed after the visual inspection is to acquire detailed photographs of the CCD Surface. This appraises the surface cleanliness and documents all embedded fiducial targets needed for accurate alignment and position measurements. Figure 1 illustrates a corner target fiducial and the detecting array definition targets.

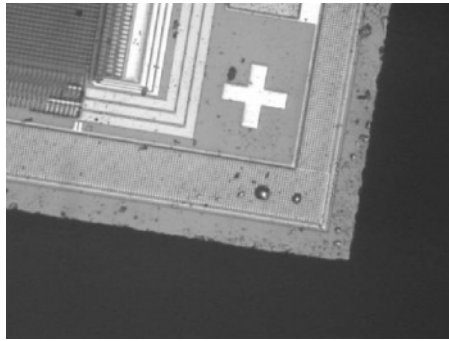


Figure 1. CCD Detailed Surface Inspection

3. mFPA DEVELOPMENT SEQUENCE

The mFPA development is a serial process performed under strict procedures to maintain surface cleanliness and the operational safety of each CCD and the mFPA as a whole.

3.1 mFPA Development Facility

The mFPA development facility was designed according to the demands of CCDs, including Electrostatic Discharge (ESD) and surface cleanliness. The LMSSC ATC facility combines full time electrical charge dissipation and electrical potential equalization procedures to ensure that static charge is dissipated before damage is done to the CCDs. The integration of the CCDs and the test processes are performed in a dedicated, class 100 cleanroom.

3.2 Baseplate Installation and Alignment

The baseplate is inspected to verify the location and geometry of the engraved reference axes position and accuracy, and the flatness of the baseplate, to design tolerances. The baseplate is integrated into the base of the alignment equipment and aligned to the reference axes. This alignment is verified after multiple cycles between the baseplate axes and the reference axes demonstrate repeatable positional data within acceptable tolerances.

3.3 Initial CCD Installation

The installation of each CCD onto the baseplate is performed using alignment tooling rods. These tooling rods are manually inserted into the mounting surface of each CCD and passed through the baseplate alignment holes. The critical elements of the insertion process are the positional tolerances between the baseplate, the CCD with the alignment rods inserted, and the tooling rods as manufactured. Detailed Geometric Dimensioning and Tolerancing (GDT) are used to capture these critical alignments between the elements. Once the CCD is positioned on the baseplate, the CCD is aligned to the baseplate axes using the positional equipment to locate and quantify the CCD fiducial position. The measurements and adjustments to the CCD are repeated until the alignment meets the defined tolerances.

3.4 mFPA CCD Installation

The remaining detectors are installed onto the baseplate and aligned to the baseplate axes using the reference axes. Measurements and adjustments are made in translation (X and Y axes), tip and tilt of each CCD surface to the reference axis plane, and focus plane (z-axis). The detectors are secured using the defined final anchoring method (adhesive injection or final mechanical torque set), and measured again to ensure the alignment requirements are maintained.

An alternative method of installing multiple CCDs is to use a 'mechanical fence' to 'roughly' position the CCDs. This allows the CCD to be 'pushed' against the fence during the installation to locate the CCDs for subsequent measurements to be made. A gap embedded in the initial design provides the opportunity to use a gap tool. Similar tooling may be used to install 'buttable' CCDs.

The final positional tolerances should be carefully reviewed to ensure CCD carrier manufacturing errors, CCD substrate installation errors, and embedded CCD fiducial manufacturing errors, which can result in achieving the final position of the CCDs to the defined requirements and tolerances.

Table 1 provides the quantified position of the 5 CCDs integrated during the validation of the mFPA development process.

Table I. Positional Data

Center	Xa (mm)	Ya (mm)	Zavg (mm)	Delta X (mm)	Delta Y (mm)	Delta Z (mm)
CCD A	382.4755	392.8217	79.137	0	0	0.0724
CCD B	319.4477	392.6492	78.9467	-63.0278	-0.1725	-0.1179
CCD C	445.5985	392.5665	79.1442	63.123	-0.2552	0.0796
CCD D	382.2269	359.9524	79.0033	-0.2486	-32.8693	-0.0613
CCD E	382.6589	425.53	79.092	0.1834	32.7083	0.0274
			79.0646		Depth of Focus =0.1975	
Location	X (mm)	(mm)	Z (mm)	Delta X (mm)	Delta Y (mm)	radians
A1	413.0025	377.4617	79.0910	61.0538	0.1625	2.66159E-03
A2	412.9325	408.1876	79.0920			
A3	351.8887	408.0351	79.0205			
A4	351.9487	377.2992	79.0000			
			79.0509			
B1	349.9747	377.2892	78.9915	61.0496	0.1869	3.06145E-03
B2	349.8943	408.0009	79.0125			
B3	288.8467	407.8222	78.8880			
B4	288.9251	377.1023	78.8810			
			78.9433			
C1	476.1255	377.2065	79.1865	61.0294	-0.1960	-3.21157E-03
C2	476.2191	407.9424	79.1925			
C3	415.1711	408.0767	79.1130			
C4	415.0961	377.4025	79.1145			
			79.1516			
D1	412.7539	344.5924	79.0400	61.0446	0.0050	8.19073E-05
D2	412.7689	375.3083	79.0700			
D3	351.7193	375.3133	78.9975			
D4	351.7093	344.5874	78.9665			
			79.0185			
E1	413.1859	410.1700	79.1370	61.0522	0.2654	4.34728E-03
E2	413.0717	440.8959	79.1645			
E3	352.0137	440.6311	79.0465			
E4	352.1337	409.9046	79.0195			
			79.0919			

The integration of these CCDs onto the baseplate is illustrated in Fig. 2.

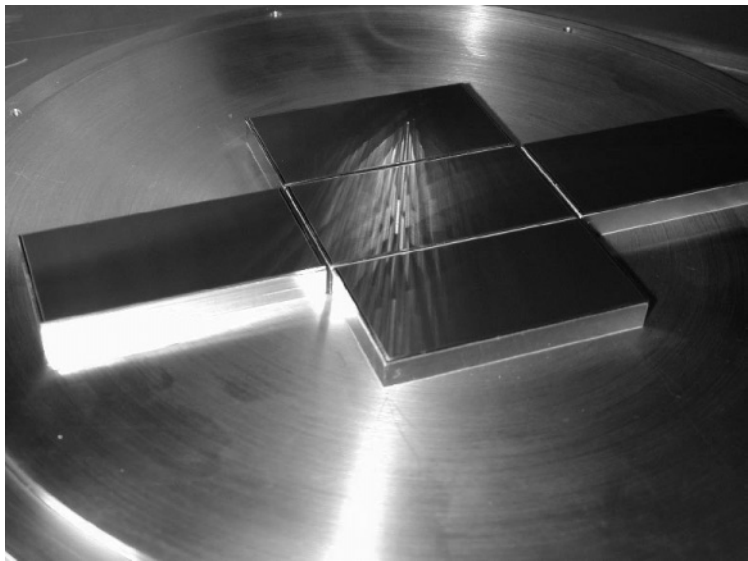


Figure 2. 5 CCD mFPA integration

A graphic illustration of the resulting alignment is provided in Fig. 3. The references noted as the center and corners are provided in Table 1. The associated values of the data points allow for the calculations for rotations to be developed. The Z-axis values at the corners enable tip/tilt measurements and average focus measurements to be calculated.

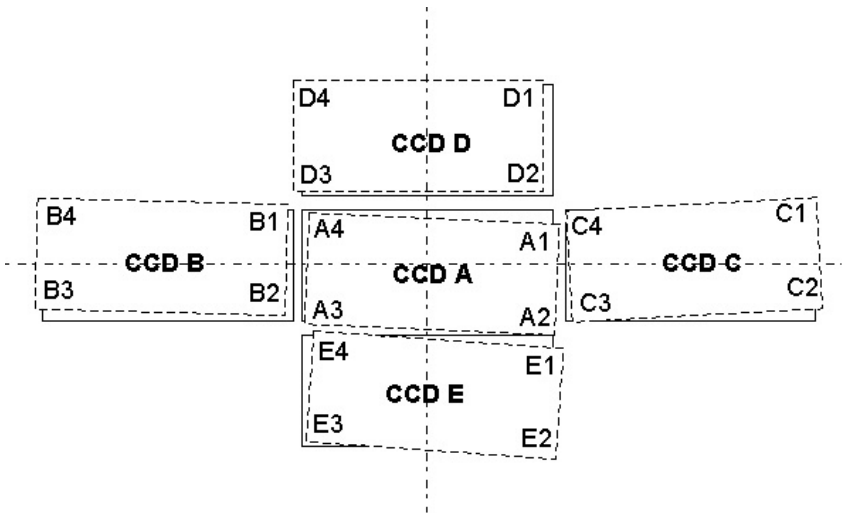


Figure 3. Exaggerated CCD alignment illustration.



A stroll through Paradise for just \$850 a week! (Courtesy G. Burley)



Sebastian Deiries, months before realizing that he has forgotten to take the lens cap off.

SECTION VII:
SPACE MISSIONS

IN-FLIGHT PERFORMANCE OF THE ADVANCED CAMERA FOR SURVEYS CCDS

Mark Clampin¹, Marco Sirianni², George F. Hartig³, Holland C. Ford²,
Garth D. Illingworth³, Bill Burmester⁴, William Koldewynd⁴, Andre R.
Martel², Adam Riess¹, Ronald J. Schrein⁴, and Pamela C. Sullivan⁵

¹Space Telescope Science Institute, ²Johns Hopkins University, ³Univ of California Obs/Lick
Observatory, ⁴Ball Aerospace and Technology Corp., ⁵NASA Goddard Space Flight Center

Abstract: *The Advanced Camera for Surveys (ACS), installed in the Hubble Space telescope in March 2002, will significantly extend HST's deep, survey imaging capabilities. ACS has met, or exceeded, all of its key performance specifications. In this paper we briefly review the in-flight performance of the instrument's CCD detectors and preview early ACS science observations.*

Key words: *Hubble Space Telescope (HST), Advanced Camera for Surveys (ACS), Charge-Coupled Device (CCD), wide field imaging, UV imaging*

1. INTRODUCTION

The Advanced Camera for Surveys (ACS) is a third generation instrument for the Hubble Space Telescope (HST). It was installed in HST during the fourth servicing mission (SM3B) in March 2002. ACS replaced a first generation axial bay instrument, the Faint Object Camera (FOC). ACS has three channels, shown schematically in Fig. 1, the Wide Field Camera (WFC), the High Resolution Camera (HRC) and the Solar Blind Camera (SBC). In this paper we will discuss the WFC and HRC CCD detectors.

WFC is a high-throughput, wide field imager (202"×202") designed for deep imaging surveys in the near-IR. WFC provides a factor of 10 gain in discovery efficiency at 800 nm, compared to the Wide Field Planetary Camera-2 (WFPC2). In this context discovery efficiency is defined as the

product of field of view (FOV) and instrumental throughput. WFC employs a 4096×4096 CCD mosaic as its focal plane detector. The plate scale of the WFC is $0.05''/\text{pixel}$, which delivers near-critical sampling at the near-IR wavelengths for which the camera is optimized.

The HRC is a near-UV to near-IR imager, which provides critically sampled images in the visible, over a $29'' \times 26''$ field of view. HRC shares its optical train with the SBC, a far-UV imaging channel utilizing a photon counting MAMA detector. The HRC focal plane detector is a 1024×1024 CCD detector, based on the Space Telescope Imaging Spectrograph (STIS) CCD. The HRC plate scale is $0.027''/\text{pixel}$, which yields fully sampled images in the visible.

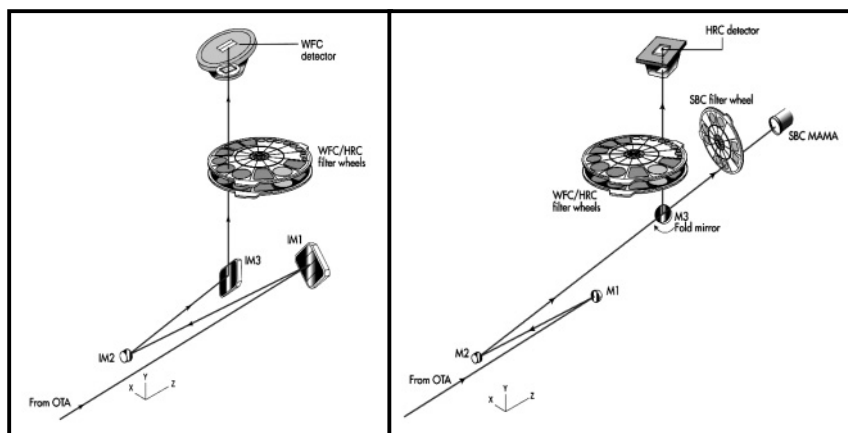


Figure 1. Schematic showing the optical designs for the WFC (left) and the HRC/SBC (right).

2. ACS CCD DESIGN

The selection of CCD detectors for ACS was based on the heritage of the STIS program [1], which employed devices designed and fabricated at Scientific Imaging Technologies (SITE). The design of the ACS CCDs is summarized below in Table 1. The HRC detector is the same basic design as the STIS CCD detector, but with a different backside process offering a significant improvement in near-UV sensitivity.

The WFC focal plane package comprises two SITE 2048×4096 CCDs butted together to provide a 4096×4096 pixel mosaic, as shown in Fig. 2. The CCD design is derived from the three-side buttable, SITE commercial 4096×2048 array (ST-002A). However, concerns regarding term degradation of charge transfer efficiency (CTE), due to the radiation environment in HST's low earth orbit, prompted a design change to minimize the number of

parallel shifts. The WFC detector's serial register is 4096 pixels long and reads out through an amplifier at each end. This design reduces the readout to 2048 parallel and 2048 serial shifts for each quadrant of the 4096×4096 mosaic. However, the device can be butted along one side only.

Table 1. Properties of the ACS CCD detectors

Camera	WFC	HRC
Process	3-phase, backside thinned, MPP	3-phase, backside thinned, MPP
AR coating	SITe VIS-AR coating	SITe UV-AR coating
Readout	2 amplifiers/CCD	4 amplifiers/CCD
Format	4096×4096 (2×2048×4096)	1024×1024
Pixel Size	15 μm ×15 μm	21 μm ×21 μm
Sensitivity	370-1050 nm	200-1050 nm

The WFC detector housing, also shown in Fig. 2, incorporates an outer shell of molybdenum and alloy 42, combined with an inner shell mounted on four two stage Peltier coolers. The WFC mosaic header is mounted on a four stage Peltier cooler stack. The housing's thermal design permits the detector mosaic to be cooled to 77 °C. Following the next servicing mission (SM4) an externally mounted aft-shroud cooling system will be installed on HST to permit cooling of the detectors to ~85 °C. The HRC detector is mounted in an exact replica of the housing employed for the STIS CCD, a single shell design, which cools the HRC CCD to 80 °C.

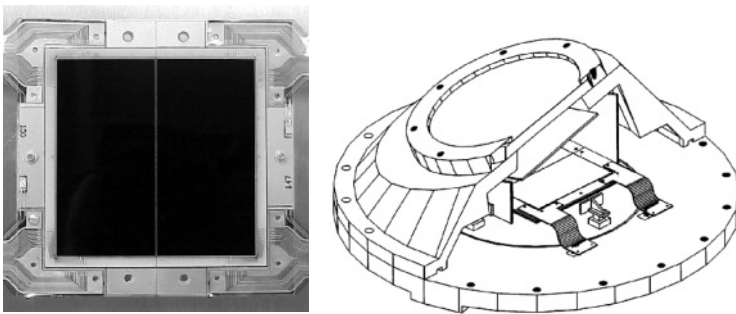


Figure 2. (left) The WFC 4096×4096 CCD mosaic package. (right) The WFC detector housing showing the double shell design, and the location of the focal plane array.

3. FLIGHT PERFORMANCE OF ACS CCDs

The orbit performance of ACS was determined during the Servicing Mission Orbital Verification (SMOV) program. SMOV comprises a series of observational programs designed to bring ACS to operational status, verify

basic functionality, and obtain preliminary calibrations so that routine science operations can be initiated.

The ACS detector systems are performing nominally. Both the WFC and HRC detector read noise figures are unchanged from pre-launch measurements made during ground testing, as shown in Table 2. Although most WFC broadband science observations are sky limited, read noise is important to narrowband observations. HRC science programs are all read-noise limited, due to the smaller pixel size.

Table 2.. Comparison of pre-launch and post-launch CCD readout noise

	Amp.	Gain	Read Noise (e ⁻) RMS			Amp.	Gain	Read Noise (e ⁻) RMS	
			ground	flight					
WFC1	A	1	4.8	4.9	HRC	A	2	4.6	4.6
	B	1	4.7	4.8		B	2	4.4	4.7
WFC2	C	1	5.2	5.2		C	2	4.7	4.7
	D	1	4.7	4.8		D	2	5.0	4.9

The measured dark currents, excluding hot pixels $>0.04 \text{ e}^- \text{pix}^{-1} \text{s}^{-1}$, are $7.5 \text{ e}^- \text{pix}^{-1} \text{hr}^{-1}$ (77°C) and $9.1 \text{ e}^- \text{pix}^{-1} \text{hr}^{-1}$ (80°C), for the WFC and HRC respectively. Remarkably, these temperatures are achieved without the aft-shroud cooling system, which will be installed during the next servicing mission (SM4). Hot pixels are a result of proton displacement damage. The primary technique for moderating the hot pixel growth rate is annealing of the CCDs at the ambient temperature. Typically, the ACS detectors reach $\sim 20^\circ \text{C}$ when CCD cooling is switched off.

Hot pixel evolution has been evaluated over several ACS annealing cycles. Hot pixels in the WFC appear at a rate of $\sim 1230 \text{ pixels day}^{-1}$. In Fig. 3, we show the evolution of hot pixels and the effect of the monthly annealing. WFC hot pixels are annealed at a rate of $\sim 60\%$, in contrast to the factor of $\sim 80\%$ for the HRC detector. In subsequent WFC anneals, existing hot pixels are annealed at very low rates such that after $\sim 7\text{-}8$ anneal cycles the cumulative fraction of annealed pixels reaches a plateau at $\sim 70\%$ [2]. Consequently, $\sim 1.5\%$ of the WFC mosaic will be covered by hot pixels after 24 months. This corresponds to the fraction of the WFC mosaic covered by cosmic rays in a 1000 sec WFC exposure.

The WFPC2 and STIS CCDs are similar to the HRC in annealing at a rate of $\sim 80\%$. Currently, the WFPC2 focal plane array has $\sim 2.5\%$ coverage by hot pixels, where WFPC2 hot pixels are defined as $>0.02 \text{ e}^- \text{s}^{-1}$. While the WFC hot pixel evolution rate is a concern, it can be handled during science operations by obtaining daily hot pixel calibration images, and dithering observation sequences so that optimal combination of science frames can be used to eliminate hot pixels.

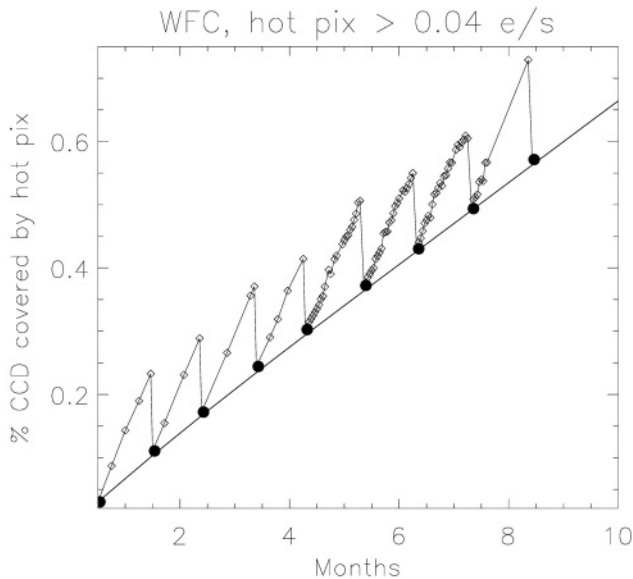


Figure 3. The growth of WFC hot pixels since launch, illustrating the effect of monthly anneals on the long-term evolution of hot pixels in the WFC [2].

Initial post-launch measurements indicated that charge transfer efficiency (CTE) for the WFC and HRC detectors was consistent with pre-launch calibrations. The radiation environment experienced in HST's orbit has caused long-term degradation of CTE in previous HST instruments including STIS [3], and WFPC2 [4]. Preliminary calibration using the extended edge pixel response (EPER) method on internal flat field images indicates a degradation of parallel CTE from 0.999999 to 0.999991 (amplifier D) during the first six months of operation. EPER measurements are not, however, a good measure for assessing the impact of CTE degradation on science observations. More relevant measurements are currently being made using crowded star fields.

The image quality obtained with the ACS is dependent upon the image delivered by the camera optics [5], and the pixel response function of the CCD detectors [6]. The WFC flight images meet specification, with 79% of the light enclosed within a 0.25" diameter at 630 nm. WFC images obtained through the primary WFC broadband filters F606W, F814W and F850LP are illustrated below in Fig. 4.

The WFC F850LP image exhibits an enhanced horizontal diffraction spike, resulting in a reduction of encircled energy at $\lambda > 800$ nm. The feature is due to a metal coating applied to the frontside of the WFC CCDs, prior to

chip mounting and thinning [7]. The metal coating was applied to prevent large image halos ($\phi > 100$ pixels) caused by long wavelength photons scattering inside the CCD's soda glass header.

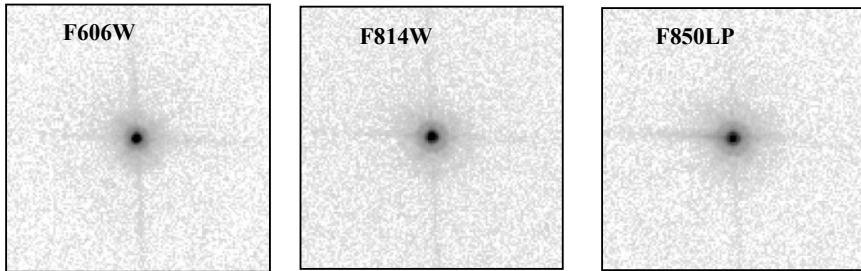


Figure 4. Images obtained with the F606W, F814W and F850LP filters in the WFC. The longer wavelength image (F850LP) shows the enhanced diffraction edge on the left horizontal diffraction spike.

Images of the HRC PSF taken through the F220W, F435W and F814W filters are shown in Fig. 5. The HRC exceeds its specification with the encircled energy at $0.25''$ equal to 0.82. The HRC PSF also exhibits a “spur” at shorter wavelengths (< 400 nm), due to a moderate amount of several low order aberrations in the optical system.

The discovery efficiency goal for WFC was closely linked to achieving high CCD quantum efficiency. The WFC CCDs have typical quantum efficiencies for backside-thinned devices with the SiTe VIS-AR process [8], with a peak quantum efficiency of $\sim 75\%$ at 600 nm. For the HRC, the primary goal was to maximize near-UV sensitivity, so the SiTe UV-AR process was employed on a backside-thinned device.

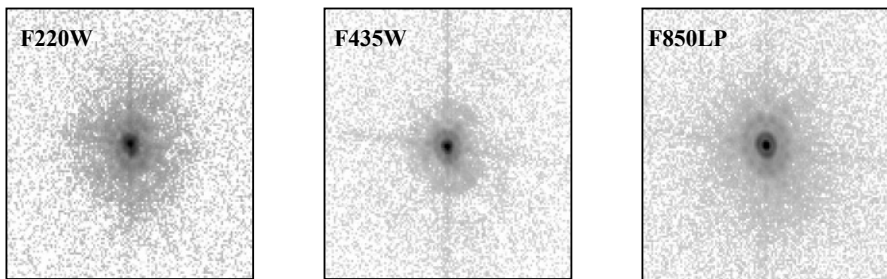


Figure 5. HRC images obtained with the F220W, F435W and F850LP filters in the WFC.

During SMOV, observations of spectrophotometric standard stars, and calibrated star fields were used to verify sensitivity predictions based on component level measurements. In Fig. 6, we present the overall instrumental throughput of the WFC and HRC cameras, including the contribution of the HST optical telescope assembly (OTA).

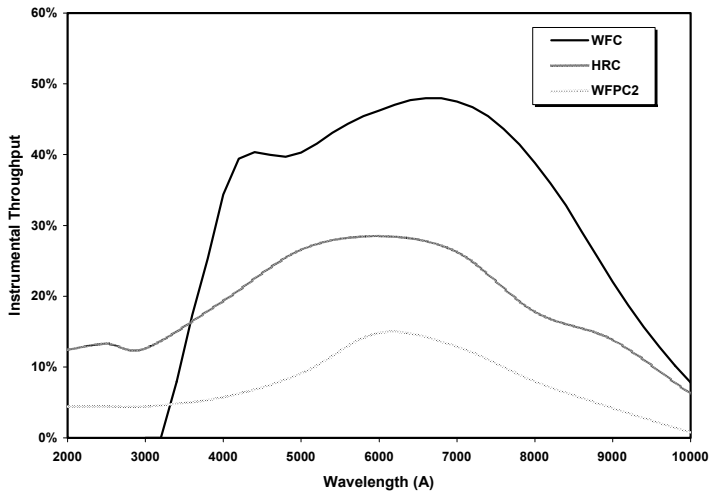


Figure 6. Overall throughput of the ACS WFC and HRC cameras including the OTA.

The limiting magnitude performance specification for ACS is stated in Table 3, with a summary of exposure time calculations using the post-launch sensitivity curves that demonstrate ACS met its requirements. The calculations consider both average and low sky background conditions, and determine the SNR for the case of an optimal aperture, equivalent to PSF fitting, and an aperture corresponding to 80% encircled energy.

Table 3. Point Source limiting magnitudes based

WFC Requirement: S/N \geq 5 for a 2600 sec observations of a F0V star of V magnitude = 27.4			HRC Requirements: S/N \geq 5 for a 2600 sec observations of a F0V star of V magnitude = 26.7		
S/N	Photometry	Sky background	S/N	Photometry	Sky background
5.8	Aperture ¹	Average ²	7.8	Aperture ¹	Average ²
6.7	Aperture ¹	Low ³	8.4	Aperture ¹	Low ³
9.0	PSF fitting	Average ²	15.0	PSF fitting	Average ²
10.4	PSF fitting	Low ³	15.8	PSF fitting	Low ³
¹ Aperture 5 \times 5 pixels (80% encircled energy)			¹ Aperture 5 \times 5 pixels (80% encircled energy)		
² Average sky V=22.7			² Average sky V=22.7		
³ Low Sky = 23.2			³ Low Sky = 23.2		

In summary, the ACS has met and exceeded its performance specifications. A demonstration of its potential for deep, imaging surveys is provided by early release observations (ERO) of the interacting galaxy Arp 188, shown in Fig. 7. In just 14 HST orbits the observations came within <1 magnitude of the limiting magnitude achieved Hubble Deep Field South [9] observations with WFPC2

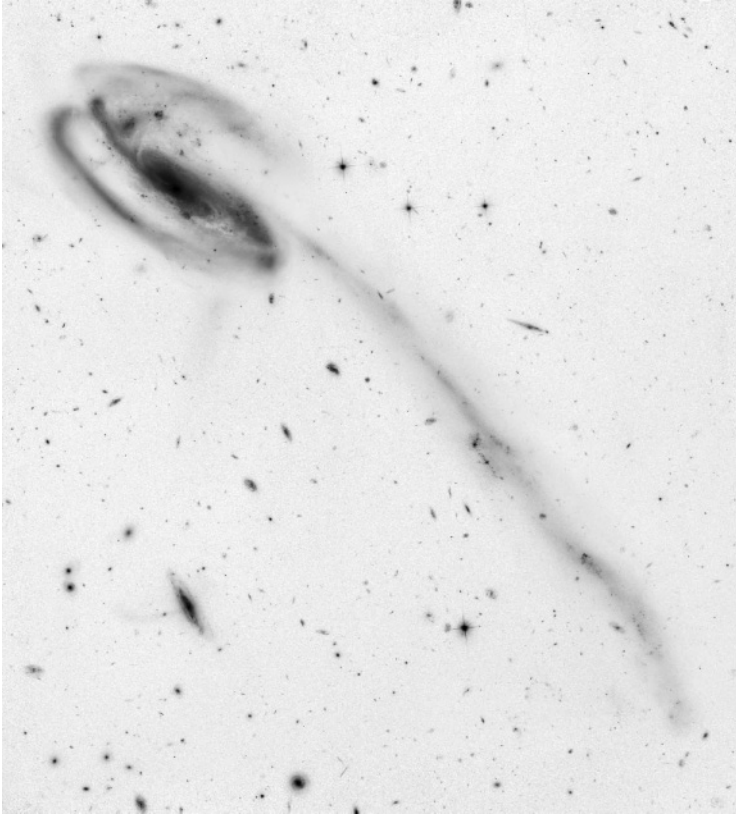


Figure 7. WFC image of Arp 188. The image is a composite built from a 6 orbit observation through F475W, a 4 orbit observation through F606W and 6 orbits through F814W. The field is $\sim 3.2''$ on each side.

4. ACKNOWLEDGEMENTS

ACS was developed under NASA contract NAS 5-32865, and this research is supported by NASA grant NAG5-7697. We are grateful for an equipment grant from the Sun Microsystems, Inc.

5. REFERENCES

- [1] Kimble, R. A. et al. 1998, *ApJL* **492**, pg. L83.
- [2] Riess, A. 2002, *STScI ISR* pgs. 02-06.
- [3] Kimble, R. A.; Goudfrooij, P.; Gilliland, R. L. 2000, *SPIE* **4013**, pg. 532.
- [4] Whitmore, B., Heyer, I, & Casertano, S. 1999, *PASP* **111**, pg. 1559.
- [5] Hartig, G. et. al. 2002, *SPIE*.

- [6] Clampin, M. et al. 1998, SPIE **3356**, pg. 332.
- [7] Sirianni, M. et al. 1998, SPIE **3355**, pg. 608.
- [8] Clampin, M. et al. 2000, SPIE **4008**, pg. 669.
- [9] Williams, R. E. et al. 2000, AJ **120**, pg. 2735.



He has just realized he forgot his swimsuit. (Courtesy G. Burley)



*"There are 99 nerds dancing on the floor
Take one down, roll it around
There are 98 nerds dancing on the floor...."*



Jim Janesick is happy because he managed to catch the Frisbee with his head....

ON THE IMPLEMENTATION AND CALIBRATION OF THE FOCAL PLANE FOR GAIA

Mario Gai¹ and Deborah Busonero²

¹*Istituto Nazionale di Astrofisica - Osservatorio Astronomico di Torino*, ²*Università degli Studi di Siena*

Abstract: *We review the focal plane specifications for GAIA, as derived from the measurement principle and payload implementation concept. Design requirements must be tailored to the needs of the mission, taking into account optical performance, detector geometry and electro-optical properties, as well as Time Delay Integration (TDI) operation at the level of both single chip characteristics and overall layout. By optimization of both mosaic manufacturing and in-flight calibration based on the scientific data, we deduce requirements comparable to those of Charge-Coupled Device (CCD) mosaics for modern ground based telescopes.*

Key words: *astrometry, space vehicles, instruments, telescopes*

1. INTRODUCTION

The European Space Agency (ESA) has selected the mission GAIA (Cornerstone 6) for launch by 2012. The goal is accurate measurements of position, proper motion and absolute parallax of every target on the sky in the visual magnitude range $V \cong 11 - 20 \text{ mag}$, i.e. about one billion objects including 1-2 % of the population of our galaxy and many solar systems and extra-galactic objects. Objects down to $V \cong 17 \text{ mag}$ will be observed by a spectro-photometric payload, providing spectral classification and radial velocity. Identification of dynamics, and of the individual and collective astrophysical characteristics of such samples, allows the reconstruction of

critical events in the Galactic history, tracing both its present content and past evolution. A more detailed description of the astrophysical goals and implementation concept of GAIA is available in literature [1] and on the internet [2]. The desired astrometric accuracy of position, parallax and annual proper motion for a $V=15\text{ mag}$ target is 10 micro-arcsec (hereafter, μas); for brighter stars the photon limited accuracy is higher, but it can be achieved only upon stringent constraint on instrument systematic error, by design, implementation and calibration at the sub-nanometer level [3].

Industrial contracts for the refinement of the implementation concept are in progress; this presentation is based on the Concept and Technology Study Report [4]. Several working groups have been appointed by ESA among the more than one hundred scientists interested in GAIA for detailed analysis of its performance and optimization of its operation. The authors are part of the On-Ground and In-Orbit Calibration Working Group.

Here we discuss the requirements for the baseline GAIA implementation concept, in terms of top-down design, operation and calibration.

GAIA is a spinning satellite (3 hour period), with continuous full-sky observation through a combination of rotation, precession and orbital motion. The orbit is the external libration point (L2) of the Earth-Sun system, at about 1.7 million km. The measurement concept, inherited from the previous mission Hipparcos, requires observation along two lines of sight, separated by a large *base angle* ($1-2\text{ rad}$), along the equatorial *great circle*. The main astrometric payload requires two telescopes, with a large Focal Plane (FP) detector: a CCD mosaic operated in Time Delay Integration (TDI) mode.

The aperture is rectangular, with collecting area 1.2 m^2 and along scan size $D=1.7\text{ m}$, corresponding to an Airy size $\sim 0''.17$ at the reference wavelength $\lambda=700\text{ nm}$. The effective focal length $F=50\text{ m}$ results in an optical scale $s \cong 4''/\text{mm} = 4\mu\text{as}/\mu\text{m} = 4\mu\text{as}/\text{nm}$. The nominal diffraction image (sinc^2 function) is binned in the across scan (low resolution) direction, producing one-dimensional signals sampled with about 4.5 pixels on the central lobe. The real image is affected by aberrations from the optical configuration, finite spectral bandwidth and other instrumental effects. The spectral bandwidth is limited only by the detector sensitivity curve (no filter present); the intrinsic stars emission provides anyway a bandwidth of $200-300\text{ nm}$, at different effective wavelength.

CCD readout is tagged against a common time scale, so that the pixel value distribution can be centered to find the transit instant of the star photo-center over reference positions on the FP (e.g. the CCD edge). The motion law maps time to the sky position through the scan velocity: $\Delta\eta = V_s \cdot \Delta t$, i.e. $\Delta x = F \cdot V_s \cdot \Delta t$, and we can express the measurement requirements in angular units on the sky, or timing or linear units on the FP, equivalently.

Hereafter, we discuss some of the requirements on to design, implementation, verification and in-flight calibration of the GAIA astrometric payload.

2. THE ASTROMETRIC FOCAL PLANE

The FP has three CCD strips devoted to target identification, the Star Mapper (SM), at the entrance of the detector. All pixels are read, selecting the Regions Of Interest (ROI) for follow-up, with signal above detection threshold. Two detections on subsequent chips are required for confirmation, to reject cosmic rays and spurious effects. They also estimate the satellite scan velocity and, for solar system objects, their differential speed. The third CCD strip is used in cold redundancy.

The main Astrometric Field (AF) provides 17 independent exposures of each selected target on subsequent chips. The AF operates in windowing mode, on the ROI identified by the SM, thus alleviating the electronics requirements. The acquisition time of the useful pixels is maximized by discarding the empty regions, 99% of the sky down to $V=20\text{mag}$, thus improving on effective bandwidth and readout noise. The star then crosses the Broad Band Photometry (BBP) region, with four CCDs endowed with color filters providing spectral classification information down to the limiting magnitude. The transit of each star is thus observed by 24 CCDs.

Ten horizontal strips are placed side by side across scan: each FP is composed of 240 chips, for a total of ~ 300 video lines (external CCDs have split outputs). A large field of view is required to achieve sufficient exposure time on every target, and to reach the desired astrometric precision; also, the FP breadth ensures superposition between subsequent TDI passages. A single CCD model is used for the whole FP, with specialized operating mode. The pixel size is $9 \times 27 \mu\text{m}$, and the logical format 2780×2150 , corresponding to $25 \times 58 \text{mm}$, respectively along and across scan. The FP area is therefore $75 \times 60 \text{cm} \cong 0.45 \text{m}^2$, corresponding to a field of view of $0.8^\circ \times 0.7^\circ \cong 0.55$, and a total 1.5Gpix . The 85% filling factor is due to the along scan gap between devices for front-end electronics interconnections. Marconi technology is assumed; the development requirements are mainly on reliability and low power operation, rather than on CCD electro-optical characteristics. The row period is $300 \mu\text{s}$, due to the satellite rotation period; vertical transfer at 30kHz and serial binning (or flushing of unused pixels) at 15MHz . This allows for useful pixel readout at 120kHz , with estimated noise $\text{RON} \cong 5e^-$.

Hereafter, we select as x coordinate the across scan direction, running along the CCD rows; y is along the scan, *i.e.* along the CCD columns, due to

the TDI operation; z is orthogonal to the nominal CCD surface, and coincident with the optical axis at the appropriate position of the field. We label the rotations around x , y and z as α -tilt, β -tilt and γ -tilt, respectively.

3. REQUIREMENT ASSESSMENT

The optical scale maps the μas measurement goal into nm level requirements, for at least some of the FP parameters; we identify the most sensitive design aspects in order to reduce the implementation criticality. We split the requirements in different classes, as associated to global measurement characteristics, to the preservation of the elementary exposure quality, and to astrometric calibration. The location process provides the position of GAIA signals with precision depending upon the telescope diffraction limit and the Signal to Noise Ratio (SNR):

$$\sigma(y) = \eta \cdot \frac{\lambda}{D} \cdot \frac{1}{\text{SNR}} \quad (1)$$

Here η is a factor taking into account geometry, finite pixel size and other instrumental aspects. Usually the image is sampled to a comparably coarse fraction of the diffraction limit (*e.g.* 2-3 pixels within λ/D), in a trade-off between resolution and field of view. Besides, from Eq. (1) the precision expected on bright stars is a very small fraction of the pixel size. This has been verified on a low cost laboratory experiment [5], in which 1/800 pixel precision has been achieved. Systematic errors, with time constant longer than the exposure, and amplitude larger than the final precision by a factor 10, were identified and effectively removed in the reduction process. The same principle can be applied to the GAIA data.

The precision associated to the elementary exposure of a $V=12\text{ mag}$ star is about $16\ \mu\text{as} \cong 4\text{ nm}$. The desired precision at the transit level (17 AF exposures) is thus at the nm level. As the link among measurements is provided by the relative CCD position along y , the detector geometry should be known with comparable precision, to exploit the limiting astrometric performance on the full magnitude range. If the instrument has sufficient precision at the single exposure level, and remains stable over longer periods, many critical FP parameters can be estimated from the data and calibrated out. In particular, sufficient image quality must be preserved on each elementary exposure, and the geometric relation among the devices must be stable over a time scale adequate for FP calibration at the $\mu\text{as} / \text{nm}$ level. The former condition mostly impacts the location process performance

for each elementary exposure, *i.e.* the random error. The latter condition allows modeling of FP parameters and systematic errors.

Given the high final precision of GAIA, the requirements on instrument stability and on instrument modeling accuracy are challenging. Also, the elementary measurement precision is high, and simultaneous detection of many stars at each time helps in building up the calibration information. The image quality requirement is evaluated with respect to tolerance on initial CCD positioning within the mosaic to on-board knowledge of the FP geometry, and finally to the calibration procedures. The reference parameter is the characteristic width along y , which must not be degraded (increased) by more than $\sim 1/10$ of its nominal value, since this has an acceptable impact on the location process efficiency, *i.e.* on the random error. Therefore,

$$\Delta y < \frac{1}{10} \cdot 2 \frac{\lambda}{D} F = \frac{\lambda F}{5D} \cong 4 \mu m \quad (2)$$

3.1 Detector manufacturing and operation constraints

The independent measurement along y is the time of transit of the target photo-center over each CCD reference position, with precision depending on the image SNR. The whole CCD strip subsequently observes the target, and we can fit the whole data set to a common law of motion in order to get a better estimate of the equivalent time of transit over a common reference. This process is effective if the main uncertainty is associated with the data, with sufficiently good knowledge of the detector geometry.

The initial CCD alignment must reduce the dead space and preserve the main measurement characteristics, *e.g.* that an object detected by SM be observed by all trailing AF CCDs. For operations, we need to retain the image quality and sufficient knowledge of the detector geometry for reading out the ROI. In data reduction, the individual exposures must be merged into a single transit measurement with a μ as-level accuracy. This requires much better knowledge on the configuration, as well as sufficient stability.

Below, we discuss each degree of freedom in the more relevant context.

3.1.1 CCD position

The x position of each CCD must be set on the FP to within one or a few columns, *i.e.* a few ten μ m, to ensure that all devices read the same targets.

The y position does not affect the measurement, provided it is known, and the dead space is dominated by the interface to the front-end electronics. We retain the above requirement of few ten μ m. They must be known to a

few μm , in order to select the ROI to within a fraction of pixel; besides, the ROI is defined with margins, because it is also affected by attitude.

The z position requirement can be derived from the image blurring due to a CCD displacement, Δz , resulting in defocusing. The image size increase Δy associated to Δz is:

$$\Delta y = \Delta z \cdot \tan \alpha \approx \alpha \Delta z = \frac{\Delta z D}{2F} \Rightarrow \Delta z < \frac{2}{5} \frac{\lambda F^2}{D^2} \cong 200 \mu\text{m} \quad (3)$$

3.1.2 CCD rotation

Rotation vs. x provides image blurring and smaller effective pixels size, which results in a mismatch between nominal clock rate and projected sidereal velocity. For small angles, α , the along scan size L decreases to $L' = L \cdot \cos \alpha < L$. At the end of the on-chip integration, the displacement between the instantaneous image provided by the optical system and the nominal on-chip image is $\Delta L = L - L'$, and the image blurring is $\Delta L/2$, assuming the CCD is driven at the nominal clock rate. Therefore,

$$\Delta y = \frac{\Delta L}{2} = \frac{1}{4} L \alpha^2 \Rightarrow \alpha < \sqrt{\frac{4}{5} \cdot \frac{\lambda F}{LD}} \cong 2.4e-2 \text{ rad} \quad (5)$$

i.e. a linear displacement of the CCD edge by about $7 \mu\text{m}$.

Rotation vs. y provides differential defocusing across the device, as the CCD columns are placed at different heights vs. the nominal FP. The across scan pixel size is reduced. However, the effect on image quality is not critical given the large tolerance on z positioning derived above. Besides, the reduction on the across scan CCD size reduces the coverage of the nominal sky strip. The few ten μm requirement on x position, in angle, becomes:

$$\beta < \frac{\Delta x}{C} \cong 5e-4 \text{ rad} \cong 2' \quad (4)$$

Rotation vs. z induces effects similar but opposite to rotation vs. x . The along scan size L increases to $L' = L / \cos \gamma > L$ for a small rotation angle γ . As above, we deduce $\gamma < 2.4e-2 \text{ rad}$, *i.e.* a linear displacement at the CCD corner of about $7 \mu\text{m}$.

3.2 Stability and calibration requirements

The difference in the time of transit of each star between CCD pairs gives an estimate of their separation Δy ($\Delta t = \Delta x / (V_s \cdot F)$), with precision depending on the target SNR, *e.g.* $4\sqrt{2} \text{ nm}$ for a $V=12 \text{ mag}$ star. Any other star on the same sky strip provides an independent estimate of the same quantity. The measurements can be averaged, in order to achieve sufficient precision through statistics. Notably, in case of variations, we do not know by a pair-wise measurement which chip is displaced; we can identify collective effects, *e.g.* global shrinking or expansion, or displacement of a single device with respect to all others.

We take the average of the stars contained in one square degree, away from the Galactic plane, in the magnitude range $V \equiv 12 - 19 \text{ mag}$, and with some conservative reduction factor. The cumulative precision achieved by such data set, taking into account number of stars and individual precision vs. magnitude, is $3.4 \mu\text{as} = 0.85 \text{ nm}$. Since the across scan size of the CCD is $\sim 4'$, the required sky strip has along scan size 15° , and it is scanned in TDI mode in 450 sec, or 7.5 min. Thus, the normal science data stream allows calibration of relevant FP parameters on a time scale below 10 min, *i.e.* much shorter than the 3 hour spin period. If the instrument is intrinsically stable over longer periods, the calibration data could be averaged over longer periods, achieving the $1 \mu\text{as} = 0.25 \text{ nm}$ level in about 90 min.

This result, although obtained in the framework of in-flight operations, is also relevant for on-ground verification of the FP, which has mechanical proper frequencies above few ten Hz for launch compatibility. Thermal variations may have typical scales of a few or several min: it is convenient that their time constant is set by design and manufacturing significantly longer than the above, *e.g.* 15-20 min, to retain the performance of the proposed calibration technique. The FP time constant can be tailored by proper choice of geometry, material and structure, and verified in the laboratory over macroscopic range (several K).

4. OPEN ISSUES AND POSSIBLE IMPROVEMENTS

The effects of small rotation vs. x/z correspond to variations of the effective pixel (and chip) along scan size, resulting in image blurring if the nominal clock rate is retained. Conversely, the image quality may be restored by the application of an optimal clock rate for each device, *i.e.* driving the FP asynchronously. It is important to verify the feasibility of this option, its impact on the FP complexity, and on its performance; in principle, asynchronous operation may induce a relevant level of system noise.

Local adaptation of the CCD clock rate may also be useful to reduce the effects of distortion, which changes the local optical scale and the angular pixel size over the FP. Variable clock rate is compatible with effective focal length variation $\Delta F / F \leq 0.5\%$; usage of a fixed (synchronous) clock rate requires $\Delta F / F \leq 0.02\%$, with more stringent optical design requirements.

Current industrial studies are trying to ease the implementation constraints of GAIA by optimization of several mission aspects, including optical design performance to allow for common CCD clocking. Also, the superposition of the images from both telescopes on a common FP (as in previous concepts analyzed for GAIA) may reduce the overall detector complexity by a factor two. The feasibility of a nearly square CCD format, about 6 cm along scan size, with pixel format $10 \times 30\ \mu\text{m}$, is under investigation. This reduces by another factor of two the single FP complexity, the chip count, and the dead space for interconnections. Also, the option of halving the satellite spin rate, and consequently the readout and telemetry rate, is considered. The latter two concepts also increase the elementary exposure time, with a negative impact on the bright limiting magnitude due to saturation.

5. CONCLUSION

The specifications of mosaic design and manufacturing are that individual CCD positions can be set to within few ten μm , provided the corners are within few μm from local x - y axis. The actual CCD position can be verified by measurements both on the ground and in orbit. The requirements seem to be compatible with the current state of the art CCD mosaic, although they are still challenging. A conceptual method for in orbit FP calibration has been discussed, and it appears to be compatible with the nm level requirements of GAIA; also, relevant aspects like FP thermal time constants, can be assessed at laboratory level on macroscopic scale.

6. ACKNOWLEDGEMENTS

We acknowledge the Italian Space Agency for financial support (contracts ASI ARS~96-77 and ASI ARS~98-92) to our studies.

7. REFERENCES

- [1] Perryman, M. A. C., de Boer, K. S., Gilmore, G., Høg, E., Lattanzi, M. G., Lindegren, L., Luri, X., Mignard, F., Pace, O., de Zeeuw, P. T., 2001, *A&A* **369**, p. 339
- [2] <http://astro.esa.int/gaia/>
- [3] Gai, M., Lattanzi, M.G., Mana, G., 1999, *Meas. Sci. Technol.* **10**, pp. 1254
- [4] de Boer, K.S., Gilmore, G.F., Høg, E., Lattanzi, M.G., Lindegren, L., Luri, X., Mignard, F., de Zeeuw, P.T., Perryman, M.A.C., Pace, O., 2000, *ESA SCI(2000)* **4**
- [5] Gai, M., Carollo, D., Delbò, M., Lattanzi, M.G., Massone, G., Bertinetto, F., Mana, G., Cesare, S., 2001, *A&A* **367**, pp. 362-370

BEHAVIOUR OF A RAYTHEON IRFPA (438×270) UNDER HIGH ENERGY PROTONS

Yann Hello¹, Jérôme Parisot¹, Sébastien Barde², Tristan Buey¹, Bertrand Le Ruyet¹, Alain Sémerly¹, Didier Tiphène¹

¹Laboratoire 'Etudes Spatiales et d'Instrumentation en Astrophysiques (LESIA), Observatoire de Paris/Meudon, ²Centre National d'Etudes Spatiales (CNES)

Abstract: *A Raytheon HgCdTe (cut-off 5 μm) 436×270 Infrared Focal Plane Array (IRFPA) is mounted at two of the three focal planes of an infrared imaging spectrometer, VIRTIS, on board the ESA/ROSETTA cometary mission. VIRTIS is comprised of a mapping spectrometer (-M) under Italian responsibility (Officine Galileo) and a high-resolution spectrometer (-H) under French responsibility (Observatoire de Paris, Meudon).*

ROSETTA will be launched in 2003 to intercept the comet Wirtanen in 2011. Almost all the measurements of the instruments will be performed at the end of the mission, after 8 years irradiation of ionising particles (mainly high energy protons from solar wind) have degraded the instruments.

In order to simulate part of the ROSETTA detector's radiation environment, we performed a set of irradiation tests under high energy protons (up to 50 MeV). This paper firstly describes the environmental conditions of the tests. As a second step, the characteristics we obtained before and after irradiation are given: detector dark current, readout noise, linearity, and operability. Those results are compared and discussed.

Key words: *cooled Infrared Focal Plane Array (IRFPA), irradiations, HgCdTe, space instrument*

1. INTRODUCTION

The journey to the comet Wirtanen will take eight years. To gain enough orbital energy to reach its target, one Mars and two Earth gravity assists are required. The space radiation during this time presents a major problem. It is the penetrating particles that pose the main problems,

which include upsets to electronics, degradation and damage to components. In this mission in particular solar protons and galactic rays will be encountered. The trapped particle radiation environment during the intermediate transfer phases can be neglected in comparison with the contribution from the solar protons. The objective of these tests was to predict the effects of space radiation on the main characteristics (especially the dark current) of the IRFPA. This purpose of this campaign was principally to improve our knowledge of the displacement damage induced by protons (only few publications of similar tests on HgCdTe can be publicly access). Only proton energies above 20 MeV, because of the attenuation by Al shielding, can reach the detector. The decreasing of solar protons at high proton energy caused us choose an irradiation facility that can accelerate protons up to a few tens MeV below 100 MeV (at 100 MeV, there is 100 times less protons than at 20 MeV).

We performed the irradiation tests at 60 MeV on a single chip detector at the cyclotron of Louvains-La-Neuve (Belgium) on the 15th of December 2001.

2. CONFIGURATION

The 60 MeV incident proton beam was 80 mm in diameter and was shot at the detector through a four-areas shield to decompose the beam in four energies: 20 MeV, 30 MeV, 40 MeV and 50 MeV.

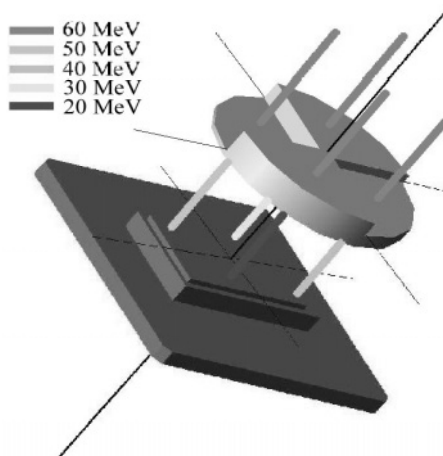


Figure 1. Irradiation flow.

Most of the radiation will happen during the long hibernation cruise, where most of the electrical systems are not operational. Thus, the test was performed using the real IRFPA hibernation parameters: 180 K and no power.

The full dose was applied to the detector in three shots, corresponding to half, once and twice the estimated total dose received by the detector for the entire hibernation cruise on board the Rosetta space probe.

Measurements of dark current, linearity, noise and flat fields were made before and after irradiation. Additional measurements of dark current were made between irradiation steps.

3. MAIN RESULTS

The profile of temperature and irradiation fluencies is given on Figure 2.

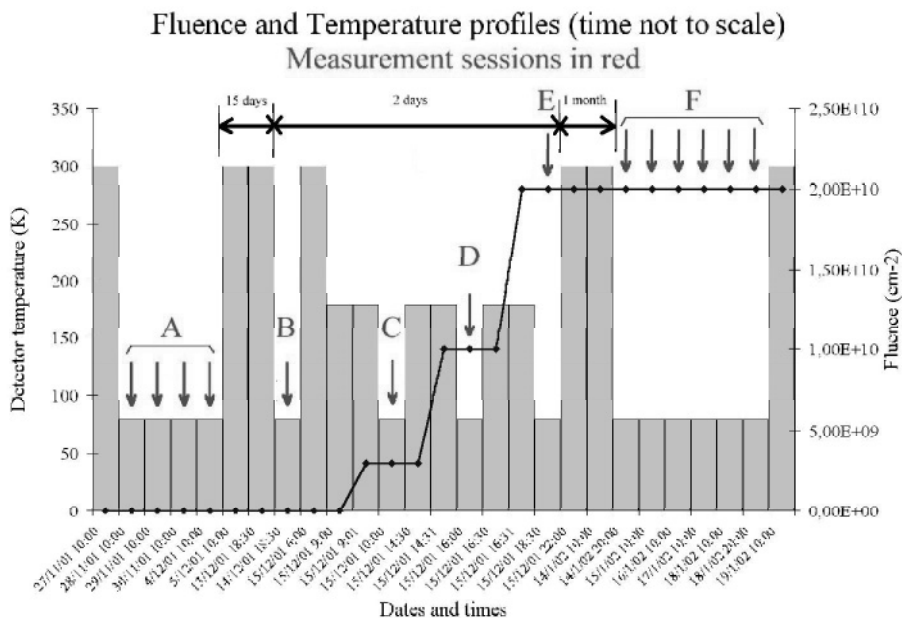


Figure 2. Temperature and irradiation fluence profile.

The largest impact that we observed (which is still very low) was on dark current. All other characteristics remained almost unaffected.

Figure 3 shows the dark current behaviour after irradiation for the four different zone (protons energy). The effect of irradiation is estimated by calculating the number of pixels whose difference of dark current is greater than a given threshold.

We observed a partial annealing of the component with time (1 month at 300 K) after the irradiation. Figure 4 shows, for the highest affected zone (30 MeV zone), the temporal behaviour of dark current.

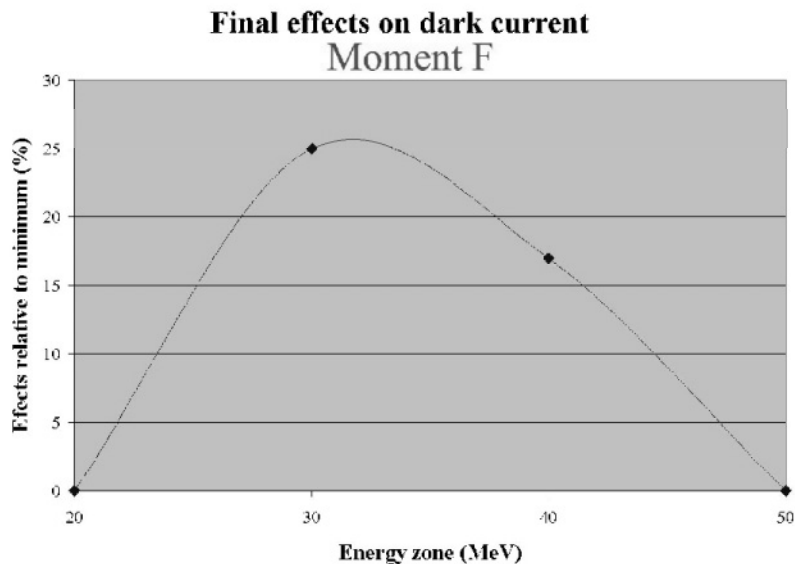


Figure 3. Dark current behaviour.

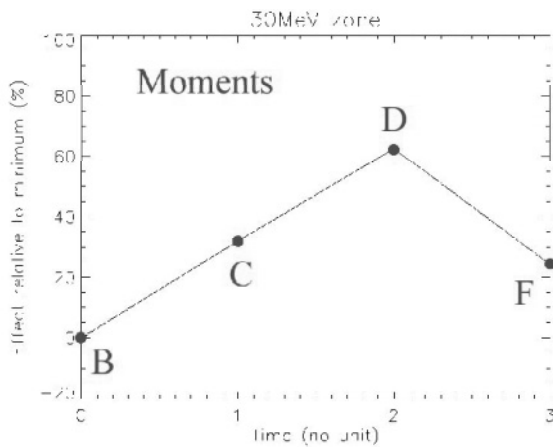


Figure 4. Temporal behaviour of the 30 MeV zone for dark current.

4. CONCLUSION

The radiation effects on the detector global performances are not significant. A partial annealing of the component has been observed after one month of non-operative conditions at 300 K.

Except for the 20 MeV zone, whose shield might be too thick (protons were stopped by the shield), the effects due to irradiation follow the simulated model that predicts a decreasing effect with proton energy.

RADIATION DAMAGE EFFECTS IN XMM-NEWTON EPIC MOS CCDS

David Lumb

Science Payloads Technology Division, Research & Science Support Department, European Space Agency, European Science Research and Technology Centre (ESTEC)

Abstract: *The effects on Charge Transfer Inefficiency (CTI) performance of radiation damage are described. The variation in performance of background rates and X-ray energy are summarised. The performance is consistent with pre-launch expectations and confirms a model that attributes most damage to Phosphorus-Vacancy (P-V) center traps. However, other trap species are also present, and the implications for photometric missions like **Hubble Space Telescope** and **Eddington** are reviewed, and the claims for novel p-channel CCDs are addressed.*

Key words: *Charge-Coupled Devices (CCDs), radiation damage, Charge Transfer Inefficiency (CTI)*

1. INTRODUCTION

The orbit of the XMM-Newton spacecraft is highly eccentric (7,000–114,000 km), and passes through the proton belts every 48 hrs. As of mid-2002 it has flown through 2 years of the Solar Maximum, experiencing several large solar flares. Measurable radiation damage has occurred, affecting the Charge Transfer Inefficiency (CTI). For reference, the pre-launch analysis predicted a fluence over the mission (dominated by solar proton flares) of $\sim 5 \times 10^8$ equivalent 10 MeV protons cm^{-2} , behind the thick Al shielding (~ 3 cm).

The EPIC MOS camera [1] employs a close-packed array of 7 MAT (now E2V) CCDs, which have high resistivity substrates for enhanced X-ray

response, and novel open electrode structures for good, soft X-ray efficiency. Radiation resistance is maximized with narrow supplementary buried channels. Our single photon X-ray counting mode is the most critical application for CTI – we require the accurate measurement of X-ray signal packets at a rate of 10^{-3} photons/pix, in the absence of any background signal between X-ray packets.

2. DAMAGE MEASUREMENT & MITIGATION

To monitor and calibrate the degradation of CTI, we employ an internal Fe^{55} radioactive source that produces X-ray photons that liberate ~ 400 and 1600 e^- charge packets in Si. This source is typically monitored near the particle belts and outside normal science operational windows.

Degradation of CTI and energy resolution is a result mainly of trapping in the parallel shift registers, and due to the well-known Phosphorus-Vacancy (P-V) defect centre. The degradation in energy resolution is comparable with expectations pre-launch (at an X-ray energy of 5.9 keV from degradation from 133 eV to 167 eV FWHM, see Fig. 1).

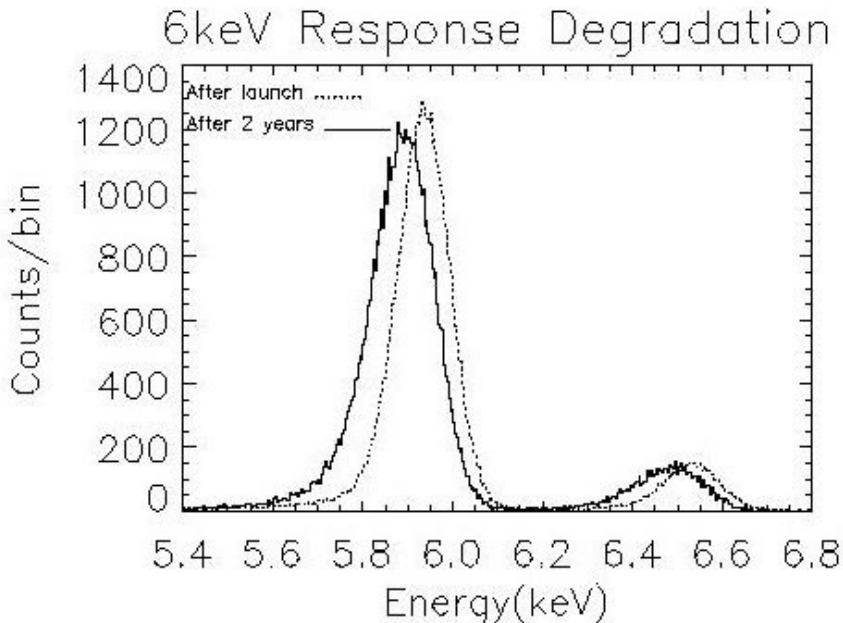


Figure 1. Comparison of response to internal X-ray calibration source immediately after launch (*dotted line*) with that of after ~ 2 yrs in orbit (*unbroken line*). Charge loss and resolution degradation is measurable, but well within expected limits.

The P-V centre trap release time at -90°C is \sim seconds. The time within $\pm 200\%$ is still unknown, but it ranges from 1 to 10 seconds. At typical photon rates of 3×10^{-5} photons/pix/sec this means that each column experiences 1 charge packet per 20 trap emission times. Measurement of CTI vs. background rate is facilitated by the highly variable background rate at low altitudes, where the rate can increase to ~ 1 charge packet per column/frame, and qualitatively confirms these time constants.

To mitigate the damage experienced, we have recently performed tests with the CCDs cooled to -120°C . This demonstrated that approximately a 65% charge loss recovery (Fig. 2). This occurs because the P-V center trap emission times lengthen by ~ 100 sec with this temperature change, and the traps tend to remain filled between charge packet arrival.

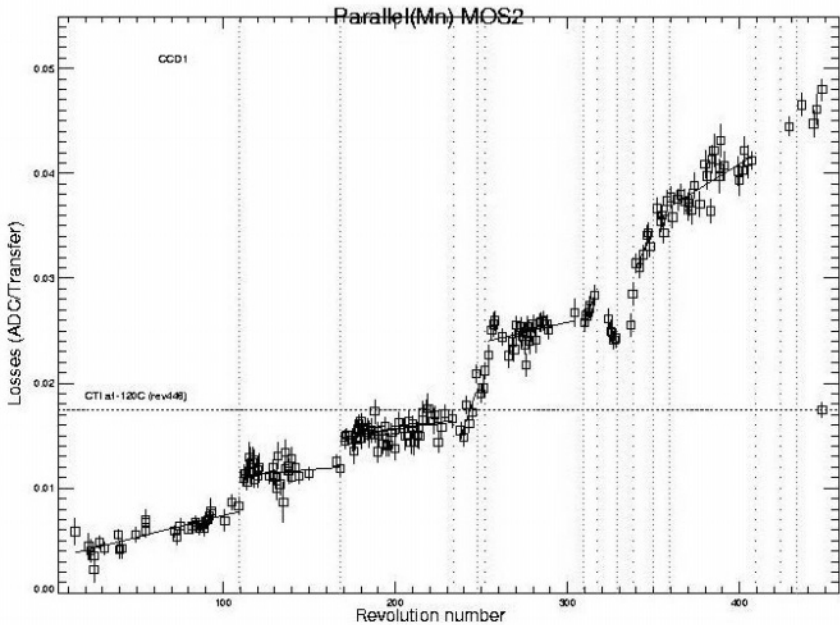


Figure 2. Trend of CTI increase with time. The last datum corresponds to improved CTI by cooling to -120°C . Vertical lines correspond to solar flare events.

A measure of energy dependence for CTI is also found. This is empirically related to the charge packet volume occupancy and also to the associated trapping time constant. We convert the fractional CTI loss to charge trapped, and find that 6 keV X-ray charge packets lose twice the amount of charge as a 1.5 keV packet.

3. IMPLICATIONS OF CTI MODELING

The fractional charge loss increases as the energy decreases. This affects applications for optical photometry. Empirical corrections carried out for HST WFPC, *e.g.*, ignores such detailed modeling, whereas background signal and exposure frame rates are important modifiers of CTI. In addition to different CTI loss with stellar magnitude, the effects of low-level background signals needs to be considered, as well as the readout history of the CCD (previous exposures, bias frames, etc.)

The predicting of effects in certain operational modes, *e.g.*, Time Delay & Integration, must be carefully considered given nominal CTI estimates from other measurements or models. The charge loss per TDI clock cycle is not the same as lost by the equivalent signal in a static integration, because the charge builds up in a packet with time. Fractional loss is relatively *less* at the start of the TDI cycle.

Claims for p-channel devices regarding radiation hardness must be treated with caution. Our measurements indicate a probable ~30% density of traps responsible for charge trapping are *not* of P-V flavour. Other traps such as di-vacancy, or a stable vacancy attracted to the p-channel dopant might be important for those p-channel devices.

It cannot be emphasized enough that taking a measurement (*e.g.*, at a single X-ray energy and after a proton irradiation at suitable fluence) is inadequate to predict the effects in a future applications. Not only must the radiation environment (ionising or non-ionising) be representative, but the mode of imaging, signal level and temperature all have strong effects on the eventual performance.

4. REFERENCES

- [1] Turner, M.J.L. et al, 2001, *Astron. & Astroph.* **365**, p. 27.

95 MILLION PIXEL FOCAL PLANE FOR USE ON THE KEPLER DISCOVERY MISSION

Robert Philbrick¹, John Geary², Edward Dunham³, David Koch⁴

¹Ball Aerospace & Technologies Corporation, ²Smithsonian Astrophysical Observatory,

³Lowell Observatory, ⁴NASA Ames Research Center

Abstract: *The primary goal of the upcoming Kepler Discovery mission is to search for terrestrial-sized planets around neighboring stars. To accomplish this mission, a space-based photometer is being developed that employs a 0.95-m aperture Schmidt telescope coupled to a very large Focal Plane Array (FPA) measuring 14''(L)× 14''(W)× 10''(D). The FPA is populated with 42 large-format custom CCD-based detectors to yield approximately 95 million pixels in the 100 sq. deg. field of view of the instrument. Over the 4 year mission the FPA will continuously measure the relative intensity of approximately 100 thousand main sequence stars ($14 \leq m_v \leq 9$) and will be capable of detecting relative changes in stellar flux on the order of 10-40 ppm (one-sigma) over transit periods ranging between 2 to 16 hours. All critical electronics are housed immediately behind the FPA, which yields a low-noise, compact design that is both robust and fault tolerant. The design and development of the FPA and custom CCD-based detectors is discussed along with the results from detailed performance models.*

Key words: Kepler, Charge-Coupled Device (CCD), Focal Plane Array (FPA), photometry

1. INTRODUCTION

The primary goal of the *Kepler* Discovery Mission [1] is to survey at least 100 sq. deg. of the sky for at least 4 years while gathering relative intensity data on approximately 100 thousand main sequence stars, ranging in brightness from $14 \leq m_v \leq 9$. To accomplish this task, a 0.95-m aperture space-based photometer is being developed by Ball Aerospace &

Technologies Corporation for the *Kepler* science team headed by the NASA Ames Research Center. The stream of stellar intensity data will be analyzed on the ground to identify planetary transient events ranging in duration from 2-16 hours. Of particular interest to the science team will be the identification of transit events corresponding to planets lying in the habitable zone [2]. The *Kepler* spacecraft will reside in a heliocentric orbit to take advantage of the benign observing environment, with the launch currently scheduled to occur in 2007.

At the heart of the *Kepler* photometer, as depicted in Fig. 1, is the Focal Plane Array Assembly (FPAA), which consists of the integrated Focal Plane Array (FPA) and Focal Plane Interface Electronics (FPI). The FPA is populated with a total of 46 CCD-based detectors and is tasked with monitoring the star ensemble. Of the 46 CCDs, 42 are dedicated to the acquisition of science data and the remaining 4 CCDs are used for fine guidance control. The 42 science CCDs are arranged onto 21 CCD modules, with each module housing 2 CCDs. The FPI lies immediately behind the FPA and supplies all critical bias, clock inputs and pre-amplification of the CCD output signals. All electrical signals are routed to/from the FPAA through cables along the spider support legs.

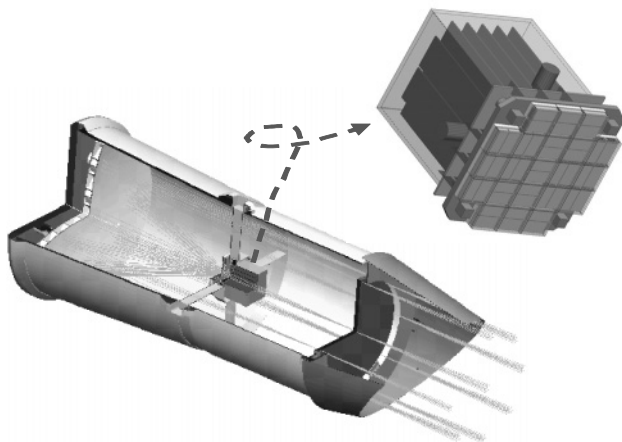


Figure 1. Transparent view of preliminary *Kepler* photometer design.

Every 90 days the *Kepler* spacecraft will undergo a 90° rotation about the optical axis to keep the solar panels optimally aligned to the sun and the passive radiator pointed to deep space. During this period a number of system level checks will be performed and an entire field of view image (*i.e.*, a 95-million-pixel image) will be downloaded, along with other telemetry data. After thermal stability is reestablished (<24 hours), the instrument restarts the continuous monitoring functions. During the monitoring periods, only select regions around each star of interest, referred to as photometric

apertures, will be downloaded to the ground. The particular photometric aperture selected for a given star will be determined through statistical analysis, as discussed by Jenkins [3].

Figure 2 shows two views of the mechanical FPAA model populated with only three CCD modules and two FPI electronics boards. The FPA is cooled using dual constant conductance heat pipes and a dedicated passive radiator. Additional details on the FPA, FPI, CCD module, and science CCD are discussed in the following sections.

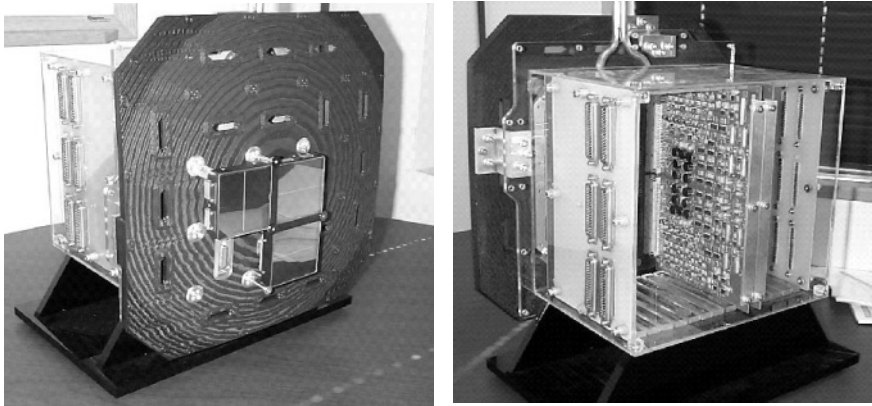


Figure 2. Front and rear views of the mechanical FPAA model (black base is not part of the FPAA).

2. FOCAL PLANE ARRAY

The FPA consists of a 14"× 14" substrate made from graphite cyanate ester onto which 25 CCD modules (21 science and 4 fine guidance) are mounted. The curvature of the substrate is designed to match the optimal focal surface of the Schmidt telescope, which is closely described by a 1.4-m spherical surface. Molybdenum inserts are spaced across the curved FPA surface to provide a mechanically stable platform and a high conductivity thermal path to the "thermal spreader" and heat pipe assembly which reside immediately behind the FPA substrate. Each CCD module mounts to the curved FPA substrate only at the inserts. The graphite composite substrate is used to provide a stable thermoelastic platform for all CCD modules. Heaters are mounted onto the "thermal spreader" and are used to actively control the temperature of the FPA. Temperature drifts over time resulting from the changing sun solar angle are not expected to exceed 0.1 °C/12 hour period and when the active control system is factored in, the actual temperature variability is expected to be considerably less than this value.

CCD modules are arranged on the FPA in a rotationally symmetrical orientation to ensure all stars are monitored in a consistent manner over time (e.g., before and after the quarterly 90° roll maneuvers). To minimize the degrading effects on the CCDs of very bright stars (i.e., $m_v < 9$), many of the brightest stars in the field of view are aligned to fall onto the FPA web light shield (see gap between modules in Fig. 3). CCD modules are installed and removed exclusively from the front of the FPA, thereby not disturbing any part of the FPI.

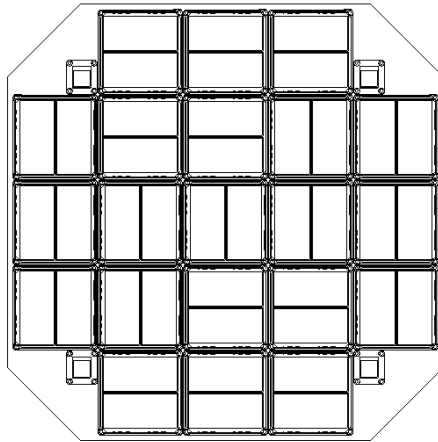


Figure 3. Top side view of Kepler FPA.

The photometer has been designed to allow a total optics plus FPA alignment tolerance budget of $\pm 150 \mu\text{m}$, which, in turn, enables the FPA to be assembled using a “bolt and go” approach. That is, if the CCDs, CCD module components, and FPA substrate are manufactured to sufficient tolerance, then all components can be simply assembled together and the resultant stack up in tolerance will be within the allotted budget. Therefore, precise focus alignment is not required for each CCD or CCD module. The photometer has an overall focus mechanism on the primary mirror that is used to bring the entire FPA into optimal focus. It should be noted here that by design optimal focus results in a total system PSF (i.e., optics plus CCD) ranging from 4-7 pixels in diameter. This broad PSF is highly desired in photometric applications such as *Kepler* [4] because it significantly reduces the sensitivity to intra-pixel variations and minimizes the number of stars that will saturate the CCDs.

3. FOCAL PLANE INTERFACE

The Focal Plane Interface (FPI) consists of 13 electronics boards and one backplane, configured in a typical card cage arrangement. Eleven boards are used to drive the 21 science CCD modules and 2 boards are used to drive the 4 fine guidance detectors. The body of the FPI is sealed from the photometer interior to minimize the possibility of outgassing contamination reaching the sensitive electro-optical components within the photometer. The FPI is vented to the exterior of the photometer through the use of a dedicated hose which runs along the length of one of the spider support legs.

Boards are installed and removed from the FPI exclusively from the rear of the FPI, thereby not disturbing any part of the FPA. Each of the 11 science module driver boards supplies all the clocks and biases to run 2 CCD modules, or 4 CCDs. The boards are designed and laid out in such a manner as to ensure that any credible single-point failure will result in the loss of only one CCD module. Fully redundant power and control signals are routed to the FPI from the CCD Signal Processor (CSP) and the LVDS timing signals routed to the FPI are fully redundant from within the CSP. The 84 science CCD outputs are driven to the CSP from the FPI using low-noise differential line drivers through individually shielded twisted pair cables. Figure 4 shows a schematic representation of the photometer electronics systems.

The CSP is tasked with supplying all clocks and control signals to the FPI and with digitizing and storing data from all 95 million pixels during the 15 min aggregation periods. Each channel on the CSP is composed of two memory banks arranged in a ping-pong configuration. So while 15 min binned data is being read out of one bank (ping) the other bank (pong) is acquiring the next 15 min worth of data. The CSP also has the ability to detect and remove transient signal events caused by incident cosmic or solar radiation. Common timing signals generated within the CSP ensure that all 42 science CCDs are operated synchronously, which significantly reduces electrical crosstalk between the 84 CCD outputs. The fine guidance CCDs on the FPA run at a 10-Hz frame rate (non-synchronous with science CCDs), but the boards and wiring associated with these CCDs are separate and decoupled from the science CCDs to minimize potential crosstalk issues. The Remote Photometer Electronics (RPE) and Solid State Recorder (SSR) perform other system level functions (not discussed in this work).

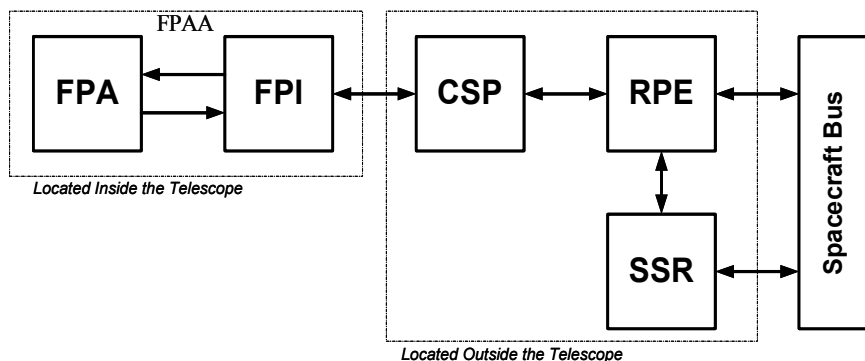


Figure 4. Block diagram of the *Kepler* photometer electronics.

4. CCD MODULE

Each science CCD module houses two CCD detectors on a common substrate. Electrical signals are routed from the CCD bondpads to a PCB located on the bottom side of the module substrate using high density, subminiature connectors and cables. Several surface mount decoupling capacitors reside on the PCB, in addition to the 51 pin main interface connector which mates to a similar connector on the FPA substrate. A field flattener lens resides above the CCDs and is supported using a 4-sided fixture. A captive screw is held in each of the four flexure support legs and is used to affix the CCD module to the FPA substrate from the front of the FPA. The legs provide mechanical support and the thermal path to the thermal spreader located on the back of the FPA.

Electrical signals are routed from the CCD bondpads to the PCB located on the bottom side of the module substrate using high density, subminiature connectors and cables. Several surface mount decoupling capacitors reside on the PCB, in addition to the 51 pin main interface connector. The main interface connector on the CCD modules mates with an opposite gender connector affixed to the FPA substrate.

The pinout of the CCD is symmetric about the row dimension and, therefore, both frontside and backside versions of the CCD can be accommodated using the aforementioned packaging scheme (see Fig. 6). The science CCDs operate in the backside illumination mode to yield high quantum efficiency over the 400 to 900 nm wavelength range of interest, to minimize intra-pixel variability and the effects of stellar variability in the UV and faint reddened background eclipsing binaries, and to provide additional flexibility in tailoring the Point Spread Function (PSF).

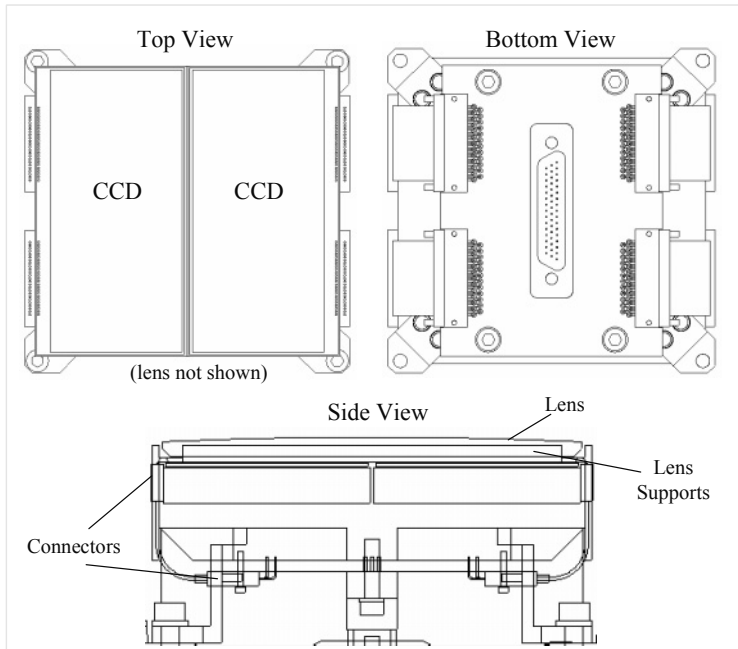


Figure 5. Schematic of a single *Kepler* science CCD module.

Two CCD manufacturers, Marconi Applied Technologies and Semiconductor Technologies Associates, have been selected to supply the science grade CCD detectors for the *Kepler* mission. Each vendor will be tasked with supplying 30 flight-grade CCDs, in addition to several mechanical, frontside evaluation grade, and engineering grade CCDs.

Each *Kepler* science detector is a CCD-based full-frame device with 2200 columns and 1024 rows, as depicted in Fig. 6. A four-phase architecture is employed in both the serial and parallel CCD registers to maximize charge capacity ($> 1 \text{ Me}^-$) and minimize clocking induced artifacts. Each pixel is $27 \mu\text{m} \times 27 \mu\text{m}$. A vertical injection structure is included and may be used to pre-flush the entire photoactive area or pre-fill select portions only.

5. FPA PERFORMANCE

The *Kepler* application is somewhat unique for a space-based telescope in that the mission involves staring at the same image scene for 4 years. In addition, because relative differential rather than absolute photometry is being performed to detect transit events on the time scale of 2 to 16 hours,

slow changes over time in optical, CCD and electronics performance are easily identified and removed from the data by detrending.

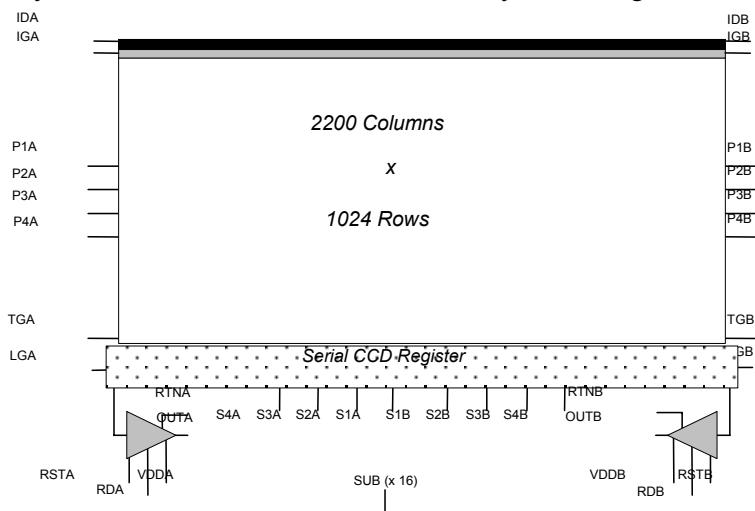


Figure 6. Block diagram of the Kepler CCD detector.

CCD performance model simulations have been run for several possible CCD operating modes and configurations [5] and the results indicate that the degradation in charge transfer efficiency resulting from exposure to the space radiation environment will not significantly degrade the performance of the CCDs over the 4-year lifetime. This is due principally to the fact that the radiation-induced traps reach a steady state population at the -90°C operating temperature, a result of the static imaging application and the fact that the trap emission time constant is 4 sec, whereas the integration period is only 2.5 sec. At higher temperatures, where the trap emission time constant is much less than the integration period, the trap population does not reach a steady state, but the impact of degraded CTE on each star in the FOV remains relatively constant over time, and again there is no significant impact on the ability to perform relative photometry. The preliminary instrument design placed the CCD operating temperature at -90°C but recent analysis appears to indicate that the CCDs could operate as warm as -60°C and possibly higher whilst enabling the photometer to meet all performance requirements at end-of-life.

System level signal-to-noise analysis shows that stellar variability is the dominant noise source for the brighter stars ($m_v < 12$) and photon shot noise for the fainter stars ($m_v \geq 12$). This, in turn, permits the CCD and FPI noise budgets to be relatively high when compared to other space-based CCD instruments. For example, at the nominal integration period of 2.5 sec and

pixel rate of 3 Mpix/sec, the maximum read noise specification for the CCDs is 25 e⁻rms.

6. CONCLUSION

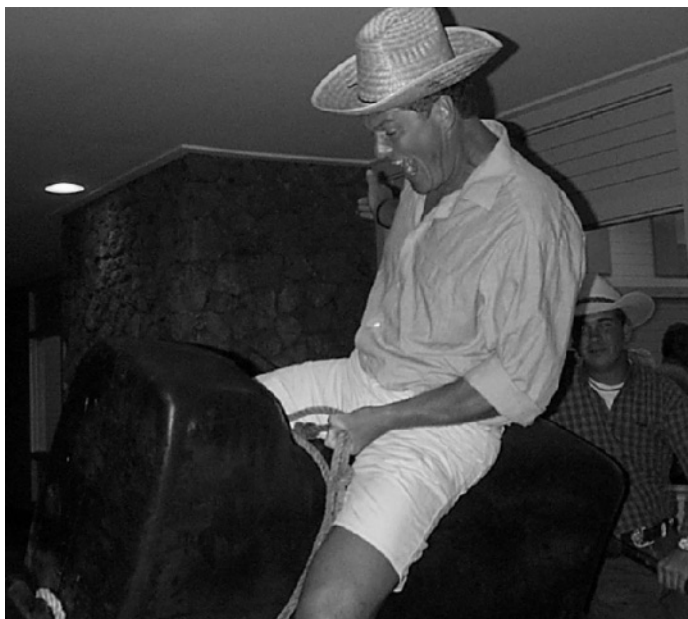
The preliminary design of the *Kepler* FPAA has been discussed. While design trades and analyses are expected to continue well into 2003, and minor changes in materials and processes will likely occur, the basic design of the *Kepler* FPAA is not expected to deviate significantly from that presented herein. Specific design trades currently under way are investigating the impact on photometer performance of raising the FPA operating temperature above the baseline -90 °C level and investigating the use of alternative materials for the FPA substrate.

7. REFERENCES

- [1] Borucki, W. J., Dunham, E. W., Koch, D. G., Cochran, W. D., Rose, J. A., Cullers, K., Granados, A., and Jenkins, J. M., 1996, *FRESIP: A Mission to Determine the Character and Frequency of Extra-Solar Planets Around Solar-Like Stars*, Astrophysics & Space Science, **241**, p. 111.
- [2] Koch, D., Borucki, W., 1996, *A Search For Earth-Sized Planets In Habitable Zones Using Photometry*, First International Conference on Circumstellar Habitable Zones, Travis House Pub. p. 229.
- [3] Jenkins, J., Witteborn, F., Koch, D., Dunham, E., Borucki, W., Updike, T., Skinner, M., Jordan, S., 2000, *Processing CCD images to detect transits of Earth-sized planets: Maximizing sensitivity while achieving reasonable downlink requirements*, SPIE Conf Proc. **4013**, p. 520.
- [4] Koch, D., Borucki, W., Jenkins, J., Webster, L., Witteborn, F., 2000, *CCD Photometry tests for a mission to detect Earth-size planets in the extended solar neighborhood*, SPIE Conf Proc. **4013**, p. 508.
- [5] Philbrick, R. H., 2002, *Modeling the Impacts of Pre-Flushing on CTE in Proton Radiation CCD-Based Detectors*, IEEE Trans. Nucl. Sci., Vol. **49**, No. 2, Pt. 2, p. 559.



All the food is gone! Who ate the food on the ride to Volcano? The forlorn travelers have called in the secret service envoy (in the back with sunglasses on). Roger Smith (back) is speechless for once.



“ I am a loooooong way from Copenhagen, Ma!” Preben Norregaard demonstrating that years of riding elks makes him a good Paniolo.

SECTION VIII:

SUB-ELECTRON NOISE FOCAL PLANE ARRAYS

L3CCDS: FAST PHOTON COUNTING FOR OPTICAL INTERFEROMETRY

Statistics of Photon Counting

Alastair Basden, Chris Haniff and Craig Mackay.
Cavendish Laboratory, University of Cambridge

Abstract: *Low Light Level Charge-Coupled Devices (L3CCDs) have a large on-chip gain which can allow a signal to be detected above the readout noise. In this paper a technique allowing photon counting at any light level is investigated, and found to add noise to the signal at higher light levels due to the statistical nature of the gain. Accurate signal estimation can be achieved with very faint signals, up to about one photon/pixel/read. Optical interferometry requires detection of very faint signals, and the use of an L3CCD is found to allow reproduction of interferometric visibilities to high precision. Custom instrumentation used for control is also detailed.*

Key words: *Low Light Level Charge-Coupled Devices (L3CCDs), controller, interferometer, photon counting, statistical gain*

1. INTRODUCTION

Low Light Level Charge-Coupled Devices (L3CCDs) are newly developed CCDs, which can give high internal gain. However, the gain process is statistical, achieved by avalanche multiplication. Therefore, the CCD output cannot be used to calculate the exact photon input, rather, it can only infer the most likely photon input. The accuracy of this prediction determines how useful the L3CCD is as a photon counting device.

Optical interferometry involves the detection of interference fringes from two or more light beams. The temporal variation of these fringes must be measured as the relative delay between the light paths is altered, requiring sampling up to 10 kHz. High speed detection can result in a very low signal, which can be lower than one photon/pixel/frame. For interferometric

spectroscopy, there is a need for a detector with at least 100 pixels in one dimension with sub-electron readout noise. The use of L3CCDs as spectroscopic detectors is investigated, with particular regard for how accurately the interferometric visibilities can be reproduced.

Section 2 discusses the statistics of photon counting, and Sec. 3 discusses the custom controller.

2. PHOTON COUNTING STATISTICS

An L3CCD is able to provide a large internal gain by passing electrons through a multiplication register, which is an extension of the serial register [1]. As electrons pass through this register, a high voltage on one of the pins can cause avalanche multiplication to occur. The probability of creating an extra electron at each stage is small (1-2%), but many such stages can lead to a large overall gain, which can be adjusted between 1 and 10,000. The probability distribution for the electron output (x) is given by:

$$P(x) = g^{-n} x^{n-1} e^{-x/g} / (n-1)! \quad (1)$$

where the mean gain, $g = (1+m/100)^r$ (for large r), m is the multiplication factor, r is the multiplication register length and n is the number of electrons entering the multiplication register. This distribution is shown in Fig. 1.

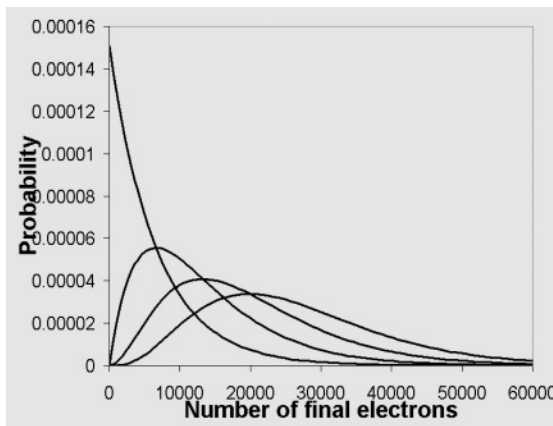


Figure 1: Probability distribution for L3CCD gain process.

The probability distribution can be used to estimate the number of received photons from a given output. The L3CCD can generate an output event with a high Signal-to-Noise Ratio (SNR) from a single electron

detected by the CCD imaging array. This allows processing of the output signal in a variety of ways. There is no spatial or temporal dispersion due to the amplification, which gives some advantages over some intensifier methods, allowing much higher mean photon arrival rates to be handled properly.

2.1 Readout Modes

There are several different ways in which we can interpret the output from the L3CCD, each of which has advantages in different situations.

2.1.1 Analogue Mode

The output is treated as with normal CCD's, the input times the mean gain. Due to the Poisson nature of the multiplication, the output noise scales as $\sqrt{2n}$, n being the number of detected photons. This is $\sqrt{2}$ greater than we would expect from photon shot noise and effectively halves the quantum efficiency of the device. This mode is best used at higher light levels.

2.1.2 Single Threshold Mode

If the input signal is low, with an average of less than 1 photon/pixel/frame, then we can assume that any detected event above a threshold level corresponds to one photon. This eliminates the dispersion caused by the multiplication process, and adding many frames gives a noise of \sqrt{n} . However, at higher light levels, there will be significant coincident losses, and we will underestimate the true input.

Where the losses are modest, they are easily estimated statistically and corrections can be introduced to improve linearity. This method only works up to a mean of about 1 event/pixel/frame.

2.1.3 Multiple Threshold Mode

For a given output signal and known gain, we can estimate the most likely value of the input number of photons. There will be errors made but at low signal levels these are small, minimising the additional noise factor.

At higher signal levels we lose accuracy progressively. This leads to noise scaling as \sqrt{n} at low light levels (standard Poisson photon shot noise statistics) where a single threshold is effectively used, and tends towards $\sqrt{2n}$ as the light level increases. In choosing the thresholds for selecting the input, a noise level (typically 6σ , where σ is the mean readout noise) is first subtracted from the signal. Then the remaining signal is placed into equal sized bins (the threshold step size), representing the predicted number of photons.

This gives the benefits of both the single threshold mode and the analogue mode, allowing photon counting at both low and higher light levels.

The threshold step size that gives the best estimate for the photon input is dependent on the gain and light level. There is more allowance for errors in the step size at lower light levels where larger steps are optimum, tending to infinity as light tends to zero (single threshold mode).

At high light levels, the ideal step size tends to the expected gain and gives noise similar to the analogue case, as shown in Fig. 2.

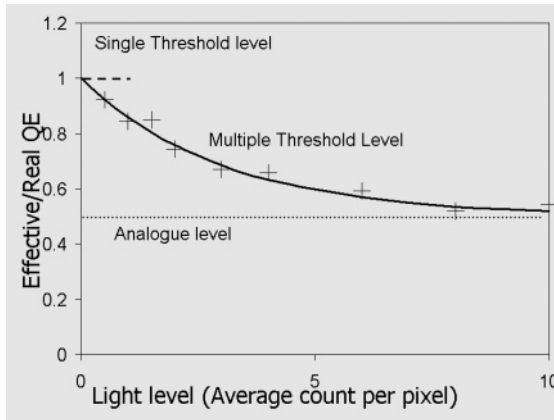


Figure 2: The effective decrease in Quantum Efficiency (QE) is also shown, due to statistical noise being added during the multiplication process.

We have investigated the ideal step size, and found that it is possible to predict from the average light level using the following relation:

$$\text{Threshold Step Size} = \text{gain} \left(1 + 0.5x(\text{mean photons per pixel})^{-3/4} \right) \quad (2)$$

This gives a good fit to the data over a wide range of gain and light levels.

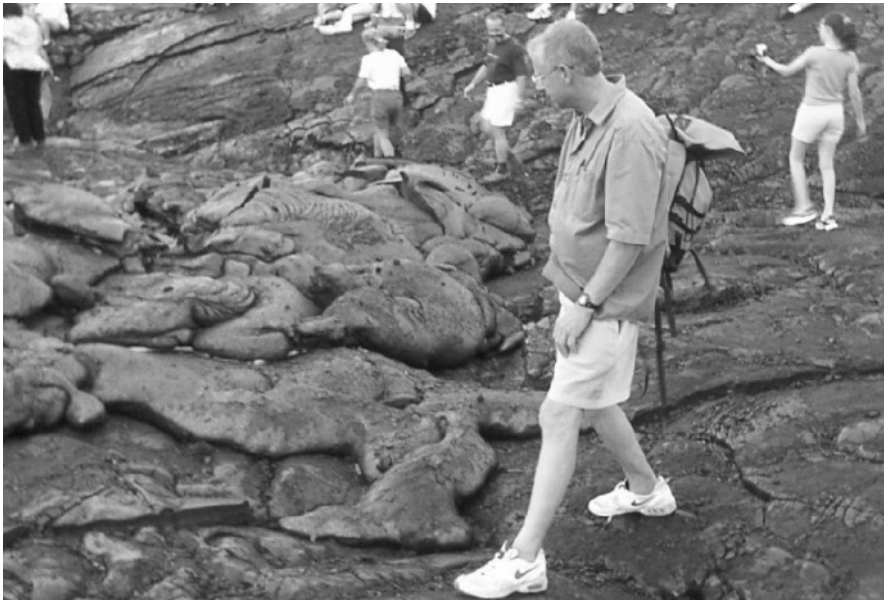
3. L3CCD CONTROLLER DESIGN

We are currently constructing a controller in our lab, capable of operating in any of the readout modes [2]. A Digital Signal Processor (DSP, Analog Devices SHARC-21160) is used to generate L3CCD control waveforms (clock and signal process) at up to 15 MHz (with capability for higher pixel rates). The DSP is controlled by an embedded web server, allowing machine independent operation. Custom circuit boards with a field programmable

gate array will convert the DSP output into CCD waveforms, and the CCD output will be digitised to 14 bits. A host PC and frame grabber (Matrox Meteor II/dig) will then be used to capture the data and provide real time analysis of the visibilities and processing of the data for telescope control feedback.

4. REFERENCES

- [1] Jerram, P., Pool, P., Bell, R., Burt, D., Bowring, S., Spencer, S., Hazelwood, M., Moody, I., Catlett, N., Heyes, P., 2000, *The L3CCD: Low Light Imaging without the need for an Intensifier*, Marconi Applied Technologies.
- [2] <http://www.mrao.cam.ac.uk/telescopes/coast/index.html>



Guy Woodhouse outruns the flowing lava...he has improved his speed since the last time we measured it (see Optical Detectors for Astronomy II, page 118).



Newest members of the "Grantcan Mai Tai Club". (don't they look cute with leis?). In the back the SOC is still deliberating to choose the awards recipients. (Courtesy G. Burley)



Gustavo Rahmer and wife Mariana enjoy the "traditional" Paniolo dinner of Frosted flakes.

L3CCD'S: LOW READOUT NOISE CCDS IN ASTRONOMY

Lucky Exposures Technique

Alastair Basden, Bob Tubbs and Craig Mackay

Institute of Astronomy, University of Cambridge

Abstract: *Perturbations in the earth's atmosphere mean that we do not get diffraction-limited images on anything but the smallest telescopes, even if they have perfect mirrors. However, changes in the atmosphere occur on timescales of order 10 ms. Images taken with exposures shorter than this will freeze the atmosphere in the image, and occasionally a flat wave front will be imaged. Shifting and adding many such images will result in a diffraction-limited picture of the sky. We report on some results obtained using a Low Light Level Charge-Coupled Device (L3CCD), on the Nordic Optical Telescope (2.5-m) in the I band. The full width half maximum of a point object is about $0.1''$, better than that given by the Hubble Space Telescope.*

Key words: *Low Light Level Charge-Coupled Device (L3CCD), Lucky Exposure (LE), Adaptive Optics (AO), diffraction limited*

1. INTRODUCTION

In the quest for the imaging of fainter objects, telescopes have grown in size. Atmospheric fluctuations mean that images produced are no longer diffraction limited, but smeared. Adaptive Optics (AO) has sought to overcome these problems by adjusting mirror surfaces in real time to correct the atmospheric effect. This, however, is not straight forward in the infrared, and more difficult in the optical. The isoplanatic patch is small ($\sim 10''$).

Changes in the atmosphere occur on timescales of order 10 ms. By imaging the sky with an exposure time less than this, it is possible to freeze the atmosphere, so that little smearing occurs in the image. If this is done many times, a flat wave front will eventually be imaged, giving a diffraction-

limited image of the sky [1,2]. Shifting and adding many such images allows us to build up a picture of the sky.

The fast frame rate means that each image may be very faint. However, reading a CCD fast usually results in a noisy signal, limiting the magnitude to which objects can be observed. A fast CCD with very low noise readout is required, characteristics that are matched by Low Light Level CCDs (L3CCDs). Tests with these chips have been successful, the elimination of read noise allowing us to reach up to ten magnitudes fainter.

2. L3CCD CHIP

An L3CCD is able to provide a large internal gain by passing electrons through the multiplication register, an extension of the serial register. As electrons pass through this register, a high voltage on one of the pins can cause avalanche multiplication to occur. The probability of creating an extra electron at each stage is small (1-2%), but many such stages can lead to a large overall gain, which can be adjusted between 1-10000. The output signal can then be much greater than the readout noise, resulting in a high signal-to-noise ratio for a single electron detected by the imaging array. Several modes are available for reading out the CCD, depending on light level, as discussed by Basden [3]. Here, we use an analogue mode, treating the output exactly as we would a conventional CCD. This leads to increased statistical noise due to the multiplication process.

3. RESULTS

The isoplanatic patch is about 60'' in the I band when using Lucky Imaging; greater than that achievable with AO. This is limited by telescope mirror imperfections. Fainter stars are affected by photon shot noise, though shifting and adding many such images removes this problem. A thinned L3CCD is able to use reference stars as faint as 17th magnitude. A sample of results is shown in Fig. 1.

3.1 Observing efficiency and quality

When using this imaging technique, we throw away a large fraction of images, resulting in poor observation efficiency. Observing efficiency can be improved at the expense of resolution, by using a larger fraction of images. This gives poorer results, though is still dramatically better than a long-exposure image, the quality degrading only slowly. The fraction of images used is determined by the required sensitivity and resolution, typically between 1-10%.

Image quality is found to be affected by the magnitude of the reference star, and by angular separation between the reference and science objects.

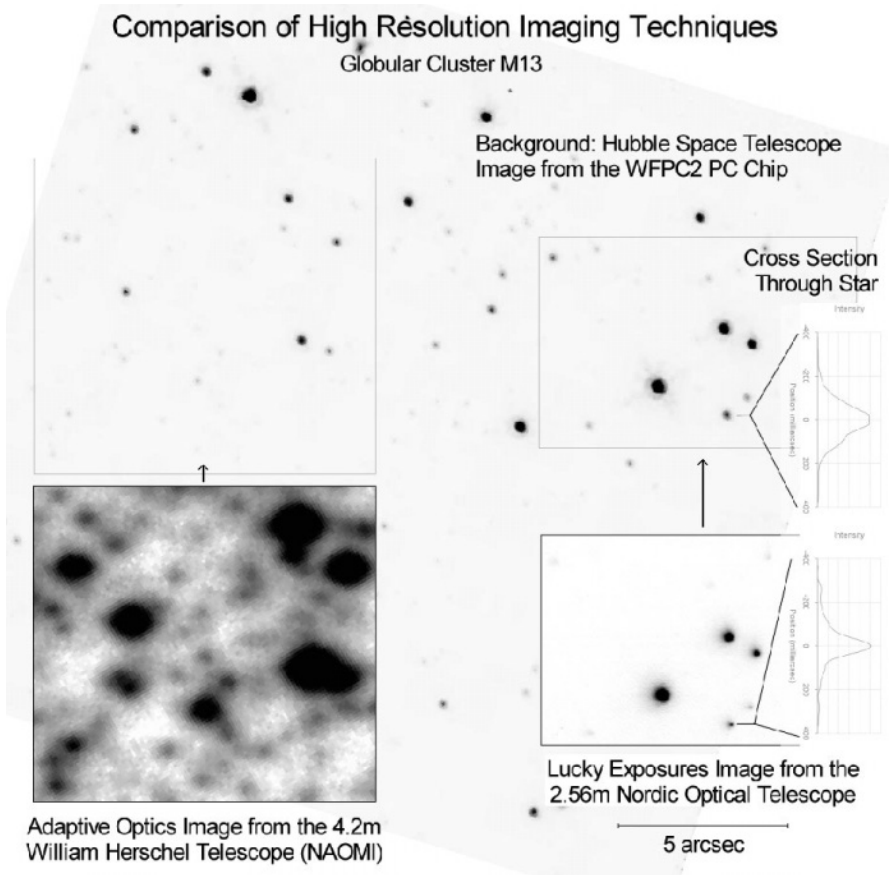


Figure 1. Comparison of imaging techniques. Background is from Hubble Space Telescope (HST), overlain with images from Adaptive Optics (AO) and Lucky Exposure (LE) techniques. The full width half maximum from each technique is: HST 0.12-0.15", AO 0.4", LE 0.1". Lucky exposure image was obtained using 3 sec of data from a 300 sec observing run.

Using 1% selection over one hour of observation on a 2.5-m telescope, the magnitude limit is $I \sim 23$ with a thinned CCD with diffraction-limited imaging (0.1-0.13" resolution), assuming seeing of about 0.5". This can be increased to $I \sim 25$ by selecting the best 10% of images, though the resolution is poorer (0.12-0.15").

Results could be improved further by using a multiple threshold readout mode [3], as this would increase the signal-to-noise levels in the faintest parts of the image, allowing greater detail.

4. HARDWARE REQUIREMENTS

There is a need to develop high-speed controllers for L3CCD's, which are capable of pixel rates up to 15-25 MHz, with multiple output channels and parallel signal chains. There is also a need for operation in several readout modes, current controllers only supporting analogue readout. Integrated hardware needs to be developed to sort, assess and process image data in real time. This is made possible by the current generation of digital signal processors, for example, Analog Devices SHARC-21160 chip, which we will use.

5. CONCLUSIONS

The Lucky Exposures imaging technique provides, at low cost, essentially the only way to achieve ground-based diffraction-limited imaging in the visible. Virtually 100% of the sky is accessible, and the isoplanatic patch is greater than with adaptive optics.

Larger telescopes can be used, dividing them up into a set of sub-apertures. The summation of independent sets will then improve the limiting magnitude.

6. REFERENCES

- [1] Tubbs, R. N., Baldwin, J. E., Mackay, C. D., Cox, G. C., 2002, *Diffraction-Limited CCD Imaging with Faint Reference Stars*, A&A **387** L21.
- [2] Baldwin, J. E., Tubbs, R. N., Cox, G. C., Mackay, C. D., Wilson, R. W., Andersen, M. I., 2001, *Diffraction-limited 800 nm imaging with the 2.56-m Nordic Optical Telescope*, A&A **368** L1.
- [3] Basden, A., Haniff, C., Mackay, C., 2002, *L3CCD's Fast Photon Counting for Optical Interferometry*, these proceedings, pg. 593.

ZERO NOISE CCD

A new readout technique

Jean-Luc Gach¹, David Darson², Christian Guillaume³, Michel Goillandeau³,
Olivier Boissin¹, Jacques Boulesteix¹, Cyril Cavadore⁴

¹Observatoire de Marseille, ²Laboratoire de Physique et de la Matière Condensée,

³Observatoire de Haute Provence, ⁴European Southern Observatory

Abstract: *We present a completely new technique to readout CCDs, which can achieve much lower noise than classical techniques used since the 70's. This technique is based on digital analysis of the CCD's output signal instead of analog filtering coupled to an original filtering method. Despite several attempts carried out in the past to implement digital Correlated Double Sampling (CDS), this is the first time that a radical improvement in readout noise performance is shown. Developed with this noise level improvement in mind, the zero noise CCD concept is presented. This is highly interesting for low light level conditions, where the detector works in readout noise regime and not in photon noise regime. This is the case particularly when concerning carrying out medium to high resolution spectroscopy, or multiplex (scanning) observations.*

Key words: *detectors, Charge-Coupled Device (CCD) readout, noise reduction*

1. READOUT NOISE LIMITATIONS WITH CLASSICAL TECHNIQUES

The problem of readout noise affects CCDs at low light levels. Despite the remarkably high quantum efficiency achievable, up to 95 %, and the very low noise, down to 2-3 e⁻, this is largely insufficient for high resolution spectroscopy where the observations are often detector noise limited. The problem is even more prevalent with multiplex instruments (*e.g.*, scanning instruments), where there is a large number of images produced. This problem has been largely discussed in [1, 2].

Usually, CCDs are read out with Correlated Double Sampling (CDS) devices. There are also other techniques, such as double ramp integration, clamp-and-sample, etc., but all are equivalent to the CDS system in terms of transfer function and signal processing. To limit readout noise, a first order low pass pre-filter with correctly matched bandwidth is placed before the CDS device. The output signal of the CDS is then converted into a digital signal with an A/N converter when this difference has been done (once per pixel) for computer acquisition. It is possible to show that in this system at high frequencies, reducing f_c , the pixel clock diminishes the readout noise of the CCD. But for lower frequencies, this readout noise becomes consistent, which means that reducing the readout speed of the CCD will no more reduce the readout noise [3].

2. BREAKING THE NOISE FLOOR

To have a lower readout noise at the same readout frequency, and principally to have much lower readout noise than the noise floor expected with a given CCD, it is then necessary to use a radically different readout technique. We removed the CDS completely and converted the signal of the CCD directly into digital information to feed a Digital Signal Processor (DSP). This scheme is well known and was introduced to read out infrared arrays in the early 1990's [4,5]. However, more recently Markelov et al. [6] developed a DSP based CCD controller it was still using a straightforward digital CDS (subtraction of two samples taken on the black level and pixel level respectively) or a classical filtering technique based on the Hegyi & Burrows optimal filter concept [7] at lower readout rates. In the case of our system, the A/D conversion rate is much higher (10 mega-samples/sec) since we have to sample several times (100-250) the reference level and the pixel level in order to have sufficient material for further digital processing. The digital flux is then processed in real time by a high computing power embedded DSP board (based on a Texas TMS320C6201), and the evaluated pixel value given by this process is returned to the classical CCD controller. This system has been designed to be completely transparent with older CCD controllers in order to avoid usefulness developments and to have an exact comparison base with an existing CCD system developed by Haute Provence Observatory. Therefore, swapping from a classical CDS system to this digital readout system is very simple. Figure 1 gives the system's synoptic.

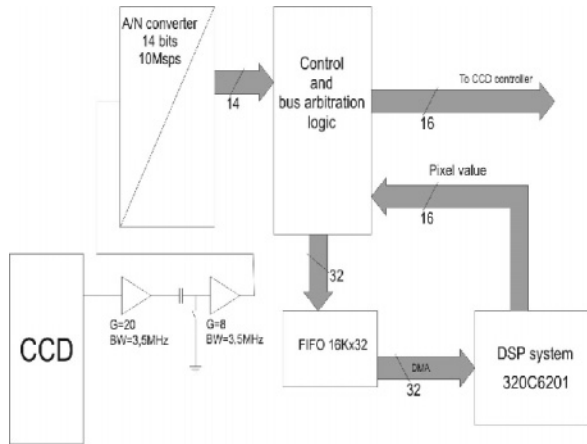


Figure 1. Synoptic of the system

Figure 2 shows a typical signal we obtained with this system and an EEV 42-20 CCD previously used in Haute Provence Observatory with a “classical CDS” controller. This graph shows clearly that samples which are very near to the reference level/pixel transition are much more correlated than the ones, which are at the opposite side of these (theoretically constant) levels.

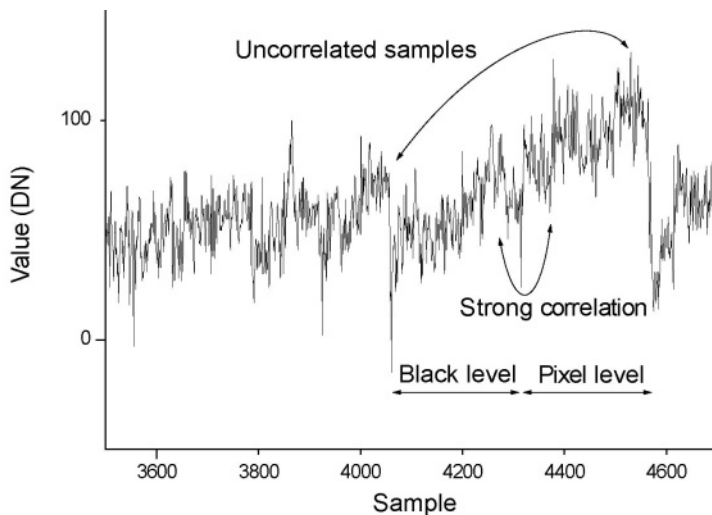


Figure 2. The sampled signal of a CCD @ 10 Mps in dark condition. One pixel has been highlighted with its black level reference and pixel level, showing that samples spaced in time are strongly uncorrelated.

Therefore one could say that the samples that are near the reference level/pixel transition (central samples) have a much higher quality than the other ones. One possibility to decrease readout noise is to give more "weight" to the samples, which are near this transition. When taking the mean of all the samples of a given level (black or pixel), one makes a simple 1st order filter. It is then possible to digitally subtract the black level from the pixel level, having a "digital double ramp integration", which is equivalent to a CDS as stated before. To give more weight to the central samples, it is necessary to give a coefficient to the samples, sum up and normalize with the sum of all the coefficients to maintain the system's gain at the same value. Each pixel value is then computed by the following formula:

$$Pix = \frac{\sum_{n=0}^{2n-1} \alpha_i S_i}{\sum_n \alpha_i} - \frac{\sum_{0}^{n-1} \alpha_i S_i}{\sum_{n=0}^{n-1} \alpha_i} \quad (1)$$

Where α_i is the i^{th} coefficient, S_i the i^{th} sample and n the amount of samples for each level (black or pixel) giving $2n$ samples per pixel. This formula can be simplified, especially for algorithmic reasons and code efficiency, giving negative coefficients for the first n^{th} coefficients (corresponding to the black level samples) and using symmetrical coefficients, by:

$$Pix = \frac{\sum_{n=0}^{2n-1} \alpha_i S_i}{2 \sum_n \alpha_i} \quad (2)$$

The first coefficients tested are plotted in Fig. 3. This shape is based on a Gaussian centred on the black/pixel level transition where the first n^{th} coefficients were inverted as explained above.

When varying the width of the Gaussian, we looked then what was the effect on the readout noise of the CCD. We obtained the results showed in Fig. 4, which plots the readout noise as a function of the Gaussian width. When the Gaussian is very large, all the coefficients have essentially the same value, the system then simply takes the mean of the samples and simulates a CDS as described before.

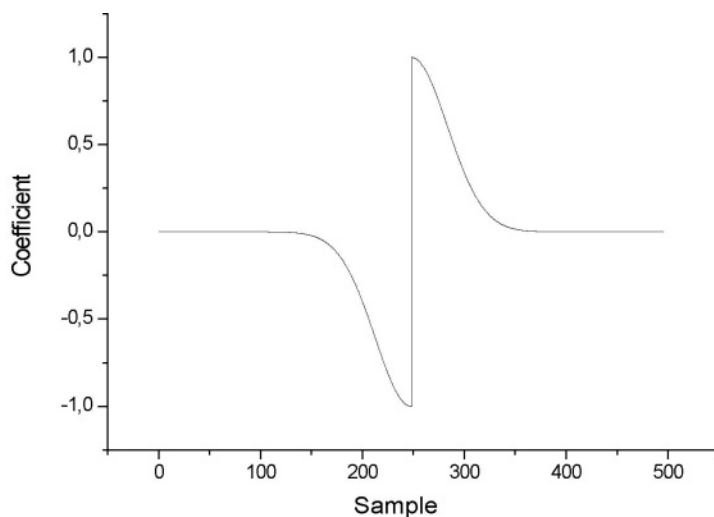


Figure 3. The filter coefficients based on a Gaussian shape where the first n^{th} coefficients were inverted.

The readout noise of the entire system was measured at 3.1 e^- , which is in accordance with the readout noise of the CCD EEV 42-20 used (EEV says 3 e^-). The first advantage of this technique is shown here: the numerical CDS adds nearly no readout noise (except preamplifier noise).

When the Gaussian width is decreased, the readout noise diminishes to a minimal value of $\sim 2.2 \text{ e}^-$ and then increases again. This is due to the fact that the central samples get more weight compared to the ones located at the edges of the black or pixel levels. For very small values of the Gaussian width, the readout noise increases since only a few number of samples are taken into account, and then the bandwidth of the system is increases dramatically, increasing the readout noise as a side effect. The Gaussian shape has been chosen randomly, therefore there would be almost no chance that this shape would minimize the readout noise. To find the best coefficients, we ran a “simulated re-cooking” program with the readout noise as cost function. We obtained the coefficients plotted in Fig. 5, which shows that this coefficient’s shape cannot be described by a simple mathematical function.

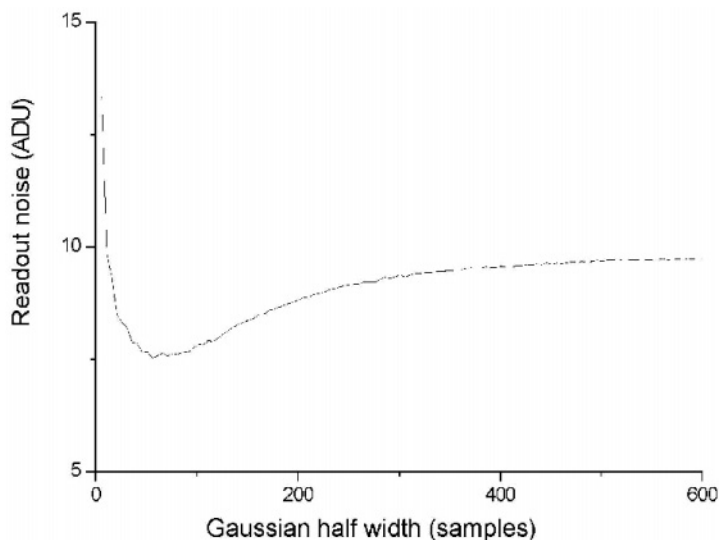


Figure 4. Readout noise obtained when varying the gaussian width shape. The conversion factor is $0.3 \text{ e}^-/\text{ADU}$.

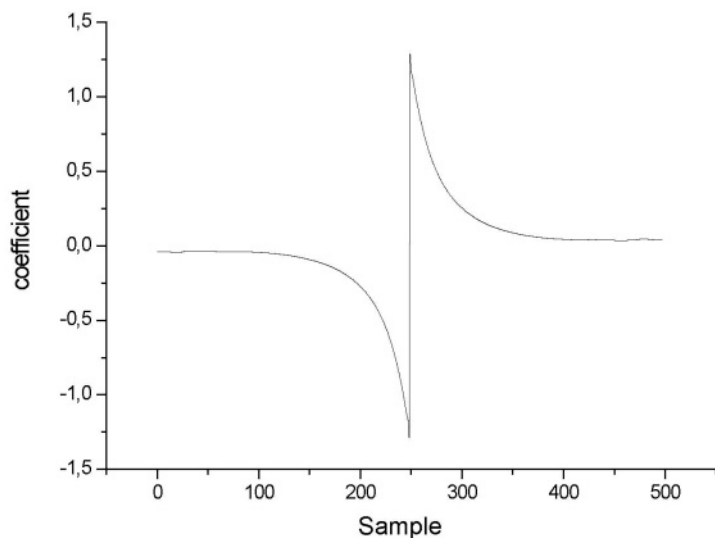


Figure 5. The optimized coefficients that minimizes the readout noise.

Using these coefficients, the readout noise fell to 1.7 e^- . This is compared with the “3 electron-noise CCD” which was read out $\sim 5 \text{ e}^-$ noise by the classical Observatoire de Haute Provence’s controller in exactly the same environmental conditions (same dewar, same location, etc.). The linearity of the camera has been measured at 100 ppm versus 1000 ppm with the classical controller. This is interpreted by the fact that the CCD’s signal is

digitized very near to the CCD's output and does not go through any complex analogic device. Therefore it is less affected by distortions and other classical analogic errors found in CDS systems.

3. ZERO NOISE CCD CONCEPT

The device we presented here still has a readout noise (1.7 e^-), and therefore it is not a zero noise CCD. Nevertheless, when it is possible to have $0.2\text{--}0.3\text{ e}^-$ readout noise, it will be possible to remove the noise completely. Since the photons (and electrons) are discrete elements (2.5 photons is obviously nonsense), the signal produced by a single electron will be above 3 to 5σ , and it will then be possible to determine precisely the amount of electrons present on one pixel. This is equivalent to a digital non-linear filtering that will completely remove the remaining noise of the image. The goal is not so far off: there is only a factor 5 left to achieve. If we look at the progression of the CDS technique since it has been introduced 30 years ago, the gain was much more, having only a few years of background. There are various technical solutions to reach this level.

First it is possible to use a more recent CCD, which has a lower intrinsic noise. The CCD technique is still in evolution and now $1\text{--}2\text{ e}^-$ devices are foreseen or already proposed.

It is also possible to couple this filtering method with a non destructive readout CCD achieving already sub-electron noise readout [8] or multiple skipper outputs.

Finally, we have only explored one digital method to extract the useful signal from the CCD's output. More complex techniques will be investigated in the future, particularly statistical analysis, non linear filters and other digital methods usually used in other digital signal processing fields.

4. CONCLUSION

We presented a promising, completely new filtering technique to readout CCDs. This technique has real potential to be an improvement since it is extremely versatile and permits extremely complex digital processing. We expect to reach the 0.3 e^- readout noise level in the future, which would permit the complete removal of CCD readout noise. This will lead to outstanding capabilities of these kind of cameras in low light level conditions.

5. ACKNOWLEDGEMENTS

We would like to thank ESO for the support for this project by providing us a cryostat to build the prototype.

6. REFERENCES

- [1] Gach J.L., Darson D., Guillaume C., Goillandeau C., Boissin O., Boulesteix J., Cavadore C., 2001, ESO Workshop: Scientific Drivers for ESO Future VLT/VLTI Instrumentation, Garching bei München, Germany, June 11-15, 2001.
- [2] Gach J.L., Hernandez O., Boulesteix J., Amram P., Boissin O., Carignan C., Garrido O., Marcelin M., Östlin G., Plana H., Rampazzo R., 2002, *Fabry-Perot Observations Using a New GaAs Photon-counting System*, PASP, vol **114**, no 799, p. 1043.
- [3] Gach J.L., Darson D., Guillaume C., Goillandeau C., Boissin O., Boulesteix J., Cavadore C., 2002, Optro 2002 conference, Paris, January 14-16, 2002.
- [4] Fowler A.M., Gatley I., 1990, ApJ, **353**, L33.
- [5] Fowler A.M., Gatley I., 1991, SPIE, **1541**, p. 127.
- [6] Markelov S.V., Murzin V.A., Borisenko A.N., Ivaschenko N.G., Afanasieva I.V., Ardilanov V.I., 2000, *Astronomical and Astrophysical Transactions*, pp. 19, 579.
- [7] Hegyi D.J., Burrows A., 1980, AJ, **85**, p. 1421.
- [8] Janesick J.R., Elliott T., Dingizian A., Bredthauer R. A., Chandler C. E., 1990, SPIE, **1242**, p. 223.



FIRST RESULTS OF AN L3CCD IN PHOTON COUNTING MODE

Jean-Luc Gach¹, Christian Guillaume², Olivier Boissin¹, and Cyril Cavadore³
¹Observatoire de Marseille, ²Observatoire de Haute Provence, ³European Southern Observatory

Abstract: *We present the first results of an L3CCD used at very high gain to achieve efficient photon counting regime observations.*

Key words: photon counting, detectors

1. INTRODUCTION

Readout noise is a problem that affects CCDs at low light levels. Despite remarkably high quantum efficiency, up to 95 %, and very low noise, down to 2-3 e⁻, CCDs are largely insufficient for high resolution spectroscopy where observations are often detector noise limited. This problem is even more critical with multiplex instruments (*e.g.*, scanning instruments), where there are a large number of images produced. This problem has been largely discussed in Gach et al. 2002 [1]. The L3CCD technology reveals new ways to achieve high quantum efficiency photon counting detectors. This paper presents the first evaluation of an L3CCD in photon counting regime and scientific conditions. The system uses a CCD65 chip with embedded avalanche gain [2], cryogenically cooled in a cryostat at -90 °C, working at 11 MHz pixel rate.

2. PHOTON COUNTING ISSUES

In photon counting mode, when the signal is above a cut level for each pixel, we assume that the pixel has received one (and only one) photon. Therefore, for high fluxes, there is a possibility that on some pixels, several photons are only counted as one. To avoid this effect, the CCD is read out as fast as possible to keep the mean flux per pixel and per image sufficiently low. The accumulation process is then performed by a computer in real time [1]. Figure 1 shows the non-linearity of a photon counting device with respect to the illumination and the frame rate.

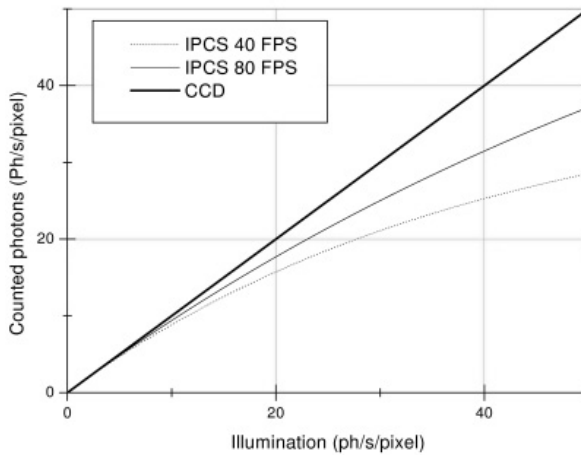


Figure 1. Linearity of a photon counting device.

With the L3CCD system it is also necessary to determine the cut level above which the output signal is considered as one photon. This depends on the readout noise of the CCD and its acquisition chain, and on the gain in the multiplication register of the L3CCD. The gain must be sufficiently high to avoid detecting false events that are a result of electronics noise. Our experience showed that 5σ is a minimum, and 10σ is preferable (where σ is the readout noise). Due to the statistical distribution of the multiplication process [3], there is a possibility, if the cut level is set too high, that the photon is missed leading to a direct QE loss. Figure 2 shows the computed Quantum Efficiency (QE) loss due to the uncertainty of the multiplication process with respect to the CCD gain and for various cut levels.

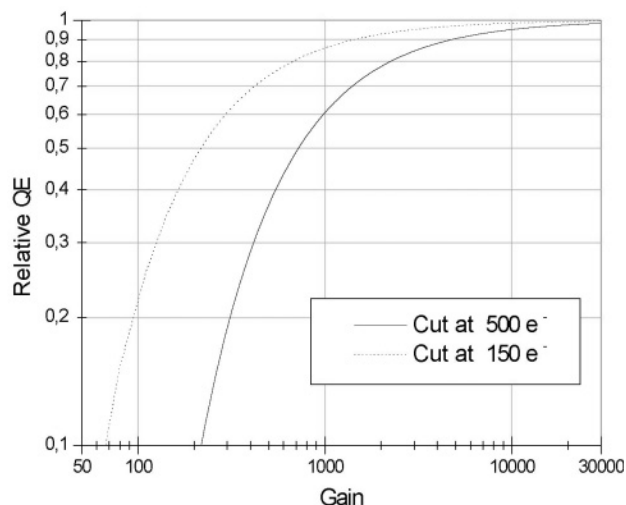


Figure 2. Relative QE vs gain and cut levels.

Therefore, to use the L3CCD in photon counting mode while maintaining a good QE, which is its principal advantage over Image Photon Counting Systems (IPCS) [4], it is necessary to use a very high gain. This gain increases when the electronic readout noise of the system is high.

3. RESULTS

Figure 3 shows an image of a standard target in photon counting mode captured with our system. Each white spot represents (at least as described before) one photon. The exposure time was 40 ms.

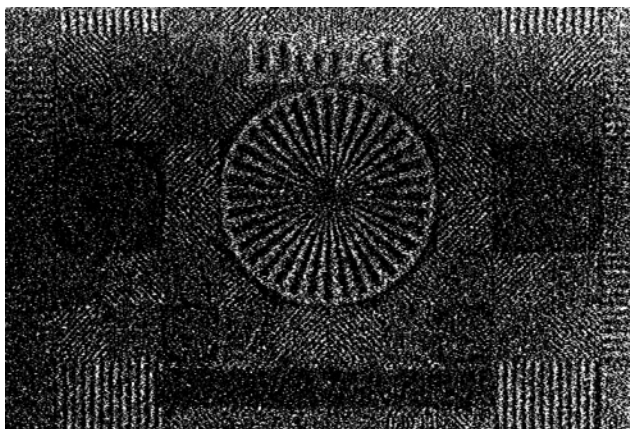


Figure 3. Photon counting regime image.

Measuring the dark current showed that, while it is decreasing for high temperatures, it reaches a minimum level for lower ones. This has been interpreted as a charge injection due to the multiplication process. This charge injection is strongly dependant on the amplification level, therefore it is necessary to maintain a low amplification value in order to keep the charge injection as low as possible. We observed this effect at a level as high as 1 photon/sec/pix, which makes this system uncompetitive for long exposures.

4. CONCLUSION

It has been shown that it is necessary to maintain a low amplification level of the L3CCD to avoid charge injection, however, this is opposed to the photon counting selection process, which requires high gain. It also opposes the readout speed necessary to maintain a good linearity that leads to noisy electronics and would therefore require a high gain.

For the moment, due to the charge injection, L3CCDs are not competitive when compared with IPCS and especially with GaAs IPCS [1]. The key issue now is to produce very low noise wideband amplifiers, down to 30 e^- with 20 MHz bandwidth, to reduce the amplification level by reducing the cut level to approximately 150 e^- . Clocking schemes that could reduce the charge injection will also be experimented with in the very near future.

5. REFERENCES

- [1] Gach J. L., Hernandez O., Boulesteix J., Amram P., Boissin O., Carignan C., Garrido O., Marcelin M., Ostlin G., Plana H., Rampazzo R., 2002, *Fabry-Perot Observations Using a New GaAs Photon-counting System*, PASP, vol **114**, no 799, p. 1043.
- [2] Jerram P., Pool P., Bell R., Burt D., Bowring S., Spencer S., Hazlewood M., Moody I., Catlett N., Heyes P., 2001, SPIE **4306**, p. 178.
- [3] Mackay C. D., Tubbs R. N., Bell R., Burt D. J., Jerram P., Moody I., 2001, SPIE **4306**, p. 289
- [4] Gach J-L., Hernandez O., Boulesteix J., Carignan C., 2002, *Fabry-Perot Observations using a new GaAs Photon-Counting System*, these proceedings, pg. 335

GLOSSARY OF ACRONYMS

We include this glossary to help the reader translate acronyms into English. The following list is a tribute to the ingenuity, or lack thereof, of inventors of acronyms in the detector community. Believe it or not, all 382 of these acronyms are used somewhere in these proceedings. This is the first, and perhaps the last, time we try this. We leave it to the “gentle” reader to judge the usefulness of the compilation.

3T	<i>3-Transistor</i>
AASC	<i>Astronomy and Astrophysics Survey Committee</i>
AAT	<i>Anglo-Australian Telescope</i>
AC	<i>Alternating Current</i>
ACS	<i>Advanced Camera for Surveys</i>
ACU	<i>Alignment and Compensation Unit</i>
ADC	<i>Analog-to-Digital Converter</i>
ADC	<i>Atmospheric Dispersion Corrector</i>
ADU	<i>Analog-to-Digital Unit</i>
AEOS	<i>Advanced Electro Optical System</i>
AF	<i>Astrometric Field</i>
AFRL	<i>Air Force Research Laboratory</i>
AG	<i>Autoguider</i>
AGN	<i>Active Galactic Nuclei</i>
AIMO	<i>Advanced Inverted Mode Operation</i>
AIP	<i>American Institute of Physics</i>
AO	<i>Adaptive Optics</i>
AOB	<i>Adaptive Optics Bonnet</i>
APD	<i>Avalanche Photodiode</i>
APS	<i>Active Pixel Sensor</i>
AQC	<i>Active Quenching Circuit</i>
AR	<i>Anti-Reflection</i>
ARC	<i>Ames Research Center (NASA)</i>
ASG	<i>Acquisition and Slow Guider</i>
ASIC	<i>Application Specific Integrated Circuit</i>
ASTEROID	<i>A System To Efficiently Read Optical/Infrared Detectors</i>
ATC	<i>Astronomy Technology Centre (Edinburgh)</i>
ATM	<i>Asynchronous Transfer Mode</i>
AURA	<i>Association of Universities for Research in Astronomy</i>
BAO	<i>Beijing Astronomical Observatory</i>
BBP	<i>Broad Band Photometry</i>
BI	<i>Back-Illuminated</i>
BIB	<i>Blocked Impurity Band</i>
BMBF	<i>Bundesministerium für Bildung und Forschung</i>
BNSC	<i>British National Space Centre</i>

BOX	<i>Buried Silicon Dioxide Layer</i>
bROS	<i>bench-mounted High Resolution Optical Spectrograph</i>
CAD	<i>Computer Assisted Design</i>
CARA	<i>California Association for Research in Astronomy</i>
CAS	<i>Chinese Academy of Sciences</i>
CCD	<i>Charge-Coupled Device</i>
CCE	<i>Charge Collection Efficiency</i>
CDS	<i>Correlated Double Sampling</i>
CELT	<i>California Extremely Large Telescope</i>
CFC	<i>Continuous Flow Cryostat</i>
CFHT	<i>Canada France Hawaii Telescope</i>
CID	<i>Charge Injection Device</i>
CMOS	<i>Complementary Metal Oxide Semiconductor</i>
CMOS-APS	<i>Complementary Metal Oxide Semiconductor-Active Pixel Sensor</i>
CNC	<i>Computer Numerically Controlled</i>
CNES	<i>Centre National d'Etudes Spatiales (France)</i>
CNR	<i>Consiglio Nazionale delle Ricerche (Italy)</i>
CNRS	<i>Centre National de la Recherche Scientifique (France)</i>
CONICA	<i>COudé Near-Infrared CAmera</i>
COO	<i>Caltech Optical Observatories</i>
CPAPIR	<i>Camera PANoramic Proche Infra-Rouge</i>
CRIRES	<i>CRyogenic, InfraRed Echelle Spectrometer</i>
CSP	<i>CCD Signal Processor</i>
CTE	<i>Charge Transfer Efficiency</i>
CTI	<i>Charge Transfer Inefficiency</i>
CTIA	<i>Capacitive Trans-Impedance Amplifier</i>
CTIO	<i>Cerro-Tololo Inter-American Observatory</i>
DC	<i>Direct Current</i>
DAC	<i>Digital-to-Analog Converter</i>
DCIXS	<i>Demonstrator Compact Imaging X-ray Spectrometer</i>
DEIMOS	<i>Deep Imaging Multi-Object Spectrograph</i>
DFG	<i>Deutsche Forschungsgemeinschaft</i>
DHE	<i>Detector Head Electronics</i>
DL	<i>Delay Line</i>
DLPH	<i>Double Layer Planar Heterostructure</i>
DLL	<i>Dynamic Link Library</i>
DLR	<i>Deutschen Zentrum für Luft und Raumfahrt</i>
DMA	<i>Direct Memory Access</i>
DN	<i>Digital Number</i>
DNL	<i>Differential Non-Linearity</i>
DOE	<i>Department Of Energy</i>
DQE	<i>Detected Quantum Efficiency</i>
DROID	<i>Distributed Readout Imaging Devices</i>
DSP	<i>Digital Signal Processor</i>
DTS	<i>Detector Test System</i>
DWG	<i>Italian Detector Working Group</i>
EEPROM	<i>Electrically Erasable Programmable Read Only Memory</i>
EEV	<i>English Electric Valve Company</i>

E2V	<i>E2V Technologies, Inc.</i>
e_h	<i>Electron-Hole</i>
ELM	<i>Edge Localized Modes</i>
ELT	<i>Extremely Large Telescope</i>
EMC	<i>Electromagnetic Compatibility</i>
EMI	<i>Electromagnetic Interference</i>
EMMI	<i>ESO Multi Mode Instrument</i>
EMIR	<i>Espectrógrafo Multiobjecto Infrarrojo (GTC)</i>
EO	<i>Earth Observation</i>
EPER	<i>Edge Pixel Extended Response</i>
EPIC	<i>European Photon Imaging Camera</i>
EPIC-MOS	<i>European Photon Imaging Camera – Multi-Object Spectrograph</i>
EPLD	<i>Erasable Programmable Logic Device</i>
ERO	<i>Early Release Observation</i>
ESA	<i>European Space Agency</i>
ESD	<i>Electrostatic Discharge</i>
ESI	<i>Echelle Spectrograph and Imager</i>
ESO	<i>European Southern Observatory</i>
ESTEC	<i>European Space Research and Technology Centre</i>
EUV	<i>Extreme UltraViolet</i>
FAME	<i>Full-sky Astrometric Mapping Explorer</i>
FBI	<i>Fully Buttable Imager</i>
FDSOI	<i>Fully Depleted Silicon On Insulator</i>
FET	<i>Field-Effect Transistor</i>
FGC	<i>Fast Guider Camera</i>
FIERA	<i>Fast Imager Electronic Readout Assembly</i>
FIFO	<i>First In First Out</i>
FINITO	<i>Fringe-tracking Instrument of NIce and TORino</i>
FITS	<i>Flexible Image Transport System</i>
FMOS	<i>Fiber Multi-Object Spectrograph</i>
FOC	<i>Faint Object Camera</i>
FOCAS	<i>Faint Object Camera And Spectrograph</i>
FORS2	<i>FOcal Reducer/low dispersion Spectrograph</i>
FOV	<i>Field of View</i>
FP	<i>Focal Plane</i>
FPA	<i>Focal Plane Array</i>
FPA	<i>Focal Plane Assembly</i>
FPGA	<i>Field Programmable Gate Array</i>
FPI	<i>Focal Plane Interface</i>
FPN	<i>Fixed Pattern Noise</i>
FSU	<i>Fringe Sensor Unit</i>
FTS	<i>Fourier Transform Spectrograph</i>
FWHM	<i>Full-Width Half-Maximum</i>
GDT	<i>Geometric Dimensioning and Tolerancing</i>
GEC	<i>Global Engineering Company</i>
GEST	<i>Galactic Exoplanet Survey Telescope</i>
GHASP	<i>Gassendi survey of Hα in SPiral galaxies</i>

GMOS	<i>Gemini Multi-Object Spectrograph</i>
GNIRS	<i>Gemini Near-Infrared Spectrograph</i>
GPS	<i>Global Positioning System</i>
g-r	<i>generation-recombination</i>
GRB	<i>Gamma Ray Burst</i>
GSAOI	<i>Gemini South Adaptive Optics Imager</i>
GSMT	<i>Giant Segmented Mirror Telescope</i>
GTC	<i>Gran Telescopio Canarias</i>
GUI	<i>Graphical User Interface</i>
HARPS	<i>High-Accuracy Radial Velocity Planetary Search</i>
HASYLAB	<i>Hamburger Synchrotronstrahlungslabor</i>
HAWAII	<i>HgCdTe Astronomy Wide Area Infrared Imager</i>
HIFI	<i>Heterodyne Instrument for the Far Infrared</i>
HRC	<i>High Resolution Camera</i>
HRI	<i>High Resolution Instrument</i>
HST	<i>Hubble Space Telescope</i>
IAC	<i>Instituto de Astrofísica de Canarias</i>
IBC	<i>Impurity Band Conduction</i>
IC	<i>Integrated Circuit</i>
ICD	<i>Interface Control Definition</i>
IfA	<i>Institute for Astronomy</i>
IFS	<i>Integral Field Spectroscopy</i>
II/LA	<i>Ion Implant/Laser Anneal</i>
IMM	<i>Istituto per la Microelettronica e Microsistemi</i>
IMS	<i>Ion Mobility Spectrometry</i>
INAF	<i>Istituto Nazionale di AstroFisica</i>
INAF-OATo	<i>Istituto Nazionale di AstroFisica – Osservatorio Astronomico di Torino</i>
ING	<i>Isaac Newton Group of Telescopes</i>
INSU	<i>Institut National des Sciences de l'Univers</i>
INSU-CNRS	<i>Institut National des Sciences de l'Univers-Centre National de la Recherche Scientifique</i>
I/O	<i>Input/Output</i>
IPCS	<i>Image Photon Counting System</i>
IR	<i>InfraRed</i>
IRAC	<i>InfraRed Array Camera</i>
IRACE	<i>InfraRed detector high speed Array Control Electronics</i>
IRAF	<i>Image Reduction and Analysis Facility</i>
IRAS	<i>InfraRed Astronomical Satellite</i>
IRC	<i>InfraRed Camera</i>
IRFPA	<i>InfraRed Focal Plane Array</i>
IRMOS	<i>InfraRed Multi-Object Spectrograph</i>
IRTF	<i>InfraRed Telescope Facility</i>
ISIS	<i>Intelligent Satellite data Information System</i>
I/SOI	<i>Imaging/Silicon-On-Insulator</i>
ISPI	<i>Infrared SidePort Imager</i>
ITL	<i>Imaging Technology Laboratory (University of Arizona)</i>
ITO	<i>Indium-Tin-Oxide</i>

I-V	<i>Current versus Voltage</i>
IWS	<i>Instrument Work Station</i>
JCMT	<i>James Clerk Maxwell Telescope</i>
JFET	<i>Junction Field Effect Transistor</i>
KBO	<i>Kuiper Belt Object</i>
KIRMOS	<i>Keck InfraRed Multi-Object Spectrograph</i>
KPNO	<i>Kitt Peak National Observatory</i>
L3CCD	<i>Low Light Level Charge Coupled Device</i>
LAOG	<i>Laboratoire d'Astrophysique de Grenoble</i>
LBC	<i>Large Binocular Camera</i>
LBF	<i>Low-level Background Facility</i>
LBNL	<i>Lawrence Berkeley National Laboratory</i>
LBT	<i>Large Binocular Telescope</i>
LCC	<i>Leadless Chip Carrier</i>
LCU	<i>Local Control Unit</i>
LDSS	<i>Low Dispersion Survey Spectrograph</i>
LE	<i>Lucky Exposure</i>
LED	<i>Light Emitting Diode</i>
LEGRI	<i>Low Energy Gamma Ray Imager</i>
LMSSC	<i>Lockheed Martin Space Systems Company</i>
LOWFS	<i>Low Order WaveFront Sensor</i>
LPE	<i>Liquid Phase Epitaxy</i>
LSB	<i>Linux Standard Base</i>
LSI	<i>Large-Scale Integration</i>
LSST	<i>Large Synoptic Survey Telescope</i>
LVDS	<i>Low-Voltage Differential-Sampling</i>
LWS	<i>Long Wavelength Spectrometer</i>
LRIS	<i>Low Resolution Imaging Spectrograph</i>
MAD	<i>Multi-conjugate Adaptive optics Demonstrator</i>
MAT	<i>Marconi Applied Technologies</i>
MBE	<i>Molecular Beam Epitaxy</i>
MCAO	<i>Multi-Conjugate Adaptive Optics</i>
MCP	<i>Micro Channel Plate</i>
MCT	<i>Mercury Cadmium Telluride</i>
MDM	<i>Micro-D Metal</i>
MEL	<i>MicroElectronics Laboratory (Lincoln Laboratory)</i>
mFPA	<i>mosaic Focal Plane Assembly</i>
MHD	<i>Magneto-HydroDynamic</i>
MIMD	<i>Multiple Instruction Multiple Data</i>
MIPS	<i>Multi-band Imaging Spectrometer</i>
MIR	<i>Mid-Infrared</i>
MIT	<i>Massachusetts Institute of Technology</i>
MIT-LL	<i>Massachusetts Institute of Technology – Lincoln Laboratory</i>
MOIRCS	<i>Multi-Object Infrared Camera and Spectrograph</i>
MOS	<i>Metal-Oxide-Semiconductor</i>
MOSFET	<i>Metal-Oxide-Semiconductor Field Effect Transistor</i>
MPP	<i>Multi-Pinned Phase</i>
MRI	<i>Medium Resolution Instrument</i>

MSPS	<i>Million Samples Per Second</i>
MTF	<i>Modulation Transfer Function</i>
MUSE	<i>Multi-Unit Spectroscopic Explorer</i>
MWIR	<i>Medium Wavelength InfraRed</i>
NAOC	<i>National Astronomical Observatory of China</i>
NAOS	<i>Nasmyth Adaptive Optics System</i>
NDRO	<i>Non-Destructive Readout</i>
NEO	<i>Near-Earth Objects</i>
NEWFIRM	<i>NOAO Extremely Wide-Field Infrared Imager</i>
NGST	<i>Next Generation Space Telescope</i>
NICMOS	<i>Near Infrared Camera and Multi-Object Spectrometer</i>
NIR	<i>Near-InfraRed</i>
NIRI	<i>Near-InfraRed Imager</i>
NIRMOS	<i>Near-InfraRed Multi-Object Spectrograph</i>
NIRSPEC	<i>Near-InfraRed Cryogenic Echelle Spectrograph</i>
NIST	<i>National Institute of Standards and Technology</i>
NMOS	<i>Negative Metal-Oxide-Semiconductor</i>
NOAO	<i>National Optical Astronomy Observatory</i>
NOVA	<i>Nederlandse Onderzoekschool voor Astronomie (The Netherlands Research School for Astronomy)</i>
NRE	<i>Non-Redundant Engineering</i>
NSF	<i>National Science Foundation</i>
NTD	<i>Neutron Transmutation Doped</i>
NTE	<i>Nuevas Tecnologías Espaciales</i>
NVO	<i>National Virtual Observatory</i>
OATo	<i>Osservatorio Astronomico di Torino</i>
OCIW	<i>Observatories of the Carnegie Institute of Washington</i>
ODI	<i>One Degree Imager (WIYN)</i>
ODT	<i>Optical Detector Team (ESO)</i>
OHP	<i>Observatoire de Haute Provence</i>
Omm	<i>Observatoire du mont Mégantic</i>
ONERA	<i>Office National d'Etudes et de Recherches Aéronautiques</i>
OPD	<i>Optical Path Difference</i>
OPTIC	<i>Orthogonal Parallel Transfer Imaging Camera</i>
OSIRIS	<i>Optical System for Imaging and low- Resolution Integrated Spectroscopy</i>
OTA	<i>Optical Telescope Assembly</i>
OTA	<i>Orthogonal Transfer Array</i>
OTCCD	<i>Orthogonal Transfer Charge-Coupled- Device</i>
OWL	<i>Overwhelmingly Large Telescope</i>
PACE	<i>Producibile Alternative to Cd(Zn)Te Epitaxy</i>
PAN	<i>Pixel Acquisition Node</i>
PanSTARRS	<i>Panoramic Survey Telescope and Rapid Response System</i>
PC-ICCD	<i>Photon Counting-Intensified CCD</i>
PEC	<i>Process Evaluation Control</i>
PCB	<i>Printed Circuit Board</i>
PCI	<i>Peripheral Component Interconnect</i>
PDR	<i>Preliminary Design Review</i>

PGA	<i>Pin Grid Array</i>
PI	<i>Principal Investigator</i>
PISCO	<i>Palomar Infrared Spectrograph with Cross- dispersed Optics</i>
PLD	<i>Programmable Logic Device</i>
PMAS	<i>Potsdam Multi-Aperture Spectrophotometer</i>
PMC	<i>PCI Mezzanine Card</i>
PMT	<i>PhotoMultiplier Tube</i>
PPS	<i>Polyphenylene Sulfide</i>
PRIMA	<i>Phase-Referenced Imaging and Micro- arcsecond Astrometry</i>
PRNU	<i>Photon Response Non-Uniformity</i>
PSF	<i>Point Spread Function</i>
P-V	<i>Phosphorus-Vacancy</i>
QDC	<i>Charge-to-Digital</i>
QE	<i>Quantum Efficiency</i>
QUOTA	<i>QUad Orthogonal Transfer Array</i>
RAI	<i>Random Access Integration</i>
RAL	<i>Rutherford Appleton Laboratory</i>
RBD	<i>Reliability Block Diagram</i>
R&D	<i>Research & Development</i>
RICL	<i>Reticle Image Composition Lithography</i>
RIO	<i>Raytheon Infrared Operations</i>
RMS	<i>Root Mean Square</i>
ROI	<i>Regions of Interest</i>
ROIC	<i>ReadOut Integrated Circuit</i>
RON	<i>Read Out Noise</i>
RPE	<i>Remote Photometer Electronics</i>
RQE	<i>Relative Quantum Efficiency</i>
RSC	<i>Rockwell Scientific Corporation</i>
RSD	<i>Relative Standard Deviation</i>
RT	<i>Real Time</i>
RTC	<i>Real Time Computer</i>
RTD	<i>Real Time Display</i>
RTOS	<i>Real-Time Operating System</i>
RTV	<i>Room Temperature Vulcanizing</i>
RTF	<i>Random Telegraph Signals</i>
RTOS	<i>Real Time Operating System</i>
SCA	<i>Sensor Chip Assemblies</i>
SBC	<i>Solar Blind Camera</i>
SBIG	<i>Santa Barbara Instrument Group</i>
SBRC	<i>Santa Barbara Research Center</i>
SCD	<i>Swept Charge Device</i>
SCP	<i>Supernova Cosmology Project</i>
SE	<i>Systems Engineering</i>
SECCHI	<i>Sun Earth Connection Coronal and Heliospheric Investigation</i>
SEU	<i>Single-Event-Upset</i>
SFD	<i>Single-stage Floating Diffusion</i>
SFD	<i>Source Follower per Detector</i>
SFS	<i>Segment Figure Sensor</i>

SHWFS	<i>Shack-Hartmann WaveFront Sensor</i>
SINFONI	<i>SINgle Far Object Near-Infrared Investigation</i>
SIRTF	<i>Space InfraRed Telescope Facility</i>
SITe	<i>Scientific Imaging Technologies</i>
SLCU	<i>SPARC Local Control Unit</i>
SM	<i>Servicing Mission</i>
SM	<i>Star Mapper</i>
SMEI	<i>Solar Mass Ejection Imager</i>
SMOV	<i>Servicing Mission Orbital Verification</i>
SNAP	<i>SuperNova/Acceleration Probe</i>
SOI	<i>Silicon-On-Insulator</i>
SPAD	<i>Single Photon Avalanche Diode</i>
SQUID	<i>Superconductive Quantum Interference Device</i>
SSOP	<i>Shrink Small Outline Package</i>
SSR	<i>Solid State Recorder</i>
SSTD	<i>Space Science and Technology Department</i>
SSTL	<i>Survey Satellite Technology Limited</i>
STEREO	<i>Solar TERrestrial RELations Observatory</i>
STIS	<i>Space Telescope Imaging Spectrograph</i>
STJ	<i>Superconducting Tunnel Junction</i>
STM	<i>ST Microelectronics</i>
STS-FGC	<i>Segment Tilt Sensor – Fast Guider Camera</i>
SURCIS	<i>SUB-one-metre Resolution Compact Imaging System</i>
SWIR	<i>Short-Wave InfraRed</i>
TASCA	<i>Tololo All Sky CAmera</i>
TDI	<i>Time Delay Integration</i>
TE	<i>Thermo-Electric</i>
TEC	<i>Thermo-Electric Cooler</i>
TEC	<i>Transition Edge Sensors</i>
TIM	<i>Time Interface Module</i>
TMS	<i>Texas Instruments</i>
TNG	<i>Telescopio Nazionale Galileo</i>
TRIDENT	<i>TRIple Imager for Detecting Earth Near T-dwarfs</i>
TSIP	<i>Telescope System Instrumentation Program</i>
TTL	<i>Transistor-Transistor Link</i>
TUFPAC	<i>Tohoku University Focal Plane Array Controller</i>
UA	<i>University of Arizona</i>
UH	<i>University of Hawaii</i>
UIST	<i>UKIRT Imager Spectrometer</i>
UKATC	<i>United Kingdom Astronomy Technology Centre</i>
UKIRT	<i>United Kingdom InfraRed Telescope</i>
UV	<i>UltraViolet</i>
UVB	<i>UltraViolet B</i>
VCS	<i>VLT Control Software</i>
VHDL	<i>Very High Speed Integrated Circuit (VHSIC) Hardware Description Language</i>
VHSIC	<i>Very High Speed Integrated Circuit</i>
VINCI	<i>VLT INTERferometer Commissioning Instrument</i>

VISTA	<i>Visible and Infrared Survey Telescope for Astronomy</i>
VLF	<i>Very Large Format</i>
VLSI	<i>Very Large Silicon System I</i>
VLТ	<i>Very Large Telescope</i>
VLTI	<i>Very Large Telescope Interferometer</i>
VME	<i>Virtual Machine Environment</i>
VME-CPU	<i>Virtual Machine Environment-Central Processing Unit</i>
VST	<i>VLТ Survey Telescope</i>
WFC	<i>Wide Field Camera</i>
WFCAM	<i>Wide Field Camera</i>
WFPC	<i>Wide Field Planetary Camera</i>
WFPC2	<i>Wide Field Planetary Camera-2</i>
WFS	<i>WaveFront Sensor</i>
WIRC	<i>Widefield InfraRed Camera</i>
WIYN	<i>Universisty of Wisconsin, Indiana University, Yale University and NOAO (telescope)</i>
XEUS	<i>X-ray Evolving Universe Spectroscopy</i>
ZIF	<i>Zero-Insertion-Force</i>

The Nerd Boat



*A group of nerds on a boat. We think they look pretty good!
Stay tuned.....Paola & Jim*

Astrophysics and Space Science Library

Volume 299: ***Open Issues in Local Star Formation***, edited by Jacques Lépine, Jane Gregorio-Hetem
Hardbound, ISBN 1-4020-1755-3, December 2003

Volume 298: ***Stellar Astrophysics - A Tribute to Helmut A. Abt***, edited by K.S. Cheng, Kam Ching Leung, T.P. Li
Hardbound, ISBN 1-4020-1683-2, November 2003

Volume 297: ***Radiation Hazard in Space***, by Leonty I. Miroshnichenko
Hardbound, ISBN 1-4020-1538-0, September 2003

Volume 296: ***Organizations and Strategies in Astronomy, volume 4***, edited by André Heck
Hardbound, ISBN 1-4020-1526-7, October 2003

Volume 295: ***Integrable Problems of Celestial Mechanics in Spaces of Constant Curvature***, by T.G. Vozmischeva
Hardbound, ISBN 1-4020-1521-6, October 2003

Volume 294: ***An Introduction to Plasma Astrophysics and Magnetohydrodynamics***, by Marcel Goossens
Hardbound, ISBN 1-4020-1429-5, August 2003
Paperback, ISBN 1-4020-1433-3, August 2003

Volume 293: ***Physics of the Solar System***, by Bruno Bertotti, Paolo Farinella, David Vokrouhlický
Hardbound, ISBN 1-4020-1428-7, August 2003
Paperback, ISBN 1-4020-1509-7, August 2003

Volume 292: ***Whatever Shines Should Be Observed***, by Susan M.P. McKenna-Lawlor
Hardbound, ISBN 1-4020-1424-4, September 2003

Volume 291: ***Dynamical Systems and Cosmology***, by Alan Coley
Hardbound, ISBN 1-4020-1403-1, November 2003

Volume 290: ***Astronomy Communication***, edited by André Heck, Claus Madsen
Hardbound, ISBN 1-4020-1345-0, July 2003

Volume 287/8/9: ***The Future of Small Telescopes in the New Millennium***, edited by Terry D. Oswalt
Hardbound Set only of 3 volumes, ISBN 1-4020-0951-8, July 2003

Volume 286: ***Searching the Heavens and the Earth: The History of Jesuit Observatories***, by Agustín Udías
Hardbound, ISBN 1-4020-1189-X, October 2003

Volume 285: ***Information Handling in Astronomy - Historical Vistas***, edited by André Heck
Hardbound, ISBN 1-4020-1178-4, March 2003

Volume 284: ***Light Pollution: The Global View***, edited by Hugo E. Schwarz
Hardbound, ISBN 1-4020-1174-1, April 2003

Volume 283: ***Mass-Losing Pulsating Stars and Their Circumstellar Matter***, edited by Y. Nakada, M. Honma, M. Seki
Hardbound, ISBN 1-4020-1162-8, March 2003

Volume 282: ***Radio Recombination Lines***, by M.A. Gordon, R.L. Sorochenko
Hardbound, ISBN 1-4020-1016-8, November 2002

Volume 281: ***The IGM/Galaxy Connection***, edited by Jessica L. Rosenberg, Mary E. Putman
Hardbound, ISBN 1-4020-1289-6, April 2003

Volume 280: ***Organizations and Strategies in Astronomy III***, edited by André Heck
Hardbound, ISBN 1-4020-0812-0, September 2002

Volume 279: ***Plasma Astrophysics, Second Edition***, by Arnold O. Benz
Hardbound, ISBN 1-4020-0695-0, July 2002

Volume 278: ***Exploring the Secrets of the Aurora***, by Syun-Ichi Akasofu
Hardbound, ISBN 1-4020-0685-3, August 2002

Volume 277: ***The Sun and Space Weather***, by Arnold Hanslmeier
Hardbound, ISBN 1-4020-0684-5, July 2002

Volume 276: ***Modern Theoretical and Observational Cosmology***, edited by Manolis Plionis, Spiros Cotsakis
Hardbound, ISBN 1-4020-0808-2, September 2002

Volume 275: ***History of Oriental Astronomy***, edited by S.M. Razaullah Ansari
Hardbound, ISBN 1-4020-0657-8, December 2002

Volume 274: ***New Quests in Stellar Astrophysics: The Link Between Stars and Cosmology***, edited by Miguel Chávez, Alessandro Bressan, Alberto Buzzoni, Divakara Mayya

Hardbound, ISBN 1-4020-0644-6, June 2002

Volume 273: ***Lunar Gravimetry***, by Rune Floberghagen
Hardbound, ISBN 1-4020-0544-X, May 2002

Volume 272: ***Merging Processes in Galaxy Clusters***, edited by L. Feretti, I.M. Gioia, G. Giovannini
Hardbound, ISBN 1-4020-0531-8, May 2002

Volume 271: ***Astronomy-inspired Atomic and Molecular Physics***, by A.R.P. Rau
Hardbound, ISBN 1-4020-0467-2, March 2002

Volume 270: ***Dayside and Polar Cap Aurora***, by Per Even Sandholt, Herbert C. Carlson, Alv Egeland
Hardbound, ISBN 1-4020-0447-8, July 2002

Volume 269: ***Mechanics of Turbulence of Multicomponent Gases***, by Mikhail Ya. Marov, Aleksander V. Kolesnichenko
Hardbound, ISBN 1-4020-0103-7, December 2001

Volume 268: ***Multielement System Design in Astronomy and Radio Science***, by Lazarus E. Kopilovich, Leonid G. Sodin
Hardbound, ISBN 1-4020-0069-3, November 2001

Volume 267: ***The Nature of Unidentified Galactic High-Energy Gamma-Ray Sources***, edited by Alberto Carramiñana, Olaf Reimer, David J. Thompson
Hardbound, ISBN 1-4020-0010-3, October 2001

Volume 266: ***Organizations and Strategies in Astronomy II***, edited by André Heck
Hardbound, ISBN 0-7923-7172-0, October 2001

Volume 265: ***Post-AGB Objects as a Phase of Stellar Evolution***, edited by R. Szczerba, S.K. Górný
Hardbound, ISBN 0-7923-7145-3, July 2001

Volume 264: ***The Influence of Binaries on Stellar Population Studies***, edited by Dany Vanbeveren
Hardbound, ISBN 0-7923-7104-6, July 2001

Volume 262: ***Whistler Phenomena - Short Impulse Propagation***, by Csaba Ferencz, Orsolya E. Ferencz, Dániel Hamar, János Lichtenberger
Hardbound, ISBN 0-7923-6995-5, June 2001

Volume 261: ***Collisional Processes in the Solar System***, edited by Mikhail Ya. Marov, Hans Rickman
Hardbound, ISBN 0-7923-6946-7, May 2001

Volume 260: ***Solar Cosmic Rays***, by Leonty I. Miroshnichenko
Hardbound, ISBN 0-7923-6928-9, May 2001

Volume 259: ***The Dynamic Sun***, edited by Arnold Hanslmeier, Mauro Messerotti, Astrid Veronig
Hardbound, ISBN 0-7923-6915-7, May 2001

Volume 258: ***Electrohydrodynamics in Dusty and Dirty Plasmas- Gravito-Electrodynamics and EHD***, by Hiroshi Kikuchi
Hardbound, ISBN 0-7923-6822-3, June 2001

Volume 257: ***Stellar Pulsation - Nonlinear Studies***, edited by Mine Takeuti, Dimitar D. Sasselov
Hardbound, ISBN 0-7923-6818-5, March 2001

Volume 256: ***Organizations and Strategies in Astronomy***, edited by André Heck
Hardbound, ISBN 0-7923-6671-9, November 2000

Volume 255: ***The Evolution of the Milky Way- Stars versus Clusters***, edited by Francesca Matteucci, Franco Giovannelli
Hardbound, ISBN 0-7923-6679-4, January 2001

Missing volume numbers have not yet been published.

For further information about this book series we refer you to the following web site:
<http://www.wkap.nl/prod/s/ASSL>

To contact the Publishing Editor for new book proposals:
Dr. Harry (J.J.) Blom: harry.blom@wkap.nl